Smart Sensors, Measurement and Instrumentation 19

Asaf Grosz
Michael J. Haji-Sheikh
Subhas C. Mukhopadhyay *Editors*

High Sensitivity Magnetometers

Springer

Smart Sensors, Measurement and Instrumentation

Volume 19

Series editor

Subhas Chandra Mukhopadhyay
School of Engineering and Advanced Technology (SEAT)
Massey University (Manawatu)
Palmerston North
New Zealand
e-mail: S.C.Mukhopadhyay@massey.ac.nz

More information about this series at http://www.springer.com/series/10617

Asaf Grosz · Michael J. Haji-Sheikh
Subhas C. Mukhopadhyay
Editors

High Sensitivity Magnetometers

Springer

Editors
Asaf Grosz
Ben-Gurion University of the Negev
Beer-Sheva
Israel

Subhas C. Mukhopadhyay
Massey University (Manawatu)
Palmerston North
New Zealand

Michael J. Haji-Sheikh
Northern Illinois University
DeKalb, IL
USA

ISSN 2194-8402 ISSN 2194-8410 (electronic)
Smart Sensors, Measurement and Instrumentation
ISBN 978-3-319-34068-5 ISBN 978-3-319-34070-8 (eBook)
DOI 10.1007/978-3-319-34070-8

Library of Congress Control Number: 2016942777

Printed on acid-free paper

This Springer imprint is published by Springer Nature
The registered company is Springer International Publishing AG Switzerland

Contents

Abstract

One approach to the development of magnetometers is the pursuit of an ideal device that meets the demands and limitations of all the possible applications. Such an ideal device must have ultra-high resolution, ultra-low power consumption, a wide dynamic range and bandwidth, as well as being ultra-miniature, inexpensive, operable over a wide range of temperatures and more, which, all together, does not seem realistic.

Since this silver bullet is currently unachievable, researchers are seeking optimal, rather than ideal, magnetometers. An optimal magnetometer is that which best fits a set of requirements dictated by a specific application. However, the large number of applications employing magnetic sensors leads to a great variety of requirements and, naturally, also to a large number of "optimal magnetometers".

The aim of this book is to assist the readers in their search for their optimal magnetometer. The book gathers, for the first time, an overview of nearly all of the magnetic sensors that exist today. This broad overview exposes the readers, relatively quickly, to a wide variety of sensors. The book offers the readers thorough and comprehensive knowledge, from basics to the state-of-the-art, and is therefore suitable for both beginners and experts.

From the more common and popular AMR magnetometers and up to the recently developed NV center magnetometers, each chapter describes a specific type of sensor and provides all the information that is necessary to understand the magnetometer behavior, including theoretical background, noise model, materials, electronics, design and fabrication techniques.

We invite students, researchers and engineers to learn more about the fascinating world of magnetic sensing.

Induction Coil Magnetometers

Kunihisa Tashiro

Abstract This chapter describes induction magnetometers with air-core coils for weak magnetic fields detection. In order to explain the historical background, the introduction provides the useful references through the author's experiences. Two detection models, the voltage and current detection model, can help to understand of the operational principle. Because the key components are the coils and electronics, practically useful design tips are summarized. Some experimental demonstration results with well-designed induction magnetometers are also mentioned.

1 Introduction

Because the study of induction magnetometers has long history in many research fields, this magnetometers are also given several names as induction sensors (ISs), induction magnetic field transducers (ITs), search coil magnetometers (SCMs), magnetic antenna, coil sensors, and pickup coils. They have been used many years to measure micropulsations of the Earth's magnetic field in ground-based stations [1], to study of magnetic field variations in space plasmas [2], and to several scientific spacecraft missions [3]. Although fluxgate is well adapted for weak magnetic field from dc to a few Hz, while induction magnetometers extend the frequency band measurement from few 100 MHz to few kHz [4]. A very important advantage of induction magnetometers is that they are completely passive sensors: they do not require any internal energy source to convert magnetic field into electrical signal. The only power consumption associated with a search coil is that needed for signal processing [5]. Induction magnetometers are one of the oldest and most well-known types of magnetic sensors, and they can cover numerous applications. Several good review papers [6–8] and handbooks [9–11] published in the 21st century may help to follow them. Although there are a lot of magnetic sensors

K. Tashiro (✉)
Spin Device Technology Center (SDTC), Shinshu University, Wakasato 4-17-1, Nagano, Japan
e-mail: tashiro@shinshu-u.ac.jp

A. Grosz et al. (eds.), *High Sensitivity Magnetometers*, Smart Sensors, Measurement and Instrumentation 19, DOI 10.1007/978-3-319-34070-8_1

are proposed, the study of induction magnetometer is still attractive to this author. One of the reason is that the technical details are still difficult to answer, clearly. The motivation of this chapter is to provide author's experiences and tips related to study the induction magnetometer.

The "first contact" of this author to the induction magnetometers was related to the biomagnetic measurements. Although SQUID sensors are common tool in this measurements at present, they did not exist when the evidence for the existence of magnetic fields from human heart [12] and brain [13] were presented. For the both magnetocardiography (MCG) and magnetoencephalograpy (MEG) measurements, the signals were measured with induction magnetometers whose operational principle was voltage detection mode. Because of the operational principle based on Faraday's induction law, the pickup coil has a magnetic (ferrite) core and large the number of windings as one-million or two-million. Although the use of a magnetic core makes the sensitivity high, the estimation of effective permeability is one of the difficult problem [14]. Because theoretical estimation of demagnetization factor only exists for an ellipsoidal body which is placed in a uniform magnetic field. This chapter does not focuses on the design of the magnetic cores. In order to weak, low-frequency magnetic field, reduction of environmental magnetic fields is necessary. The design and construction of magnetic shielded room [15] were very important for the success of the first MEG measurements. In other words, the necessity of the magnetic shielded room is a barrier to install the MEG system for local hospitals. In case of the first MCG measurements, the environmental noise was suppressed by the use of the signal conditioning circuit and gradiometer, two pickup coil connected in anti-parallel direction. In fact, the author also confirmed that the possibility to detect the MCG signal outside the magnetic shielded room [16]. It should be noted that the electrical interferences should be reduced by choosing suitable grounding points and simple electrical shielding enclosure, Faraday cage.

The motivation to start studying the induction magnetometers was not for the MCG measurements; it was the demands for a magnetic shield evaluation. Compared with the geomagnetic field (dc field), the amplitude of environmental magnetic fields at 50/60 Hz in our living environmental is low. And the performance in dc fields is usually limited by the internal magnetic field produced by own magnetic layers, so that the fluxgate is enough to the evaluation in dc performance [17]. When the magnetic shield to be evaluated is placed with a sufficient distance from electrical devices or power lines, the amplitude of environmental magnetic field at 50/60 Hz were usually less than 0.1 μT. The magnetic shielding factor is usually defined by the ratio of external to internal field strength. If the evaluation of magnetic shielding factor is larger than 100,000, the corresponding magnetic field inside the magnetic shield is less than 1 pT. Although SQUID sensors can be used for this evaluation, the interferences of urban RF noises should be reduced because they disturbs the measurement results [18]. Compared with a commercially available fluxgate, the advantages of induction magnetometers are very attractive [19].

Although SQUID sensors have several advantages in the sensitivity and spatial resolution, the maintenance of liquid nitrogen or helium is indispensable. For a young researcher, who used SQUID sensors as a tool, this demerit made troubles and disappointment. The most impressive paper for this author was written by R.J. Prance in 2003 [20]. The title is "Compact room-temperature induction magnetometer with superconducting quantum interference device level field sensitivity". This induction magnetometer was the current detection model which is based on the definition of self-inductance. To the best of author's knowledge, the first paper related to the current detection model was proposed by M.A. Macintyre in 1980 [21]. In this optimization, the estimation of the coil inductance is very important [22]. This kind of induction magnetometers were not only used for MCG measurements [23], but also to measure magnetic fields produced by nerve action currents of a 2 kg lobster [24]. Because the pickup coil does not require to keep inside liquid nitrogen or helium, they can approach to the object as possible. In the current detection model, the magnetic flux linkage of the coil is converted to the induced voltage with a transimpedance amp, or current-to-voltage converter. Because the induced current can be used to produce a well-controlled magnetic field, it could be combined with a SQUID device. Some practical applications were proposed as a clip-on SQUID current probe [25], SQUID magnetometer with a room-temperature pickup coil for impedance magnetocardiography [26] and superconducting induction magnetometer [27].

This chapter focuses on the current detection model. In the section two, induction magnetometers are categorized into two detection models. The equivalent circuits for both models are explained through Faraday's law, definition of inductance, and Ohm's law. In the section three, the coil design is explained. The main point is the estimation of self-inductance for several shapes of coils. Although the theoretical estimation of self-inductance for any shapes of coils does not exist, good approximations are useful in practical use. In the section four, some tips of the electronics design are provided. In general, a high-sensitive magnetometer is not only sensitive to magnetic field, but also to electrical interferences. The suppression of the interferences, a stable grounding point for the electronics should be provided. In the section five, experimental demonstration results with well-designed induction magnetometers are mentioned.

2 Operational Principle

Although the fundamental explanation through the two equivalent circuits was presented in previous paper [28], this section describes more simple explanation with modified figures. First of all, the induction magnetometers are categorized into two models. The theoretically backgrounds for both models are mentioned with several equations. Finally, advantages of the current detection model are explained with an example of both the calculated and measured results.

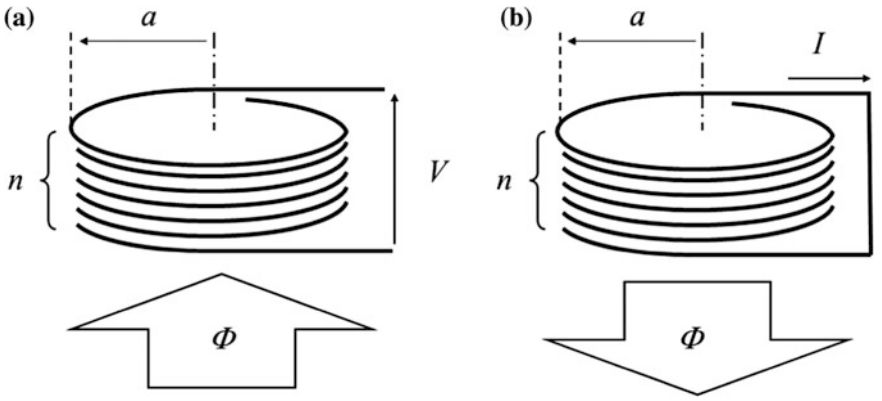

Fig. 1 **a** Faraday's induction law and **b** definition of inductance for the explanation of voltage and current detection models

2.1 Two Detection Models

The basis of induction magnetometer can be explained by two detection models, voltage detection model and current detection model. Figure 1 shows Faraday's induction law and definition of inductance for explanation of both models.

Figure 1a shows the model based on Faraday's law for the explanation of voltage detection model. When a homogeneous magnetic field, $\mu_0 H$ [T], at frequency, f [Hz], is crossed with a coil having mean radius, a [m], the induced voltage, V [V], is expressed by the following equations:

$$V = -\frac{d\Phi}{dt} \tag{1}$$

$$V = -j\omega n S \mu_0 H = -j2\pi^2 f n a^2 \mu_0 H \tag{2}$$

where j is an imaginary number and n is the number of coil windings. It means that the both waveform of the magnetic field and induced voltage has phase difference in 90°. If an ideal integrator integrates the induced voltage, the output voltage waveform corresponds to the objective magnetic field.

Figure 1b shows a model based on the definition of inductance for the explanation of current detection model. The relationship between the current, I [A], and flux linkage, Φ [Wb], is expressed by the following equations:

$$\Phi = LI \tag{3}$$

$$I = \frac{nS\mu_0 H}{L} = \frac{\pi n a^2 \mu_0 H}{L} \tag{4}$$

where L [H] is the inductance of the coil. If an ideal current-to-voltage converter, or transimpedance amplifier, converts the induced current, the output waveform corresponds to the objective magnetic field. In practical use, it should be considered a finite resistance in the coil, R [Ω], and input resistance in the instrumentation, R_{in} [Ω]. Because the equivalent circuits of both detection types are regarded as a simple RL circuit, cutoff frequencies f_{c} can be defined.

$$f_c = \frac{R + R_{\mathrm{in}}}{2\pi L} \tag{5}$$

Although the coil resistance of an ideal superconducting coil is zero, connecting wire between the coil and instrumentation may cause as coil resistance. SQUID sensors does not have the connecting wire between the coil and instrumentation. From the view point of an engineer related to induction magnetometer, this kind of sensor is based on current detection model. The pickup coil in SQUID sensor not only convert to the objective magnetic field to induced current, but also passes magnetic flux to the superconducting interference device, SQUID. SQUID with a flux closed loop, FLL, is the instrument which can convert a magnetic flux to output voltage.

2.2 Voltage Detection Model

Figure 2a shows the voltage detection model. Based on Thevenin's theorem, the pickup coil can be replaced with parameters of R, L, and V. Figure 2b shows the equivalent circuit model. From the Kirchhoff's voltage law (KVL), the current I can be expressed by the following equations:

$$V = L\frac{dI}{dt} + (R + R_{\mathrm{in}})I \tag{6}$$

$$I = \frac{V}{R + R_{\mathrm{in}}} \frac{1}{1 + j\left(\frac{2\pi Lf}{R + R_{\mathrm{in}}}\right)} = \frac{V}{R + R_{\mathrm{in}}} \frac{1}{1 + j\left(\frac{f}{f_{\mathrm{c}}}\right)} \tag{7}$$

Because the output current is as same as the induced current, the output voltage, V_{out} [V], is expressed by:

$$V_{\mathrm{out}} = R_{\mathrm{in}} I_{\mathrm{out}} = R_{\mathrm{in}} I = \frac{R_{\mathrm{in}}}{R + R_{\mathrm{in}}} \frac{1}{1 + j\left(\frac{f}{f_{\mathrm{c}}}\right)} \times V \tag{8}$$

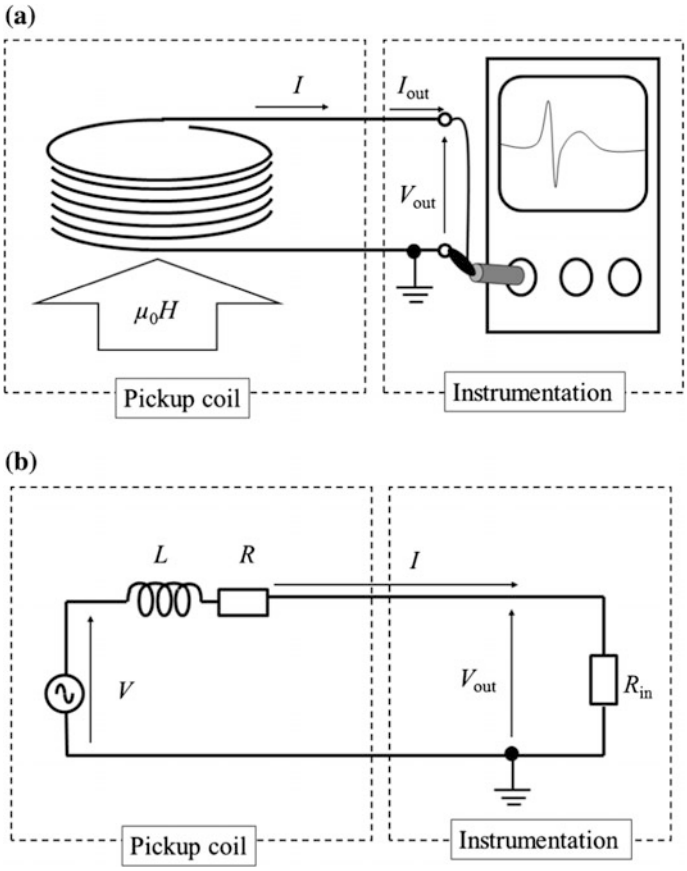

Fig. 2 Voltage detection model. **a** Model. **b** Equivalent circuit

The frequency response of the output voltage can be considered by two frequency regions where the resistance or the inductance is dominant. If the frequency of the objective field is low as $f \ll f_c$:

$$V_{out} = \frac{R_{in}}{R + R_{in}} \times V = -j \frac{R_{in}}{R + R_{in}} \times 2\pi^2 na^2 \times f \times \mu_0 H \tag{9}$$

and if the frequency of the objective field is high as $f \gg f_c$:

$$V_{out} = -j \frac{R_{in}}{R + R_{in}} \frac{f_c}{f} \times V = -\frac{R_{in}}{L} \times \pi na^2 \times \mu_0 H \tag{10}$$

At the low frequency region, it is same to Faraday's induction law when the R_{in} is very large as $R_{in} \gg R$. The output voltage is proportional to the frequency. At the high frequency region, it is same to the definition of inductance. The output voltage is proportional to the magnetic field, and does not depend on the frequency. It may cause a misunderstanding because the output voltage is also proportional to the input resistance as amplifier gain. If the input resistance is infinity, the cutoff frequency is also infinity so that the output voltage is expressed by the Faraday's induction law. If the input resistance has a finite value, the cutoff frequency has also finite value. It means that the output voltage should be considered with both Faraday's induction law and definition of inductance. Although the resistance of an ideal integrator is infinity, the value is limited to a finite value in practical. When the detection of relatively high frequency field as MHz frequency range, the input resistance of the instrumentation, a spectrum analyzer or network analyzer, is usually 50 or 75 Ω to prevent the reflection phenomenon.

2.3 Current Detection Model

Figure 3a shows the current detection model with a transimpedance amplifier. Because the plus pin of the OPamp is connected to the ground, the input resistance is zero in ideal case, $R_{in} = 0$, and the pickup coil is in a virtual short. Figure 3b shows the equivalent circuit. The induced current is expressed by:

$$I = \frac{V}{R}\frac{1}{1+j\left(\frac{2\pi Lf}{R}\right)} = \frac{V}{R}\frac{1}{1+j\left(\frac{f}{f_c}\right)} \tag{11}$$

Although the oscilloscope, or other analyzer for measuring the output voltage, has a finite input resistance, R_{in}', the OPamp controls the output voltage, V_{out} [V], as follows:

$$V_{out} = -IR_f = -\frac{R_f}{R}\frac{1}{1+j\left(\frac{f}{f_c}\right)}V \tag{12}$$

The frequency response of the output voltage can be also considered by two frequency regions where the resistance or the inductance is dominant. If the frequency of the objective field is low as $f \ll f_c$:

$$V_{out} = -\frac{R_f}{R}V = -j\frac{R_f}{R} \times 2\pi^2 na^2 \times f \times \mu_0 H \tag{13}$$

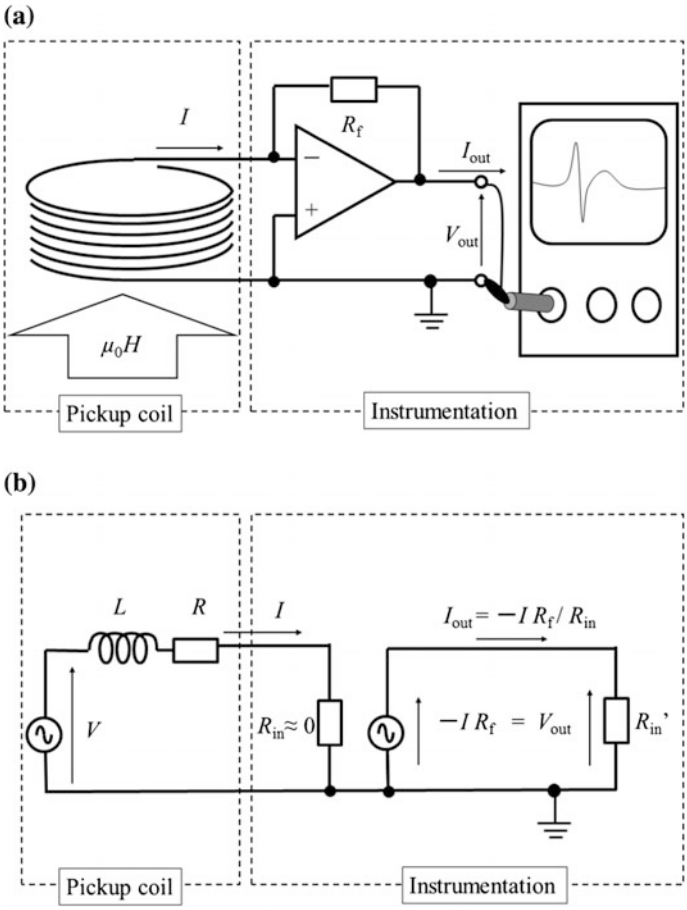

Fig. 3 Current detection model. **a** Model. **b** Equivalent circuit

and if the frequency of the objective field is high as $f \gg f_c$:

$$V_{out} = -j\frac{R_f f_c}{R f} V = -\frac{R_f}{L} \times \pi n a^2 \times \mu_0 H \tag{14}$$

At the low frequency region, the output voltage is (R_f/R) times than that of the voltage detection model. Although an increase in n makes the output voltage large in the voltage detection model, the value of R becomes large. Because Johnson noise is proportional to $R^{1/2}$, the noise floor level of the magnetometer becomes worse. Although a low-noise voltage amplifier could be used for the voltage detection model, the gain of a commercially available amplifier is usually limited to

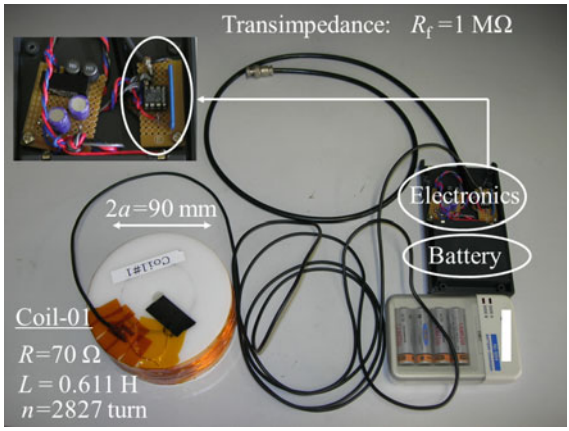

Fig. 4 An induction magnetometer with an air-core pickup coil. The operational principle is the current detection model [19]

1000, or 60 dB. In contrast, the value of R_f can be achieved larger than 100,000, or 100 dB, with a commercially available OPamp.

2.4 Comparison of Frequency Response

From the simple equivalent models, both detection models have similar manner related to frequency response; the output voltage is proportional to the frequency in low frequency region and does not depend on the frequency in high frequency region. Compared with both models, the ideal values of R_{in} are different; $R_{in} \to \infty$ for voltage detection model and $R_{in} \to 0$ for current detection model. Figure 4 shows an induction magnetometer with an air-core pickup coil, whose design was based on the current detection model [19]. The frequency responses are categorized into three regions;

I. Low frequency in voltage detection model ($f < f_c$): Eq. (9),
II. Low frequency in current detection model ($f < f_c$): Eq. (13),
III. High frequency in both detections model ($f > f_c$): Eqs. (10) and (14).

At the region III, the sensitivity is same because the typical values of both R_{in} in the input resistance of an instrument for voltage detection model and R_f in the transimpedance for current detection model are 1 MΩ. Figure 5 shows the frequency responses of the induction magnetometer with the coil (a). Plots represent the experimental results, and lines represent the theoretical estimation results. It does not only explain the validity of the theoretical estimations, but also the advantages of the current detection model. This magnetometer exhibit the linear response from 18 Hz to 10 kHz without an integrator. If the linear and wide response is required, a frequency compensation circuit is useful which described in

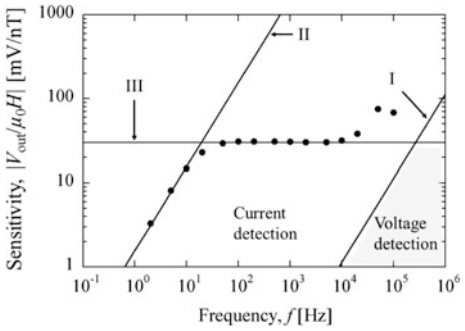

Fig. 5 Comparison of frequency response on the sensitivity between the voltage and current detection model. The pickup coil is Coil-01. [28] (a = 45 mm, n = 2827, R = 70 Ω, L = 0.611 H, $R_f = R_{in}$ = 1 MΩ)

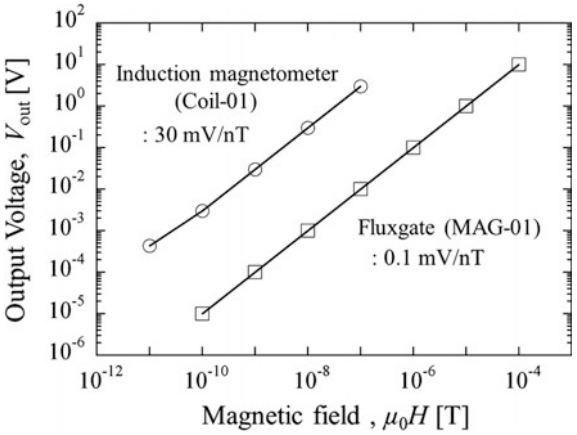

Fig. 6 Linearity of the induction magnetometer (Coil-01) compared with a fluxgate magnetometer. The evaluation frequency is 100 Hz [19]

Sect. 3. It seems that a resonance phenomenon is found in the range between 10 and 100 kHz. It was caused by the stray capacitance of the cable which is connected between the coil and electronics. In order to obtain the linear and flat response, stray capacitances should be small. In contrast, if the frequency of objective field is already defined, the use of resonance phenomenon, which should be categorized as third detection model, is the best way.

2.5 Remarks

To give the straightforward understandings for induction magnetometers, some remarks are mentioned with some experimental and theoretical estimation results. The first remark is that the induction magnetometer based on current detection model has an advantage in the sensitivity compared with a fluxgate. Figure 6 shows an example of the measured linearity compared with a fluxgate (MAG-03,

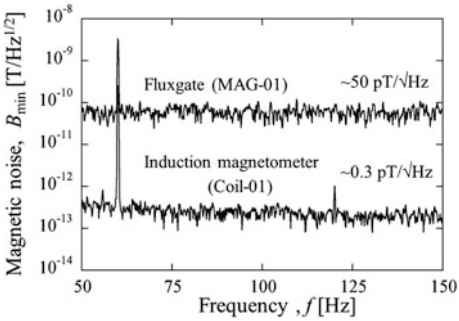

Fig. 7 Noise floor level measured inside a magnetic shield [19]

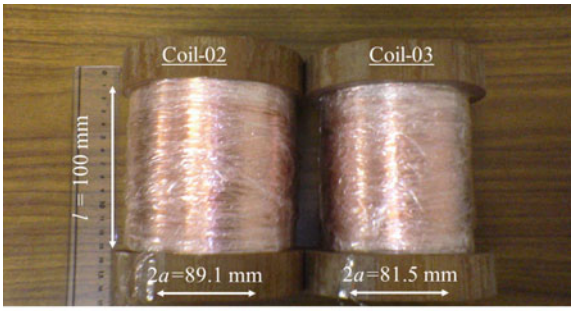

Fig. 8 Two pickup coils for induction magnetometers based on current detection model [29]

Bartington). The induction magnetometer had a linear sensitivity as 30 mV/nT, and it was in good agreement with the theoretical estimation. Compared with the fluxgate, the sensitivity is 300 times. Although it could gain combined with an instrumentational amplifier as described in Sect. 5, it is a challenging to suppress both the electrical interferences and environmental magnetic field. Figure 7 shows an example of the noise floor level measured inside a magnetic shielding. The measured range was from 50 to 150 Hz with 0.125 Hz in a bandwidth, and the averaging was 4 times. The measured noise floor level was as low as 300 fT/Hz$^{1/2}$ which is one of the advantage for the weak and low-frequency magnetic field detection.

Other remarks are related to the design of coil parameters. Figure 8 shows two pickup coils for induction magnetometers based on current detection model [29]. Although the values of mean diameter of the coils are similar as Coil-01, the numbers of turns are different. According to the design based on the voltage detection model, the number of turns makes the sensitivity high. In contrast, the best sensitivity can achieve the magnetometer with Coil-01 based on the current detection model. The values of sensitivity in III region are 30, 6.5 and 2.4 mV/nT

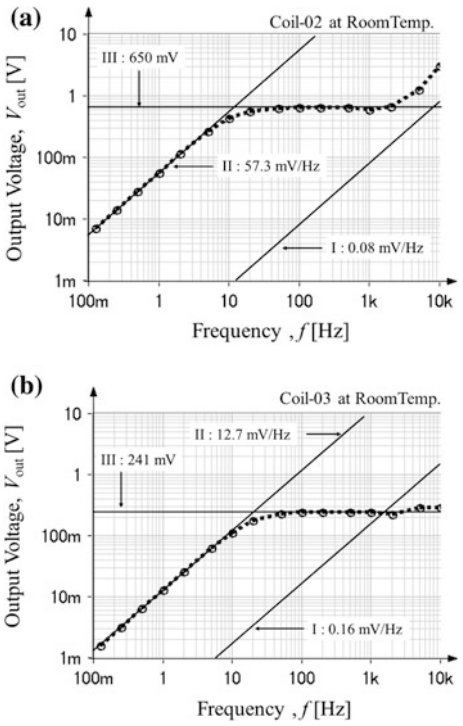

Fig. 9 Comparison of frequency response between the induction magnetometers. *Plots* represent the measured results [29] and *lines* represents the theoretical estimation results. **a** Coil-02. **b** Coil-03

for Coil-01, 02 and 03, respectively. The frequency responses of the current detection model strongly depends on the coil inductance, the design of coil shape and parameters is very important. Figure 9 shows the frequency responses of Coil-02 and Coil-03 for the magnetic field of 100 nT. The electronics was the same as Coil-01; R_f = 1 MΩ. Because of the numbers of turns, the sensitivity in the region I of Coil-03 is twice compared with Coil-02. In contrast, the sensitivity based on the current detection model, region II and II, for Coil-02 is twice or more compared with that for Coil-03. It should be noted that the value of the cutoff frequency was also low in Coil-02. If the lowest cutoff frequency is required, the use of Brooks coil as Coil-01 is one of the smart solution which described in Sect. 2.

The final remark in this section is the temperature stabilization. This is not only the problem for the induction magnetometer, but also all magnetic sensors for practical use. The reason of the high sensitivity in region II relies on the coil resistance. From the view point of the voltage detection model design, this resistance define the voltage gain of a pre-amplifier as (R_f/R). For example, this value becomes as high as 83.1 dB for the Coil-01. However, it is well known that the resistance has temperature dependency. In the extreme case, the resistance value of copper wire becomes about 1/8 when it is dipped in a liquid nitrogen (77 K).

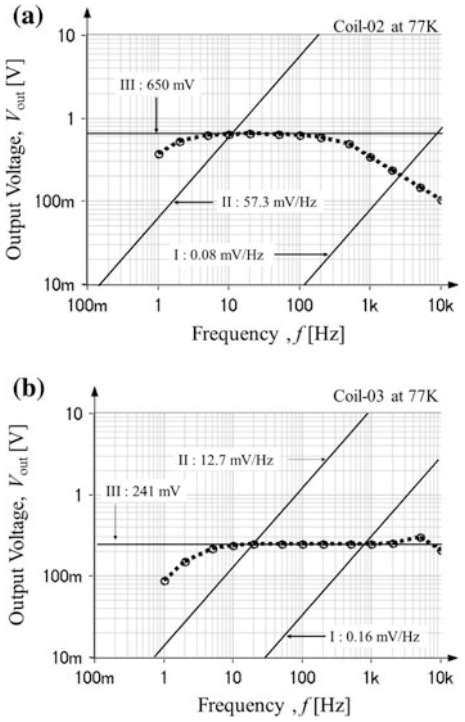

Fig. 10 Comparison of frequency response between the induction magnetometers cooled in a liquid nitrogen. *Plots* represent the measured results [29] and *lines* represents the theoretical estimation results. The amplitude of the measured magnetic field was 100 nT. **a** Coil-02. **b** Coil-03

Figure 10 shows the frequency responses of Coil-02 and Coil-03 cooled in a liquid nitrogen for the magnetic field of 100 nT. In conclusion, the temperature dropping makes the flat frequency response wide, and the sensitivity does not change in the region III.

3 Coil Design

The estimation of coil inductance is very important to design induction magnetometer based on current detection model. Although the estimation of the inductance for ideal solenoid coil is well known, it could not be used for the other shapes of coils. The study of inductance estimation contains long historical background and difficult mathematics [30]. From the point of engineers related to development of the induction magnetometer, it is not easy to follow all the details.

Figure 11 shows the shapes of coil which are selected for practical use. In order to estimate the inductance, suitable approximations should be chosen. In 1995, K. Kajikawa and K. Kaiho confirmed the accuracy of the several approximations for a circular coil of rectangular cross section with the help of computer calculations

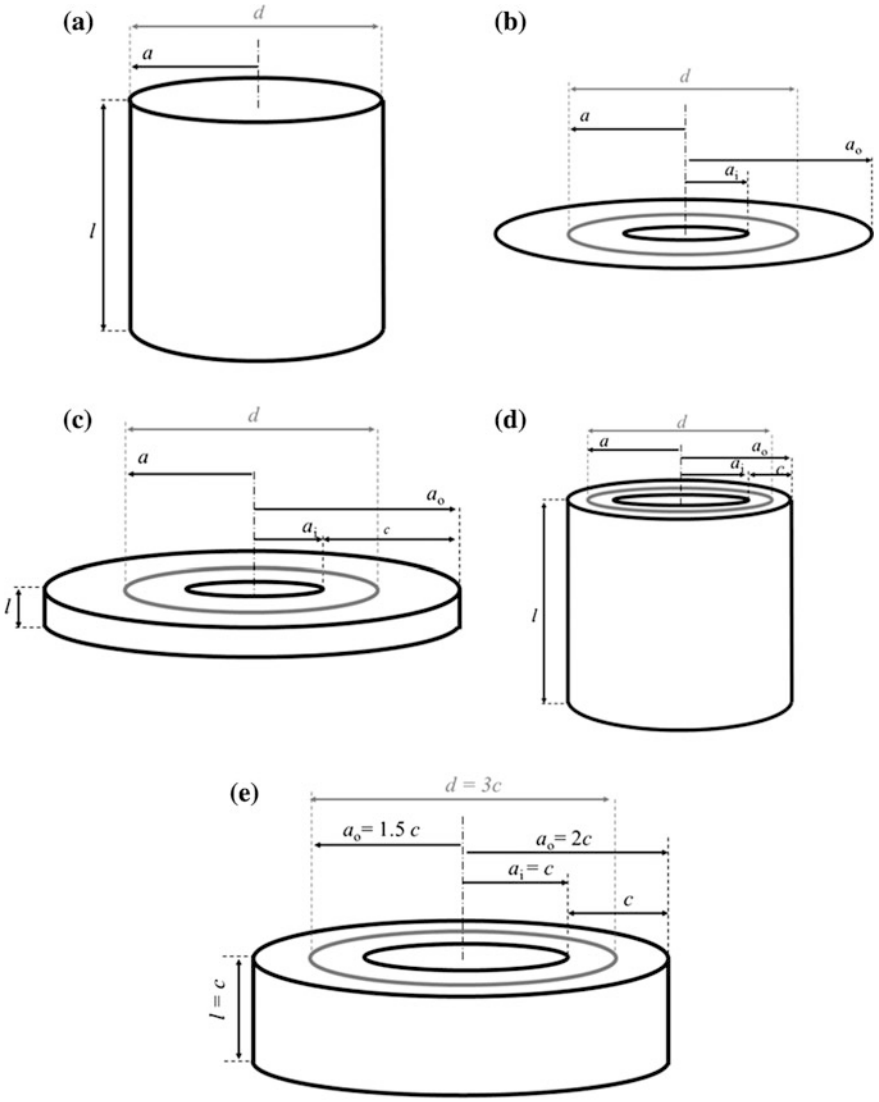

Fig. 11 Coil shapes for estimation of self-inductance. The parameters written in the figures are: a_i, a_o and a represent the inner, outer and mean radius, respectively. c and l represent the coil width and length, respectively. **a** Thin solenoid coil ($c = 0$). **b** Flat spiral coil ($l = 0$). **c** Short solenoid coil ($d < l$). **d** Long solenoid coil ($l > d$). **e** Brooks coil ($l = a_i = c$, $a = 1.5c$, $a_o = 2c$, $d = 3c$)

[31]. According to their excellent works, it was reported that the five approximations are enough to estimate the inductance within three digit accuracy. For the induction magnetometer design, the selection in this section is more simplified into four general shapes and one special shape, Brooks coil. All the estimations can be calculated by a simple calculator as Excel program.

3.1 Thin Solenoid Coil

The inductance of a single-layered solenoid coil with negligible coil winding width is expressed by

$$L = C_{\text{nagaoka}} \frac{\mu_0 \pi a^2 n^2}{l} \tag{15}$$

where μ_0 (H/m) is the permeability in vacuum, a (m) is radius of the coil, n is number of the coil windings, l (m) is length of the solenoid coil, and C_{nagaoka} is the Nagaoka coefficient. For the ideal solenoid coil, the value of C_{nagaoka} is 1. In practical case, the existence of open ends should be taken in account even if the solenoid coil has relatively long length. The Nagaoka coefficient is defined by

$$C_{\text{nagaoka}} = \frac{4}{3\pi} \frac{1}{k'} \left[\frac{k'^2}{k^2} (K - E) + E - k \right] \tag{16}$$

where k and k' are the elliptic module and complementary elliptic module, K and E are complete elliptic integral of the first and second kind, respectively. In order to calculate with a simple calculator as Excel spreadsheet program, approximations proposed by C. Hastings [32] are very useful. The calculation of values of estimation error are lower than 0.01 % [33].

$$k = \sqrt{\frac{4r^2}{4r^2 + l^2}}, \quad k'^2 = 1 - k^2, \tag{17}$$

$$\begin{aligned} K = K(k) &= \int_0^{\pi/2} \frac{1}{\sqrt{1 - k^2 \sin^2 \theta}} d\theta \\ &\approx \left(1.3862944 + 0.1119723k'^2 + 0.0725296k'^4\right) \\ &\quad + \left(\frac{1}{2} + 0.1213478\,k'^2 + 0.0288729k'^4\right) \ln(1/k'^2) \end{aligned} \tag{18}$$

$$\begin{aligned} E = E(k) &= \int_0^{\pi/2} \sqrt{1 - k^2 \sin^2 \theta} d\theta \\ &\approx \left(1 + 0.4630151k'^2 + 0.1077812k'^4\right) \\ &\quad + \left(0.2452727k'^2 + 0.0412496k'^4\right) \ln(1/k'^2) \end{aligned} \tag{19}$$

3.2 Flat Spiral Coil

According to the reference [31], Spielrein's approximations are known to calculate the inductance for a flat spiral coil with negligible coil winding width. To calculate the inductance, the aspect ratio γ should be used to select the suitable approximation.

$$\lambda = \frac{a_i}{a_o} \tag{20}$$

If $\gamma < 0.5$,

$$\begin{aligned} L =& \mu_0 \frac{n^2 a_o}{4\pi(1-\lambda)^2} \times \\ & \left\{ \frac{8\pi}{3} \left[2G - 1 - \lambda^3 \left(\pi \ln 2 - 2G + 1 - \frac{\pi}{12} + \frac{\pi}{2} \ln \frac{1}{\lambda} \right) \right] \right. \\ & \left. + \pi^2 \left[\frac{3}{20}\lambda^5 + \frac{15}{448}\lambda^7 + \frac{175}{13824}\lambda^9 + \frac{2205}{360448}\lambda^{11} + \frac{14553}{4259840}\lambda^{13} \right] \right\} \end{aligned} \quad [\mathrm{H}] \tag{21}$$

where,

$$2G = \int_0^{\pi/2} \frac{\varphi d\varphi}{\sin \varphi} = 1.8319311883544380301\ldots \tag{22}$$

Else if $\gamma > 0.5$,

$$\begin{aligned} L =& \mu_0 \frac{n^2 a_o}{1+\tau} \times \\ & \left\{ \left[\ln \frac{4}{\tau} - \frac{1}{2} \right] + \tau^2 \left[\frac{1}{24} \ln \frac{4}{\tau} + \frac{43}{288} \right] + \tau^4 \left[\frac{11}{2880} \ln \frac{4}{\tau} + \frac{1}{150} \right] \right\} \end{aligned} \tag{23}$$

where,

$$\tau = \frac{1-\lambda}{1+\lambda}. \tag{24}$$

3.3 Short Solenoid Coil (d > l)

This shape of coils is popular for the pickup coil of an induction magnetometers. The inductance of Coil-04, Coil-05, a one turn coil for high frequency field

detection, described in Sect. 5, was also estimated by this approximation. The estimation of the inductance for this coil shape is known as Lyle's approximation. According to the reference [31], it was pointed that there was a mistake in the approximation described in the original Lyle's paper. Lyle's approximation is acceptable when the values of (l/d) is lower than 1.0 within the 0.1 % error. Because approximation has a lot of terms, it should be divided into several parts to calculate a Excel program as follows. The Lyle's approximation could be expressed by

$$L = \mu_0 a n^2 \times (A_0 + A_2 + A_4 + A_6) \tag{25}$$

where,

$$u = \frac{l^2}{c^2} \ln \frac{l^2 + c^2}{l^2}, \tag{26}$$

$$v = \frac{c^2}{l^2} \ln \frac{l^2 + c^2}{c^2}, \tag{27}$$

$$w = \frac{l}{c} \tan^{-1} \frac{c}{l}, \tag{28}$$

$$w' = \frac{c}{l} \tan^{-1} \frac{l}{c}, \tag{29}$$

$$A_0 = \ln \frac{8a}{l^2 + c^2} + \frac{1}{12} + \frac{u + v}{12} - \frac{2}{3}(w + w'), \tag{30}$$

$$A_2 = \frac{1}{96a^2} \left\{ \left(3l^2 + c^2\right) \ln \frac{8a}{l^2 + c^2} + \frac{1}{2} l^2 u - \frac{1}{10} c^2 v - \frac{16}{5} l^2 w + \frac{69}{20} l^2 + \frac{221}{60} c^2 \right\} \tag{31}$$

$$A_4 = \frac{1}{30720a^4} \left\{ \left(-30l^4 + 35l^2 c^2 + \frac{22}{3} c^4 \right) \ln \frac{8a}{l^2 + c^2} - \frac{115l^4 - 480l^2 c^2}{12} u - \frac{23}{28} c^4 v + \frac{256}{21} \left(6l^4 - 7l^2 c^2\right) w - \frac{36590l^4 - 2035l^2 c^2 - 11442c^4}{840} \right\}, \tag{32}$$

$$
\begin{aligned}
A_6 = \frac{1}{6881280a^6}\Bigg\{ & \left(525l^6 - 1610l^4c^2 + 770l^2c^4 + 103c^6\right)\ln\frac{8a}{l^2+c^2} \\
& + \left(\frac{3633}{10}l^6 - 3220b^4c^2 + 2240l^2c^4\right)u - \frac{359}{30}c^6v \\
& - 2048\left(\frac{5}{3}l^6 - 4l^2c^2 + \frac{7}{5}l^2c^4\right)w + \frac{2161453}{840}l^6 \\
& - \frac{617423}{180}l^4c^2 - \frac{8329}{60}l^2c^4 + \frac{108631}{840}c^6\Bigg\}.
\end{aligned} \tag{33}
$$

3.4 Long Solenoid Coil ($d < l$)

This shape of coils is also popular for the pickup coil of an induction magnetometers. According to the reference [31], there are two candidates for the suitable approximations, Butterworth's or Dwight approximation. For the design of induction magnetometers, Dwight approximation is acceptable. The values of inductance for Coil-02, Coil-03 and Coil-06 can be estimated by this approximation [22, 34]. If the coil width is very thick, $(c/d) > 0.8$, and the coil length as similar as the mean diameter, $1 < (l/d) < 1.2$, the shape of the coil should be re-designed. The Dwight's approximation could be expressed by

$$
L = \frac{\mu_0\pi a^2n^2}{l}\left(C_{\text{nagaoka}} + \Delta L_0 + \Delta L_2 + \Delta L_4 + \Delta L_6\right) \tag{34}
$$

where,

$$
m = \frac{d}{\sqrt{d^2+4l^2}}, \tag{35}
$$

$$
\begin{aligned}
\Delta L_0 = & -\frac{2}{3}\frac{c}{d} + \frac{1}{3}\frac{c^2}{d^2} \\
& + \frac{4d}{3\pi l}\left\{\frac{1}{4}\frac{c^2}{d^2}\left(\ln\frac{4d}{c} - \frac{23}{12}\right) - \frac{1}{80}\frac{c^4}{d^4}\left(\ln\frac{4d}{c} - \frac{1}{20}\right)\right. \\
& \left. - \frac{1}{896}\frac{c^6}{d^6}\left(\frac{23}{20}\ln\frac{4d}{c} - \frac{4547}{5600}\right)\right\},
\end{aligned} \tag{36}
$$

$$
\begin{aligned}
\Delta L_2 = & \frac{c^2}{d^2}\frac{d}{l}\left\{\frac{m}{6} - \frac{5}{24}m^3 + \frac{m^5}{3} - \frac{95}{128}m^7 + \frac{217}{128}m^9\right. \\
& \left. - \frac{2135}{512}m^{11} + \frac{21571}{2048}m^{13} - \frac{895895}{32768}m^{15}\right\},
\end{aligned} \tag{37}
$$

$$\Delta L_4 = \frac{c^4}{d^4}\frac{d}{l}\left\{\frac{m}{36} - \frac{17}{180}m^3 + \frac{53}{96}m^5 - \frac{1265}{576}m^7 + \frac{38857}{4608}m^9 - \frac{3913}{128}m^{11} + \frac{2206281}{20480}m^{13} - \frac{1519375}{4096}m^{15}\right\}, \tag{38}$$

$$\Delta L_6 = \frac{c^6}{d^6}\frac{d}{l}\left\{-\frac{1}{120}m^3 + \frac{15}{112}m^5 - \frac{1117}{672}m^7 + \frac{1183}{96}m^9 - \frac{76461}{1024}m^{11} + \frac{4043831}{10240}m^{13} - \frac{15637479}{8192}m^{15}\right\}. \tag{39}$$

3.5 Brooks Coil (l = ai = c, a = 1.5c, ao = 2c, d = 3c)

Although the inductance of Brooks coil could be estimated by Lyle's approximation, the historical background should be mentioned according to the handbook of inductance calculation written by F.G. Grover:

> Maxwell found that for maximum inductance with a given length to a chosen wire, the mean diameter of the turns should be 3.7 times the dimension of the square cross section. This result, although often quoted, is only approximate. The more accurate formulas for the inductance now available show that the ratio lies quite close to $2a / c = 3\ldots$ Accordingly, Brooks has proposed that a coil for which $2a / c = 3$ is, for all practical purposes, one of the optimum form and has the advantage over that yielded by mathematical analysis of simplicity of the proportions. Such a coil offers, in fact, an inductance only 2 parts in 100,000 less than the maximum attainable with the wire in question. [30]

This shape of coil can achieve maximum inductance for a given length of winding wire, and the estimation error of the inductance is less than 3 % [22]. The inductance of the Brooks coil is given by

$$L = 1.6994 \times 10^{-6} \times an^2 \tag{40}$$

It should be noted that the cutoff frequency is defined by the size of the Brooks coil. The resistance of a coil is given by

$$R = \frac{2\pi an}{s} \times \rho \tag{41}$$

where s [m^2] and ρ [Ωm] represents the cross section and resistivity of the wire, respectively. With the values of the inductance and resistance, the cutoff frequency for the Brooks coils is given by

$$f_c = \frac{R}{2\pi L} = \frac{\rho}{1.6994 \times 10^{-6} sn} = \frac{\rho}{1.6994 \times 10^{-6} \beta c^2} \tag{42}$$

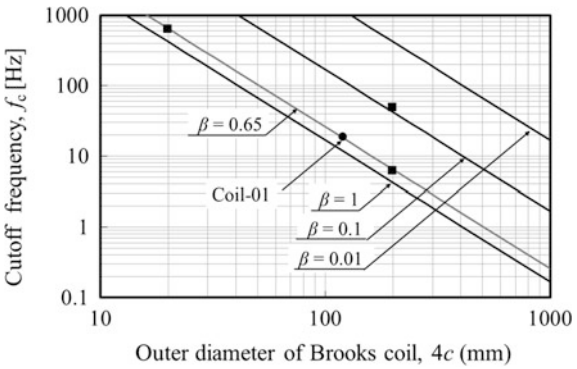

Fig. 12 Cutoff frequency as a function of outer diameter of Brooks coil

where β represents the spacing factor of the Brooks coil. If the ideal high-conductor density coil, the value of β closes to 1. Figure 12 shows the cutoff frequency as a function of outer diameter of Brooks coils, as a parameter of the spacing factor. The values for Coil-01 and other Brooks coils described in previous reports are also plotted. In practical design, the reasonable value of β is 0.65. In previous reports [19, 22, 28, 35], the values of β were overestimated because of the definition of s based on the square cross section. It should be corrected that the definition of the s is

$$s = \pi \frac{\delta^2}{4} \tag{43}$$

where δ [m] represents the diameter of the wire.

4 Electronics Design

The basis of the electronics design for the current detection model was proposed by Macintyre in 1980 [21]. Design of the electronics is not only related to the coil design, but also to reduction of both the environmental magnetic field and electrical interferences. This section provides some useful tips for the design of this induction magnetometer for practical use.

4.1 Optimum Design

Figure 13 shows the equivalent circuit of the induction magnetometer. An op-amp has both an input noise voltage and current density, e_n [V/Hz$^{1/2}$] and i_n [A/Hz$^{1/2}$], respectively. Considering both the op-amp noise and thermal noise in the resistance.

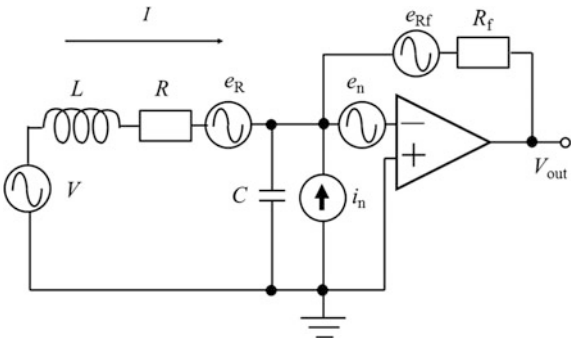

Fig. 13 Equivalent circuit of an induction magnetometer based on the current detection model

For example, typical values of a low noise op-amp LT1028 (Linear Technology) are 0.9 V/Hz$^{1/2}$ and 1 pA$^{1/2}$, respectively [36]. The values of both R and R_f correspond to thermal voltage noise source e_R [V/Hz$^{1/2}$] and e_{Rf} [V/Hz$^{1/2}$], respectively. The total voltage noise, V_n [V/Hz$^{1/2}$], in output voltage is defined by all the voltage and current noises, which define the noise floor level of the induction magnetometer, B_{min} [T/Hz$^{1/2}$]:

$$B_{min} = \frac{V_{noise}}{|V_{out}/\mu_0 H|} \tag{44}$$

where $|V_{out}/\mu_0 H|$ [V/T] represents the sensitivity of the induction magnetometer which defined by (13) for low frequency region, II, and (14) high frequency region, III. They are expressed by

$$\left|\frac{V_{out}}{\mu_0 H}\right| = \frac{R_f}{R} \times 2\pi^2 na^2 \times f, \quad \text{for region II,} \tag{45}$$

$$\left|\frac{V_{out}}{\mu_0 H}\right| = \frac{R_f}{L} \times \pi na^2 \quad \text{for region III,} \tag{46}$$

From this author's experiences, the thermal voltage in coil resistance, e_R, is usually main contribution to the noise floor level. For the practical use, the values of e_R and V_{noise} could be given by

$$e_R = \sqrt{4kTR} \tag{47}$$

$$V_{noise} = \frac{R_f}{R} e_R \tag{48}$$

where k [J/K] represents the Boltzman constant ($\sim 1.38 \times 10^{-23}$) and T [K] represent the room temperature. The value of $(4kT)^{1/2}$ could be estimated as $(1/8) \times 10^{-9}$ at room temperature. It should be recommended that the value of V_{noise} should be set larger than 1 μV/Hz$^{1/2}$ because of the limitation of a

conventional instrumentations to measure the voltage signal. The noise floor level could be estimated by

$$B_{\min} = \frac{L}{\pi n a^2}\sqrt{\frac{4kT}{R}} \tag{49}$$

The estimated value for the Coil-01 was 0.51 pT/Hz$^{1/2}$ and the corresponding value of the output noise voltage was 15 μV/Hz$^{1/2}$ with the transimpedance of 1 MΩ. In general, the measured noise floor level is decreased by the square number of averaging. As mentioned in Sect. 2, the measured value of 0.3 pT/Hz$^{1/2}$ with 4 times averaging, which agreed with the estimation result. The estimated values for the Coil-02 and Coil-03 were also 0.52 and 0.47 pT/Hz$^{1/2}$, and the corresponding values of the output noise voltage were 3.42 μV/Hz$^{1/2}$ and 1.23 μV/Hz$^{1/2}$ with the tranimpedance of 1 MΩ, respectively. Although the numbers of windings for Coil-02 and Coil-03 are larger than that for Coil-01, the values of noise floor level are similar. If the shape of coil is Brooks coil, the size and spacing factor also define the noise floor level. With the estimation of both the inductance and resistance described in Sect. 3, the noise floor level is rewritten by

$$B_{\min} = 1.6994 \times 10^{-7}\sqrt{\frac{16kT\beta}{27\pi^3 c\rho}} \tag{50}$$

This results notice that the noise floor level does not depend on the wire diameter or number of winding coil, because they are defined by the values of the coil width and spacing factor. It should be mentioned that an decrease in the spacing factor produces an decrease in the noise floor level. Figure 14 shows the noise floor level as a function of the outer diameter of Brooks coil, as a parameter of the spacing factor. Lines represent the theoretical results calculated by Eq. (45), where parameters are $\rho = 1.78 \times 10^{-8}$ [Ωm], $k = 1.38 \times 10^{-23}$ [J/K] and $T = 300$ [K], respectively. The circle and square plots represent the Coil-01 and other Brooks coils described in Ref. [22], respectively.

4.2 Frequency Compensation

A simple explanation of a frequency compensation circuit for a transimpedance amplifier was given by R.J. Prance [37]. Figure 15 shows the equivalent circuit of the induction magnetometer with a frequency compensation. Optional passive elements of a resistor, R_1[Ω], and capacitor, C_1 [F], extend the frequency region II. Figure 16 shows the transimpedance as a function of the frequency. The values of R_1 and C_1 define a cutoff frequency f_1 [Hz] to be set the desired value of the cutoff frequency for induction magnetometer. The values of R and C_1 define a cutoff frequency f_2 [Hz] to be set the cutoff frequency defined by the values of both the

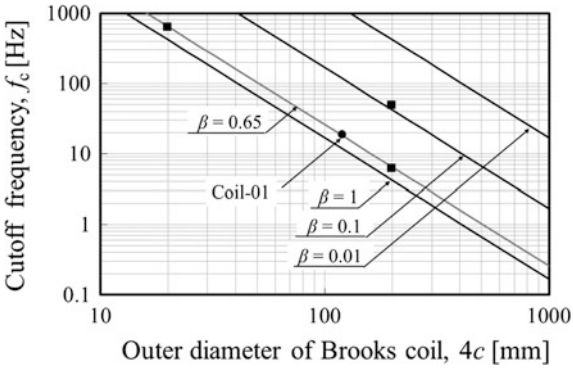

Fig. 14 Noise floor level as a function of the outer diameter of Brooks coil, as a parameter of the spacing factor

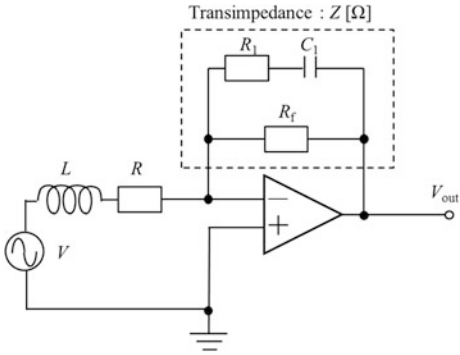

Fig. 15 Equivalent circuit of the induction magnetometer with frequency compensation transimpedance amplifier [37]

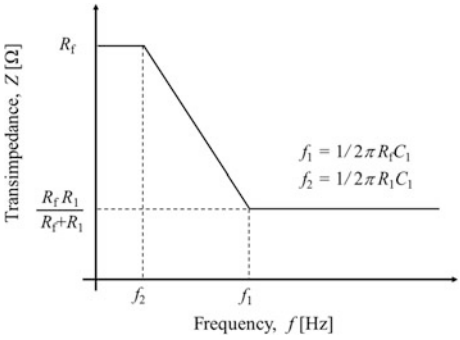

Fig. 16 Transimpedance of the frequency compensation transimpedance amplifier as a function of the frequency

inductance and resistance of the coil. The values of R_f and R_1 define the transimpedance in the region III.

Figure 17 shows the comparison of the sensitivity for the induction magnetometer with and without this compensation circuit. Although the sensitivity in the region III is decreased, it provides a wide and flat frequency response. Figure 18 shows an example of the measured frequency response. The coil is Coil-01, and the

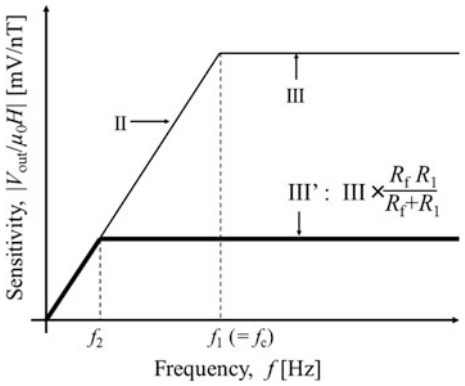

Fig. 17 Sensitivity with a conventional and frequency compensation transimpedance amplifier

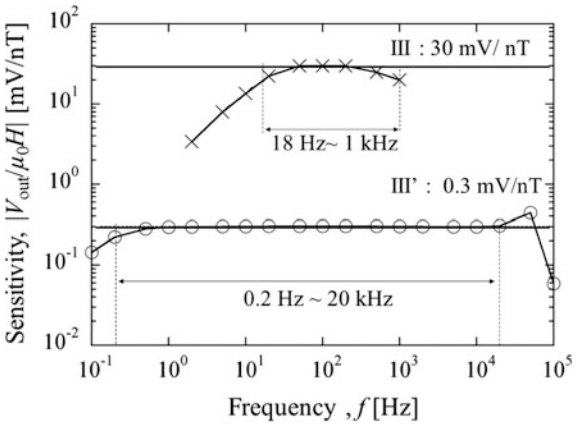

Fig. 18 Measured sensitivity of the induction magnetometer Coil-01 as a function of the frequency [38]. *Cross* and *circle plots* represent the results with a conventional and frequency compensation transimpedance amplifier, respectively

electronics is the conventional or frequency compensation transimpedance amplifier. The values of R_f, R_1, C_1 are 1 MΩ, 10 kΩ and 0.88 μF, respectively. Although the sensitivity becomes as 1/100 times with the frequency compensation transimpedance circuit, the linear frequency response of 0.3 mV/nT was confirmed from 0.2 Hz to 20 kHz.

4.3 Reduction of Noise

To detect weak and low-frequency field, reduction of environmental magnetic field and electrical interferences is necessary work. There are two keywords: differential structure and grounding points for both coil and electronics [39]. Figure 19 shows an example of induction gradiometer. The pickup coil consists of two coils, Coil-01, which are connected in serial, differentially. When a uniform magnetic field is crossed to both coil, the induced voltage is cancelled. Because

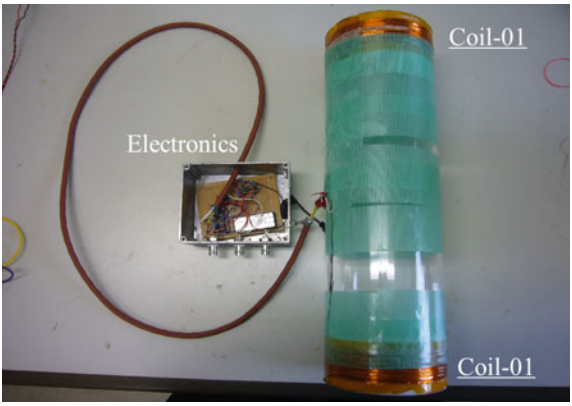

Fig. 19 An example of induction gradiometer

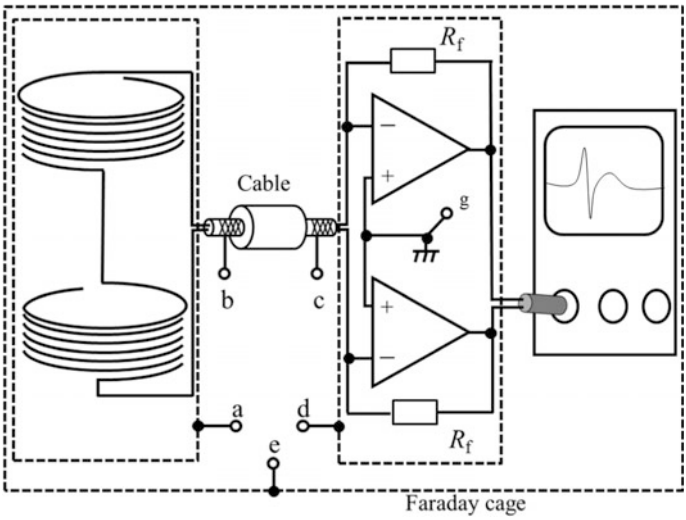

Fig. 20 A schematic design of the induction gradiometer [39]

environmental magnetic field could be regarded as a uniform magnetic field, this pickup coil could be reduced it. The electronics is differential-input-type transimpedance amplifier. Figure 20 shows the schematic design of this induction gradiometer. Because a conventional op-amp has a finite offset voltage, this structure could be reduced it. This amplifier also help to reduce the electrical interferences due to the unstable grounding point. The Dotted lines represent conducting material for electrical shielding.

The reduction of electrical interferences needs several or endless trials. The keyword is "never give up". Figure 21 shows the induction gradiometer after finding

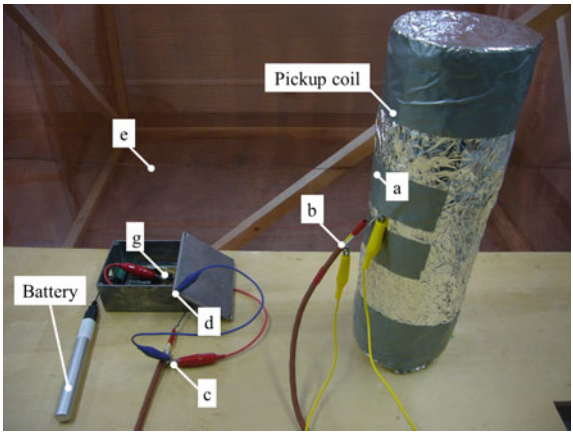

Fig. 21 An example of induction gradiometer after finding a condition of suitable grounding points [39]

a condition of suitable grounding points. The points "a" and "d" represent the contacting points on the electrical shield for the pickup coil and the converter, respectively. The points "b" and "c" represent the contacting point on the cupper mesh layer of the cable. The point "e" represents the contacting point on the Faraday cage. The point "g" represents the grounding point of the transimpedance amplifier. The resistance values of the cables, used for the connecting points, should be less than 0.2 Ω. An example of the grounding procedure in detail is described in [39].

5 Application Tips

The motivation of this section is to provide some inspirations for future development related induction magnetometers. This section provides some useful tips for the design of this induction magnetometer for practical use.

5.1 MHz Fields Detection

To the best of author's knowledge, the state-of-the-art performance of the induction magnetometers was presented by Korepanov's group [6]. From personal communications with Prof. Valery Korepanov and Ms. Vira Pronenko in 2010, it was confirmed that the noise floor level was 100 fT/Hz$^{1/2}$ at 1 Hz for low frequency type (0.3 mHz–200 Hz), 10 fT/Hz$^{1/2}$ at 1 kHz for middle frequency type (1 Hz–20 kHz), and 2 fT/Hz$^{1/2}$ at 50 kHz for high frequency type (10 Hz–600 kHz). On the other hand, the definition of the sensor to measure magnetic fields around MHz range is not clear because both magnetometers and antennas cover this frequency range. To measure this frequency range involves several applications; NMR/MRI devices, metal detection systems for security gates, high efficiency motor with

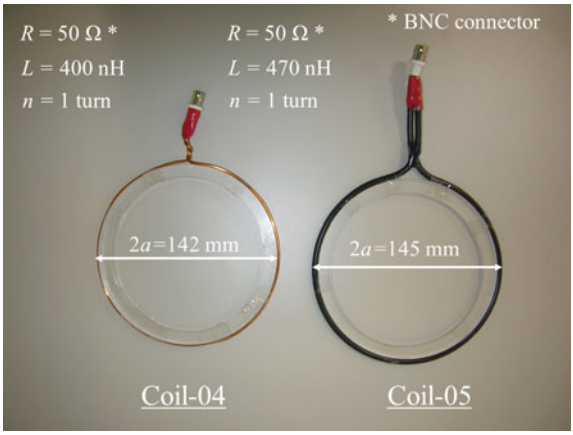

Fig. 22 Coils for detection magnetic fields around MHz range

PWM control, etc. An interested report was presented by Coillot's groups [4]. Although their developed magnetometer achieved a best noise floor level of 30 fT/Hz$^{1/2}$ at 2 kHz, it became worse for higher frequency region. The noise floor level was 100 fT/Hz$^{1/2}$ at 80 kHz, and 1 pT/Hz$^{1/2}$ at 400 kHz.

Figure 22 shows an example of coils to detect magnetic fields around MHz range. The first report on this sensor of Coil-04 was presented and EMSA2010 conference, and the paper was published in 2013 [40]. In order to suppress undesired stray capacitance, the number of coil windings is one. The value of inductance can be estimated by the Lyle's approximation described in Sect. 3. Although the values of resistance were less than 10 Ω, the values of effective resistance become 50 Ω which is defined by the equivalent input resistance of the instrumentation, spectrum analyzer. The wire of Coil-05 is made of BNC cable whose inner wire and metal shielded layer are used for the coil and electrical shield, respectively [41]. Figure 23 shows the experimental setup for the evaluation. All of the experiments were conducted in an electromagnetically shielded room (Iida EMC center, Nagano, Japan).

In this frequency range, the field has both the magnetic and magnetic properties. In order to generate a magnetic field of 10 nT, an electromagnetic field of 3 V/m was calibrated with an electric field sensor. Figure 24 shows an example of the measured frequency response based on the voltage detection model. Plots represent the measured output voltage for the calibration field and noise floor level [41], and lines represent the estimation results. The absolute error of the output voltage between the measurement and estimation was less than ±1 dBμV between 0.3 and 2 MHz. From the measured noise floor level, the sensitivity limit at 1 MHz was 1 nT. Figure 25 shows an example of the measured frequency response based on the current detection model. Although the value of transimpedance was 1 kΩ because of the enough sensitivity, the values could be set up to 10 MΩ if an environment for weaker electromagnetic field calibration environment is prepared. The measured results were good in agreement with the estimated results in region II. From the measured noise floor level, the sensitivity limit at 1 MHz was 20 nT

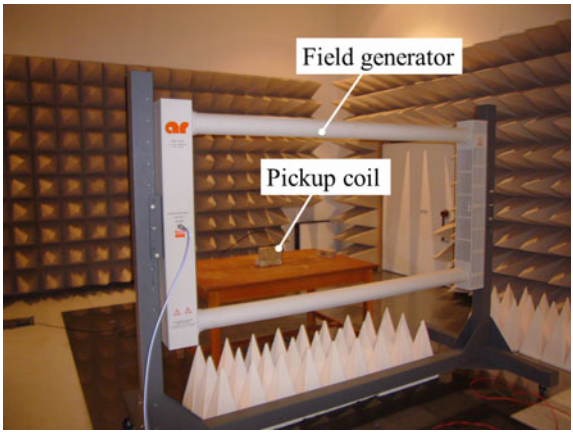

Fig. 23 Experimental setup for evaluation of induction magnetometer for MHz range

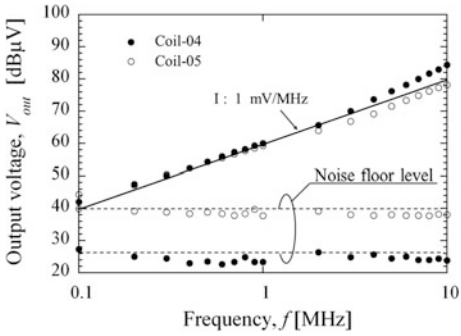

Fig. 24 An example of frequency response based on voltage detection model. The value of calibration field was 10 nT [41]

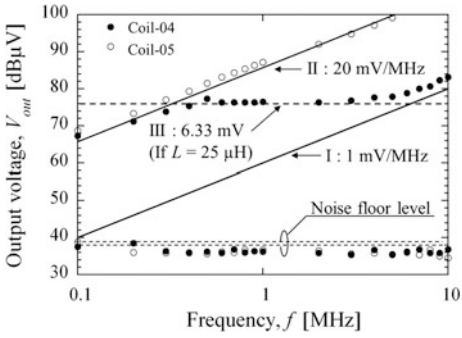

Fig. 25 An example of frequency response based on current detection model. The values of calibration field and transimpedance were 10 nT and 10 kΩ, respectively [41]

which was 20 times values compared with the voltage detection model. To share future success related to induction magnetometers, it should be mentioned unsolved question related to estimation of inductance in high frequency region. Although the estimated cutoff frequency for both coils are larger than 10 MHz, the Coil-04

operated as region III after the cutoff frequency around 3 MHz. If the value of the inductance is 25 μH, this phenomenon is explained by the basis described before.

5.2 *Nondestructive Evaluation*

Based on both the electrical and magnetic properties, magnetic field can be used to inspect an object without destruction. The famous applications are a security gate in airport and metallic contamination detection system in the food industry. Because of the sensitivity of induction magnetometer based on voltage detection model, the frequency of magnetic field is usually larger than 100 kHz. However, it does not penetrate inside a conductive material, when the frequency of the magnetic field is high. For example, the skin depth corresponds to 0.2 mm at 100 kHz for a material made of copper. The use of a low-frequency magnetic field has an advantage with an induction magnetometer based on current detection model.

From the author's point of view, the nondestructive evaluation is not only for the industry application, but also for both the engineering education and material science. Figure 26 shows an example for the engineering education for children. Several cheese are wrapped an aluminum foil as samples, and a staple made of a stainless SUS304 is embedded into a sample. Children made a fun when a sample with a staple was found without unwrapped the aluminum foil. While the austenitic stainless material SUS304 does not have magnetism, stress-induced martensitic transformation gives it magnetic properties. Most of the possible contaminants are fragmented metal with sharp edges caused by degradation during processing in a machine. In particular, the austenitic stainless material SUS304 accounts for over 60 % of all stainless material in production.

Figure 27 shows the magnetic contamination detection system [34, 42]. This system consists of two coils, electronics, current source with power amplifier and oscilloscope. To access the inspection area, a sample folder made of nonmagnetic

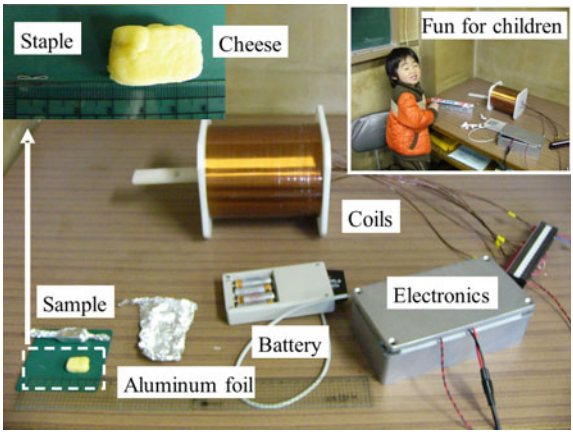

Fig. 26 An example for engineering education for children. Although magnetic field is invisible, children made a fun when a sample with a staple was found without unwrapped the aluminum foil

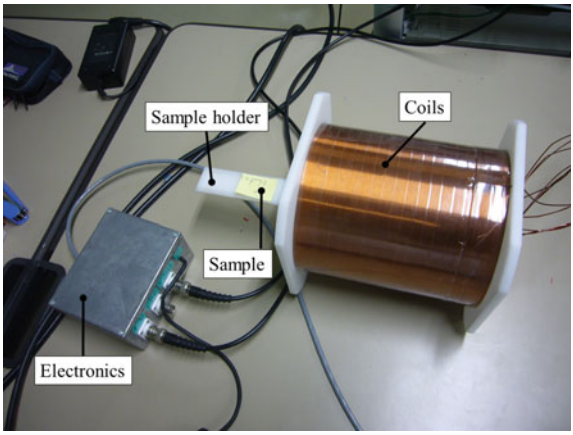

Fig. 27 Magnetic contamination detection system [34]

material is used. Figure 27 shows the schematic diagram of this system. When a uniform magnetic flux crosses this differential structured detection coil, a current is not induced. However, an induced current appears in the detection coil if the balance of the magnetic flux is disturbed by a magnetic material (Fig. 28). Figure 29 shows the coil for producing a uniform magnetic field, Coil-06. Although this coil is used for the generation of magnetic field inside the coil, the basis of induction magnetometers is useful for this design. The values of inductance, resistance and cutoff frequency are 30.5 H, 841 Ω, and 4.39 Hz, respectively. Because of the low cutoff frequency, the reactance is dominant component to provide a current for generation of magnetic field. This coil can produce magnetic field as 0.2 T/A. Figure 30 shows the coil detection coil having a differential structure, Coil-07. Two thin solenoid coil are connected in serial, differentially.

To share future success related to induction magnetometers, it should be mentioned unsolved question related to perfect balance and material science. Figure 31 shows examples of the output waveform. The frequency of the excitation is 10 Hz,

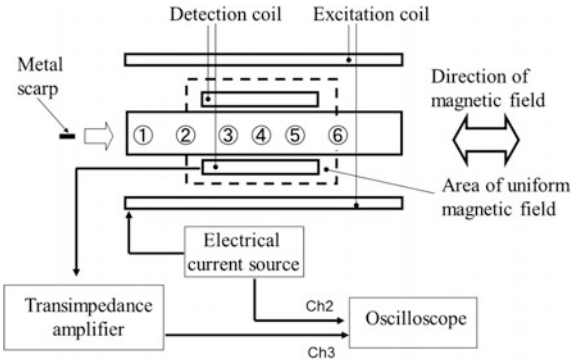

Fig. 28 Schematic design of the magnetic contamination detection system [34]

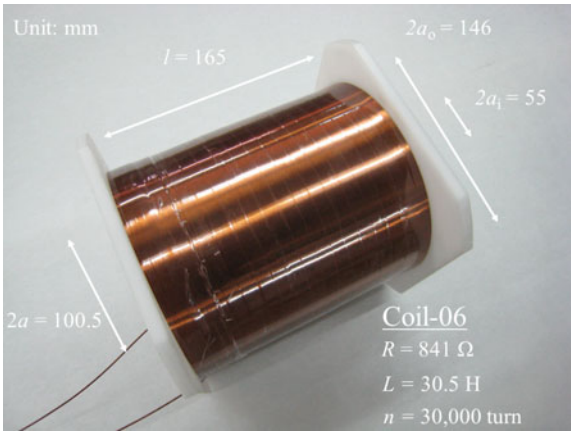

Fig. 29 Excitation coil for generating a uniform magnetic field, Coil-06 [34]

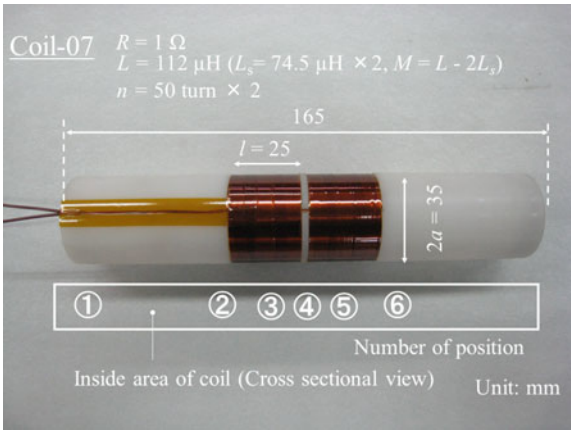

Fig. 30 Detection coil having a differential structure. Coil-07 [34]

and the waveform of current are also plotted. Because of the high sensitivity, the output waveform was saturated when the diameter of the sample iron was 0.1 mm. In contrast, the output voltage was not balanced when the magnetic was not placed. Although an finite offset voltage was suppressed by the both differential input type transimpedance amp and a high pass filter, drift phenomenon in output voltage of a few V was observed. Due to the imperfection of the coil balance, the components of both the excitation and power-line frequency also appear in the output voltage. Figure 32 shows the summary of the output voltage as a function of the wire diameter, as a parameter of the wire length. The response for iron wire was acceptable because the values of output voltage depended on both the wire length and diameter. However, the response for SUS304 wire needed to explain some physical model because the values of output voltage was limited by the wire

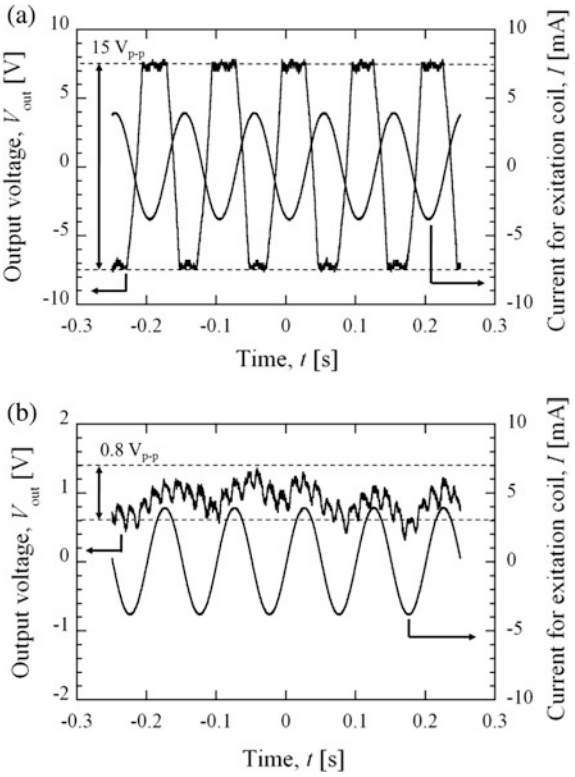

Fig. 31 Examples of output waveforms of the system [42]. **a** Fe wire (ϕ = 0.1 mm, l = 10 mm). **b** Without sample

diameter. Although a qualitative explanation was described [42], the quantitative explanation is still unsolved (Fig. 28).

5.3 Biomagnetic Measurement

As mentioned before, the first MCG and MEG measurements were demonstrated by induction magnetometer, so that the motivation of biomagnetic measurement is enough reason to study induction magnetometers. The detail of the first MCG measurement by this author was already described in previous [16], the progress of this research is mentioned, here. It should be noted that this continuous study were supported by author's master student, Mr. Takahiro Yamamoto, and all experimental results were written in his master thesis. Figure 33 shows explanation of a MCG signal distortion caused by filters. Because the induction gradiometer with two Coil-01 has a cutoff frequency around 18.5 Hz, the values of R and S wave amplitude were decreased and increased. In contrast, the band pass filter (BPF) and

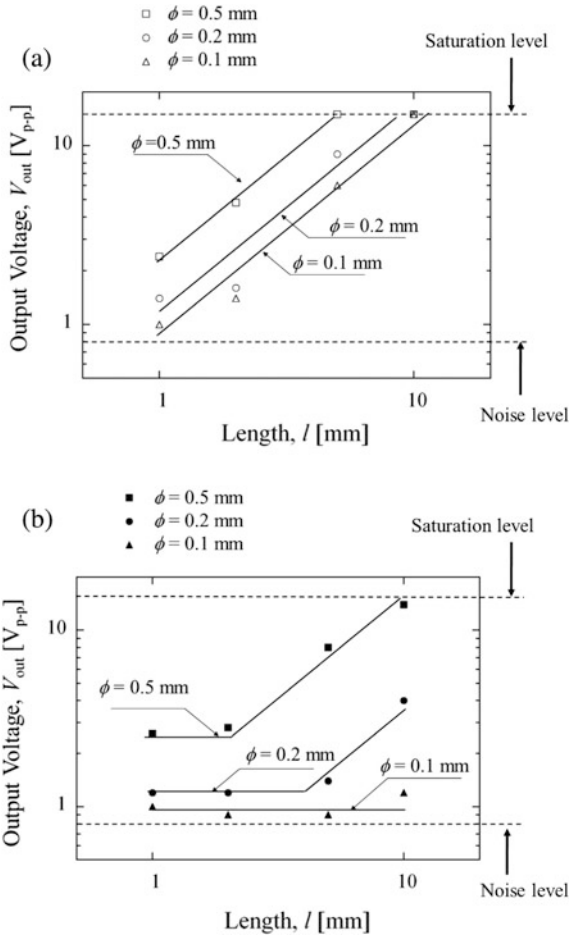

Fig. 32 Measured output voltage as a function of the wire diameter, as a parameter of the wire length [42]. **a** Fe wire. **b** SUS304 wire

band eliminate filter (BEF) does not distort the MCG signal, significantly. This results are agreed with the previous experimental results [16]. Figure 34 shows the new electronics of the induction gradiometer for MCG measurements. Compared with the previous electronics, the transimpedance amplifier has frequency compensation circuit which provides a new cutoff frequency of 0.3 Hz. All the measurements was conducted inside a Faraday cage, and a suitable grounding condition was selected. Figure 35 shows the confirmation of the MCG measurement with this induction gradiometer. The MCG signal was generated by one turn coil, and the output voltage signal was measured by a PC with LabView Program. Although the power-line frequency noise of 60 Hz were superposed, the measured signal was good in agreement with the generated MCG signal. Figure 36 shows the demonstration of MCG measurement from a human heart.

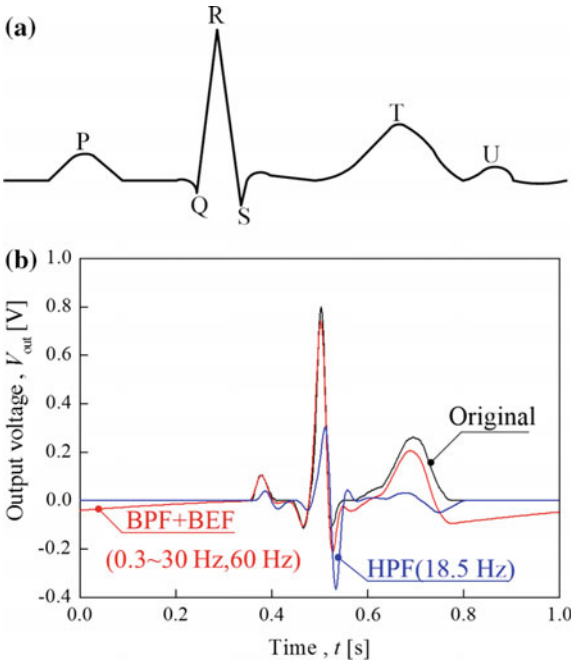

Fig. 33 Explanation of a MCG signal distortion caused by filters. **a** MCG signal. **b** Effect of filters on the MCG signal waveform

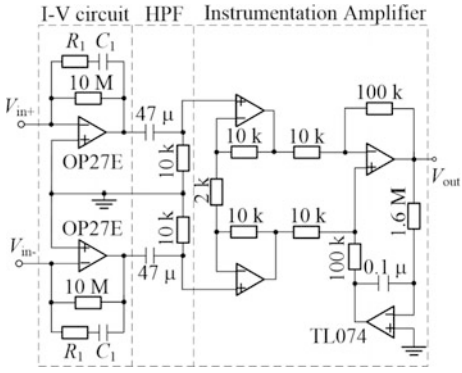

Fig. 34 Electronics in the induction gradiometer for MCG measurements

To share future success related to induction magnetometers, it should be mentioned unsolved question related to design of magnetic core. Although this induction magnetometer is possible to measure the MCG signal, the spatial resolution is not enough to estimate the current source in the object. In order to design a suitable magnetic core to reduce the size of pickup coils, the estimation of effective permeability related to the demagnetizing factor is a key point. Because exact calculation of the demagnetization factor for ellipsoidal bodies exists, it is widely used for

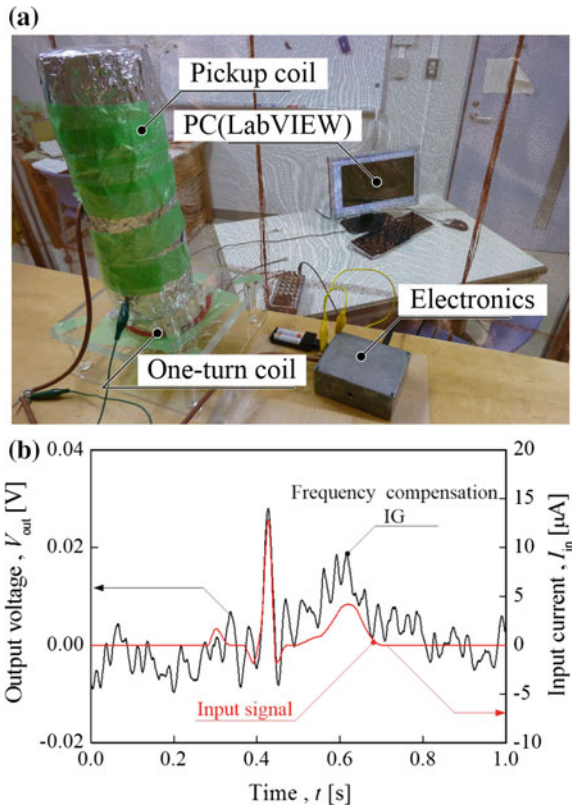

Fig. 35 Measurement result of MCG signal generated by one turn coil. **a** Experimental setup. **b** Measured results (100 times averaging)

the estimation of the effective permeability for ellipsoidal core or relatively long rod core. Unfortunately, this estimation is not acceptable for the dumbbell-shaped core [14], which was used for the first MCG measurement in 1963 [12].

5.4 Zero-Power Induction Magnetometer

To share future success related to induction magnetometers, it should be mentioned unsolved last question related to power consumption. Low power consumption is one of the advantages in induction magnetometer. After all, zero-power induction magnetometer is considerable feature for future trillion sensors world with wireless sensor network. Figure 37 shows an example of zero-power induction magnetometer, magnetic field alarm. It consists of a coil with a dumbbell-shaped core, Cockcroft-Walton circuit and piezo buzzer. It is not only a self-generation component powered by magnetic energy harvesting, but also a sonification device which notices the existence of environmental magnetic field; This alarm is activated

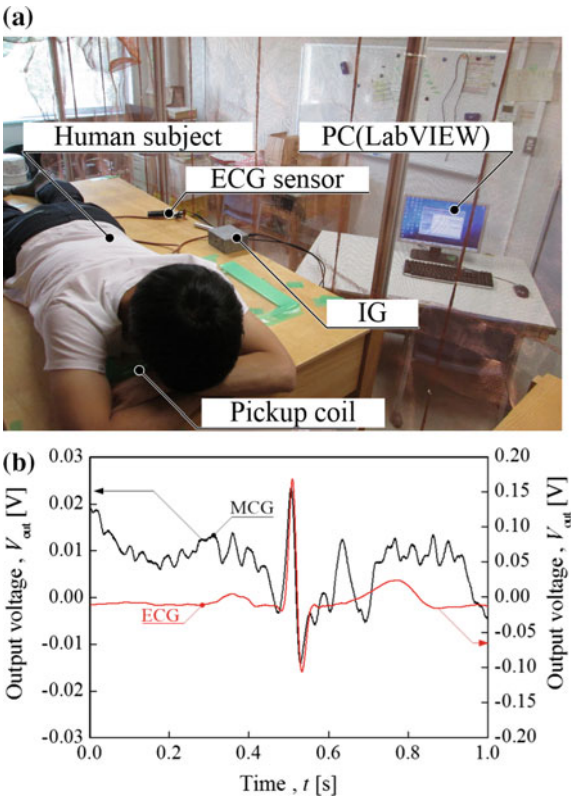

Fig. 36 MCG measurement result from a human heart. **a** Experimental setup. **b** Measured results (100 times averaging)

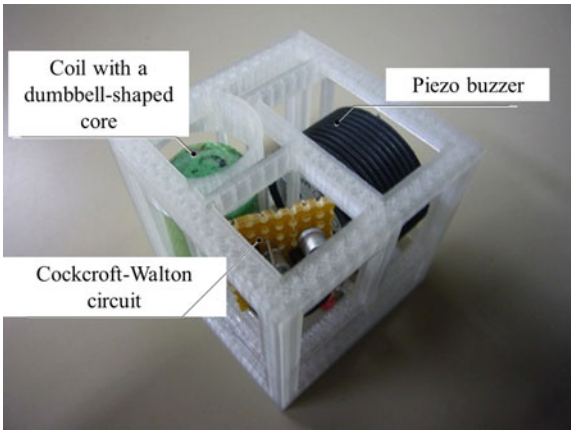

Fig. 37 An example of zero-power induction magnetometers, magnetic field alarm

when a magnetic field of 100 μT at 60 Hz was crossed to the coil. Although the details of this design will be published [43], the basis is as same as the induction magnetometer based on current detection model.

6 Conclusion

This chapter described the technical background and useful information to design induction magnetometers. In Sect. 1, from the author's point of view, the study of induction magnetometers were summarized. Some useful review papers and handbooks were also introduced. In Sect. 2, the operational principle was categorized into two, voltage and current detection models. To mention the motivation, some remarks were also presented with previous results. In Sect. 3, because the estimation of inductance is key point to design induction magnetometers based on the current detection model, useful approximations were summarized. In Sect. 4, several tips were summarized to design the electronics for weak and low-frequency magnetic fields. Although some optimization procedures were proposed, the simplified estimation of noise floor level described in this section could be useful for practical. In Sect. 5, some application related to induction magnetometers were summarized. To share future success related to induction magnetometers, several unsolved questions were also mentioned.

Acknowledgements I would like to great thank Prof. S.C. Mukhopadhyay, "Chandra-san" for me, in Massey University for providing this opportunity to summary the 10 years' study of induction magnetometers, and continuous supports when we were supervised by Prof. S. Yamada in Kanazawa University. I'd like to great thank Prof. I. Sasada in Kyushu University for giving an interested study topic related to magnetic shield which led to study this induction magnetometers. I'd like to great thank Prof. H. Wakiwaka in Shinshu University for valuable discussions related to not only magnetic sensors but also magnetic shield, actuator and other magnetic applications. I'd like to special thank students who supported this continuous study; Mr. A. Kakiuchi, A. Matsuoka, S. Inoue, Y. Uchiyama and T. Yamamoto and other students who belonged to our laboratory. It needed 10 years' study to detect a MCG signal form a human heart. It will be my great pleasure if this summary will help to lead the future success related to induction magnetometers given by young researchers.

References

1. H.C. Seran, P. Fergeau, An optimized low-frequency three-axis search coil magnetometer for space research. Rev. Sci. Instrum. **76**, 044502 (2005)
2. V.E. Korepanov, The modern trends in space electromagnetic instrumentation. Adv. Space Res. **32**, 401–406 (2003)
3. A. Roux, O. Le Contel, C. Coillot, A. Bouabdellah, B. de la Porte, D. Alison, S. Ruocco, M.C. Vassal, The search coil magnetometer for THEMIS. Space Sci. Rev. **141**, 265–275 (2008)
4. C. Coillot, J. Moutoussamy, R. Lebourgeois, S. Ruocco, G. Chanteur, Principle and performance of a dual-band search coil magnetometer: a new instrument to investigate fluctuating magnetic fields in space. IEEE Sens. J. **10**, 255–260 (2010)
5. E. Paperno, A. Grosz, A miniature and ultralow power search coil optimized for a 20 mHz to 2 kHz frequency range. J. Appl. Phys. **105**, 07E708 (2009)
6. V. Korepanov, R. Berkman, L. Rakhlin, Y. Klymovych, A. Prystai, A. Marussenokov, M. Afanassenko, Advanced field magnetometers comparative study. Measurement **29**, 137–146 (2001)

7. J. Lenz, A.S. Edelstein, Magnetic sensors and their applications. IEEE Sens. J. **6**, 631–649 (2006)
8. S. Tumanski, Induction coil sensors—a review. Meas. Sci. Technol. **18**, R31–R46 (2007)
9. P. Ripka, Magnetic sensors and magnetometers: Artech house (2001)
10. G. Müsmann, Y. Afanassiev, Fluxgate magnetometers for space research, BoD (2010)
11. S. Tumanski, Handbook of magnetic measurement, CRC Press, USA (2011)
12. G. Baule, R. Mcfee, Detection of magnetic field of heart. Am. Heart J. **66**, 95–96 (1963)
13. D. Cohen, Magnetoencephalography: evidence of magnetic fields produced by alpha-rhythm currents. Science, **161** (1968)
14. K. Tashiro, H. Wakiwaka, G. Hattori, Estimation of effective permeability for dumbbell-shaped magnetic cores. IEEE Transac. Magnet. **51**(1), 4, (2015) (to be published)
15. D. Cohen, A shielded facility for low-level magnetic measurements. J. Appl. Phys. **38**, 1295–1296 (1967)
16. K. Tashiro, S. Inoue, H. Wakiwaka, Advancement in sensing technology: new developments and practical applications (Chapter 9: Design of induction gradiometer for MCG measurement) vol. 1 (Springer, Berlin, 2013), pp. 139–164
17. K. Tashiro, H. Wakiwaka, K. Matsumura, K. Okano, Desktop magnetic shielding system for the calibration of high-sensitivity magnetometers. IEEE Trans. Magn. **47**, 4270–4273 (2011)
18. K. Tashiro, K. Nagashima, A. Sumida, T. Fukunaga, I. Sasada, Spontaneous magnetoencephalography alpha rhythm measurement in a cylindrical magnetic shield employing magnetic shaking. J Appl Phys, vol. 93, no. 15, pp. 6733–6735, 2003
19. K. Tashiro, Optimal design of an air-core induction magnetometer for detecting low-frequency fields of less than 1 pT. J. Magn. Soc. Jpn. **30**, 439–442 (2006)
20. R.J. Prance, T.D. Clark, H. Prance, Compact room-temperature induction magnetometer with superconducting quantum interference device level field sensitivity. Rev. Sci. Instrum. **74**, 3735–3739 (2003)
21. S.A. Macintyre, A portable low-noise low-frequency 3-axis search coil magnetometer. IEEE Trans. Magn. **16**, 761–763 (1980)
22. K. Tashiro, H. Wakiwaka, A. Kakiuchi, A. Matsuoka, Comparative study of air-core coil design for induction magnetometer with current-to-voltage converter, in *Proceedings of second international conference on sensing technology (ICST2007)* (2007), pp. 590–594
23. K.P. Estola, J. Malmivuo, Air-core induction-coil magnetometer design. J. Phys. E-Sci Instrum **15**, 1110–1113 (1982)
24. J.P. Wiksow, P.C. Samon, R.P. Giffard, A low-noise low imput impedance amplifier for magnetic measurements of nerve action currents. IEEE Transac. Biomed. Eng. **BME-30**, pp. 215–221 (1983)
25. M.C. Leifer, J.P. Wikswo, Optimization of a clip-on squid current probe. Rev. Sci. Instrum. **54**, 1017–1022 (1983)
26. A. Kandori, D. Suzuki, K. Yokosawa, A. Tsukamoto, T. Miyashita, K. Tsukada, K. Takagi, A superconducting quantum interference device magnetometer with a room-temperature pickup coil for measuring impedance magnetocardiograms. Jpn. J. Appl. Phys. Part 1-Regular Papers Short Notes & Rev. Papers **41**, 596–599 (2002)
27. R. Sklyar, Superconducting induction magnetometer. IEEE Sens. J. **6**, 357–364 (2006)
28. K. Tashiro, S. Inoue, H. Wakiwaka, Sensitivity limits of a magnetometer with an air-core pickup coil. Sens. Transduc. J. **9**, 171–181 (2010)
29. K. Tashiro, I. Sasada, Contact less current sensor with magnetic shaking techniquie (Preliminary studies on ultra-low noise induction sensor). JSAEM Stud. Appl. Electromagnet. Mech. **15**, 35–40 (2005)
30. F.W. Grover, Inductance calculations: dover phenix editions (2004)
31. K. Kajikawa, K. Kaiho, Usable range of some expression for calculation of the self-inductance of a circular coil of rectangular cross section. TEIONKOHGAKU **30**, 324–332 (1995). (in Japanese) (This article improved previous work given by J. Hak: El. u. Maschinenb. 51, 477 (1933))

32. H. Hastings, Approximations for digital computers (Sheet No. 46 and 49), Princeton, (1955). (This information referred to a Japanese book: S. Moriguchi, K. Udagawa and S. Hitomatsu, "IWANAMI SUUGAKU KOUSHIKI", Iwanami publishing, 22th edition, Vol. III, pp. 79–81, 2010)
33. K. Tashiro, H. Wakiwaka, T. Mori, R. Nakano, N.H. Harun, N. Misron, Sensing technology: current status and future trends IV (Chapter 7: Experimental Confirmation of Cylindrical Electromagnetic Sensor Design for Liquid Detection Application) (Springer, Berlin, 2014), pp. 119–137
34. K. Tashiro, A. Kakiuchi, A. Matsuoka, H. Wakiwaka, A magnetic contamination detection system based on a high sensitivity induction gradiometer. J. Jpn. Soc Appl Electromag. Mech. **17**, S129–S132 (2009)
35. K. Tashiro, Proposal of coil structure for air-core induction magnetometer. Proc. IEEE Sens. **2006**, 939–942 (2006)
36. Linear Technology, LT1028, Data sheet
37. R.J. Prance, T.D. Clark, H. Prance, Compact broadband gradiometric induction magnetometer system. Sens. Actuators a-Phys. **76**, 117–121 (1999)
38. K. Tashiro, Broadband air-core Brooks-coil induction magnetometer. SICE - ICASE **2006**, 179–182 (2006)
39. K. Tashiro, H. Wakiwaka, S. Inoue, Electrical interference with pickup coil in induction magnetometer, in *Proceedings of the 2011 Fifth International Conference on Sensing Technology (ICST2011)* (2011), vol. 90–93
40. K. Tashiro, S. Inoue, H. Wakiwaka, H. Yasui, H. Kinoshita, Induction magnetometer in MHz range operation. Sens. Lett. **11**, 153–156 (2013)
41. K. Tashiro, S. Inoue, Y. Uchiyama, H. Wakiwaka, H. Yasui, H Kinoshita, Induction magnetometer with a metal shielded pickup coil for MHz range operation. IEE J. Transac. Fundam. Mat. **131**(7), 490–498 (2010) (in Japanese) doi:10.1541/ieejfms.131.490
42. K. Tashiro, S. Inoue, K. Matsumura, H. Wakiwaka, A magnetic contamination detection system with a differential input type current-to-voltage converter, in *The Fourth Japan-US Symposium on Emerging NDE Cabpabilities for a Safer World* (2010), pp. 94–99
43. K. Tashiro, A. Ikegami, S. Shimada, H. Kojima, H. Wakiwaka, Design of self-generating component powered by magnetic energy harvesting—magnetic field alarm (Springer, Berlin, 2015), 21 pages (to be published)

Parallel Fluxgate Magnetometers

Michal Janosek

Abstract This chapter gives a brief overview of parallel fluxgate development, technology and performance. Starting from theoretical background through derivation of fluxgate gating curves, the fluxgate sensor is explained on its typical examples, including sensors with rod-, ring- and race-track core. The effects of geometry, construction and magnetic material treatment on parallel fluxgate noise are discussed in detail–noise levels as low as 2 $pT_{rms} \cdot Hz^{-0.5}$ are possible with state-of-the-art devices. Basic applications of fluxgate magnetometers are given and a quick overview of commercial devices is presented, concluded with recent advances in bulk, miniature, digital and aerospace devices.

1 Background

The parallel fluxgate sensor dates back to the 1930s [1] and most of this early knowledge remains valid until today, although refined by recent findings in the field of sensor noise, core magnetic materials and new principles of signal extraction. Since the early times, the noise level of several nanoteslas has continuously decreased due to evolution in electronic circuits and core materials to units of pT in a 10-Hz bandwidth.

The parallel fluxgate sensor in its simplest form is sketched on Fig. 1 (left)—the time-varying excitation flux Φ_E created in the ferromagnetic core via the excitation field intensity H_E (produced by the excitation coil) and the "measured" field H_M are in *parallel*.

A fluxgate sensor is basically a magnetic field sensor relying on induction law. For its simplest form of Fig. 1 (left), its output voltage U_i present at the pick-up coil terminal P is approximated by the following equation:

$$U_i = -N \cdot S \cdot \left(\frac{dB_E}{dt} + K \cdot \mu_0 \mu_r \cdot \frac{dH_M}{dt} + K \cdot \mu_0 \cdot H_M \frac{d\mu_r}{dt} \right) \quad (1)$$

M. Janosek (✉)
Department of Measurement, Faculty of Electrical Engineering,
Czech Technical University in Prague, Technicka 2, Prague, Czech Republic
e-mail: janosem@fel.cvut.cz

A. Grosz et al. (eds.), *High Sensitivity Magnetometers*, Smart Sensors,
Measurement and Instrumentation 19, DOI 10.1007/978-3-319-34070-8_2

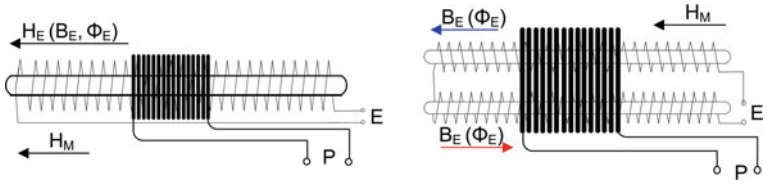

Fig. 1 (*Left*) Simplest parallel fluxgate with a rod-core. (*Right*) Modification with two cores

where H_M is the measured external magnetic field intensity with an eventual time-varying component, B_E is the alternating excitation flux density in the ferromagnetic core due to the excitation field intensity H_E, N is the number of turns of the pick-up coil, S is the core cross-sectional area, μ_0 is the permeability of vacuum and K is a dimension-less coupling coefficient of the core to the field H_M (real core geometry is far from an ellipsoid). The first term in parentheses is present because this simple sensor directly transforms also the excitation flux Φ_E to the pick-up coil, which is the basic disadvantage of this design. The second term is due to the eventually time-varying measured field H_M. However the key principle of a fluxgate sensor is in the last term of the equation—the alternating excitation ("drive") field H_E, which periodically causes the saturation of the magnetic material used in the fluxgate core, modulates the core permeability which has in turn a non-zero time derivative.

The sensor presented in Fig. 1 (left) is however impractical, although sometimes used in low-cost devices. Two cores can be used instead of one core, with each core having an opposite direction of the excitation flux, whereas the pick-up coil shares both of the cores—see Fig. 1 (right). If the core magnetic properties are same for both of them, the first term of Eq. 1—with eventually large disturbing amplitude—is effectively suppressed by the common pick-up coil.

If the measured magnetic field H_M is constant, the second term is also zero and only the third term of Eq. 1 remains as fluxgate output. In agreement with [2] and [3] we can then write for the fluxgate output voltage:

$$U_i(t) = -NS \cdot \mu_0 H_M \cdot \frac{d\mu_r}{dt} \frac{1-D}{[1+D(\mu_r-1)]^2} \tag{2}$$

The "coupling coefficient" K in Eq. 1 was replaced by an equation introducing the dimension-less demagnetization factor D of a ferromagnetic body (fluxgate core).

2 The Physical Model

2.1 Fluxgate Transfer Function

The sensor depicted in Fig. 1 (right) can be used for deriving the parallel fluxgate operation principle. As we have two core slabs sharing the same, but opposite-in-direction excitation field H_E (yielding in time-varying $\Phi_E(B_E)$ in the

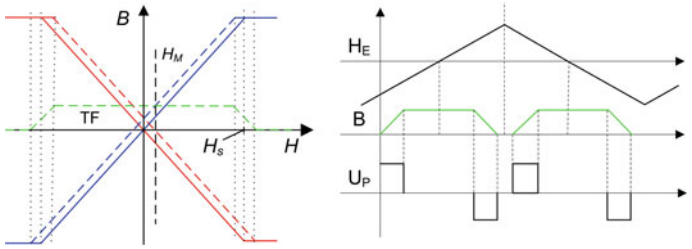

Fig. 2 (*Left*) Transfer function—ideal BH curve. (*Right*) Output voltage derivation with triangular excitation

core), we can draw the corresponding B-H loops for each core (which correspond to one-half of the magnetizing cycle) as seen in Fig. 2 (left). The core B-H loop was simplified to an ideal one with no magnetic hysteresis with H_S standing for the field intensity where it becomes saturated; the red curve corresponds to the lower core of Fig. 1 (right) and the blue one to the upper core. Without any external field H_M (solid curves), if both characteristics are summed, the net change of B during the half excitation cycle is zero. A non-zero external measured field H_M however effectively adds to the exciting field H_E and the resulting B-H loops are shifted (dashed curve). After their summation for both cores we obtain an effective "B-H transfer function" TF or "gating-function": the flux in the core (core flux density) is being periodically gated by the excitation field, the threshold is set by the H_S value and size of the external field H_M.

Now considering a triangular waveform of the excitation field H_E as in Fig. 2 (right) and applying the transfer function TF to it, we can derive the output voltage at the pick-up coil U_P as the core flux density B derivative. It can be seen that the output voltage is at twice the frequency of H_E and its magnitude and also phase lag would be proportional to the measured field H_M.

When taking into account also the material hysteresis, the transfer function will modify accordingly [2] as shown in Fig. 3 (left). However the approach-to-saturation

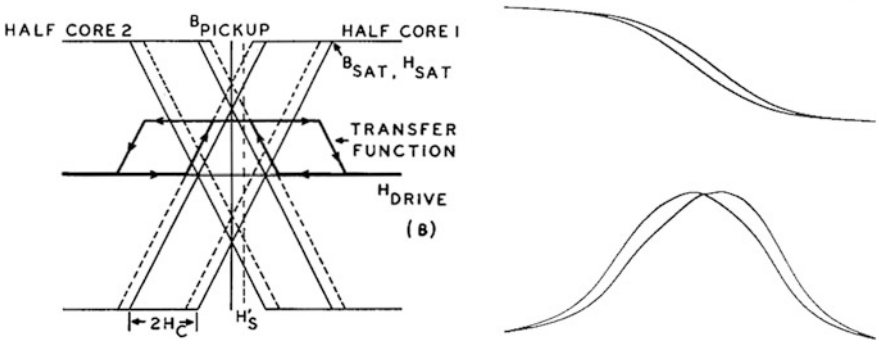

Fig. 3 (*Left*) Gating function with hysteresis from [2]. (*Right*) Real gating function from [3]

shown in Figs. 2 (right) and 3 (left) is not realistic—in Fig. 3 (right) a real BH loop and the corresponding gating function are shown.

An analytical approach to derive the fluxgate output signal was done as early in 1936 [1] and since then many improvements in the model were achieved, also by applying a Fourier-transform to the pulse-train shown in Fig. 2 (right), see [2–5]. However the original Aschenbrenner's approach is shown below since it gives a simple analytical demonstration of the origin of second harmonic in the fluxgate output signal.

Let's have a very simple approximation of the BH magnetizing curve [1], assuming the coefficients $a > 0,\ b > 0$:

$$B = a \cdot H - b \cdot H^3 \tag{3}$$

At each of the magnetic cores of Fig. 1 (right), the measured field H_M and the harmonic excitation field $H_E = A \sin \omega t$ are summed up:

$$H_{1,2} = H_M \pm H_E = H_M \pm A \sin \omega t \tag{4}$$

The corresponding flux density B in each of the two cores is then expressed using Eq. 3:

$$B_{1,2} = a(H_M \pm A \sin \omega t) - b(H_M \pm A \sin \omega t)^3 \tag{5}$$

$$\begin{aligned} B_{1,2} = {} & a \cdot H_M - b \cdot H_M^3 - \frac{3}{2} b \cdot A^2 \cdot H_M \\ & \pm \left(a \cdot A - 3b \cdot A \cdot H_M^2 - \frac{3}{4} b \cdot A^3 \right) \sin \omega t \\ & + \frac{3}{2} b \cdot A^2 H_M \cos 2\omega t \ \pm \ \frac{1}{4} b \cdot A^3 \sin 3\omega t \end{aligned} \tag{6}$$

If both cores are of equal cross-section S, the flux is then added by the means of common pick-up coil and after summing we get the remaining terms:

$$\begin{aligned} \Phi &= S \cdot (B_1 + B_2) \\ &= 2S \cdot \left(a \cdot H_M - b \cdot H_M^3 - \frac{3}{2} b \cdot A^2 \cdot H_M + \frac{3}{2} b \cdot A^2 H_M \cos 2\omega t \right) \end{aligned} \tag{7}$$

The only time-varying component is at the second harmonic of excitation field frequency:

$$\Phi(t) = 3S \cdot b \cdot A^2 \cdot H_M \cos\ 2\omega t \tag{8}$$

Again we see that the time-varying output is at the second harmonics of the excitation frequency and its amplitude is directly proportional to the measured, static field H_M. If H_M was time-varying, there would be also a signal at the fundamental frequency. In reality, however, also higher-order even harmonics are

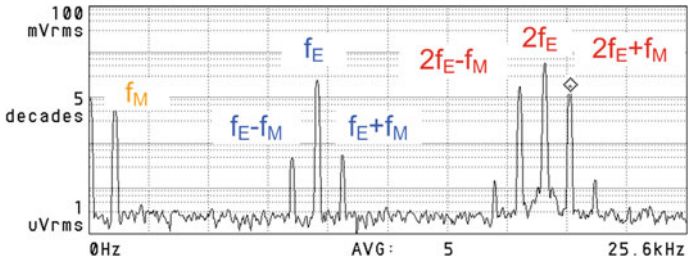

Fig. 4 The ac-driven fluxgate output spectrum

present, due to the nature of the B-H loop (hysteresis, approach to saturation) and non-sinusoidal excitation waveforms with higher harmonics. These effects are taken into account by the modern fluxgate models [2–5].

2.2 *The Fluxgate as a Modulator*

A real-world output of a fluxgate sensing a field H_M with both ac and dc component can be seen in Fig. 4—f_M is the frequency of alternating component and f_E is the excitation signal frequency. Signal at f_E which is present due to non-ideal symmetry of the sensor: i.e. the complementary terms of Eq. 6 are not exactly of the same amplitude and phase, so they do not subtract completely. The signal exactly at the second harmonics $2f_E$ is due to the dc component of H_M. The measured field H_M is thus modulated on the excitation second harmonics. However due to the non-ideal symmetry of the sensor, it appears modulated also on the fundamental excitation frequency f_E. This applies not only to dc but also to the ac signal at f_M, which appears at $2f_E \pm f_M$ and $f_E \pm f_M$.

It can be concluded from the spectrum in Fig. 4 that an alternating signal is amplitude-modulated with a carrier on the 2nd harmonics of fluxgate excitation frequency, while the amplitude of the carrier is proportional to the dc component of the signal. This can be proven by substituting $H_M + B{\cdot}\cos(\psi t)$ for H_M in Eq. 8. If the excitation field would contain higher harmonics, there will be also higher modulation harmonics present in the spectra and the higher-order even harmonics will contain the information about the measured magnetic field.

3 The Parallel Fluxgate Noise

The fluxgate noise generally exhibits a $1/f$ behavior with a noise amplitude spectral density $(\mathrm{ASD} = \sqrt{\mathrm{PSD}})$ as low as 2–3 $\mathrm{pT_{rms}\ Hz^{-0.5}}$ @ 1 Hz, typically $\sim 10\ \mathrm{pT_{rms}\ Hz^{-0.5}}$. However, the noise due to the magnetometer electronic circuitry mostly limits at least the white noise floor (amplifier noise, detector phase

noise etc.), which makes measuring the fluxgate noise difficult and subject to large statistical errors.

The actual fluxgate noise can be related to three effects—stochastic behavior of the Barkhausen noise, or better explained as irreversible rotation and domain wall-displacement process during the fluxgate magnetizing cycle [6–8], thermal white noise [9] and an excessive, small-scale noise [10] which is seen at many fluxgates with supposedly low Barkhausen noise. The latter is believed to originate from inhomogeneous, stochastic magnetoelastic coupling of the non-zero magnetostrictive core to external stresses [11] rather to magnetostrictive movement itself [12]. The white noise of the pick-up coil does not have much influence, since although with increasing coil turns resistance increases but also the voltage sensitivity increases.

An important factor is the coupling of the "internal" fluxgate core noise to the actual sensor noise via the core demagnetization factor D. It can be written [13]:

$$B_{SensorNoise} \cong DB_{CoreNoise} \tag{9}$$

For Barkhausen noise, it was shown by van Bree [6], that minimum detectable signal H_0, which is equal to noise for SNR 0 dB, can be expressed as

$$H_{0(Bh)} = \frac{B_S}{\mu_0 \mu_r} \sqrt{\frac{\tau}{N_B \cdot t_m}} \tag{10}$$

where τ is the magnetization period lower limit (inverse of excitation frequency), t_m is the measurement time, B_s is the saturation flux density and N_B is the density of Barkhausen volumes after Bittel and Storm [8]. For the lower limit of $N_\mathrm{B} = 10^4$, $\tau = 10^{-6}$ s, $t_\mathrm{m} = 1$ s and $\mu_\mathrm{r} = 8000$ [6], H_0 yields in about 2×10^{-6} A/m (2 pT in air) which corresponds to the state-of-the art materials with low Barkhausen noise [14].

The white noise is usually estimated according to the (thermal) fluctuating current in the core: the component perpendicular to the core axis creates magnetic field noise, which couples to the pick-up coil [9]—Eq. 11.

$$I_{core}\left[\frac{A_{rms}}{\sqrt{\mathrm{Hz}}}\right] = \sqrt{\frac{4kT}{R_{core}}} \tag{11}$$

This "white-noise current" is also present at the 2nd harmonics. In this case, Eq. 11 should take into account the core "effective resistance" Re{Z} due to the skin-effect. However, since now we are considering only the correlated component at the 2nd harmonics, the noise couples to the pick-up coil only by the (low) residual transformer term of Eq. 1.

For usual core volumes, the predicted white noise is at least an order of magnitude below the observed fluxgate noise: for the race-track sensor [9] with 2 $\mathrm{pT_{rms}\,Hz^{-0.5}}$ @ 1 Hz the white noise was about 0.39 $\mathrm{pT_{rms}\,Hz^{-0.5}}$. In a single-domain fluxgate [14], white noise about 50 fT was reported utilizing a cross-spectral measurement technique.

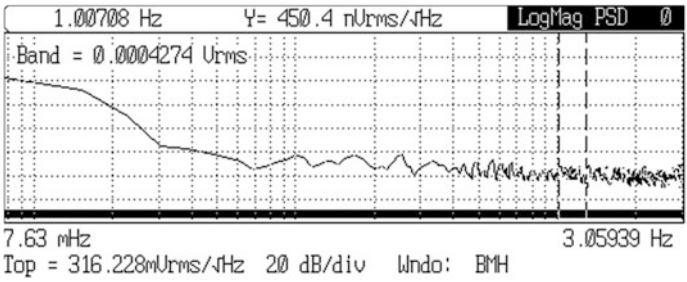

Fig. 5 Typical fluxgate magnetometer noise (TFM100G2, 100 kV/T, SR770)

A typical fluxgate noise is depicted below in Fig. 5—the low-noise TFM100G2 magnetometer of Billingsley A&D exhibits approximately 1/f character between 10 and 300 mHz and almost white response starting at 1 Hz with ASD about 4.5 pT_{rms} $Hz^{-0.5}$, which is a limit of the electronics, not the sensor itself.

4 Fluxgate Geometry and Construction

The core geometry plays an important role in constructing the parallel fluxgate sensor: the sensors can be roughly divided in two families according to core geometry. Rod sensors utilize cores with open magnetic path, ring-cores and race-tracks use closed path cores.

4.1 Rod Sensors

The design using two magnetic rods as in Fig. 1 (right) with a common pick-up coil was used already in 1936 by Aschenbrenner and it is also often referred as "Förster configuration" after the researcher and manufacturer F. Förster who utilized it. An example is in Fig. 6 with two thin Permalloy cores in glass tubes, on top of which the excitation coils are wound [compare to Fig. 1 (right)]. Alternatively, there can be two pick-up coils anti-serially connected which would be wound directly on the excitation coils—the so-called "Vacquier configuration" patented by V. Vacquier in 1941.

The advantage of rod sensors is low demagnetization factor due to the favorable ratio of cross-section and length which is in the direction of measured field. The disadvantage is that due to the open magnetic path the level of saturation is different across the core length, causing problems with sensor offset. The pick-up coil is then placed not to cover the noisy, unsaturated core ends [15].

Fig. 6 The rod fluxgate (Förster type) before assembly

4.2 Ring-Core and Race-Track

As stated previously, the construction of a parallel fluxgate should assure good symmetry to suppress unwanted excitation signal and also possibly to reduce the noise by strong excitation field: this can be obtained with a closed-path magnetic core. In terms of Eq. 4, the sensor can be virtually divided to two "core halves" with opposite excitation field direction—see Fig. 7. The key advantage of the ring-core [Fig. 7 (left)] is the possibility to rotate the pick-up coil in order to obtain best suppression of the residual excitation signal (due to transformer term in Eq. 1). Its disadvantage is the relatively large demagnetization factor decreasing its sensitivity when compared to the rod designs. To decrease the demagnetization factor, a sensor with an oval, race-track shape of ferromagnetic core [Fig. 7 (right)] is often designed. However its balance is not easily achieved as for ring-cores.

4.3 Bulk Sensors and Micro-fluxgates

The classical parallel fluxgate is a bulk-type, i.e. it uses magnetic core material from magnetic tape/wire or even a bulk material with wire-wound excitation and pick-up

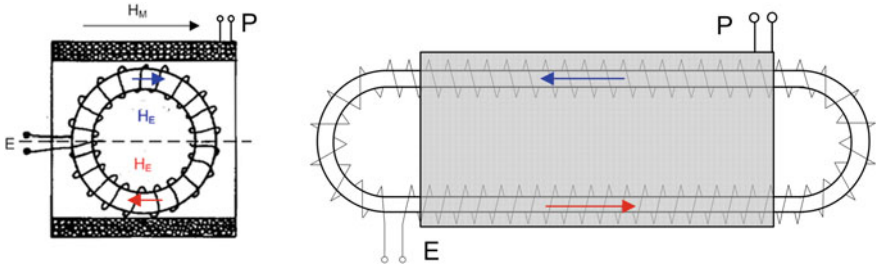

Fig. 7 (*Left*) The ring-core with H_E in "core halves." (*Right*) The race-track sensor

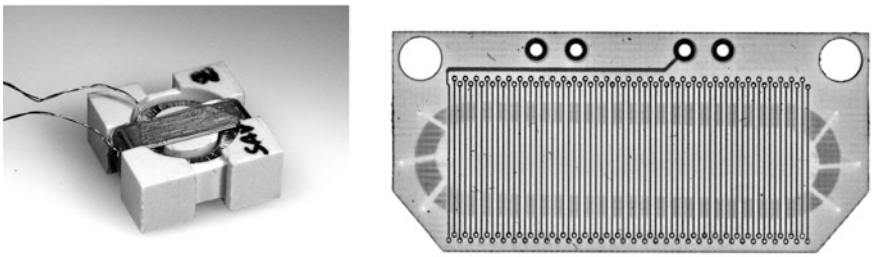

Fig. 8 (*Left*) The real 12-mm-dia ring-core is a typical bulk sensor. (*Right*) The 30-mm long race-track is created in PCB technology

coils. The final core shape in larger sensors is then obtained by winding the magnetic tape [16] or the annealed wire [14] to a core holder [Fig. 8 (left)]; a stress-free alternative is etching or arc-cutting the final core shape from a wide magnetic tape [17]. The advantage of bulk fluxgates is their high sensitivity due to large cross-section and high number of pick-up coil turns, and also low demagnetization factor achievable with long sensors. Disadvantages are their cost and mass which start to be a limiting factor even in aerospace applications where bulk fluxgates still find use [18]. An approach to at least simplify the manufacturing design has been done with PCB fluxgate sensors [19]—Fig. 8 (right), however despite the comparable size their parameters are inferior to that of classical ones mostly due to residual stresses after manufacturing (bonding of the ferromagnetic core) [20]. Electroplated ring-core fluxgates on PCB substrates have been presented by Butta [11], the thin layer was advantageous for high-frequency performance of the sensor.

Fluxgate micro-sensors appear since the end of 1980s. Their limitation is mostly very low sensitivity, resulting in 1-Hz ASD about 1 nT_{rms} $Hz^{-0.5}$ even when using excitation frequencies in the range of 1 MHz. The way of magnetic core manufacturing is often limited by desired sensor design: the need for solenoid coils and integrating the core mostly leads to MEMS devices; CMOS devices rely on flat-coils with worse coupling to the ferromagnetic core. An integrated micro-sensor core would require electrolytic deposition [21], integrating the etched tape [22] or sputtering [23].

5 Fluxgate Noise and Ferromagnetic Core

During the 80 years of fluxgate development, it has been finally understood that the core parameters are the key for a low-noise, high-sensitivity sensor [14, 16, 24]. The ferromagnetic core for a parallel fluxgate should fulfill several requirements arising from Eq. 2 and the principle of operation; these requirements affect several different parameters. Table 1 shows the list of required parameters and the most affected property.

Table 1 Influence of core parameter on fluxgate performance

Core parameter	Primary effect	Secondary
Low demagnetization factor	Sensitivity	Noise
Low Barkhausen noise	Noise	–
Low magnetostriction, low applied stresses	Offset	Noise
High permeability	Sensitivity	Power consump.
Approach to saturation	Noise	–
Thickness/resistivity	Losses	High f operation
Curie temperature	Operating range	Noise

5.1 Core Shape—Demagnetization Factor

Keeping the core demagnetization factor D low (lowest for rod-type sensors) not only allows for high sensitivity to external fields (Eq. 2) but also provides better ratio to the "core noise"—see Eq. 9. Thus a common practice to decrease sensor noise, if the limits of improving the magnetic material are reached, is to decrease D.

The demagnetization factor of a ring-core with a diameter d and effective core thickness T was estimated from a number of calculations and measurements [13]:

$$D \cong 0.223\ (T/d) \tag{12}$$

However it is relatively easy to model D it in today's FEM packages for arbitrary shapes. In Fig. 9 (left), the demagnetization factor of a 10-mm ring-core was calculated using ANSYS and also FLUX 3D software. The ferromagnetic tape was 20 μm thick and 2.6 mm wide with μ_r = 15,000. The resulting demagnetization factors for 5, 18 and 46 tape turns agree well with that calculated by Eq. 12. The relation between fluxgate noise and the demagnetizing factor due to Eq. 9 as proposed by Primdahl was later proved for large ring-core sensors [25]—the typical dependence is depicted in Fig. 9 (right). The increased noise at very low D values appears due to the fact that a smaller cross-section causes loss of SNR, assuming the existence of external induced noise coherent to the 2nd harmonic.

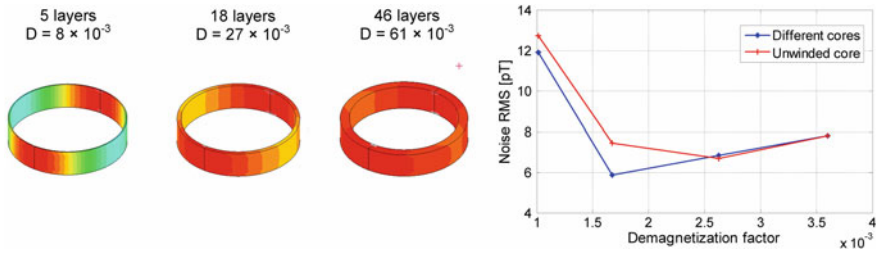

Fig. 9 (*Left*) Calculated demag. factor D of 10-mm ring [25]. (*Right*) Noise versus D for 50-mm rings

5.2 Core Material and Processing

Historically, the core materials were iron [1] or ferrites [3]. Later crystalline Ni-Fe started to be used in the form of tapes or rods ending up with specially annealed Molybdenum-Permalloy tapes [26] which are still being utilized in space research [18]. With these crystalline materials, the cores have to be annealed with the material already in its final shape. The inherent advantage of Permalloys is their high Curie temperature, allowing for high temperature operation, however special care of the material composition is necessary to achieve near-zero magnetostriction. Since 1980s there is a widespread use of amorphous materials, mostly in form of thin tapes and wires, which do not require hydrogen annealing in the final form and are less mechanically sensitive. Cobalt-based amorphous materials tend to be the best candidates for the sensors [16] however also in this case sufficient annealing process is necessary to obtain the same or better performance than the heritage Mo-Py cores.

Low Barkhausen noise is generally obtained in materials with very low area of the hysteresis loop with prevalent domain-wall rotations rather than domain-wall movements. This is achieved usually by perpendicular-field or stress annealing of the magnetic material to introduce perpendicular anisotropy, thus promoting domain-wall motion rather than sudden jumps due to the domain wall movement [16, 24]. Influence of Curie temperature on noise was studied by Shirae for various amorphous compositions [27]—a strong correlation between low Curie temperature and low fluxgate noise was found.

Since the end of the 20th century, nanocrystalline materials receive great attention because of their good thermal stability and stable phase, which makes them suitable for down-hole drilling [28] and possibly in space research. However their disadvantage is the relatively high saturation induction, requiring high excitation power and higher noise even after proper annealing.

6 The Feedback Compensated Magnetometer

The diagram of a typical feedback-compensated fluxgate magnetometer is on Fig. 10. The magnetometer usually uses feedback in order to achieve better stability and linearity of the device: the measured field is zeroed by an artificial field with opposite sign, created either by a coil shared for also for voltage pick-up, or by a separate compensating coil. The standard means of achieving the compensation field is using an integrating regulator feeding a feedback resistor or driving an active current source.

Alternatively, for full-vector magnetometers, the feedback coils can be integrated to a triaxial coil system where the orthogonal sensor triplet is placed, assuring high homogeneity of the compensating field and suppressing the parasitic sensitivity to perpendicular fields [30]. Also the mutual influence of feedback fields of the closely located sensors is suppressed.

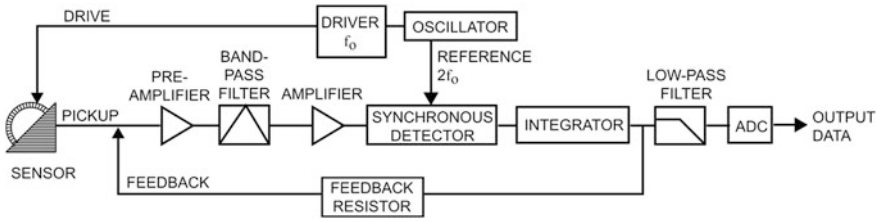

Fig. 10 The feedback compensated magnetometer from [29]

The sensitivity of the compensated magnetometer depends—by its operating principle—only on the coil constant of the compensating coil. The open-loop sensitivity (given by number of pick-up coil turns, core volume, demagnetization factor, permeability, drive waveform etc.) then affects the noise or resolution of the magnetometer, which ideally remains the same as in open-loop. The magnetometer linearity can be in tens of ppm and its gain stability better than 20 ppm/K, which in a good design is limited by the thermal expansion of the compensating coil (and its support) rather than by the electronics itself [30]. However, even for best magnetometers, the real-world limiting factor affecting the magnetometer resolution is the sensor offset and its temperature drift, which are not suppressed by the feedback loop. The offset is frequently caused by the non-ideal excitation waveform, which may contain parasitic signal at second-harmonic, which is not suppressed due to finite balance of the pick-up coil and the two ferromagnetic cores (or core halves). The core itself can be further affected by perming (i.e. large field shock, which causes change in the core remanence). Another significant contribution to the offset is the core in-homogeneity and its magnetostrictive coupling to inhomogeneous external stresses [12]; much lower contribution is to be expected from the electronics, such as amplifier non-linearity and detector offset. A detailed study of influence of the electronics on magnetometer parameters was presented by Piel [31].

6.1 Magnetometer Electronics

6.1.1 Analog

Signal processing of the pick-up voltage in an analog design normally uses an appropriate circuit for phase-sensitivite, dc-coupled down-conversion of the modulated signal on 2nd excitation harmonics (synchronous detector—phase sensitive detector/mixer)—this is done mainly when the fluxgate output signal at the pickup-coil can be “tuned” by a resonant capacitor to suppress higher-order even harmonics. Another detection possibility is “in time-domain” by integrating the output voltage [20]. Alternatively, it is possible to “short-circuit” the output

fluxgate terminals by a current-to-voltage converter and then process the pulse-like signal proportional to the gated flux [32]. Other techniques use the information of time-lag of the fluxgate output pulses in a special detector circuit [33, 34].

After the detector circuit, the feedback regulator (integrator) stage assures the feedback current, which is sensed, filtered and its value processed in an A/D converter. The fluxgate excitation (oscillator + driver in Fig. 10) in reality does not use sine-wave or triangular excitation signals, as shown in the derivation of the fluxgate output function. In order to save power, either pulse excitation using H-bridge is used [20] or the excitation circuit is "tuned", i.e. the excitation waveform is generated by switches and the non-linear inductance of the excitation circuit is tuned to serial-parallel resonance obtaining sharp excitation peaks. In that way the losses in the excitation circuit can be lowered only to ohmic losses of the excitation winding, moreover it was shown that the amplitude of the excitation signal has an inverse proportional effect on sensor noise [35].

6.1.2 Digital

Early digital magnetometer designs ended up with higher noise than the analog fluxgate with its D/A converter, however at least in space applications the trend is to integrate the electronics to an ASIC which can be further radiation-hardened for aerospace applications. The signal path historically utilized appropriate analog-to-digital converters and signal processing in DSP/FPGA together with D/A converters for feedback [36].

Recently, the fluxgate sensor was successfully integrated in an higher-order delta-sigma feedback loop electronics [37]—the power consumption of the corresponding ASIC (Fig. 11), which carries out the signal demodulation, feedback compensation and digital readout, was only 60 mW and the magnetometer performance was at least equivalent to 20-bit+ analog magnetometers with delta-sigma ADC's [38].

7 Applications

The first fluxgate applications appeared in the field of geomagnetic studies [1] and later also in the military or defense sector—"flux-valves" served for detection of ships or submarines [39]. After WWII, fluxgates have been extensively used in compasses/gyrocompasses in shipping and aviation [40], they have also found their use in attitude control of rockets or missiles and later they started to be used also on satellites [41]. Fluxgate sensors have been used in planetary studies since the early Apollo missions [26] and remained in their form almost unchanged—despite improved electronics—in the aerospace segment up to today [18]. Geophysical prospecting used aircraft-mounted fluxgates from the very beginning, and since

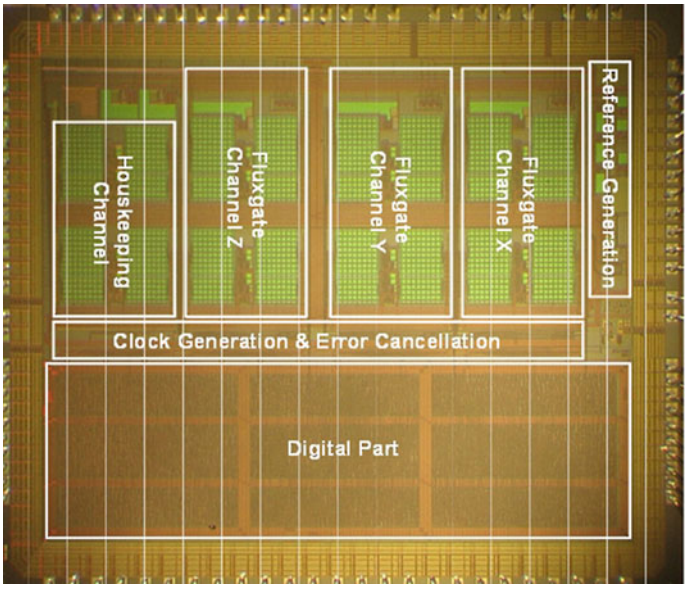

Fig. 11 Microphotograph of the MFA fluxgate ASIC. Reprinted from [37] with kind permission of the author

1980s, sufficient methods appeared to precisely calibrate the sensors, which allowed their use even onboard spacecraft for satellite-based geophysical research [42, 43].

One of the most common applications of a fluxgate for ground-based surveys is a magnetic gradiometer, consisting mostly of two aligned uniaxial sensors or two triaxial sensor heads. For a single-axis gradiometer, the estimated gradient dB_x/dx would be an approximation from two sensor readings B_{x1} and B_{x2} in a distance d:

$$\frac{\partial B_x}{\partial x} = \lim_{d \to 0} \frac{B_{x1} - B_{x2}}{(x_1 - x_2)} \cong \frac{B_{x1} - B_{x2}}{d} = \frac{\Delta B_x}{\Delta x} \tag{13}$$

Equation 13 implies the high requirements on individual fluxgate sensor noise if the sensor spacing d should be reasonable, i.e. below 1 m. Metal or UXO (Unexploded Ordnance) detectors using fluxgate find application also in underwater mine-hunting [44] and because of the cheap computational power now available, they are even constructed as full-tensor gradiometers which allow for localizing the magnetic dipole.

There also exist fields in biomedicine where fluxgate (gradiometers) have found their application: magneto-relaxometry (MRX) [45] and magneto-pneumography (MPG) [46]. Parallel fluxgate—or at least their principle—are also used for contact-less, precise dc/ac current measurements [34, 47].

8 Commercial Fluxgates

8.1 Magnetometers

There are actually very few suppliers who would sell good-quality fluxgate sensors separately—complete magnetometers are mostly offered. One common configuration is a triaxial magnetometer with analog outputs, the transfer constant (sensitivity) is mostly 100,000 V/T. Such instruments are for example of TFM100G2 (Billingsley Aerospace & Defense, USA), MAG03 (Bartington, UK), FGM3D (Sensys, Germany), TAM-1 or LEMI 024 of Laboratory of Electromagnetic Innovations (Lviv, Ukraine). Digitalization of these analog instrument outputs is upon the user or a special hardware is available from the manufacturers. Magnetometers which feature digital outputs (d-) are e.g. the Billingsley DFMG24, LEMI-029, the 3-axis magnetometer of Förster, Germany and FVM-400 of MEDA, USA. Table 2 summarizes most important parameters of the mentioned magnetometers.

8.2 Fluxgate Gradiometers/UXO Detectors

Table. 3 shows parameters of several commercially available gradiometers (UXO detectors), as manufactured by Schonsted (WV, USA), Förster (Germany), Geoscan (UK) or Bartington (UK). Although the gradiometer noise can be a parameter for selecting the best instrument, in reality, the gradiometer resolution is given by gradiometer calibration (astatization) which limits its real-world performance: the large, homogeneous Earth's field will cause false response unless the gradiometer is perfectly aligned or calibrated.

Table 2 Parameters of several commercial magnetometers

Magnetometer type	Range (±μT)	Noise (1 Hz) ($pT_{rms}/\sqrt{Hz}$)	3-dB BW (kHz)	Offset drift (nT/K)	Power (W)
TFM100G2	100	5–10	0.5/4	0.6	0.4
MAG03	70	6–10–20	3	0.1	0.5
FGM3D	100	15	2	0.3	0.6
LEMI 024	80	6	0.5	N/A	0.35
d—FVM-400	100	N/A	0.05/0.1	N/A	0.55
d—DFMG24	65	20	0.05	0.6	0.75
d—LEMI-029	78	6 (w/comp)	0.18	N/A	0.5
d—Förster 3-Axis	100	35	1	1	3.6

Table 3 Parameters of several commercial gradiometers

Gradiometer type	Base (m)	Resolution (nT/m)	Mass (kg)	Power (W)
Schonsted GA52Cx	0.5	N/A	1.1	0.2
Förster Ferex (0.6 m, w/logger)	0.65	1.5	4.9	2
Geoscan FM256	0.5	2	2.5	0.5
Bartington GRAD601 (w/logger)	1	<1	1.3	1.1

9 State of the Art—Recent Results

Recent achievements, either in the field of sensors, or in final magnetometers/gradiometers, are mainly determined by improving the ferromagnetic core material and sensing technologies.

9.1 Bulk Sensors, Magnetometers and Gradiometers

A fluxgate magnetometer with high-temperature rating of +250 °C was presented by Rühmer [28], the sensor core utilized nanocrystalline Vitroperm VP800R. Similar study was done before by Nishio [48] for Mercury exploration satellite, where the sensor characteristics were measured in −160 to +200 °C range.

Noise of a miniature, 10-mm diameter amorphous ring-core fluxgate was shown to decrease by field-annealing down to 6 pT_{rms} $Hz^{-0.5}$ @ 1 Hz [24] which is comparable to the state-of-the-art 17-mm aerospace sensors of the Danish Technical University [30] and also crystalline Mo-Py sensors used by the Geophysics and Extraterrestrial Physics group of the Technical University Braunschweig, Germany [18]. By decreasing the demagnetization factor by optimizing core geometry and the core cross-section of large ring-cores, it was shown by the author that 2 pT_{rms} $Hz^{-0.5}$ can be achieved even with an as-cast tape [25]. The problem with low sensitivity of miniature fluxgates was addressed by Jeng [49] who showed an improvement of 2× in the miniature magnetometer noise by using information from multiple even harmonics.

A study relating the magnetostrictive coupling of fluxgate core to external stresses with fluxgate noise was done by Butta [11]. The origin of the fluxgate offset was recently studied by Ripka [12] and it is—together with excessive noise—believed to be the effect of (local) magnetoelastic coupling, if other sources like perming or offset due to electronics are excluded.

In the field of gradiometers, the state-of-the art in axial devices is still the construction of DTU [50] with two triaxial vectorially-compensated heads, separated by 60 cm: the achieved resolution was 0.1 nT_{rms} m^{-1}. An underwater "real-time-tracking autonomous vehicle" developed at Naval Surface Warfare

Center, FL, USA [51] exhibited noise below 0.3 nT m^{-1} $Hz^{-0.5}$ @ 1 Hz, after compensating the vehicle noise. Recently, a similar full-tensor gradiometer vectorially compensated by a compact-spherical-coil was shown by Sui [52], which has the perspective to further decrease the gradiometer error and increase its sensitivity due to common compensation of the homogeneous field for all the 4 × 3 sensors.

9.2 *Micro-fluxgates*

A low-noise MEMS microfluxgate with nanocrystalline core embedded by chemical etching and with 3D solenoid coils was presented by Lei [22]. The sensor size was 6 × 5 mm^2 and the noise was as low as 0.5 nT $Hz^{-0.5}$ @ 1 Hz. Texas Instruments has recently published a CMOS-integrated Förster-type micro-fluxgate for contactless current sensing using a gradiometric arrangement [53]. It is also intended for closed-loop current measurement, where it replaces the common Hall-probe in the yoke gap. Its microphotograph is in Fig. 12: the Förster sensor is shown together with the excitation and signal-processing electronics. The microfluxgate operates at 1 MHz, achieves 0.2 mA resolution and was released as "DRV421". Recently, also a standalone micro-fluxgate in a 4 × 4 mm^2 QFN chip was released, with a noise of 1.5 nT $Hz^{-0.5}$ @ 1 kHz [54].

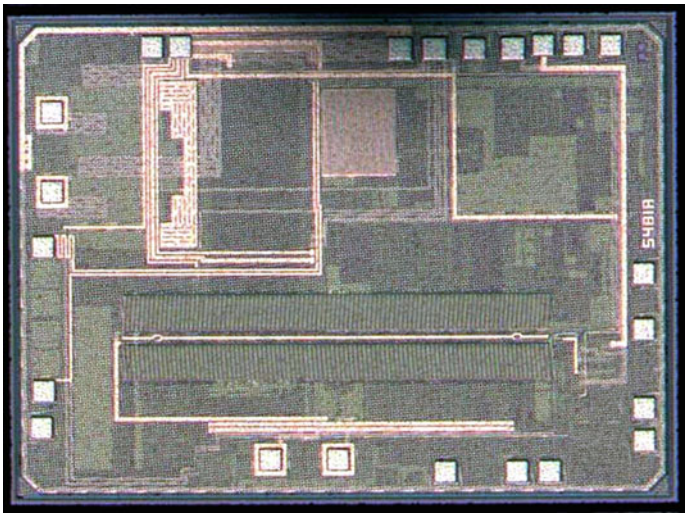

Fig. 12 The CMOS integrated Förster fluxgate, reproduced with kind permission of Texas Instruments, Inc

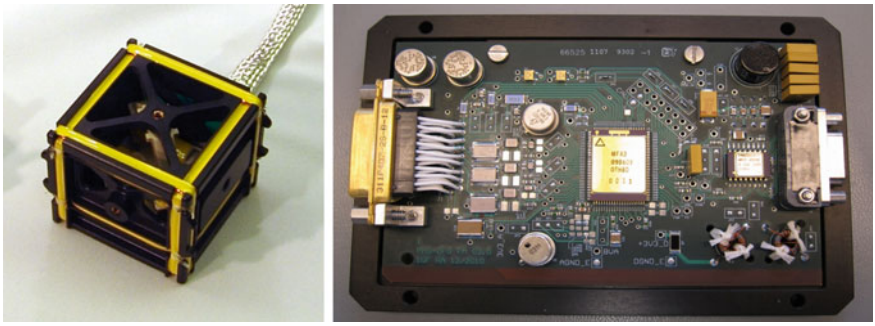

Fig. 13 The magnetic sensor and digital electronics of MMM mission (flight model, not to scale) —reproduced with kind permission of Werner Magnes /IWF Graz

9.3 Space Applications

An offset-reduction technique proposed by DTU for satellite missions [55] allowed to decrease offset drift of the heritage analog magnetometer design [30] to ±0.5 nT in a 73 °C range—the temperature changes in the excitation resonant circuit were compensated by an adaptive control of the detector phase. The digital-detection delta-sigma magnetometer of the THEMIS mission (launched 2007, still active) achieved offset stability of approximately 0.05 nT/K in the −55 to 60 °C temperature range [18]. These parameters became the state-of-the art in space fluxgate magnetometers.

The recently successful ROSETTA Explorer and its lander PHILAE used fluxgate magnetometers; the instrument noise was about 22 pT_{rms} in 0.1–10 Hz band [56]. The SWARM multi-satellite mission, launched in 2013, carries onboard several atomic magnetometers and also traditional fluxgates from DTU Denmark, and is now producing valuable data for a new Earth's field model and other geophysical observations [43]. A similar NASA "Magnetospheric Multiscale Mission" was launched in March 2015; the spacecraft carries analog and also delta-sigma-loop-integrated magnetometers with custom ASIC developed at the IWF Graz, Austria [37]—see Fig. 13. Multiple magnetometers have been used and large effort was made to achieve magnetic cleanliness [38].

References

1. H. Aschenbrenner, G. Goubau, Eine Anordnung zur Registrierung rascher magnetischer Störungen. Hochfrequenztechnik und Elektroakustik **47**(6), 177–181 (1936)
2. D.I. Gordon, R.H. Lundsten, R. Chiarodo, Factors affecting the sensitivity of gamma-level ring-core magnetometers. IEEE Trans. Magn. **1**(4), 330–337 (1965)
3. F Primdahl, The fluxgate mechanism, part I: the gating curves of parallel and orthogonal fluxgates. IEEE Trans. Magn. **6**(2), 376–383 (1970)

4. J.R. Burger, The theoretical output of a ring core fluxgate sensor. IEEE Trans. Magn. **8**(4), 791–796 (1972)
5. A.L. Geiler et al., A quantitative model for the nonlinear response of fluxgate magnetometers. J. Appl. Phys. **99**(8), 08B316 (2006)
6. J.L.M.J. van Bree, J.A. Poulis, F.N. Hooge, Barkhausen noise in fluxgate magnetometers. Appl. Sci. Res. **29**(1), 59–68 (1974)
7. M. Tejedor, B. Hernando, M.L. Sánchez, Reversible permeability for perpendicularly superposed induction in metallic glasses for fluxgate sensors. J. Magn. Magn. Mater. **133**(1), 338–341 (1994)
8. H. Bittel, L. Storm, *Rauschen. Eine Einfuehrung zum Verstaendnis elektrischer Schwankungserscheinungen*. (Springer, Berlin, 1971) (1)
9. C. Hinnrichs et al., Dependence of sensitivity and noise of fluxgate sensors on racetrack geometry. IEEE Trans. Magn. **37**(4), 1983–1985 (2001)
10. D. Scouten, Sensor noise in low-level flux-gate magnetometers. IEEE Trans. Magn. **8**(2), 223–231 (1972)
11. M. Butta et al., Influence of magnetostriction of NiFe electroplated film on the noise of fluxgate. IEEE Trans. Magn. **50**(11), 1–4 (2014)
12. P. Ripka, M. Pribil, M. Butta, Fluxgate Offset Study. IEEE Trans. Magn. **50**(11), 1–4 (2014)
13. F. Primdahl et al., Demagnetising factor and noise in the fluxgate ring-core sensor. J. Phys. E: Sci. Instrum. **22**(12), 1004 (1989)
14. R.H. Koch, J.R. Rozen, Low-noise flux-gate magnetic-field sensors using ring-and rod-core geometries. Appl. Phys. Lett. **78**(13), 1897–1899 (2001)
15. C. Moldovanu et al., The noise of the Vacquier type sensors referred to changes of the sensor geometrical dimensions. Sens. Actuators A **81**(1), 197–199 (2000)
16. O.V. Nielsen et al., Analysis of a fluxgate magnetometer based on metallic glass sensors. Meas. Sci. Technol. **2**(5), 435 (1991)
17. P. Ripka, Race-track fluxgate sensors. Sens. Actuators, A **37**, 417–421 (1993)
18. H.U. Auster et al., in *The THEMIS fluxgate magnetometer*. The THEMIS Mission (Springer, New York, 2009), pp. 235–264
19. O. Dezuari et al., Printed circuit board integrated fluxgate sensor. Sens. Actuators, A **81**(1), 200–203 (2000)
20. J. Kubik, M. Janosek, P. Ripka, Low-power fluxgate sensor signal processing using gated differential integrator. Sens. Lett. **5**(1), 149–152 (2007)
21. O. Zorlu, P. Kejik, W. Teppan, A closed core microfluxgate sensor with cascaded planar FeNi rings. Sens. Actuators A **162**(2), 241–247 (2010)
22. J. Lei, C. Lei, Y. Zhou, Micro fluxgate sensor using solenoid coils fabricated by MEMS technology. Meas. Sci. Rev. **12**(6), 286–289 (2012)
23. E. Delevoye et al., Microfluxgate sensors for high frequency and low power applications. Sens. Actuators A **145**, 271–277 (2008)
24. P. Butvin et al., Field annealed closed-path fluxgate sensors made of metallic-glass ribbons. Sens. Actuators A Phys. **184**, 72–77 (2012)
25. M. Janosek et al., Effects of core dimensions and manufacturing procedure on fluxgate noise. Acta Phys. Pol. A **126**(1), 104–105 (2014)
26. M.H. Acuna, Fluxgate magnetometers for outer planets exploration. IEEE Trans. Magn. **10**, 519–523 (1974)
27. K. Shirae, Noise in amorphous magnetic materials. IEEE Trans. Magn. **20**(5), 1299–1301 (1984)
28. D. Rühmer et al., Vector fluxgate magnetometer for high operation temperatures up to 250 °C. Sens. Actuators A Phys. **228**, 118–124 (2015)
29. A. Matsuoka et al., Development of fluxgate magnetometers and applications to the space science missions. Sci. Instrum. Sound. Rocket Satell. (2012)
30. O.V. Nielsen et al., Development, construction and analysis of the "Oersted" fluxgate magnetometer. Meas. Sci. Technol. **6**(8), 1099 (1995)

31. R. Piel, F. Ludwig, M. Schilling, Noise optimization of racetrack fluxgate sensors. Sens. Lett. **7**(3), 317–321 (2009)
32. F. Primdahl et al., The short-circuited fluxgate output current. J. Phys. E Sci. Instrum. **22**(6), 349 (1989)
33. B. Andò et al., in *Experimental investigations on the spatial resolution in RTD-fluxgates*. IEEE Instrumentation and Measurement Technology Conference, 2009 (IEEE 2009), pp. 1542–1545
34. D. High, Sensor Signal Conditioning IC for Closed-Loop Magnetic Current Sensor (Texas Instruments, 2006)
35. P. Ripka, W.G. Hurley, Excitation efficiency of fluxgate sensors. Sens. Actuators A **129**(1), 75–79 (2006)
36. J. Piil-Henriksen et al., Digital detection and feedback fluxgate magnetometer. Meas. Sci. Technol. **7**(6), 897 (1996)
37. W. Magnes et al., in *Magnetometer Front End ASIC*. Proceedings of 2nd International Workshop on Analog and Mixed Signal Integrated Circuits for Space Applications, (Noordwijk, 2008) pp. 99–106
38. C.T. Russell et al., The magnetospheric multiscale magnetometers. Space Sci. Rev. 1–68 (2014)
39. D.T. Germain-Jones, Post-war developments in geophysical instrumentation for oil prospecting. J. Sci. Instrum. **34**(1), 1 (1957)
40. W.L. Webb, Aircraft navigation instruments. Electr. Eng. **70**(5), 384–389 (1951)
41. S.F. Singer, in *Measurements of the Earth's Magnetic Field from a Satellite Vehicle*. Scientific uses of earth satellites (Univ. Michigan Press, Ann Arbor,1956), pp. 215–233
42. M.H. Acuna et al., in *The MAGSAT Vector Magnetometer: a Precision Fluxgate Magnetometer for the Measurement of the Geomagnetic Field*. NASA Technical Memorandum (1978)
43. T.J. Sabaka et al., CM5, a pre-Swarm comprehensive geomagnetic field model derived from over 12 yr of CHAMP, Ørsted, SAC-C and observatory data. Geophys. J. Int. **200**(3), 1596–1626 (2015)
44. Y.H. Pei, H.G. YEO, in *UXO Survey Using Vector Magnetic Gradiometer on Autonomous Underwater Vehicle*. OCEANS 2009, MTS/IEEE Biloxi-Marine Technology for Our Future: Global and Local Challenges (2009), pp. 1–8
45. F. Ludwig et al., Magnetorelaxometry of magnetic nanoparticles with fluxgate magnetometers for the analysis of biological targets. J. Magn. Magn. Mater. **293**(1), 690–695 (2005)
46. J. Tomek et al., Application of fluxgate gradiometer in magnetopneumography. Sens. Actuators A **132**(1), 214–217 (2006)
47. T. Kudo, S. Kuribara, Y. in *Takahashi, Wide-range ac/dc Earth Leakage Current Sensor Using Fluxgate with Self-excitation System*. IEEE Sensors (2011), pp. 512–515
48. Y. Nishio, F. Tohyama, N. Onishi, The sensor temperature characteristics of a fluxgate magnetometer by a wide-range temperature test for a Mercury exploration satellite. Meas. Sci. Technol. **18**(8), 2721 (2007)
49. J. Jeng, J. Chen, C. Lu, Enhancement in sensitivity using multiple harmonics for miniature fluxgates. IEEE Trans. Magn. **48**(11), 3696–3699 (2012)
50. J.M.G. Merayo, P. Brauer, F. Primdahl, Triaxial fluxgate gradiometer of high stability and linearity. Sens. Actuators A **120**(1), 71–77 (2005)
51. G. Sulzberger et al., in *Demonstration of the Real-time Tracking Gradiometer for Buried Mine Hunting while Operating from a Small Unmanned Underwater Vehicle*. IEEE Oceans (2006)
52. Y. Sui et al., Compact fluxgate magnetic full-tensor gradiometer with spherical feedback coil. Rev. Sci. Instrum. **85**(1), 014701 (2014)
53. M. Kashmiri et al., in *A 200kS/s 13.5 b Integrated-fluxgate Differential-magnetic-to-digital Converter with an Oversampling Compensation Loop for Contactless Current Sensing*. IEEE International Solid-State Circuits Conference-(ISSCC), 2015 (IEEE, 2015), pp. 1–3

54. Texas Instruments Inc., DRV425—Fluxgate Magnetic-Field Sensor (2015), http://www.ti.com/lit/ds/symlink/drv425.pdf
55. A. Cerman et al., in *Self-compensating Excitation of Fluxgate Sensors for Space Magnetometers.* IEEE Instrumentation and Measurement Technology Conference Proceedings, 2008 (IEEE, 2008), pp. 2059–2064
56. K.-H. Glassmeier et al., RPC-MAG the fluxgate magnetometer in the ROSETTA plasma consortium. Space Sci. Rev. **128**(1–4), 649–670 (2007)

Orthogonal Fluxgate Magnetometers

Mattia Butta

Abstract Orthogonal fluxgate is a particular type of fluxgate, which recently gained popularity. As all fluxgate sensors it is based on the gating of magnetic flux in a ferromagnetic core; however, in orthogonal fluxgates the excitation field and the measured field are orthogonal. This leads to different sensor structure, most notably to the absence of an excitation coil, making the construction of an orthogonal fluxgate very simple. In this chapter we will first analyse the principle of operation of orthogonal fluxgates in order to explain the mechanism which generates the output signal. Then, we will examine how the sensor is build, especially the structure of the core and the techniques typically used in order to minimize the amplitude of excitation current. Next, a particular type of orthogonal fluxgate–the so-called coil-less fluxgate—is presented: its name comes from the lack of the pick-up coil, for the output voltage is derived directly from the core's termination thanks to helical anisotropy of the core.The most important part of the chapter is however focused on fundamental mode orthogonal fluxgate; in this type of sensor a large dc bias is added to the excitation current in order to suppress the Barkhausen noise, that is the main source of noise in fluxgates. The resulting output has very low noise: we show how, properly designing the core geometry and modifying the anisotropy by annealing we can achieve noise as low as 1 pT/$\sqrt{\text{Hz}}$ at 1 Hz. Another part of the chapter is focused on magnetic gradiometers based on orthogonal fluxgates, typically used when the sensor has to be used in noisy environment and the magnetic field to be measured has large gradient and small amplitude. Finally a comparison with similar sensors, such as wire-based GMI, is presented: we show similarities and differences, especially regarding the methods for signal extractions and we explain why orthogonal fluxgates perform better.

M. Butta (✉)
Czech Technical University in Prague, Prague, Czech Republic
e-mail: buttamat@fel.cvut.cz

A. Grosz et al. (eds.), *High Sensitivity Magnetometers*, Smart Sensors, Measurement and Instrumentation 19, DOI 10.1007/978-3-319-34070-8_3

1 Introduction

Fluxgates are very common sensors of magnetic field with large range of applications when high resolution is required form a room temperature operated sensor. However, in the common language the term "fluxgate" typically refers only to one particular type of fluxgate, the parallel one. As a matter of fact, there is another type of fluxgate, namely the orthogonal one, which is often disregarded.

In fact, orthogonal fluxgates have been invented almost simultaneously to parallel fluxgates; the first patent about orthogonal fluxgates dates back to 1952 [1]. Then, this principle was forgotten for long time since most of the focus of the scientific community was on parallel fluxgates, which apparently gave better results.

In the last decade, however, orthogonal fluxgates gained new popularity, especially thanks to the availability of new magnetic microwires, which allowed us to manufacture small orthogonal fluxgates competitive to parallel fluxgates.

2 Principle of Operation

All types of fluxgates are based, as the name suggests, on the gating of the magnetic flux in a ferromagnetic material. In a fluxgate we therefore always have a core composed of ferromagnetic material; this core is periodically saturated in opposite directions by an excitation field applied to it. During the transition from one saturated state to the opposite one we can observe the fluxgate effect. In a sense, the fluxgate effect might look different for parallel and orthogonal fluxgate, but in fact in both cases both working modes are based on the saturation of the core, and therefore on the gating of the magnetic flux. In both cases you need saturation to make a fluxgate work, whether parallel or orthogonal.

Let us now examine how the orthogonal fluxgate measures and external magnetic field. Before that, however, let us define what we mean by orthogonal fluxgate and especially why we call it orthogonal.

In Fig. 1 we can see the basic structure of a parallel and orthogonal fluxgate. There are different configurations for parallel fluxgates; in this case we depict a race-track core to highlight the sensing portions of the core where the measured field and the excitation field are parallel.

In a parallel fluxgate the excitation coil is wound around the core so that it creates an excitation field H_{ex} parallel to the sensed field H_m. An orthogonal fluxgate, on the contrary is composed, in its simplest shape by a cylindrical ferromagnetic core surrounded by a toroidal excitation coil. Still the sensed field is the axial direction of the core, however the excitation field generated by toroidal coil is a circular field. In this case the excitation field lays in the X-Y plane which is orthogonal to the sensed direction, that is Z axis (correspondent to the axis of the

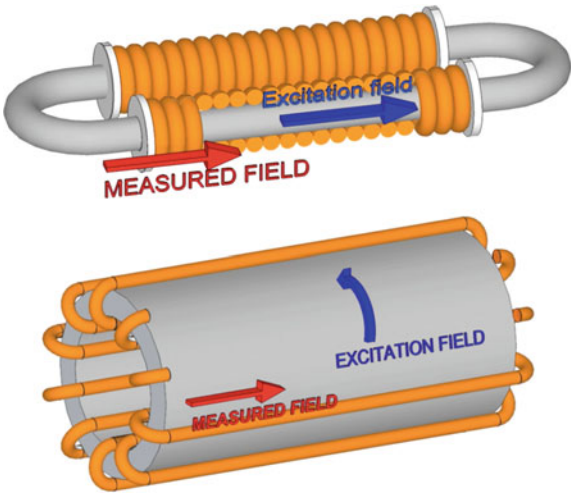

Fig. 1 Basic structures of parallel (*upper*) and orthogonal (*lower*) fluxgates

core). That is why we define this sensor *orthogonal*, because the excitation and the sensed field are mutually orthogonal.

Even if trivial, we should point out this does not mean that the excitation field H_{ex} is linear; in fact, as we can see in Fig. 1 it is circular. By stating that H_{ex} is orthogonal to H_Z, we simply say it is always perpendicular to H_Z along the whole circumference (it never leaves the X-Y plane).

Although the cylindrical core is currently not the most common shape for a orthogonal fluxgate is useful to use it for describing the working principle of the sensor, not only because it was historically the first structure proposed, but also because it allows us to easily understand how the sensor work.

Let us consider an isotropic magnetic core in shape of a cylinder. The core is exposed to a circumferential field H_Φ produced by the toroidal coil (not shown in the drawing) and an external field H_Z in axial direction (Fig. 2a). Let us assume a simplified hysteresis curve of the ferromagnetic material as depicted in Fig. 2b; this is clearly not true for real magnetic materials, but this simplification helps us to understand the basic principle of the orthogonal fluxgate.

While H_Z is constant, H_Φ varies in time as a sine wave (Fig. 2c) because the excitation coil is a sine wave. We further assume that H_Z is much smaller than the amplitude of H_Φ and much smaller than the field necessary to saturate the core H_S (also this is a simplification, in real ferromagnetic material there is not a clear border between saturated and non-saturated state). Under this assumption, and keeping in mind the isotropy of the material we analyze what happens to the magnetization when H_Φ varies in time.

When H_Φ is low enough so that the total field $H_{tot} = (H_\Phi^2 + H_Z^2)^{1/2} < H_S$ the core is not saturated. Therefore, M has the same direction of the total field H_{tot}, and increases its magnitude as H_{tot} increases. Once H_Φ is large enough to make $H_{tot} > H_S$ then it is easy to understand from the hysteresis loop that the amplitude of

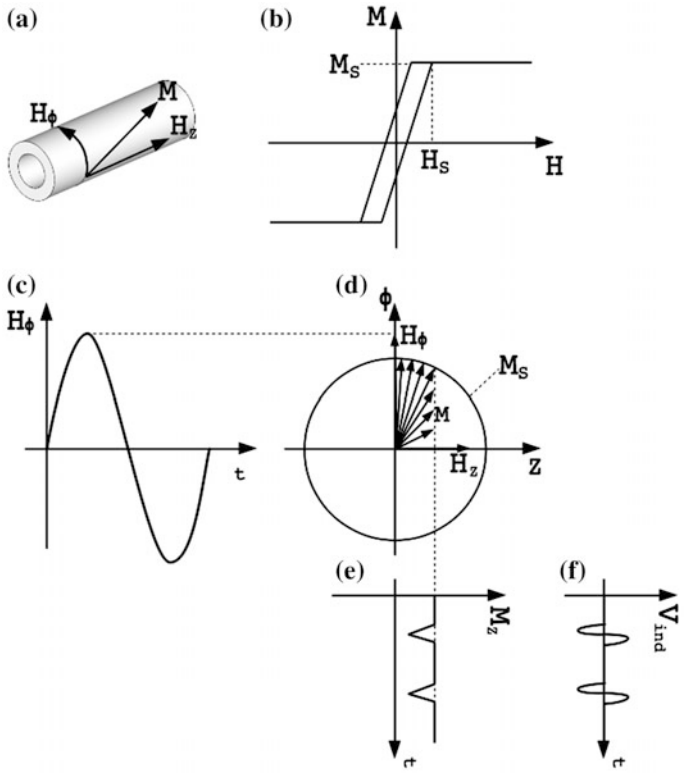

Fig. 2 Working principle of the orthogonal fluxgate

M cannot further increase because it reached its maximum value M_S. At this stage M rotates over the circumference corresponding to $M = M_S$.

If we pay now attention we realize that in the first period when the core is not saturated, M_Z, that is the projection of M on Z-axis, is constant (because H_Z is constant). However, when the core enters into saturation and M start rotating M_Z decreases (Fig. 2d).

When we consider the whole period of H_Φ, we easily find out that M_Z rises back to its original value when H_Φ decreases and H_{tot} returns back to a value lower than H_S; everything happens again for the semi-period when H_Φ is negative. In that case the core is saturated in negative direction as soon as $H_{tot} < -H_S$, and again M rotates making M_Z decrease again (Fig. 2e).

By taking the time derivative of M_Z we obtain a signal proportional to the voltage induced in the pick-up coil (which is the derivative of the flux in axial direction). Because there are two drops of M_Z for each period of H_Φ, it is straightforward that the output signal is at the second—and higher order even—harmonic (Fig. 2f).

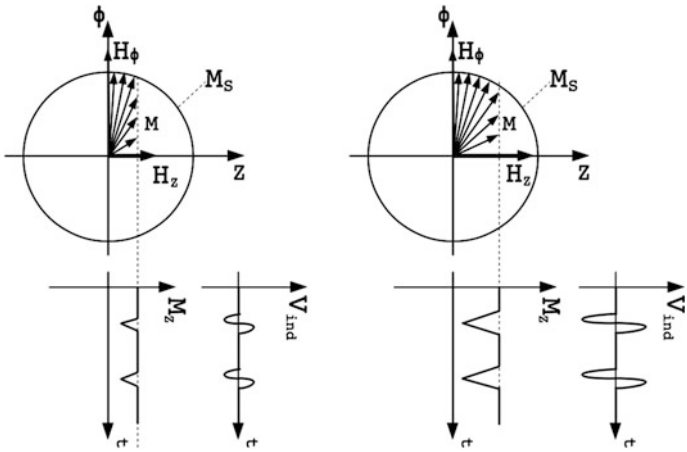

Fig. 3 Mechanism which brings to different induced voltage for different H_Z field in an orthogonal fluxgate

Let us consider a different value of H_Z. What happens if H_Z is larger? Simply, the maximum value of M_Z will be larger. In this case the saturation is reached for lower value of H_Φ (because the contribution of H_Z to the total field H_{tot} is larger), and—most important—the derivative of M_Z will be larger because the drop of M_Z is larger. Therefore, for larger H_Z we obtain larger second harmonic in the output voltage (Fig. 3).

It is easy to understand that if H_Z becomes negative then the polarity of the output voltage is reversed.

As we stated in the assumptions this mechanism works for low H_Z. If H_Z is large enough to saturate the core then there is only rotation of M_Z; in this case if H_Z increases there is no change in M_{Zmax} which is equal to M_S, because M_Z cannot increase more than M_S. Finally, we would have an increment of H_Z without any change in the output voltage, that means the sensor is saturated.

While the core should not be saturated in axial direction, an important condition is large saturation of the core in circumferential direction given by large amplitude of H_Φ. If saturation in circumferential direction is not achieved there is no drop of M_Z and therefore no voltage induced in the pick-up coil. In order to get a properly working orthogonal fluxgate large saturation should be always achieved in circumferential direction.

This model [2] assumes the core to be isotropic. In case of a non-negligible anisotropy we should also consider the contribution of the anisotropy energy in determining the direction of the magnetization [3]. Nonetheless the basic principle of operation still applies.

3 Core Shape

3.1 Cylindrical Core

As already mentioned the cylindrical core was the first structure originally proposed for an orthogonal fluxgate, as it was the simplest possible core. A toroidal coil, in fact, is not so simple to be manufactured around a cylinder (while automatic winding machines are available for ring cores used in parallel fluxgates). However, it allows generating a large excitation field by winding a large enough number of turns.

We know that saturation is a key point for proper functionality of a fluxgate. Moreover, if we want a low noise and largely linear sensor we must necessarily apply an excitation field large enough to bring the core into deep saturation. By using a cylindrical core excited by a toroidal coil this can be rather easily achieved.

Two other structures were originally proposed for orthogonal fluxgates [1]. In the first one a wire simply passes through the cylinder carrying the excitation current I (Fig. 4).

In this case the current flowing through the wire generates a circular magnetic field H similarly to the toroidal coil. In a way, you can consider the wire passing through the core together with the return wire a single turn toroidal coil. While this structure is certainly easier to be implemented because it does not require complicated winding of many turns it also has the disadvantage of producing a much lower magnetic field than a toroidal coil.

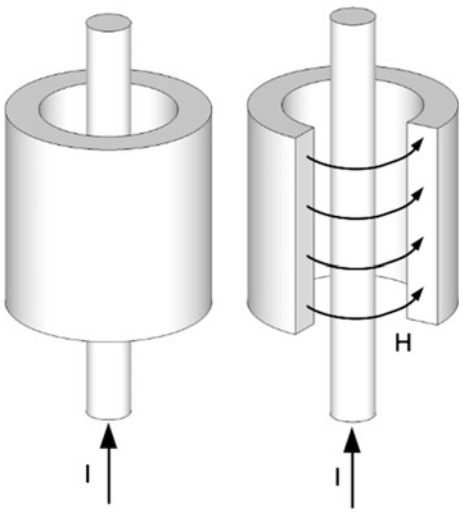

Fig. 4 Orthogonal fluxgate based on a cylinder of ferromagnetic material and a wire carrying the excitation current (the image on the *right* shows a section of the cylinder)

3.2 Wire Based Orthogonal Fluxgate

This structure does not make use of a cylinder but employs a ferromagnetic wire as a core (Fig. 5). The excitation current directly flows through the ferromagnetic wire creating a circular magnetic field inside it. Therefore, also in this case the core is saturated in circumferential direction as seen in the previous structures.

Wire-based orthogonal fluxgates share the same disadvantage previously mentioned for cylinder base fluxgate excited by a single wire that is the circumferential excitation field is limited. However, the structure is simplified: in this case all we need for the core is single ferromagnetic wire, which serves both as magnetic core and as excitation element since it carries itself the excitation current.

In other words we get rid of the excitation coil. This opportunity attracted new interests to orthogonal fluxgate since it is very important in the prospective of miniaturization of magnetic sensor as currently required by the market.

As we mentioned, the excitation field produced by the current flowing in the ferromagnetic wire cannot be compared to the much larger magnetic field produced by a toroidal coil; nonetheless, the current state of art of material sciences allows us to produce both amorphous an nanocrystalline microwires with very soft magnetic behavior and a diameter spanning from 10 to 100 μm. Therefore, nowadays we have magnetic microwires suitable for orthogonal fluxgates.

3.3 Composite Wires

Orthogonal fluxgates based on wires became immediately very popular because they eliminate the need of an excitation coil, so simplifying the structure of the sensor. However they have a disadvantage: the center of the wire is generally non-saturated. This is due to the fact that the circumferential field H_Φ produced by the excitation current is not constant at every distance from the center of the wire. Following Ampere's law, H_Φ linearly rises from 0 in the center of the wire to its

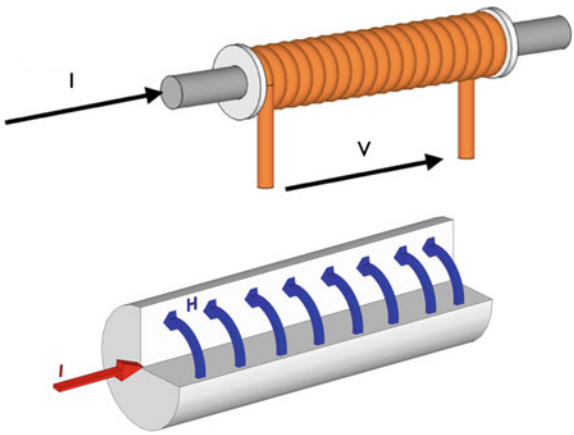

Fig. 5 Wire-based orthogonal fluxgate: the current flows through the wire and produces a circular field in it

maximum at the edge of the wire. In the center of the core therefore there will be a portion of the wire which is not saturated because the excitation field H_Φ is lower than the field necessary to saturate the wire's material. We can certainly increase the excitation field using a larger current, and we can use a very soft magnetic material; in this way we can reduce the portion of the core which is not saturate, however there will always be an inner part of the core which is not saturated.

Add to that there is the effect of the skin effect, which cannot be disregarded. In this case the current drifts to the border of the wire, making the circumferential field lower in the middle [4]; therefore the larger is the skin effect the larger is the area of non-saturated inner section of the wire.

One might think that a non-saturated inner part of the core is simply a portion of the core which does not act as a fluxgate, given that it is not saturated, therefore the only problem is a limited amount of the total ferromagnetic material contributing to the fluxgate effect. As a matter of fact there are other disadvantages when the central part of the core is not saturated. The most immediate problem is that such portion of the wire can be magnetized in axial direction by a large H_Z, and the excitation field will never be large enough to restore it in its original state. This causes a hysteresis in the characteristic of the fluxgates. Moreover, there is not a brick-wall transition between the saturated and the non-saturated regions of the wire. That is, we could have parts of the wire which still partially acts as fluxgate by being "close" to saturation, but they do not work properly due to the fact that they are not "fully" saturated. This carries a noisy contribution to the total output signal.

In order to avoid such effects composite wires have been proposed [5, 6]. The main idea is to use wires with a copper core and an electroplated shell of ferromagnetic material, typically permalloy ($Ni_{80}Fe_{20}$). Copper has much lower resistivity (17 nΩ m) than the permalloy has (200 nΩ m). Therefore, we can expect that most of the current flows in the copper than the permalloy; in this way we can compensate the tendency of the current to draw to the border of the wire by giving a low resistivity way to flow through in the center of the wire.

Yet, for large enough excitation frequency the skin effect cannot be disregarded. In this case a more complex structure has been proposed [7] to overcome such problem. The wire is composed by a glass coated copper core. A thin layer of gold is sputtered over the glass coating to create a conductive surface over it. Later, electrodeposition of permalloy (or generally speaking, any other soft magnetic material) is performed on the gold layer (Fig. 6). The terminations of the wire are not gold sputtered, therefore neither electroplated. Therefore, the excitation current

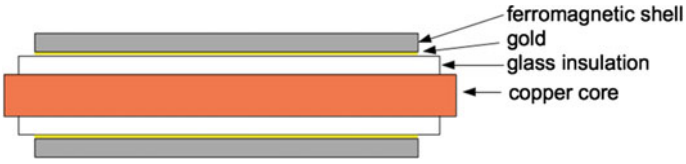

Fig. 6 Bi-phase wire with glass insulation between copper core and ferromagnetic shell

can be injected in the copper core without any electric contact to the ferromagnetic shell. In this way the glass coating of the copper provides an efficient electric insulation between the copper and the ferromagnetic layer which prevents the current to drift to the wire's border due to skin effect at any frequency. This makes much easier to saturate the wire and it has been proved to reduce by a factor of three the current necessary to saturate a fluxgate core.

3.4 Multi-Wire Core

One of the disadvantages of orthogonal fluxgates based on microwire is the low sensitivity when compared to parallel fluxgates (typically with bulk cores), or even orthogonal fluxgates based on tubular core. This is simply due to the small cross sectional area of the ferromagnetic core. Generally speaking the sensitivity of a fluxgate depends on many factors (quality factor of the pick-up coil, permeability of the core, excitation frequency, demagnetizing factor of the core…) nevertheless, as a rule of the thumb we can say that if the amount of ferromagnetic material of the core is low we can expect low sensitivity.

In order to overcome this problem orthogonal fluxgates with multiple wires core have been proposed. It is important to point out that in such sensors the wires are not electrically in contact along their lengths, since an insulating layer (either few μm of glass coating for melt spun wires or thin layer of epoxy for electroplated wires) avoid electric contact between them. Therefore, from the electrical point of view the act as independent wires in parallel.

The dependence of sensitivity on the number of wires used in the core has been studied [8]. It was found out that the sensitivity increases almost exponentially over the number of wires. For instance, if 16 wires are used instead of a single wire, the sensitivity becomes 65 times larger. This was shown [9] to be not simply due to a larger amount of ferromagnetic material inside the pick-up coil, as a core with the same cross-sectional but a single wire has lower sensitivity of a core with two wires, each of them with half of the cross sectional area.

Later it was shown that such effect disappears if the wires are kept far enough (at least five times their diameter) instead of closely packed. This indicates that the origin of such exponential growth of the sensitivity is the magnetic interaction of the wires.

Subsequently, it has been suggested [10] that such increment of the sensitivity was due to the improvement of the quality factor of the circuit composed by the pick-up coil and the parallel tuning capacitor. Such hypothesis was later confirmed in [11].

It is important to note that sensitivity is only one factor of the signal-to-noise ratio. If we increase the sensitivity but simultaneously we increase also the noise of the same quantity we do not have advantage whatsoever. However, it was found out that the increment of sensitivity obtained using multiple wires as a core does not only increase the sensitivity but also decreases the noise [12].

4 Spatial Resolution

We have already discussed about the greatest advantage of orthogonal fluxgates that is the absence of the excitation coil when the excitation field is generated by the current flowing through the wire serving as core. Another important advantage is very high spatial resolution in X-Y plane (that is the plane orthogonal to axial direction of the wire). Classical parallel fluxgates have either a ring or race-track core where two active parts of the core sense the external magnetic field to be measured. If the field is not uniform but it has a gradient these two branches of the core sense different fields, as shown in Fig. 7 where one part of the core senses H_{XA} whereas the other part senses H_{XB}. Because the pick-up coil collects the flux from both parts the total output signal will be an average of H_{XA} and H_{XB}, and there is no way to discriminate them. From this point of view the spatial resolution of the sensor is limited by the width of its core. When we consider the orthogonal fluxgate it is straightforward to understand why its spatial resolution is much higher. Indeed, orthogonal fluxgates can be built based on microwire cores. This means that in the X-Y plane the limiting dimension is the diameter of the wire, typically some tens of μm for the smallest sensors up to 100–150 μm. In Z direction, that is the direction corresponding to the axis of the wire the length of the core is still of several cm, nevertheless by using wire core in orthogonal fluxgate we are able to strongly improve the spatial resolution at least in the X-Y plane. For instance, using 120 μm diameter magnetic wires as core for orthogonal fluxgate, magnetic domains of steel can be observed by mapping the magnetic field above its surface [13].

It has to be noted that parallel fluxgates have been developed using ultra-thin cores using either magnetic tapes or electrodeposited [14] or sputtered [15] cores. In

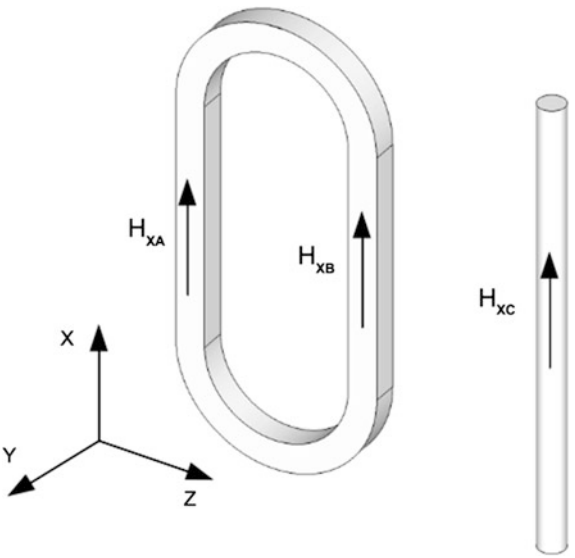

Fig. 7 Spatial resolution of parallel and orthogonal fluxgate

this case the parallel fluxgates gains his spatial resolution in one of the dimensions of the X-Y plane, yet the second dimension is intrinsically limited by the ring or race-track shape to be much larger.

5 Coil-Less Fluxgate

If the absence of the excitation coil is convenient, the lack of both coils is certainly better. The natural evolution of orthogonal fluxgate based on wire core was then to get rid not only of the excitation coil but also of the pick-up coil. This was obtained using the so-called coil-less fluxgate [16].

The sensor is still a fluxgate with a ferromagnetic wire periodically saturated in opposite polarities by an ac current flowing through it. However the second or higher order even harmonics are not derived from the voltage obtained using a pick-up coil wound around the wire. The second harmonic is taken out from the voltage at the wire's terminations, V_{wire} (Fig. 8).

It was found out that the second harmonic in V_{wire} is linearly dependent on the magnetic field applied in axial direction as long as the wire has helical anisotropy. This effect was first shown in composite wires creating helical anisotropy by twisting the wire (torque in opposite direction was applied at the wire's terminations). In this case the helical anisotropy was mechanical induced anisotropy. Later it was shown that the same effect can be achieved by field induced helical anisotropy: the magnetic wire was electroplated under the effect of an helical field which in turns gives built-in helical anisotropy in the electroplated layer without need to mechanically twist the wire afterwards [17].

It is worthy to highlight that such effect occurs only if there is helical anisotropy in the wire. Regular wires with axial (or circular) anisotropy do not have any field

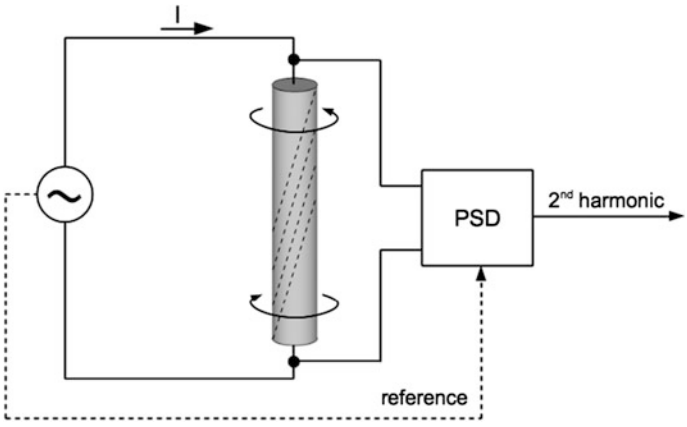

Fig. 8 Basic structure of a coil-less fluxgate based on torque induced helical anisotropy

depended second harmonic in the voltage on their terminations. The fact that the helical anisotropy is the cause of the appearance of the field dependent second harmonic is clear when we consider that the sensitivity of the coil-less fluxgate increases as the angle of anisotropy increases; eventually the sensitivity becomes negative when the helical direction of the anisotropy is reversed.

5.1 Working Mechanism

By observing the structure of a coil-less fluxgate one might find some similarities to magnetoimpedance sensors. In fact, the working principle at the base of coil-less fluxgate is completely different from magnetoimpedance; the first clue is the much lower frequency this phenomenon appears at (typically where magnetoimpedance effect is negligible). Most important, the sensor does not work if the core is not well saturated, exactly like in fluxgates.

Underlying the coil-less sensor there is still the same working mechanism of the orthogonal fluxgate we have previously analyzed. The only difference is that such mechanism now is rotated by an angle γ corresponding to the angle of skew angle of helical anisotropy (Fig. 9).

The mechanism is still the same: the circumferential field H_Φ makes the magnetization M rotate, while H_Z is the axial field which has to be measured. However, now the axes are rotated by an angle γ; therefore the actual field which makes M rotate is not the whole H_Φ field but only its component $H_\Phi\perp$, that is the component of H_Φ perpendicular to the easy axis of magnetization (E.A.). This is the reason why the larger is the angle of the helical anisotropy the larger is the current we must use to achieve saturation of the wire. Indeed, the larger is γ the lower is $H_\Phi\perp$, that is the field which brings the wire into saturation.

If we consider H_Z we easily realize that due to the rotation of the reference axis, now H_Z has also a component $H_Z\perp$ perpendicular to E.A, the same direction of $H_\Phi\perp$. Because H_Z is constant (or at low frequency) we can consider $H_Z\perp$ as a dc offset to $H_\Phi\perp$. In other words, $H_\Phi\perp$ makes M rotate back and forward by bringing

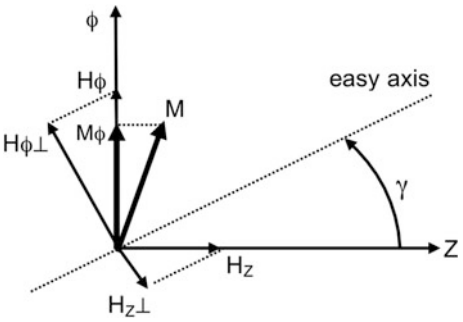

Fig. 9 Working principle of the coil-less fluxgate

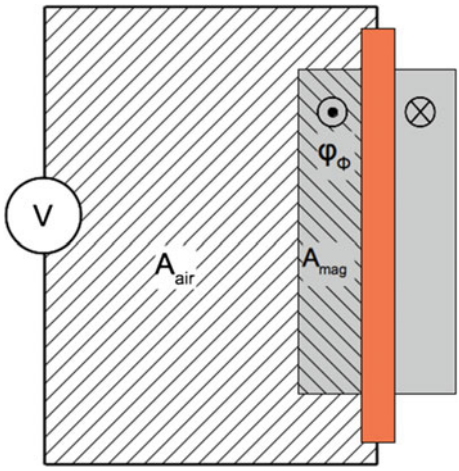

Fig. 10 One-turn coil of the coil-less fluxgate

it into saturation in both polarities, and $H_Z\perp$ shifts this mechanism bringing M into saturation more on one polarity than on the opposite polarity.

The voltage at wire's terminations V_{wire} is composed of two contributions: a resistive component given by the product of the current I_{wire} time the resistance of the wire R_{wire} plus the inductive voltage V_{ind}.

$$V_{wire} = R_{wire} \cdot I_{wire} + V_{ind} \tag{1}$$

V_{ind} is the derivative of the circumferential flux. Let us consider the axial cross section of a composite copper core—magnetic shell wire (Fig. 10): if we consider the circuit composed of the inner copper core plus the return wire we have a single-turn-coil whose area is composed by A_{air} (the cross section of the air) and A_{mag} (the cross section of the magnetic shell). The voltage induced at the termination of this coil is then given by the derivative of the total flux of the air and the circumferential flux φ_{air} of the magnetic shell φ_Φ.

Now, let's go back to the working mechanism. We have seen that the magnetization M rotates due to the excitation field $H_\Phi\perp$, and this process is shifted by a dc component $H_Z\perp$. If we measure the voltage V_{ind}, we shall see that a component of M corresponding to its projection on Φ axis, namely M_Φ, which is responsible for the circumferential flux φ_Φ. Therefore, the shifting of the rotation of M due to $H_Z\perp$ has effect also on φ_Φ and therefore V_{ind}. That is why we can see this effect at wire's terminations. Indeed, if we observe the circumferential B-H loop (i.e. circumferential B vs. circumferential H [18]) we see that the B-H loop is shifted by external field H_Z.

In other words, the helical anisotropy does not only create a component of H_Z which shifts the magnetization process, but it also allows us to detect the flux on wires terminations by bringing a portion of what is typically the axial flux on the circumferential axis due to rotation of axis.

5.2 Sensitivity

The main problem of coil-less fluxgate is the low sensitivity. As a matter of fact with classical composite Cu (50 μm diameter)—Permalloy (10 μm shell thickness) wires sensitivity up to 10–15 V/T can be achieved for few cm long wires. This is quite low and unfortunately we cannot simply increase it by adding more turns to the pick-up coil because there is no pick-up coil.

Also, we cannot simply amplify V_{wire} because it usually contains a large resistive component $R_{wire} \cdot I_{wire}$ which does not carry any information but it contributes to reach a peak value of the voltage which determines saturation of the amplifying electronics.

A solution is to use a bridge to suppress the restive part of the voltage. Yet, V_{ind} will be composed of peaks (corresponding to the fast transition from one saturated state to the opposite one) which only shift to the left or the right in time domain. Ideally we would like to have no voltage at all for $H_Z = 0$ and peaks arising only for $H_Z \neq 0$. This can be achieved using a double bridge with two microwires having opposite direction of magnetization [19].

Other alloys than permalloy have been used to produce coil-less fluxgate giving larger sensitivity; for instance in Co-rich amorphous wire 400 V/T sensitivity has been achieved at 30 kHz [20]. In composite wire Cu—$Co_{19}Ni_{49.6}Fe_{31.4}$ sensitivity of 120 V/T at 20 kHz was reported [21].

5.3 Linearity and Noise

Unfortunately the coil-less fluxgate has relatively large noise. For example in [22] a coil-less fluxgate base on composite Cu-Permalloy wires with 3 nT/$\sqrt{\text{Hz}}$ noise at 1 Hz has been reported. This is believed to be mainly due to low sensitivity. As a matter of fact the noise could be lower with Co-based alloy microwires, which have larger sensitivity but data of their noise have not been reported yet.

Coil-less fluxgate behaves better in terms of linearity, which is an important parameter for this kind of sensor, since non-linearity cannot be compensated by feedback method given that there is no coil to create a feedback field.

Open loop linearity error of coil-less fluxgate could be as low as ±0.5 % in a ±50 μT range and it drops to ±0.2 % in a ±40 μT range [22].

6 Fundamental Mode Orthogonal Fluxgates

As we mentioned before, one of the reasons why orthogonal fluxgates have been disregarded for many decades was their worse performances when compared to classical parallel fluxgates, and this was particularly true when it came to noise.

Everything changed in 2002 when Sasada proposed the so-called fundamental mode orthogonal fluxgate [23]. The structure of the sensor is the very same of wire-based orthogonal fluxgate: the core is composed of a magnetic wire excited by a current flowing through it while the output voltage is obtained using a pick-up coil wound around the magnetic wire. The only difference is that a large dc bias is added to the traditional ac current. How large is the dc bias? And what is its purpose?

The dc bias should be large enough to permanently saturate the wire in one direction. Its amplitude therefore depends on the B-H loop of the particular wire used as a core; different ferromagnetic material generally speaking require different dc bias to fall into permanent saturation only in one direction.

The question now is: why should I keep the wire saturated only in one direction? So far we have always considered the magnetization periodically alternating its saturation state in opposite direction, so why do we now change the operative mode?

In fact, it turns out most of the noise in fluxgate sensors is due to Barkhausen noise originated during the reversal of magnetization from one saturated state to the opposite. The main idea behind fundamental mode orthogonal fluxgate is to suppress the Barkhausen noise by eliminating the reversal of magnetization: if the core is permanently saturated in one direction no reversal of magnetization occurs and there Barkhausen noise is strongly reduced.

However, how is the output voltage obtained if the core does never reverse its magnetization? Clearly, the working mode previously explained does not hold anymore. In this case the output signal is not obtained by extracting the second harmonic as in traditional fluxgates (both orthogonal and parallel), but the first harmonic. That's why the sensor is in fact said to work in fundamental mode, because the output signal is at the fundamental frequency.

The reason why the signal is now at the fundamental frequency is easy to understand if we analyze the behavior of the magnetization calculating the position it acquires to minimize its total energy.

Let us consider a simple isotropic wire saturated by an $I_{ac} + I_{dc}$ current, which in turn generates circular magnetic fields $H_{ac} + H_{dc}$. If no other field is present the magnetization M simply lays on circumferential direction too (Fig. 11).

However, if an external dc field H_Z is applied in axial direction the magnetization is deviated away from the circumferential direction by a generic angle α between Φ direction (where $H_{ac} + H_{dc}$ lays) and Z direction (where H_Z lays). The angle α depends on the amplitude of both $H_{ac} + H_{dc}$ and H_Z: the larger is $H_{ac} + H_{dc}$ the lower is α, the larger is H_Z the larger is α (Fig. 12). The position of M is indeed determined by minimizing the total energy [24]:

$$E = -\mu_0 \cdot M \cdot (H_{ac} + H_{dc}) \cdot \cos(\alpha) - \mu_0 \cdot M \cdot H_Z \cdot \cos(\pi/2 - \alpha) \qquad (2)$$

For a given H_Z field we now consider how α changes in the time domain, considering that the circumferential field has a time varying component H_{ac}. When H_{ac} is maximum the total field on circumferential direction is $H_{dc} + |H_{ac}|$ and α is minimum; when H_{ac} reaches its minimum value the total field on circumferential

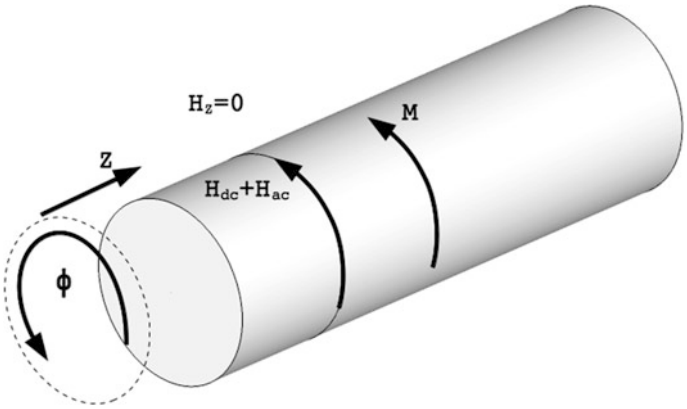

Fig. 11 Excitation field and magnetization in a fundamental mode orthogonal fluxgate without axial field

direction is $H_{dc} - |H_{ac}|$ and α is maximum. If we consider now the projection of M on Z-axis M_Z we find out that M_Z oscillates with the same frequency of H_{ac}. Then it is sufficient to wind a coil around the wire to pick-up the magnetic flux corresponding to M_Z and obtain and output voltage with the same frequency of the excitation current (Fig. 13).

It is easy to realize that in case H_Z is zero α is permanently zero because there is no field, which can deviate M away from circumferential direction. Therefore M always lays on Φ direction and there is no component M_Z whatsoever. As a result, given that $M_Z = 0$, the voltage induced in the pick-up coil is also zero. The voltage is then only induced when H_Z is applied in axial direction and gives us a measure of H_Z. Of course, the larger is H_Z the larger is the deviation of M from

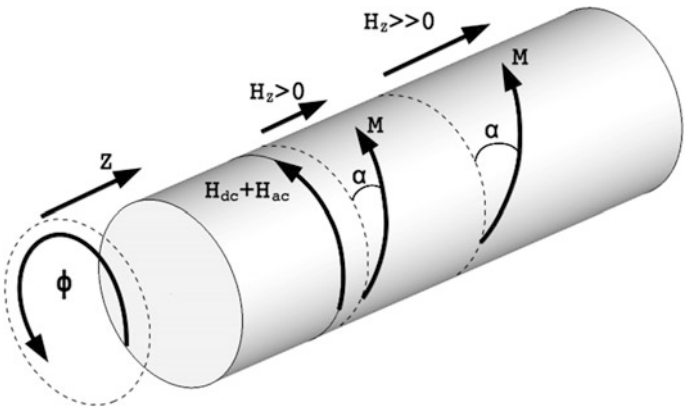

Fig. 12 Deflection of the magnetization in a fundamental mode orthogonal fluxgate with two different values of axial field H_Z

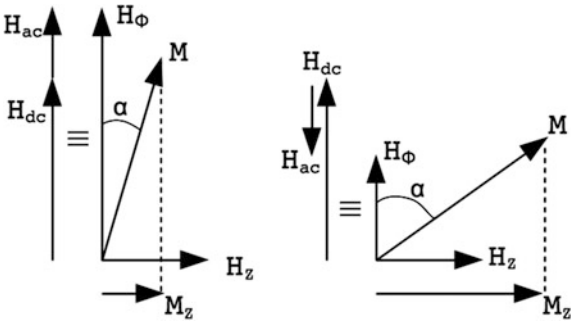

Fig. 13 Working principle of the fundamental mode orthogonal fluxgate

circumferential direction, and therefore the larger is the voltage induced in the pick-up coil: this is how we can finally measure the amplitude of H_Z.

6.1 Sensitivity

One of the most common mistakes is to think that if the core is deeply saturated then the sensor cannot work properly; many believe that if the core is fully saturated (a condition which anyway cannot be totally achieved) then the output voltage is zero. This leads them to think that it is necessary to let the core to be unsaturated for low values of H_{ac}, because if the core is practically always saturated then there is not output voltage; as a result many use low dc bias current because they are afraid that a deeply saturated core would make the sensor not working. This is simply not true: even if the core is deeply saturated, the sensor will keep working properly. The magnetization in fact rotates to meet the angle α where the minimum total energy condition is met even the core is in deep saturation. Of course, the larger is the dc bias the lower is the resulting sensitivity of the sensor. This can be easily understood by considering the working principle of the fluxgate in fundamental mode previously explained.

For a given amplitude of the ac current I_{ac} the sensitivity drops as we increase the dc bias I_{dc} (Fig. 14). This is due to the fact that a larger I_{dc} makes the magnetization M rotate toward the circumferential axis Φ, so that the amplitude of the oscillation of M is reduced. In other words, M is more strongly attracted by $H_{dc} + H_{ac}$ and α oscillates less, giving in turn lower variation of M_Z (which finally gives us the output voltage).

On the other hand, for a given I_{dc} the larger is I_{ac} the larger is the sensitivity (Fig. 14). In this case it is straightforward to understand why: if we increase H_{ac} angle α swings to a larger extend giving as a result a larger variation of M_Z.

Finally, by tuning the amplitude of I_{dc} and I_{ac} one can obtain the desired sensitivity. The choice of I_{dc} and I_{ac} however is not so straightforward as one might think. The resulting noise strongly depends on these two parameters.

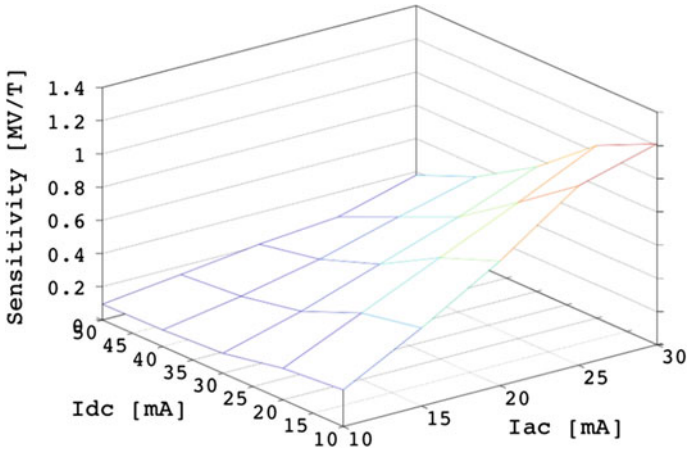

Fig. 14 Sensitivity of the fundamental mode orthogonal fluxgate as a function of both ac current and dc bias

6.2 Noise

As we mentioned before, the fundamental mode orthogonal fluxgate had immediately a large success due to its lower noise compared to traditional orthogonal fluxgates. Paperno has clearly demonstrated [25] that the dc bias itself is the reason why the noise drops by comparing the noise of the very same fluxgate operated without dc bias (in traditional 2nd harmonic mode) and with dc bias (in fundamental mode). By only changing the operative mode the noise drops by one order of magnitude.

In that paper about 20 pT/$\sqrt{\text{Hz}}$ noise at 1 Hz has been achieved. Later on the noise was reduced to 10 pT/$\sqrt{\text{Hz}}$ in tubular [26] and wire based [27] sensors.

By properly designing the geometry and using magnetic microwires with circular anisotropy finally 1 pT/$\sqrt{\text{Hz}}$ noise at 1 Hz has been achieved [28].

6.3 Excitation Parameters

The first key point to obtain the minimum noise from an orthogonal fluxgate in fundamental mode is to properly select the excitation parameters I_{ac} and I_{dc}. As we mentioned before a larger I_{dc} reduces the sensitivity whereas a larger I_{ac} increases the sensitivity. However, we should always keep in mind that sensitivity is only one side of the coin when it comes to noise. Indeed, we should also consider the intrinsic magnetic noise of the core alongside the sensitivity. If we reduce the dc bias the sensitivity certainly increases, but the magnetization risks to fall out of saturation during the part of the period when I_{ac} approaches its minimum value [29].

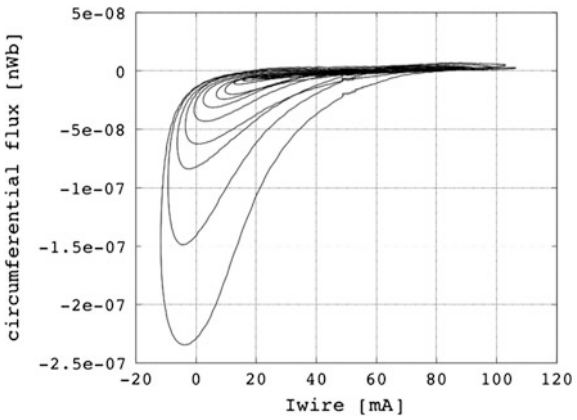

Fig. 15 Minor circumferential loops of a magnetic wire excited by a current with constant dc value (45 mA) and different ac amplitude

It turns out that the noise depends on the area (that is the energy) of the minor loop of the core B-H loop [30] (Fig. 15). This was later confirmed analytically in [31].

If we now plot the noise at 1 Hz (or at any arbitrary point when the noise has $1/f$ behavior) for different I_{ac} amplitude (keeping the same I_{dc}), we observe how the noise has three different regions where it differently behaves (Fig. 16). At first, when I_{ac} is low, the noise rapidly decreased for higher values of I_{ac}. In this region most of the noise is due to noise of the signal conditioning circuit. The minor loop energy is so low that the noise of electronics overlooks it. In fact we observe that the noise behaves roughly as the inverse of the sensitivity given that the noise of electronics is constant and the sensitivity increases for larger I_{ac}.

For larger I_{ac} the minor loop energy rapidly increases, in fact it increases much more rapidly than the sensitivity does, therefore the final noise recalculated in magnetic units eventually rises (and approaches the same slope of the minor loop

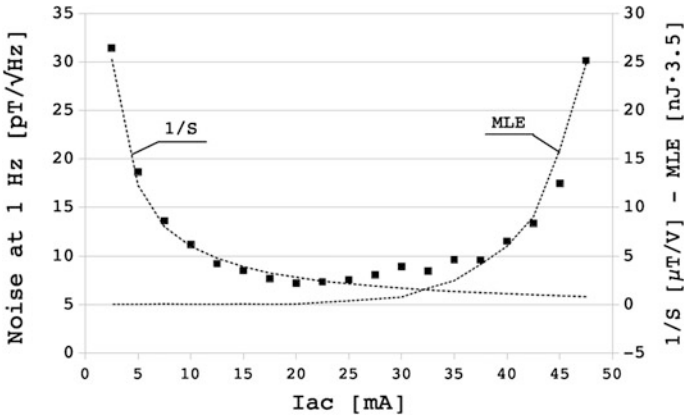

Fig. 16 Noise at 1 Hz of a fundamental mode orthogonal fluxgate (*squares*), inverse of the sensitivity (1/S) and minor loop energy (MLE) as a function of the I_{ac} for a I_{dc}

energy). In the middle between these two regions there is third region when the minimum energy is obtained. In this region the sensitivity is large enough to make the noise of the electronic negligible and reveal the actual magnetic noise of the core, yet I_{ac} is not too large to cause excessive minor loop energy (Fig. 16).

The minimum noise for a given I_{dc} is therefore found by selecting an amplitude of I_{ac} large enough to overcome the noise of the signal conditioning circuit but not too large to make the magnetization fall out of saturation and have the magnetic noise rise.

So far we considered only the case when I_{dc} was constant and I_{ac} was varying. If we now consider an increasing I_{dc} we find out the minimum energy is shifted in the bottom right direction (Fig. 17). For a larger value of I_{dc} the sensitivity, as we saw, decreases then it is necessary a larger I_{ac} to obtain the same sensitivity, which defeats the noise of signal conditioning circuits. At the same time higher saturation is achieved then the value of the minimum noise slightly decreases.

Then, one might think that an extremely large value of I_{dc}, with proper amplitude of I_{ac}, can eventually lead us to very low noise. Unfortunately there is a limit to the amplitude of the excitation current due to excessive heat a large current might cause.

Another important parameter is the frequency of I_{ac}. In this case the tradeoff is between a frequency which should not be too low to return a low sensitivity and not too large to let the current be too much affected by the skin effect. For Unitika AC-20 microwires the optimal range of frequency is between 70 and 130 kHz.

6.4 *Effect of the Anisotropy*

In the previous description of the working principle of fundamental mode orthogonal fluxgate we disregarded the effect of anisotropy by assuming the material was

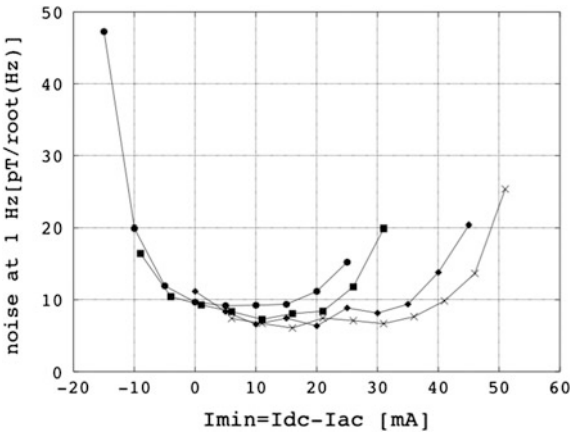

Fig. 17 Noise at 1 Hz of a fluxgate excited using different I_{dc} and I_{ac}. Every *line* corresponds to a value of I_{dc}: *circles* 35 mA, *squares* 41 mA, *diamonds* 50 mA, *crosses* 56 mA. The horizontal axis is the minimum value of the excitation current that is the most critical point in the hysteresis curve of the wire

isotropic. This is in fact not true, for anisotropy is typically found in magnetic wires. Anisotropy can positively or negatively affect the behavior of the sensor depending on its direction. If the anisotropy is out of circumferential axis an offset will arise in the output signal. The reason is easy to understand if we consider the contribution of the anisotropy to the position of the magnetization M. When we consider the total energy of M we should now consider also the energy due to the anisotropy calculated as:

$$E = -\mu_0 \cdot M \cdot (H_{ac} + H_{dc}) \cdot \cos(\alpha) - \mu_0 \cdot M \cdot H_Z \cdot \cos(\pi/2 - \alpha) + k_u \cdot \sin^2(\gamma - \alpha) \tag{3}$$

where γ is the angle of the anisotropy with the respect of the circumferential direction and k_u the anisotropy constant.

In other words, the anisotropy tries to pull the magnetization to its direction as well as magnetic fields do. Let us consider now the case when $H_Z = 0$; we would expect the output signal to be null too. However, if the anisotropy is out of circumferential direction the magnetization will be located at an angle α in between the direction of anisotropy and the circumferential axis as a compromise between $H_{dc} + H_{ac}$ which try to turn M counterclockwise and the anisotropy which try to turn M clockwise. Also in this case the angle α oscillates with the same frequency of I_{ac} given that α is maximum for $H_{dc} - |H_{ac}|$ and α is minimum for $H_{dc} + |H_{ac}|$. As a result a voltage is induced in the pick-up coil even if $H_Z = 0$.

On the other hand if the anisotropy lays in circumferential direction it has a positive effect on the fluxgate operated in fundamental mode. In this case the anisotropy works alongside the dc bias to keep the magnetization into saturation and reduce the noise.

This can be better understood by observing what happens when we increase the circumferential anisotropy by annealing the wire under the effect of a dc current flowing into the wire.

The technique is based on the principle that annealing a ferromagnetic material under the influence of magnetic field large enough to achieve saturation generates an anisotropy in the direction of the field [32]. This has been extensively used to change the anisotropy of magnetic materials for many applications, including fluxgates [33].

In this case we desire the anisotropy to be in circumferential direction, therefore we inject a large dc current in the wire to create a circumferential field. Figure 18 shows the circumferential B-H loop of an AC-20 wire from Unitika before and after annealing at 200 °C for 4 h with 90 mA dc current flowing through it. Note that the annealing is not obtained by joule effect caused by the wire but by an infrared furnace.

We can see that the effect of annealing under dc current is an increment of the circumferential anisotropy as the circumferential B-H loop appears more squared, therefore the circumferential one becomes the easy direction of magnetization. The anisotropy can be increased annealing for longer time or at higher temperature (still

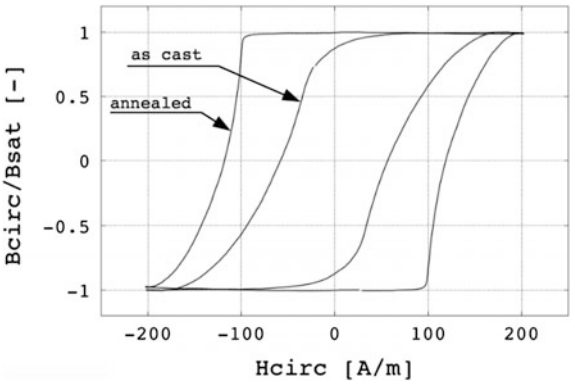

Fig. 18 Circumferential B-H loop of a magnetic wire as cast and after annealing at 200 °C for 4 h with 90 mA dc current flowing through it

keeping below Curie temperature) up to a technical limit where the anisotropy does not further increase.

If we now consider the fluxgate excited by $I_{dc} + I_{ac}$ we easily realize the minor loop energy is strongly reduced by the presence of a strong circumferential anisotropy. The magnetization keeps well saturated on the upper floor of the hysteresis curve; in order to fall out of saturation M should reach the knee of the B-H loop which is now located at lower value of H. In other words at the same value of $H_{dc} - |H_{ac}|$ while for as-cast wire M could be already at the knee on a annealed wire M is still in saturation. This brings a strong reduction of the magnetic noise, but of course it decreases the sensitivity too. Nevertheless, at low frequency the balance of lower magnetic noise but lower sensitivity brings lower final noise. For instance, in Fig. 19 we can see the noise spectrum of a 65 mm long fluxgate based on as-cast wires compared to the spectrum of a sensor based on wires annealed 45 min at 150 °C under the effect of 200 mA current. As we can clearly see the noise at 1 Hz decreased from 2.5 to 1 pT/$\sqrt{\text{Hz}}$ due to the large anisotropy created by annealing.

However, we see that for frequency higher than 40 Hz the noise of annealed core sensor is larger, for it earlier reaches the white noise region. This white noise is in

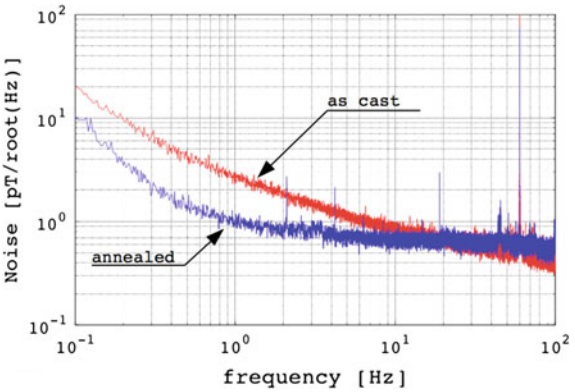

Fig. 19 Noise of a fundamental mode orthogonal fluxgate base on as cast wire and annealed wire

fact the noise of the noise of signal conditioning circuit, which emerges due lower sensitivity of the sensor.

6.5 Suppression of the Offset

One of the drawbacks of the anisotropy, as we mentioned before, is that any component of the anisotropy out of circumferential direction causes an offset in the output signal of the fluxgate.

It is vital to avoid the presence of axial field during annealing, in order to be sure the magnetization is as most circumferential as possible during the thermal treatment returning a circumferential anisotropy.

Another reason why we should avoid axial field during annealing is that the inner part of the core is exposed to lower circumferential field, therefore it is not saturated. In this inner region of the wire an axial field, if present, induces axial anisotropy, which makes the internal part of the core to be magnetized axially; as a result we would see a magnetic field measured by the sensor even at $Hz = 0$ because of the field generated by the internal part of the wire (Fig. 20).

There is in fact a smart method to suppress the offset caused by non-circular component of the anisotropy, and it consists of periodical switching of the dc bias and subsequently subtraction of the output voltages obtained with each polarity [34].

This method is based on the fact that if the dc bias is reversed the sensitivity changes polarity but the offset remains unchanged. The reason why the sensitivity is reversed—if we switch the polarity of the dc bias—can be seen in Fig. 21. Let us consider the case of positive dc bias (Fig. 21a) and increasing H_{ac}. For a given H_Z field to be measured, the magnetization M rotates counterclockwise as

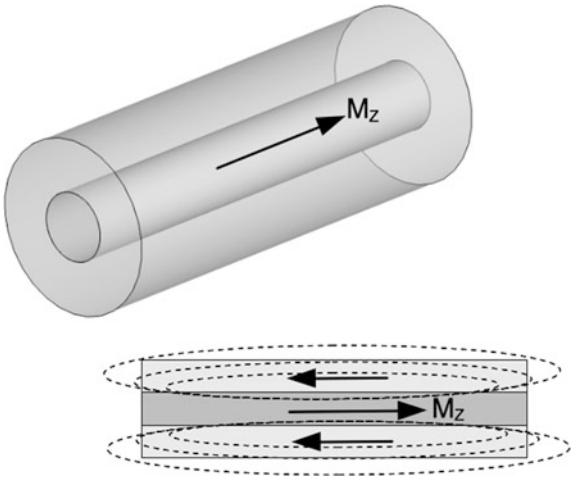

Fig. 20 Wire with axially magnetized inner region: the back-flux-lines will pass through the outer shell of the wire causing offset

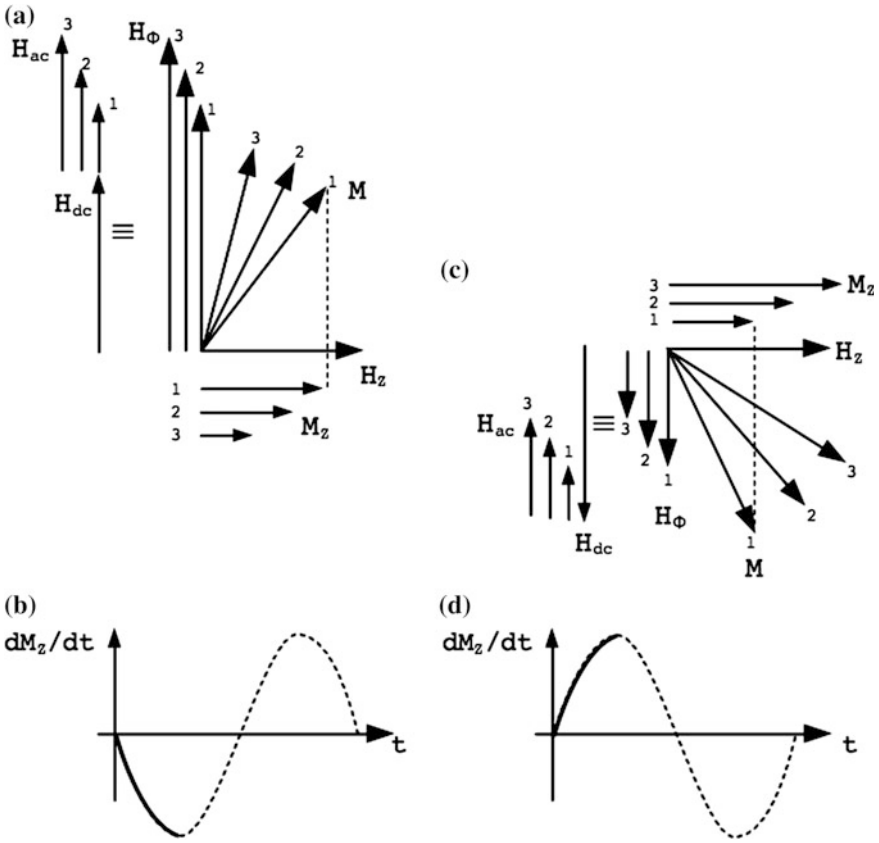

Fig. 21 Reversal of sensitivity for different polarity of dc bias

$H_\Phi = H_{dc} + H_{ac}$ increases. As a consequence the component of M in axial direction M_Z decreases. Therefore, a negative voltage is obtained at the pick-up coil, as this voltage is proportional to the derivative of the axial flux, and therefore of M_Z. In the second quarter of period H_{ac} decreases, so M rotates clockwise, M_Z increases, its derivative is positive and therefore a positive voltage is induced in the pick-up coil. The resulting waveform of the output voltage is summarized in Fig. 21b, including also the second half of the period.

Everything is reversed when the dc bias is negative. For negative H_{dc}, if H_{ac} increases the amplitude of the total excitation field H_Φ becomes smaller, and therefore M rotates counterclockwise (Fig. 21c); however, since M in in the fourth quadrant a counterclockwise rotation implies M_Z increases, therefore a positive voltage induced in the pick-up coil. Vice versa, in the second quarter of period, when H_{ac} decreases the voltage induced in the pick-up coil will be negative. If we now compare the voltage output obtained with positive H_{dc} (Fig. 21b) and the

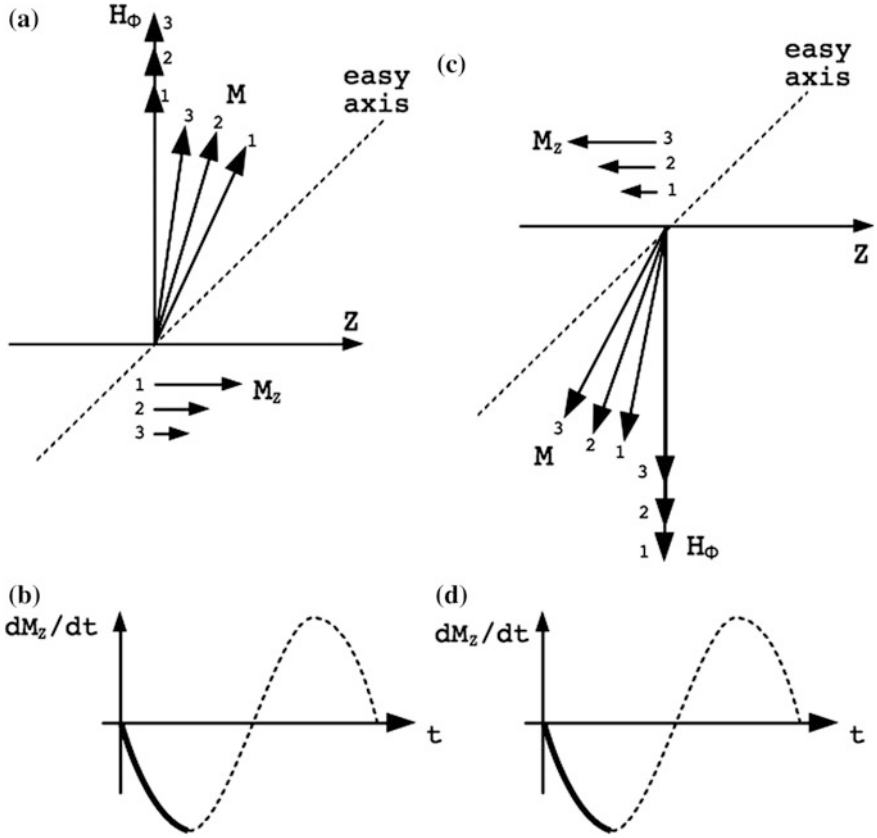

Fig. 22 Offset caused by non-circular anisotropy, equal for both positive and negative dc bias

voltage obtained with negative bias (Fig. 21d) we easily see the voltages are π radians shifted, therefore when one gets the real part of such voltage, the sign is reversed.

So far we considered the material to be isotropic. Let us now consider an off-circumferential anisotropy. In this case we have output voltage even at $H_Z = 0$, that is we have an offset. Let us repeat the same procedure used before to derive the polarity of the output voltage: if the dc bias is positive, for increasing H_{ac} we have increasing H_Φ. Then M, which lays between Φ axis and easy axis of magnetization rotates counterclockwise, giving a decreasing M_Z (Fig. 22a), and therefore a negative voltage (Fig. 22b).

If the dc bias is negative the magnetization, given the symmetry of the anisotropy, lays in the third quadrant. If H_{ac} increases then the absolute value of H_Φ decreases and M rotates clockwise (Fig. 22c). In this case M_Z increases but it is negative, so the output voltage is negative exactly as it was for positive dc bias (Fig. 22d).

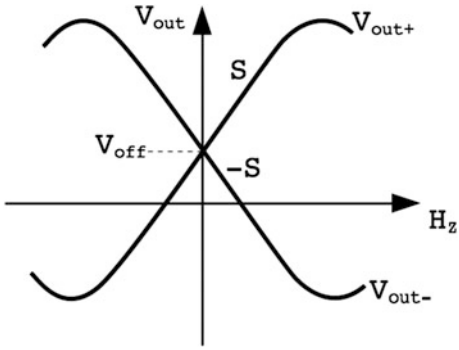

Fig. 23 Response of a fundamental mode orthogonal fluxgate with offset for positive (V_{out+}) and negative (V_{out-}) dc bias

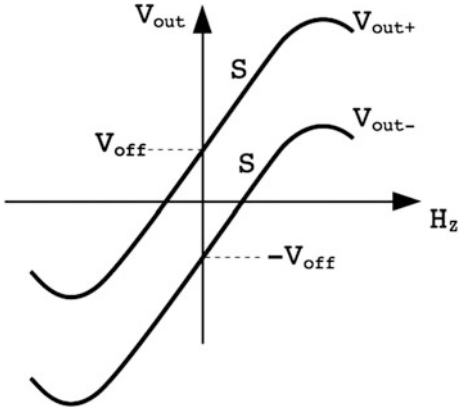

Fig. 24 Response of a fundamental mode orthogonal fluxgate with offset obtained switching both dc bias and ac current

In other words, when we switch the polarity of the dc bias the output voltage keeps the same polarity.

Generally speaking, given a fluxgate operated in fundamental mode the output characteristic after demodulation, shown in Fig. 23, can be described as $V_{out+} = S \cdot H_Z + V_{off}$ for positive dc bias and $V_{out-} = -S \cdot H_Z + V_{off}$ for negative dc bias, where S is the sensitivity and V_{off} is the offset voltage.

If we now subtract the voltages obtained with positive and negative dc bias we obtain

$$V_{out} = V_{out+} - V_{out-} = (S \cdot H_Z + V_{off}) - (-S \cdot H_Z + V_{off}) = 2S \cdot H_Z \qquad (4)$$

and we get rid of the offset.

As an alternative, one can switch both H_{dc} and H_{ac} (simply by flipping the polarity of the wire). In this case the sensitivity does not change sign but the offset does (Fig. 24):

$$V_{out+} = S \cdot H_Z + V_{off} \tag{5}$$

for $+H_{ac}$ and $+H_{dc}$

$$V_{out-} = S \cdot H_Z - V_{off} \tag{6}$$

for $-H_{ac}$ and $-H_{dc.}$

In order to cancel the offset we can simply add the voltage obtained with both polarities:

$$V_{out} = V_{out+} + V_{out-} = (S \cdot H_Z + V_{off}) + (S \cdot H_Z - V_{off}) = 2S \cdot H_Z \tag{7}$$

This solution is somehow more efficient from the practical implementation point of view because it only requires switching of the polarity of the excitation current while the output voltage can be simply integrated with the same integrator without need of performing difference of two voltages.

With this method we can efficiently suppress the offset. However, switching of the dc bias can generate additional noise to the output signal due to the spikes originated when the polarity is inverted. This problem can be solved by excluding from demodulation a few periods immediately after the switching in order to let any transient deplete. This can be done quite easily if digital signal conditioning is used as in [35]. Recently Karo Hikaru has implemented an analog signal conditioning circuit where the spikes due to switching of dc bias are removed using a solid state switches. Even if this technique efficiently reduced the noise due to the spikes the orthogonal fluxgate in fundamental mode with switched bias has significantly larger noise than the same sensor with non-switched bias (in this case it was 10 pT/$\sqrt{\text{Hz}}$ vs. 3 pT/$\sqrt{\text{Hz}}$ at 1 Hz). This gap is expected to be filled by synchronizing the switching time in order to avoid a quick transient form 0 V to the voltage of the pick-up coil when this is non-zero.

6.6 Temperature Stability

Alongside noise, another important issue for magnetic sensors is the stability versus temperature. For many applications indeed it is necessary to use magnetic sensor in environments where the temperature is not constant and in some case it can change several tens of degrees. In this case is it essential to verify how stable the output of the fluxgate is. For this reason it is important to characterize sensitivity and offset of the sensor for a large range of temperature.

The sensitivity is an important parameter but any change of open-loop sensitivity can be easily compensated by operating the fluxgate in feedback [36]; therefore, as long as we do not observe a consistent loss of sensitivity any moderate drift of sensitivity due to the temperature is not an issue.

Unfortunately offset cannot be compensated by feedback, therefore it is very important to produce sensors with low temperature drift of the offset. Fundamental mode orthogonal fluxgate has shown to have a very large temperature coefficient of offset [37], up to 59 nT/°C which is totally unacceptable. However, it was found out the offset drift is very similar for positive and negative dc bias (most probably due to the fact that the main cause of offset drift is the influence of temperature on anisotropy); this means that if we apply the dc bias switching techniques we used to cancel the offset we do not only suppress the offset at one temperature but we also strongly reduce the offset drift. By applying dc bias switching the offset drift was strongly reduced to 0.2–0.5 nT/K. While this is still larger then fluxgates properly designed for temperature stability which return offset drift as low as 0.044 nT/K [38], 0.02 nT/K [39] or 0.007 nT/K [40], switched fundamental mode orthogonal fluxgate still offers comparable or better offset drift than many commercially available parallel fluxgates which normally have 0.1–0.6 nT/K temperature coefficient.

6.7 Geometry of the Core

Dimensions and shape of a fluxgate strongly influence the performances of the sensor. In some applications we have constrains imposed by the maximum size allowed for the sensors. In some other cases we are freer to choose the size of the fluxgate. In both cases it is important to understand how the performances of the fluxgate depend on its geometry to maximize the results.

As we mentioned before, the orthogonal fluxgate has a huge advantage compared to parallel fluxgate, given that its cross section is often tens of μm to 100–150 μm. Therefore, in the X-Y plane the sensor's core has a very small dimension. When it comes the length, however, the choice of size is very important because it strongly affects the sensitivity and the noise of the fluxgate.

In order to understand why, we should first consider the behavior of the magnetic flux when a magnetic wire of a finite length and saturated in circumferential direction (as we do in fundamental mode orthogonal fluxgates) is placed in a region with uniform magnetic field. In Fig. 25 we can see that the magnetic flux converges to the microwire not only from the wire's terminations but also along its length. In fact, only a small part of the flux enters in the wire from its end; most of the flux enters in the wire from its outer cylindrical surface. Therefore we observe the flux to be minimum at the termination and then gradually increase up to the maximum in the center of the wire. In the second half of the wire everything is reversed and the flux symmetrically leaves the wire [41].

If we plot the flux inside the microwire we obtain a sort of bell showing the maximum flux in the center of the wire and rapidly drops at the terminations. As a practical consequence we derive that it is not necessary to wind the pick-up coil along the whole length of the core. We can keep the terminations of the wire out of the pick-up coil, because they bring negligible contribution to the output signal.

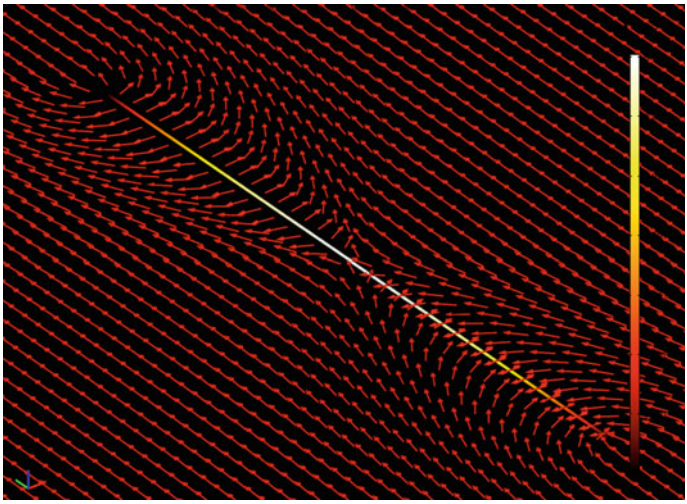

Fig. 25 Convergence of the magnetic flux to the core of a fluxgate in a uniform field

If we now consider wires with different length we find out that due to lower demagnetizing factor the longer is the wire the higher is the flux in the wire (Fig. 26).

This means that a fluxgate based on longer wire core has larger sensitivity, number of turns of the pick-up coil being equal. As a result also the final noise of the sensor decreases for longer wires. Does this mean that we can indefinitely decrease the noise of the fluxgate simply building a longer sensor? Of course not, there is a limit to the noise reduction that we can achieve by increasing the length of the core, and we can see it very well in Fig. 27a where the noise at 1 Hz is plotted

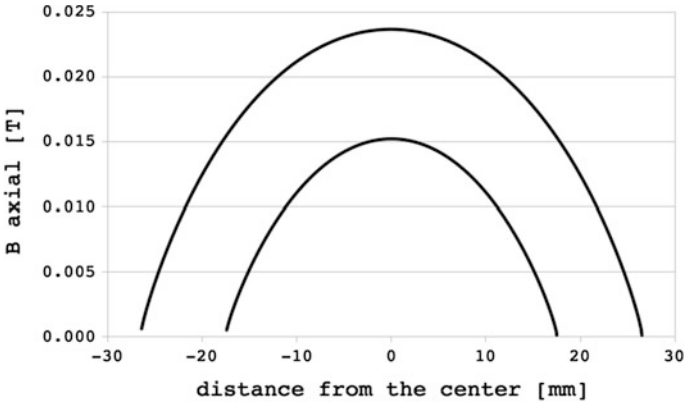

Fig. 26 Distribution of the field in the core of the fluxgate for 35 and 55 mm long cores

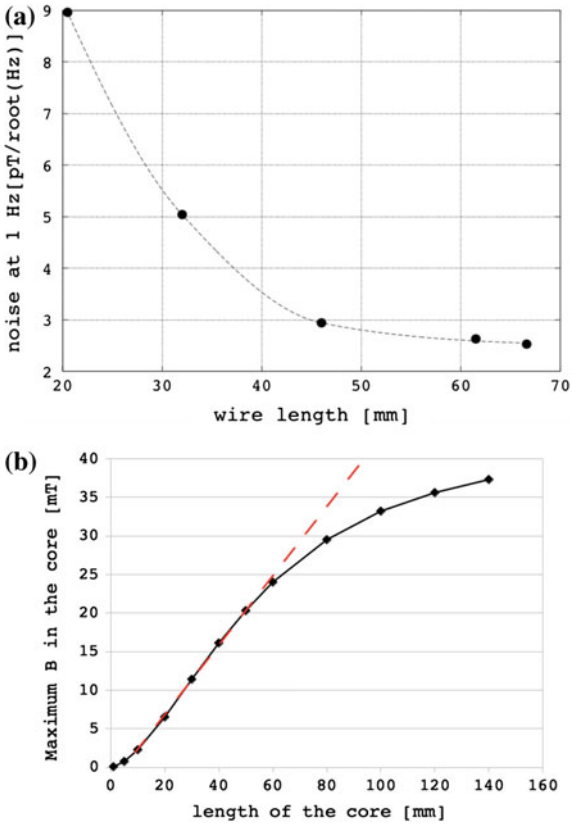

Fig. 27 Dependence of the noise at 1 Hz (**a**) and maximum B in the core (**b**) on the core length

versus the wire length for as cast double wire core (excited at 35 mA at 100 kHz and 40 mA dc bias).

As the length approaches 65 mm the noise does saturates to about 2.5 pT/$\sqrt{\text{Hz}}$, which looks like the minimum achievable noise with as cast wires.

The reason of such saturation in the reduction of the noise is simple to understand if we consider the amplitude of the flux inside the microwire versus the length (Fig. 27b). The flux rapidly increases if we increase the length till 60 mm; then, for longer cores, the flux still increases but with lower slope. The difference between these slopes is crucial; as we increase the wires' length we certainly increase the sensitivity but we also linearly increase the Barkhausen noise, simply because we have more magnetic material. For wires lower than 60 mm, the flux in the wire increases more rapidly than the magnetic noise because the slope in Fig. 27b is steep. Therefore, it makes sense to use a longer wire because the increase in sensitivity is larger than the increase of intrinsic magnetic noise. For longer wires however the sensitivity increases with the same rate as magnetic noise, therefore the advantage of a larger sensitivity is compensated by a similar increment of magnetic noise.

This means that it makes sense to increase the length of the core only until the magnetic flux, and therefore the sensitivity, increases more rapidly of the intrinsic magnetic noise of the wire. Generically speaking this length is different for different wires; as a rule of the thumb one can either calculate or measure (simply by induction method) the flux in the wire—taking as a reference the flux in the center of the wire—and plot it versus the length of the wire. The length where the flux has inflection is the limit length; increasing the length of the wire over this limit length does not contribute to decrease the noise.

7 Gradiometer Based on Orthogonal Fluxgate

With extensive development of orthogonal fluxgate operated in fundamental mode a very low noise magnetic sensor became available. Such low-noise fluxgate is then aimed to measure very low magnetic fields; quite often such low fields are generated locally either by magnetized material (e.g. magnetic nanoparticles used in biotechnologies) or by very tiny electric currents (e.g. magnetic field produced by beat of human heart). In both cases the sensor is certainly exposed to a very low magnetic field, but this field rapidly decreases as we get away from its source. It has been shown that fundamental mode orthogonal fluxgate can be used to measure adult human heart by placing the sensor very close to the patient chest [42], but this is not the best way to measure such low magnetic field. Indeed, instead of magnetic field one should measure the gradient of magnetic field, for the field rapidly drops as the distance increases generating a large gradient. If we simply measure the uniform magnetic field the measurement should be performed in a shielded environment to suppress, first of all, the Earth's magnetic field and other sources of uniform magnetic field much larger than the tiny field we are interested in. By using a gradiometer this can be avoided and we can just measure the gradient of magnetic field.

In a sense a first example of gradiometer based on orthogonal fluxgate was presented in [13] where they measured the magnetic field produced by magnetic domains of steel plates by using a fluxgate core composed of a bended wire: the first half of the wire was placed very close to the steal plate whereas the second half of the wire was kept 1 mm above in order to expose it only to the uniform field.

However, the first actual gradiometer based on orthogonal fluxgate was presented in [43]. In this case two 30 mm long fluxgate probes originally designed to measure homogeneous field where used to measure gradient by arranging them 50 mm apart and connecting in anti-series their pick-up coils.

In this case, we do not have a single core with two pick-up coils, but we have two different cores each of them with its own pick-up coil, and we derive the difference of the induced voltages to get rid of the response to the homogeneous field. The reason why two cores, instead of a single core, are used comes from smart method used to match the response to the homogenous field in order to fully suppress it.

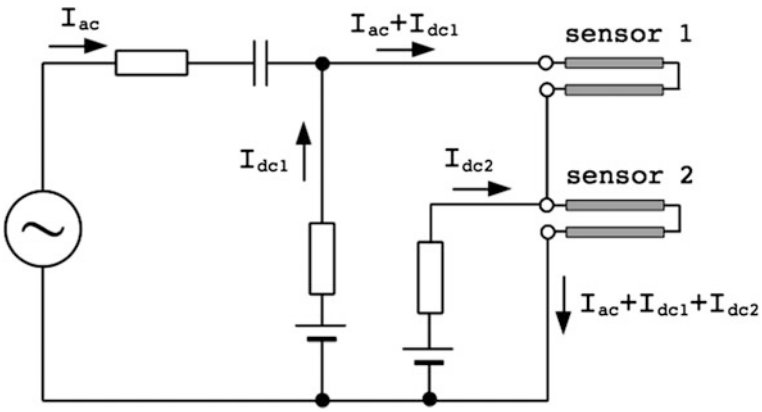

Fig. 28 Schematics of a gradiometer based on orthogonal fluxgate in fundamental mode with correction of sensitivity obtained using additional dc current on sensor 2

As a matter of fact it is almost impossible to build two sensors with sufficiently similar sensitivity to obtain negligible response to the homogenous field when the difference of the induced voltages is derived, even if the cores are excited by the same excitation current, and are composed of the same material with the same geometry.

Therefore, it is necessary to manually match the sensitivities of the sensors used in the gradiometer. This is typically done by either moving the coils or by changing the number of turns of the pick-up coil, yet it is very difficult to obtain a good match of the sensitivities.

In this case a smart technique is used to efficiently suppress the response to the homogenous field. This method is based on the fact that the sensitivity of a fundamental mode orthogonal fluxgate monotonically decreases if we increase the dc bias, as we saw in Fig. 14. Therefore, we can change the sensitivity of the sensor with larger sensitivity by increasing its dc bias in order to match the sensitivity of the second sensor. The simple schematics is shown in Fig. 28: alongside I_{ac} and I_{dc1} which flow through both sensors an additional current I_{dc2} is added to the one of the sensor to obtain fine tuning of its sensitivity. With this method the suppression ratio of the gradiometer is easily increased more than two orders of magnitude. Finally a gradiometer with 200 (pT/m)/$\sqrt{\text{Hz}}$ noise at 1 Hz can be obtained.

8 Signal Extraction and Operative Frequency

Sensors similar to fundamental mode orthogonal fluxgate have been proposed, during the last years, by developers devoted to giant magnetoimpedance (GMI) and classified as off-diagonal GMI. Even if such sensors failed to reach the same quality

of fundamental mode orthogonal fluxgate (the lowest noise reported so far was 1 pT/√Hz at 30 Hz and presumably 6–7 pT/√Hz at 1 Hz—derived from the 1/*f* curve even if actual data are not show [44]), it is worthy to analyze them, as this gives us the opportunity to better understand some features of orthogonal fluxgates, because this can teach us something how to properly extract signal from these sensors.

The structure of the sensor is the very same, a magnetic core—typically a wire—excited by an ac current plus a dc bias and a pick-up coil wound around it.

The first immediate difference is the method used to extract signal from the voltage induced in the pick-up coil. If large saturation of the core is achieved then the output voltage is very close to a sine-wave at fundamental frequency, therefore tuning of the pick-up coil is not necessary to achieve resonation at the desired frequency (on the contrary this is done in parallel fluxgate to retrieve the second harmonic buried in larger harmonics). However, phase sensitive detection is used in fundamental mode orthogonal fluxgate in the very same way it is performed in parallel fluxgates. This can be achieved by a standard lock-in amplifier or any other type of phase sensitive demodulation. Using a lock-in amplifier to extract a specific frequency from a voltage where that frequency is already prevalent to a large extend might look excessive. Developers of off-diagonal GMI often use simpler method to extract signal from the voltage induced in the pick-up coil, also because—as we will later discuss—off-diagonal GMIs are operated at larger frequencies than orthogonal fluxgates (up to several tens of MHz). In this case using synchronous demodulation with low noise is rather challenging. A cheaper alternative is to use as simple peak detector, which can be easily manufactured using diode-capacitor scheme [45].

A typical response of off-diagonal GMI obtained a peak detector is shown in Fig. 29.

The curve shows two pseudo-linear regions from 0 to about ±150 A/m, then after a peak the amplitude of the voltage decreases. Developers of off-diagonal GMI use a bias field H_0 to move the working point to the middle of one of the two pseudo-linear regions to use it as characteristic of the sensor [46].

Using this approach one might calculate the derivative of the curve shown if Fig. 29 and derive where the sensitivity (i.e. the slope of the curve) is maximum and set the H_0 bias there. In the same way one can easily realize that the sensitivity is zero for $H = 0$.

On the other hand, scientists working on fundamental mode orthogonal fluxgates use phase sensitive demodulation. This means that not only we extract a specific frequency from the picked-up voltage, but we also derive its real part instead of the total amplitude as peak detectors do. Let us consider again the same sensor whose response was shown in Fig. 29. If we extract the real part of the fundamental harmonic we obtain an actual linear response in the ±100 A/m instead of two pseudo-linear parts (Fig. 30).

It is clear that such response is much more suitable for a sensor, because it does not require a bias field H_0 to achieve a linear and antisymmetric characteristic. Moreover, it can be seen that the sensitivity at $H = 0$ is larger than the sensitivity at

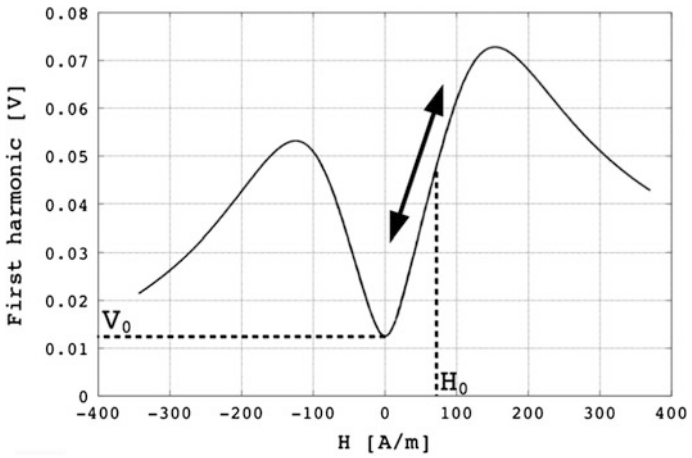

Fig. 29 Typical characteristic of off-diagonal GMI sensor obtained by measuring the amplitude of the voltage induced in the pick-up coil. A bias field H_0 is used to move the working point into the linear region

the bias field $H_0 > 0$ (where the slope is already decreasing because it is approaching the peak). So, considering the real part of the fundamental harmonic we obtain an actual linear characteristic and the highest possible sensitivity. It is possible this is achieved only by changing the signal conditioning techniques? In fact, it is.

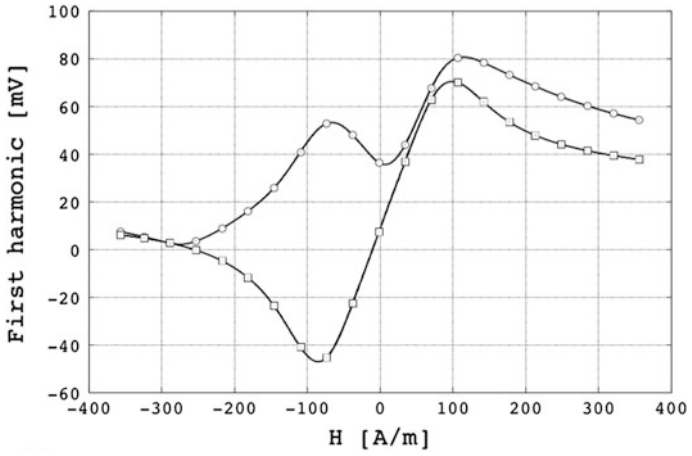

Fig. 30 Characteristic of fundamental mode orthogonal fluxgate (*squares*) and off-diagonal GMI (*circles*) for the very same sensor operated under the same conditions (I_{dc} = 20 mA, I_{ac} = 40 mA, f = 10.4 MHz)

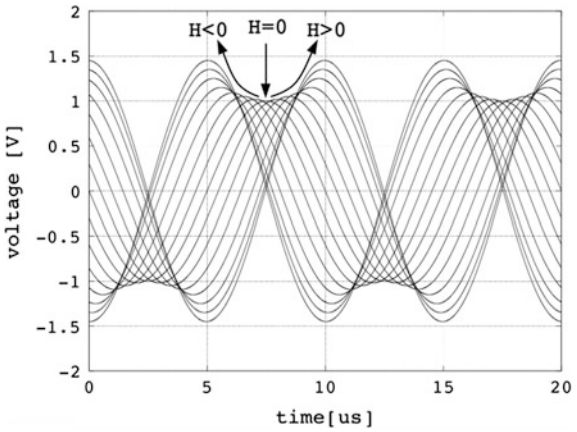

Fig. 31 Induced voltage in high-V_0-sensors for different value of measured field around $H = 0$

What is missing in the peak detector method used by the developers of off-diagonal GMI is the information about the phase. The voltage induced in the pick-up coil does not contain information about the measured field only in its amplitude but also in its phase.

In Fig. 29 we can see that the amplitude of the voltage it is not zero at $H = 0$ but it reaches its minimum value V_0. This means that around $H = 0$ the amplitude of the voltage does not significantly change; however, if we observe the voltage in time domain we would see a voltage with basically an unchanged amplitude shifting to the left or to the right according to the measured magnetic field. This means that around $H = 0$ the amplitude is steady whereas the phase of the voltage is changing (Fig. 31). In the ideal case when $V_0 = 0$ the phase simply switches by π radians exactly at $H = 0$; in actual cases $V_0 > 0$ and there is always a finite, although sometime narrow, range around $H = 0$ where the information about the field is not contained in the amplitude of the voltage but in its phase.

In some particular case V_0 is very large and it gets close to the maxima of the voltage amplitude response. If we simply use the amplitude response with a field

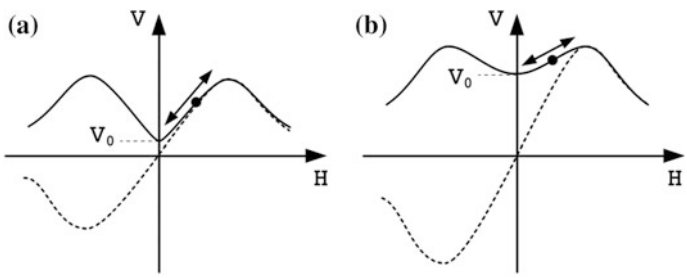

Fig. 32 Two responses of different sensors with low and large V_0, in amplitude (*solid line*) and real part (*dotted line*)

bias as developers of off-diagonal GMIs do, we might think that the sensitivity is very poor because of the lower slope we can obtain out of such response.

Using such method to extract information from the sensor's output voltage one can try to maximize the sensitivity by selecting the excitation parameters, which return low V_0 and then larger slope at the bias field H_0. This approach is however misleading: one might think that a response such the one in Fig. 32b has low sensitivity due to the slope at H_0, but this is not true. The sensor in fact has a large sensitivity, we are only extracting the signal in a very inefficient way. If we consider the real part of the voltage instead of its amplitude we find out the sensor has very large sensitivity (dotted lines in Fig. 32b), even larger that the response shown in Fig. 32a; we were mislead because we were looking at the amplitude while a considerable amount of the signal was represented by the phase.

Therefore, the method used in off-diagonal GMI to extract the signal is simply a very inefficient method to gather the information about the magnetic field we want to measure; such method should then be used only if the frequency is so high to make unpractical to used proper phase sensitive detection.

As already mentioned, an important difference between the fundamental mode orthogonal fluxgate and off-diagonal GMI is the excitation frequency: fundamental mode orthogonal fluxgates are often excited by an ac current with low frequency (100 kHz in [27], 40 kHz in [28], 1–32 kHz in [25], 130 kHz in [26]) whereas off diagonal GMI is operated at much higher frequency (1 MHz in [46], 10 MHz in [48], 1 MHz in [50] in ribbons). The main reason for this difference in the operative frequency is that orthogonal fluxgates based on microwires are traditionally operated at ∼kHz frequency, in order to easily saturate the wire, whereas GMI sensors

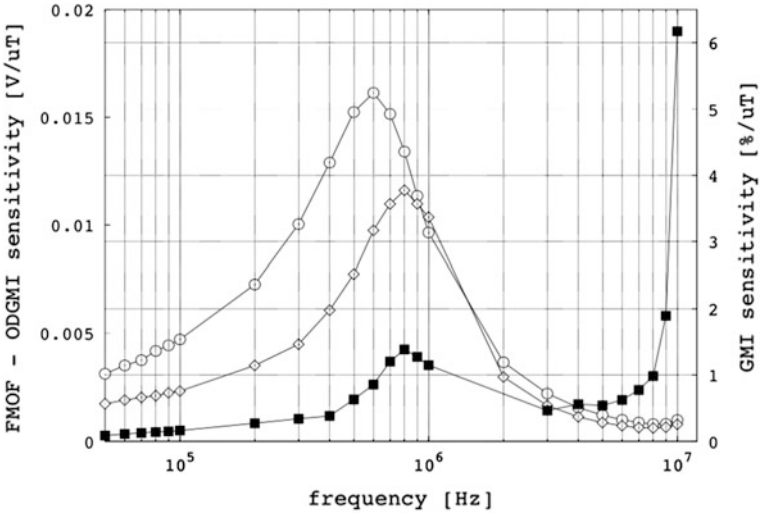

Fig. 33 Dependence of the sensitivity of fundamental mode orthogonal fluxgate (*circles*), off-diagonal GMI (*diamonds*) and classical GMI (*black squares*) on frequency

are excited by ac current in ∼MHz range in order to achieve significant skin effect, for this is the main cause of GMI effect [50].

Therefore, when using off-diagonal GMI sensors they usually operate them at high frequency as well. Another reason which brings many researches to use high frequency is that the induced signal is expected to be larger for higher frequency. However, this is not always true.

As previously mentioned, we must take into account that higher frequency makes the current drift to the border of the wire; as a consequence H_Φ is too low in the central part of the wire to achieve saturation. Therefore, as the frequency raises the thickness of the saturated shell of the wire decreases: even if the frequency is higher the amplitude of the rotating M is lower and eventually the induced voltage is lower than the voltage induced at lower frequency.

This can be clearly seen in Fig. 33 where the sensitivity for both fundamental mode orthogonal fluxgate and off-diagonal GMI are plotted versus frequency (for I_{dc} = 40 mA, I_{ac} = 18 mA). The sensitivity for off-diagonal GMI has been measured considering bias the middle point between $H_Z = 0$ and the value of H_Z where the peak in the characteristic was reached. The sensitivity of off-diagonal GMI clearly results lower than the sensitivity of fundamental mode orthogonal fluxgate (because sensitivity at $H = 0$ is larger than the one at $H = H_0$).

First of all we notice a resonance, due to the stray capacitance of the pick-up coil; some users tune the excitation frequency to the resonance frequency in order to maximize the sensitivity. This technique is useful in classical second harmonic fluxgate, because it helps to retrieve a small second harmonic buried in a large first harmonic signal. However, when working on fundamental mode orthogonal fluxgate the induced voltage is already at the desired frequency. If the wire is properly saturated the output voltage will be basically sinusoidal, therefore there is no need to use resonance frequency to retrieve a specific harmonic from a signal with multiple harmonics. Using resonance frequency is not always convenient, because the value of the resonance frequency may drift with temperature. Moreover, when we operate the sensor at resonance frequency we do not increase the actual signal generated from the sensor, but we simply amplify it by tuning the capacity and the inductance of the sensor; nonetheless the intrinsic signal coming from the rotation of the magnetization will be only due by the amplitude of the rotating M and its frequency, regardless how the signal is tuned at the pick-up coil. This means that operating the sensor at resonance frequency does not increase the amount of information in the signal provided by the sensor, it merely increases its amplitude.

In fact, this can be advantageous in case the main source of the noise in the magnetometer is the noise of the electronics. In this case it is useful to have an induced voltage as large as possible in order to decrease the equivalent noise of the magnetometer by dividing the electronic noise by a large sensitivity.

Excluding this specific case, using resonance frequency gives a large sensitivity which is just the result of a mere amplification, and eventually does not improve the signal-to-noise ratio of the signal. Since our goal is to analyze the intrinsic noise of the sensor, we disregard the frequency range where resonance occurs.

We can then consider two main regions in Fig. 33: the first is at frequency up to ~200 kHz before the resonance effect appear, the second is at frequency larger than ~3 MHz where the resonance has disappeared. Comparing these two regions we clearly notice the effect of the frequency: in the first region (up to ~200 kHz) the sensitivity increases linearly due to larger frequency (induction law). At this stage the skin effect is still negligible, therefore the only parameter affecting the sensitivity is the frequency. In the second region (above ~3 MHz) the sensitivity not only stops increasing as we should expect from the induction law, but it even drops at values considerably lower than those obtained for $f < 200$ kHz.

This means that skin effect is not negligible anymore for $f > 3$ MHz: the skin effect is substantially reducing the thickness of the saturated shell making the amplitude of the flux decrease and finally the sensitivity to drop. For this reason it is more convenient to operate the sensor in the first region, where skin effect is still negligible.

Moreover, Fig. 33 is useful because it helps also to understand the working principle of the sensor. Alongside the sensitivity of fundamental model orthogonal fluxgate and ODGMI in the same graph also the classical GMI sensitivity is shown. This is the off-diagonal GMI, or simply the classical GMI, that is the dependence of the wire impedance on H_Z. The value of classical GMI sensitivity is shown in percentage relative to the impedance at $H_Z = 0$ per μT. We observer that, excluding a small resonance, the classical GMI sensitivity is very small up to 3 MHz, then it rapidly increases. This confirms that the skin effect becomes significant for $f > 3$ MHz, as previously derived.

In other words, the giant magnetoimpedance effect is not involved at all in the mechanism which brings to the development of the signal in what is called off-diagonal GMI, since GMI effect arises only at frequencies where the off-diagonal GMI sensitivity is already vanishing.

As a matter of fact, the so called off-diagonal GMI sensors are a degraded version of orthogonal fluxgates in fundamental mode excited at too large frequency and with inefficient method for signal extraction.

References

1. Alldredge, USA Patent 2,856,581, 1952
2. F. Primdahl, The fluxgate mechanism, Part I: the gating curves of parallel and orthogonal fluxgates. IEEE Trans. Magn. **MAG-6**(2), 376–383 (1970)
3. M. Butta, P. Ripka, Two-domain model for orthogonal fluxgate. IEEE Trans. Magn. **44**(11), 3992–3995 (2008)
4. J.P. Sinnecker, K.R. Pirota, M. Knobel, L. Kraus, AC magnetic transport on heterogeneous ferromagnetic wires and tube. J. Magn. Magn. Mater. **249**(1–2), 16–21 (2002)
5. P. Ripka, X.P. Li, F. Jie, Orthogonal fluxgate effect in electroplated wires. IEEE Sens. (2005)
6. X.P. Li, Z.J. Zhao, T.B. Oh, H.L. Seet, B.H. Neo, S.J. Koh, Current driven magnetic permeability interference sensor using NiFe/Cu composite wire with a signal pick-up LC circuit. Phys. Status Solidi A **201**, 1992–1995 (2004)

7. M. Butta, P. Ripka, G. Infante, G.A. Badini-Confalonieri, M. Vázquez, Bi-metallic magnetic wire with insulating layer as core for orthogonal fluxgate. IEEE Trans. Magn. **45**(10), 4443–4446 (2009)
8. X.P. Li, J. Fan, J. Ding, H. Chiriac, X.B. Qian, J.B. Yi, A design of orthogonal fluxgate sensor. J. Appl. Phys. **99**(8), Article number 08B313 (2006). ISSN 0021-8979
9. X.P. Li, J. Fan, J. Ding, X.B. Qian, Multi-core orthogonal fluxgate sensor. J. Magn. Magn. Mater. **300**(1), e98–e103 (2006)
10. P. Ripka, X.P. Li, F. Jie, Multiwire core fluxgate. Sens. Actuators, A **156**(1), 265–268 (2009). ISSN 0924-4247
11. P. Ripka, M. Butta, F. Jie, X.P. Li, Sensitivity and noise of wire-core transverse fluxgate. IEEE Trans. Magn. **46**(2), 654–657 (2010). ISSN 0018-9464
12. F. Jie, N. Ning, W. Ji, H. Chiriac, X.P. Li, Study of the noise in multicore orthogonal fluxgate sensors based on Ni-Fe/Cu composite microwire arrays. IEEE Trans. Magn. **45**(Sp. Iss. SI), 4451–4454 (2009). ISSN 0018-9464
13. Y. Terashima, I. Sasada, Magnetic domain Imaging using orthogonal fluxgate probes. J. Appl. Phys. **91**(10), 8888–8890 (2002). ISSN 0021-8979
14. J. Kubik, L. Pavel, L. Ripka, P. Kaspar, Low-power printed circuit board fluxgate sensor. IEEE Sens. J. **7**(2), 179–183
15. E. Delevoye, A. Audoin, A. Beranger, R. Cuchet, R. Hida, T. Jager, Microfluxgate sensors for high frequency and low power applications. Sens. Actuators, A **145** (SI), 271–277 (2008)
16. M. Butta, P. Ripka, S. Atalay, F.E. Atalay, X.P. Li, Fluxgate effect in twisted magnetic wire. J. Magn. Magn. Mater. **320**(20), E974–E978 (2008)
17. M. Butta, P. Ripka, G. Infante, G.A. Badini-Confalonieri, M. Vázquez, Magnetic microwires with field induced helical anisotropy for coil-less fluxgate. IEEE Trans. Magn. **46**(7), 2562–2565 (2010)
18. P. Ripka, M. Butta, M. Malatek, S. Atalay, F.E. Atalay, Characterization of magnetic wires for fluxgate cores. Sens. Actuators, A **145**(special issue), 23–28 (2007)
19. M. Butta, P. Ripka, J.P. Navarrete, M. Vázquez, Double coil-less fluxgate in bridge configuration. IEEE Trans. Magn. **46**(2), 532–535 (2010)
20. S. Atalay, V. Yagmur, F.E. Atalay, N. Bayri, Coil-less fluxgate effect in CoNiFe/Cu wire electrodeposited under torsion. J. Magn. Magn. Mater. **323**(22), 2818–2822 (2011)
21. S. Atalay, P. Ripka, N. Bayri, Coil-less fluxgate effect in $(Co_{0.94}Fe_{0.06})_{72.5}Si_{12.5}B_{15}$ amorphous wires. J. Magn. Magn. Mater. **322**(15), 2238–2243(2010)
22. M. Butta, P. Ripka, M. Vazquez et al., Microwire electroplated under torsion as core for coil-less fluxgate. Sens. Lett. **11**(1, SI), 50–52 (2013)
23. I. Sasada, Orthogonal fluxgate mechanism operated with dc biased excitation. J. Appl. Phys. **91**(10), 7789–7791 (2002). ISSN 0021-8979
24. D. Jiles, *Introduction to Magnetism and Magnetic Materials* (Chapman & Hall, London, 1991). ISBN 0-412-38640-2
25. E. Paperno, Suppression of magnetic noise in the fundamental-mode orthogonal fluxgate. Sens. Actuators, A **116**(3), 405–409 (2004). ISSN 0924-4247
26. E. Paperno, E. Weiss, A. Plotkin, A tube-core orthogonal fluxgate operated in fundamental mode. IEEE Trans. Magn. **44**(11), 4018–4021 (2008)
27. I. Sasada, H. Kashima, Simple design for orthogonal fluxgate magnetometer in fundamental mode. J. Magn. Soc. Jpn. **33**, 43–45 (2009)
28. M. Butta, I. Sasada, Method for offset suppression in orthogonal fluxgate with annealed wire core. Sens. Lett. **12**, 1295–1298 (2014)
29. M. Butta, S. Yamashita, I. Sasada, Reduction of noise in fundamental mode orthogonal fluxgates by optimization of excitation current. IEEE Trans. Magn. **47**(10), 3748–3751 (2011)
30. M. Butta, I. Sasada, Sources of noise in a magnetometer based on orthogonal fluxgate operated in fundamental mode. IEEE Trans. Magn. **48**(4), 1508–1511 (2012)
31. C. Dolabdjian, B. Dufay, S. Saez, A. Yelon, D. Menard, Is low frequency excess noise of GMI induced by magnetization fluctuations? in *International Conference on Materials and Applications for Sensors and Transducers (ICMAST)*, 2013, Prague, Czech Republic

32. F. Johnson, H. Garmestani, S. Y. Chu, M.E. McHenry, D.E. Laughlin, Induced anisotropy in FeCo-based nanocrystalline ferromagnetic alloys (HITPERM) by very high field annealing. IEEE Trans. Magn. **40**(4), 2697–2699 (2004)
33. P. Butvin, M. Janosek et al., Field annealed closed-path fluxgate sensors made of metallic-glass ribbons. Sens. Actuators, A **184**, 72–77 (2012)
34. I. Sasada, Symmetric response obtained with an orthogonal fluxgate operating in fundamental mode. IEEE Trans. Magn. **38**(5), 3377–3379 (2002)
35. Eyal W., Eugene P. Noise investigation of the orthogonal fluxgate employing alternating direct current bias. J. Appl. Phys. **109**, 07E529 (2011)
36. P. Ripka (ed.), *Magnetic Sensors and Magnetometers* (Artech House, Norwood, MA, 2001). ISBN: 1580530575
37. M. Butta, I. Sasada, M. Janosek, Temperature dependence of offset and sensitivity in orthogonal fluxgate operated in fundamental mode. IEEE Trans. Magn. **48**(11), 4103–4106 (2012)
38. A. Moldovanu, E.D. Diaconu, C. Ioan, E. Moldovanu, Magnetometric sensors with improved functional parameters. J. Magn. Magn. Mater. **157**(158), 442–443 (1996)
39. Y. Nishio, F. Tohyama, N. Onishi, The sensor temperature characteristics of a fluxgate magnetometer by a wide-range temperature test for a Mercury exploration satellite. Meas. Sci. Technol. **18**(8), 2721–2730 (2007)
40. A. Cerman, J.M.G. Merayo, P. Brauer et al., Self-compensating excitation of fluxgate sensors for space magnetometers, in *IEEE Instrumentation And Measurement Technology Conference*, vols. 1–5, pp. 2059–2064 (2008)
41. M. Butta, I. Sasada, Effect of terminations in magnetic wire on the noise of orthogonal fluxgate operated in fundamental mode. IEEE Trans. Magn. **48**(4), 1477–1480 (2012)
42. Shoumu Harada, Ichiro Sasada, Feng Hang, Development of a one dimensional fluxgate array and its application to magnetocardiogram measurements. IEEJ Trans. Fundam. Mater. **133**(6), 333–338 (2013)
43. I. Sasada, S. Harada, Fundamental mode orthogonal fluxgate gradiometer. IEEE Trans. Magn. **50**(11) (2014)
44. M. Malatek, B. Dufay, S. Saez, C. Dolabdjian, Improvement of the off-diagonal magnetoimpedance sensor white noise. Sens. Actuators, A **204**, 20–24 (2013)
45. B. Dufay, S. Saez, C. Dolabdjian, A. Yelon, D. Ménard, Characterization of an optimized off-diagonal GMI-based. IEEE Sens. J. **13**(1), 379–388 (2013)
46. D. Ménard, D. Seddaoui, L.G.C. Melo, A. Yelon, B. Dufay, S. Saez, C. Dolabdjian, Perspectives in giant magnetoimpedance magnetometry. Sens. Lett. **7**(3), 339–342 (2009)
47. K. Goleman, I. Sasada, A triaxial orthogonal fluxgate magnetometer made of a single magnetic wire with three U-Shaped branches. IEEE Trans. Magn. **43**(6), 2379–2381 (2007)
48. B. Dufay, S. Saez, C. Dolabdjian, D. Seddaoui, A. Yelon, D. Ménard, Improved GMI sensors using strongly-coupled thin pick-up coils. Sens. Lett. **7**(3), 334–338 (2009)
49. L. Kraus, Off-diagonal magnetoimpedance in stress-annealed amorphous ribbons. J. Magn. Magn. Mater. **320**(20), E746–E749 (2008)
50. K. Knobel, M. Vázquez, L. Kraus, *Giant Magneto Impedance, Handbook of Magnetic Materials*, vol. 15 (Elsevier, K.H.J. Buschow, 2003)

Giant Magneto-Impedance (GMI) Magnetometers

Christophe Dolabdjian and David Ménard

Abstract This chapter is about recent advances in giant magneto-impedance (GMI) magnetometer development. The emphasis is put on their performances in terms of equivalent magnetic noise. We first present the physical principles and outline the model of the GMI effect. Next, we establish the relation between the GMI sensing element and the associated electronic conditioning circuits, thus providing expressions for the performances of the device. Our approach is pragmatic and aimed at scientists and engineers concerned with sensitive magnetic measurements. It is hoped that our presentation of the topic will be useful to workers in the field who wish to compare GMI to other magnetic sensors.

1 Introduction

The magneto-impedance (MI) effect refers to the change in the electrical impedance of a ferromagnetic metal due to the application of an external magnetic field. While it was observed and qualitatively understood several decades ago [1], it was not until the development of magnetically ultrasoft metals that the effect was recognized for its potential for magnetic field sensing in the 1990s [2]. By 1994, several groups had reported large impedance variation in CoFeSiB amorphous microwires [3–7] and the term giant magneto-impedance (GMI) was gradually adopted to qualify the effect. In the subsequent years, the effect was observed in a variety of soft magnetic wires and ribbons and the initial phenomenological models were extended into quantitative models. The vast amount of work involved during this first decade of "GMI re-discovery" is too numerous to be properly reported her, but

C. Dolabdjian (✉)
Université de Caen Normandie, Caen, France
e-mail: christophe.dolabdjian@unicaen.fr

D. Ménard
Polytechnique Montréal, Montréal, Canada
e-mail: david.menard@polymtl.ca

A. Grosz et al. (eds.), *High Sensitivity Magnetometers*, Smart Sensors, Measurement and Instrumentation 19, DOI 10.1007/978-3-319-34070-8_4

the interested reader may find a comprehensive review of the development over that period in Ref. [8].

Magneto-impedance is a general property of any ferromagnetic metals. However, the effect can be particularly spectacular in ultra-soft magnetic wires and ribbons, whether amorphous or nanocrystalline [8]. The most widely used materials are CoFeSiB-based soft amorphous wires (exact composition varies among different research group). Wires or ribbons can be fabricated, for instance, by in-rotating water quenching [9, see also 10], glass-coated melt spinning [11] and melt extraction [12]. A fairly large number of GMI studies, over the last two decades, have also been dedicated to studies of the effect of various annealing procedures on the GMI response. It is generally accepted that soft amorphous materials with slightly negative magnetostriction coefficient, submitted to a proper stress, current, or combined stress and current annealing, yield the largest GMI ratio and highest sensitivity.

The present chapter is mostly concerned with the exploitation of the GMI effect for the development of magnetic sensors as magnetometers. Section 2 presents the physical basis for modelling the effect. For simplicity, we focus on single domain wires with uniform circumferential anisotropy, thus avoiding any difficulties associated with the details of the domain structure and domain-wall dynamics and of non-uniform anisotropy distribution. While the magnetic susceptibility, and therefore the GMI, can be related to the domain-wall dynamics at low-to-moderate frequencies (such that the domain-wall motion is not damped), we chose to ignore these effects for the following reasons. Domain structures are hard to predict and to control in these ultra-soft magnetic metals, they are most likely a source of magnetic noise, but fortunately they are relatively easy to eliminate, using a small dc bias current, which we usually do in practice.

We also chose not to focus on details of model interpretation, particularly on the confusion or misunderstandings associated with the established link between GMI and ferromagnetic resonance, along with the use of a non-local permeability due to the inclusion of an exchange term in the equation of motion for the magnetization. We will limit ourselves by stating that the non-local permeability, leading to so-called exchange-conductivity effects, have been demonstrated to set fundamental limits on the performance of GMI sensors [13, 14]. The interested reader will find a discussion of these issues in Ref. [15]. Finally, we also chose to limit our discussion to the linear behavior, which leads to simple analytic treatment. A numerical treatment of the non-linear regime has been presented, for instance, in Ref. [16].

In Sect. 3, we are concerned with the sensitivity and noise of an idealized GMI sensor. Contrary to the widespread practice of using the GMI ratio

$$\frac{\Delta Z}{Z} = \frac{Z(B) - Z\left(B_{ref}\right)}{Z\left(B_{ref}\right)}, \tag{1}$$

as a figure of merit, here we adopt the pragmatic point of view that the main criterion relevant to the design of highly sensitive GMI (or low noise GMI)

magnetometers is the maximum voltage sensitivity, defined as the derivative of voltage across the GMI sample, at the applied magnetic field at the static working point (bias field) B_0,

$$\left.\frac{\partial V}{\partial B}\right|_{B=B_0}, \tag{2}$$

expressed in V/T. As was recently discussed [17], the GMI ratio is not particularly meaningful as a metric for sensitive magnetometry and it can be misleading in the comparison of the performance between GMI wires from different sources.

Section 4 considers the design of a GMI-based magnetometer, that is, a device which outputs a voltage linearly proportional to the measured field in the full output dynamic range. An overview of the conditioning electronics is presented, along with the estimation of the associated performances. To conclude, the state of art of recent GMI magnetometer development is given.

2 Physics of Magneto-Impedance

2.1 Phenomenology of the MI Effect

Consider a magnetic wire of length l and radius a, driven by a longitudinal electrical current i_{ac} and placed in a longitudinal static magnetic field H_0, as shown in Fig. 1. It is found experimentally that the electrical impedance of the wire depends sensitively upon the longitudinal component of the applied static field. The phenomenon is referred to as magneto-impedance. The complex impedance, $Z = R + iX$, of the wire is obtained from the ratio of the voltage v_{ac} across the wire and the drive current i_{ac},

$$Z = \frac{v_{ac}}{i_{ac}} = \frac{\ell}{2\pi a}\left.\frac{e_z}{h_\varphi}\right|_{surface}, \tag{3}$$

where e_z is the surface longitudinal electric field, and h_φ the circumferential magnetic field. For nonmagnetic conductors, the ratio of the fields on the right hand side of Eq. (3), which corresponds to the surface impedance, is directly calculated from Maxwell's equations. The procedure results in the electrical impedance, which depends on the electromagnetic skin depth.

For magnetic conductors, we may assume a similar dependence of the impedance, provided the classical (non magnetic) skin depth is replaced by an effective skin depth which depends upon the magnetic field. Thus, the normalized impedance will be expressed as

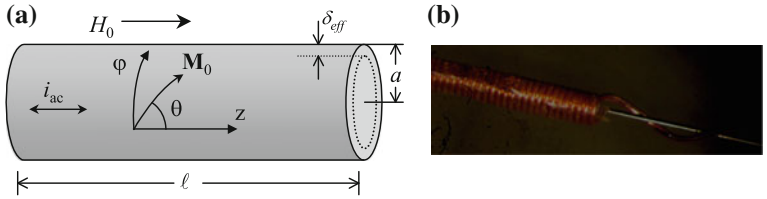

Fig. 1 **a** Ferromagnetic metallic wire driven by an AC current and submitted to a longitudinal magnetic field to be measured. **b** Picture of a wire with an associated coil

$$\frac{Z}{R_{dc}} = \frac{ka}{2}\frac{J_0(ka)}{J_1(ka)}, \tag{4}$$

where R_{dc} is the dc resistance of the wire, and

$$k = \frac{1-i}{\delta_{eff}}, \tag{5}$$

is the radial propagation constant, related to the effective skin depth

$$\delta_{eff} = \sqrt{\frac{2}{\omega\,\sigma\,\mu_{eff}}}. \tag{6}$$

In Eq. (6), ω is the angular frequency, σ is the electrical conductivity, and μ_{eff} is the effective permeability.

In order to observe a strong MI effect, the effective penetration depth, δ_{eff}, of the electromagnetic field must be much smaller than the radius, a, of the wire. When this is the case, the ratio of the Bessel functions in the right hand side of Eq. (4) equals the imaginary unit i, and Eq. (4) reflects the inverse dependence of the normalized impedance on the effective skin depth

$$\frac{Z}{R_{dc}} = \frac{1+i}{2}\frac{a}{\delta_{eff}}. \tag{7}$$

Equation (7) is generally valid for the GMI response of microwires in the MHz range. However, for frequencies of a few kHz or less, or for sub-micron structures, the situation may be such that the skin depth is much larger than the transverse dimension of the sample. For such cases, the ratio of Bessel functions in the right hand side of Eq. (4) may be expanded in series, which yields

$$Z = R_{dc} + \frac{i\omega\ell}{8\pi}\mu_{eff}. \tag{8}$$

In this limit, we would refer to the effect as magnetoinductive. Since μ_{eff} is generally complex, both the real and imaginary parts of Z may vary appreciably with the field.

The effective permeability, defined by Eqs. (4)–(6), is a useful concept to discuss the physics of the GMI effect. However, it merely displaces the problem from a calculation of the impedance to a calculation of the effective permeability. For the important case of a wire with helical anisotropy, relatively simple, approximate expression for the effective permeability, may be obtained.

2.2 *Effective Permeability*

Consider the cylindrical coordinate system in which the static field H_0 is applied longitudinally along the z-axis, as shown in Fig. 1, with a circumferential easy axis of anisotropy. When there is no applied field, the magnetization is circumferential, that is $\theta = 90°$. Thus, the circumferential component of the dynamic magnetic field produced by the driving current is parallel to the static magnetization. If the drive current is small enough to avoid nonlinear effects, there should be no response from the magnetization, and the material behave as a normal nonmagnetic conductor. Thus, for a circumferential magnetization the effective permeability is trivially μ_0. If the wire is magnetically saturated along the z axis, that is $\theta = 0°$, the coupling between the magnetization and the circumferential field is maximum. This corresponds to a transverse effective permeability which is defined as μ_t. For the general case ($0° \leq \theta \leq 90°$), μ_0 and μ_t are related to the diagonal component of the impedance tensor defined in a helical coordinate system with the z' axis at an angle θ from the z axis, that is, parallel to the static magnetization $\mathbf{M}_0$. As an example, for a circumferential uniaxial anisotropy characterized by an energy $K\sin^2\theta$, K is the anisotropy constant (J/m^3), the anisotropy field is given by $H_k = 2\,K/\mu_0 M_s$ and the static equilibrium is given by $\cos\theta = H_\theta/H_k$. The tensor is then rotated by an angle θ in order to be oriented along the wire axis. The procedure leads to a general effective scalar permeability[1].

$$\mu_{eff} = \left(\sqrt{\mu_t}\cos^2\theta + \sqrt{\mu_0}\sin^2\theta\right)^2. \tag{9}$$

The heart of the problem consists of calculating the transverse effective permeability μ_t. Note that, despite the fact that the permeability which enters Maxwell's equations is a 3×3 tensor, the magnetic behavior is effectively determined by a simple scalar effective transverse permeability,

[1]See Eq. (49) or Ref. [14]

$$\mu_t/\mu_0 = 1 + m_\varphi/h_\varphi. \tag{10}$$

This follows from the constraint $h_r = -m_r$ on the out-of-plane components of the fields, which is a consequence of the dipolar field associated with the radial k-vector, and also from the fact that the components of the fields parallel to the static magnetization do not contribute to the magnetic response. One may alternatively work in terms of a tensor of surface impedance and apply the constraints subsequently, in order to obtain an effective scalar impedance, as was done in Ref. [14].

The effective transverse permeability is calculated from the ferromagnetic torque equation of motion

$$\frac{d\mathbf{M}}{dt} = -|\gamma|\mu_0 \mathbf{M} \times \left(\mathbf{H} + d_{ex}^2 \nabla^2 \mathbf{M}\right) - \mathbf{R}. \tag{11}$$

where $|\gamma|/2\pi$ =28 GHz/T is the gyromagnetic ratio, μ_0 is the permeability of free space, $\mathbf{M}$ is the magnetization vector, and $\mathbf{H}$ is the "Maxwellian" magnetic field, which includes external, dipolar, and demagnetizing fields. While the effective anisotropy field has not been included here for simplicity, it can be easily accounted for, as will be discussed below. The exchange effective field, which arises from non-uniform magnetization vector, is expressed in terms of the exchange length

$$d_{ex} = 2A/\mu_0 M_s^2, \tag{12}$$

where A is the exchange stiffness. In Eq. (11), $\mathbf{R}$ is a phenomenological relaxation term, which can take various mathematical forms, such as a viscous damping (Gilbert term) or a relaxation (modified Bloch-Bloembergen term) or both terms, as

$$\mathbf{R} = \frac{\alpha}{M_s}\mathbf{M} \times \frac{d\mathbf{M}}{dt} + \frac{\mathbf{M} - \mathbf{M}_0}{\tau}, \tag{13}$$

where $\mathbf{M}_0$ is the static part of the magnetization. The Gilbert parameter α is dimensionless and relates to viscous damping, whereas the Bloch-Bloembergen $1/\tau$ term corresponds to a relaxation rate in rad/s. The calculation of the effective permeability from Eq. (11) has been described in detail in previous publications [13, 14].

Let us first consider a wire magnetically saturated in the z direction. Equation (11) is solved in cylindrical coordinates, in a small signal approximation. This leads to a k dependent susceptibility tensor,

$$\begin{pmatrix} m_r \\ m_\varphi \end{pmatrix} = \begin{pmatrix} \chi & -i\kappa \\ i\kappa & \chi \end{pmatrix} \begin{pmatrix} h_r \\ h_\varphi \end{pmatrix}. \tag{14}$$

The tensor components are given by

$$\chi = \frac{\omega_M \tilde{\omega}_H}{\tilde{\omega}_H^2 - \tilde{\omega}^2}, \quad \kappa = \frac{\omega_M \tilde{\omega}}{\tilde{\omega}_H^2 - \tilde{\omega}^2}, \tag{15}$$

where

$$\omega_M = \gamma \mu_0 M_0, \tag{16}$$

$$\tilde{\omega} = \omega - i/\tau, \tag{17}$$

$$\tilde{\omega}_H = \gamma \mu_0 H_0 + i\alpha\omega + \omega_M d_{ex}^2 k^2, \tag{18}$$

are in units of angular frequency. Note the implicit condition $m_z = 0$, which arises from the small signal approximation. Equation (14) describes the response of the dynamic magnetization to an internal dynamic field. The effect of anisotropy and demagnetizing fields, which is neglected here, can be included in Eq. (18) by the replacement of H_0 by an effective internal field. In the *local approximation*, exchange interaction is neglected, and the last term in k^2 is omitted from Eq. (18).

Due to the skin effect, the wave vector k will be perpendicular to the surface of the wire and the fields are expected to vary with the radial coordinate in terms of Bessel functions. Maxwell's equations will then lead to the relations

$$h_r = -m_r, \tag{19}$$

$$h_\varphi = \frac{k_0^2}{k^2 - k_0^2} m_\varphi, \tag{20}$$

where $k_0 = (1 - i)/\delta_0$ relates to the non magnetic skin depth obtained with $\mu_{eff} = \mu_0$ in Eq. (6). With the observation that $k^2/k_0^2 = \mu_{eff}/\mu_0$, Eq. (20) simply restates that $\mu_{eff}/\mu_0 = 1 + m_\varphi/h_\varphi$. The combination of Eqs. (14) and (19) enables one to solve for the scalar transverse permeability

$$\frac{\mu_t}{\mu_0} = 1 + \frac{m_\varphi}{h_\varphi} = \frac{\tilde{\omega}_{AR}^2 - \tilde{\omega}^2}{\tilde{\omega}_R^2 - \tilde{\omega}^2}. \tag{21}$$

where the complex resonance

$$\tilde{\omega}_R^2 = \tilde{\omega}_H(\tilde{\omega}_H + \omega_M), \tag{22}$$

and antiresonance

$$\tilde{\omega}_{AR}^2 = (\tilde{\omega}_H + \omega_M)^2, \tag{23}$$

angular frequencies have been defined for convenience.

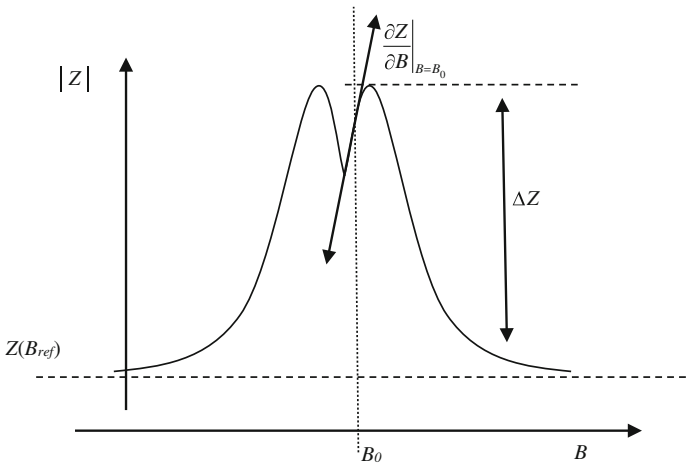

Fig. 2 Characteristic GMI response of a wire as a function of a longitudinal applied field

In the local approximation, Eq. (21) may be substituted directly in Eq. (9), with the proper θ dependence of the effective internal field, which will yield the effective skin depth and thus, the permeability of the wire. Otherwise, the exchange term in Eq. (18) leads to a k-dependent transverse permeability, or equivalently, to spatial dispersion of the permeability. Since μ_t depends on k, which also depends on μ_t, the non-local approach requires a self-consistent solution. Detailed analysis has been presented in Refs. [13, 14].

In summary, combining Eqs. (5), (6), (8) and (20) leads to the normalized impedance

$$\frac{Z}{R_{dc}} = \sqrt{\frac{i\omega\sigma\mu_0 a^2}{4}}\left(\sqrt{\frac{\tilde{\omega}_{AR}^2 - \omega^2}{\tilde{\omega}_R^2 - \omega^2}} + \tan^2[\theta(H_0)]\right)\cos^2[\theta(H_0)]. \tag{24}$$

In Eq. (24), θ is presented as an explicit function of the static external applied field H_0, emphasizing the two mechanisms of impedance variation: magnetization reorientation as a function of the field and field-dependent transverse permeability. Figure 2 illustrates a characteristic GMI impedance variation as the function of a longitudinal applied magnetic, as modeled by Eq. (24). As illustrated, the calculation provides an evaluation of the two figures of merit, defined in Eqs. (1) and (2).

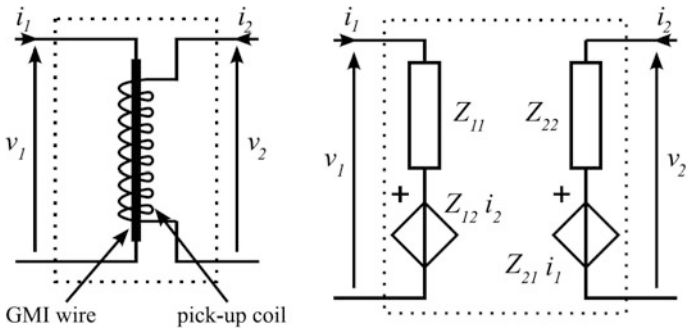

Fig. 3 Sensing element schematic and its associated two port network model illustrating the different terms of the impedance matrix given in Eq. (25) [18]

3 GMI Sensors

3.1 Two-Pole Network Model

Here, we describe how a GMI element can be engineered into a sensor, using a two-port network approach [18]. A schematic of the sensing element is illustrated in Fig. 3, along with the associated two-port network model. It consists of a GMI wire inside a long solenoid or pick-up coil.

The GMI sensing element may be described by its field-dependent impedance matrix $[Z(B_{ext})]$, where $B_{ext} = \mu_0 H_{ext}$ is the longitudinal component of the external magnetic induction.[2] Its expression is

$$\begin{pmatrix} v_1 \\ v_2 \end{pmatrix} = [Z(B_{ext})] \begin{pmatrix} i_1 \\ i_2 \end{pmatrix} = \begin{bmatrix} Z_{11} & Z_{12} \\ Z_{21} & Z_{22} \end{bmatrix} \begin{pmatrix} i_1 \\ i_2 \end{pmatrix}, \tag{25}$$

where v_p and i_p are the voltage across or current into port p (1 or 2), as illustrated in Fig. 3. For operation at low field amplitude in a closed field configuration (feedback loop), the external magnetic induction may be written as

$$B_{ext} = B_0 + b(t), \tag{26}$$

where B_0 is the static working point (bias field) and $b(t)$ is the measured ac signal. Under a small signal approximation, the first order expansion of the impedance components yields

[2]Due to strong demagnetizing effect and assuming that we measure fields that are much smaller than the saturation magnetization, the GMI elements are essentially sensitive to the longitudinal component of the field.

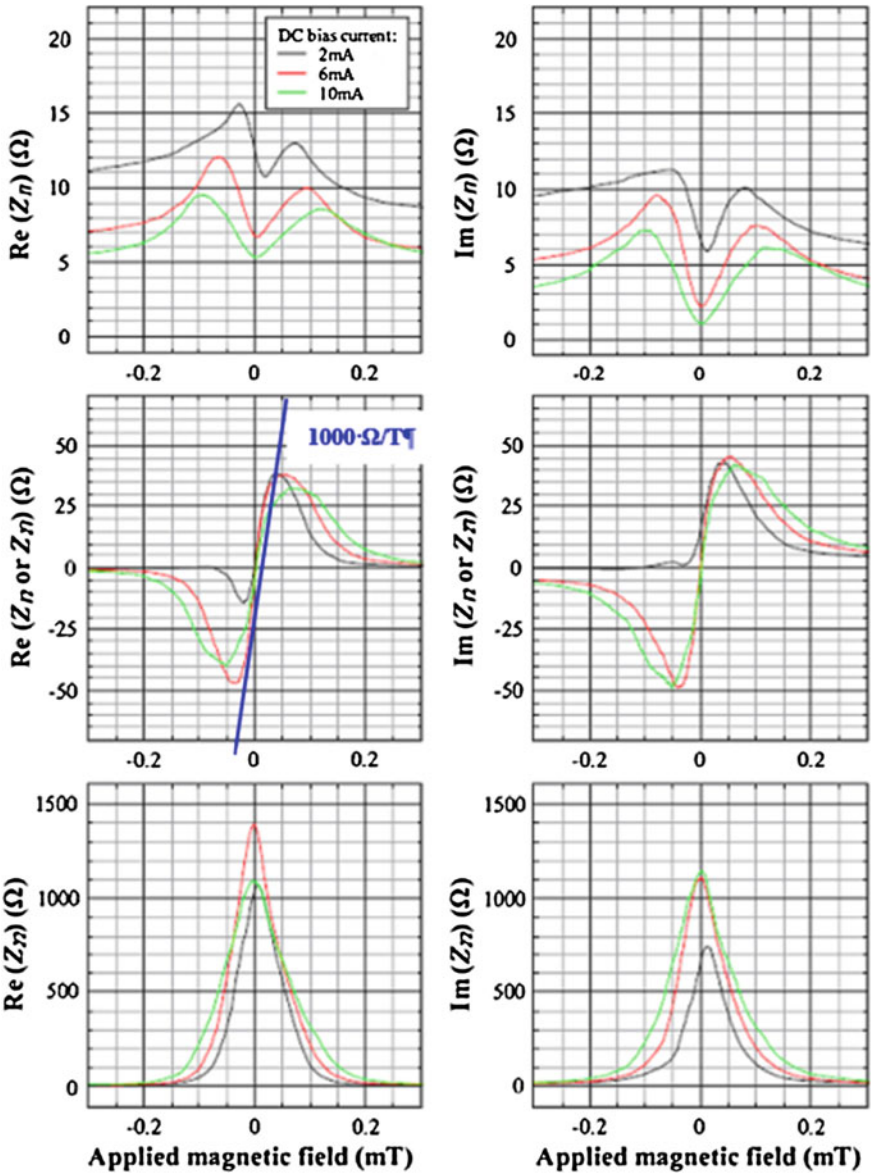

Fig. 4 Real and imaginary parts of the components of the impedance matrix, $Z_{ij}(B)$, as a function of the applied magnetic field for three dc bias currents. Measurements were performed for an excitation frequency, f_0, of 300 kHz. On the Re(Z_{12}) curve, we show an estimated differential variation of the impedance sensitivity, $S_{12-\Omega}$, at a zero field working point in Ω/T [18]

$$Z_{ij} = Z_{ij_0}(B_0) + \left.\frac{\partial Z_{ij}}{\partial B}\right|_{B=B_0} \cdot b(t) = Z_{ij_0} + S_{ij-\Omega} \cdot b(t), \tag{27}$$

where $Z_{ij0} = Z_{ij}(B_0)$ is the impedance at the bias field and $\partial Z_{ij}(B)/\partial B$ (= $S_{ij-\Omega}$) are the intrinsic sensitivity of the corresponding impedance components, in units of Ω/T.

As implied by Eq. (25), there are four different configurations for excitation and detection, each related to a component of the impedance matrix. Examples of measured impedance components, $Z_{ij}(B)$, as a function of applied field are presented in Fig. 4 [18].

The matrix components, in Eq. (25), are given by [19]

$$[Z] = \begin{pmatrix} \frac{l}{2\pi a}\left(Z_M \cos^2\theta_M + Z_N \sin^2\theta_M\right) & N(Z_N - Z_M)\sin\theta_M \cos\theta_M \\ N(Z_N - Z_M)\sin\theta_M \cos\theta_M & \frac{2\pi a N^2}{l_c}\left(Z_M \cos^2\theta_M + Z_N \sin^2\theta_M\right) \end{pmatrix}, \tag{28}$$

where l, l_c, and N are the length of the wire, the length of the pick-up coil, the number of turns of the coil, N, respectively. This expression of the impedance matrix can also be extended to include the parasitic capacitance of the pick-up coil, C_{coil}, yielding [19]

$$[Z'] = \begin{pmatrix} Z_{11} - \frac{jZ_{12}Z_{21}C_{coil}\omega_0}{1+jZ_{22}C_{coil}\omega_0} & \frac{Z_{12}}{1+jZ_{22}C_{coil}\omega_0} \\ \frac{Z_{12}}{1+jZ_{22}C_{coil}\omega_0} & \frac{Z_{22}}{1+jZ_{22}C_{coil}\omega_0} \end{pmatrix}, \tag{29}$$

where ω_0 is angular frequency of the sinusoidal current excitation of amplitude I_{ac}.

3.2 Sensitivity of the Sensor

The output voltage V_{out} of the sensor, ideally proportional to the measured field, depends upon several factors, including the intrinsic sensitivity, the driving current and the conditioning electronics. Let us consider a typical lock-in detection scheme in any of the four configurations *A*, *B*, *C* or *D*, as illustrated in Fig. 5. The classical single wire configuration (*A* configuration), which was treated in Sect. 2, consists of a direct measurement of the wire electrical impedance, whereas the so-called off-diagonal or wire-coil configuration (*B* configuration), corresponds to an excitation current through the GMI wire, with a voltage detection across the pick-up coil.

The excitation and detection stages consist of a voltage generator, e_{g1}, having an internal resistance, R_1, and associated with carrier compensation circuitry. The detector is a lock-in amplifier, locked to the excitation frequency, f_0 [18]. The output sensitivity, also called the transfer, T_r, at the lock-in amplifier output, expressed in V/T, is defined as

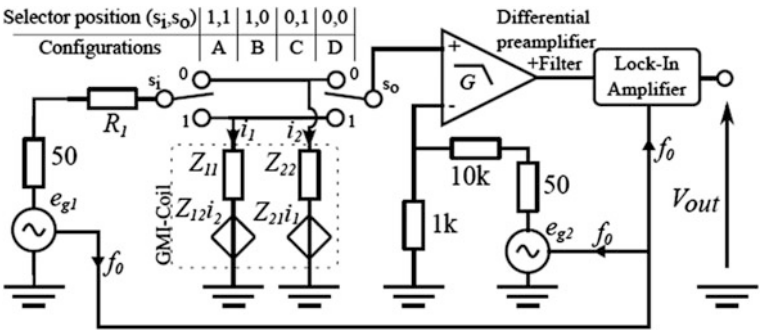

Fig. 5 Diagram of the two-pole network sensor and its associated signal conditioning (preamplifier + detector) [18]

$$T_{r_X} = \frac{\partial V_{out}}{\partial B}. \tag{30}$$

where $X = (A, B, C \text{ or } D)$ indicates the measuring configuration and V_{out} is the output voltage. Assuming a linear response, the sensitivity can be obtained from $S_{ij\,-\Omega}$, Z_{ij0} and the circuit elements. The Fourier transform of the voltage at the lock-in output is given by

$$V_{out}(\omega) \approx G\left[I_{ac}\left(Z_{ij_0}(\omega_0) + \left.\frac{\partial Z_{ij}(\omega_0)}{\partial B}\right|_{B=B_0} \cdot b(\omega) + k_{DS} z_{n_{ij}}(\omega)\right) + k_{DS} e_{n_X}(\omega_0)\right], \tag{31}$$

where G and k_{DS} are the gains associated with the preamplifier and the detector, $z_{n_{ij}}(\omega)$ is the equivalent impedance spectral noise density source, in $\Omega/\sqrt{\text{Hz}}$ and $e_{n_X}(\omega)$ is the equivalent conditioning voltage noise, in $\text{V}/\sqrt{\text{Hz}}$. At the working frequency and the static working point (bias field), the output sensitivity is

$$T_{r_X} = G\, I_{ac} \frac{\partial Z_{ij}(\omega_0)}{\partial B} = \frac{I_{ac}}{2} \frac{\partial Z_{ij}(\omega_0)}{\partial B}, \tag{32}$$

and the equivalent voltage noise

$$v_n(\omega) = G k_{DS}\, I_{ac}\; z_{n_{ij}}(\omega) + G\, k_{DS}\, e_{n_X}(\omega_0) = \frac{1}{\sqrt{2}}\left[I_{ac}\, z_{n_{ij}}(\omega) + e_{n_X}(\omega_0)\right], \tag{33}$$

where the right hand terms in Eqs. (32) and (33) were obtained by setting $G = 1/2$ and $k_{DS} = \sqrt{2}$, where k_{DS} is a correction factor varying from $\sqrt{2}$ to 1, depending upon the type of synchronous detector or lock-in used [20, 21]. Here, we consider a product detector using a sinusoidal function, at the same frequency and in phase with the carrier.

With an ideal sinusoidal current generator ($R_1 \gg Z_{11}$ or Z_{22}) and a high input preamplifier impedance, the sensitivity of the sensor is simply given by

$$T_{r_x} \approx \frac{\partial \left| Z_{ij}(\omega_0) \right|}{\partial B} \frac{I_{ac}}{2}. \tag{34}$$

The specifics of electronic conditioning are further discussed below. Details may be found in Ref. [18].

3.3 Equivalent Magnetic Noise of the Sensor

3.3.1 Intrinsic Magnetic Noise

It is well known that thermal fluctuations of the magnetization set fundamental limits to the signal-to-noise ratio of magnetic sensors, with a response depending upon the magnetization direction of their sensing elements, with magnetoresistive element as an example [22]. Estimation of the impact of the magnetization fluctuations on the equivalent magnetic noise of GMI sensors was first discussed in [23] and subsequently developed in [24]. More recently, the contribution of the hysteresis losses to the low-frequency noise was considered for the *A* configuration [25] and extended to the *B* configuration in Ref. [26].

Based on the equipartition theorem and a simplified physical model of the GMI response, the intrinsic magnetic noise is expressed by Ménard et al. [23]

$$\overline{z_{n_{ij}}^2(\omega)} \approx \left(\frac{\partial Z_{ij}}{\partial \theta} \right)^2 S_{\theta\theta}^2(\omega) \approx \left(\frac{\partial Z_{ij}}{\partial \theta} \right)^2 \left(\frac{4 k_B T \chi''}{2\pi f \mu_0 M_s^2 \vartheta} \right), \tag{35}$$

where $S_{\theta\theta}$ is the spectral density of the magnetization direction fluctuations, χ_t, the magnetic susceptibility, ϑ, the effective volume of the wire, μ_0 the permeability of free space, and $k_B T$, the thermal energy. The imaginary part of the susceptibility, χ'', is related to various dissipation mechanisms. For example, Eq. (35) implies that a viscous damping, proportional to the frequency, yields a frequency independent noise (white noise), whereas frequency independent hysteresis losses, should result in $1/f$ noise at low frequency.

The equivalent magnetic power noise spectral density, in T^2/Hz, is given by the magnetic part of the voltage noise spectral density, Eq. (33), divided by the transfer, Eq. (34), that is

$$\overline{b_n^2(f)} = 2 \frac{\overline{z_{n_{ij}}^2(\omega)}}{\left| \partial Z_{ij}(f_0)/\partial B \right|^2}. \tag{36}$$

In Ref. [27], it was shown that magnetic contribution to white noise is given by

$$\left|\frac{\partial Z_{ij}(f_0)}{\partial B}\right|^2 = \left|\left(-\frac{\sin\theta}{\mu_0 H_{\text{int}}}\right)\frac{\partial Z_{ij}}{\partial \theta}\right|^2. \tag{37}$$

Then, assuming a wire with circumferential anisotropy, the magnetization as a function of field is given by $M/M_s = \cos\theta = H_0/H_k$, and the internal field by $H_{\text{int}} = \left(H_k^2 - H_0^2\right)/H_k$. The sensor is usually operated at a few MHz, with a dc bias field approximately equal to $H_0 = H_k/2$. In these conditions, using Eqs. (35)–(37), an estimate of the equivalent magnetic power noise spectral density, is given by

$$\overline{b_n^2(f)} = \left(\frac{4\mu_0 k_B T \chi''}{\pi f \vartheta}\right)\frac{H_{\text{int}}^2}{|\sin\theta|^2 M_s^2} = \frac{3\mu_0 k_B T}{\pi \vartheta}\frac{H_k^2}{M_s^2}\frac{\chi''}{f}. \tag{38}$$

Assuming a worst case scenario, provided by $\chi'' \approx M_s/H_k$, a very rough estimate of the equivalent magnetic power noise spectral density, in the low frequency regime is

$$\overline{b_n^2(f)} \approx \left(\frac{3\mu_0 k_B T}{\pi \vartheta}\frac{H_k}{M_s}\right)\frac{1}{f}. \tag{39}$$

A lower limit to $1/f$ excess noise, at low frequency, is given by the theoretical intrinsic magnetic white noise, [17]

$$\overline{b_n^2(f)} \approx \frac{Z_{11}^2}{|\partial Z_{11}(f)/\partial B|^2}\left(\frac{4k_B T\alpha}{\gamma \mu_0^2 H_K^3 \vartheta}\right), \tag{40}$$

where γ and α are the gyromagnetic ratio and the dimensionless Gilbert damping parameter, respectively. In principle, the Johnson noise of the dc resistance of the GMI sensor, which is included in Eq. (42), should be considered also as an intrinsic noise contribution. In contrast, as discussed below, the white noise regime has been limited so far by the conditioning electronics.

To conclude, the low frequency equivalent magnetic noise spectral density is expected to scale with the impedance sensitivity ratio, with the square root of the absolute temperature, and inversely with the square root of the wire volume. While the analysis above must be considered to be a very rough estimate of the equivalent GMI magnetic noise, numerical values suggest that thermal magnetic noise arising from thermal fluctuations of the magnetization could be a significant contribution to the low frequency intrinsic noise of the sensing element. Further theoretical and experimental studies are required to address this issue in the future.

3.3.2 Noise from the Conditioning Electronics

The output equivalent noise of the system can be estimated based on the classical conditioning circuitry illustrated in Fig. 4. Assuming a well-conditioned electronic circuit, there are three main sources of this noise.

The first is noise induced by the voltage generators, e_g. Signal instability of sinusoidal sources are generally characterized by the single sideband noise spectral density expressed in decibel below the carrier per hertz (dBc/Hz), in direct relation to the output amplitude of the source. This allows one to evaluate the voltage power noise spectral density of the two generators shown in Fig. 4 to be

$$e_{ng_i}^2(f) = \frac{e_{g_i}^2}{10^{\mathrm{dBc}/10+3}} \quad (i = 1, 2), \tag{41}$$

where e_{ng_i} is the amplitude of the sinusoidal signal generator. The order of the dBc, around 100–140 dB at 1 Hz, depends upon the generator performance. The amplitude, e_{g2}, of the second generator is usually related to e_{g1} since the amplitudes of the signals at the inverting and non-inverting inputs of the preamplifier need to be approximately equal. Consequently, the noise level of the second generator, $e_{ng2}(f)$, may be expressed as functions of $e_{ng1}(f)$ and of circuit elements.

The second noise source is that of the preamplifier, which may be summarized by its $(e_n(f) - i_n(f))$ model, considering an input voltage white power $e_{2npreamp}(f)$ and an input current, $i_{2npreamp}(f)$.

The third source is the Johnson noise of each resistor, R, of the setup, including that of the GMI element, expressed as

$$e_{nR}^2 = 4k_B TR, \tag{42}$$

where k_B (1.38×10^{-23} J K^{-1}) is the Boltzmann constant and T (300 °K) is the electronic operating temperature.

Considering an AM signal at the preamplifier input of the form A_c [1 + m cos ($\omega_m t$)] cos($\omega_0 t$), where ω_m is the angular frequency of the sensed field, $b(t)$, and ω_0 is that of the excitation (driving) current, $I_{ac}(t)$. The filtered demodulated signal is multiplied by cos($\omega_0 t$). Consequently, the output noise spectral density is increased by a factor $G \cdot k_{DS}$, due to the quadratic sum of the noise of the sidebands which have to be considered (cf. Eq. 33). This effectively results in a decrease by a factor k_{DS} of the signal to noise ratio. Consequently, we can express the equivalent output white noise power spectral density given at the output, after demodulation and low-pass filtering, by

$$e_{n_X}^2(f) \approx G^2 k_{DS}^2 \left\{ \left(\frac{\left| Z_{ij_0}(f_0) \right|}{R_1} \right)^2 \left[2e_{ng1}^2(f) + e_{nR1}^2 \right] + e_{npreamp}^2 + e_{nRx}^2 + R_x^2 i_{npreamp}^2 \right\}. \tag{43}$$

Finally, the equivalent magnetic noise spectral density of the setup, b_{nX}, in pT/$\sqrt{\text{Hz}}$, is defined as the ratio of the electronic noise spectral density (in V/$\sqrt{\text{Hz}}$) to the sensitivity (in V/T), $b_{nX} = e_{nX}/T_{rX}$.

We note that this description leads to a good estimation of the experimental noise and also that the magnetic noise spectral density is dominated either by the excitation or detection stages, depending upon whether the excitation currents, or sensor sensitivity, are high or low. The non-trivial noise behavior exhibited by each configuration (A, B, C, D), leads to a better understanding of the sensor noise limitations. The configuration in which the signal at the coil terminals is measured (often named off-diagonal, $X = B$) appears, at present, to be the most efficient in decreasing the electronic conditioning equivalent output magnetic noise spectral density. Details may be found in Ref. [28].

Overall, the GMI equivalent magnetic noise due to the two main noise source contributions (intrinsic 1/f noise and white conditioning electronic contribution noise) is described by

$$\begin{aligned}\overline{b_{nx}^2(f)} &\approx \overline{b_n^2(f)} + \overline{e_{nx}^2(f)}\Big/T_{rx}^2(f) \\ &\approx 3\mu_0 \frac{k_B T}{\pi f \vartheta}\frac{H_K}{M_S} + \frac{k_{DS}^2\left\{\left(\left|Z_{ij_0}(f_0)\right|/R_1\right)^2\left[2e_{ng1}^2(f) + e_{nR1}^2\right] + e_{npreamp}^2 + e_{nRx}^2 + R_x^2 i_{npreamp}^2\right\}}{\left|\partial Z_{ij}(f_0)/\partial B\right|^2 I_{ac}^2}\end{aligned} \tag{44}$$

4 Magnetometer Development

4.1 Conditioning Electronics

There are two principal modes of excitation of a GMI sensor: the classical sine wave generation [18] and pulsed generation [29, 30]. Examples are shown in Figs. 6 and 7. The first provides a single frequency, the second a multiple frequency excitation mode.

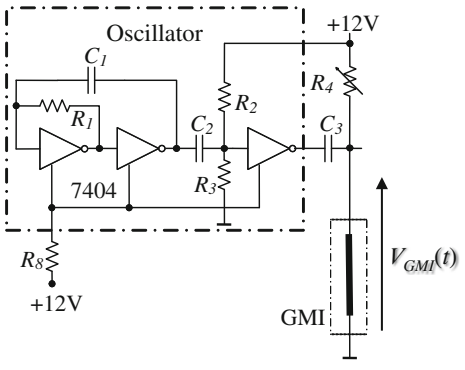

Fig. 6 Typical electronic design based on a pulse generator [31]

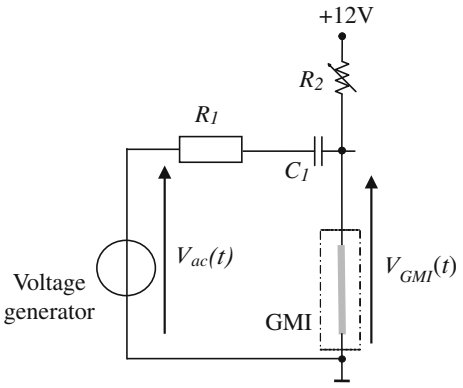

Fig. 7 Typical electronic design based on a sine-wave generator [28]

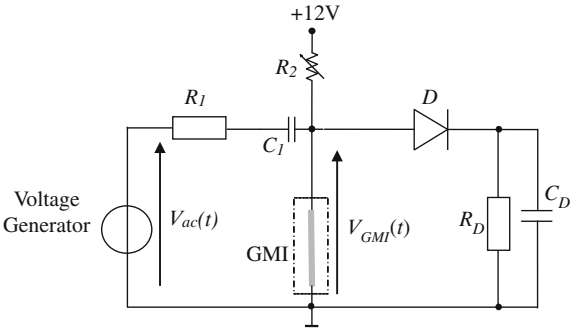

Fig. 8 Classical electronic peak detector associated to a MIG wire as sensor

Based on the Fourier formalism and considering a linear system, both modes are quite similar due to the fact that the first harmonic amplitude dominates for both signals. In both cases, a dc bias current is usually used. This helps to reduce the equivalent magnetic noise of the sensor [31]. There are some other approaches for conditioning electronics, such as a Colpitts oscillator [32], exploiting the GMI wire resonance, but we do not treat them here.

Similarly, there are different types of detectors, such as a peak detector or a lock-in. A typical peak detector is shown in Fig. 8.

4.2 Magnetic Feedback Loop

A GMI magnetometer must exhibit appropriate linearity and magnetic field dynamic range. This can be achieved by using a negative feedback technique, applying a feedback magnetic field. This is applied to the GMI wire via a coil

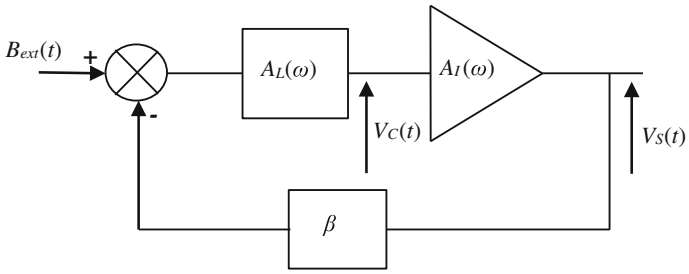

Fig. 9 Sketch view of feedback loop principle

wound around the wire, as illustrated in Fig. 1b. This field locked loop principle is common to several magnetometers. Figure 9 illustrates a typical experimental configuration. The output of the preamplifier, $V_C(t)$, is applied to a low-pass filter, $A_I(\omega)$, to get the magnetometer output signal, V_S (t). The latter is fed back to the GMI coil through a resistor.

Considering a small signal, the system is assumed to be locked on the working point having the highest transfer coefficient T_r ($T_r > 0$). The transfer between the detector and the differential amplifier output is given by

$$A_L(\omega) = \frac{A_L(0)}{1 + j\omega/\omega_L}, \tag{45}$$

where $A_L(0)$ and ω_L are the low frequency gain and cutoff frequency of the amplifier, respectively. Similarly, the transfer function of the low-pass filter is

$$A_I(\omega) = \frac{A_I(0)}{1 + j\omega/\omega_I}, \tag{46}$$

where $A_I(0)$ and ω_I are the low frequency gain and cutoff frequency of the amplifier, respectively. Combining the two, the loop factor of the magnetometer is [33]

$$A(\omega) = T_r\, \beta\, A_L(\omega) A_I(\omega), \tag{47}$$

where β is the ratio of the magnetic flux density applied to the magnetic wire to the feedback current feeding the GMI coil (in units of T/V). Finally, the classical overall small signal transfer function of the magnetometer expresses as a standard second order transfer function is

$$T(\omega) = T_{Mag}\left(\frac{\omega_N^2}{\omega_N^2 - \omega^2 + j\omega\omega_L}\right) \cong \frac{1}{\beta}\left(\frac{\omega_N^2}{\omega_N^2 - \omega^2 + j\omega\omega_L}\right), \tag{48}$$

where $T_{Mag} = \frac{T_r A_I(0) A_L(0)}{1 + T_r \beta A_I(0) A_L(0)} \approx \frac{1}{\beta}$ and $\omega_N^2 = T_r\, \beta A_I(0) A_L(0)\, \omega_I\, \omega_L$.

Let us now consider the large signal behavior of the magnetometer. Around the working point, at which the transfer coefficients are maximal, a rough estimation of the dynamic range available at the pseudo-integrator is [33]

$$-H_{Peak}\ T_r A_L(0) \leq V_c(t) \leq H_{Peak}\ T_r A_L(0). \tag{49}$$

where $H_{Peak} \approx H_k/2$. It yields that the slew-rate (the maximum rate of change of output voltage per unit of time) at the magnetometer output is limited to

$$\left|\frac{\partial V_S(t)}{\partial t}\right| \approx H_{Peak}\ T_1 A_L(0) A_I(0) \omega_I. \tag{50}$$

This limitation is encountered when a large field step takes place, shifting the magnetic flux density applied to the sensor out of the $\pm H_{peak}$ range. This limitation is quite similar to the large signal response of a locked system. The slew rate limitation also appears for large sinusoidal $B_{ext}(t)$ signals. Further, it requires a low-pass filter time constant, higher than the slew rate. If nothing else in the system saturates, the equivalent magnetic slew rate is deduced from the previous equation to be

$$\left|\frac{\partial B(t)}{\partial t}\right| \approx H_{Peak} T_r \beta A_L(0) A_I(0) \omega_I. \tag{51}$$

In the literature, there are some examples of optimized giant magneto-impedance effect magnetometers [26, 28, 29, 34]. Their performances are in good agreement with the analysis presented here, in terms of equivalent magnetic noise and performance. Table 1 summarizes the state-of-the-art of GMI magnetometer (or sensor) performances.

As an example, the field response model for the sensing element and the noise model are in good agreement with experimental results [26, 28]. Here, the sensing element consists of a thin pick-up coil wound directly on a 100 μm diameter CoFeSiB amorphous ferromagnetic wire (M_s = 561 kA/m, α = 0.02, ρ = 129 μΩ cm). The length of the pick-up coil, l_c, was equal to that of the wire, l, and is about 2.5 cm. The number of turns of the coil, N, is approximately 500 turns/layer. The noise performance of the magnetometer is, approximately, 1.7 pT/$\sqrt{\text{Hz}}$ in the white noise region. It has a bandwidth of about dc-70 kHz, a full scale of 100 μT and a measured slew rate of higher than 450 T/s. A sketch view of the electronic design and the associated equivalent spectral magnetic noise density are shown in Fig. 10.

Table 1 State-of-the-art of GMI sensor or magnetometer performances

Refs.	Mode	Material	Geometry	Current excitation	Excitation frequency (MHz)	Detector	Feed-back loop	Noise level (pT/$\sqrt{Hz}$)	Bandwidth (Hz)	Dynamic range (μT)
[26, 28]	B	CoFeSiB, 2.5 cm, Ø 30 μm Coil 500 turns	Wire	Sinusoidal	1	Peak detector	Yes	35 @ 1 Hz	100,000	±100
[29]	A	CoFeSiB (1 cm, Ø 30 μm)	Wire	Pulsed	16	Peak detector	Yes	1000 @ 1 Hz	70,000	±25
[32]	B	CoFeNiBSiMo, 1 cm, Ø30 μm Coil 85 turns	Wire	Sinusoidal 2 mA	4	Switch	Yes	10 @ 300 Hz	1000	±250
[34]	B	CoFeSiB, 2 cm, Ø 30 μm Coil 200 turns	Wire	Pulsed	0.4	Switch	No	50 @ 1 Hz	40	±10
[35]	B	$Co_{67}Fe_4Si_8B_{14}Cr_7$ (11 cm × 1 mm × 17 μm) Coil 290 turns (8 cm, Ø 9 mm)	Ribbon	Sinusoidal 10 mA_{rms} 3 mA_{rms}	0.8 0.29	SR840 Analog multiplier	No Yes	17 @ 1 Hz 70 @ 1 Hz	– 10	±1.5 ±75
[36, 37]	D	Fe78Si9B13 (1.2 cm × 2 mm × 20 μm) Coil 100 turns (6 mm)	Ribbon	Pulsed 20 mA	0.3	Peak detector	no	5 kHz	2000	±250
[38]	B	CoFeSiB (1 cm, Ø 30 μm) Coil 600 turns	Wire	Pulsed	0.03	Analog multiplier	no	3 @ 1 Hz	–	>10
[39]	A	Copper path (2 cm × 0.8 mm × 18 μm) under a thin film of CoNbZr (25 × 25mm2 × 4 μm)	Wire	Sinusoidal 20 dBm	600 800	Spectrum analyser No demodulation Phase	No	0.71 @ 500 kHz 1.3 @ 1 Hz		
[40]	A	$Co_{66}Fe_4Si_{15}B_{15}$ (1 cm × 1 mm × 20 μm)	Ribbon	Sinusoidal 10 mA	0.1	Analog multiplier	Yes			±200
[41]	A	$Fe_{75}Si_{15}B_6Cu_1Nb_3$/ $Cu/Fe_{75}Si_{15}B_6Cu_1Nb_3$ [1 cm × 6 cm × (20 μm/40 μm/20 μm)]	Ribbon-multilayer	Sinusoidal	0.16	Lock-in	NO	1000	1000	

(continued)

Table 1 (continued)

Refs.	Mode	Material	Geometry	Current excitation	Excitation frequency (MHz)	Detector	Feed-back loop	Noise level (pT/$\sqrt{\text{Hz}}$)	Bandwidth (Hz)	Dynamic range (μT)
[42, 43]	A	$Fe_{75}Si_{15}B_6Cu_1Nb_3$/ $Cu/Fe_{75}Si_{15}B_6Cu_1Nb_3$ (1 cm × 6 cm × (20 μm/40 μm/20 μm))	Ribbon-multilayer	Sinusoidal	0.6	Lock-in	no	13,000 @ 100 Hz	100	
[44]	B	$Co_{67}Fe_4Si_8B_{14}Cr_7$ (8 cm × 1 mm × 17 μm) Coil 490 turns	Two ribbons	Sinusoidal 1.2 mA_{rms}	0.29	Lock-in	Yes	5.9 @ 1 Hz	15	±75
[45, 46]	A	$Co_{67}Fe_4Mo_{1,5}Si_{16,5}B_{11}$ (3.5 cm × 0.5 mm × 25 μm)	Ribbon	Sinusoidal 10 mA_{rms}	30	Peak detector	yes			±1000
[47]	A	CoNbZr (3 windings - 0.5 cm × 30 μm × 4.3 μm)	Wire	Sinusoidal 40 mA_{rms}	0.37	Spectrum analyser No demodulation	No	1.7 @ 500 kHz		
[48]	B	Co, 2 cm, Ø120 μm Coil 400 turns	Thin film	Sinusoidal	0.4	Lock-in	No	10 @ 2 Hz	5	
[49]	A	Unitika, 4 × 0.3 cm, Ø15 μm	Wire	Sinusoidal	18–30	frequency	yes			±100
[50]	A	$Fe_{4:35}Co_{68,15}Si_{12,15}B_{15}$, 0.3 cm, Ø30 μm	Wire	pulsed	50	peak detector	no		10^6	±100
[51]	A	$[Py/Ti]_3/Cu/[Ti/Py]_3$, (2 mm × 130 μm × 590 nm)	μstripe-multilayer	Sinusoidal	120	Peak detector	No	122	100,000	

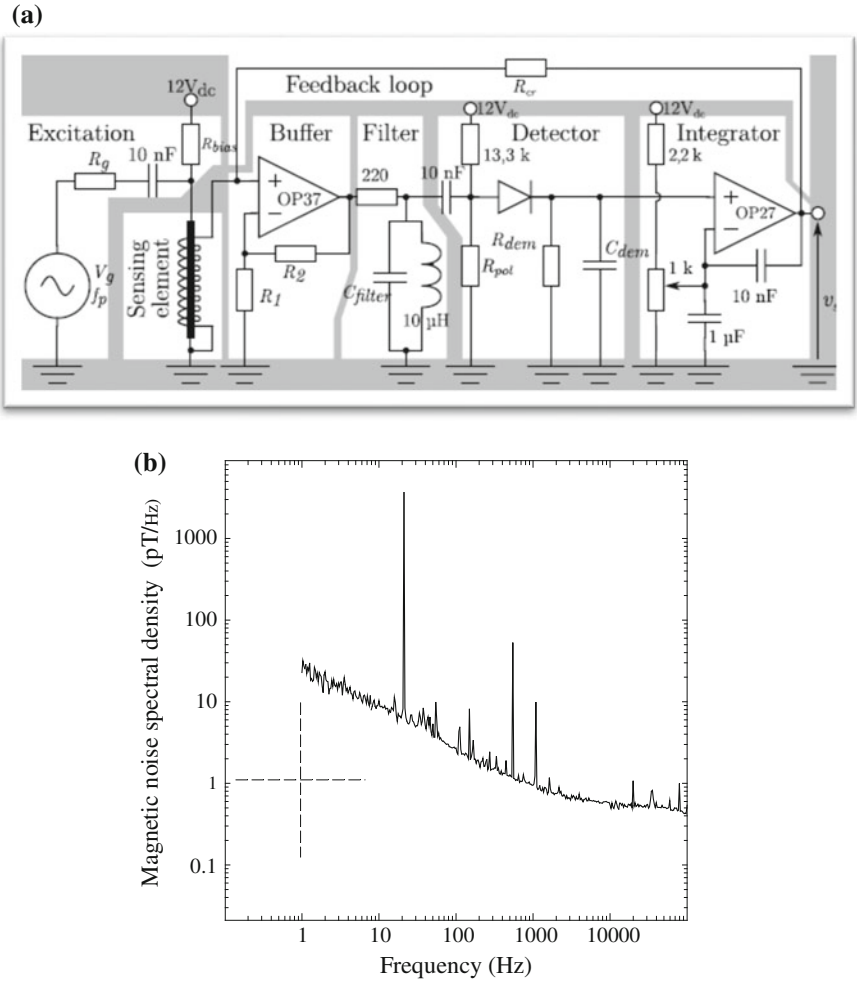

Fig. 10 Sketch view of a full electronic GMI magnetometer design (**a**) and associated equivalent spectral magnetic noise (**b**) [26, 28]

5 Conclusions

While the development of GMI sensor technologies started about two decades ago, advances in the engineering of magnetometers with a systematic evaluation of their noise performances have mostly taken place over the last 10 years. GMI magnetometry in wires, ribbons, single or multi layered films is steadily progressing and is still an active field of research. So far, impressive GMI magnetometer demonstrations have been carried out, exhibiting performances competitive with state-of-the-art low-cost magnetometers operating at room temperature. GMI

sensors are also currently considered to be promising candidates for the development of multi-sensor arrays, which could considerably extend their range of applications. Major short-term challenges include the reduction of their low-frequency excess noise and the improvement of their long term magnetic stability. These points have to be addressed, keeping sight of their energy consumption and manufacturing costs, along with other issues pertaining to material studies and optimization.

Acknowledgements We thank Professor Arthur Yelon for his suggestions on the manuscript. Financial support from the Natural Sciences and Engineering Research Council of Canada is gratefully acknowledged.

References

1. E.P. Harrison, G.L. Turney, H. Rowe, Nature **135**, 961 (1935)
2. K. Kawashima, T. Kohzawa, H. Yoshida, K. Mohri. IEEE Trans. Magn. **29**, 3168 (1993)
3. F.L.A. Machado, B.L. da Silva, S.M. Rezende, C.S. Martins, J. Appl. Phys. **75**, 6563 (1994)
4. R.S. Beach, A.E. Berkowitz, Appl. Phys. Lett. **64**, 3652 (1994)
5. L.V. Panina, K. Mohri, Appl. Phys. Lett. **65**, 1189 (1994)
6. V. Rao, F.B. Humphrey, J.L. Costa-Kramer, J. Appl. Phys. **76**, 6204 (1994)
7. J. Velásquez, M. Vázquez, D.-X. Chen, A. Hernando, Phys. Rev. B **50**, 16737 (1994)
8. M. Knobel, M. Vázquez, L. Kraus, in *Handbook of Magnetic Materials*, ed. by K.H. J. Buschow (Elsevier, London, 2003), vol. 15, p. 497
9. T. Masumoto, A. Inoue, M. Hagiwara, US Patent No. 4,523, 626 (1995)
10. I. Ogasawara, S. Ueno, IEEE Trans. Magn. **31**(2), 1219–1223 (1995)
11. H. Chiriac, T.A. Ovari, Prog. Mater Sci. **40**(5), 333–407 (1996)
12. P. Rudkowski, J.O. Ström-Olsen, U.S. Patent 5,003,291 26 March 1991
13. L. Kraus, J. Magn. Magn. Mater. **195**, 764–778 (1999)
14. D. Ménard, A. Yelon, J. Appl. Phys. **88**, 379 (2000)
15. P. Ciureanu, L.-G. Melo, D. Ménard, A. Yelon, J. Appl. Phys. **102**(073908), 1–8 (2007)
16. D. Seddaoui, D. Ménard, B. Movaghar, A. Yelon, J. Appl. Phys. **105**(083916), 1–12 (2009)
17. D. Menard, D. Seddaoui, L.G.C. Melo, A. Yelon, B. Dufay, S. Saez, C. Dolabdjian, Sensor Lett. **7**, 439–442 (2009)
18. B. Dufay, S. Saez, C. Dolabdjian, A. Yelon, D. Menard, IEEE Sens. J. **11**(6), 1317–1324 (2011)
19. B. Dufay, S. Saez, C. Dolabdjian, A. Yelon, D. Menard, IEEE Sens. J. **13**(1), 379–388 (2013)
20. L. Ding, S. Saez, C. Dolabdjian, Sens. Lett. **5**(1), 248–251 (2007)
21. M. Lam Chok Sing, C. Dolabdjian, C. Gunther, D. Bloyet, J. Certenais. Rev. Sci. Instrum. **67** (3), 796–804 (1996)
22. W.F. Egelhoff Jr., P.W.T. Pong, J. Unguris, R.D. McMichael, E.R. Nowak, A.S. Edelstein, J. E. Burnette, G.A. Fischerd, Sens. Actuators, A **155**(2), 217–225 (2009)
23. D. Ménard, G. Rudkowska, L. Clime, P. Ciureanu, S. Saez, C. Dolabdjian, D. Robbes, A. Yelon, Sens. Actuators, A **129**(1–2), 6–9 (2006)
24. L. Melo, D. Menard, A. Yelon, L. Ding, S. Saez, C. Dolabdjian, J. Appl. Phys. **103**(3), 1–6 (2008)
25. C. Dolabdjian, S. Saez, A. Yelon, D. Menard, Key Eng. Mater. **605**, 437–440 (2014)
26. B. Dufay, E. Portalier, S. Saez, C. Dolabdjian, A. Yelon, D. Ménard, *EMSA'14 Conference*, 5–7 July, Vienne (2014)

27. L. Melo, D. Menard, A. Yelon, L. Ding, S. Saez, C. Dolabdjian, J. Appl. Phys. **103**(3), 1–6 (2008)
28. B. Dufay, S. Saez, C. Dolabdjian, A. Yelon, D. Menard, I.E.E.E. Trans, Magn. **49**(1), 85–88 (2013)
29. L. Ding, S. Saez, C. Dolabdjian, L. Melo, D. Menard, A. Yelon, IEEE Sens. J. **9**(2), 159–168 (2009)
30. L. Panina, K. Mohri, Appl. Phys. Lett. **65**(9), 1189–1191 (1994)
31. L. Ding, S. Saez, C. Dolabdjian, P. Ciureanu, L. Melo, D. Ménard, A. Yelon, Sens. Lett. **5**(1), 171–175 (2007)
32. T. Uchiyama, K. Mohri, L.V. Panina, K. Furuno. IEEE Trans. Mag. **31**, 3182–3184 (Nagoya University, Japan) (1995)
33. A. Boukhenoufa, C. Dolabdjian, D. Robbes, IEEE Sens. J. **5**(5), 916–923 (2005)
34. T. Uchiyama, K. Mohri, Y. Honkura, L.V. Panina, IEEE Trans. on Magn. **48**(11), 3833–3839 (2012)
35. M. Malátek, L. Kraus, Sens. Actuators, A **164**(1–2), 41–45 (2010)
36. Y. Geliang, B. Xiongzhu, X. Chao, X. Hong, Sens. Actuators, A **161**(1–2), 72–77 (2010)
37. Y. Geliang, B. Xiongzhu, Y. Bo, L. YunLong, X. Chao, IEEE Sens. J. **11**(10), 2273–2278 (2011)
38. T. Uchiyama, S. Nakayama, K. Mohri, K. Bushida, Physica status solidi (a) **206**(4), 639–643 (2009)
39. S. Yabukami, K. Kato, Y. Ohtomo, T. Ozawa, K.I. Arai, J. Magn. Magn. Mater. **321**, 675–678 (2009)
40. S.S. Yoon, P. Kollu, D.Y. Kim, G.W. Kim, Y. Cha, C.G. Kim, IEEE Trans. Magn. **45**(6), 2727–2729 (2009)
41. F. Alves, L.A. Rached, J. Moutoussamy, C. Coillot, Sens. Actuators, A **142**(2), 459–463 (2008)
42. F. Alves, J. Moutoussamy, C. Coillot, L. Abi Rached, B. Kaviraj, Sens. Actuators, A **145**, 241–244 (2008)
43. F. Alves, B. Kaviraj, L.A. Rached, J. Moutoussamy, C. Coillot, in *Solid-State Sensors, Actuators and Microsystems Conference* (2007). TRANSDUCERS 2007. International, 2581–2584 (2007)
44. L. Kraus, M. Malatek, M. Dvorak, Sens. Actuators, A **142**, 468–473 (2008)
45. M. Kuzminski, K. Nesteruk, H. Lachowicz, Sens. Actuators, A **141**(1), 68–75 (2008)
46. K. Nesteruk, M. Kuzminski, H.K. Lachowicz, Sens. Transduce. Mag. **65**, 515–520 (2006)
47. S. Yabukami, H. Mawatari, N. Horikoshi, Y. Murayama, T. Ozawa, K. Ishiyama, K. Arai, J. Magn. Magn. Mater. **290**, 1318–1321 (2005)
48. E. Paperno, Sens. Actuators, A **116**(3), 405–409 (2004)
49. C.M. Cai, K. Usami, M. Hayashi, K. Mohri, IEEE Trans. Magn. **40**(1), 161–163 (2004)
50. K. Bushida, K. Mohri, T. Uchiyama, IEEE Trans. Magn. **31**, 3134–3136 (1995)
51. E. Fernández, A. García-Arribas, J.M. Barandiaran, A.V. Svalov, G.V. Kurlyandskaya, C. Dolabdjian, IEEE Sensors **15**(11), 6707–6714 (2015)

Magnetoelectric Magnetometers

Mirza I. Bichurin, Vladimir M. Petrov, Roman V. Petrov and Alexander S. Tatarenko

Abstract Key features of magnetoelectric (ME) sensors for measuring the magnetic field, electric current and microwave power are discussed. ME sensors are shown to have advantages over semiconductor ones in the sensitivity, low price and radiation resistance. To predict the feasibility of a composite for sensor application, we propose the nomograph method based on given parameters of the composite components. The sensor sensitivity depends on the construction and the materials parameters of the ME composite and bias magnetic field. ME laminates offer opportunities for low frequency (10^{-2}–10^{3} Hz) detection of low magnetic fields (10^{-12} Tesla or below) at room temperature in a passive mode of operation. Any other magnetic sensor does not reveal such combinations of characteristics. Current sensing based on ME effect is a good choice for many applications due to galvanic isolation between the current and measuring circuit. For increasing the sensor sensitivity one needs to use the ME composite based on materials with high magnetostriction and strong piezoelectric coupling. Microwave power sensors based on composite materials have a wide frequency range up to hundreds of gigahertz, stable to significant levels of radiation, and a temperature range from 0 K to the Curie temperature. In the microwave region, it is possible to use selective properties of ME materials, that enables one to create a frequency-selective power sensor with fine-tuning.

1 Introduction

In this chapter under the magnetoelectric (ME) sensors, we understand the devices recording the magnetic field, current in conductor, microwave power and so on, at that the ME composites are the working material of these devices. In the ME composites ferromagnetism and ferroelectricity occur simultaneously and coupling between the two is enabled and connected with the ME effect. The ME effect is defined as the dielectric polarization response of a material to an applied magnetic

M.I. Bichurin (✉) · V.M. Petrov · R.V. Petrov · A.S. Tatarenko
Novgorod State University, Veliky Novgorod, Russia
e-mail: mirza.bichurin@novsu.ru

A. Grosz et al. (eds.), *High Sensitivity Magnetometers*, Smart Sensors, Measurement and Instrumentation 19, DOI 10.1007/978-3-319-34070-8_5

field, or an induced magnetization change upon application of an external electric field [1, 2]. The Tellegen's gyrator was the first offered ME device [3], which was realized later based on layered structure of Terfenol—PZT [4]. The main interest of researchers referring to design of magnetic field sensors was connected with obtained high value of ME effect. This result showed the opportunity of design based on ME composites of high sensitivity magnetic field sensors working at room temperature [5]. The latest obtained results in the area of magnetic sensor design presented in the review of Viehland et al. [6].

The chapter is organized as follows:

In Sec. 2, we briefly discuss the ME effect in composites; define ME voltage coefficients (MVC) at the low-frequency, electromechanical (EMR) and ferromagnetic resonance (FMR) ranges and make an example of calculation of MVC by nomographs. In Sec. 3, the results of the investigations of the ME magnetic field sensors including the physical and noise models; fabrication and electronics with applications examples are reported. In Sec. 4, we present the ME current sensors with physical model and fabrication and electronics. In Sec.5, the ME microwave power sensors are considered. The equivalent circuit and fabrication of such sensors are described.

2 Magnetoelectric Composites

In ME composites the induced polarization P is related to the magnetic field H by the expression, $P = \alpha H$, where a is the second rank ME-susceptibility tensor. The (static) effect was first observed in antiferromagnetic Cr_2O_3. But most single phase compounds show only weak ME interactions and only at low temperatures [7]. However, composites of piezomagnetic/piezoelectric phases are also magnetoelectric [8, 9]. When said composites are subjected to a bias magnetic field H, a magnetostriction induced strain is coupled to the ferroelectric phase that results in an induced electric field E via piezoelectricity. The ME susceptibility, $\alpha = \delta P/\delta H$, is the product of the piezomagnetic deformation $\delta l/\delta H$ and the piezoelectric charge generation $\delta P/\delta l$ [10]. Here we are primarily interested in the dynamic ME effect. For an ac magnetic field δH applied to a biased laminate composite, one measures the induced voltage δV. The ME voltage coefficient $\alpha_E = \delta E/\delta H = \delta V/t\ \delta H$(or $a = \varepsilon_o \varepsilon_r\ \alpha_E$), where t is the composite thickness and ε_r is the relative permittivity [10]. The ME effect was first observed in single crystals [11] of single phase materials a little more 50 years ago, and subsequently in polycrystalline single phase materials. The largest value of α_{ME} for a single phase material is that for Cr_2O_3 crystals [11], where $\alpha_{ME} = 20$ mV/cm Oe. In last few years, strong magneto-elastic and elasto-electric coupling has been achieved through optimization of material properties and proper design of transducer structures. Lead zirconate titanate (PZT)-ferrite, PZT-Terfenol-D and PZT-Metglas are the most studied composites to-date [12–14]. One of largest ME voltage coefficient of 500 V cm^{-1} Oe^{-1} was reported recently for a high permeability magnetostrictive

piezofiber laminate [14]. These developments have led to ME structures that provide high sensitivity over a varying range of frequency and dc bias fields enabling the possibility of practical applications [15, 16].

In order to obtain high ME couplings, a layered structure must be insulating, in order that it can be poled to align the electric dipole moments. The poling procedure involved heating the sample to 420 K, and re-cooling to 300 K under an electric field of E = 20–50 kV/cm. The samples are then placed between the pole pieces of an electromagnet (0–18 kOe) used for applying a magnetic bias field H. The required ac magnetic field δH = 1 Oe at 10 Hz–100 kHz applied parallel to H is generated with a pair of Helmholtz coils. The ac electric field δE perpendicular to the sample plane is estimated from the measured voltage δV. The ME coefficient a_E is measured for three conditions: (1) transverse or $\alpha_{E,31}$ for H and δH parallel to each other and to the disk plane (1,2) and perpendicular to δE (direction-3), (2) longitudinal or $\alpha_{E,33}$ for all the three fields parallel to each other and perpendicular to sample plane and (3) in-plane $\alpha_{E,11}$ for all the three fields parallel to each other and parallel to sample plane. An ME phenomenon of fundamental and technological interests is an enhancement in the coupling, when the electrical or magnetic sub-system undergoes resonance: i.e., electromechanical resonance (EMR) for PZT and ferromagnetic resonance (FMR) for the ferrite. As the dynamic magnetostriction is responsible for the electromagnetic coupling, EMR leads to significant increasing in the ME voltage coefficients. In case of resonance ME effects at FMR an electric field E produces a mechanical deformation in the piezoelectric phase, resulting in a shift in the resonance field for the ferromagnet. Besides, the peak ME voltage coefficient occurs at the merging point of acoustic resonance and FMR frequencies, i.e., at the magnetoacoustic resonance [10]. Then we discuss the estimations of ME effects in the different frequency ranges.

2.1 Low-Frequency ME Coupling

We consider more often used in practice the transverse fields' orientation that corresponds to E and δE being applied along the X_3 direction, and H and δH along the X_1 direction (in the sample plane). The expression for the transverse ME voltage coefficient is [17, 18]

$$\alpha_{E,31} = \frac{E_3}{H_1} = \frac{-V(1-V)({}^{m}q_{11} + {}^{m}q_{21})^{p}d_{31}}{{}^{p}\varepsilon_{33}({}^{m}s_{12} + {}^{m}s_{11})v + {}^{p}\varepsilon_{33}({}^{p}s_{11} + {}^{p}s_{12})(1-V) - 2^{p}d_{31}^{2}(1-V)} \quad (1)$$

For symmetric trilayer structures, using the 1-D approximations, the expression for transverse ME voltage coefficient takes on the form:

$$\alpha_{E,31} = \frac{V(1-V)x}{\varepsilon_0[{}^{m}s_{11}V + {}^{p}s_{11}(1-V)]} \quad (2)$$

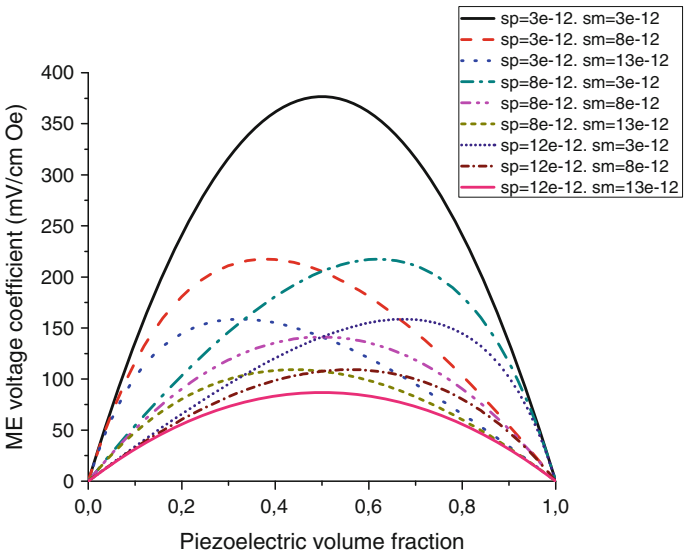

Fig. 1 Piezoelectric volume fraction dependence of transverse ME voltage coefficient for symmetric layered structure of magnetostrictive and piezoelectric components with different compliencecs

where $x = ({}^{m}q_{11} + {}^{m}q_{12})\frac{{}^{p}d_{31}}{{}^{p}\varepsilon_{33}/\varepsilon_0}$, $s_p = {}^{p}s_{11}(1 - {}^{p}v)$, $s_m = {}^{m}s_{11}(1 - {}^{m}v)$, ${}^{p}s_{11}$, ${}^{m}s_{11}$, ${}^{p}d_{31}$ and ${}^{m}q_{11}$ are compliance, and piezoelectric and piezomagnetic coupling coefficients for piezoelectric and piezomagnetic layers, respectively, ${}^{p}\varepsilon_{33}$ is the permittivity of piezoelectric layer. In Eq. 2, the electromechanical coupling factor is assumed to satisfy the condition: ${}^{p}K_{31}^2 = {}^{p}d_{31}^2/{}^{p}s_{11}{}^{p}\varepsilon_{33} \ll 1$.

For convenience we suggest using the nomograph method that facilitates the efficient estimates of ME voltage coefficients from given parameters of composite components (Figs. 1 and 2).

For the bilayer structure, the ME voltage coefficient should be calculated taking into account the flexural deformations. On the foregoing assumptions, our model enables deriving the explicit expression for ME voltage coefficient:

$$\frac{\delta E_3}{\delta H_1} = \frac{[1{}^{p}s_{11} + {}^{m}s_{11}r^3]{}^{m}q_{11}{}^{p}d_{31}/{}^{p}\varepsilon_{33}}{{}^{p}s_{11}[2r{}^{m}s_{11}(2 + 3r + 2r^2) + {}^{p}s_{11}] + {}^{m}s_{11}^2 r^4} \tag{3}$$

Equation 3 is written in a simplified form under assumption ${}^{p}K_{31}^2 \ll 1$ similarly to deriving Eq. 2 (Figs. 3 and 4).

2.2 ME Coupling at Bending Mode

Next we consider ME coupling under small-amplitude flexural oscillations of a bilayer rigidly clamped at one end. The bilayer deflection should obey the equations

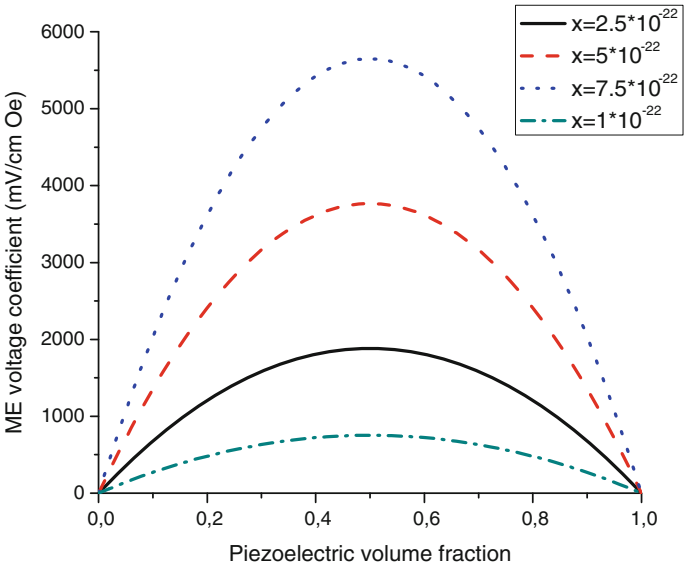

Fig. 2 Piezoelectric volume fraction dependence of transverse ME voltage coefficient for symmetric layered structure of magnetostrictive and piezoelectric components at different × values

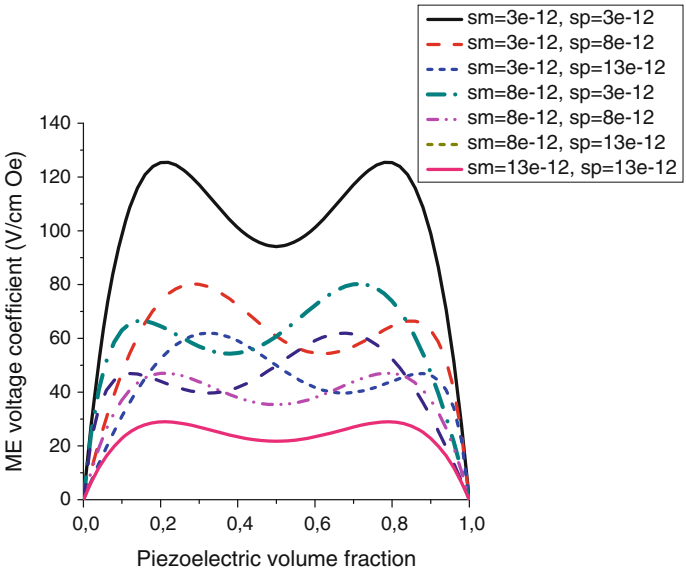

Fig. 3 Piezoelectric volume fraction dependence of transverse ME voltage coefficient for bilayer of magnetostrictive and piezoelectric components with different compliencecs

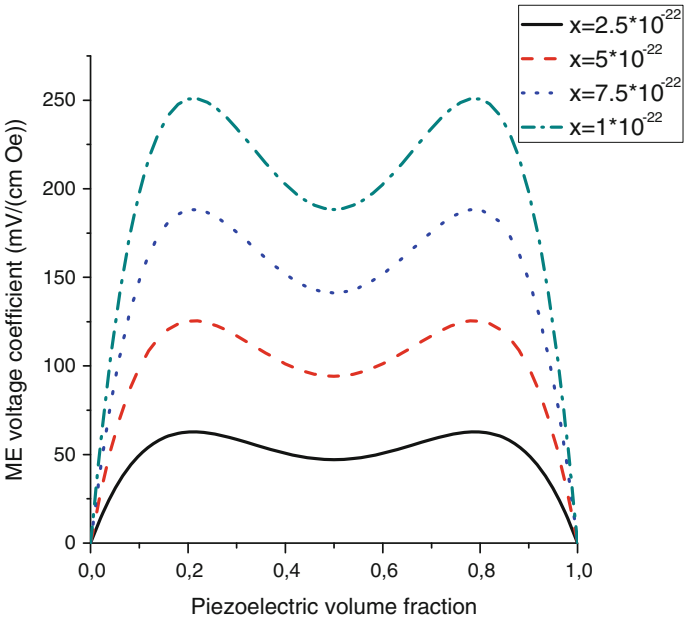

Fig. 4 Piezoelectric volume fraction dependence of transverse ME voltage coefficient for bilayer of magnetostrictive and piezoelectric components at different × values in SI units with $x = {}^{m}q_{11}{}^{p}d_{31}\varepsilon_0/{}^{p}\varepsilon_{33}$

of bending motion provided in our models in Ref. [18]. To solve these equations, we used the boundary conditions that the bilayer deflection and its derivative vanish at clamped end of the bilayer and rotational moment and transverse force vanish at free end. Under assumption ${}^{p}K_{31}^2 \ll 1$ and ${}^{m}K_{11}^2 \ll 1$ (${}^{m}K_{11}^2 = {}^{m}q_{11}^2/({}^{m}s_{11}{}^{m}\mu_{11})$ with ${}^{m}\mu_{11}$ denoting the absolute permeability of magnetic layer), the resonance condition is cosh(kL) • cos(kL) = −1 where k is wave number.

The ME voltage coefficient at bending mode frequency can be estimated as

$$\alpha_{E31} = \frac{{}^{m}Y^{H} \cdot {}^{m}t \cdot {}^{p}d_{31} \cdot {}^{p}Y^{E} \cdot {}^{m}q_{11}(2 \cdot z_0 + {}^{m}t) \cdot (2 \cdot z_0 - {}^{p}t)}{2D\Delta \cdot {}^{p}\varepsilon_{33}}(r_4 r_1 + r_2 r_3) \qquad (4)$$

where $k^4 = \frac{\omega^2 \rho t}{D}$, D, ρ, t, and L are cylindrical stiffness, density, total thickness, and length of sample, $\Delta = (r_1^2 + 2r_1 r_3 + r_3^2 - r_2^2 + r_4^2)kL$, $r_1 = \cosh(kL)$, $r_2 = \sinh(kL)$, $r_3 = \cos(kL)$, $r_4 = \sin(kL)$. Equation (8) shows that the bending resonance frequency is determined by equation Δ = 0 and depends mainly on elastic compliances and volume fractions of initial components, and ratio $\frac{L}{\sqrt{t}}$. The peak ME voltage coefficient is dictated by Q value, piezoelectric and piezomagnetic coupling coefficients, elastic compliances and volume fractions of initial components (Figs. 5, 6, 7 and 8).

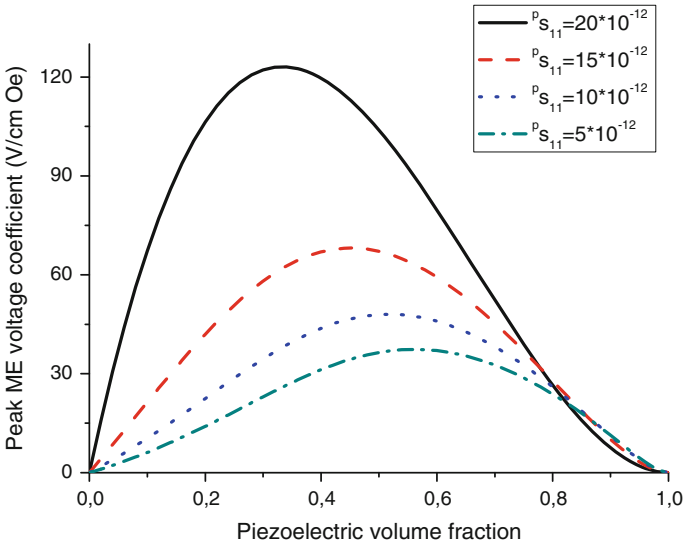

Fig. 5 Piezoelectric volume fraction dependence of peak ME voltage coefficient at bending mode of magnetostrictive-piezoelectric bilayer for ${}^{m}s_{11} = 5 \times 10^{-12}$ m^2/N and ${}^{p}s_{11} = 5 \times 10^{-12}$ m^2/N (1), ${}^{p}s_{11} = 10 \times 10^{-12}$ m^2/N (2), ${}^{p}s_{11} = 15 \times 10^{-12}$ m^2/N (3), and ${}^{p}s_{11} = 20 \times 10^{-12}$ m^2/N (4)

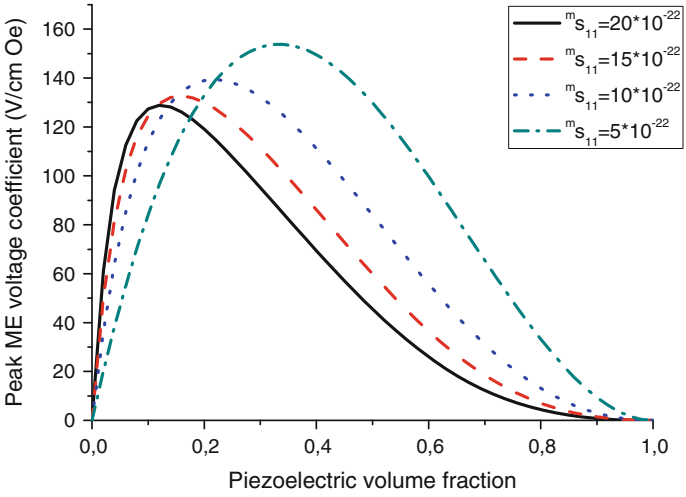

Fig. 6 Piezoelectric volume fraction dependence of peak ME voltage coefficient at bending mode of magnetostrictive-piezoelectric bilayer for ${}^{p}s_{11} = 5 \times 10^{-12}$ m^2/N and ${}^{m}s_{11} = 5 \times 10^{-12}$ m^2/N (1), ${}^{m}s_{11} = 10 \times 10^{-12}$ m^2/N (2), ${}^{m}s_{11} = 15 \times 10^{-12}$ m^2/N (3), and ${}^{m}s_{11} = 20 \times 10^{-12}$ m^2/N (4)

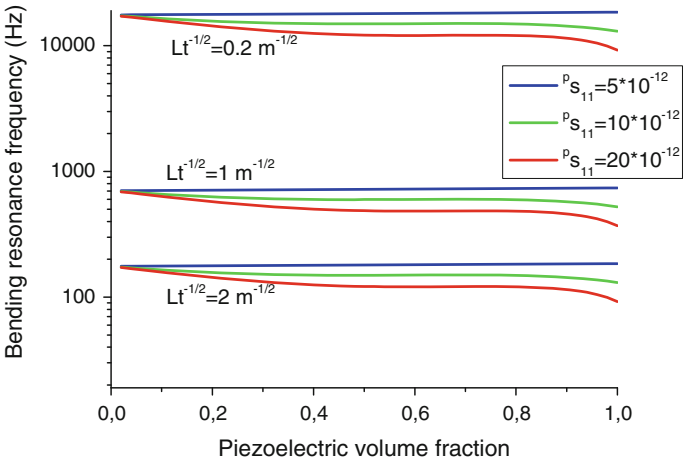

Fig. 7 Piezoelectric volume fraction dependence of bending resonance frequency of magnetostrictive-piezoelectric bilayer for ${}^{m}s_{11} = 5 \times 10^{-12}$ m^2/N and ${}^{p}s_{11} = 5 \times 10^{-12}$ m^2/N (1), ${}^{p}s_{11} = 10 \times 10^{-12}$ m^2/N (2), ${}^{p}s_{11} = 15 \times 10^{-12}$ m^2/N (3), and ${}^{p}s_{11} = 20 \times 10^{-12}$ m^2/N (4). Curves (a), (b), and (c) correspond to $Lt^{-½} = 0.2$ m^{½}, 1 m^{½}, and 2 m^{½}, correspondingly

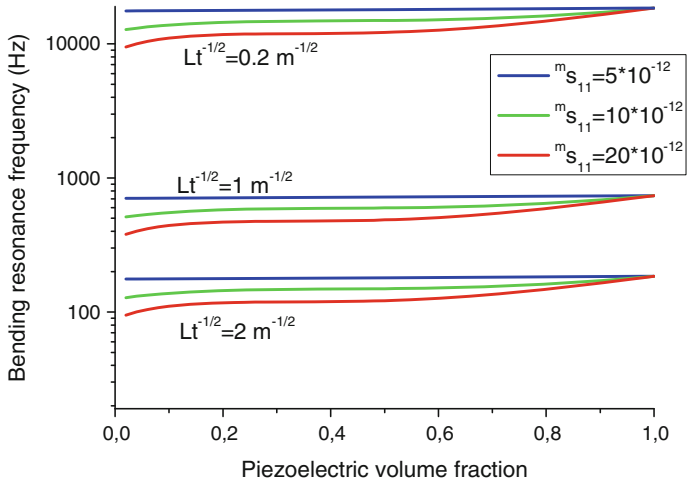

Fig. 8 Piezoelectric volume fraction dependence of bending resonance frequency of magnetostrictive-piezoelectric bilayer for ${}^{p}s_{11} = 5 \times 10^{-12}$ m^2/N and ${}^{m}s_{11} = 5 \times 10^{-12}$ m^2/N (1), ${}^{m}s_{11} = 10 \times 10^{-12}$ m^2/N (2), ${}^{m}s_{11} = 15 \times 10^{-12}$ m^2/N (3), and ${}^{m}s_{11} = 20 \times 10^{-12}$ m^2/N (4). Curves (a), (b), and (c) correspond to $Lt^{-½} = 0.2$ m^{½}, 1 m^{½}, and 2 m^{½}, correspondingly

2.3 ME Coupling at Axial Mode of Electromechanical Resonance

Next we consider small-amplitude axial oscillations of the layered structures formed by magnetostrictive and piezoelectric phases. The displacement should obey the equation of media motion provided in Ref. [18]. To solve this equation, we used the boundary conditions for a bilayer that is free at both ends. Under assumption ${}^{p}K_{11}^{2} \ll 1$, the fundamental EMR frequency is given by

$$f = \frac{1}{2L}\sqrt{\frac{{}^{p}s_{11} + r^{m}s_{11}}{{}^{p}s_{11}{}^{m}s_{11}(r^{p}\rho + {}^{m}\rho)}} \tag{5}$$

and the peak ME voltage coefficient at axial mode frequency is

$$\begin{aligned} \frac{\delta E_3}{\delta H_1} &= \frac{8Q_a}{\pi^2}\frac{r^{m}q_{11}{}^{p}d_{31}/{}^{p}\varepsilon_{33}}{(r^{m}s_{11} + {}^{p}s_{11})(r+1)} \quad \text{or} \\ \frac{\alpha_E}{Q_a} &= \frac{8}{\pi^2}\frac{V(1-V)^{m}q_{11}{}^{p}d_{31}/{}^{p}\varepsilon_{33}}{[V^{m}s_{11} + (1-V)^{p}s_{11}]} \end{aligned} \tag{6}$$

where Q_a is the quality factor for the EMR resonance.

It should be noted that Eqs. (5) and (6) for resonance frequency and ME voltage coefficient are valid for both bilayer and trilayer structures. It is easily seen from Eqs. (6), that the piezoelectric volume fraction dependence of ME voltage coefficient divided by Q value is similar to that of low frequency ME coefficient (Eq. 2). EMR frequency versus piezoelectric volume fraction is shown in Figs. 9 and 10.

2.4 ME Coupling in FMR Region

For calculating the electric field induced shift of magnetic resonance line, we consider a bilayer of ferrite and piezoelectric. The ferrite component is supposed to be subjected to a bias field H_0 perpendicular its plane that is high enough to drive the ferrite to a saturated state. Next, we use the law of elasticity and constitutive equations for the ferrite and piezoelectric and the equation of motion of magnetization for ferrite phase.

The shift of magnetic resonance field can be expressed in the linear approximation in demagnetization factors due to electric field induced stress [18]:

$$\delta H_E = -\frac{M_0}{Q_1}\left[Q_2\left(N_{11}^{E} - N_{33}^{E}\right) + Q_3\left(N_{22}^{E} - N_{33}^{E}\right) - Q_4 N_{12}^{E}\right], \tag{7}$$

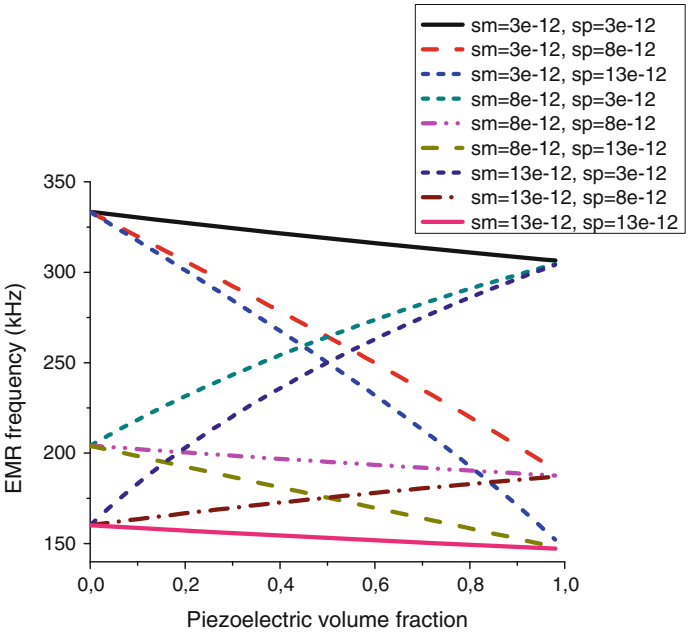

Fig. 9 EMR frequency versus piezoelectric volume fraction for longitudinal mode of 10 mm long magnetostrictive-piezoelectric layered structure

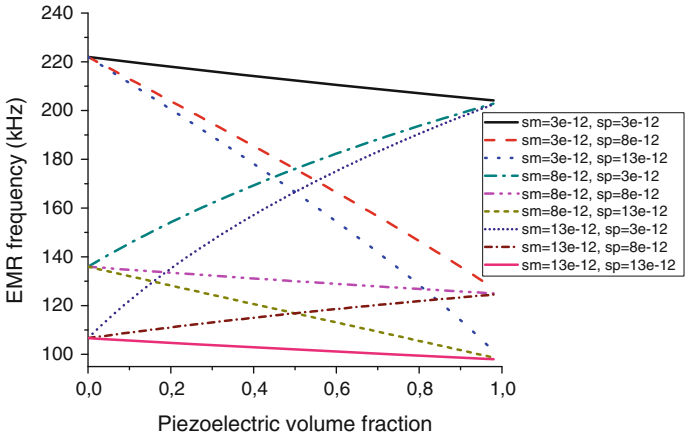

Fig. 10 EMR frequency versus piezoelectric volume fraction for longitudinal mode of 15 mm long magnetostrictive-piezoelectric layered structure

where

$$Q_1 = 2H_3 + M_0 \sum_{i \neq E} \left[\left(N_{11}^E - N_{33}^E \right) + \left(N_{22}^E - N_{33}^E \right) \right];$$

$$Q_2 = \left[H_3 + M_0 \sum_{i \neq E} \left(N_{22}^i - N_{33}^i \right) \right];$$

$$Q_3 = \left[H_3 + M_0 \sum_{i \neq E} \left(N_{11}^i - N_{33}^i \right) \right];$$

$$Q_4 = 2M_0 \sum_{i \neq E} N_{12}^i.$$

In Eq. 7, N_{kn}^i are effective demagnetization factors describing the magnetic crystalline anisotropy field (i = a), form anisotropy (i = f), field and electric field induced anisotropy (i = E).

As an example, we consider a specific case of magnetic field $\boldsymbol{H}$ along [111] axis. The shift of FMR field versus ferrite volume fraction is shown in Figs. 11. and 12. Electric field dependence of FMR field shift is presented in Fig. 13.

To obtain the estimates of ME coefficients from nomographs referred to above, one should use the material parameters of composite components. The relevant parameters of several materials that are most often used in ME structures are given in Table 1.

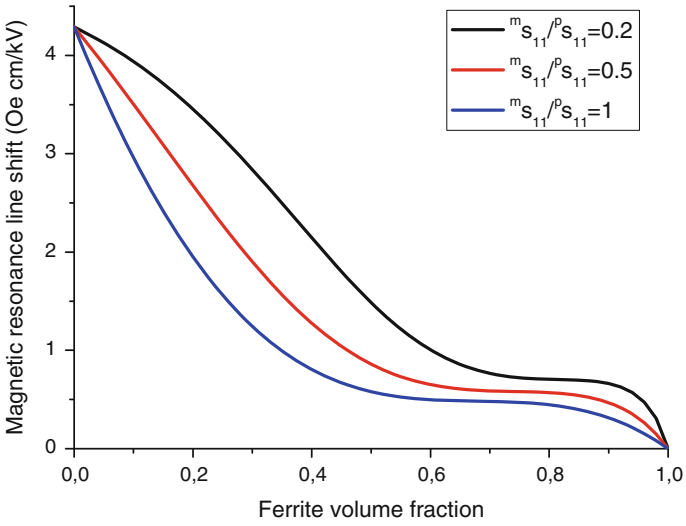

Fig. 11 Ferrite volume fraction dependence of magnetic resonance line shift at E = 1 kV/cm for ferrite-piezoelectric bilayer for $\left|\frac{\lambda_{111}}{M_s}\right| = 0.16 \times 10^{-8}$ Oe^{-1}

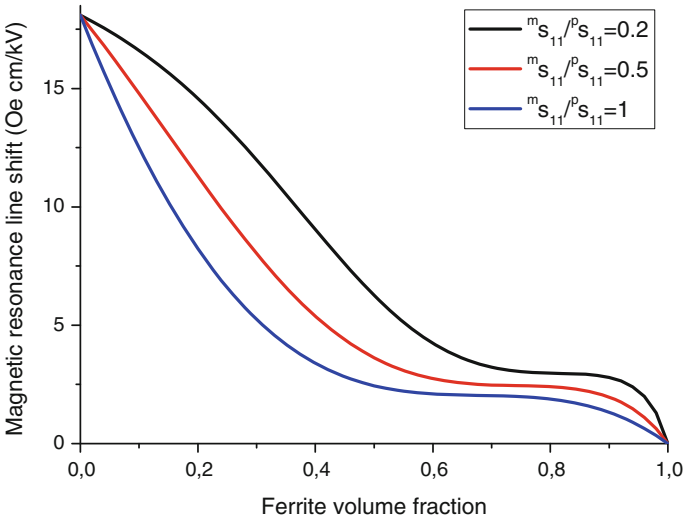

Fig. 12 Ferrite volume fraction dependence of magnetic resonance line shift at E = 1 kV/cm for ferrite-piezoelectric bilayer for $\left|\frac{\lambda_{111}}{M_s}\right| = 0.68 \times 10^{-8}$ Oe^{-1}

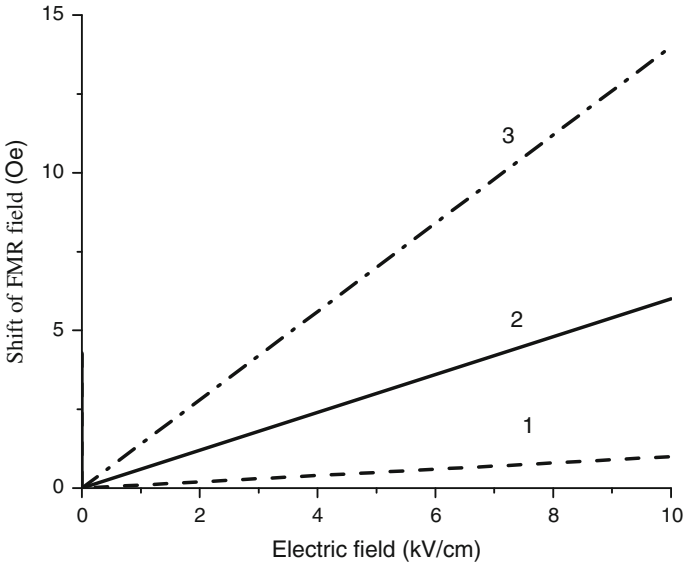

Fig. 13 Estimated shift of FMR field versus applied electric field at 9.3 GHz for the bilayers of YIG and PZT (*1*), NFO and PZT (*2*), and LFO and PZT (*3*) with equal thicknesses of magnetic and piezoelectric components

Table 1 Material parameters for piezoelectric and magnetostrictive materials used for fabrication of layered structures

Material	s_{11} (10^{-12} m^2/N)	s_{12} (10^{-12} m^2/N)	q_{33} (10^{-12} m/A)	q_{31} (10^{-12} m/A)	d_{31} (10^{-12} m/V)	d_{33} (10^{-12} m/V)	λ_{100} (10^{-6})	$\varepsilon_{33}/\varepsilon_0$
PZT	15.3	−5	–	–	−175	400	–	1750
BTO	7.3	−3.2	–	–	−78		–	1345
PMN-PT	23	−8.3			−600	1500		5000
YIG	6.5	−2.4			–	–	1.4	10
NFO	6.5	−2.4	−680	125	–	–	23	10
LFO	35	−12					46	10
Ni	20	−7	−4140	1200				
Metglas	10	−3.2	14000	−3000	–	–		

As an example of ME structure, we consider the bilayer of Ni and PZT with piezoelectric volume fraction 0.5. Based on data in Table 1, we get ${}^{m}s_{11} = 20 \times 10^{-12}$ m^2/N, ${}^{p}s_{11} = 15.3 \times 10^{-12}$ m^2/N, ${}^{p}d_{31} = -175 \times 10^{-12}$ m/V, ${}^{m}q_{11} = -4140 \times 10^{-12}$ m/A, ${}^{p}\varepsilon_{33}/\varepsilon_0 = 1750$. Figure 4 at point A reveals the low-frequency ME voltage coefficient $\alpha_{E,31} = 190$ mV/(cm Oe). Then, Fig. 5 gives the peak ME voltage coefficient $\alpha_{E,31} = 20$ V/(cm Oe) at bending resonance frequency and Fig. 2 gives the peak ME voltage coefficient $\alpha_{E,31} = 70$ V/(cm Oe) at axial resonance frequency. Q-value is assumed to be equal to 100.

In the section we presented a new quick test of ME composites using nomographs and showed its application.

3 Magnetic Field Sensors

3.1 Background

A sensor is known to be a device that detects changes in quantities and provides a corresponding output. The magnetoelectric (ME) sensor represents a structure with ME coupling with two electrodes for connecting to the voltmeter. The action of the sensor is based on the magnetoelectric effect. A composite of magnetostrictive and piezoelectric materials is expected to be magnetoelectric since a deformation of the magnetostrictive phase in an applied magnetic field induces an electric field via piezoelectric effect.

The ME effect in composites of magnetostrictive and piezoelectric phase is determined by the applied dc magnetic field, electrical resistivity, volume fraction of components, and mechanical coupling between the two phases. The ME interaction is a result of magnetomechanical and electromechanical coupling in the magnetostrictive and piezoelectric phases, and stress transfer through the interface between these two phases. It should be noted that both the magnetomechanical response in magnetostrictive phase and electromechanical resonance in piezoelectric phases are possible origin of ME output peaks.

To obtain the maximal ME output, the bias and ac magnetic fields should be simultaneously applied to the sample. For measuring either of these fields, the value of second field should be specified. In an ac magnetic field sensor, the reference bias magnetic field can be generated by both permanent magnet and electromagnet [19]. Making a dc (ac) magnetic field sensor implies using the additional magnetic system to produce the ac (dc) reference field as in Fig. 14.

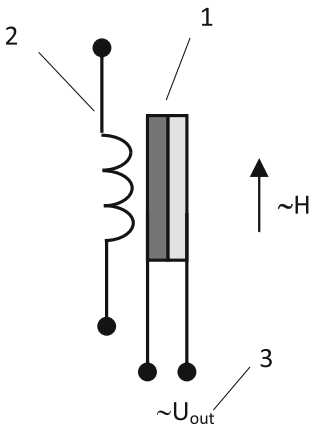

Fig. 14 The equivalent circuit of ac (dc) magnetic field sensor. *1* and *2* are the ME composite sample and dc (ac) electromagnet

3.2 Physical Model

The static ME effect can be measured by using the electromagnet with Helmholtz coils between the electromagnet poles. The Helmholtz coils generate the dc magnetic field in the ME composite. Applying the dc magnetic field to the ME layered structure induces the output dc voltage across the piezoelectric layer. The relation between output voltage and magnetic fields can be described by sensitivity. The sensitivity of the ME sensor is determined by following expression: $S = \alpha_E \cdot {}^{p}t$ where $\alpha_E = \Delta E/\Delta H$ is ME voltage coefficient and ${}^{p}t$ is the piezoelectric layer thickness with ΔE and ΔH denoting the induced voltage and applied magnetic field.

The variation of static ME sensitivity, $(\Delta E/\Delta H)_H$, as a function of magnetic field H, at room temperature is shown in Fig. 15. It is observed that the sensitivity *S* initially increases up to a certain magnetic field and finally attains a maximum

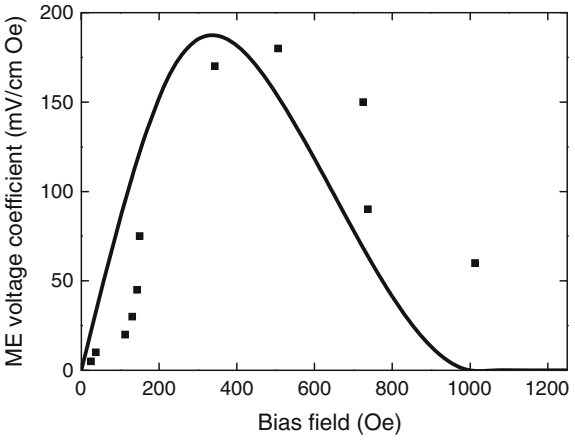

Fig. 15 Theoretical ME voltage coefficient versus H and data for bilayer of NFO and PZT

value and then decreases with an increase in applied dc magnetic field. This is because the magnetostrictive coefficient reaches saturation at a certain value of magnetic field. Beyond saturation the magnetostriction and the strain thus produced would also produce a constant electric field in the piezoelectric phase making the sensitivity decrease with increasing magnetic field.

The increases in $(\Delta E/\Delta H)_H$ with magnetic field is attributed to the fact that the magnetostriction reaches its saturation value at the time of magnetic poling and produces a constant electric field in the ferroelectric phase. Therefore, beyond a certain field, the magnetostriction and the strain thus produced would produce a constant electric field in the piezoelectric phase. Also, the possible reason for decrease in $(\Delta E/\Delta H)_H$ after certain magnetic field is attributed to the saturation state of the magnetic phase which does not show any response to the increased applied magnetic field therefore stress transfer through the interface between magnetic and electric phase decreases with magnetoelectric coupling $(\Delta E/\Delta H)$.

3.3 Noise Sources and Their Mitigation

Recent investigations of ME laminates sensors have shown that they have remarkable potential to detect changes in magnetic fields. It was shown that the feasibility of detecting magnetic field changes on the order of 10^{-12} T at near quasi-static frequencies of $f > 1$ Hz. This is an important achievement because the ME sensor does not itself require powering; rather it can harvest magnetic energy from inductances as a stored charge across a capacitor. Thus, ME laminates are small, passive magnetic field sensors with the potential of pico-Tesla sensitivity at low frequencies while operated at room temperature. The potential for ME sensors resides with the fact that there are no other present generations of magnetic sensors having the following key requirements [6, 20]: (i) extreme sensitivity ($\sim$pT/Hz$^{1/2}$), allowing for better magnetic anomaly detection; (ii) zero power consumption to foster long-term operation; (iii) operation at low frequencies, $f \sim 1$ Hz; (iv) miniaturize size, enabling deployment of arrays; (v) passive; and (vi) low cost. It should be noted that ME laminate sensors are the only ones with the potential to achieve all key requirements. However, in spite of this potential, there are no available technologies that can fulfill requirements referred to above. The integration of ME laminates into an appropriate detection scheme has yet to be achieved. This detection scheme must be simple and capable of detecting anomalies in the time domain capture mode without either signal averaging or phase referencing.

Commonly, noise is defined as any undesirable disturbance that obstructs the relevant signal passage. It is of importance in the measurement of minute signals. Reducing the noise effect on the detection device is important since the sensitivity of a sensor is often limited by noise level. We will consider some simple ways to reduce noise.

The sensor itself and the measurement circuit contribute some inherent noise. This kind of noise cannot be removed since it comes from stochastic phenomena: thermal and radiation fluctuations between sensor and environment, generation and

recombination of electron-hole pair, and current flows across a potential energy barrier in materials.

Development in the noise reduction of magnetostrictive/piezoelectric laminate sensors has been carried out in the past decade. Particularly, a 1 Hz equivalent magnetic noise of 5.1 pT $Hz^{-1/2}$ has been obtained, which is close to that of the optically pumped ultralow magnetic field sensors [21]. First of all, this was enabled by improved methods of interfacial bonding that can decrease the equivalent magnetic noise floor up to 2.7×10^{-11} T $Hz^{-1/2}$ [22]. Then, optimal poling conditions for the piezoelectric phase result in an increase in ME voltage coefficient by a factor of 1.4. The equivalent magnetic noise at $f = 1$ Hz was reported to equal 13 to 8 pT $Hz^{-1/2}$ [23].

Magnetic flux concentration was found to enhance the ME coefficient of an ME sensor. A dumbbell-shaped sensor with an enhanced ME coefficient and reduced equivalent magnetic noise was reported [24], in which the dumbbell shape leads to concentration of magnetic flux. ME laminates with dumbbell-shaped Metglas layers exhibited 1.4 times lower required dc magnetic bias fields and 1.6 times higher magnetic field sensitivities than traditional rectangular-shaped ME laminates.

It was found that Mn-doped PMN-PT single crystals have the advantages of high piezoelectric coefficient and extremely low tan δ. Experimentally, an ultralow equivalent magnetic noise of 6.2 pT $Hz^{-1/2}$ was obtained at 1 Hz of the multi-push–pull mode for Metglas/PMN-PT single crystals [25].

3.4 Fabrication

The combination of magnetostrictive amorphous ferromagnetic ribbons with piezoelectric materials, allows obtaining magnetoelectric laminated composites, that show an extremely high sensitivity for magnetic field detection. Magnetic alloys epoxyed to Polyvinylidene Fluoride (PVDF) piezoelectric polymer give as result magnetoelectric coefficients above 80 V/cm Oe. Also, high temperature new piezopolymers as polyimides are can be used for the magnetoelectric detection at temperatures as high as 100 °C.

ME three-layer can be constructed sandwich-like with longitudinal magnetostrictive operation and transverse piezoelectric response laminated composites by gluing two equal magnetostrictive ribbons to opposite sides of polymer piezoelectric films with an adhesive epoxy resin [6]. Magnetostrictive ribbons belonging to the family of Fe–Co–Ni–Si–B, Fe-rich metallic glasses have a measured magnetostriction that ranges between $\lambda s \approx 8$–30 ppm and maximum value for the piezomagnetic coefficient $d_{33} = d\lambda/dH$ of about $0.6–1.5 \times 10^{-6}$/Oe. This last parameter will modulate the magnetoelectric response of the composite as a function of the applied bias magnetic field. Concerning the piezoelectric material we firstly used the well-known polymer PVDF, the well-known piezoelectric polymer, with glass transition and melting temperatures about −35 and 171 °C, respectively, but a Curie temperature of ≈100 °C. This makes its piezoelectric

response to decay quickly above 70 °C. To develop a ME device being able to operate at higher temperatures, new amorphous piezoelectric polymers of the family of the polyimides were tested. It should be noted that its main parameters are a glass transition temperature of $Tg \approx 200$ °C and a degradation temperature of $Td \approx 510$ °C, temperatures that make these polyimides suitable for our purposes. Taking advantage of the magnetoelastic resonance effect that enhances the magnetostrictive response, all measurements have been taken at resonance. For that, the static magnetic field H_{DC} necessary to induce the maximum amplitude of that resonance was first determined. The induced magnetoelectric voltage in the sandwich laminate (through two small silver ink contacts located at both opposite magnetostrictive ribbons) was measured by the following procedure: under a H_{AC} magnetic excitation applied along the length direction, the magnetostrictive ribbons will elongate and shrink along the same direction. This will make the piezoelectric polymer film to undergo an ac longitudinal strain, inducing a dielectric polarization change in its transverse direction. Thus, we can determine simultaneously the ME response dependence as the bias field H_{DC} changes; and at the H_{DC} value for the maximum magnetoelastic resonance amplitude, the ME voltage dependence vs the applied ac magnetic excitation.

The highest ME response has been reported for laminated magnetostrictive/piezoelectric polymer composites. ME voltage coefficient of 21.5 V/(cm Oe) for a METGLAS 2605 SA1/PVDF (Metglas, Conway, SC, USA) laminate was achieved at non-resonance frequencies and is, so far, the highest response obtained at sub-resonance frequencies [6]. At the longitudinal resonance mode, energy transference from magnetic to elastic, and vice versa, is maximum. This energy conversion at the resonance turns out to be very sharp for ME laminates, while frequency bandwidth for applications based in this EMR enhancement effect remains limited. ME voltage coefficient of 383 V/(cm Oe) on cross-linked P (VDF-TrFE)/METGLAS 2605 SA1 is the highest reported to date. In order to avoid the observed sensitivity decrease when increasing temperature, the same L-T structured magnetoelectric laminates was fabricated with the same magnetostrictive constituents but using a 40/60 copolyimide as high temperature piezoelectric constituent.

Efforts to get wider bandwidths for EMR and ME applications have been mainly based on magnetic field tuning procedures either in bimorph or tri-layered structures, but the maximum achieved frequency of operation has been some tenths of kHz. Another way to get high frequencies of operation can be based on the relationship between length and resonant frequency value of magnetostrictive ribbons at the magnetoelastic resonance. So, our efforts are now focused on fabricating short magnetoelectric L-T type laminates showing good magnetoelectric response at high frequencies. Nevertheless, the higher the resonant frequency the lowest the amplitude of the resonance and as a first consequence, the magnetoelectric response will be also decreased. It is clear that a compromise between length of the device and so working frequency, and induced magnetoelectric signal, must be achieved. Thus, a device 1 cm long for which the resonant (working) frequency rises to 230 kHz was developed. The measured magnetoelectric voltage coefficient is about

15 V/(cm Oe) when PVDF is used as piezoelectric constituent. Thus a 0.5 cm long device that will work at a resonant frequency about 500 kHz is expected to be constructed. This fact, combined with the use of a high temperature piezopolymer as the polyimides previously described, can lead to a very useful class of magnetoelectric laminates working simultaneously at high temperature and within the radiofrequency range, both characteristics of great interest for low distance near field communications in aggressive environments (i.e., the desert, a tunnel or fighting a fire).

Combining the excellent magnetoelastic response of magnetostrictive amorphous ferromagnetic ribbons with piezoelectric polymers, the short length magnetoelectric laminated composites that show an extremely high sensitivity for magnetic field detection was fabricated.

3.5 *Review of Recent Results*

The magnetic sensors based on magnetoelectric composites for the practical purposes including the use in biomagnetic imaging have been of considerable interest in recent years [26–37]. Migratory animals are capable of sensing variations in geomagnetic fields as a source of guidance information during long-distance migration. It is well known that geomagnetic fields are on the order of 0.4–0.6 Oe and have different inclinations at different locations. The Earth's mean field and its inclinations at many points over much of the Earth's surface are known to be tabulated. Accordingly, geomagnetic field sensors could be used in guidance and positional location. There are many types of magnetic sensors: for example, superconducting quantum interference devices or giant magnetoresistance spin valves. However, these sensors require very low operational temperatures liquid nitrogen in order to achieve high sensitivity. Fluxgate sensors based on exciting coil have been investigated for many years to detect dc magnetic and geomagnetic fields. This widely used sensor is relatively cheap and temperature independent; however, its magnetic hysteresis, offset value under zero magnetic field, and large demagnetization factor restrict design considerations. Recently, new types of passive ac and active dc magnetic field sensors have been developed based on a giant magnetoelectric ME effect. They are simple devices that work at room temperature. The laminated composites, such as magnetostrictive Terfenol-D or ferrite layers together with Pb Zr_{1-x},Ti_x O_3 PZT ones, have been found to possess giant ME effects of between 0.1 and 2 V/cm Oe under dc magnetic bias of $H_{dc} < 500$ Oe. Furthermore, a larger ME coefficients of up to 22 V/cm Oe under $H_{dc} < 5$ Oe have recently been reported for Metglas/PZT-fiber laminates at quasistatic frequency, which is 10 times larger than prior reports for laminates and 10^4 times larger than that of single phases. As a result, using a Metglass/PZT-fiber ME sensor enables one to detect precisely both geomagnetic fields and their inclinations along various axes of a globe. This ME sensor is a Metglas/PZT-fiber laminate with a 100 circle coil wrapped tightly around it. The PZT fibers were 200 μm in thickness and were

laminated between four layers of Metglas by use of a thin layer epoxy; the thickness of each Metglas layer was 25 μm, and the total dimensions of the laminates were $100 \times 6 \times 0.48$ mm^3. The working principal of the ME sensor is that an input magnetic field changes the length of the Metglas via magnetostriction, and because the PZT fibers are elastically bound to the Metglas layers through an epoxy interfacial layer, the PZT fibers also change their length and generate an output voltage via piezoelectricity. Detection of the Earth's magnetic field was performed by applying a 1 kHz ac magnetic field H_{ac} via a 10 mA ac input to the coil and by measuring the dc voltage and its phase induced in the PZT fibers by a lock-in amplifier SR-850. Over the range of $-1.5 < H_{dc} < 1.5$ Oe, V_{ME} was linearly proportional to H_{dc} and equal to 300 mV under a $H_{dc} = 1$ Oe. This value is 10^3 times as large as that of a corresponding Terfenol-D/PZT dc magnetic field sensor operated at 1 kHz. Another important finding was that, unlike Terfenol-D/PZT magnetic sensors, V_{ME} for Metglas/PZTfiber sensors was not dependent on H_{dc} history (i.e., no hysteretic phenomena). This is very important to a stable and repeatable detection of dc magnetic fields and their variations. In addition, when the sign of H_{dc} was changed, a dramatic 180° phase shift was found. This shift could be used to distinguish the direction along which changes in H_{dc} occur with respect to the length long axis of the sensor. This is an important advantage compared to fluxgate. Previously, it was reported that V_{ME} from a Metglas/PZT fiber laminates was strongly anisotropic, offering good sensitivity to magnetic field variations only along its length direction. In the other two perpendicular directions, only very weak signals were found with changes in H_{dc}. These unique properties of Metglas/PZT-fiber ME sensors are due to the ultrahigh relative permeability r of Metglas, which is 10^3 times larger than that of Terfenol-D or nickel ferrite. Correspondingly, the high r of Metglas results in an ultrasmall demagnetization field, enabling a high effective piezomagnetic coefficient at low biases.

Thus sensitivities of a few pico-Tesla to hundreds of femto-Tesla for 1–30 MHz magnetic fields are required for use in biomagnetic imaging. A possible approach for achieving such sensitivities is a bilayer ME sensor operating under frequency modulation at bending resonance [6]. It is of interest to compare the low-frequency and resonance ME voltage coefficients in representative bilayer composite systems. One of the best values for low-frequency ME voltage coefficient, $\sim$52 V/cm Oe, was measured in samples of Metglas and a piezofiber and was attributed to high q value for Metglas and excellent magnetic field confinement field due to high permeability. A recent study that compared the low-frequency and resonance ME effects in bilayers of composites with permendur and ferroelectric PZT and PMN-PT and piezoelectric langatate and quartz [36]. The highest ME voltage coefficient of 1000 V/cm Oe at bending resonance among these systems was measured for a permendur-langatate bilayer. But the highest resonance ME voltage coefficient to-date, 20 kV/cm Oe, was reported for AlN-FeCoSiB for measurements under vacuum that reduces damping of bending resonance in air [26, 27]. A very high ME sensitivity was also reported under bending resonance in a cantilever of FeCoSiB and PZT with inter-digital electrodes.

Table 2 Properties of modern magnetic field sensors [6, 20]

Sensor type	Sensitivity (at 1 Hz) (Tesla/$Hz^{1/2}$)	Measuring mode
High-temperature superconducting quantum interference devices (SQUID)	5×10^{-14}	T < 77 K
Giant magnetoresistance (GMR) spin valve	4×10^{-10}	T = 300 K I = 1 mA
Hybridizing a GMR sensor with a superconducting flux-to-field transformer	10^{-12}	T = 77 K I = 5 mA
Chip-size atomic magnetometer	5×10^{-11}	f = 10 Hz
Magnetoelectric magnetometer	3×10^{-11} 2×10^{-15}	T = 300 K T = 300 K at resonance frequency ($10^{5\ Hz}$)

ME sensitivity optimization should take into account the environmental or external noise sources, such as thermal fluctuation and mechanical vibration. These external noises will be dominating factors that affect the sensor's sensitivity in practical applications. For ME sensors, the dominant ones are the thermal fluctuation and mechanical vibration sources. Thermal fluctuation noise is pyroelectric in origin, where the spontaneous polarization of the piezoelectric phase is temperature dependent, resulting in a dielectric displacement current in response to temperature changes; whereas the vibrational noise is piezoelectric in origin, where the spontaneous polarization is coupled to pressure and stress changes, via piezoelectricity. As for all magnetic field sensors, it is important that ME sensors be designed by such a means that optimizes its abilities to cancel these external noise.

Comparative characteristics of modern magnetic field sensors are presented in Table 2.

In the case of the push-pull laminate, the extreme enhancement in the sensitivity limits ($\sim 10^{-15}$ T/$Hz^{1/2}$) at EMR is nearly equivalent to that of a SQUID sensor operated a 4 K and 15 mA.

ME laminates offer much potential for low frequency 10^{-2}–10^{3} Hz detection of minute magnetic fields (10^{-12} T or below), at room temperature, in a passive mode of operation, such combinations of characteristics are not available in any other magnetic sensor.

4 Current Sensors

4.1 Background

Current sensors are very essential kind of product. There are many different types of sensors that are designed on different physical principles. The most common types of sensors have been developed on the use of a resistive shunt, current transformer,

magnetoresistance and Hall sensor. A new type of sensors on ME effect has good isolation, it has small dimensions and weight and at the same time, a significant advantage in sensitivity. Different variants of designs have been investigated. Operating principle of ME current sensor is based on measuring the electromagnetic field generated by current [38]. The value of the electromagnetic field allows one to estimate the magnitude of the current flowing in the conductor. Next, the use of ring-type magnetoelectric laminate composites of circumferentially magnetized magnetostrictive Terfenol-D and a circumferentially poled piezoelectric Pb(Zr,Ti)O_3 (PZT) which have high sensitivity to a vortex magnetic field is suggested [39–41]. At room temperature, an induced output voltage from this ring laminate exhibited a near-linear response to an alternating current (ac) vortex magnetic field H_{ac} over a wide magnetic field range of $10^{-9} < H_{ac} < 10^{-3}$ T at frequencies between sub-Hz and kHz. A significant improvement of sensors sensitivity for this type devices through the use of current transduction mode was proposed in [42]. Such a sensor, according to a study [43] has an increased sensitivity to ultra-low magnetic fields and leakage currents. This circumferential-mode quasiring ME laminate can detect AC currents (noncontact) 10^{-7} A, and/or a vortex magnetic field 6×10^{-12} T. Next, a self-powered current sensor consisting of the magnetostrictive/piezoelectric laminate composite and the high-permeability nanocrystalline alloys is presented in [44]. However, this design can measure only ac current, which significantly limits its use. Next, we consider the dc current sensor based on ME element with the modulating coil.

The ME current sensor uses the ME effect as a basis of its measurements. The ME effect is a polarization response to an applied magnetic field, or conversely a magnetization response to an applied electric field. ME behaviour exists as a composite effect in multiphase systems of piezoelectric and magnetostrictive materials. Magnetostrictive-piezoelectric laminate composites have much higher ME coefficients than that of single-phase materials or particulate composites. In a magnetostrictive-piezoelectric layered structure the interaction between magnetic and electric subsystems occurs through mechanical deformation. It means that the ME effect is much stronger at frequencies corresponding to elastic oscillations called resonance frequencies. In current sensor applications the induced ME voltage coefficient is more important than the induced ME electric field coefficient, as voltage is the physical quantity measured. The sensor is designed for detecting ac and dc currents in electrical circuits [45–47] on range from 0 up to 1, 10 or 100 A depending on destination.

ME current sensors can be designed on different principles. In the first case, the operation principle work of ME element is nonresonant, in the second case the principle is resonance. As a sensitive element of the sensor in both cases can used the same design of ME element. The design of nonresonant ME current sensors was considered in the paper [45], and the design of resonant ME current sensors in the paper [46, 47]. An input-to-output ME current sensor was also developed, which includes the internal current conductor as a source of information about the current, and a surface-mounted sensor placed directly on the conductor with the current to be measured. We consider here the basic principles of work of ME current sensors of non-resonant type based on the low-frequency ME effect and next the resonant

type, working on one excited in the piezoelectric phase of magnetoelectric material of a resonant electromechanical oscillations. Also there are ac and dc ME sensors. ME ac current sensor is a special case of the direct current sensor, as it doesn't contain the modulating coil and generator and, therefore, simpler to manufacture. ME dc sensor can operate as an ac sensor without design modification.

4.2 Physical Model

The equivalent circuit of the device is represented in Fig. 16. The principle of operation of the sensor is based on measuring the potential appearing at the output of ME element due to ME effect under the influence of external modulation magnetic fields and bias magnetic field. ME sensor dc will differ from the ME sensor ac only additional baseband generator.

We can carry out modeling of current sensor using known basic formula of electrophysics and using an expression for determine of ME coefficient. When the solenoid is included into the structure of current sensor, the well-known expression for the calculation of the magnetic field inside the solenoid can be used:

$$H = \frac{N \cdot I}{l} \tag{8}$$

where H is magnetic field inside the solenoid, I is measured current in the conductor, l is the length of the solenoid, N is the number of turns of the solenoid.

Let us write the expression for the ME coefficient, expressing the intensity of the electric field:

$$E = H \cdot \alpha_E \tag{9}$$

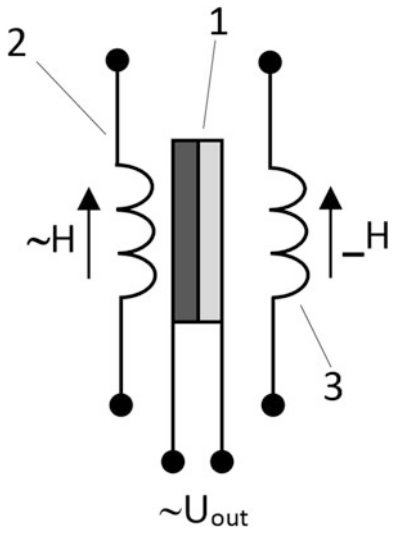

Fig. 16 The equivalent circuit of ME dc current sensor. *1* is ME element, *2* is ac solenoid coil, *3* is dc solenoid coil for measurement dc current

where is ME coefficient, E is intensity the electric field in ME material. Due to the ME effect, an electric potential equal to $U = dE$ appears across the ME element, where d is piezoelectric thickness. The expression (8) we substitute in (9) and obtain, respectively:

$$U = \alpha_E \frac{N \cdot I \cdot d}{l} \tag{10}$$

If in scheme of current sensor an amplifier is used, then in the expression should include the gain factor K_g and the measured current is expressed in terms of output voltage of the sensor as follows:

$$U_s = K_g \alpha_E \frac{N \cdot I \cdot d}{l} \tag{11}$$

The coefficient α_E depending on the operation mode can be written for different cases: nonresonant case for bending mode, for operation at the longitudinal resonance, for a thickness resonance.

According to expression (11) output voltage directly proportional to the flowing current and number of turns of the solenoid and is inversely proportional to the magnetic permeability of ME composite. The design of ME sensor was developed on the basis of these theoretical positions. Estimation of the parameter Us gives the result: when $N = 500$, $I = 1.2$ A, $d = 3$ mm, $l = 10$ mm, $\alpha_E = 2.5$ V/A, $K_g = 10$, then we obtain the output voltage equal to 4.5 V, which is in good agreement with experiment.

4.3 Fabrication

The design of ME sensor in the general case consists of a driver and a measuring head which includes ME element. The scheme of driver depends on the required measurement.

4.3.1 ME Element

ME element is the sensitive part of ME current sensor and consists, for example, of piezoelectric and magnetostrictive layers as shown in Fig. 17. Layered structure based on piezoceramic PZT plate in this case had 0.38 mm of thickness, 10 mm of

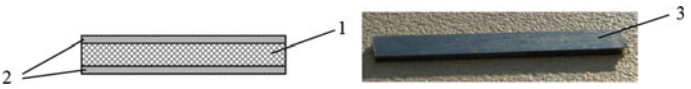

Fig. 17 Structure of ME element: (*1*) is PZT, (*2*) is Metglas, (*3*) is ME element

length and 1 mm of wide was investigated in [45]. Piezoelectric was polarized in the thickness direction. The electrodes are applied on two sides of the piezoelectric plate. The electrodes are made from three layers of Metglas and correspond in size the PZT plate. Thickness of one layer of Metglas was about 0.02 mm. Joint of layered design was done by gluing. Various types of adhesives including epoxy glue can be used. In general case, several piezoelectric plates instead of one can be used to increase the sensitivity. Also number of Metglas layers may be different in dependence on the required sensitivity. The electrical signal is taken from the surface of Metglas plates.

4.3.2 Measuring Head

Measuring head is an important element of the sensor shown in Fig. 18. ME element is placed in the inductance coil where a permanent magnetizing field and a variable modulation magnetic field are created.

Bonding the ME element to the coil inductance is very important. ME element must be fixed at one end only to avoid pinching magnetostrictive layer on the rest of the surface element. Also there is a current coil as shown in Fig. 18.

4.3.3 Sensor Schematic

In nonresonant case the scheme of current sensor consists of a generator that is tuned to the frequency, for example, about 500 Hz. Generator is connected to the inductance coil for generation of magnetic modulation field and then the signal from the ME sensor leading-out wires is amplified and fed to a peak detector. Current coil creates a constant magnetic field proportional to the current strength. If it is required, sensor's circuit can contain a microprocessor with internal analog-to-digital converter for signal conversion. Block diagram of dc sensor is shown in Fig. 19. In resonant case the scheme of current sensor similar with one, but sensitivities of the scheme some more about from ten to hundred times.

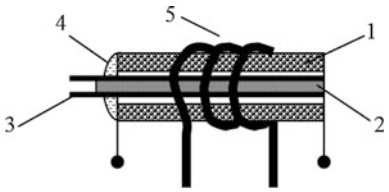

Fig. 18 Design of ME sensor measuring head: (*1*) is inductance coil, (*2*) is ME element, (*3*) is leading-out wire of ME element, (*4*) is glue, (*5*) is current coil

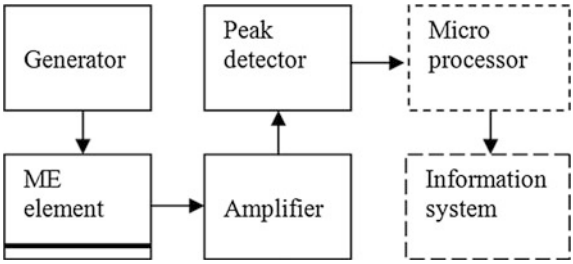

Fig. 19 Block diagram of dc sensor

4.3.4 Construction

ME current sensor is a system consisting of ME element, generator, rectifier (or peak detector), permanent magnet, two coils one of which is wound on another and case. The construction of the dc ME sensor is presented in Fig. 20.

The design of ac sensors is similar to that of electromagnetic field. The difference between these types of sensors is that the ac sensor is mounted near the conductor with alternating current around which is formed an alternating magnetic field. A dc sensors can also be used as ac sensors. The sensitivity of such sensors will depend on ME material properties and ac current frequency, because the amplitude-frequency

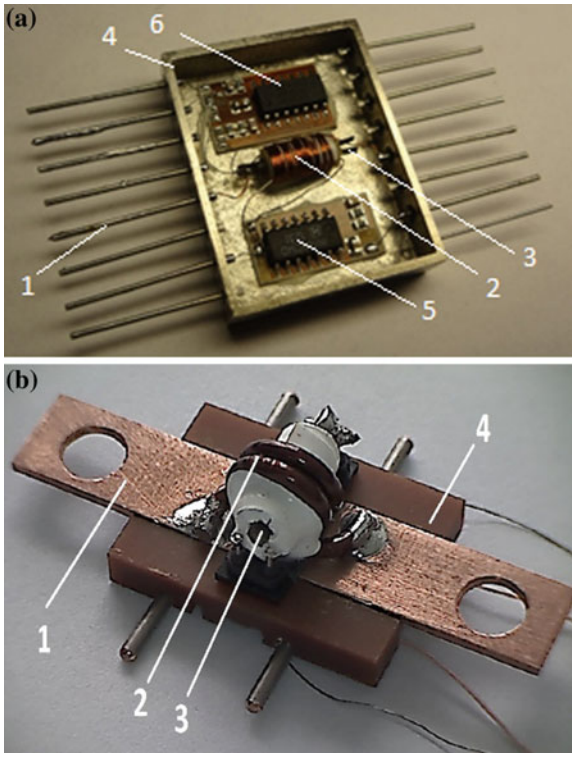

Fig. 20 Design of ME current sensor's prototype: **a** nonresonant sensor, **b** resonant sensor. (*1*) Is leading-out wire for detected current, (*2*) is current coil, (*3*) is ME element, (*4*) is the chipset case, (*5*) is generator, (*6*) is amplifier

characteristic of the ME element is non-linear and strongly depends on the frequency. The maximum sensitivity of sensors will be at various resonant frequencies, and just below that, in the low frequency range are mostly up to several kHz. To increase the accuracy, it is necessary to choose materials with the lowest magnetic hysteresis loop.

4.3.5 Electronics

Standard instruments used in measuring bench are the regulated power supply and the oscilloscope. The measurement setup includes two power supplies APS-7315 (Aktakom), multimeter HM 8112-3 (HAMEG instr.), oscilloscope ACIP-4226-3 (Aktakom) and an electromagnet, Fig. 21. First power supply provides a constant current for measurement, the second provides power supply measurement scheme, oscilloscope or multimeter is necessary for control the output voltage.

4.3.6 Measurement Data

ME element includes piezoelectric PZT layer with dimensions 10 × 5 × 1 mm and several layers of Metglas was researched and performed to optimize the sensor design.

ME element characteristics modulated by output voltage depending on the generator's frequency at the magnetic field of 3 mT is shown in Fig. 22. The curve has a non-linear form, with maxima at 1000 Hz and at electromechanical resonant frequency about 176 kHz. The resonance frequency depends on the linear dimensions of the element.

Data in Fig. 22 enable one to choose the oscillator frequency for the bias coil.

Characteristic of ME element output voltage depending on the magnetizing field at the frequency of 500 Hz is shown in Fig. 23. ME element characteristic has a strong maximum at bias field of 5 mT. The use of the linear characteristic part located from 0.5 to 4.5 mT or part from 6 to 8 mT is possible for the development of current sensors. We selected the first part for minimizing the magnetizing field.

Using data in Fig. 23 is convenient to choose the area in which will be carried out measurements of dc. For the development of the current sensor can be choose different zones of represented curve. For example, areas with the better linearity,

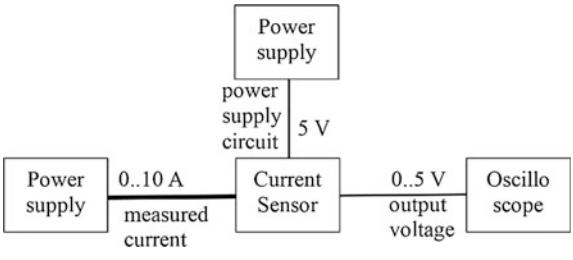

Fig. 21 Setup for measurement of dc current sensors

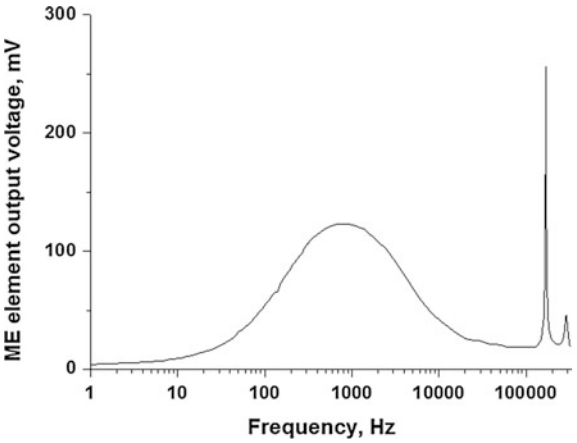

Fig. 22 ME element characteristic modulated by output voltage depending on the generator's frequency at the magnetizing field of 3 mT

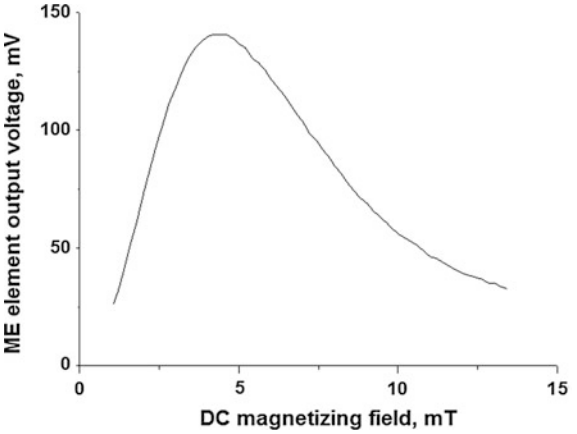

Fig. 23 Characteristic of ME element output voltage depending on dc field at the frequency of 500 Hz

starting from 0.5 to 2.5 mT, then from 6 to 8 mT and finally, one can choose a non-linear areas and use methods of compensation or transformation.

For development ME current sensor important the choice of the optimal ME structure. Theoretical modelling of symmetric and asymmetric ME structures is discussed in detail in [48]. After selecting the optimal of ME structure can start the measurement characteristics of ME sensor.

The output signal can be adjusted picking up the desired number of turns in current coil. Using the different number of current coil turns to increase the output signal in addition to the amplifier is possible. The magnetic field applied to ME element will more strong at increasing the current coil turns, and accordingly, will more big output voltage from ME element. Graph of the current sensor output voltage depending on the measured constant field and different number of the current coil turns is shown in Fig. 24. Current sensor can be used on different level of current depending on the number of turns of the current coil. In addition, sensitivity to direct current can be adjusted by using the gain of the amplifier.

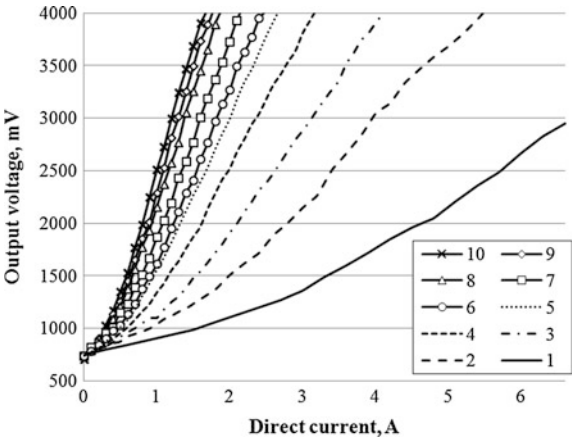

Fig. 24 Current sensor output voltage depending on direct current and different number of the current coil turns (from 1 to 10)

For the developed sensors the sensitivity of 1 A sensor is bigger than 3 V/A, for 5 A sensor sensitivity is about 0.68 B/A. The linearity of characteristic is within 1 %. Current consumption of the sensor is 2.5 mA. The increase in the number of coil current turns raises the sensitivity to the current. The sensor's design for a certain current can be calculated using the ratio of turns and sensitivity of the sensor.

The Table shows the dc sensors data. The information about the sensors HO8-NP production of LEM Holding SA, CSLW6B5 produced by Honeywell Inc., TLI4970 production of Allegro MicroSystems and also data of ME sensor discussed in [8] are presented in the table. ME sensors have higher sensitivity and lower current consumption compared to traditional sensors as it is evident from the Table 3 data.

Table 3 Comparative characteristics of dc sensors

Sensor features	HO8-NP	CSLW6B5	ACS712ELCTR-05B-T	Magnetoelectric sensor
Measuring principle	Hall effect measuring principle	Miniature ratiometric linear Hall-effect sensor	Hall-effect sensor	Magnetoelectric effect
Primary current, measuring rang I_{PM} (A)	0–20	±5	±5	0–5
Sensitivity (V/A)	0.1	0.2	0.185	0.68
Supply voltage (V)	5 ± 10 %	4.5–10.5	5 ± 10 %	5 ± 10 %
Current consumptions (mA)	19	9	10	2.5
Accuracy (%)	1	0.5	1.5	1
Output voltage range U_{out} (V)	2.5–0.5	2.7–3.7	2.5–4.5	0.7–4.1
Size in mm	24 × 12 × 12	16.2 × 14 × 10	6 × 5 × 1.75	30 × 20 × 10

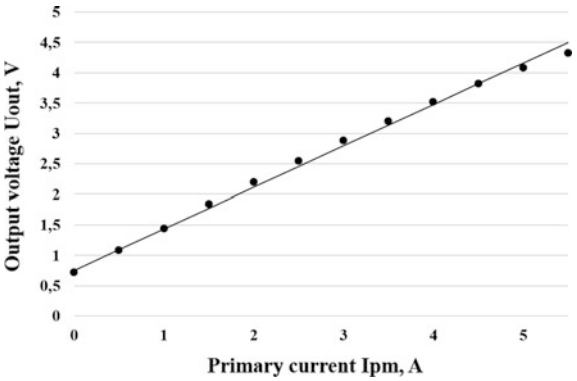

Fig. 25 Current sensor output voltage depending on dc

Figure 25 shows the characteristic of the dc current sensor for current up to 5 A.

In the future designs using of gradient ME materials and sensors placed directly on electric conductor will be explored. Using the layered structures based on compositionally graded materials enables making the sensors that can operate with no bias magnetic field applied [48]. Development of new highly sensitive ME materials will allow to develop industrial sensors are easily mounted on any surface without changing the design of the measured devices. Integrated ME sensors using MEMS or semiconductor technology in the future will also be developed.

5 Microwave Power Sensors

Almost all microwave devices use the sensor to measure any physical value that typically converts microwave oscillations in the measured signal. The operating principle of the majority of microwave power meters, called wattmeter's, is based on measuring changes in temperature or resistance elements in which the energy of electromagnetic oscillations is dissipated.

5.1 Measurement of Powerful Microwave Signal

There are various sensors for measuring the microwave power.

The calorimeters are used to measure power in the range from a few milliwatts to several hundred kilowatts. The principle of operation concludes in the equivalent conversion of electromagnetic wave energy into thermal energy calorimetric body, usually this is a water. Bolometers and thermistors: their operation is based on the transformation of the incident power into heat and the changing in resistance of the resistive element that is sensitive to temperature. Detector diodes are used for power up to 100 kW, operating range up to 100 GHz. Hall elements are used as a

walk-through power sensors in the microwave range. Meters with an absorbing wall: the principle of operation is based on the absorption of microwave power in the waveguide walls as a sensing element used semiconductor. Work of ponderomotive wattmeter is based on the mechanical action of the electromagnetic field on the conductor. Electron-beam method (Thomas method) is based on the interaction of the electron beam and the microwave field.

The disadvantages of such sensors include: non-linearity in strong magnetic fields, narrow dynamic and frequency range, a limited range of operating temperatures, the need for the voltage supply, the presence of residual stresses, low resistance to static electricity and radiation exposure [49, 50, 51, 52]. One of the most promising ways to improve the microwave power sensors is the use of ME material [12, 53]; the use of which allows to improve the performance of devices, expand their functionality and, in some cases, to create sensors with properties which are unobtainable in other types of sensors.

5.2 *Equivalent Circuit*

Sensors based on the ME materials have a wide frequency range from dc to tens of gigahertz, stable when exposed to significant levels of radiation, temperature range from 0 K to the Curie temperature of used components. ME composite materials consist of magnetostrictive and ferroelectric phases [15]. By selecting a certain of the original components in such systems it can be obtained ME interaction, sufficient for practical application. ME microwave power sensors are based on the resonant circuit [54].

For engineering calculations of resonant devices is a convenient method of analysis, in which the transmission line and the microwave resonator is considered as a bound system. The degree of coupling is characterized by a coefficient which presents the main characteristics of the transmission line with resonator: coefficient of reflection, transmission and absorption of electromagnetic microwave energy. The problem is solved in two steps: first, it is need to solve the equation of power balance (either by analyzing the equivalent circuits), that give us general expressions for the characteristics of the transmission line with resonator. Then, the coupling coefficients calculated for specific cases of resonator location in a microwave transmission line. Thus consider two types of losses: heat losses and reemission losses of electromagnetic energy in the transmission line.

Resonator quality factor Q, which is determined only on the basis of heat loss is own quality factor, reemission loss and loaded quality factor of the ME resonator are calculated as follows:

$$Q_0 = \frac{\omega W}{P_T}; Q_c = \frac{\omega W}{P_c}; \frac{1}{Q_L} = \frac{1}{Q_0} + \frac{1}{Q_c} \tag{12}$$

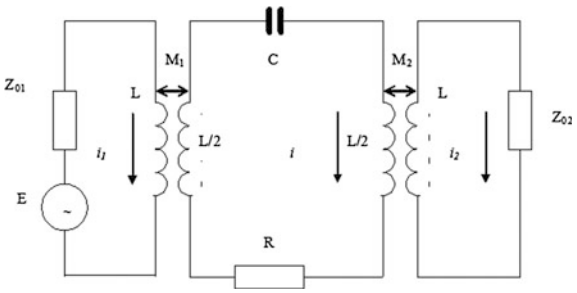

Fig. 26 The equivalent circuit of the resonator which is an element of coupling of transmission lines

where: ω is angular frequency, W is energy stored in the resonator for the period of oscillation, P_T is power of heat loss; P_c is power transferred in the transmission line by waves which reradiated by resonator.

The coupling coefficient of the resonator with microwave transmission line is defined as the ratio of the own quality factor to quality factor of coupling:

$$K = \frac{Q_0}{Q_c} \tag{13}$$

For calculation of coefficients of reflection, transmission and absorption we obtain the energy relations for the system of two transmission lines connected by ME resonator. Transmission and reflection coefficients is defined as the ratio of the amplitudes fields considering only the basic wave type. The equation of power balance in the system at resonance is follows:

$$P_{in} = P_{in}T^2 + P_{in}R^2 + P_{in}A^2 \tag{14}$$

where T is transmission coefficient; R is reflection coefficient; A is absorption coefficient.

Relations for the transmission, reflection and absorption coefficients can be obtained by analysis of the equivalent circuit (Fig. 26). The resonator in the equivalent circuit is represented as *LCR* oscillation circuit. Full input and output impedance of the transmission line can be calculated by analysis of the equivalent circuit first, and then it is possible to calculate the transmission and reflection coefficients, submitted through the coupling coefficient. This equivalent circuit can be applied to analysis of microstrip and waveguide resonant microwave power sensors.

Either all coefficients can be obtained by solving the equation of power balance. At the same coupling between the resonator and the input and output transmission lines, these formulas take the form:

$$T = \frac{K}{1+K}; R = \frac{1}{1+K}; A = \frac{2K}{(1+K)^2} \tag{15}$$

The coupling coefficient is calculated as follows:

$$K = \frac{1-R}{R} = \frac{|T|}{1-|T|} \tag{16}$$

To use the obtained general relations in specific cases it is necessary to calculate the coupling coefficients of the resonator with the transmission line. Considerable practical interest present a combination of a ME resonator with microstrip transmission line, which leads to a number of wideband, compact and easy-to-manufacture devices. The coupling coefficient in this case can be represented as:

$$K = \frac{2V\chi''_{+} z_0 \varepsilon}{\pi h^2 \lambda_v Z}\left(\operatorname{arctg}\frac{Z}{z_0\sqrt{\varepsilon}} + \frac{1}{3}\operatorname{arctg}\frac{3Z}{z_0\sqrt{\varepsilon}}\right)^2 \tag{17}$$

$$\chi''_{+} = \frac{8\pi M_0}{\Delta H}$$

where: M_0 is the saturation magnetization of the ferrite component; ΔH is the half-width of the FMR line; z_0 is characteristic impedance of a microstrip transmission line; V is volume of the ME resonator; χ''_{+} is a magnetic susceptibility at resonance; Z is wave impedance of free space; ε is the permittivity of the substrate, h is the substrate thickness; λ is wavelength transmission line.

Thus, using the expression for the coupling coefficient and the general formulas for the characteristics of the transmission line it can be calculated coefficients of reflection, transmission and absorption for different schemes of inclusion of ME resonators, and therefore devices.

The degree of coupling is characterized by the coefficient of transmission of microwave electromagnetic energy. Here we consider the transmission coefficient when the ME resonator is as heterogeneity in the transmission line.

If the transmission line is completely matched, power absorbed by ME resonator can be written as:

$$P_{ab} = \varkappa P_{in} \tag{18}$$

where the absorption coefficient is given by:

$$\varkappa = \frac{4K}{(1+K)^2 + \xi^2} \tag{19}$$

where: K is ME coupling coefficient of the resonator to the transmission line, is normalized detuning of magnetic field from the resonance values:

$$\xi = \frac{H_p - H_0 + \delta H_E}{\Delta H} \tag{20}$$

where: Hp is the value of the resonance field for a given frequency; H_0 is constant magnetizing field; δH_E is the value of resonance shift under the influence of applied electric field; ΔH is the half-width of the resonance curve of ME sample.

Absorption of microwave power by the ME material can be described by an effective magnetic microwave field $\boldsymbol{h}$ due to the ME interaction, while the absorbed power is equal to:

$$P_{ab} = k_l \boldsymbol{h}^2 \tag{21}$$

where k_l is coefficient depending on the shape and properties of the sample and equal for the disk, magnetized perpendicular or spherical sample:

$$k_l = \frac{\pi M_0}{\Delta H} \mu_0 \omega V \tag{22}$$

for disk, magnetized tangential:

$$k_l = \frac{2\pi M_0}{\Delta H} - \frac{4\pi M_0 + H_0}{4\pi M_0 + 2H_0} \mu_0 \omega V \tag{23}$$

where V is sample volume.

Magnetoelectric susceptibility tensor $\widehat{\chi}^{ME}$ is determined as:

$$\widehat{\chi}^{ME} = \widehat{\chi}^{M} \frac{h}{e} \tag{24}$$

where $\widehat{\chi}^{M}$ is magnetic susceptibility tensor

From the Formula (22) follows that electric field arising in ME element of microwave power sensor:

$$e = \frac{\widehat{\chi}^{M} \sqrt{\frac{4KP_{in}}{k_l\left[(1+K)^2 + \xi^2\right]}}}{\widehat{\chi}^{ME}} \tag{25}$$

The voltage on the ME element, which is a planar structure with electrodes (as capacitor) is:

$$U = ed = d\frac{\widehat{\chi}^{M} \sqrt{\frac{4KP_{in}}{k_l\left[(1+K)^2 + \xi^2\right]}}}{\widehat{\chi}^{ME}} \tag{26}$$

where: d is the distance between the electrodes.

Sensitivity of microwave power sensor can be calculated by the formula:

$$K_U = d\frac{\widehat{\chi}^{ME}\sqrt{\frac{4K}{k_l\left[(1+K)^2+\xi^2\right]}}}{\widehat{\chi}^{M}} \tag{27}$$

Analysis of the formula (27) shows that for increasing the sensitivity of the microwave power sensor is necessary to use a material with a large ME susceptibility. Increasing the sensitivity will also decrease the magnetic susceptibility and the coupling coefficient. To obtain maximum sensitivity is necessary to provide adjustment of ME resonator on the resonant frequency.

5.3 *Fabrication*

5.3.1 Microstrip Resonant Microwave Power Sensor

The topology of the microstrip resonant microwave power sensor [54] is shown in Fig. 27.

ME material (5) is placed in the hole in the substrate (8), while its thickness must be equal to the thickness of the substrate. At the location of the ME material stripe loops (3) and (4) long 3λ/8 and λ/8, respectively established area of circular polarization of the microwave field. ME material at the same time is in the field of a

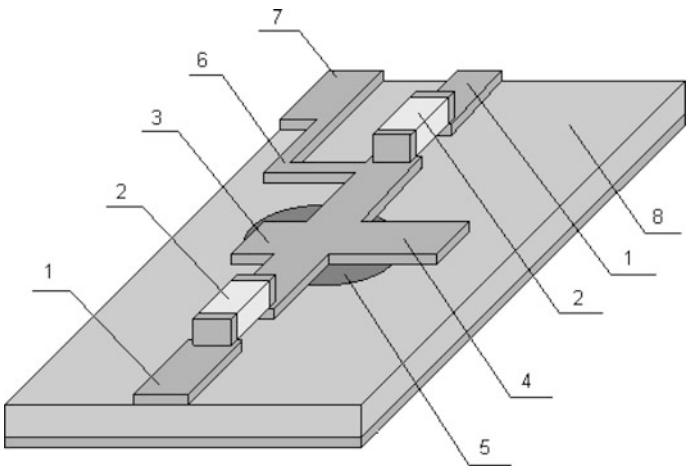

Fig. 27 The topology of the microstrip microwave power sensor. (*1*) Is supply lines; (*2*) the coupling capacitor; (*3*, *4*) strip resonator; (*5*) ME material; (*6*) the inductive element; (*7*) the capacitive element; (*8*) substrate

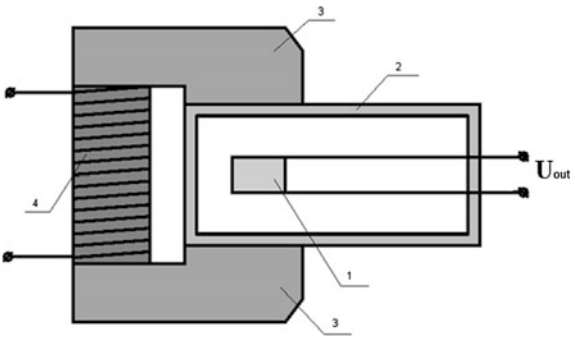

Fig. 28 ME waveguide microwave power sensor. (*1*) Is ME element; (*2*) the waveguide; (*3*) electromagnet poles; (*4*) the electromagnet coil

permanent magnet that produces magnetic bias field. The value of the magnetizing field determines the operating frequency of the sensor. On the electrodes of ME resonator due to passing through the sensor microwave power as a result of the ME interaction will appear ac voltage proportional to the incident power. The ac voltage, in the form of repeating the bending around amplitude-modulated RF signal through a low-pass filter (6 and 7) is connected to a measuring device. Coupling capacitors (2), without affecting the microwave signal, prevent the spread of low-frequency voltage across the RF channel.

Presented power sensor can be used as a detector of amplitude-modulated microwave oscillations.

5.3.2 Waveguide Resonance Microwave Power Sensor

Microwave power sensor (Fig. 28) is a waveguide device. ME element is placed in the area of circular polarization, while being in a constant magnetic field of electromagnet which create magnetic bias field at resonance frequency. The value of the magnetizing field will determine the operating frequency of the sensor. On the electrodes of ME material will appear ac voltage repeating form of the bending around of the microwave signal and proportional to the measured power.

Presented sensor operates at a frequency determined by the voltage of resonant constant magnetic field. The frequency rearrange of the waveguide microwave power sensor is achieved by varying the value of the magnetizing field. The waveguide sensor can be used as a detector of an amplitude-modulated microwave oscillations.

5.3.3 ME Microwave Power Sensor Based on Toroidal Resonator

Figure 29 shows the design of the sensor on the basis of the toroidal resonator [55]. ME element (1) is placed at an antinodes of the ac electric field and simultaneously in the field of the permanent magnet (3). Coil (5) based on thin-film technology are

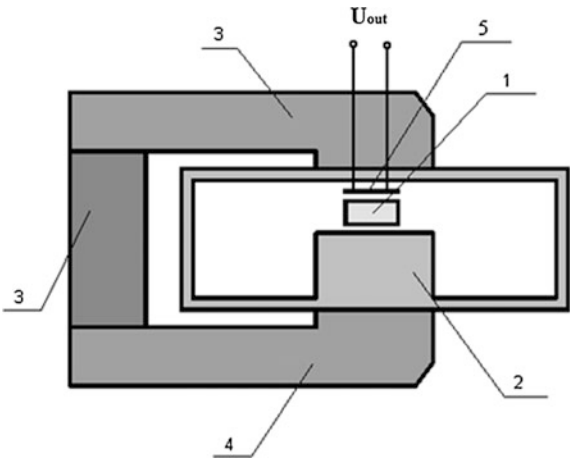

Fig. 29 ME microwave power sensor based on a toroidal resonator. (*1*) Is ME element; (*2*) the toroidal resonator; (*3*) the permanent magnet; (*4*) electromagnet poles. (*5*) coil

placed directly on the surface of the resonator ME. The value of resonance magnetizing field will determine the operating frequency of the sensor.

Under the action of the ac electric field on ME resonator through the piezoelectric and magnetostrictive action around the ME resonator will appear low-frequency ac magnetic field. Due to inductive coupling of ME resonator and the coil on the electrodes arise EMF in the shape corresponding to the bending around of the amplitude-modulated microwave signal, and the amplitude is proportional to the measured power. Presented sensor operates at a fixed frequency determined by the voltage of the constant magnetic field and the self-resonant frequency of the toroidal resonator. When using an electromagnet, and a mechanical adjustment of the toroidal resonator it can be changed the operating frequency of the sensor.

The main advantage of ME microwave power sensor on the basis of the toroidal resonator is: (1) the ability to measure high power levels at which the traditional ferrite sensors and ME sensors operating in an ac microwave field are in the saturation regime; (2) ac microwave electric and magnetic fields sufficiently separated and haven't influence simultaneously at large ME resonators.

6 Conclusions

In this chapter we considered the main constructions, equivalent circuits and characteristics of ME sensors for measuring the magnetic field, current in conductor and microwave power. It was showed that ME sensors have some advantages over semiconductor ones, for example based on Hall effect, in the sensitivity, low price and radiation resistance.

Obtained results are as follows:

(1) The nomograph method is suggested for the efficient estimates of ME voltage coefficients from given parameters of composite components. This facilitates to evaluate the feasibility of the composite for sensor application.
(2) The potential for ME sensors is notable due to the fact that there are no other present generations of magnetic sensors having the following key requirements: extreme sensitivity ($\sim$pT/Hz$^{1/2}$), allowing for better magnetic anomaly detection; zero power consumption to foster long-term operation; operation at low frequencies, $f \sim 1$ Hz; miniaturize size, enabling deployment of arrays; and low cost.
(3) The theory predicts that the highly sensitive ME laminate can be designed by increasing the ME voltage coefficient.
(4) ME sensitivity optimization should take into account the environmental or external noise sources, such as thermal fluctuation and mechanical vibration. These external noises will be dominating factors that affect the sensor's sensitivity in practical applications. For ME sensors, the dominant ones are the thermal fluctuation and mechanical vibration sources. It is important that ME sensors are designed by such a means that optimizes its abilities to cancel these external noise.
(5) The output voltage of ME current sensor was found to be a function of the detecting input current under various dc magnetic bias fields. The sensor sensitivity depends on constructive and material parameters of ME composite and bias magnetic field. The operating point for the ME current sensor has been selected. Current sensing based on ME effect is a good choice for many applications due to galvanic isolation between the sensed circuit and the measuring circuit. Using push-pull mode of ME composite will enable an improvement of the sensors. For increasing the sensor sensitivity one needs to use the ME composite based on materials with high magnetostriction and piezoelectric coupling.
(6) Analysis of characteristics of the microwave power sensors shows that one of the most promising ways to improve the sensors is the use of ME materials, which allows improving the performance of devices, expand their functionality and, in some cases, to create sensors with properties which are unobtainable in other microwave power sensors. Sensors based on composite materials have a wide frequency range up to hundreds of gigahertz, stable to significant levels of radiation, temperature range is from 0 K to the Curie temperature. In the microwave range, it is possible to use selective properties of ME materials, that allows to create a frequency selective power sensor with the possibility of adjustment.

Future prospects:

Although a large number of parameters of ME sensors would be attained, however, several important issues remain to be solved, including, the following.

(1) Increasing the sensitivity and design of sensor for simultaneous measuring the orientation and magnitude of dc and ac magnetic field.
(2) Design of contactless sensor and one for measuring the current at different range from leakage current up to 100 A.
(3) Realization of frequency tuning and design of sensor at different range of microwave power.

References

1. M.I. Bichurin, D. Viehland (eds.) *Magnetoelectricity in Composites* (Pan Stanford Publishing, Singapore, 2012), 273 p
2. C.-W. Nan, M.I. Bichurin, S. Dong, D. Viehland, G. Srinivasan, J. Appl. Phys. **103**, 031101 (2008)
3. B.D.H. Tellegen, Philips Res. Rep. **3**, 81 (1948)
4. J.Y. Zhai, J.F. Li, S.X. Dong, D. Viehland, M.I. Bichurin, J. Appl. Phys. **100**, 124509 (2006)
5. M.I. Bichurin, V.M. Petrov, R.V. Petrov, Y.V. Kiliba, F.I. Bukashev, A.Y. Smirnov, D.N. Eliseev, Ferroelectrics **280**, 199 (2002)
6. Y. Wang, J. Li, D. Viehland, Mater. Today **17**, 269 (2014)
7. H. Schmid, Ferroelectrics **162**, 317 (1994)
8. J. Van Suchtelen, Philips Res. Rep. **27**, 28 (1972)
9. J. van den Boomgaard, A.M.J.G. van Run, J. van Suchtelen, Ferroelectrics **14**, 727 (1976)
10. M.I. Bichurin, D. Viehland, G. Srinivasan, J. Electroceram. **19**, 243–250 (2007)
11. D.N. Astrov, Sov. Phys. JETP **13**, 729 (1961)
12. S. Dong, J. Zhai, F. Bai, J.F. Li, D. Viehland, Appl. Phys. Lett. **87**, 062502 (2005)
13. C.-W. Nan, G. Liu, Y. Lin, H. Chen, Phys. Rev. Lett. **94**, 197203 (2005)
14. S. Dong, J. Zhai, J. Li, D. Viehland, Appl. Phys. Lett. **89**, 252904 (2006)
15. M.I. Bichurin, V.M. Petrov, S. Priya, Magnetoelectric Multiferroic Composites (Chap. 12), in *Ferroelectrics—Physical Effects*, ed. by M. Lallart (InTech, 2011), p. 277
16. J. Zhai, Z. Xing, S. Dong, J. Li, D. Viehland, J. Am. Ceram. Sos. **91**, 351 (2008)
17. G. Harshe G, Magnetoelectric effect in piezoelectric-magnetostrictive composites. PhD thesis, The Pennsylvania State University, College Park, PA, 1991
18. M.I. Bichurin, V.M. Petrov, in *Modeling of Magnetoelectric Effects in Composites*, vol. 201. Springer Series in Materials Science (Springer, New York, 2014), 108p
19. M.I. Bichurin, V.M. Petrov, R.V. Petrov, Y.V. Kiliba, F.I. Bukashev, A.Y. Smirnov, D.N. Eliseev, Ferroelectrics **280**, 365 (2002)
20. J. Gao, Y. Wang, M. Li, Y. Shen, J. Li, D. Viehland, Mater. Lett. **85**, 84–87 (2012)
21. J. Clarke, R.H. Koch, The impact of high-temperature superconductivity on SQUID magnetometers. Science **242**, 217–223 (1988)
22. Y.J. Wang, J.Q. Gao, M.H. Li, Y. Shen, D. Hasanyan, J.F. Li, D. Viehland, Phil. Trans. R. Soc. A **372**, 20120455 (2014)
23. Y. Wang, D. Gray, J. Gao, D. Berry, M. Li, J. Li, D. Viehland, H. Luo, J. Alloy. Compd. **519**, 1–3 (2012)
24. Y. Wang, D. Gray, D. Berry, J. Li, D. Viehland, IEEE Trans. Ultrason. Ferroelectr. Freq. Control **59**, 859–862 (2012)
25. Y. Wang, J. Gao, M. Li, D. Hasanyan, Y. Shen, J. Li, D. Viehland, H. Luo, Appl. Phys. Lett. **101**, 022903 (2012)
26. X. Zhuang, S. Saez, M. Lam Chok Sing, C. Cordier, C. Dolabdjian, J. Li, D. Viehland, S.K. Mandal, G Sreenivasulu, G. Srinivasan, Sens. Lett. **10**, 961 (2012)
27. R. Jahns, H. Greve, E. Woltermann, E. Quandt, R. Knöchel, Sens. Actuators, A **183**, 16 (2012)

28. T. Onuta, Y. Wang, S.E. Lofland, I. Takeuchi, Adv. Mater. (2014). doi:10.1002/adma.201402974
29. S. Marauska, R. Jahns, C. Kirchhof, M. Claus, E. Quandt, R. Knochel, B. Wagner, Sens. Actuators, A **189**, 321 (2013)
30. J. Petrie, D. Viehland, D. Gray, S. Mandal, G. Sreenivasulu, G. Srinivasan, A.S. Edelstein, J. Appl. Phys. **111**, 07C714 (2012)
31. J.R. Petrie, J. Fine, S. Mandal, G. Sreenivasulu, G. Srinivasan, A.S. Edelstein, Appl. Phys. Lett. **99**, 043504 (2011)
32. Y. Wang, D. Gray, D. Berry, J. Gao, M. Li, J. Li, D. Viehland, Adv. Mater. **23**, 4111 (2013)
33. E. Lage, C. Kirchhof, V. Hrkac, L. Kienle, R. Jahns, R. Knöchel, E. Quandt, D. Meyners, Nat. Mater. **11**, 523 (2012)
34. C. Kirchhof, M. Krantz, I. Teliban et al., Appl. Phys. Lett. **102**, 232905 (2013)
35. A. Piorra, R. Jahns, I. Teliban et al., Appl. Phys. Lett. **103**, 032902 (2013)
36. G. Sreenivasulu, V.M. Petrov, L.Y. Fetisov, Y.K. Fetisov, G. Srinivasan, Phys. Rev. B **86**, 214405 (2012)
37. T.T. Nguyen, F. Bouillault, L. Daniel, X. Mininger, Finite element modeling of magnetic field sensors based on nonlinear magnetoelectric effect. J. Appl. Phys. **109**, 084904 (2011)
38. M.I. Bichurin, V.M. Petrov, R.V. Petrov, Y.V. Kiliba, F.I. Bukashev, A.Y. Smirnov, D.N. Eliseev, Ferroelectrics **280**, 365 (2002)
39. S.X. Dong, J.F. Li, D. Viehland, J. Appl. Phys. **96**, 3382 (2004)
40. S.X. Dong, J.F. Li, D. Viehland, Appl. Phys. Lett. **85**, 2307 (2004)
41. Shuxiang Dong, John G. Bai, Junyi Zhai et al., Appl. Phys. Lett. **86**, 182506 (2005)
42. S. Zhang, C.M. Leung, W. Kuang, S.W. Or, S.L. Ho. J. Appl. Phys. **113**, 17C733 (2013)
43. S.X. Dong, J.G. Bai, J.Y. Zhai, J.F. Li, G.Q. Lu, D. Viehland, S.J. Zhang, T.R. Shrout, Appl. Phys. Lett. **86**, 182506 (2005)
44. Jitao Zhang, Ping Li, Yumei Wen, Wei He et al., Rev. Sci. Instrum. **83**, 115001 (2012)
45. R.V. Petrov, N.V. Yegerev, M.I. Bichurin, S.R. Aleksić, Current sensor based on magnetoelectric effect, in *Proceedings of XVIII-th International Symposium on Electrical Apparatus and Technologies SIELA 2014*, , Bourgas, Bulgaria, 29–31 May 2014
46. I.N. Solovyev, A.N. Solovyev, R.V. Petrov, M.I. Bichurin, A.N. Vučković, N.B. Raičević. Sensitivity of magnetoelectric current sensor, in *Proceedings of 11th International Conference on Applied Electromagnetics—IIEC 2013*, Niš, Serbia, 1–4 Sept 2013, pp. 109–110
47. R.V. Petrov, I.N. Solovyev, A.N. Soloviev, M.I. Bichurin, Magnetoelectic current sensor, in *PIERS Proceedings*, Stockholm, Sweden, 12–15 Aug 2013, pp. 105–108
48. M. I. Bichurin, V.M. Petrov, Modeling of magnetoelectric interaction in magnetostrictive-piezoelectric composites, in *Advances in Condensed Matter Physics* (2012)
49. E.L. Ginzton, *Microwave Measurements* (McGraw-Hill, Inc., London, 1957)
50. A. Fantom, *Radio Frequency and Microwave Power Measurement*, IET (1990), 278p
51. M.I. Bichurin, S.V. Averkin, G.A. Semenov, The magnetoelectric resonator. Patent 2450427RU
52. A.S. Tatarenko, M.I. Bichurin, Electrically tunable resonator for microwave applications based on hexaferrite-piezoelectrc layered structure. Am. J. Condens. Matter Phys. **2**, #5 (2012)
53. M.I. Bichurin, V.M. Petrov, G.A. Semenov, Magnetoelectric material for components of radio-electronic devices. Patent 2363074RU
54. M.I. Bichurin, S.N. Ivanov, Selective microwave power detector. Patent 2451942RU
55. M.I. Bichurin, A.S. Tatarenko, V. Kiliba Yu, Magnetoelectric microwave power sensor. Patent 147272RU

Anisotropic Magnetoresistance (AMR) Magnetometers

Michael J. Haji-Sheikh and Kristen Allen

Abstract Anisotropic magnetoresistive (AMR) based magnetometers are used in devices as varied as global positioning systems to provide dead reckoning capability and in automotive ignition systems to provide crankshaft rotational position. Presented are data and methods that can assist in the design and implementation of these systems and a method to design a Helmholtz coil system to test these devices. The transverse and longitudinal behavior of individual AMR sensors along with group (proximity) behavior is addressed with both data and modeling. The design of a 3-axis measurement system goes from basic electromagnetics to the use of COMSOL and the verification of the measurement system using a commercial 3-axis magnetometer.

1 Background

When William Thompson (Lord Kelvin) discovered the Anisotropic Magnetoresistance (AMR) effect in 1897 [1] it was but a curiosity of physics. Significant effort through the early part of the Twentieth Century was made in an effort to model and understand this effect. Though, to use AMR to its maximum effect it would take another sixty years of development (including the microelectronics revolution) to make usable thin-films for sensors and memory. In the 1960s, the invention of the integrated circuit along with the space race led to advances in thin film deposition processes that produced high quality magnetic films. The search for a material to be a lightweight non-volatile memory material for space applications, led researchers to develop devices from AMR materials [2] to satisfy these requirements. This memory is called magnetic random access memory or MRAM. Corporations as diverse as IBM, Philips Electronics, TI, and Honeywell have developed variants over the years on this theme. Philips Electronics and

M.J. Haji-Sheikh (✉) · K. Allen
Department of Electrical Engineering, Micro-Electronic Research and Development Center, Northern Illinois University, Dekalb, IL 60115, USA
e-mail: mhsheikh@niu.edu

A. Grosz et al. (eds.), *High Sensitivity Magnetometers*, Smart Sensors, Measurement and Instrumentation 19, DOI 10.1007/978-3-319-34070-8_6

Honeywell entered the Market in the 1960s, 1970s and into the present day using AMR thin film magnetometers. Over that time period, researchers studied the effect of depositing films under magnetic fields [3, 4] and the sources of noise that would effect low field measurements [5]. Recently, the topic of permalloy deposition in static magnetic fields has become of interest again as shown in this recent paper by García-Arribas et al. [6]. Commercial uses of AMR magnetometers consist of high current detection (overload current detection in power distribution), position sensing, tachometry, low magnetic field anomaly detection, and multi-axis compasses.

2 Physical Model

Magnetoresistance can be broken into two types, ordinary and anisotropic. Ordinary magnetoresistance is often exhibited by non-magnetic metal and semiconductors. The effect is due to the shorting out of the Hall voltage which then increases the path length of the electrons which in turn increases the resistance. The ordinary magnetoresistance equation is

$$\frac{\Delta\rho}{\rho_0} = C \cdot \mu \cdot B^2 \tag{1}$$

where C is a constant, μ is the mobility, and B is the normal magnetic field. This effect is mostly used in indium antimonide magnetoresistors produced by Asahi Chemical Industry. The InSb compound semiconductor can have extremely high mobilities (60,000–80,000 cm^2/V s). During the late 1980s and early 1990s GM research advocated the use of InSb sensors in crank-sensor applications [7] and deployed some of these sensors in vehicles such as their Cadillac luxury line.

Automotive AMR sensors come in two types: High-field sensors that sense primarily angle; Low-field that sense magnitude. The range of what is considered high field depends on the application. A high field sensor for an AMR device is an in-plane field level that is high enough to keep the sensor in saturation. It is common to discuss field levels in magnetic sensors in units of Oersteds or Oe since a Tesla is quite a large unit for normal uses. For many AMR sensors this corresponds to greater than 25–30 Oe. A low-field sensor operates below the onset of saturation. Figure 1 shows the response of a single AMR resistor element. The lower region behaves in somewhat a sinusoidal manner while the next region is somewhat linear and the last region is the saturation region. This curve is often described as $\cos^2$ behavior

$$\frac{\Delta R}{R_0} = \Delta R_{max} \cos^2 \theta. \tag{2}$$

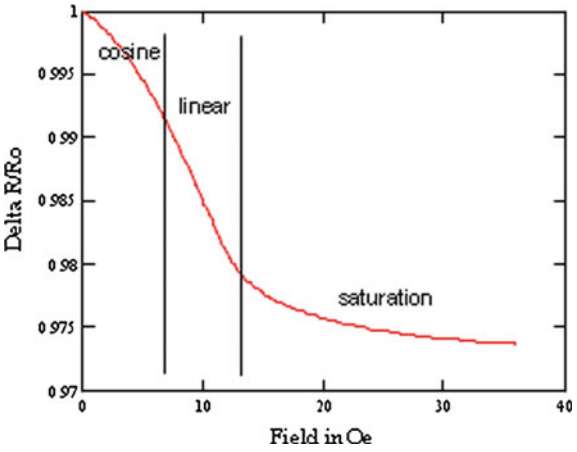

Fig. 1 The transverse magnetoresistance curve for a 37.5 nm and 35 μm wide resistor. This field response curve is entirely dependent on geometry of the sensor (width and thickness)

A solid monograph on the design of AMR sensors, as defined through the 1990s and published in 2001 is authored by Tumanski [8]. Tumanski defines a broader set of application devices and analyzes some giant magnetoresistive (GMR) devices where this article only will consider AMR devices. Tumanski outlines much of the design criteria for various magnetic sensors and is a pioneer in the use of AMR sensors for many commercial applications.

2.1 Theoretical Behavior

The ordinary magneto-resistance effect is present in all metals and was first observed by Hall [9] in his groundbreaking paper on "A New Action of the Magnet on Electric Currents" in 1879 then followed by William Thompson's discovery of the AMR effect in 1897. After almost of a century of work by various researchers such as Birss [10] and Stoner and Wolforth [11], the material went from a curiosity to a commercial success in transformer cores, to modern magnetic sensors and magnetic memory. The theoretical models can date back to the research work done by the people at IBM's Watson Research Center [2, 12]. A physical model put forth [2] is the increase in resistance due to s-d interband scattering. Magnetoresistance can be broken into two types, ordinary and anisotropic. Additionally Batterel and Galinier [13] pointed out a novel effect that appears in AMR materials, this effect is described as the planer hall effect and come out of the tensor analysis of the AMR effect. This effect is often used in MRAM (magnetic random access memory) not generally used in magnetometry. The anisotropy constant can be determined by the planer hall effect according to Chang [14].

2.2 The Resistivity Tensor

A physical model for the behavior of an AMR sensor is a necessary step to allow these sensors to be used in design. Most models start with trying to fit data and theory to a resistor below the saturation point. As we were designing sensors for various saturation mode applications, it was painfully obvious that that method was not applicable to the situation presented. Testing shows that rotating a saturating field created a very well defined sinusoidal behavior. This did not match the $\cos^2\theta$ behavior outlined in a plurality of journal papers. For us to use an equation in our modeling at the time, we needed to rethink this equation. An experiment to develop this physical model was devised at the time that would incorporate everything we knew about measuring resistors. Figure 2 shows the basic resistor design used to develop a Maxwell's equations based model to characterize the behavior of saturated elements. The basic concept is to use Kelvin connected resistors that have a well defined current launching structure that will behave in a manner which can make extracting behavior a simple mathematical exercise. A common measurement technique for these films has been to use a Vander Pauw structure. The Vander Pauw structure is not useful for these type of magnetic tests due to the current never following a straight line in one of these structures.

Figure 3 is a graph of the data generated for a group of magnetoresistive elements tested in the saturation region [15].

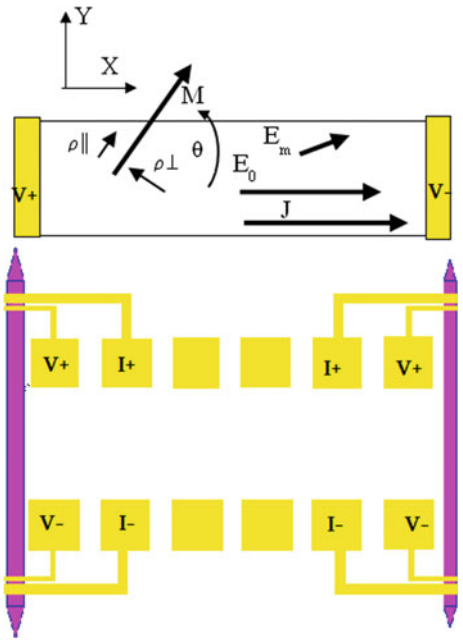

Fig. 2 CAD layout of a typical AMR thin film Kelvin resistor along with a schematic of the vectors present in the given device. *This image is care of Honeywell's Sensing and Control Division*

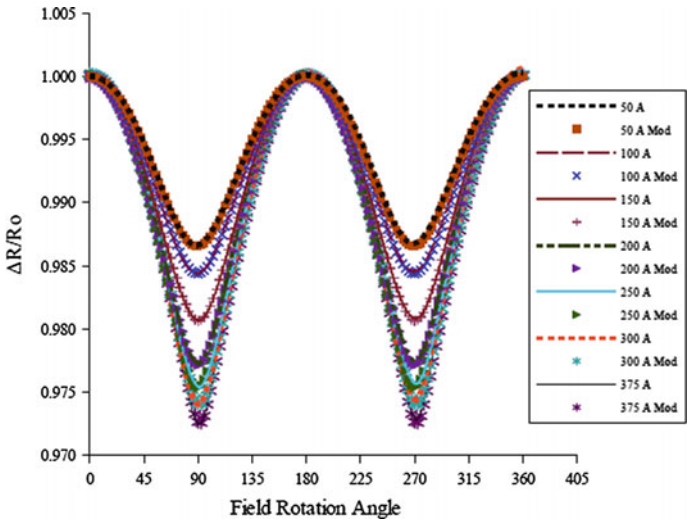

Fig. 3 Saturated magnetoresistors tested through 360°. The data is from Haji-Sheikh et al. [15]. This graph also includes the results of modeling

The sensor model behavior is the result of solving a 2d tensor that starts by assuming isotropic and anisotropic behavior for a magnetoresistor. The error often made in this solution is the dropping of one of the current elements that relates to the transverse current in a resistor. The full tensor to solve for the saturated magnetoresistance is as follows

$$P'_{total} = \begin{bmatrix} \rho_0 & 0 \\ 0 & \rho_0 \end{bmatrix} + \begin{bmatrix} \rho' + \Delta\rho' \cos(2\theta) & \Delta\rho' \sin(2\theta) \\ \Delta\rho' \sin(2\theta) & \rho' - \Delta\rho' \cos(2\theta) \end{bmatrix} \tag{3}$$

By solving the following relationship,

$$\vec{E} = \rho\vec{J} \tag{4}$$

where E is the electric field and J is the current density. The modified AMR relationship can be shown to be similar to the Mohr's circle as described in Nye [16] and is as shown in equation,

$$\rho_{eff} = \rho_0 + \rho' \sqrt{\left(1 + \frac{\Delta\rho'}{\rho'}\cos(2\theta)\right)^2 + \left(\frac{\Delta\rho'}{\rho'}\sin(2\theta)\right)^2} \tag{5}$$

with the only difference from a mechanical system is the lack of off-axis shear components. So that the measured resistance is

Table 1 Coefficients of fit for permalloy magnetoresistors

	Film thickness						
	5.0 nm	10.0 nm	15.0 nm	20.0 nm	25.0 nm	30.0 nm	37.5 nm
A	0.97923	0.97580	0.97340	0.97090	0.97050	0.96968	0.97000
B	0.01420	0.01640	0.01695	0.01695	0.01726	0.01722	0.01630
C	0.480	0.480	0.572	0.572	0.718	0.769	0.845

$$V = \rho_{eff} \frac{length}{area} \cdot I \quad or$$
$$V_{total} = I_s R_0 \left[A + B\sqrt{(1 + C\cos(2\theta))^2 + (C\sin(2\theta))^2} \right] \tag{6}$$

The value of R_0 is also experimentally determined since it represents the resistance with no applied field (Table 1).

These empirical results allow for a high precision fit to the permalloy and are consistent with Maxwell's equations. For a sensor below saturation the modeling is not so simple. Many things influence the results including the proximity of the other sensor elements, length, width, and thickness. Some automotive designs operate between 0.1 and 0.2 T (1000–2000 G) which is far above the sensor saturation level. Above saturation, proximity and geometry don't have much of an effect but below saturation these effects become designable parameters and can have a significant effect on the overall results.

2.3 *Cross Axis Behavior Unsaturated Single Resistor Element*

The range of what is considered high field changes from sensor to sensor design. A high field sensor for an AMR sensor is an in-plane field level that is high enough to keep the sensor in saturation. It is common to discuss field levels in magnetic sensors in units of Oersteds or Oe (Gauss in air). For many AMR sensors this corresponds to greater than 15–30 Oe. A low-field sensor operates below the onset of saturation. Figure 4 shows the response of a single AMR element with different thicknesses. This behavior is representative of the rotation of micro-magnetic domains. These domains will rotate until they reach a maximum angle which will be a number somewhat lower than ninety degrees.

The below saturation mode in automotive sensing is not as common as the above saturation mode sensors but it does show up in current sensing in electric vehicles and in sensing the Earth's magnetic field. The high-current sensors are generally designed as meander sensors but have to take in account the design parameters an not needed for the above saturation devices. Figure 5 shows various representations of the magnetization and behaviors of the sensors below saturation.

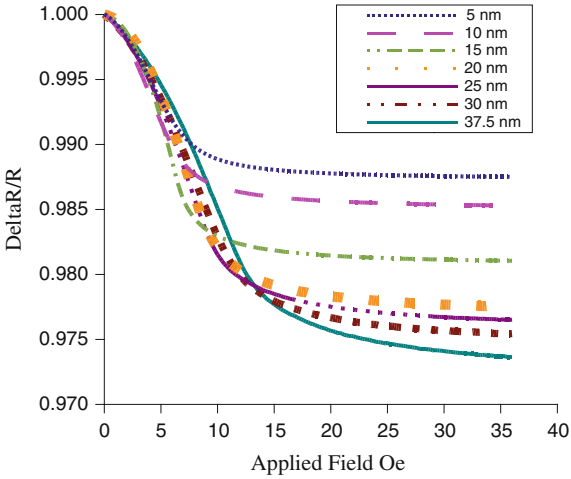

Fig. 4 Transverse magnetoresistance curves from a 5 to 37.5 nm thick 35 μm wide resistor. The saturation region of this curve is controlled by geometry. Thinner films have a lower saturation field and a lower maximum change in resistance

The Stoner-Wohlforth model is often used to represent the behavior of magnetoresistors within the full range of hysteresis, as shown in Fig. 5. To approach magnetization rotation, we can look at minimizing the energy of the magnetic system so from Chikazumi and Charap [17] we get,

$$E = -K_u \cos^2(\theta - \theta_0) - M_s H \cos\theta \tag{7}$$

where M_s is the saturation magnetization, H is the external field, θ is the angle between H and M_s and θ_o is the angle between H and the easy axis (EA). The anisotropy constant K_u acts like the spring constant for a rotating spring and is the energy that it takes to return the magnetization back to the original position. It is important to characterize the permalloy out of any particular deposition process since no two deposition systems will produce identical material. The two main numbers that are needed to be compared from machine to machine are the values of H_c and H_k. The H_c value represents the easy-axis hysteresis and the H_k represents the hard-axis slope between the saturation levels. There are commercial B-H

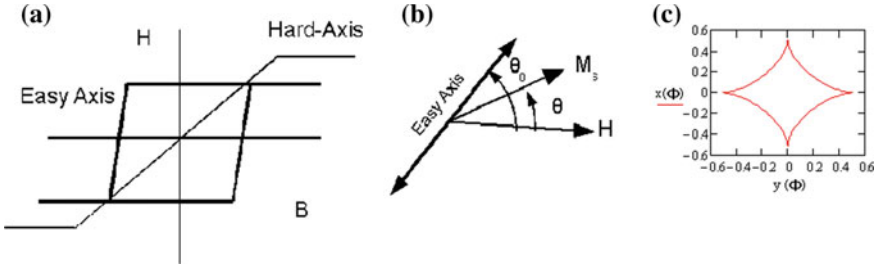

Fig. 5 **a** The B-H behavior of an ideal thin film. **b** A magnetic free body diagram representing the thin-film resistor. **c** A plot of the Stoner-Wohlforth asteroid is shown

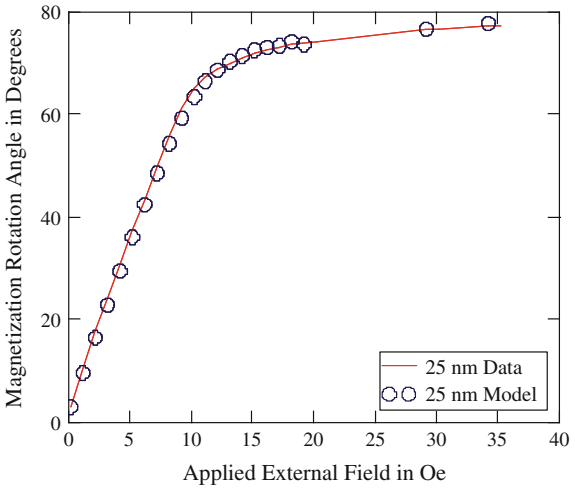

Fig. 6 The angle θ versus applied external field H. Also shown is the results of attempting to create a model to fit the rotation of the magnetization with H. There is significantly more transition than the S-W predicts

looping systems that will measure these values inductively directly on a deposited substrate. That means that Eq. (8) needs to be matched to an actual test structure. To extract θ for a given design, the following equation can be used to extract the angle

$$|\cos\theta| = \sqrt{\frac{1}{4C}\left[\left(\left(\frac{V_0}{I_S R_0} - A\right)\frac{1}{B}\right)^2 - C^2 - 1 + 2C\right]} \tag{8}$$

where the values of A, B, and C come from Eqs. (8) and (9). The angle θ can be plotted against applied θ. A graph of this is shown in Fig. 6 for a 25 nm. Equation (12) is a first attempt to model the behavior using a magnitude tensor ratio

$$\Delta\theta = \frac{M}{2K_u}H = \frac{M_0\sqrt{(1+\alpha\cos 2\theta)^2 + (\alpha\sin 2\theta)}}{2K_u\sqrt{(1+\delta\cos 2\theta)^2 + (\delta\sin 2\theta)}} \tag{9}$$

where M_o is considered to vary rhombohedrally and K_u is also varying in the same fashion. The values for δ and for α are also experimentally determined and the equation is solved transcendentally.

The model can then be substituted into Eq. (4) and compared to the original data. The initial data and experiments indicates that this model can fit actual data. The relationships then can create a conceptual basis for a more complete model in the future.

It is important to reinsert the rotation data (Fig. 7) into the model to determine if the magnetization rotation model works. This is to match the modeled data to the

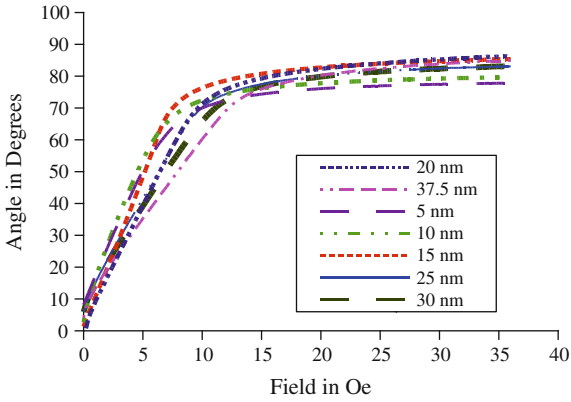

Fig. 7 Rotation angle for resistors of the same width and different thicknesses. It is clear that the thicknesses change the maximum rotation angle. The maximum angle of rotation appears to be actually lower for the thinner resistors. Width equals 35 μm

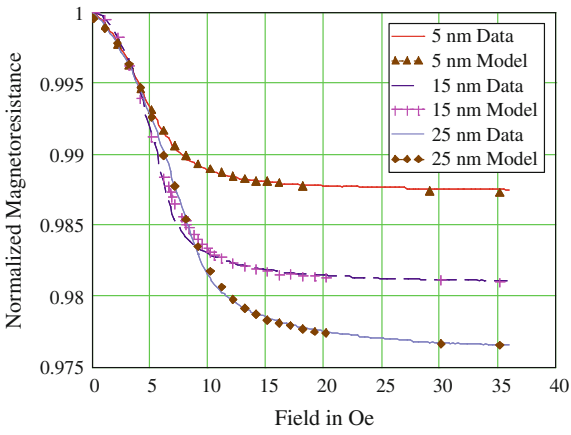

Fig. 8 This is a graph of magnetic response of single resistors of constant width but varying thickness. This graph demonstrates the behavior of the model versus the actual sensor results. Unfortunately the model is not as predictive as necessary. but it does show the relationship between the earlier saturation model and the below saturation behavior

original data. The result for this comparison is shown in Fig. 8. Normally this data is fitted using a piecewise model as shown in Tumanski [8] but this new approach allows the model to be appear contiguous.

2.4 Longitudinal Axis Behavior Unsaturated Single Resistor Element

An important sensor response that needs to be understood is the off-axis behavior. This off-axis behavior is most interesting when looking at a 45° field to the current direction and then when the field is rotated 180° from the magnetization direction. The resistors force the magnetization to line up with the resistor direction and without an applied external field the magnetization and the current is parallel to the current direction. With these responses, hysteresis is defined. This is specific to a below saturation element and

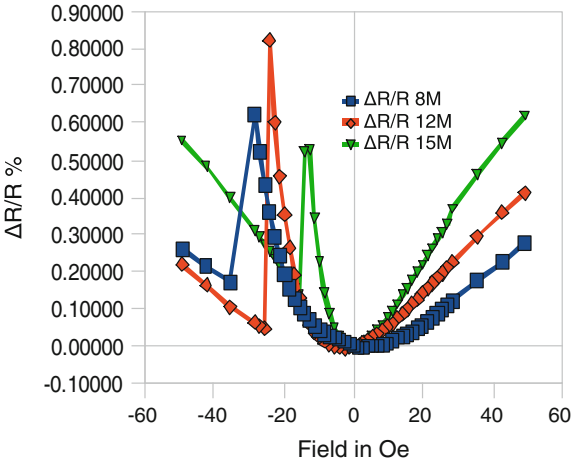

Fig. 9 45° off-axis behavior for three different widths of a resistor with the same thickness. The results up until the switching field show a behavior (as they should) similar to a barber-pole sensor

often a source of error. The schematic in Fig. 5 shows an ideal hysteresis behavior and we can compare this with Fig. 9 which shows the 45° off-axis applied field behavior. The first quadrant applied field is in the direction in which the magnetization is set (right side) and the third quadrant applied field is in the opposite direction of the set magnetization (left side). This displays two effects need to produce a compass chip. One of these effects is the asymmetry of the resistor response and the other is the hysteresis caused by the reversal of the magnetization.

The hysteresis effect that is often observed in certain sensors can be demonstrated by applying the field at forty-five degrees to the resistor. Each measurement point is around a milligauss so that the domain reversal happens in a narrow field range. To demonstrate the reversal effect at its strongest, a group of individual resistors were bias longitudinally. These resistors were on four wafers to reduce the effect of manufacturing variability on the experiment. There was no attempt to reproduce this data with the effect of proximity on this set of samples. According to Tanaka, Yazawa and Masuya [18], in their study of magnetization reversal in cobalt thin films, the magnetization reversal is always proceeded by a non-coherent rotation process and is heavily influenced by crystalline grain orientation. During the processing of permalloy films often multiple layers are deposited to build up the target thickness. The single layer films have Bloch wall displacement where multilayer devices have Neel wall displacement [19]. This multilayer structure lowers the switching field. The films in the following graphs have multiple layers (2 minimum and 10 maximum). They exhibit switching fields that are strongly affected by the thickness of the films and by the width of the patterned resistors. The results in Fig. 9 demonstrate the behavior of a single resistor element being biased by an external magnetic field at forty-five degrees. As expected, the resistor behaves much as a barber-pole sensor behaves until the switching field is reached. When the magnetization reversal occurs, the resistance change mirror images the right half plain behavior.

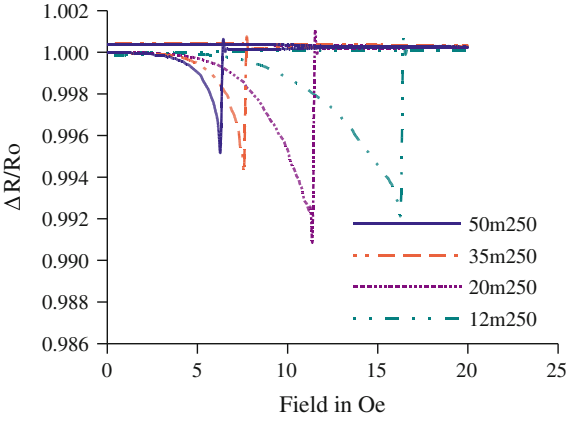

Fig. 10 Resistance of individual resistors biased magnetically along the current direction. The resistor thickness is 25 nm and all resistors are the same length

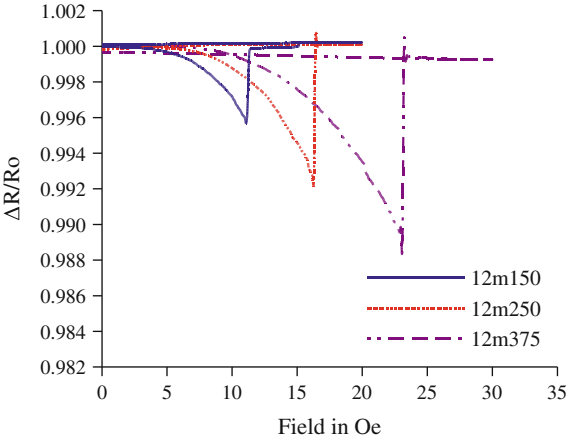

Fig. 11 Resistance of individual resistors biased magnetically along the current direction. The resistor thickness varies from 15, 25, 37.5 nm and the width is 12 μm and all resistors are the same length

The next set of graphs show the results of using an external bias field along the resistor direction and in the opposite direction of the magnetization for that resistor. Figures 10, 11, 12, 13 and 14 demonstrate the effect of patterning and film thickness on the reversal field for an 81 % Ni/19 % Fe permalloy film. It is clear that the switching field drops with patterned resistor width. In Fig. 10, the film thickness was 25 nm (250 Å) and the resistors appear to go through a single reversal point which would indicate that there is a certain amount of coherency in this behavior. In Fig. 11 the comparison is with a constant resistor width (12 μm) and varying the thickness from 15, 25, and 37.5 nm. This shows that the switching field is increasing with increasing film thickness. This is consistent with the increasing magnetic material volume.

The effects of using a very narrow resistor i.e. 6 μm as patterned, is shown in Fig. 12 while Figs. 13 and 14 show 15 and 20 μm resistors. Several things come out of these figures. The effect of edge in support of the magnetization reversal is

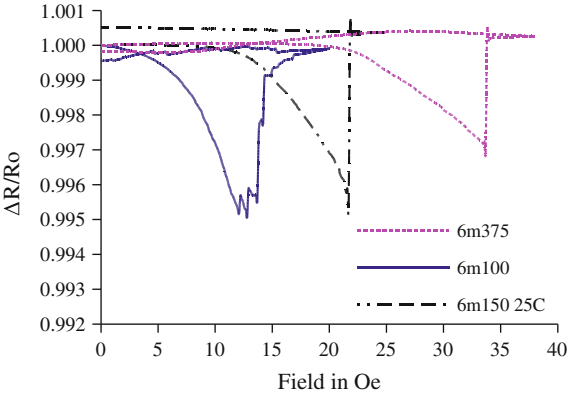

Fig. 12 Resistance of individual resistors biased magnetically along the current direction. The resistor thickness varies from 15, 25, 37.5 nm and the width is 6 μm and all resistors are the same length

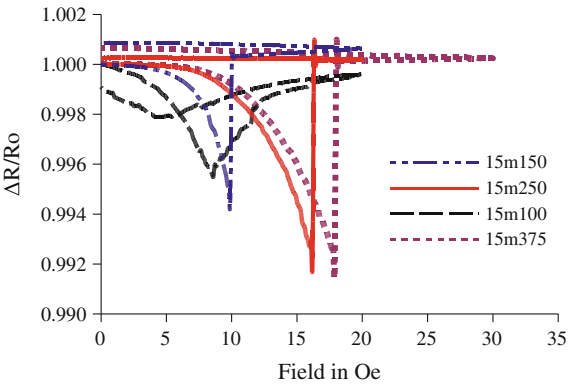

Fig. 13 Resistance of individual resistors biased magnetically along the current direction. The resistor thickness varies from 10, 15, 25, 37.5 nm and the width is 15 μm and all resistors are the same length. The domain reversal is not as sharp at 10 nm

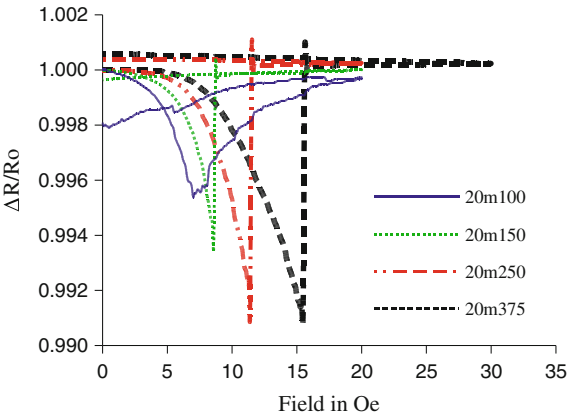

Fig. 14 Resistance of individual resistors biased magnetically along the current direction. The resistor thickness varies from 10, 15, 25, 37.5 nm and the width is 20 μm and all resistors are the same length. The domain reversal is not as sharp at 10 nm

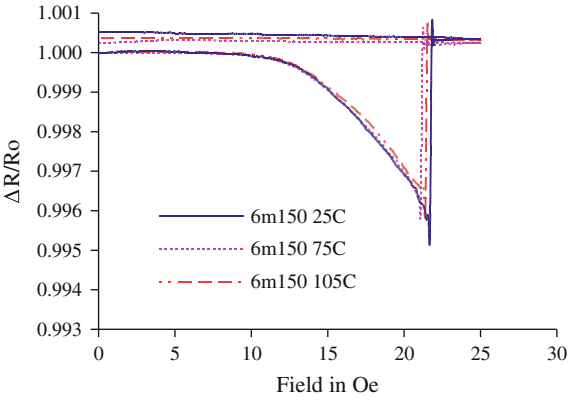

Fig. 15 Resistance of an individual resistor biased magnetically along the current direction. The resistor thickness is 15 nm and the width is 6 μm. This experiment was performed at 3 different temperatures and shows the magnetization reversal is relatively independent of temperature

quite strong. As the resistor gets narrower the field required to reverse the magnetization gets higher. This is consistent with present design philosophy and theory. The thickness also has an effect on the reversal of the magnetization. Not only does the thinner sensors demonstrate lower magnetization reversal, the thinnest sensors (10 nm) show significant anisotropy dispersion. This dispersion is not evident in the thicker resistors. Also, this dispersion effect is also interactive with the support from the edge effect. This is also demonstrated with the 10 nm sample which, when the resistor was patterned at 6 μm, the apparent dispersion was reduced and the reversal point was increased. This dispersion effect, in the range of the test, does not seem to be as strong as the thickness to width ratio from 15 nm and up. Additional measurement in this range could support a strong micro-domain numerical model.

Another question that was attempted to be answered by this experiment was whether or not temperature, in a narrow range, has an effect on the reversal value. Figure 15 shows the resistance of an individual resistor biased magnetically along the current direction. The resistor thickness is 15 nm and the width is 6 μm. This resistor was chosen because of the strong magnetization reversal value above 20 Oe. This experiment was performed at 3 different temperatures and shows the magnetization reversal is relatively independent of temperature in that narrow range.

The magnetization rotation angle was calculated for the resistors going through domain reversal. This calculation is shown in Fig. 16 and demonstrates that the magnetization rotates somewhere between 50° and 65° of rotation prior to reversing direction. Interestingly enough, the 35 μm resistor shows a result that implies that some portion of the resistor is rotating past 90° since the resistance is starting to decrease smoothly prior to reversal.

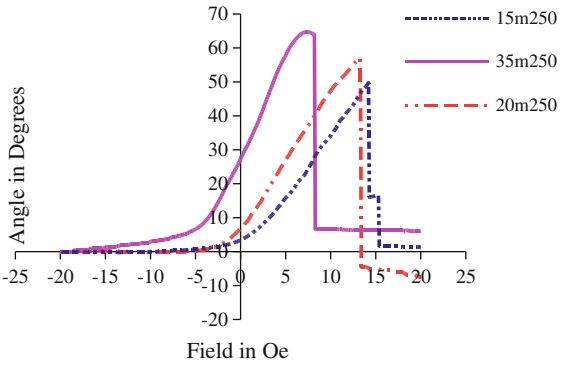

Fig. 16 Calculated angles for longitudinally biased resistors using Eq. (11) to determine the edge effect. The three resistors were next to each other on the same silicon substrate. The magnetization reversal occurs between 50° and 65° of rotation prior to reversing direction

2.5 *Cross Axis Behavior for the Unsaturated Barber-Pole*

Since the resistance change is coupled to the current direction, a different type of sensor was developed. Commercial entities such as Philips and Honeywell have produced compass chips using a design called the barber-pole. Unlike the previous structures, the barber-pole steers the current 45° to resistor direction. This allows the maximum field to be 90° to the resistor direction and improves magnetization control. One of the primary uses of an AMR sensor is for a below saturation direction sensor. The normal behavior of an AMR resistor can be characterized as an even function sensor i.e. symmetrical about "y" axis. The resistance of these barber-pole structures in a ninety degree applied field is shown in Fig. 17.

Figure 18 is a single element barber-pole resistor. The resistor is 35 μm in width and has 45° shorting straps. The np in the graph means we are setting the magnetization in the negative direction and sweeping the field in the positive direction, and the nn means that we are setting the field in the negative direction and sweeping the field in the negative direction. These samples had a fixed offset field i.e. bias field of 0, 5, and 10 Oe. The classic compass chip behavior is obtained by summing resistor values that have different shorting +45 (and + current) shorting bars and −45 (and −current) to linearize the main sensing region. The resistance of these structures is inverse to the desired behavior, the wider structures have lower resistances which in turns says that the larger the resistor bridge the better the compass, but in general a more expensive part. These resistors are sensitive to magnetization reversals so that it is important to have a calibration routine that includes a magnetization reset function. A barber-pole sensor when placed in a

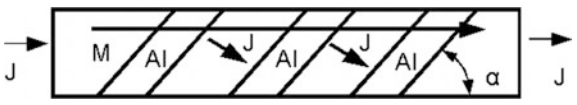

Fig. 17 Barber-pole sensor element, aluminum shorting straps for redirecting the current

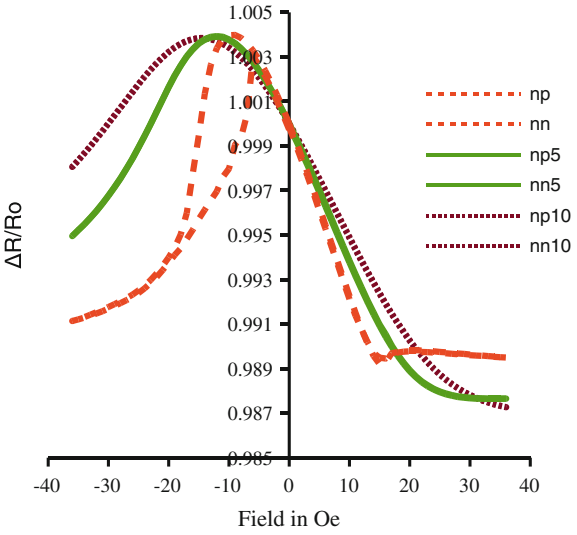

Fig. 18 Single element barber-pole resistor. The resistor is 35 μm in width and has 45° shorting straps. The np means, negative set field/positive sweep, and nn means negative set field/negative sweep. No number means no longitudinal bias while the 5 means 5 Oe and the 10 means 10 Oe

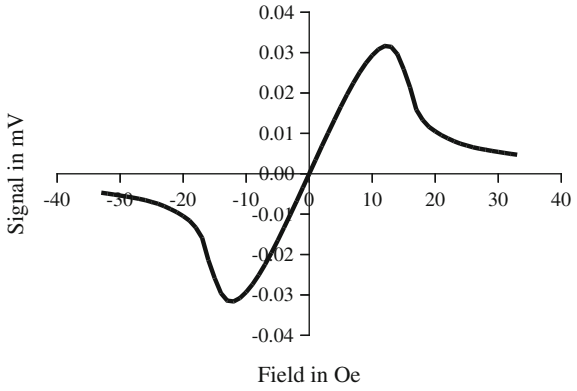

Fig. 19 Bridge response calculated for a 4 resistor array with no proximity effect. The proximity effect will increase the sensitivity of the sensor by as much as a factor of 5

saturating field behaves similar to a non-barber pole sensor except that the phase is shifted by forty-five degrees.

Figure 19 shows a bridge response calculated from a 4 resistor Wheatstone bridge with no proximity effect. The proximity effect will be shown in the next section. The source resistor data comes from the resistor in Fig. 18. The proximity effect will increase the sensitivity of the sensor by as much as a factor of 5. The advantage of a barber-pole magnetometer is that you get a very sensitive resistor along with high linearity and good directional sense. Unfortunately these sensors need either a magnet to support a consistent magnetization direction or some form of set-reset circuitry and corresponding structures.

2.6 Proximity Effect

The proximity effect, in AMR sensors, is unique in sensing. Anisotropic magetoresistors change sensitivity when placed in close proximity of each other, which is quite unlike any other sensors. Two pressure sensors next to each other do not change their sensitivity, two flow sensing elements cannot either. This effect is caused by the coupling of each sensing element magnetically. A good demonstration of this effect can be visually demonstrated by using inexpensive compasses and placing them in close proximity of each other. Each compass starts effecting the previous compass till all the compasses have more effect on each other then the Earth's magnetic field has on the compasses. Figure 20 is a schematic of a resistor array used to demonstrate the effect of proximity.

So in the sensor element, as the space between each element get closer, the effective transverse sensitivity increases. The proximity effect has been modeled by B.B. Pant [20] and is as follows,

$$\alpha(r) = 2 \cdot \left(\frac{r}{(1+2 \cdot r)}\right) + \left(\frac{r}{(2 \cdot (1+r)^2)}\right) \cdot \left(\frac{\pi^2}{2} - 4\right) \tag{10}$$

where $\alpha(r)$ is the geometric correction factor based on the distance r that is the resistor separation distance. This factor is then used as a correction factor for the demagnetization factor,

$$G(r, t, w) = \frac{t}{w} \cdot \alpha(r) \tag{11}$$

The demagnetization factor $G(r, t, w)$ is now a function of the gap $(\alpha(r))$, the thickness t, and the resistor width w. Table 2 shows how a this factor can be used to find equivalent thickness, width, and gaps for designing in proximity. These values are quite reasonable. Figure 21 demonstrates the demagnetization factor $G(r, t, w)$ by holding the gap to 6 μm and varying the resistor width from 12 to 35 μm. These results show a significant sensitivity difference between the elements. The sensitivity is usually represented by

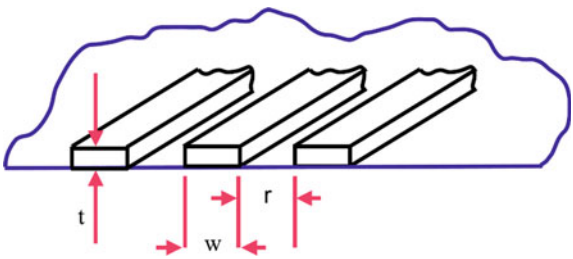

Fig. 20 Multiple resistor strip model for proximity effects

Table 2 Geometric correction factors for 2 different bridge designs

	Gap μm	α (r)	t (μm)	w (μm)	G (r, t, w)
r1	6	0.9803	0.035	20	0.00170
r2	3	0.9448	0.020	11	0.00172

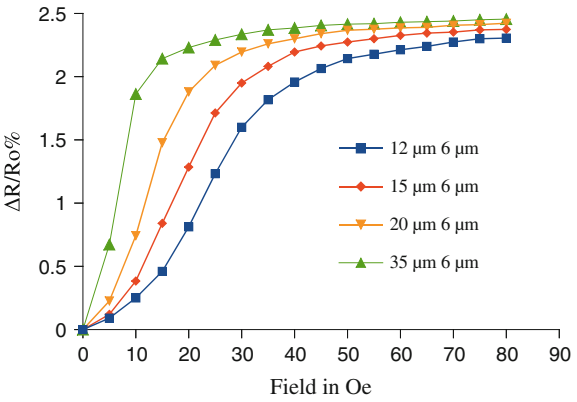

Fig. 21 The demagnetization factor $G(r, t, w)$ effect demonstrated by holding the gap to 6 μm and varying the resistor width from 12 to 35 μm

$$S = \frac{dR}{R_0 dB} \tag{12}$$

where R is the resistance at the starting point in the field range of interest, dR is the change in the resistance, and the dB is change in the magnetic flux. Unfortunately, proximity does not effect resistors being biased longitudinally, which does effect the usefulness of the proximity effect in 0°–90° Wheatstone bridge configured sensors. Narrow resistors as shown Figs. 10, 11, 12, 13 and 14 have reversal values much higher than the wider resistors therefore producing a much larger hysteresis loop, but a better low field sensor (less than 10 Oe). Wider resistors produce a much better medium field range sensor i.e. greater than 11 Oe but lower than saturation since the hysteresis is usually less than 10 Oe.

3 Noise Sources and Behavior

Noise sources and the behavior of permalloy thin films at dc to high frequency have been studied since these materials have been used for magnetic recording heads. There are multiple reasons for noise in AMR materials but the most common source is Barkhausen noise. Baldwin and Pickles [19] in 1971 experimented with thin permalloy films to determine what model that the Barkhausen noise behaves like. The term Barkhausen noise often refers to the erratic pops that are often heard in older sound systems which use soft-magnetic materials. In the analysis above, the

flux applied to the test samples were varied linearly over time. The conclusions for this was to determine that the Barkhausen noise in the materials analyzed were due to statistical fluctuations. For an exponential distribution function i.e. the power spectrum G_p the concept that was put forward to analyze the effect with a breakable spring model,

$$f(z, z_0) = kz0 \leqslant z \leqslant z_0 \tag{13}$$

$$f(z, z_0) = 0z \leqslant 0,\ z \geq \quad z_0 \tag{14}$$

and the exponential distribution function,

$$z_0 n(z_0) = N \exp(-z_0/Z) \tag{15}$$

then by integrating,

$$\begin{aligned} G_p(b) = (1/A_u) \int_{\infty}^{0} dz_0 n(z_0) \left[\int_{L_p} \exp(-jpz) f(z, z_0) dz \right]^2 \\ - \left[\int_{L_p} dz \int_{0}^{\infty} dz_0 n(z_0) f(z, z_0) \right]^2 \delta(p) \end{aligned} \tag{16}$$

we get

$$\frac{G_p(p)}{P_c^2} = \frac{4}{NA_u} \frac{1}{(pZ)^{-1}} \left(\left((pZ)^2 \frac{(pZ)^2 - 1}{(pZ)^2 + 1} \right) + \ln[(pZ)^2 + 1] \right) + \delta(p) \tag{17}$$

and the coercive pressure is,

$$P_c = \frac{1}{2} NkZ^2 \tag{18}$$

N and Z are density and length parameters, L_e is the length of the wall travel perpendicular to the wall, z_0 is the defect range, A_u is the are of the domain wall p is the spatial frequency.

Shape anisotropy and defects have an effect on higher frequency behavior, this was demonstrated by Grimes et al. [21]. They experimented on thin permalloy films by patterning repeated arrays of holes in the film. This showed that a variation of thicknesses and hole patterning created compensating demagnetization factors. Another form of error is hysteresis caused by the formation and annihilation of edge walls in the sensor elements. This was demonstrated by Mattheis et al. [22] by using high fields perpendicular to the resistor. The edge walls were observed using Kerr microscopy. Additionally, the pinning mechanism at the edge walls was observed

by seeing cross-tie walls on thin permalloy films using scanning electron microscopy with polarization analysis was used to image the surface magnetic domain structure after exposure of the permalloy film to an ac field as shown by Lee et al. [5]. Recently, Zhang et al. [23] have demonstrated Y-factor noise measurements for sub-micron permalloy arrays. Their test setup was configured using co-planer waveguides and patterned permalloy. The noise figures were extracted from the following equation

$$F = \frac{N_a + kT_0G_s}{kT_0G_s} \tag{19}$$

where F is the noise figure, k is Boltzmann's constant, G_s is the system power gain, N_a is the added system noise, and T_0 is 290 K. The noise voltage density for the permalloy array will vary with bias voltage and will produce various ferromagnetic resonance peaks. The noise, from the measurements, is Johnson-Nyquest noise which comes from the real part of an RLCG model. The noise voltage density for this array approach is

$$V_N = 4NkT\Delta R \tag{20}$$

where N is the total number of array elements and $\Delta R + R$ is the output of the measurement system. The measurements in this analysis show even low noise voltage density for frequency measurements in the 2–10 GHz frequency range. This was less than 1 nV^2/Hz except at resonance where it was 2 nV^2/Hz at resonance which is quite low.

4 Fabrication Methods

Over the years, various physical deposition methods have been used as techniques to create sensing films. These methods include e-beam evaporation, filament evaporation, ion beam deposition and sputter deposition. The sputter deposition methods include DC (Direct Current), DC-magnetron, RF (radio-Frequency), and RF magnetron plasma deposition. The most effective method used to manufacture the AMR sensors is a combination of radio frequency magnetron plasma deposition and strong enough magnets to bias the film during deposition. This allows the film to be deposited incorporating the minimum in trapped gases since the plasma can run in a pressure as low as 1 mTorr. Plasma deposited films will trap gasses as shown in van Hattum et al. [24] who shows that the argon incorporation can be as high as four percent in the film. Early deposition experiments using rf-plasma showed that this gas incorporation can create delaminations of the film. The stresses from these trapped gases can effect the maximum magnetoresistive change and stability of the sensor. Another important variable to control during the deposition phase is the system base pressure. Base pressure in the 10^{-8} Torr range will

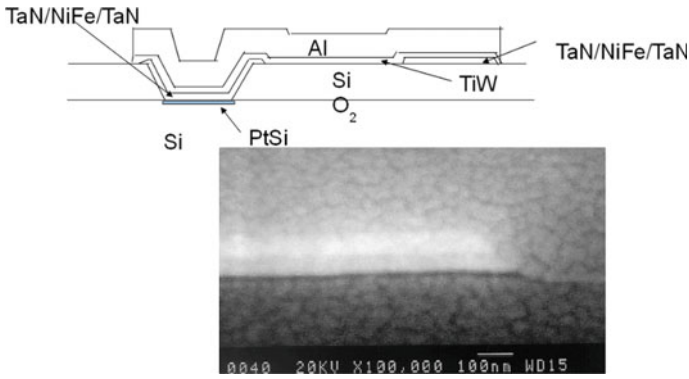

Fig. 22 Monolithic AMR sensor element. The total element is around 1500 nm thick. *From the Author*

minimize oxygen incorporation in the film. When creating a sensor film it is important to protect the permalloy (AMR sensor film) as much as possible from oxidation. Iron and nickel oxides will reduce the range of the sensor and create a much higher H_c which will increase the stiffness of the film. Many process chemicals will attack the permalloy film if it is left unprotected. The relatively high iron contact makes the film rather sensitive to chlorine compounds. To prevent these problems from happening, many people use a thin protective coating of tantalum nitride. The film than can be handled like any other metallic film and patterned with photoresist without the worry of contamination. A dry etch is recommended at this point since the protective films are usually wet etch resistant and most wet permalloy etches are inconsistent at best. The most common way of etching permalloy is to use an neutral beam ion-mill [15]. Figure 22 shows a schematic of a scanning electron microscope image of an AMR sensor element on a monolithic device. The sensing film, TaN/NiFe/TaN, is deposited on an integrated circuit with the semiconductor contacts open. The film is then coated with positive acting photoresist and exposed through a patterned photomask. All areas with semiconductor contacts are covered with resist and also the pattern for the sensor is covered with the resist.

After the ion-milling process and after the photoresist is removed, every contact will be covered with a residual stack of material. The advantage of this is that this residual material acts as an electromigration barrier for the contact also. The TiW/Al wiring layer is deposited on the surface and pattered and then the entire wafer is coated with silicon nitride. To reduce process stresses, the assembly is annealed in forming gas for at least 30 min at temperatures greater than 400 °C. This step will lower the resistance of the permalloy and maximize the magnetoresistance. To analyze the effects of the thickness on crystallography, several different samples were sent to Argonne National Labs advanced photon source. The results show that as the NiFe thickness increases the face centered cubic [111] becomes enhanced [25]. This enhancement can explain the change in film behavior in films less than 10 nm in thickness.

5 Using a Magnetometer to Calibrate a 3 Axis Helmholtz System

To demonstrate the one application of an AMR magnetometer, a 3 axis Helmholtz low field system was chosen. To evaluate a sensor design the magnitude and direction of the generated magnetic fields must be known or easily determined. Since the magnetometers to be tested are capable of measuring the surrounding magnetic fields along the x, y, and z axes, the system must be able to generate magnetic fields in these three directions simultaneously. These design requirements are fulfilled by the proposed arrangement of three pairs of Helmholtz Coils placed along the three orthogonal directions. A pair of Helmholtz Coils is separated by the value of their shared radius. However, when there are three sets of coils all with the same coil radius and separated by that same coil radius along the x, y, and z directions, an intersection would need to occur between these coils. Therefore, in the system ultimately derived and laid out below, the three pairs are separated by their diameter. This structure will be referred to as a modified Helmholtz Coil system. The proposed arrangement of three pairs of Helmholtz Coils placed will be placed along the three orthogonal directions. A pair of Helmholtz Coils is separated by the value of their shared radius. The Biot-Savart Law for calculating the magnetic field at a point along the axis of a loop of wire is shown in Eq. (21):

$$B = \frac{\mu_0 I R^2}{2\left(R^2 + a^2\right)^{3/2}} \tag{21}$$

defined by two coils placed in series. These two coils have the same radius and current magnitude/direction and are represented by this equation, μ_0 is the magnetic permeability of free space, I is the coil current, R is the radius of the coil, and a is the distance between the coil and the point at which the measurement is taken, which can be anywhere along the coil axis. From this equation, an equation can be derived to calculate the magnetic field for a pair of coils, Helmholtz coils. This is Eq. (22):

$$B = \frac{\mu_0 (NIR^2)}{2\left(R^2 + (R/2)^2\right)^{3/2}} \tag{22}$$

Here the total current, I, is calculated from the current supplied to a coil and the number of turns of wire for a coil, N. The coils are separated by a distance equal to the radius of the coils, R. The point at which the measurement is taken, a is half of the radius, $R/2$. The two coils are in series with the same current direction so that the magnetic fields generated by the two are additive. Each coil is the same with respect to all the quantities of interest, the entire equation describing one coil can be multiplied by two. Simplifying Eq. (3), results in Eq. (4):

$$B = (4/5)^{3/2} \frac{\mu_0 NI}{R} \tag{23}$$

Equation (21) can be used to calculate the magnetic field obtained from a pair of true Helmholtz Coils—where the coils are separated by their shared radius. However, to account for the fact that each pair of coils will instead be separated by their diameter rather than their radius for the reasons discussed above, Eq. (24) is derived from Eq. (21) where a now represents half the diameter of the coils or the radius, R.

$$B = \frac{\mu_0 (NIR^2)}{2(R^2 + R^2)^{3/2}} \tag{24}$$

Simplifying this equation results in Eq. (25):

$$B = (1/2)^{3/2} \frac{\mu_0 NI}{R} \tag{25}$$

Equation (25) is the equation that ultimately describes each pair of coils in one direction for the coil system designed within this thesis. The magnetic field generated by each pair of coils along their shared axis can be determined when the number of turns, current, and radius are specified. Alternately, this equation can be rearranged to solve for a different unknown; for example, it will be useful to solve for the number of turns of wire needed to achieve a desired magnetic field value. It can be seen that the numerical constant in Eq. (25), describing what will be referred to as the modified pair of Helmholtz Coils, is smaller than the constant that appears in Eq. (23), which describes the true pair of Helmholtz Coils. This is to be expected, as separating the coils by a larger distance and measuring the magnetic field at a further point from the two sources generating the field should reduce the measured field. The result of this solution will require a greater number of wire turns for a given current. Also an increase supplied current to generate a given field value in the modified coil system could be used, more than would be required by the true Helmholtz Coil system. The consequence of this fact will require a greater number of wire turns or more current supplied to generate a given field value in the modified coil system than would be required by the true Helmholtz Coil system. There are many calibration techniques that have been developed for magnetometers utilizing different methods. An example of a physical method is the swinging compass procedure, which has long found use in sea navigation. This process requires that the magnetic field values be recorded using the ship's compass for the eight cardinal directions and these values are then compared with reference values to obtain the offset in measurements [26]. Generally, this method is two-dimensional and not very precise and so will not be suitable when working with a three-axis magnetometer in this application. For compensating the external hard and soft error sources, which once again take the form of an ellipsoid shape rather than sphere that is offset from the origin, numerical methods using matrices

are commonly employed and are considered to be the simpler and less accurate linear approach. In this approach, it is sought to do away with this mathematical approach in compensating for these errors. Helmholtz coils have found use in compensating the internal biasing errors of magnetometers. With regards to the tri-axis design, existing designs tend to attempt to hold true to the requirement that the separation between the coils be their shared radius, which again requires that the design allow for the intersection and overlap of coils, making the realization of the actual system more complex [27]. Here, the design to be explored keeps the coil system design simple to realize by separating the coils by their diameter instead.

Once it was determined that the test system for the magnetometers would be of a modified Helmholtz design for all three axes, the specifics of the design were laid out. Originally, the limiting factors of the design were to be that a total magnetic field capable of being generated by the system was to be about 6 G—as that was the limit of the range of one of the magnetometers to be tested with the system. In addition, the current was originally limited to 5A and was therefore the value used in the initial calculations. The reason for this was to plan for the event in which there would be difficulties in obtaining six power supplies with a higher current rating. The physical coil system was to be assembled using six aluminum bicycle rims with a diameter of 16.5 in. (radius of 8.25 in.), each wrapped with 16 gauge insulated copper wire. Before continuing, vector relationship equations must be employed to determine the required magnetic field that must be generated for each of the three axes, such that the resultant magnetic field vector has a magnitude of roughly 6 G through the center of the system. A magnetic field vector of 3 G along each of the x, y, and z axes will give a resultant vector magnitude of 5.20 G through the center of the system.

Now, if Eq. (25) is employed and rearranged to solve for N, the number of windings of copper wire needed for each of the bicycle rims can be estimated given the requirement that for each pair, about 3 G of magnetic field be generated when 5A of current is supplied to each pair. This equation predicts that roughly 28 windings are necessary for each of the six bicycle rim coils.

In order to better visualize the magnetic fields predicted to be generated by the entire tri-axis coil system, the software package COMSOL was used to simulate the coil system design using the Magnetic Fields package. From within the COMSOL model, the six aluminum rims, the current to be supplied to the coils, the number of wrappings of copper wire, etc. could all be specified. The final simulation results are shown in Fig. 23 which shows an individual slice of the three dimensional simulation. Figure 24 shows the complete three dimensional model results. Similar to the calculated scenario, this simulation specified an 8.25 in. radius for the coils, a current of 5A supplied to each pair of coils and 28 wrappings for each of the coils. It can be seen that at the very center of the assembly about 5.5 G is the predicted value of the magnetic field according to the color legend. This does compare very closely with the vector magnitude of 5.20 G and direction through the center of the system that was calculated above.

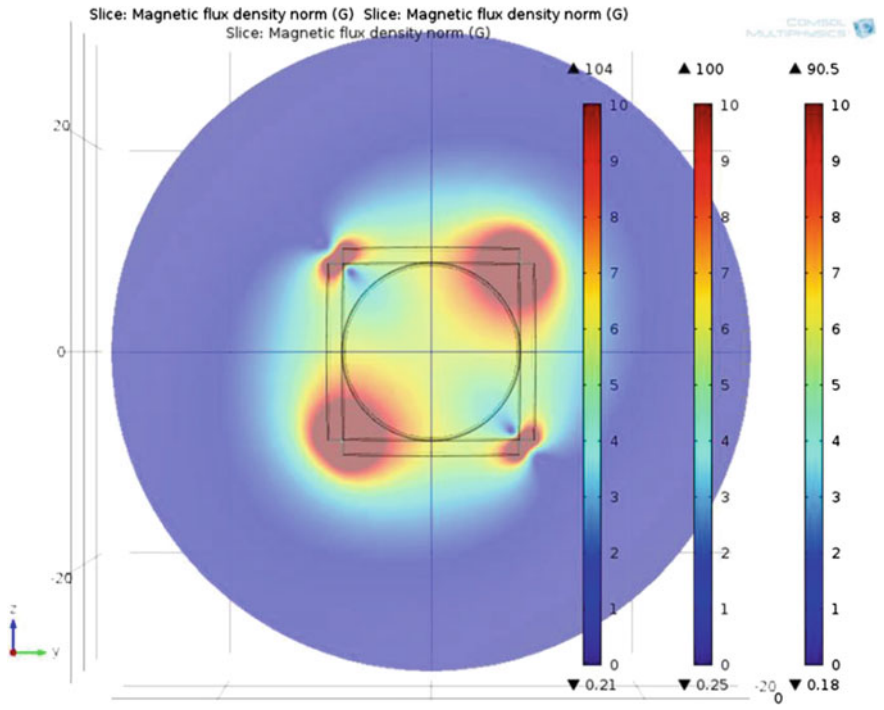

Fig. 23 One-dimension of the Comsol model of the three-axis Helmholtz coil test system

It should be noted that for this modified Helmholtz Coil design, the COMSOL model shows that the fields within the system are not as uniform as what would be expected from the true Helmholtz Coil design.

It can be seen in Fig. 23 that there are various "hot spots" near adjacent coils that create an overall less than uniform pattern of the magnetic field in the system. Regardless, the center point of the system, where the magnetometer will be placed, shows a "sweet spot" for the field which Eq. (6) can predict fairly accurately. Using the results of the COMSOL simulation, the six bicycle rims were hand wrapped with 28 turns of the copper wire with the goal of achieving the roughly 6 G of magnetic field at center of the physical assembly. Figure 25 shows the actual physical assembly of the coil system. The base of the assembly seen in this figure is also constructed of aluminum, chosen like the bicycle rims for its non-magnetic properties and hence, not a source of magnetic distortion to the system. Finally, the rod extending to the center of the system from a three axis manipulator located to the left of the system is also aluminum and this is where the magnetometer will be placed. Each coil was wrapped twice, with 28 turns going in the clockwise (CW) direction and another 28 turns counterclockwise (CCW) (Fig. 25).

For the three pairs of coils for the x, y, and z direction, each wrapped in the clockwise and counterclockwise direction, a total of six power supplies were

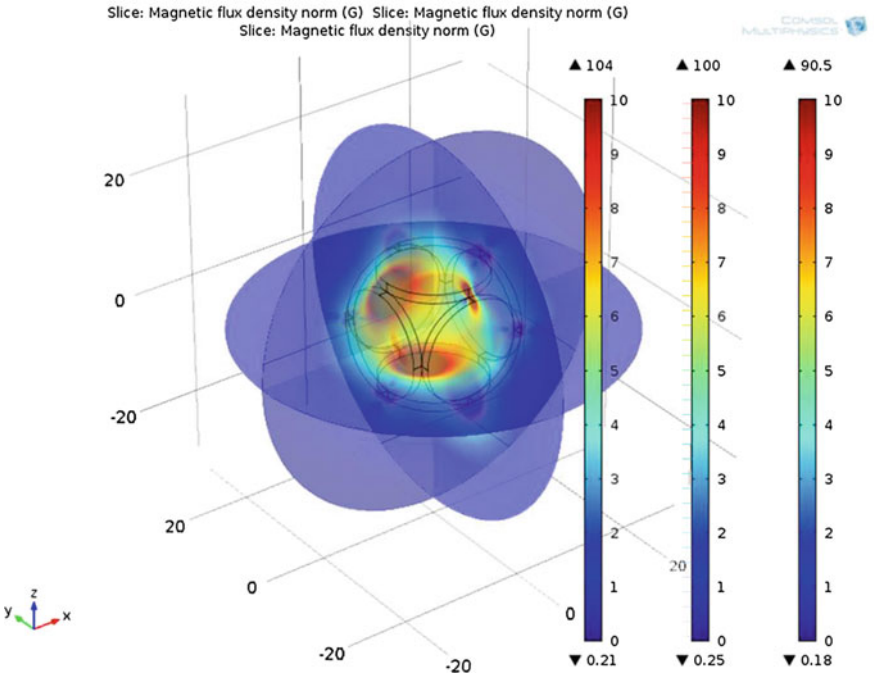

Fig. 24 Full three dimensional model of the three-axis Helmholtz test system

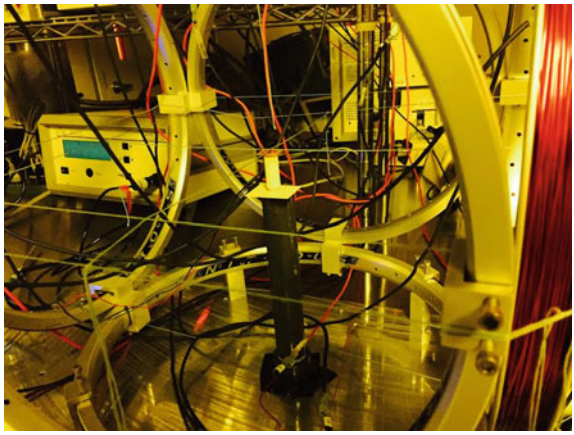

Fig. 25 Modified 3-axes Helmholtz Coil design. The strings were used to help square the sensor in the test area

needed for the assembly. This setup is useful in the absence of switching power supplies, because to otherwise switch the direction of the current, the leads would have to manually be switched between the CW and CCW sets of wrappings and checked each time for accuracy. Also, with two directions of wrappings, there exists the possibility of running both sets of coils at the same time with different currents

supplied to the two sets, if an offset value of magnetic field needs to be generated by the second set to adjust the overall magnetic field for the system. Two Honeywell chips, the HMC5843 and HMC5883L were considered for use in testing the coil system. The HMC5843 chips were already available for use and provided the opportunity to construct a hybrid circuit, while the HMC5883L breakout boards were purchased fully assembled. These two chips were very similar in design and operation. The HMC5883L was designed to be the successor to the HMC5843 and boasted a few improvements, including a smaller size, less connections, the ability to measure a larger range of fields, etc.

The HMC5843 chip was explored first. The chip itself has dimensions of 4 mm x 4 mm × 1 mm with 20 pads, each with a width of 0.25 mm (about 10 mils) and spacing between the pads of 0.25 mm. Using AutoCAD, a layout for the design of a hybrid circuit was constructed. The design was simple, requiring only that there be conducting traces from the chip pad to larger printed pads at the edges of the alumina substrate for the purposes of making external connections to the chip. An additional AutoCAD layer was specified for printing a dielectric layer onto the substrate to function as a solder dam to prevent leeching of solder applied to the conducting pads out to the traces. Figure 26 shows the completed hybrid circuit with the HMC5843 chip soldered to the printed circuit and wired to the connector. Wires soldered to the magnetometer were then fed outside of the coil system an Arduino Nano placed at the base of manipulator. The magnetometer is a slave device with a unique hardware address and must be connected to a master that can supply the power, clock, collect the data, etc. The Arduino was then connected by way of an USB to a computer which ultimately supplied the power to the Arduino. It also ran the Arduino IDE with code uploaded to the Nano that collected the magnetic fields data along the x, y, and z axes and calculated the overall vector magnitude and angles. The results of testing the physical coil assembly and magnetometer with the Arduino code when 5A of current was supplied to each of the three pairs of coils. It can be seen that the x and y axis values are in agreement with

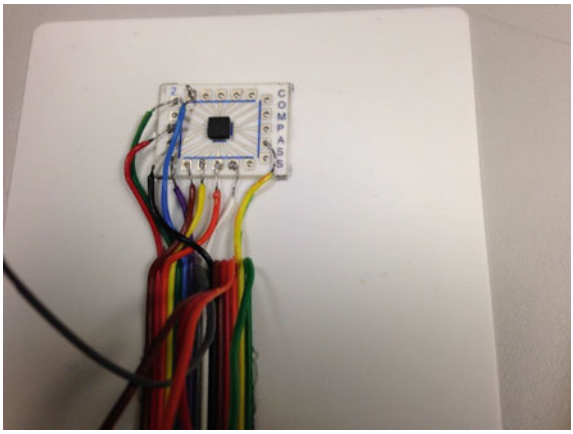

Fig. 26 HMC5843 hybrid circuit with external connections

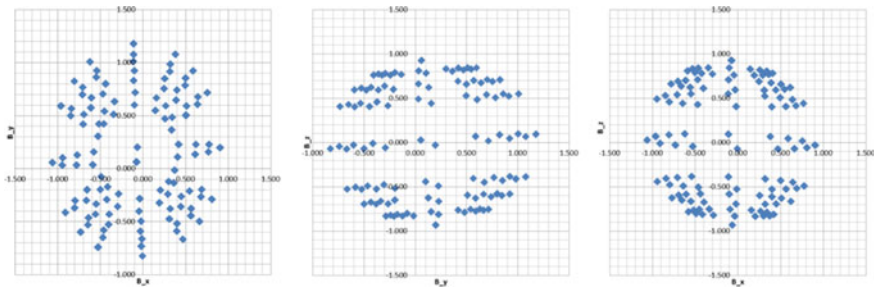

Fig. 27 Plot of the corrected output of the HMC5883L magnetometer in x-z, y-z, and x-y with various offset currents to compensate the Earth's field. Centered, spherical magnetic field data with an offset current applied in the z coil set

Eq. (25), which once again, predicts 3 G of field under these conditions. The discrepancy is mainly with the z axis measurement, as it showed the greatest variation from 3 G, with roughly 2 G of magnetic field. And, it was this measurement that reduced the magnitude of the resultant field to 4.748 G. Recall that the mathematical prediction was 5.20 G while the COMSOL model predicted 5.5 G. The fact that the experimental model resulted in a total magnetic field value significantly different from both the COMSOL model and the mathematical calculations would be expected, as the latter two are considered more ideal or simplistic than the real world situation in which the experimental model operates. Real world conditions include the presence of Earth's magnetic field along with many other potential sources of stray magnetic fields—the surrounding power supplies, computers, etc. in the lab are just a few examples.

The following graphs show the results of using the HMC5883L chip to find sources of magnetic field distortion (Fig. 27).

6 Commercial Devices

Commercial sensing opportunities for AMR magnetometers are broken into two basic areas. The first of these is for feedback for process control systems and the second use generally for safety equipment. Automotive sensors are usually used for engine control as well as safety equipment. The feedback control applications are often position sensing and can be very similar to automotive applications, but many are static position devices. These static position devices often set the range of motion for robotic and automatic equipment. A common commercial device is the meander sensor. Meander sensors can be used to measure anything from ring-magnets to high-current fields generated by power lines.

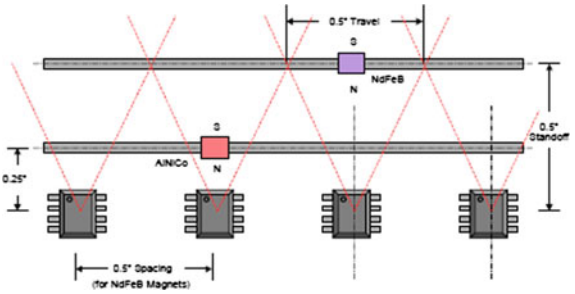

Fig. 28 Honeywell's HMC1501 array. The outputs can be compared to determine position of the sliding magnets, from Honeywell Application Notes [28]

6.1 Discrete Devices

Common uses for the discrete AMR devices often are low field applications. The low field applications are mostly compass applications but some applications like linear position sensors may use an array of discrete sensors. An example of an array of position sensors is shown in Fig. 28.

This arrangement of sensors can be used with either multi-channel analog to digital converters and computer algorithms or can be used with a series of amplifiers and comparators an a purely analog circuit.

6.2 Automotive Applications (Monolithic IC)

In the early 1970s a small group of engineers began a revolution in automotive sensing using magnetic sensors. These individuals perceived that magnetic sensing could replace the mechanical points in the automotive ignition system. By that time optical ignition systems had been used in automotive racing, but these systems proved unreliable in field testing due to their tendency to perform poorly in less than ideal conditions. A team at Honeywell's MicroSwitch Division saw that the Hall Effect sensor along with a vane could replace the cam and points in an automotive ignition system. This team installed this first solid state vane switch in a 1960s Ford Mustang and drove into the future. This first introduction of a point-free magnetic sensor based ignition system open the door to computerized automotive control systems. These developments allowed the automotive manufacturers to reduce emissions of primary pollutants. Modern engine control systems now monitor intake air, crank position, cam position, and exhaust gases. In the early 1990s, automotive manufacturers were looking to meet more stringent emissions criteria. The criteria were essentially no misfire during start-up, and no fuel tank vapor leaks. To improve the quality of the signal and to simplify the control system by removing unneeded components the spark distributor was replaced by the gear-tooth sensor. It was in this environment that the first automotive grade anisotropic magnetoresistive sensor [29, 30] was introduced. This sensor is a

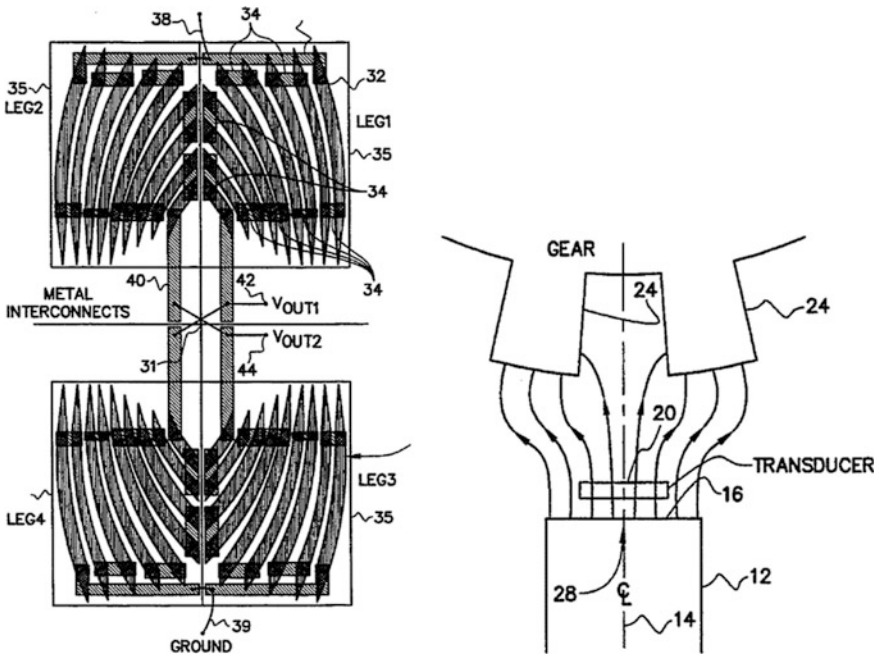

Fig. 29 First automotive grade gear tooth AMR sensor element. This sensor element in combination with the process patent created a monolithic sensor that could withstand 185 °C ambient [29, 30]

monolithic sensor—monolithic means that the sensor and the circuitry exists on the same chip and is shown in Fig. 29. Previous AMR monolithic sensors (high current sensors) produced by the Honeywell team were limited by process technology to 85 °C, these sensors have now been replaced by newer technology. Previous AMR monolithic sensors (high current sensors) produced by the Honeywell team were limited by process technology to 85 °C, these sensors have now been replaced by newer technology. The Hall Effect sensor, which is still used by the majority of automotive platforms, requires that the direction of the field be oriented out of plane. The Hall Effect sensor is mounted in such a way that the sensor is essentially sitting on top of the magnet and the gear tooth sensor passes just short of the sensor surface. Figure 30 shows an automotive crankshaft with target from the early 1990s. The problem with this sensor configuration is that the gap spacing is the distance between the surface of the Hall sEffect sensor and the magnetic target and is dependent on the over-molding, fit and engine wear. The form of the waveform coming off of the gear-tooth is roughly sinusoidal with an dc offset. When a Hall Effect sensor is placed close to a gear-tooth it produces a high dc offset and a high amplitude waveform. As the spacing opens up, the offset reduces and the peak-to-peak values reduce significantly. To maximize the sensors usefulness, the Hall Effect sensor electronics require a partial rotation of the gear-tooth target to

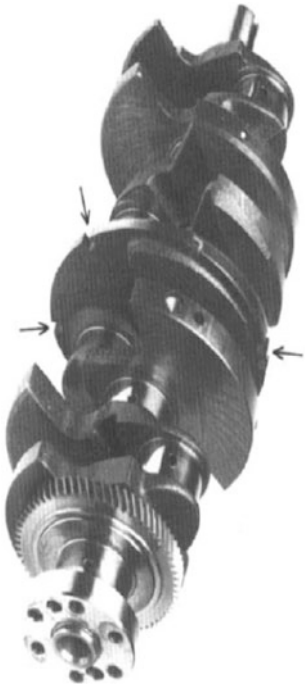

Fig. 30 Early 1990s crankshaft with target. The *arrows* show the target [31]

calibrate the sensor. This causes excess unburned hydrocarbons to be released in the atmosphere during start-up.

On the other hand, the Anisotropic MagnetoResistor (AMR) sensor depends on the in-plane magnetic fields. The AMR sensor is sensitive to the ratio of the in-plane fields which can be quite consistent over several millimeters. This consistency and high signal to noise ratio makes the AMR sensor quite desirable for start-up conditions. Unlike the Hall Effect sensor, the circuitry used for the AMR sensor can be relatively simple temperature compensated dc operational amplifier (Hall Effect sensors can also be dc but the gap spacing is significantly smaller, as much as 25–50 %). The AMR sensor can be near zero-speed at start-up, which means that the sensor can detect the first gear-tooth transition. The AMR sensor can be used with an encoded target rather than a gear-tooth target. The encoded target can be found in U.S. Manufactured vehicles built by General Motors after 1997 (C5 Corvette). Other automotive applications in which AMR sensors can be used are as follows, wheel-speed, gear-shift, automatic transmission sensing, and compass applications. In the early days of AMR automotive sensing, there was a concern for stray fields effecting the AMR sensors. This was allayed by a group of Honeywell design engineers who surveyed all the possible sources of stray fields in the greater Chicago area.

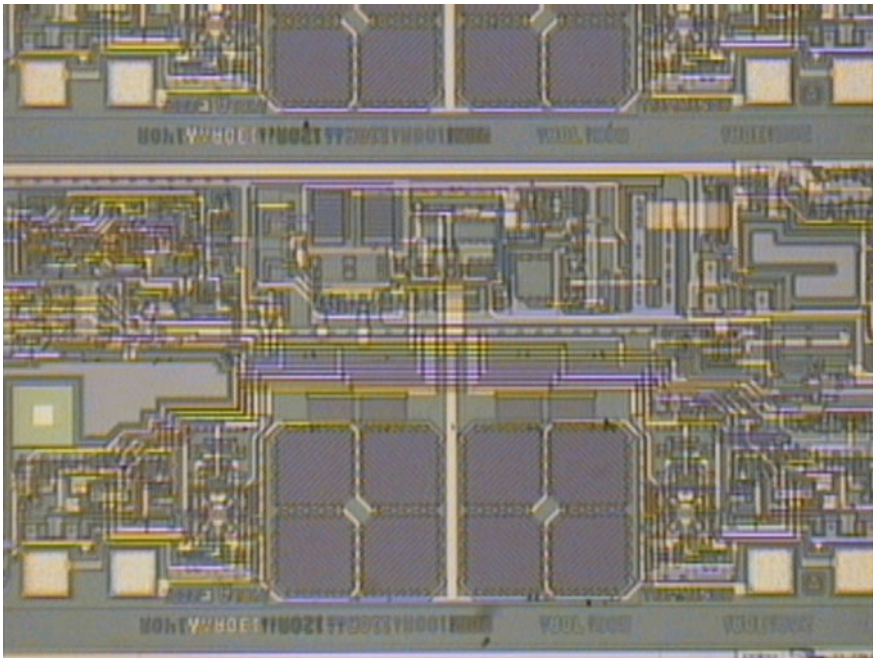

Fig. 31 Prototype speed and direction sensor manufactured by Honeywell's MicroSwitch Division in the early 2000s. The monolithic device is made from ion-milled permalloy and double level metal. The sensors are ±45° meander sensors. The logic family is I2L. *Photo care of Author*

The stray fields were discovered to be much less than the fields needed to cause a significant error in the sensor. Figure 31 shows a prototype permalloy speed [32] and direction sensor built by Honeywell's Microswitch Division. This device has two separate permalloy sensors spaced far enough apart to create a phase shift. This phase shift along with simple digital logic allows the device to detect direction along with rotational speed for a ring magnet. The application envisioned for this device was an anti-lock brake sensor that could a car from rolling backwards on a steep hill.

7 Advances in AMR Magnetometry

The bulk of work in AMR magnetometry over the last 15 years has focused on improving modeling of AMR sensors. A significant amount of work has been performed to analyze permalloy nanowires and nanodots. Recent work by Corte-León et al. [33] looks at the effect of pinning at the corners of 150 nm structures. They noted that even these nanostructures magnetic response is still dominated by the AMR effect while they were studying how to determine the best

way to analyze magnetization reversal. The effect of aspect ratio is studied by Singh and Mandel [34] along with temperature effects. Spin-waves in permalloy nanostructures are studied by Nguyen et al. [35] using high frequency measurement techniques with good correlation of theory for experimental. Many new papers are studying these physical properties of nanowires, but this has not been translated to the area practical magnetometry. Most modern advances in AMR magnetometry has been in the commercial sphere and can be found during cursory searches on patent agencies. A recent advancement on the planer hall device was filed with the U.S. Patent and Trademark Office by Klien et al. [36] and a modification of the dual track automotive sensor was filed by Pant and Lakshman [37]. Significant work still needs to be done in trying to characterize the three dimensional tensor that represents the magnetoresistor also connecting that to the basic mechanisms. Nanoscale work is showing that even though the resistors are getting smaller, the AMR effect may exist at a very fundamental level.

Acknowledgments The Authors would like to thank the many fine engineers, technicians and production operators at Honeywell's Sensor Fab in Richardson, Texas for helping collect reams of data on the behavior of permalloy from 1994 to 2002. We would also like to thank Misty Haji-Sheikh for patiently editing this work. Additionally, like the lead author, many of the people have moved on to other careers such Bob Biard (Honeywell Retired), Wayne Kilian, Ron Foster, and John Schwartz (Honeywell Retired), but all have had a part in this work in some way or another.

References

1. W. Thompson, On the electro-dynamic qualities of metal: effects of magnetization on the electric conductivity of nickel and of iron. Proceedings of the Royal Society of London, vol. 8, (1897), pp. 546–550
2. T.R. McGuire, R.I. Potter, Anisotropic magnetization in ferromagnetic 3d alloys. IEEE Trans. Magn. **MAG-11**(4), 1018–1037 (1975)
3. L.I. Maissel, R. Glang, *Handbook of Thin Film Technology* (McGraw-Hill Handbooks, New York City, 1970)
4. B.B. Pant. Magnetoresistive sensors. Sci. Honeyweller **8**(1), 29–34 (1987)
5. Y. Lee, A.R. Koymen, M.J. Haji-Sheikh, Discovery of cross-tie walls at saw-tooth magnetic domain boundaries in permalloy films. Appl. Phys. Lett. **72**(7), 851–852 (1998)
6. A. García-Arribas, E. Fernández, A.V. Svalov, G.V. Kurlyandskaya, A. Barrainkua, D. Navas, J.M. Barandiaran, Tailoring the magnetic anisotropy of thin film permalloy microstrips by combined shape and induced anisotropies. Euro. Phys. J. B **86**(4), 136 (2013)
7. J.P. Heremans, Magnetic field sensors for magnetic position sensing in automotive applications (invited review). Mat. Res. Soc. Symp. Proc. **1**, 63–74 (1997)
8. S. Tumanski, *Thin Film Magnetoresistive Sensors* (IOP, Bristol, U.K., 2001)
9. E.H. Hall, On a new action of the magnet on electric currents. Am. J. Math. **2**(3), 287–292 (1879)
10. R.R. Birss, *Symmetry and Magnetism* (North Holland, Amsterdam, The Netherlands, 1964)
11. E.C. Stoner, E.P. Wohlfarth, A mechanism of magnetic hysteresis in heterogeneous alloys. Philos. Trans. R. Soc. A: Phys. Math. Eng. Sci. **240**(826), 599–642 (1948)
12. D.A. Thompson, L.T. Romankiew, A.F. Mayadas, Thin film resistors in memory, storage and related applications. IEEE Trans. Magn. **MAG-11**(4), 1039–1050 (1975)

13. C.P. Batterel, M. Galinier, Optimization of the planer hall effect in ferromagnetic thin films for device design. IEEE Trans. Magn. **MAG-5**(1), 18–28 (1969)
14. C.-R. Chang, A hysteresis model for planar hall effect in the films. IEEE Trans. Magn. **36**(4), 1214–1217 (2000)
15. M.J. Haji-Sheikh, G. Morales, B. Altuncevahir, A.R. Koymen, Anisotropic magnetoresistive model for saturated sensor elements. Sens. J. IEEE **5**(6), 1258–1263
16. J.F. Nye, *Physical Properties of Crystals: Their Representation by Tensors and Matrices* (Oxford University Press, Oxford, 1985)
17. S. Chikazumi, S.H. Charap, *Physics of Magnetism* (Krieger Pub Co, Malabar, 1978)
18. T. Tanaka, K. Yazawa, H. Masuya, Structure, magnetization reversal, and magnetic anisotropy of evaporated cobalt films with high coercivity. IEEE Trans. Magn. **MAG-21**(5), 2090–2096 (1985)
19. J.A. Baldwin Jr., G.M. Pickles. Power spectrum of Barkhausen noise in simple materials. J. Appl. Phys. **43**(11), 4746–4749 (1972)
20. B.B. Pant, Effect of interstrip gap on the sensitivity of high sensitivity magnetoresistive transducer. J. Appl. Phys. **79**, 6123 (1996)
21. C.A. Grimes, P.L. Trouilloud, L. Chun, Switchable lossey/non-lossey permalloy thin films. IEEE Trans. Magn. **33**(5), 3996–3998 (1997)
22. R. Mathias, J. McCord, K. Ramstöck, D. Berkov, Formation and annihilation of edge walls in thin-film permalloy stripes. IEEE Trans. Magn. **33**(5), 3993–3995 (1997)
23. H. Zhang, C. Li, R. Divan, A. Hoffmann, P. Wang, Broadband mag-noise of patterned permalloy thin films. IEEE Trans. Magn. **46**(6), 2442–2445 (2010)
24. E.D. van Hattum, D.B. Boltje, A. Palmero, W.M. Arnoldbik, H. Rudolph, F.H.P.M. Habraken, On the argon and oxygen incorporation into SiOx through ion implantation during reactive plasma magnetron sputter deposition. Appl. Surf. Sci. **255**, 3079–3084 (2008)
25. S.C. Mukhopadhyay, Y.-M.R. Huang, *Sensors: Advancements in Modeling, Design Issues, Fabrication and Practical Applications*, 1st edn. (Springer, Berlin, 2008)
26. N. Bowditch, *The American Practical Navigator: An Epitome of Navigation* (National Imagery and Mapping Agency, Bethesda, 2002)
27. HCS1: Helmholtz Coil System. HCS1 product datasheet, Barrington Instruments
28. Honeywell's Application Notes, Applications of Magnetic Position Sensors
29. M.J. Haji-Sheikh, TaN/NiFe/TaN Anisotropic Magnetic Sensor Element. Patent Number 5,667,879, 16 Sept 1997
30. D.R. Krahn, Magnetoresistive proximity sensor. U.S. Patent 5,351,028 A
31. J. Heremans, Solid state magnetic field sensors and applications. J. Phys. D Appl. Phys. **26**, 1149–1168 (1993)
32. M. Haji-Sheikh, M. Plagens, R. Kryzanowski, Magnetoresistive speed and direction sensing method and apparatus. U. S. Patent Number 6,784,659
33. H. Corte-León, V. Nabaei, A. Manzin, J. Fletcher, P. Krzysteczko, H.W. Schumacher, O. Kazakova, Anisotropic magnetoresistance state space of permalloy nanowires with domain wall pinning geometry. Sci. Rep. **4**(6045) (2014) doi:10.1038/srep06045
34. A.K. Singh, K. Mandal, Effect of aspect ratio and temperature on magnetic properties of permalloy nanowires. J. Nanosci. Nanotechnol. **14**(7), 5036–5041 (2014)
35. T.M. Nguyen, M.G. Cottam, H.Y. Liu, Z.K. Wang, S.C. Ng, M.H. Kuok, D.J. Lockwood, K. Nielsch, U. Gösele, Spin waves in permalloy nanowires: the importance of easy-plane anisotropy. Phys. Rev. B **73**, 140402(R) (2006)
36. L. Klein, A. Grosz, M.O.R. Vladislav, E. Paperno, S. Amrusi, I. Faivinov, M. Schultz, O. Sinwani, High resolution planar hall effect sensors. Patent Application US 20140247043 A1
37. B.B. Pant, L. Withanawasam, Anisotropic magneto-resistance (amr) gradiometer/magnetometer to read a magnetic track. Patent Application US 20130334311 A1

Planar Hall Effect (PHE) Magnetometers

Vladislav Mor, Asaf Grosz and Lior Klein

Abstract The planar Hall effect (PHE) is intimately related to the anisotropic magnetoresistance (AMR). However, while AMR-based magnetic sensors have been commercially available for decades and are widely used in a variety of applications, PHE-based sensors have been mostly the subject of research. The reason for that is most probably the superior performance that has been exhibited by the AMR sensors. In this chapter, we review the work that has been done in the field of PHE sensors with emphasis on the PHE sensors developed by the authors. The performance of these sensors exceeds the performance of commercially available AMR-based sensors and has the potential of competing even with bulkier ultra-sensitive sensors such as flux-gate and atomic magnetometers. We review the physical origin of the effect, the use of shape to tailor the magnetic anisotropy on demand and the optimization process of the fabrication details of the sensor and its amplification circuit.

1 Physical Background

The interplay between spin polarized current and magnetic moments gives rise to many challenging and intriguing phenomena. The emergence of the field of spintronics [1, 2] highlighted phenomena encountered in heterostructures such as giant

V. Mor · L. Klein
Department of Physics, Nano-Magnetism Research Center, Institute of Nanotechnology and Advanced Materials, Bar-Ilan University, 52900 Ramat-Gan, Israel
e-mail: vladislav.mor@gmail.com

L. Klein
e-mail: Lior.Klein@biu.ac.il

A. Grosz (✉)
Department of Electrical and Computer Engineering, Ben-Gurion University of the Negev, P.O. Box 653, 84105 Beer-Sheva, Israel
e-mail: asaf.grosz@gmail.com

A. Grosz et al. (eds.), *High Sensitivity Magnetometers*, Smart Sensors, Measurement and Instrumentation 19, DOI 10.1007/978-3-319-34070-8_7

magnetoresistance, tunneling magnetoressitance, spin-torque, etc. Several additional important phenomena are encountered in a single compound, such as the dependence of the longitudinal resistivity ρ_{xx} and that of the transverse resistivity ρ_{xy} on the orientations of the current density J and the magnetization M. For polycrystalline magnetic conductors (including ferromagnetic *3d* alloys) the dependence is given by:

$$\rho_{xx} = \rho_{\perp} + \left(\rho_{\parallel} - \rho_{\perp}\right) \cos^2 \theta \tag{1}$$

$$\rho_{xy} = \frac{1}{2}\left(\rho_{\parallel} - \rho_{\perp}\right) \sin 2\theta \tag{2}$$

where $\rho_{\parallel}$ and $\rho_{\perp}$ are the resistivities for magnetization parallel and perpendicular to the current, respectively, and θ is the angle between J and M (see Fig. 1). The variation of ρ_{xx} is called the anisotropic magnetoresistance (AMR), while the variation of ρ_{xy} is called the planar Hall effect (PHE) [3, 4].

The AMR and PHE can be more complicated when the magnetic conductor is crystalline. In this case, in addition to the angle between J and M, the angles between each of the two vectors and the crystal axes may also be relevant, and the magnetotransport tensor ρ_{ij} is expressed as a function of the direction cosines, α_i, of the magnetization vector [5],

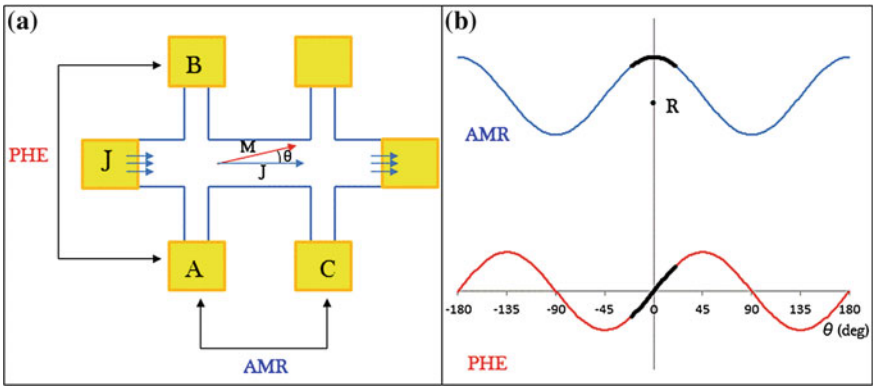

Fig. 1 **a** A sketch of a typical pattern used for measuring AMR and PHE. **b** The dependence of the longitudinal and transverse resistance on the angle θ between the current J and the magnetization M demonstrating AMR (*blue graph*) and PHE (*red graph*), respectively

$$\rho_{ij}(\alpha) = \sum_{k,l,m...=1}^{3} \left(\begin{array}{r} a_{ij} + a_{kij}\alpha_k + a_{klij}\alpha_k\alpha_l + a_{klmij}\alpha_k\alpha_l\alpha_m \\ + a_{klmnij}\alpha_k\alpha_l\alpha_m\alpha_n + \cdots \end{array} \right) \tag{3}$$

where *i, j = 1,2,3* and the *a*'s are expansion coefficients. As usual, $\rho_{ij}(\alpha) = \rho^s_{ij}(\alpha) + \rho^a_{ij}(\alpha)$ where, ρ^s_{ij} and ρ^a_{ij} are symmetric and antisymmetric tensors, respectively. As the AMR and PHE are symmetric, only the symmetric part of the tensor is used to extract the AMR and PHE equations to replace Eqs. (1) and (2).

Theoretical treatment of AMR and PHE in *3d* itinerant ferromagnets has been mainly done in the framework of two channel *sd*—scattering model. In this model, conduction (carried primarily by *s* electrons) is divided into spin-up and spin-down currents which flow in parallel and mix via a spin-orbit interaction which depends on the angle between the *k* vector of the conduction electron and the orientation of the magnetic moments.

The AMR of *3d* magnetic alloys is on the order of several percent and their room temperature resistivity is on the order of 50 μΩ cm . Therefore, typically the PHE amplitude given by $(\rho_{\parallel} - \rho_{\perp})$ is on the order of 1 μΩ cm. For films with thickness on the order of 100 nm, the actually measured ΔR is on the order of 0.1 Ω.

Much larger PHE amplitudes are obtained in GaAs(Mn) [6], manganites [7], and magnetites [8], and for this reason the PHE in these compounds is termed giant. The origin of the giant PHE is not high AMR ratio but much larger ρ_{xx}.

2 PHE Sensors

The dependence of the PHE signal on the angle between the magnetization direction in the magnetic conductor and the direction of the current that flows through it is used for magnetic field sensing. For such a use the magnetic conductor should have uniform magnetization, and the magnetization direction should change predictably, reversibly and without hysteresis in the presence of an applied magnetic field. To obtain such a behavior, the layer should have magnetic anisotropy, commonly with an easy axis parallel to the current direction. When these conditions are met, the PHE signal indicates the magnetization direction which indicates the magnitude of the applied magnetic field in the film plane, in a perpendicular direction to the current direction.

In comparison with AMR sensors, PHE sensors have several intrinsic advantages. The AMR as a function of the angle θ between the current and the magnetization has its largest slope at $\frac{\pi}{4} + \frac{n\pi}{2}$ whereas the PHE as a function of θ has its largest slope at $\frac{n\pi}{2}$. Since it is easier to fabricate sensors where in the absence of an applied magnetic field θ is equal to $\frac{n\pi}{2}$ PHE sensors are simpler and cheaper to manufacture.

Furthermore, the AMR signal is measured on top of a large dc component associated with the average resistance (see Fig. 1b). Therefore, temperature and aging drifts which affect the dc component are extremely detrimental to AMR sensors. To obtain an output voltage which reflects the AMR signal without the dc component, AMR sensors are commonly used in a Wheatstone bridge configuration of four AMR sensors. Such a design is not needed in PHE sensors whose dc component is zero (see Fig. 1b).

Different types of PHE sensors have been reported:

1. Sensors with a single ferromagnetic layer with magnetic anisotropy which is induced during growth by applying a magnetic field and by using an antiferromagnetic pinning layer.
2. Sensors with multi ferromagnetic layers separated by non-magnetic conductors. These sensors are commonly called spin valve PHE sensors.
3. Sensors that are called PHE Bridge (PHEB) sensors but in fact are AMR sensors in a common Wheatstone bridge configuration.
4. Sensors with a single ferromagnetic layer and shape induced magnetic anisotropy due to their elliptical shape. This is the type of sensors with the best reported magnetic field resolution and we will elaborate on the properties of these sensors in the following sections.

2.1 PHE Sensors with Field Induced Magnetic Anisotropy

Uniform and reversible response of a sensing ferromagnetic layer in a PHE sensor has been obtained by inducing uniaxial magnetic anisotropy during growth. A common structure of such sensors consists of a ferromagnetic $Ni_{80}Fe_{20}$ layer coupled to an antiferromagnetic IrMn layer. A field on the order of several hundreds of Oersteds induces magnetic anisotropy and aligns the pinning direction of the IrMn layer [9–12].

2.2 Spin-Valve PHE Sensors

PHE sensors that consist of at least two ferromagnetic layers separated by non-magnetic layers are commonly called PHE sensors with spin-valve structure (Fig. 2). This term refers to the fact that such magnetic multilayer structures are used to obtain a spin-valve effect; namely, that for a given voltage the current flow is high or low depending on the relative orientation of the magnetization in neighboring magnetic layers (parallel or anti-parallel). Following are spin valve structures that are used to fabricate PHE sensors.

A common structure used for spin-valve PHE sensors is $Ta/Ni_{80}Fe_{20}/Cu/Ni_{80}Fe_{20}/IrMn/Ta$ [13–28]. The structure is commonly deposited on silicon dioxide in dc magnetron sputtering system. The first Ta layer is a seed layer, the

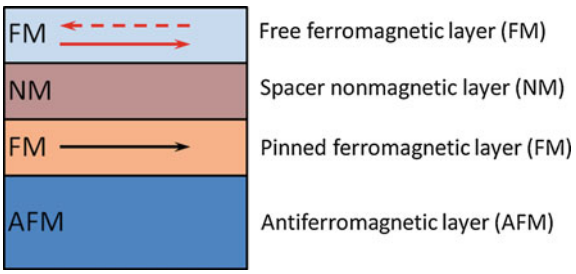

Fig. 2 A typical layer structure of a spin-valve PHE sensor

first $Ni_{80}Fe_{20}$ layer is the free magnetic layer, the Cu layer serves as the non-magnetic metallic spacer, the second $Ni_{80}Fe_{20}$ layer is the pinned ferromagnetic layer, the IrMn layer is an antiferromagnetic layers that pins the $Ni_{80}Fe_{20}$ layer below, and the second Ta layer is a capping layer.

The layers are commonly sputtered in a working pressure of several mTorr with a magnetic field on the order of several hundreds Oersted parallel to the film plane. The role of the field is to induce magnetic anisotropy in the ferromagnetic layers and define the exchange bias between the antiferromagnetic layer and the neighboring ferromagnetic layer. Typical thicknesses are: Ta—5 nm, free NiFe—4–20 nm, Cu—1–4 nm, pinned NiFe—1–12 nm, IrMn—10–20 nm.

A sensitivity of 15.6 mΩ/Oe was reported for a structure with free layer thickness of 20 nm and pinned layer thickness of 2 nm [29]. Other reports indicate sensitivity of less than 10 mΩ/Oe [16, 21, 24, 30]. Other spin valve structures include Co/Cu/Py [31–33], Co/Cu multilayers [34], NiFe/FeMn/NiFe [35], and Ta/NiFe/CoFe/Cu/CoFe/IrMn/Ta [14]. However, for these structures either sensitivity data are missing or the sensitivity is lower than for the Ta/$Ni_{80}Fe_{20}$/Cu/Ni80Fe20/IrMn/Ta structures.

In these sensors the spin valve structure is used to induce the required magnetic properties. There are no reports of additional transverse voltage in relation to the spin valve effect itself; namely, the large variations in the longitudinal resistivity as a function of the magnetic configuration. The measured PHE signal is simply the average contribution of all layers in connection with the AMR of each layer.

2.3 PHE Bridge Sensors

The term PHE bridge (PHEB) sensors [9–12, 24, 36–41] has been used to describe AMR sensors in different Wheatstone bridge configurations. Two main types have been considered: (a) sensors where the arms are straight and form a square; (b) sensors where the arms form a ring shape [42]. The two basic shapes have been further developed into meander-like shapes to increase the signal (see Fig. 3). In all these configurations at zero applied field the angle between the internal magnetization and the current is around 45° as required for AMR sensors and not parallel or anti-parallel as required for PHE sensors.

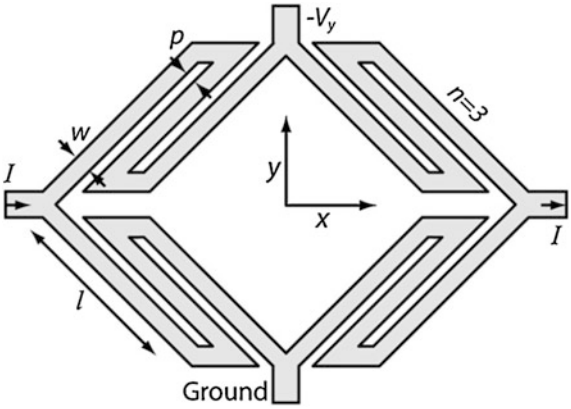

Fig. 3 Planar Hall effect Bridge (PHEB) configuration with multi segments per branch (*Source* Ref. [10])

The bridge configuration which is useful for eliminating effects of thermal drifts, and the angle between the current and the internal magnetization when no field is applied give rise to a dependence of the output voltage on the magnetization direction which is similar to that obtained for PHE; nevertheless, these are in fact AMR sensors whose output is determined by the integrated AMR response of the entire bridge structure. Such sensors have demonstrated a resolution of 2 nT/$\sqrt{\text{Hz}}$ at 1 Hz [10].

3 Elliptical PHE Sensors

Starting from this section we concentrate on elliptical PHE sensors which exhibit magnetic field resolution of $\sim$200 pT/$\sqrt{\text{Hz}}$ at 1 Hz and less than 1 nT/$\sqrt{\text{Hz}}$ at 0.1 Hz.

The elliptical shape of these sensors induces uniaxial magnetic anisotropy parallel to the long axis of the ellipse. For sensing, a current is driven along the long axis of the ellipse and the transverse voltage due to the PHE is measured across the short axis of the magnetic ellipse (see Fig. 4).

We start with describing the fabrication process and then we introduce the main factors which are used to analyze the operation of the sensor: the equivalent circuit, the signal and noise models and the resulting resolution.

3.1 Fabrication

The sensors are fabricated by the following steps:

1. We start with an undoped Si wafer (orientation: (100) $\pm$ 0.9°, resistivity $> 100\Omega$ cm, micro roughness ≤ 5 Å).

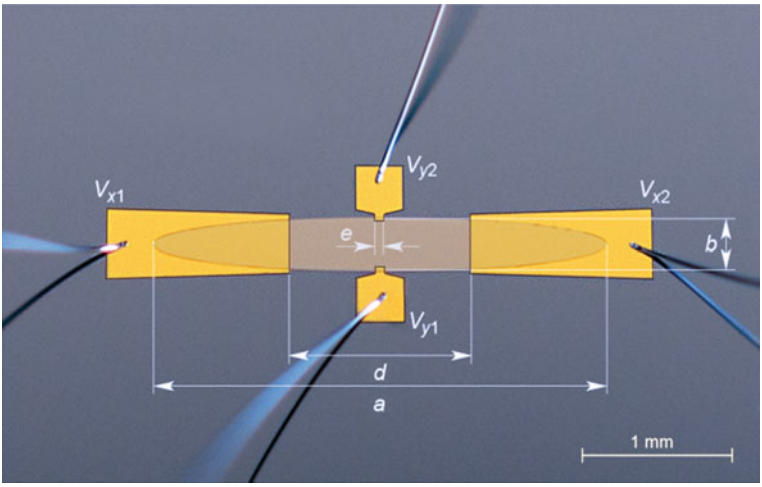

Fig. 4 An elliptical PHE sensor with its dimensions. The elliptical part is made of permalloy capped with tantalum. The current leads (V_{x1}, V_{x2}) and the voltage leads (V_{y1}, V_{y2}) are made of gold

2. Ellipses are patterned on the wafer by a liftoff process using MJB-4 Mask-aligner, photoresist S1813 and developer MICROPOSIT® MF®-319.
3. Permalloy ($Ni_{80}Fe_{20}$) films capped with tantalum are sputtered in a UHV-evaporation and sputtering system (BESTEC). Prior to deposition, the wafer is treated with Ar^+ beam using 3 cm dc Ion Source Filament Cathode (ITI) in order to remove resist and developer residue that can remain after development process. Base vacuum before deposition is less than 5×10^{-7} mBar, and it rises to 3×10^{-3} mBar during deposition. Gas is introduced into the upstream end of the ion source through the gas feed tube where it is ionized. The Permalloy is sputtered at a rate of $1.76\,\text{Å}/s$ and a capping layer of tantalumn (3 nm) is deposited on top in situ immediately after Permalloy to prevent oxidation.
4. The wafer is immersed in NMP for liftoff.
5. Current and voltage leads are patterned at a second liftoff process.
6. The gold contacts are sputtered on top of an adhesion layer of chrome (4 nm) in BESTEC. Before deposition the wafer is treated with Ar^+ beam. The gold layer thickness is $\sim$1.5 times the thickness of the magnetic layer.
7. The wafer is immersed in NMP heated to 80 °C for liftoff.

The liftoff process described in (2), (3) and (4) can be replaced by a wet etching process. In this process the new stage (2) is former stage (3) performed on an unprocessed wafer. Stage (3) is former stage (2) with reversed lithography (namely the remaining photoresist defines the ellipses. Stage (4) is replaced by wet etching with 32 % HCl. The etching is stopped by H_2O.

3.2 Equivalent Circuit

The equivalent electrical circuit of the PHE sensor and its preamplifier is presented in Fig. 5. The equivalent circuit includes the PHE voltage source which generates a V_y voltage across the sensor y-terminals, the sensor resistance across the y-terminals, R_y, the sensor internal thermal and $1/f$ noise sources $e_{thermal}$ and $e_{1/f}$ respectively, and e_{amp}, the total preamplifier noise, referred to its input (including the voltage noise, current noise, and the noise of the feedback resistors R_f and R).

3.3 Signal

The sensitivity of a PHE sensor is defined as the ratio between the PHE voltage V_y and the magnetic field B applied in the film plane perpendicular to the easy axis (and the current direction). When B is small compared to the total effective anisotropy field (H_k) which is the sum of the sensor shape induced anisotropy H_{sa} and the excess anisotropy H_{ea}, the sensitivity can be expressed as follows [43]

$$S_y = \frac{V_y}{B} = 10^4 \frac{V_x}{R_x} \cdot \frac{\Delta\rho}{t} \cdot \frac{1}{H_{sa} + H_{ea}} \tag{4}$$

where V_x is the bias voltage across the x-terminals, R_x is the sensor resistance across the x-terminals, t is the sensor thickness, and $\Delta\rho$ is the sensor average electrical resistivity ($\Delta\rho = \rho_{\parallel} - \rho_{\perp}$).

We express the sensor resistance across the x-terminals R_x, while neglecting the resistance of the gold leads and the interface resistance between the leads and the sensor as:

$$R_x = \frac{C_1 \cdot \rho \cdot d}{t \cdot b} \tag{5}$$

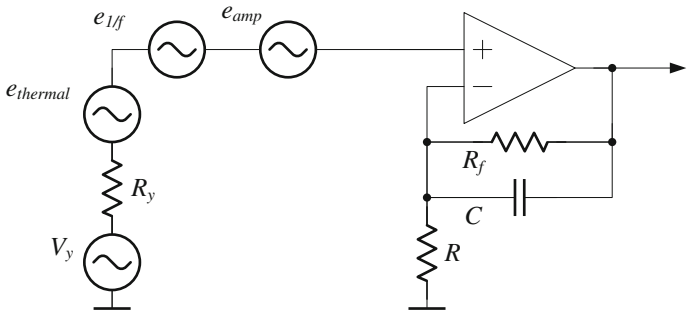

Fig. 5 Equivalent electrical circuit of the PHE sensor

In this expression, C_1 is a constant not much larger than 1 which is used to reflect the previously mentioned approximations.

3.4 Noise

The total noise of a PHE sensor e_Σ has three main components: 1/*f* noise, thermal noise, and preamplifier noise:

$$e_\Sigma = \sqrt{e_{1/f}^2 + e_{\text{thermal}}^2 + e_{amp}^2} \tag{6}$$

3.4.1 Thermal Noise

The thermal noise (sometimes referred to as Johnson noise) is generated by thermal agitation of electrons in a conductor and is defined by:

$$e_{\text{thermal}} = \sqrt{4k_B T R_y} \tag{7}$$

where k_B is the Boltzmann constant, T is the temperature, and R_y is the sensor resistance across the *y*-terminals:

$$R_y = \frac{C_3 \cdot \rho \cdot b}{t \cdot e \cdot C_2} \tag{8}$$

where C_3 similarly to C_1 is a constant not much larger than 1, and C_2 is a constant larger than 1 that relates the real, rectangle shaped volume between the *y*-terminals to the effective conduction area.

3.4.2 1/*f* Noise

The sensor 1/*f* noise is described using the Hooge empirical formula:

$$e_{1/f} = \sqrt{V_x^2 \frac{\delta_H}{N_c \cdot Vol \cdot f^\alpha}} \tag{9}$$

where V_x is the bias voltage, δ_H is the Hooge constant [44, 45], N_c is the "free" electron density and is equal to 1.7×10^{29} 1/m^3 for $Ni_{80}Fe_{20}$ Permalloy [45], f is the frequency, α is a constant, and *Vol* is the effective volume, where the electrons are contributing to the conduction process in a homogeneous sample [45].

Considering the effective conduction volume described using C_2 in Eq. (8), *Vol* can be approximated by:

$$Vol = C_2 \cdot t \cdot b \cdot e \tag{10}$$

3.4.3 Amplifier Noise

e_{amp} is the total preamplifier noise, referred to its input (including the voltage noise, current noise, and the noise of the resistors). The feedback resistors R_f and R are selected to be small enough so their noise contribution can be neglected. Consequently,

$$e_{amp} = \sqrt{v_{amp}^2 + \left(R_y i_{amp}\right)^2} \tag{11}$$

where v_{amp} and i_{amp} are the operational amplifier voltage and current noise respectively. The voltage and current noise of the operational amplifier possess both white and pink (1/*f*) noise components and can be expressed using the following expressions:

$$v_{amp} = v_{amp0}\sqrt{1 + \frac{f_{c1}}{f^{\alpha_1}}} \tag{12}$$

$$i_{amp} = i_{amp0}\sqrt{1 + \frac{f_{c2}}{f^{\alpha_2}}} \tag{13}$$

where v_{amp0} and i_{amp0} are the level of the voltage and current white noise densities respectively, f_{c1} and f_{c2} are the voltage and current noise densities corner frequency respectively and α_1 and α_2 are constants.

3.5 Equivalent Magnetic Noise

The sensor equivalent magnetic noise (sometimes referred to as resolution or minimal detectable field) is defined as

$$B_{eq} = \frac{e_\Sigma}{S_y} = \frac{\sqrt{e_{1/f}^2 + e_{\text{thermal}}^2 + e_{amp}^2}}{10^4 \frac{V_x}{R_x} \cdot \frac{\Delta\rho}{t} \cdot \frac{1}{H_{sa} + H_{ea}}} \tag{14}$$

In the following sections we describe a series of steps we have made to improve the magnetometer resolution with special emphasis on the low frequency noise.

4 Magnetic Behavior of Elliptical PHE Sensors

As mentioned above, the operation of PHE sensors requires magnetic anisotropy. In elliptical PHE sensors the magnetic anisotropy is induced by the dependence of the magnetostatic energy on the direction of the magnetization relative to the principal axes of the ellipse. Compared to previously discussed methods for the magnetic anisotropy induction (e.g. field induction or induction using an anti-ferromagnetic layer), anisotropy induction using the sensor shape has several important advantages:

1. The direction and magnitude of the magnetic anisotropy is determined by the pattern shape.
2. In principle, for ideal magnetic ellipsoids with no intrinsic magnetic anisotropy, the anisotropy field, which is inversely proportional to the signal [see Eq. (4)], can be made as small as required.
3. The anisotropy is achieved using a single magnetic layer which makes the fabrication simple. Furthermore, due to the fact that the anisotropy is not achieved via interaction with other layers, the magnetic sensing element can be as thick and big as required which is important for decreasing the $1/f$ noise.

For elongated and flat ellipsoids $(a \geq b \gg c)$, one can define and calculate the demagnetization factors [43, 46],

$$\frac{N_a}{4\pi} = \frac{c}{a}(1-e^2)^{1/2}\frac{K-E}{e^2} \tag{15}$$

$$\frac{N_b}{4\pi} = \frac{c}{a}\frac{E-(1-e^2)K}{e^2(1-e^2)^{1/2}} \tag{16}$$

$$\frac{N_c}{4\pi} = 1 - \frac{cE}{a(1-e^2)^{1/2}} \tag{17}$$

where a, b and c are the axes of the ellipsoid. N_a, N_b and N_c are the demagnetizing factors (corresponding to a, b and c respectively). K is a complete elliptic integral of the first kind and E is a complete elliptic integral of the second kind, whose argument is $e = \left(1 - \frac{b^2}{a^2}\right)^{\frac{1}{2}}$. The behavior of the ellipsoid when H is applied in the ab plane can be described by the Stoner-Wohlfarth Hamiltonian $\mathcal{H} = K_u \sin^2\theta - M_s H \cos(\alpha - \theta)$ [47] where the anisotropy constant K_u is given by $K_u = \frac{1}{2}M_s^2(N_b - N_a)$. So the shape-induced anisotropy field (H_{sa}) is

$$H_{sa} = M_s(M - L) \tag{18}$$

Using asymptotic expansions of K and E in the limit $a \gg b \gg c$ [46] we obtain

$$H_{sa} \sim 4\pi M_s \frac{c}{b} \sim 10,807 \frac{c}{b} Oe \tag{19}$$

Using this approximation we estimate the shape-induced anisotropy of a thin ellipse (thickness t) with principle axes a and b $(a \geq b \gg t)$ as

$$H_{sa} \sim 4\pi M_s \frac{t}{b} \sim 10,807 \frac{t}{b} Oe \tag{20}$$

As shown below, the effective anisotropy field does not go to zero when t/b goes to zero. Therefore, we denote by H_{sa} the calculated shape-induced anisotropy field and by H_k the actual effective anisotropy field.

The ideal magnetic ellipsoid is expected to exhibit a single magnetic domain behavior with uniform magnetization. Figures 6 and 7 present two types of experiments which demonstrate the effective single domain behavior of the thin ellipses.

Figure 6 demonstrates the effective single domain behavior by showing that if the magnetization is tilted away from the easy axis by an external field, it returns completely to the easy axis when the applied magnetic field is set to zero. This is demonstrated by measuring the PHE with and without the field. The small variations in the zero-field signals are consistent with the expected effect of a small ambient field.

Figure 7 shows the dependence of the switching Field H_s on α measured on elliptical sensor with long axis of 1 mm. The line is the expected for coherent rotation [47]

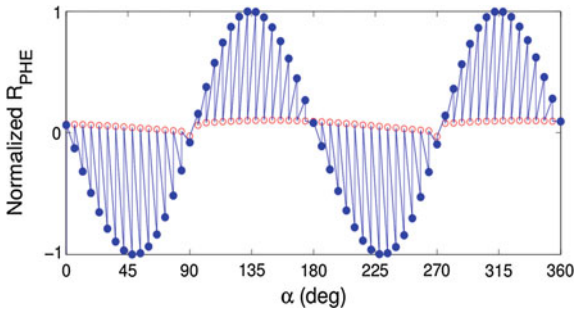

Fig. 6 Demonstration of effective single-domain behavior of large elliptical sensors. The normalized PHE is measured across an elliptical sensor as a function of the angle α between H and J. The dimensions of the ellipse are 2 mm length, 0.25 mm width, and 60 nm thickness, the current J is applied along the long axis of the ellipse. For each α, the voltage is measured twice: with H = 100 Oe (full symbols) and with H = 0 (empty symbols). (*Source* Ref. [43])

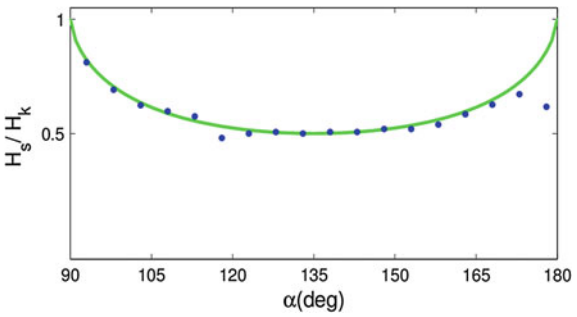

Fig. 7 The switching field H_s divided by the anisotropy field H_k as a function of α. The line is a fit to the Stoner–Wohlfarth model. The dimensions of the ellipse are 1 mm length, 0.125 mm width, and a 60 nm thickness. (*Source* Ref. [43])

$$H_s(\alpha) = \frac{H_k}{\left[\sin^{\frac{2}{3}}\alpha + \cos s^{\frac{2}{3}}\alpha\right]^{\frac{3}{2}}} \tag{21}$$

where H_k is the actual effective anisotropy field. We note that for α close to 180° the experimental points deviate from the theoretical prediction indicating that in this narrow range of angles the magnetization reversal cannot be described in terms of coherent rotation. This however does not affect the functionality of the sensors which are used to detect fields much smaller than the anisotropy field.

To determine the effective H_k of the sensors, we apply a small field perpendicular to the easy axis and measure the slope of θ versus $H_\perp$. Figure 8 represents the experimentally extracted H_k for elliptical sensors in a wide range of sizes as a function of b/t, where t is the film thickness, and b is the short axis of the ellipse.

We compare the analytical approximation with the experimental results (see Fig. 8) and note that the experimental value of H_k has a lower bound. Namely, there is an excess anisotropy which is sample dependent and its magnitude is typically on the order of 5 Oe. The origin of this excess anisotropy is yet to be determined. We

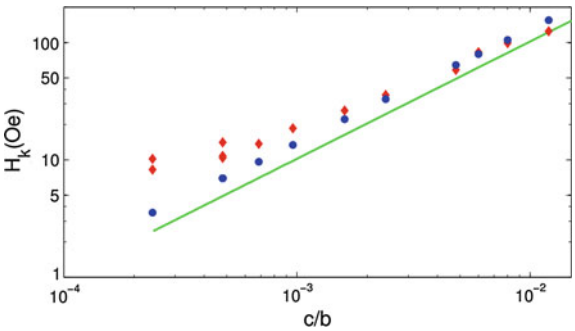

Fig. 8 The theoretical anisotropy field of ellipsoids with principle axes a, b and c [continuous line according to Eq. (19)] and the experimental (*diamonds*) and simulated (*dots*) shape anisotropy field for ellipses with principle axes a and b and thickness $t = c$ as a function of c/b. (*Source* Ref. [43])

therefore write H_k as a sum of two contributions: the expected anisotropy field due to shape denoted by H_{sa} and an excess anisotropy field denoted by H_{ea}.

We compare the analytical approximation with OOMMF [48] simulations and note that the approximation in Eq. (19) is quite good for $a/b \geq 8$.

We have also performed simulations for ellipses and rectangles and have found that the analytical approximation is better for elongated ellipses. The simulations also indicate the effective single domain behavior for ellipsoids and ellipses in a very wide range of sizes, whereas rectangular samples are much less stable. The ellipses with axes ratio of 6:1 and above behave quite like a single domain particle and the behavior improves with increasing axes ratio.

We note that the size dependence of the switching properties of Permalloy ($Ni_{80}Fe_{20}$) ellipses was also investigated by other groups using magnetoresistance measurements and magnetic force microscopy. A single-domain configuration was observed in the elements with the range of aspect ratios from 5 to 10. More complex domain structures appear in the lower aspect ratio and thicker samples [49].

Surprisingly, the single-domain-like behavior is observed even for very large ellipses [43]. This has a practical importance since the big ellipses have a very small H_k which means that their sensitivity can be higher.

$$S = \frac{V_y}{I} \cdot \frac{1}{H_k} \propto \frac{1}{H_k} \tag{22}$$

We have obtained H_k as small as 8 Oe and S as big as 200 $\frac{\Omega}{T}$.

5 Operation and Optimization of Elliptical PHE Sensors

5.1 *Exciting the Sensor Using AC Current*

As previously explained, the preamplifier consists of voltage and current noise sources at its input, both possessing white and 1/*f* components [see Eqs. (12) and (13)]. Our magnetometer is designed for optimal resolution at ultra-low frequencies starting from the mHz range. Since the 1/*f* noise of the elliptical PHE magnetometer is extremely low, even ultra-low noise operational amplifiers will introduce an additional, significant 1/*f* noise at frequencies below 1 Hz (see for example LT1028 by Linear Technology).

A probable solution is to use chopper or auto-zero amplifiers. Those amplifiers show minimal drift and zero 1/*f* noise at their input. However, even state-of-the-art commercially available amplifiers of this type (see for example ADA4528-1 by Analog Devices) demonstrate white noise levels five times higher compared to the white noise level of a standard ultra-low noise operational amplifier and therefore did not constitute a potential solution in this case.

To overcome this limitation we have excited our sensor using ac current as opposed to the classic approach of dc current excitation. Exciting the sensor using

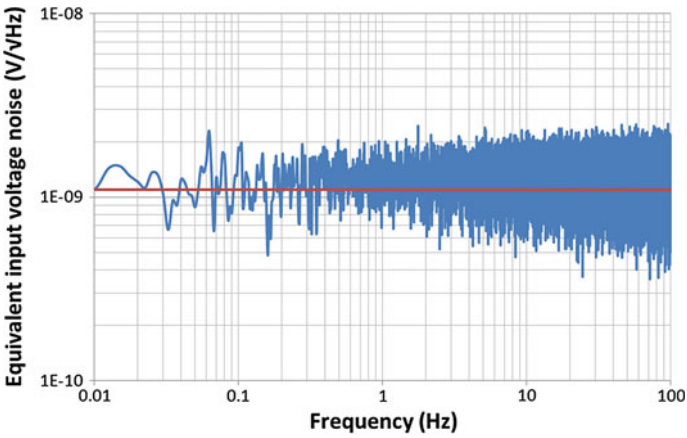

Fig. 9 Equivalent input voltage noise versus frequency for a LT1028 operational amplifier with an output demodulation at 1.12 kHz. Both the measured noise and the fit are shown (*blue* and *red line* respectively)

ac current translates its output signal and its intrinsic 1/*f* noise to frequencies where the 1/*f* noise of the preamplifier can be neglected. The preamplifier output signal can then be demodulated back to baseband using analog or digital synchronous detector.

Compared to chopper amplifiers which modulate the signal inside the amplifier, modulation of the signal inside the sensor itself results in an equivalent white noise behavior of the amplifier with a drastically lower noise level.

Figure 9 shows the amplitude spectral density of the LT1028 preamplifier equivalent input noise, measured after demodulation without excitation current. One can see that the preamplifier noise is white from 10 mHz to 100 Hz. The measured white noise level of ~ 1.1 nV/$\sqrt{\text{Hz}}$ is in good agreement to the reported white noise level in the LT1028 op-amp datasheet. The graph in Fig. 9 was acquired using a digital demodulation at a frequency of 1.12 kHz.

5.2 *Optimization of the Sensor Thickness*

The PHE sensor 1/*f* noise is inversely proportional to the sensor volume [see Eq. (9)]. Since the sensor signal is inversely proportional to the sensor thickness, it is also inversely proportional to its volume [see Eq. (4)]. As a result, there is an optimal thickness for which the sensor equivalent magnetic noise is minimal.

Our magnetometer is optimized to operate at ultra-low frequencies where the 1/*f* noise component of the sensor is dominant over its thermal noise and the preamplifier white noise.

In the limit where the 1/*f* noise is dominant, only the first term under the square root of Eq. (6) remains relevant. The parameters $H_{ea}, \frac{\Delta\rho}{\rho}$, and ρ do not depend on the sensor thickness for $t > 20$ nm; therefore, they are considered as constants for the thicknesses we use. By substituting the expressions for H_{sa}, R_x, *Vol* and R_y into Eq. (14) we obtain:

$$B_{eq} = \sqrt{\frac{\delta_H}{N_c \cdot C_2 \cdot t \cdot b \cdot e \cdot f^{\alpha}}} \frac{(10^4 t + b + H_{ea}) \cdot C_1 \cdot d \cdot \rho}{10^4 \cdot \Delta\rho \cdot b^2} \tag{23}$$

We note that the equivalent magnetic noise in Eq. (23) depends only on the sensor dimensions and the material properties.

Optimizing t for minimal value of B_{eq} yields:

$$t_{opt} = \frac{H_{sa} \cdot b}{10^4} \tag{24}$$

We find that for this thickness:

$$H_{sa} \approx H_{ea} \tag{25}$$

We now substitute Eq. (24) into Eq. (23) and obtain the sensor low-frequency equivalent magnetic noise at the optimal thickness:

$$B_{\min} = \sqrt{\frac{\delta_H}{N_c \cdot C_2 \cdot e \cdot f^{a}}} \frac{2\sqrt{H_{ea}} C_1 \cdot d \cdot \rho}{10^2 \cdot \Delta\rho \cdot b^2} \tag{26}$$

To appreciate the sensitivity of B_{eq} on deviations from the optimal thickness, we calculate changes in B_{min} denoted as $B_{eq} = B_{min} \cdot \delta B_{eq}$ as a result of relative changes in the sensor thickness denoted as $\delta t = (t_{opt} \pm t)/t_{opt}$.

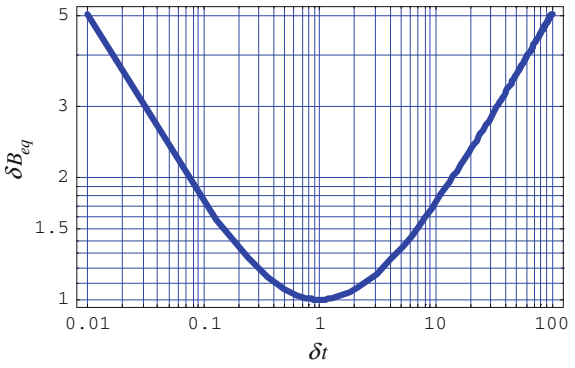

Fig. 10 Relative change in the equivalent noise as a result of deviations from the optimal thickness

This yields

$$\delta B_{eq} = \frac{1}{2}(1+\delta t)\sqrt{\frac{1}{\delta t}} \tag{27}$$

A plot of Eq. (27) (see Fig. 10) shows that a ten-fold deviation of the sensor thickness from its optimum value results in almost two-fold increase in the sensor equivalent magnetic noise.

5.3 *Optimization of the Driving Current*

Theoretically, if the sensor power consumption is not limited, the excitation current should be as high as possible to bring the equivalent magnetic noise to a minimum at all frequencies. However, the ability of the sensor to dissipate the excessive heat is limited and therefore, at a too high current, the sensor becomes thermally unstable, which degrades its equivalent magnetic noise.

The excitation current should be selected according to the bandwidth requirements of the specific application. In frequencies significantly higher or lower than 1 Hz, thermal or 1/*f* noise, respectively, will dominant over other noise sources regardless of the excitation current. On the other hand, the unique case of a bandwidth ranging from sub-Hz frequencies and up to tens or hundreds of Hz requires a more sophisticated approach for the selection of the excitation current based on an experimental optimization process.

In this case of intermediate frequencies the optimal current must yield best possible magnetic field resolution at frequencies where the 1/*f* noise dominants but also at frequencies where the white noise sources are dominant.

To find the optimal excitation current for the intermediate frequency range, we have measured the sensor equivalent magnetic noise between 0.01 and 10 Hz for currents in the range of 10–100 mA. We have changed the current by small steps

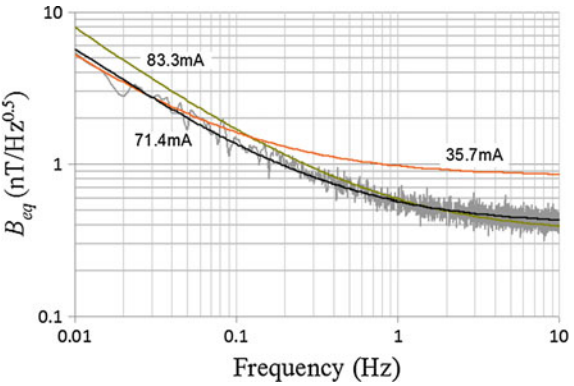

Fig. 11 Equivalent magnetic noise versus frequency. For the optimum excitation current amplitude of 71.4 mA, both the sensor noise and the noise fit are shown. For other excitation current amplitudes only the noise fits are shown. (*Source* [50])

measuring at each step the sensor gain and noise. Figure 11 shows the sensor equivalent magnetic noise as a function of frequency for three cases: a too high, a too low and optimal excitation current.

The sensor was excited with ac current. The sensor output was amplified using a low-noise operational amplifier (LT1028). The amplifier output was sampled by a 24-bit ADC (PXI-5421) and demodulated using a digital synchronous detector. A 100 Hz low-pass filter at the output of the synchronous detector was used to band-limit the signal. As the input voltage noise of the LT1028 operational amplifier flattens at around 1 kHz, we have excited the sensor at 1.22 kHz to avoid the amplifier 1/*f* noise and 50 Hz power network harmonics. The sensor gain was measured using a calibrated solenoid and was found to be flat from 10 mHz to 100 Hz. The sensor noise was measured inside a seven layer magnetic shield to suppress low-frequency interferences. A similar experimental setup is shown in Fig. 12. The experimental sensor parameters are listed in Table 1.

From Fig. 11, one can see that the sensor equivalent magnetic noise at the optimal excitation current is either the lowest one or does not practically differ from the noise values at the other excitation currents. A too low excitation current provides similar results at low frequencies but worse results at higher frequencies, where the 1/*f* noise is not so dominant. At a too high excitation current, the equivalent magnetic noise at high frequencies is similar to that of the optimal current, but is degraded at low frequencies due to thermal drift.

5.4 Equivalent Input Magnetic Noise

By increasing the sensor volume (see Fig. 13) and decreasing white noise associated with the pre-amplifier we have managed to considerably improve the equivalent magnetic noise of our PHE sensors and obtain a magnetic field resolution of 200 pT/$\sqrt{\text{Hz}}$ at 1 Hz and less than 1 nT/$\sqrt{\text{Hz}}$ at 0.1 Hz [51].

Figure 14 shows the 5 mm PHE sensor equivalent magnetic noise as a function of frequency compared to the equivalent magnetic noise of a high-resolution commercial AMR sensor of a model HMC1001 by Honeywell.

6 Future Prospects and Applications

The current resolution of the elliptical PHE-sensors exceeds the resolution of the highest performance commercial AMR sensors and the resolution of other MR sensors. However, there are prospects for improving the resolution of these sensors by more than an order of magnitude to reach field resolution in the femto-Tesla range. In the following we address several routes for improved resolution: (a) increasing the signal (b) increasing the measured field and (c) decreasing the noise.

There are two main ways to increase the signal. The AMR ratio of the used Permalloy films is on the order of 1–2 %. However, based on reports in the

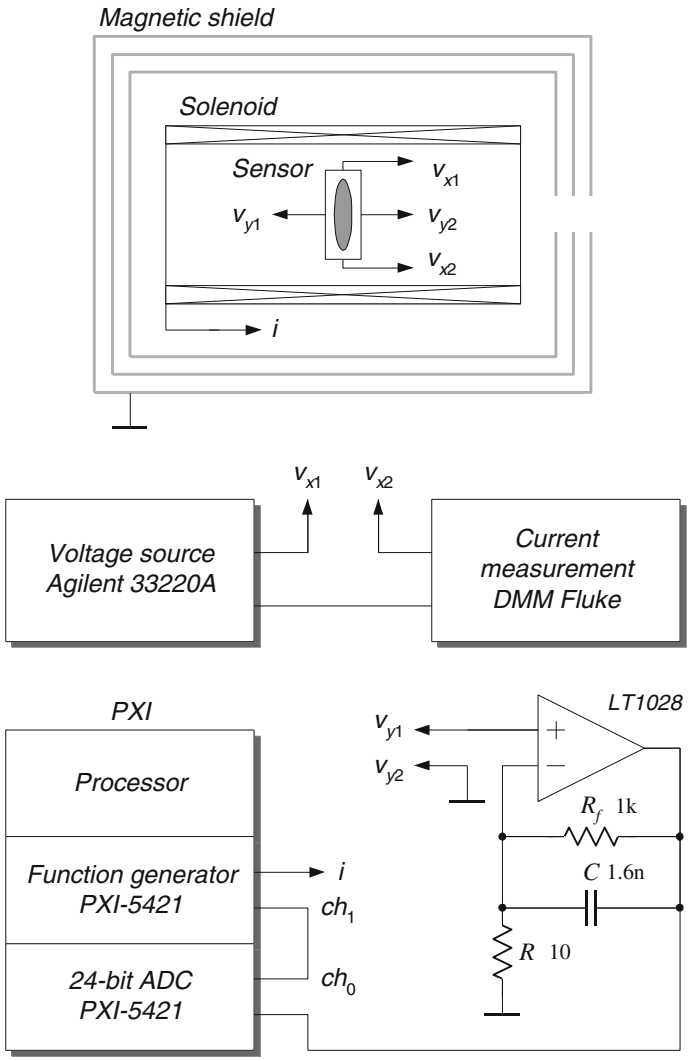

Fig. 12 An experimental setup similar to the one used for the excitation current optimization process. (*Source* Ref. [43])

literature, optimization of deposition conditions may reasonably yield an improvement of at least a factor of 2. We note that the equivalent magnetic noise is inversely proportional to the AMR ratio. Another way to increase the signal is by reducing the excess anisotropy H_{ex} which sets a lower bound for the total effective uniaxial anisotropy. The origin of the excess anisotropy is not fully understood at this stage. We believe that it is related to internal intrinsic magnetocrystalline anisotropy which can be suppressed by the optimization process of the growth

Table 1 Parameters of the PHE sensor experimental model

Parameter	Value	Units	Parameter	Value	Units
a	3	mm	H_a	3.84	Oe
b	0.375	mm	H_k	3.45	Oe
t	120	nm	$\Delta\rho/\rho$	1.6	%
d	1.2	mm	ρ	2.7×10^{-7}	Ohm m
e	0.06	mm	α	1.5	
R_x	9.97	Ohm	δH	2.73×10^{-3}	
R_y	5.08	Ohm	N_c	17×10^{28}	$1/m^3$
I_x	71.4	mA			

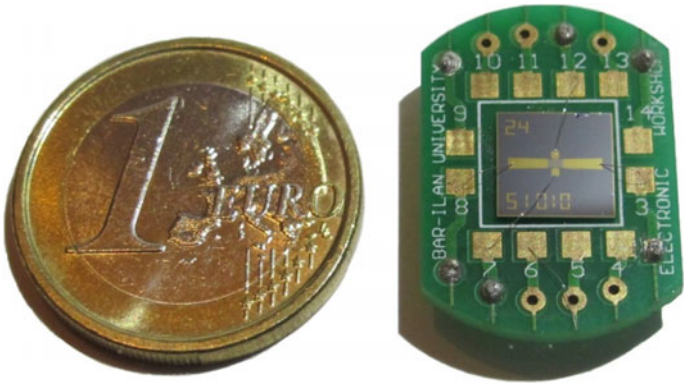

Fig. 13 A 5 mm PHE sensor mounted on its carrier, placed next to 1 EURO coin for scale

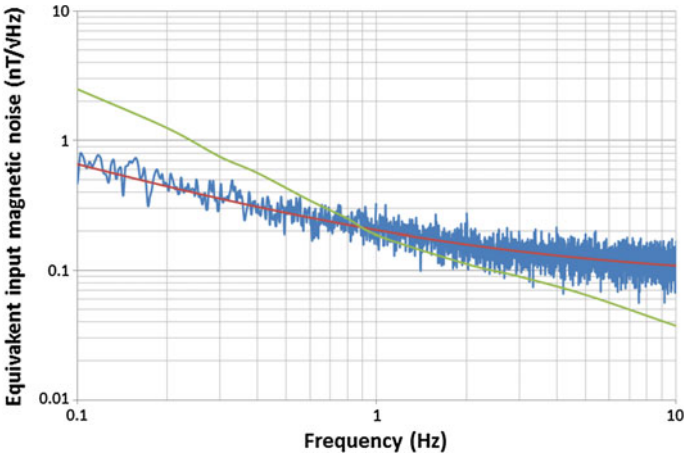

Fig. 14 The equivalent magnetic noise of a 5 mm elliptical PHE sensor (*blue line*—measured noise, *red line*—fit) compared to the equivalent magnetic noise of a high-resolution commercial AMR sensor of a model HMC1001 by Honeywell (*green line*)

conditions. We note that Eq. (26) equivalent magnetic noise is proportional to $\sqrt{H_{ea}}$.

The amplification of the field is commonly achieved by using magnetic flux concentrators. In the case of elliptical PHE sensors the integration of such concentrators is relatively simple. We note that flux concentrators have been used to increase the applied field by more than an order of magnitude.

The decrease of the noise can be achieved in several ways: by optimizing the sensor geometrical parameters including the parameters of the current and voltage leads and by optimizing the measuring method (amplitude and frequency of the excitation current, amplification circuit, etc.). Based on the above, even without exploring other material systems, a low frequency femto-Tesla resolution with the elliptical PHE sensors is within reach. In addition to the field resolution advantage of these sensors, there are other important advantages. They are simpler than the AMR sensors, their anisotropy is tailored by shape which enables the simple fabrication on the same chip of sensors with easy axes which differ in their orientation and the strength of the effective anisotropy field. Furthermore, they are quite robust and stable, a feature which decreases considerably the need to "refresh" the sensor. These features of the sensors make them suitable for a wide range of applications. They may compete with the low-cost low-resolution magnetic sensors such as Hall

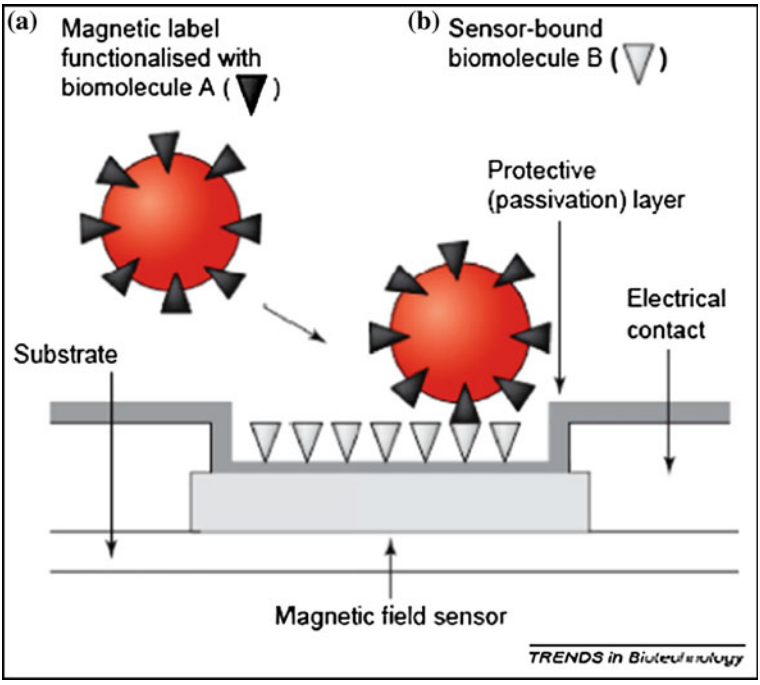

Fig. 15 Simplified scheme for biomolecule detection. Biomolecule with label (*A*) connecting to the sensing surface by creating a bridge with a complementary biomolecule (*B*). This event can be registered with a magnetic field sensor. Figure taken from [52]

sensors, which are widely used in the automotive industry. Currently, it appears that this industry does not need the improved resolution; however, it could be that once cheap, high-resolution sensors are available, the need will also arise.

PHE sensors have been suggested for various medical diagnostic applications; particularly, as a central part in lab-on-a-chip systems [52] (see Fig. 15). In such systems, better resolution means more sensitive diagnosis. Thus the use of elliptical PHE sensors in such systems may have important medical benefits. Furthermore, they can also become relevant for detecting magnetic fields generated by the human body in connection with heart and neural activity.

Another important field of application is related to magnetic anomaly detection of ferrous objects (for example: vehicles, submarines, etc.) The possible mass production of PHE sensors make them relevant for smart-dust [53] applications which require the distribution of a large number of sensors.

References

1. S.A. Wolf, A.Y. Chtchelkanova, D.M. Treger, Spintronics—a retrospective and perspective. IBM J. Res. Dev. **50**, 101–110 (2006)
2. S.A. Wolf, D.D. Awschalom, R.A. Buhrman, J.M. Daughton, S. von Molnár, M.L. Roukes et al., Spintronics: a spin-based electronics vision for the future. Science **294**, 1488–1495 (2001)
3. F.G. West, Rotating-field technique for galvanomagnetic measurements. J. Appl. Phys. **34**, 1171–1173 (1963)
4. C. Goldberg, R.E. Davis, New galvanomagnetic effect. Phys. Rev. **94**, 1121–1125 (1954)
5. T.T. Chen, V.A. Marsocci, Planar magnetoresistivity and planar hall effect measurements in nickel single-crystal thin films. Physica **59**, 498–509 (1972)
6. H.X. Tang, R.K. Kawakami, D.D. Awschalom, M.L. Roukes, Giant planar hall effect in epitaxial (Ga, Mn) as devices. Phys. Rev. Lett. **90**, 107201 (2003)
7. Y. Bason, L. Klein, J.B. Yau, X. Hong, C.H. Ahn, Giant planar hall effect in colossal magnetoresistive La0.84Sr0.16MnO3 thin films. Appl. Phys. Lett. **84**, 2593–2595 (2004)
8. X.S. Jin, R. Ramos, Y. Zhou, C. McEvoy, I.V. Shvets, Planar hall effect in magnetite (100) films. J. Appl. Phys. **99**, 08C509 (2006)
9. A.D. Henriksen, B.T. Dalslet, D.H. Skieller, K.H. Lee, F. Okkels, M.F. Hansen, Planar hall effect bridge magnetic field sensors. Appl. Phys. Lett. **97**, 013507 (2010)
10. A. Persson, R.S. Bejhed, F.W. Osterberg, K. Gunnarsson, H. Nguyen, G. Rizzi et al., Modelling and design of planar hall effect bridge sensors for low-frequency applications. Sens. Actuat. a-Phys. **189**, 459–465 (2013)
11. F.W. Osterberg, G. Rizzi, M.F. Hansen, On-chip measurements of Brownian relaxation of magnetic beads with diameters from 10 nm to 250 nm. J. Appl. Phys. **113**, 154507 (2013)
12. A. Persson, R.S. Bejhed, H. Nguyen, K. Gunnarsson, B.T. Dalslet, F.W. Osterberg et al., Low-frequency noise in planar hall effect bridge sensors. Sens. Actuat. a-Phys. **171**, 212–218 (2011)
13. S.J. Oh, T.T. Le, G.W. Kim, C. Kim, Size effect on NiFe/Cu/NiFe/IrMn spin-valve structure for an array of PHR sensor element. Phys. Status Solidi A **204**, 4075–4078 (2007)
14. N.T. Thanh, K.W. Kim, O. Kim, K.H. Shin, C.G. Kim, Microbeads detection using planar hall effect in spin-valve structure. J. Magn. Magn. Mater. **316**, E238–E241 (2007)

15. B. Bajaj, N.T. Thanh, C.G. Kim, in *Planar Hall Effect in Spin Valve Structure for DNA Detection Immobilized with Single Magnetic Bead.* 7th IEEE Conference on Nanotechnology, vol. 1–3 (2007), pp. 1037–1040
16. N.T. Thanh, B.P. Rao, N.H. Duc, C. Kim, Planar hall resistance sensor for biochip application. Phys. Status Solidi A **204**, 4053–4057 (2007)
17. S. Oh, N.S. Baek, S.D. Jung, M.A. Chung, T.Q. Hung, S. Anandakumar et al., Selective binding and detection of magnetic labels using PHR sensor via photoresist micro-wells. J. Nanosci. Nanotechno. **11**, 4452–4456 (2011)
18. D.T. Bui, M.D. Tran, H.D. Nguyen, H.B. Nguyen, High-sensitivity planar hall sensor based on simple gaint magneto resistance NiFe/Cu/NiFe structure for biochip application. Adv. Nat. Sci, Nanosci. Nanotechnol. **4**, 015017 (2013)
19. M. Volmer, J. Neamtu, Micromagnetic characterization of a rotation sensor based on the planar hall effect. Phys. B **403**, 350–353 (2008)
20. M. Volmer, M. Avram, A.M. Avram, in *On Manipulation and Detection of Biomolecules Using Magnetic Carriers*. International Semiconductor Conference (2009), pp. 155–8
21. T.Q. Hung, S.J. Oh, B.D. Tu, N.H. Duc, L.V. Phong, S. AnandaKumar et al., Sensitivity dependence of the planar hall effect sensor on the free layer of the spin-valve structure. IEEE Trans. Magn. **45**, 2374–2377 (2009)
22. T.Q. Hung, J.R. Jeong, D.Y. Kim, H.D. Nguyen, C. Kim, Hybrid planar hall-magnetoresistance sensor based on tilted cross-junction. J. Phys. D Appl. Phys. **42**, 055007 (2009)
23. B.D. Tu, L.V. Cuong, T.Q. Hung, D.T.H. Giang, T.M. Danh, N.H. Duc et al., Optimization of spin-valve structure NiFe/Cu/NiFe/IrMn for planar hall effect based biochips. IEEE Trans. Magn. **45**, 2378–2382 (2009)
24. B. Sinha, S. Anandakumar, S. Oh, C. Kim, Micro-magnetometry for susceptibility measurement of superparamagnetic single bead. Sens. Actuat. a-Phys. **182**, 34–40 (2012)
25. M. Volmer, J. Neamtu, Electrical and micromagnetic characterization of rotation sensors made from permalloy multilayered thin films. J. Magn. Magn. Mater. **322**, 1631–1634 (2010)
26. M. Volmer, J. Neamtu, Magnetic field sensors based on permalloy multilayers and nanogranular films. J. Magn. Magn. Mater. **316**, E265–E268 (2007)
27. T.Q. Hung, B.P. Rao, C. Kim, Planar hall effect in biosensor with a tilted angle of the cross-junction. J. Magn. Magn. Mater. **321**, 3839–3841 (2009)
28. Z.Q. Lu, G. Pan, Spin valves with spin-engineered domain-biasing scheme. Appl. Phys. Lett. **82**, 4107–4109 (2003)
29. B.D. Tu, L.V. Cuong, T.H.G. Do, T.M. Danh, N.H. Duc, Optimization of planar hall effect sensor for magnetic bead detection using spin-valve NiFe/Cu/NiFe/IrMn structures. J. Phys. Conf. Ser. **187**, 012056 (2009)
30. T.Q. Hung, S. Oh, J.R. Jeong, C. Kim, Spin-valve planar hall sensor for single bead detection. Sens. Actuat. a-Phys. **157**, 42–46 (2010)
31. M. Volmer, J. Neamtu, Optimisation of spin-valve planar hall effect sensors for low field measurements. IEEE Trans. Magn. **48**, 1577–1580 (2012)
32. K.M. Chui, A.O. Adeyeye, M.H. Li, Detection of a single magnetic dot using a planar hall sensor. J. Magn. Magn. Mater. **310**, E992–E993 (2007)
33. M. Volmer, J. Neamtu, in *Micromagnetic Analysis and Development of High Sensitivity Spin-valve Magnetic S*ensors. 5th International Workshop on Multi-Rate Processes and Hysteresis, vol. 268 (Murphys, 2010)
34. C. Christides, S. Stavroyiannis, D. Niarchos, Enhanced planar hall voltage changes measured in Co/Cu multilayers and Co films with square shapes. J. Phys. Condens. Mat. **9**, 7281–7290 (1997)
35. K.M. Chui, A.O. Adeyeye, M.H. Li, Effect of seed layer on the sensitivity of exchange biased planar hall sensor. Sens. Actuat. a-Phys. **141**, 282–287 (2008)
36. T.Q. Hung, S. Oh, B. Sinha, J.R. Jeong, D.Y. Kim, C. Kim, High field-sensitivity planar hall sensor based on NiFe/Cu/IrMn trilayer structure. J. Appl. Phys. **107**, 09E715 (2010)

37. F.W. Osterberg, G. Rizzi, T.Z.G. de la Torre, M. Stromberg, M. Stromme, P. Svedlindh et al., Measurements of Brownian relaxation of magnetic nanobeads using planar hall effect bridge sensors. Biosens. Bioelectron. **40**, 147–152 (2013)
38. S. Oh, S. Anandakumar, C. Lee, K.W. Kim, B. Lim, C. Kim, Analytes kinetics in lateral flow membrane analyzed by cTnI monitoring using magnetic method. Sens. Actuat. B-Chem. **160**, 747–752 (2011)
39. S. Oh, P.B. Patil, T.Q. Hung, B. Lim, M. Takahashi, D.Y. Kim et al., Hybrid AMR/PHR ring sensor. Solid State Commun. **151**, 1248–1251 (2011)
40. F. Qejvanaj, M. Zubair, A. Persson, S.M. Mohseni, V. Fallahi, S.R. Sani et al., Thick double-biased IrMn/NiFe/IrMn planar hall effect bridge sensors. Magn. IEEE Trans. **50**, 1–4 (2014)
41. F.W. Osterberg, A.D. Henriksen, G. Rizzi, M.F. Hansen, Comment on "Planar Hall resistance ring sensor based on NiFe/Cu/IrMn trilayer structure" [J. Appl. Phys. 113, 063903 (2013)], J. Appl. Phys. **114** (2013)
42. B. Sinha, T. Quang Hung, T. Sri Ramulu, S. Oh, K. Kim, D.-Y. Kim, et al., Planar hall resistance ring sensor based on NiFe/Cu/IrMn trilayer structure. J. Appl. Phys. **113**, 063903 (2013)
43. V. Mor, M. Schultz, O. Sinwani, A. Grosz, E. Paperno, L. Klein, Planar hall effect sensors with shape-induced effective single domain behavior. J. Appl. Phys. **111**, 07E519 (2012)
44. T. Musha, Physical background of Hooge's α for 1/f noise. Phys. Rev. B **26**, 1042–1043 (1982)
45. M.A.M. Gijs, J.B. Giesbers, P. Beliën, J.W. van Est, J. Briaire, L.K.J. Vandamme, 1/f noise in magnetic Ni80Fe20 single layers and Ni80Fe20/Cu multilayers. J. Magn. Magn. Mater. **165**, 360–362 (1997)
46. J.A. Osborn, Demagnetizing factors of the general ellipsoid. Phys. Rev. **67**, 351–357 (1945)
47. C. Tannous, J. Gieraltowski, A Stoner-Wohlfarth model redux: static properties. Phys. B **403**, 3563–3570 (2008)
48. M.D. Donahue, D. Porter, OOMMF. http://math.nist.gov/oommf/
49. C.C. Chang, Y.C. Chang, W.S. Chung, J.C. Wu, Z.H. Wei, M.F. Lai et al., Influences of the aspect ratio and film thickness on switching properties of elliptical permalloy elements. Magn. IEEE Trans. **41**, 947–949 (2005)
50. A. Grosz, V. Mor, E. Paperno, S. Amrusi, I. Faivinov, M. Schultz, et al., Planar hall effect sensors with subnanotesla resolution. IEEE Magn. Lett. **4**, 6500104 (2013)
51. A. Grosz, V. Mor, S. Amrusi, I. Faivinov, E. Paperno, L. Klein, A high resolution planar hall effect magnetometer for ultra-low frequencies. IEEE Sensors J. **16**, 3224–3230 (2016)
52. D. Grieshaber, R. MacKenzie, J. Voros, E. Reimhult, Electrochemical biosensors—sensor principles and architectures. Sens. Basel **8**, 1400–1458 (2008)
53. J.M. Kahn, R.H. Katz, K.S.J. Pister, Emerging challenges: mobile networking for smart dust. Commun. Netw. J. **2**, 188–196 (2000)

Giant Magnetoresistance (GMR) Magnetometers

Candid Reig and María-Dolores Cubells-Beltrán

Abstract Since its discovering in 1988, the Giant Magnetoresistance (GMR) effect has been widely studied both from the theoretical and the applications points of view. Its rapid development was initially promoted by their extensive use in the read heads of the massive data magnetic storage systems, in the digital world. Since then, novel proposals as basic solid state magnetic sensors have been continuously appearing. Due to their high sensitivity, small size and compatibility with standard CMOS technologies, they have become the preferred choice in scenarios traditionally occupied by Hall sensors. In this chapter, we analyze the main properties of GMR sensors regarding their use as magnetometers. We will deal about the physical basis, the fabrication processes and the parameters constraining their response. We will also mention about some significant application, including developments at the system level.

1 Physical Background

The electric current in a magnetic multilayer consisting of a sequence of thin magnetic layers separated by thin non-magnetic layers is strongly influenced by the relative orientation of the magnetizations of the magnetic layers [1, 2]. More specifically, the resistance of the magnetic multilayer is low when the magnetizations of the magnetics layers are parallel but higher when the magnetizations of the neighbouring magnetic layers are antiparallel. This is due to the spin-dependent scattering. The spontaneous relative orientation between adjacent magnetic layers depend on the the thickness of the spacer layer. Then, by applying an external magnetic field, a change from antiferromagnetic to ferromagnetic (or viceversa) coupling can be achieved, so changing the resultant resistance value.

C. Reig (✉) · M.-D. Cubells-Beltrán
University of Valencia, Valencia, Spain
e-mail: candid.reig@uv.es

M.-D. Cubells-Beltrán
e-mail: m.dolores.cubells@uv.es

A. Grosz et al. (eds.), *High Sensitivity Magnetometers*, Smart Sensors, Measurement and Instrumentation 19, DOI 10.1007/978-3-319-34070-8_8

The magnetoresistance (MR) ratio is, then, generally defined as:

$$\frac{\Delta R}{R} = \frac{R^{\uparrow\downarrow} - R^{\uparrow\uparrow}}{R^{\uparrow\uparrow}} \tag{1}$$

Such behaviour has important applications, initially focusing on magnetic information storage technology. In this sense, P. Grunberg and A. Fert received the Nobel Prize in Physics in 2007 for the discovering of the effect [3].

There are several kind of structures that can display GMR effect [4, 5]. In fact, there have been described and used granular materials with such effect [6]. For engineered applications, multilayer structures are preferred due to their integration feasibility [7]. Typical multilayered structures consist of two or more magnetic layers of a Fe–Co–Ni alloy, as can be permalloy, separated by a very thin non magnetic conductive layer, as can be Cu [5], as sketched in Fig. 1 (left). With magnetic films of about 4–6 nm width and a conductor layer of about 35 nm, magnetic coupling between layers is slightly small. With this configurations, MR levels of about 4–9 % are achieved, and spreading the linear ranges of about 50 Oe [5], good for sensing applications. The figures of merit of these devices can be improved by continuously repeating the basic structure.

Spin valves are a particular configuration of a sandwich structure. In spin valves, an additional antiferromagnetic (*pinning*) layer is added to the *top* or *bottom* part of the structure, as shown in Fig. 1 (right). In this sort of structures, there is no need of an external excitation to get the antiparallel alignment. In spite of this, the pinned direction (easy axis) is usually fixed by raising the temperature above the knee temperature (at which the antiferromagnetic coupling disappears) and then cooling it within a fixing magnetic field. Obviously, so obtained devices have a temperature limitation below the knee temperature. Typical values displayed by spin valves are a MR of 4–20 % with saturation fields of 0.8–6 kA/m [4].

For linear applications, and without excitation, pinned (easy axis) and free layers are preferably arranged in a crossed axis configuration (at 90°), as depicted in Fig. 2. In this way, the linear range is improved and the sign of the external field is detected without the need of an additional magnetic biasing. The response this structure is given by Freitas et al. [8]:

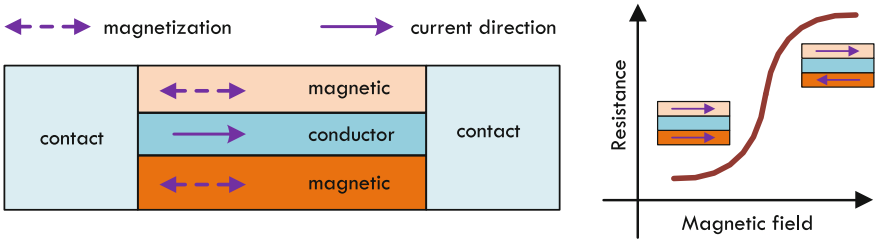

Fig. 1 (*left*) Basic GMR multilayer structure, (*right*) typical response of a basic GMR structure

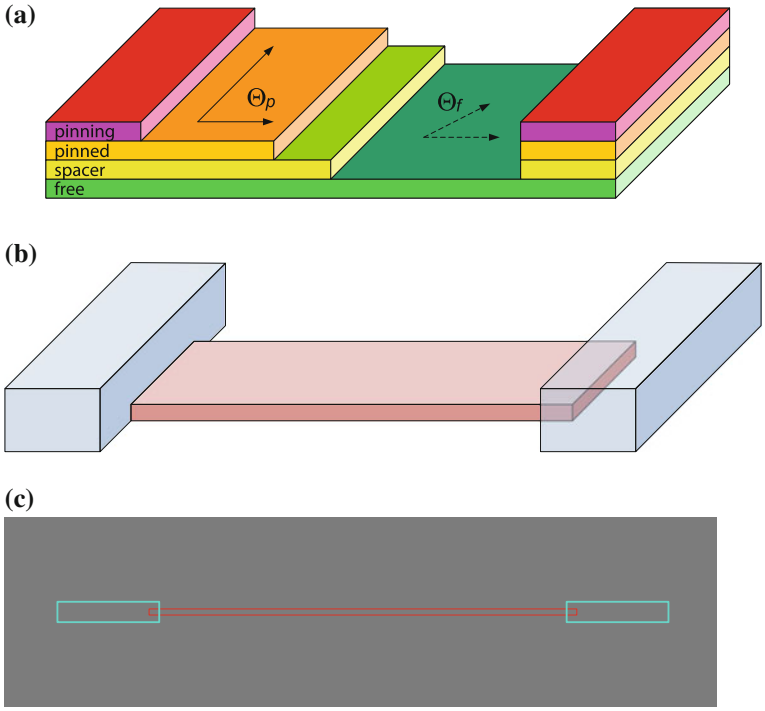

Fig. 2 Basic spin valve scheme: **a** multilayer structure in crossed axis configuration, **b** typical implementation, **c** simplest lithography masks set

$$\Delta R = \frac{1}{2}\left(\frac{\Delta R}{R}\right) R_{\square} \frac{iW}{h} \cos\left(\Theta_p - \Theta_f\right) \tag{2}$$

where $(\Delta R/R)$ is the maximum MR level (5–20 %), $R_{\square}$ is the sensor sheet resistance 15–20 $\Omega/\square$), L is the length of the element, W is its width, h is the thickness, i is the sensor current, and Θ_p and Θ_f are the angle of the magnetization angle of pinned and free layers, respectively. Assuming uniform magnetization for the free and pinned layers, for a linearized output, $\Theta_p = \pi/2$ and $\Theta_f = 0$.

As a practical example, in [9], the spin valve structure was deposited by ion beam sputtering (IBD) onto 3″ Si/SiO_2 1500 Å substrates with a base pressure of $1.0 \times 10^{-8} - 5.0 \times 10^{-8}$ Torr. For IBD deposition, a Xe flow was used for a deposition pressure of 4.1×10^{-5} Torr. The spin valve structure was Ta(20 Å)/NiFe(30 Å)/CoFe(20 Å)/Cu(22 Å)/CoFe(25 Å)/MnIr(60 Å)/Ta(40 Å). This structure has demonstrated to give magnetoresistance responses of about 6–7 %, linear ranges of about 20 Oe and sheet resistivities of about 10–15 $\Omega/\square$) [9]. Deposition rates ranged from 0.3 to 0.6 Å/s. A 40 Oe field was applied to the substrates during the deposition step in order to state the easy axis in the pinned and free layers. The

wafer was 90° rotated between both depositions to ensure a crossed-axis spin valve configuration.

Nano-oxide layers (NOL) inserted in the pinned layer and above the free layer have been found to increase the magnetoresistance ratio up to 19 % [10]. The enhancement of GMR is attributed to the specular scattering effect of the conduction electrons at the metal/insulator interfaces.

In [11], the specular spin valve structure was Ta(3 nm)/NiFe(3 nm)/MnIr(6 nm)/CoFe(1.6 nm)//NOL//CoFe(2.5 nm)/Cu(2.5 nm)/CoFe(1.5 nm)/NiFe(2.5 nm)//NOL//CoFe(2.0 nm)/Ta(0.5 nm). NOL layers were formed in a 15 min natural oxidation step at atmospheric pressure in the deposition tool load lock. The natural oxidation process, keeping its simplicity, has proven to be well effective. Finally, the samples were annealed at 270 °C under vacuum and cooled under a 3 kOe magnetic field applied parallel to the pinned and free layer easy axis.

Giant magnetoresistance can also find in other structures. We collect two illustrative examples. Pena et al. [12] report on giant magnetoresistance in ferromagnet/superconductor superlattices. On the other hand, Pullini et al. [13] describe GMR in multilayered nanowires. In any case, a magnetic/non-magnetic interface is required in order to allow the spin-electron scattering producing the effect.

2 Fabrication

The fabrication of giant magnetoresistance (GMR) devices involves a sort of techniques including deposition, patterning and encapsulation in a similar fashion to those related to standard CMOS processes. Because doping and implantation are not required, they can be considered as low temperature processes. As a guideline, three to five lithography steps are required for fabricating basic GMR devices. They can be deposited on silicon wafers but glass, sapphire or flexible substrates can also be considered.

On Bi-CMOS processes, silicon, silicon oxide and aluminum are the basis materials, as well as the dopants (Boron, Phosphorus, Arsenic, Antimony and related compounds). In the case of GMR devices, the fabrication of magnetic layers requires the use of additional magnetic materials (Iron, Cobalt, Nickel, Manganese, and their alloys), different metals (e.g. Copper, Ruthenium) and additional oxides (Al_2O_3, MgO …), not usually found in conventional semiconductor facilities. Each of these materials has particular requirements in terms of deposition technology and conditions or system contamination that need to be specifically considered and optimized. As a high-lighting example we should mention the deposition of layers with preferentially aligned magnetic moment which requires the use of a polarizing magnet placed inside the deposition system, therefore not easily compatible with hot deposition tools.

2.1 Deposition

As before mentioned, GMR structures are composed of multilayered engineered structures based on nanometric to sub-nanometric thick layers of ferromagnetic materials (e.g.: Co, CoFe, NiFe) separated by a non-magnetic spacer (Cu). Isolation layers are also commonly required. Therefore, adequate deposition techniques namely those using ultra-high vacuum systems and providing a thorough control of the thickness of the deposited layers are essential for the proper functionality of so obtained devices.

2.1.1 Sputtering

Cathodic sputtering is one of the more common physical vapor deposition technique used for depositing thin films onto substrates. Such sputtering process occurs when an accelerated ion hits a solid target material. If the ion kinetic energy is high enough, atoms are extracted from the matrix. A vacuum reaction chamber (usually lower than 10^{-7} Torr) is required. A high voltage is applied to the target holder so producing an electrical discharge that allows the ionization of the gas and hence leads to the plasma. The produced ions are then attracted toward the cathode, hitting the target. The ions with energy above the threshold can extract atoms from the target material. These atoms are deposited onto the substrate, usually facing the target, and thus forming a layer of material.

Regarding specific GMR devices, this method offers the possibility to deposit from a target composed of different materials (alloy or mosaic target). Due to this, sputtering is one of the preferred techniques to deposit metallic and magnetic layers in GMR de-vices. It is also commonly used for the deposition of metallic non-magnetic contacts and also insulating oxides.

2.1.2 Ion Beam Deposition (IBD)

The IBD technique is not as extended as traditional sputtering but it provides a good film thickness uniformity and higher deposition control due to the low deposition rates employed, enabling also epitaxial growth under particular conditions and higher deposition textures. Deposition parameters such as ion flux, energy and sputtered species, as well as the angle of incidence, can be more independently controlled. In this case, the plasma is created and confined in an ion gun being then accelerated towards the target through voltage applied into a grid set. Furthermore, the basic configuration of a typical IBD system normally includes an assist gun, used either for assisted deposition or ion-milling etching. An automatically

interchangeable target holder (4–8 targets) can be used in GMR multilayer deposition without vacuum break, with deposition rates below 1 nm/s.

2.1.3 Chemical Vapor Deposition (CVD)

CVD thin films deposition is based on the decomposition and/or reaction of different gaseous compounds. In this way, the considered material is directly deposited onto the substrate surface from a gas phase.

Deposition usually occurs at high temperatures >300 °C, therefore not compatible with magnetic multilayers. However, since the deposition rates can be very large (therefore fast deposition) and it is a conformal deposition (thus, excellent step coverage), this method is mainly used in the deposition of insulating and passivation layers (silicon oxide or silicon nitride) leading to good quality layers with moderate cost equipment.

2.2 Patterning

GMR structures can be patterned in a similar way than common devices in typical CMOS processes. Well-known ultraviolet (UV) lithography through hard or software designed masks, together with physical or chemical etching processes can be used. In this way, a good ratio cost/reliability is achieved with defined features down to ~ 1 μm. The patterning process of a GMR device consists of sequential steps of pattern design and transfer as illustrated in Fig. 3, with typically three lithography steps, including that for opening contacts.

2.2.1 Photolithography

The photolithography process includes three steps: (i) coating of the sample with a proper photoresist (a radiation sensitive polymer solution); (ii) exposure of the resist, patterning a certain design (mask), previously prepared; (iii) development of the transferred pattern.

Coating

The photoresist is deposited onto the surface of the sample by spin-coating, with controlled conditions of speed, time and amount of resist for a proper thickness and homogeneity of the sensitive layer, which is crucial for the lithography resolution [14]. It is usually required a surface pre-treatment (such as hexamethyldisilizane, HMDS) for promoting the adhesion, and a post-treatment (soft-baking, 80–100 °C) for removing solvents and stress.

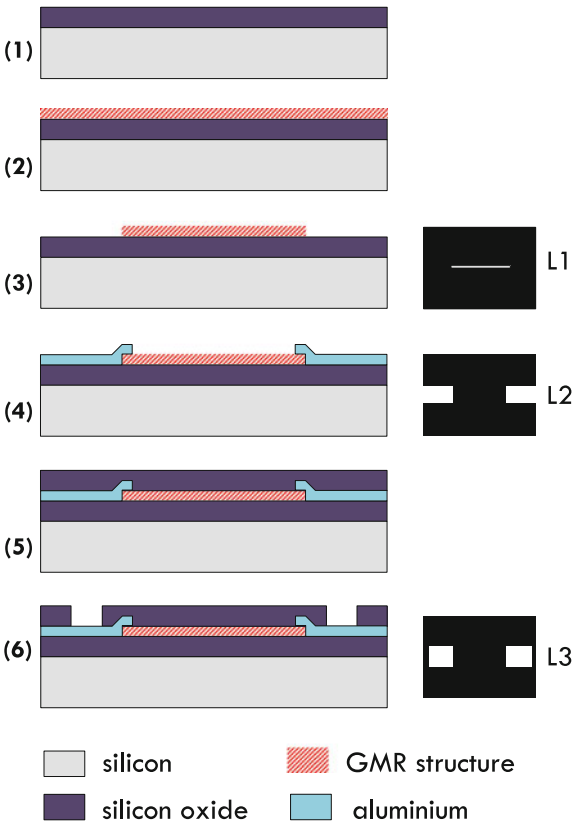

Fig. 3 Typical steps of the patterning procedure in microfabrication of basic GMR devices

Lithography

By using UV radiation (wavelength typically ranging 0.5–0.1 μm) with focused laser beams (direct write systems) or lamps (hard mask aligners), resolutions below 1 μm can be obtained. Due to the commonly limited production volumes of GMR devices, direct write systems are particularly interesting. In this case, a spot of the light beam moves trough the surface in those zones that need to be illuminated, with the help of a precision X-Y system, together with a switching light mechanism. The fabrication of physical masks is, then, not required. This is a versatile and low cost, but slow process (the full exposure of a 150 mm wafer can take more than 12 h, depending on he particular design). If higher resolutions are demanded (<0.5 μm), X-ray, electron or ion beam systems can be used [15].

Development

The development is usually assisted by a soft-baking step before the resist developer is sprayed or spin-coated onto the sample surface. With positive resists, exposed regions have turn soluble during the exposure and are removed at this moment. For negative resits, exposed regions turn harder and remain after

developing. In any case, the sample is then washed to stop the development process and dried. The pattern has been printed into the resist layer.

2.2.2 Pattern transfer techniques

We will consider two options: etching and lift-off.

Etching

It is a process concerning the capability of removal undesired portions of a deposited layer. Such a selective property is provided by the patterned resist mask, but also by the characteristics of the involved layers. The starting point is usually the film to be patterned deposited on a substrate with the desired pattern defined in the top resist mask,

Dry etching. Physical (dry) etching is commonly achieved by using plasma etching (reactive etching or an ion beam system) providing a controlled removal of material. Ion beam etching (ion milling), in particular, offers slow (below 0.2 nm/s) but very controlled and stable etching ratios and it is usually used for the patterning of GMR devices [15]. It is an anisotropic process with etching efficiency depending on the material type and the incident angle [16].

Wet etching. For chemical (wet) etching, corrosive properties of some substances (usually acids) are used. In this way, wet etching can be patterned with polymer based resists, due to their intrinsic organic nature, resistant to the inorganic acids action. Tables with specific etchers for the different materials, with associated speeds can be found in the literature [17]. Due to its aggressive and isotropic nature, wet etching is not commonly used for patterning GMR structures and is mostly used for processes like opening contacts/vias.

3 Noise

Real performances of GMR magnetometers can only be estimated when compared with their intrinsic noise sources. The noise power spectrum density (PSD) is commonly given in V^2/Hz. Often, is much more convenient to use the amplitude spectrum density (ASD), expressed in $V/\sqrt{Hz}$ for comparison with voltage signals. The sensitivity for a magnetoresistance signal, S_V is usually given in V/V/T. Typical values for GMR sensors are 20–40 V/V/T, e.g., 20–40 nV/nT when they are biased with 1 V. For comparing different sensors, it is recompensable to use the field equivalent noise power spectra density, sometimes called *detectivity*. It corresponds to the PSD divided by the sensitivity. For example, if a sensor displays a noise of $10\,nV/\sqrt{Hz}$ at a given frequency and a sensitivity of 25 V/V/T, its detectivity will be 400 pT for 1 V bias.

3.1 Types of Noise in GMR Magnetometers

3.1.1 Thermal Noise

The most relevant noise is the thermal noise (also called Johnson-Nyquist noise or white noise), which is directly related to the resistance of the sensor. It is a *white* noise, so it is independent of the frequency. It was first observed by Johnson [18] and interpreted by Nyquist [19]. It is expressed as:

$$S_V(\omega) = \sqrt{4Rk_BT} \tag{3}$$

where R is the sensor resistance, k_B is the Boltzmann constant and T is the temperature. For example, a 1 kΩ resistor at room temperature has $4\,\mathrm{nV}/\sqrt{\mathrm{Hz}}$.

3.1.2 1/*f* Noise

The origin of the 1/*f* noise or 'pink' noise or Flicker noise is on resistance fluctuations, so it can only revealed by applying a current into the sensor. Its dependence with the frequency is described by the following phenomenological formula:

$$S_V(\omega) = \frac{\gamma_H R^2 I^2}{N_C f^\beta} \tag{4}$$

where γ_H is a dimensionless constant proposed by Hooge [20], R is the sensor resistance, I is the bias current, N_C is the number of current carriers, f is the frequency and β is an exponent typically in the order of 1. 1/*f* noise can exhibit a non magnetic and a magnetic component with possible different slopes. The size and the shape of the sensors have a strong effect on the 1/*f* noise. Due to its average nature, and as followed by Ec. 4, small GMR sensors display more 1/*f* noise than bigger ones. By considering equally thin sensors, the 1/*f* noise is roughly inversely proportional to their area [21].

3.2 Noise Measurement in GMR Devices

Noise measurement is a difficult task that needs to be carefully performed. A standard measurement system should comprise the sensor (device-under-test, DUT), a low noise biasing source (usually batteries), a low noise amplifier (it can be composed of different stages), filtering and acquisition/processing system, as this depicted in Fig. 4. In some occasions, last two parts can be replaced by a spectrum analyzer. A particular implementation is also shown in Fig. 4 including a National Instruments data acquisition (DAQ) card (24 bits of resolution, 200 kHz bandwidth

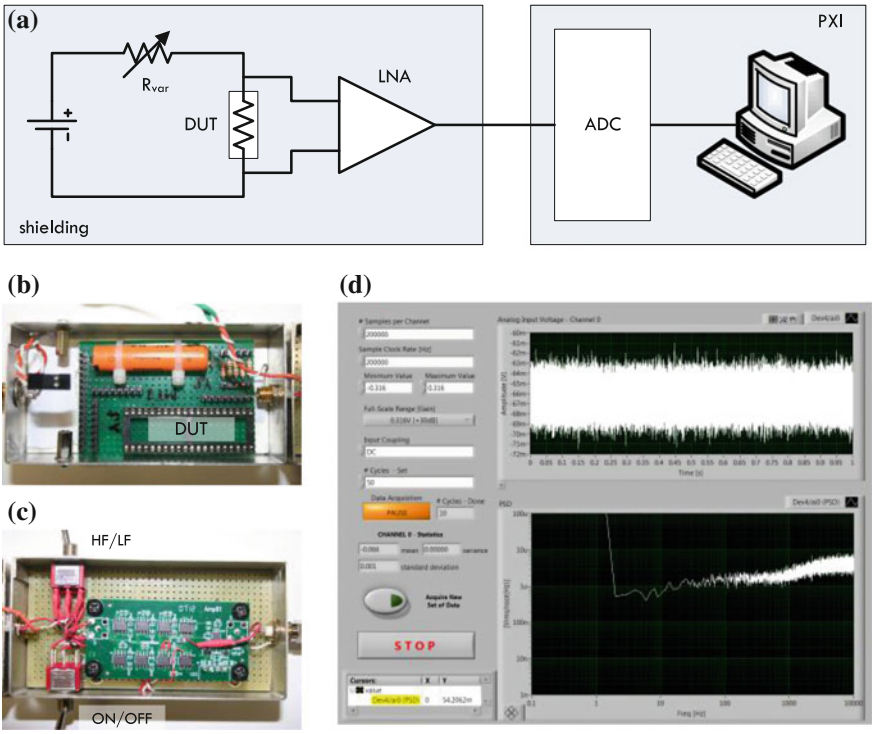

Fig. 4 Noise measurement system: **a** basic setup, **b** detail of the bias and shielding of the DUT, **c** a specifically designed LNA, **d** aquisition and processing software

and noise spectral density of $8\,\mathrm{nV}/\sqrt{\mathrm{Hz}}$ at 1 kHz) and a low-noise amplifier ($2\,\mathrm{nV}/\sqrt{\mathrm{Hz}}$ noise in a frequency band from 0.3 Hz to 100 kHz and voltage gain of 1000). Devices and bias batteries are shielded. A LabView program is used for controlling the system and obtaining the ASD.

As a representative example, we will give noise data on spin valves based on multilayered structures [Ta(20 Å)/NiFe(30 Å)/CoFe(20 Å)/Cu(22 Å)/CoFe(25 Å)/MnIr(60 Å)/Ta(40 Å)] patterned on strips of $3 \times 200\,\mu\mathrm{m}^2$. Measured sensitivity was 20 mV/mT (1 mA bias). Measured bandwidth was above 1 MHz [22]. The measured noise is shown in Fig. 5a, b. The $1/f$ behaviour is clearly observed and the thermal noise limit well defined. If we take into account the measured sensitivity, we can draw the detectivity understood as the field equivalent noise, that is drawn in Fig. 5c, d. The benefits of the frequency is clearly stated. The increase of the bias current has an impact on the field detectivity at higher frequencies, but there is no effect in the $1/f$ regime [21].

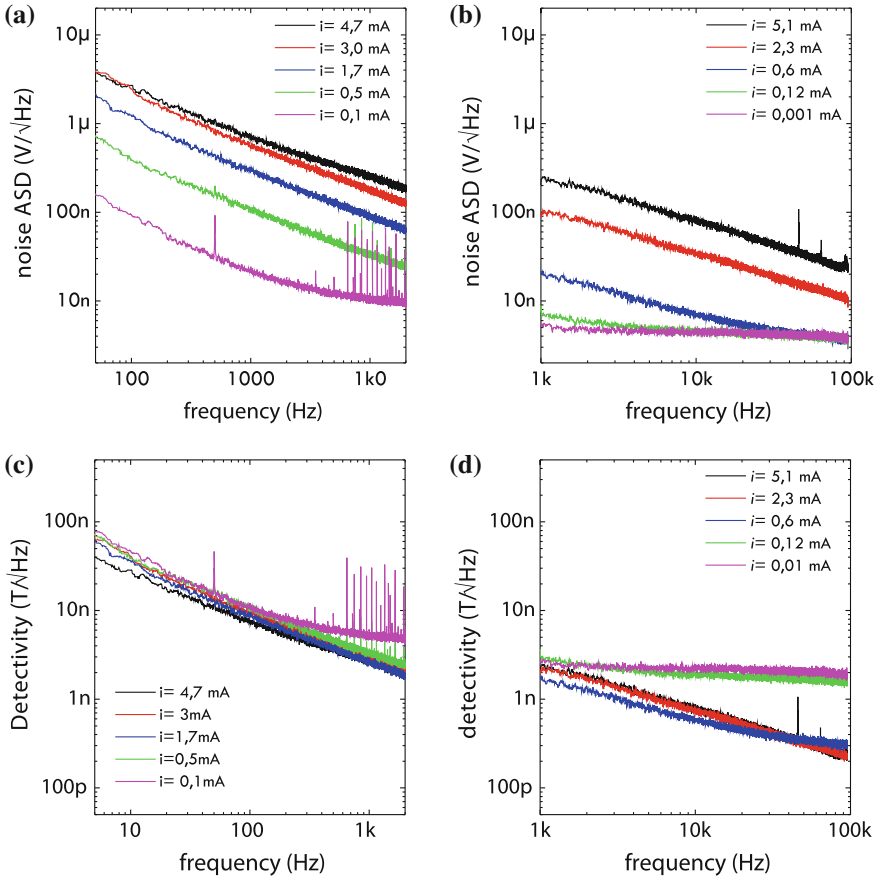

Fig. 5 Noise measurement data on $3 \times 200\ \mu m^2$ spin valves as described in [22]: **a** low frequency noise, **b** high frequency noise, **c** low frequency detectivity, **d** high frequency detectivity

3.3 Improving the Detectivity

Once the main parameters have been introduced, we follow with some suggestion for improving the detectivity in GMR based magnetometers, as discussed in [23].

- Structures with high sensitivity (high MR level) should be considered in order to maximize the output signal. Then, the signal to noise ratio (SNR) needs to be calculated. In this sense, tunnel magnetic resistance (TMR) devices display sensitivities higher than those from GMR, but with a noise level that is typically three times higher. Then, a triple MR level is required for achieving the same SNR. On the other hand, linear ranges should be kept as narrow as possible in

Table 1 Field equivalent noise of GMR as dependant on the dimensions

	Size	Noise at 1 Hz	White noise	Power consumption
Small GMR	150 × 4 μm^2	10 nT	50 pT	5 mW
Large GMR	1 mm^2	100 pT	20 pT	100 mW

order that the pendent in the response (and then the sensitivity) is as high as possible [see Fig. 1 (right)]

- Due to the statistical nature of noise, this is reduced with the increasing of the sensor size, by means of the Hooge parameter. From [21], the values in Table 1 can be extracted.
- The frequency of operation should be stated as high as possible in order to minimize the 1/*f* noise effect. This can hardly done by modulating the measured field with additional loops or by placing the sensing elements onto oscillating cantilevers [23].
- The use of flux guide concentrators allows, in some cases, to have a magnetic field amplification up to one hundred. In addition, the deposition of high permeability materials is compatible with the patterning and deposition processes described above.

4 Thermal Effects

The temperature is always a limiting parameter in electronics. Every electronic device has temperature depending response arising from its physical nature. Regarding specific GMR electrical current sensors, not only the resistance (and then the sensor impedance) varies with the temperature. Also the MR level (and then the sensitivity) does.

The resistance of GMR sensors, like common resistances, is a function of the temperature. For GMR based devices, and in the usual range of utilization, this dependence can be considered as linear, and can be defined by a temperature coefficient (TEMPCO) as following:

$$TCR(\%) = 100 \times \frac{1}{R_{T_0}} \frac{\Delta R}{\Delta T} \tag{5}$$

An analogue relationship can be defined for the thermal dependence of sensitivity, as:

$$TCS(\%) = 100 \times \frac{1}{S_{T_0}} \frac{\Delta S}{\Delta T} \tag{6}$$

When a full bridge configuration is considered, this thermal dependence is partially compensated and is expected to be low. Due to the inherent voltage offset of sensors configured as bridges, the temperature drift of the offset voltage must be specified::

$$TCV_{off}(\%) = 100 \times \frac{\frac{\Delta V_{off}}{\Delta T}}{V_{off,T_0}} \tag{7}$$

Moreover, the output voltage has also a thermal dependence, defined as:

$$\begin{aligned} TCV_o(\%) &= 100 \times \frac{1}{\Delta T}\frac{V_{o,T_i} - V_{o,T_0}}{V_{o,T_0}} \\ V_{o,T_i} &= V_{out,T_i} - V_{off,T_i} \end{aligned} \tag{8}$$

Experimental parameters are only related to the nature of the GMR structures, and they have been measured elsewhere. In Fig. 6 we show typical values for full bridge sensors composed of equal spin valve elements, as described in [22]. From these graphs we can extract $TCR \approx 0.11$ %/°C, $TCV_{off} < 10$ μV/°C and $TCS \approx -0.15$ %/°C.

Compensation techniques

Assumed that thermal effects cannot be completely eliminated, various methods of temperature compensation have been reported in the literature addressed to reduce the thermal drift output of Wheatstone bridge type sensors. These methods can be differentiated as noninvasive and invasive. As noninvasive we mean a technique consisting of the addition of different circuit elements in series or parallel to the bridge in order to reduce its thermal drift, as described, for example in [24]. A temperature sensor, a fixed resistor, some kind of active network (diode or transistor) or a fixed current source have been successfully applied. This way, the addition of one of the above elements results in a change of the bridge supply voltage due to the temperature variation, which produces a valid compensation.

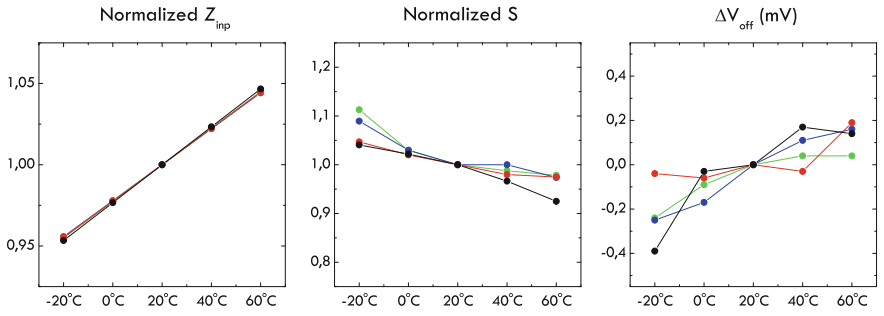

Fig. 6 Experimental thermal parameters of typical GMR structures

A slightly different approach consists of the connection of a temperature variable gain instrumentation amplifier in cascade at the output of the bridge. On the other hand, a Wheatstone bridge can also be temperature compensated by means of the modification of its original configuration. In this case, we should ensure that the terminals of the bridge are externally accessible. This group of techniques can be considered as invasive, due that the conditioning circuitry in common commercial sensors make the bridge terminals often inaccessible. An excellent revision of these works is made in [25]. In addition, in the same work is presented a novel application of the Generalized Impedance Converter (GIC) as a thermal compensating biasing circuit for specific magnetoresistive sensors.

5 Electronic Interfaces

From the macroscopic point of view, a GMR sensor behaves as a resistance. In this sense, in order to get a useful electrical signal, traditional schemes applied to resistive sensors can be considered.

5.1 Resistive Bridges

Although single elements or basic voltage dividers can be also considered, to arrange a resistive senor in a bridge configuration has clear advantages in terms of the signal level, linearization, voltage offset and immunity against external undesired perturbations. As a clear example, we can observe the benefits of such configuration from data in 6. In this sense, we can make use of bridges with a unique sensing element, half bridges or full Wheatstone bridges. For getting half bridge sensors, and due to the requirement of polarization of the magnetic moments of the layers, two of the four sensing elements must be inactive, usually got by depositing patterned magnetic shielding layers [26]. It should be noted that, if a full Wheatstone bridge is considered, the fabrication involves two steps (see Fig. 7).

5.2 Amplification

Due to the low signals involved, low noise amplifiers (LNA) are usually necessary. Noise sources in operational amplifiers can be:

- *Input-referred voltage noise*. It can be modeled with a noise voltage source. As an example, such a noise is typically : $30\,\mathrm{nV}/\sqrt{\mathrm{Hz}}$ @1 kHz in a 741 general purpose opamp and lower than $1\,\mathrm{nV}/\sqrt{\mathrm{Hz}}$ in an specific LNA.

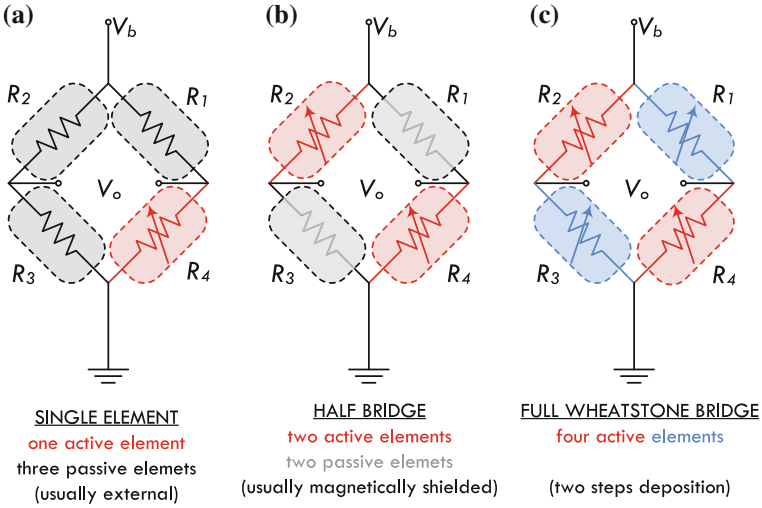

Fig. 7 Arrangements of GMR elements in bridges: **a** Single element, **b** Half bridge, **c** Full wheatstone bridge

- *Input-referred current noise*. It can be modeled as two noise current sources pumping currents through the two differential input terminals). Its value can range from : $10\,\text{pA}/\sqrt{\text{Hz}}$ @1 kHz in general purpose amplifiers to : $10\,\text{fA}/\sqrt{\text{Hz}}$ @1 kHz in specific LNAs.
- *Flicker* (1/*f*) *noise*. Due to the fabrication process, the IC device layout and the device type. It has a rate of $\sim$3 dB/oct for CMOS amplifiers, $\sim$4.0 dB/oct for bipolar amplifiers and $\sim$5 dB/oct for JFET amplifiers,

In this sense, lock-in amplifiers (LIA) [27] and *chopper* amplifiers [28] are the preferred choices.

5.3 Biasing

The correct use of GMR devices implies a proper biasing scheme both from the electric and magnetic point of view. Assuming a resistor bridge configuration, a constant voltage source can be used to feed the sensor, through two opposite vertex of the bridge. The differential output voltage is taken from the remaining pins. Nevertheless, it has been demonstrated that thermal characteristics (temperature drifts) of spin valve based sensors are notably improved by using a constant current source for the sensor feeding [29]. In addition, it has been demonstrated that an ac biasing applied GMR based devices notably improves their performance in terms of linearity, hysteresis, offset and noise [30].

Once the sensor is fed and the bias point set, it can be slightly modified by applying an external magnetic field. This external magnetic field adds (with sign) to

the measured signal and the operation point is then shifted. In a certain way, an offset correcting coil can also be understood as an additional biasing, as presented here. When no helping coils are present, a permanent magnet can also be used. In this case the system has to be carefully designed. A proper magnetic biasing can, for example, to convert to bipolar a GMR device, by displacing the quiescent point to the middle of the output function [30].

5.4 Resistance to Time Approaches

Regarding interfacing, in typical resistor-based sensor applications (such as GMR), the resistive sensing devices are usually dc biased. The generated output signal is taken as an analogue dc voltage level, by employing traditional resistance-to-voltage (*R–V*) conversion approaches and, commonly, by also making use of amplifiers and filters, as previously described. As well known, these voltamperometric solutions usually display undesired voltage offsets that need to be specifically calibrated/corrected or taken into account. When compared with *R–V* converters, front-end schemes using ac excitation have been demonstrated highly advantageous for wide range devices or with unknown nominal/baseline values by improving the immunity to voltage offset, noise and frequency disturbs [15]. These approaches perform resistance-to-frequency (*R–f*) or voltage-to-frequency (*V–f*) conversions so providing a direct quasi-digital output whose frequency depends on the sensor resistance value. In addition, since the ac excitation of the sensor is made through a closed feedback loop, the output frequency is theoretically independent from the power supply level. They generally do not require any calibration procedure and/or manual adjustments and the output signal can be directly connected to the digital part of a system, making these solutions particularly interesting for A/D mixed-signal applications. Moreover, these solutions can be easily used in integrated CMOS designs and SoCs since they are typically implemented with a reduced number of active/passive components.

We can consider several approaches as described in Fig. 8.

A simple astable multivibrator implemented with transistors (not necessarily bipolar), as this depicted in Fig. 8a has an oscillation period given by:

$$T = \ln(2)(R_2C_1 + R_3C_2) \tag{9}$$

then, by making R_2 and/or R_3 variable, we get our objective.

An oscillator can also be implemented by using an integrated 555 circuit, as shown in Fig. 8b. In this case, we get a square wave with a high level during t_1 and a low level during t_2, being:

$$t_1 = \ln(2)(R_1 + R_2)C; t_2 = \ln(2)(R_2)C \quad \text{so} \quad T = \ln(2)(R_1 + 2R_2)C \tag{10}$$

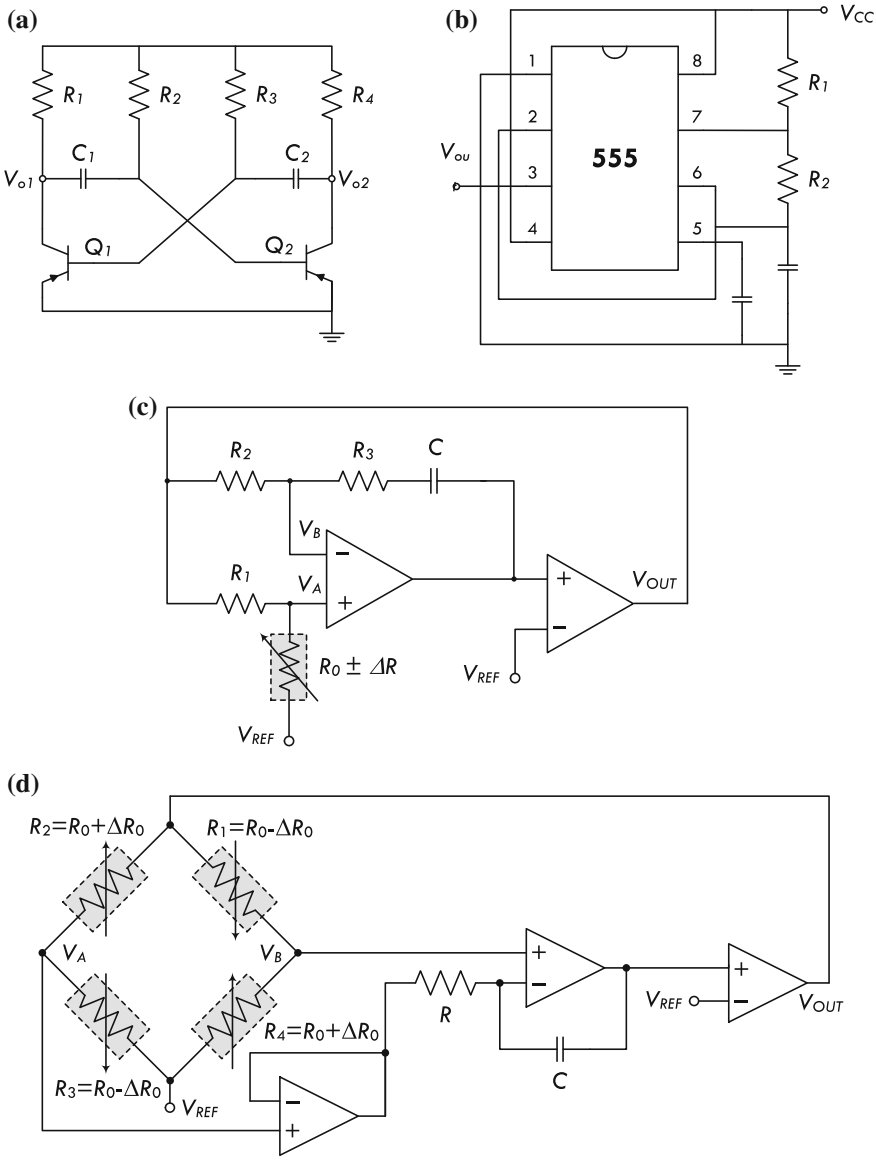

Fig. 8 Differente *R*-to-*t* approaches for resistive GMR devices: **a** basic transistor based astable, **b** astable with 555 IC, **c** circuit with operational amplifiers for single resistors, **d** circuit with operational amplifiers for resistive bridges

More complex approaches can be developed with active elements like opamps as displayed in Fig. 8c and detailed in [31]. In this case,

$$T = \frac{4C_1}{R_1} R_0 (R_0 \pm \Delta R_0) - R_1 R_3 \tag{11}$$

If we are dealing with resistive bridges, we can make use of the circuit in Fig. 8d, where:

$$f = \frac{1}{2RC} \left(\frac{R_4}{R_1 + R_4} \frac{R_3}{R_2 + R_3} \right) \tag{12}$$

Circuits shown in Fig. 8c, d have been successfully used with discrete elements and in integrated circuit form and for GMR spin valve sensing elements and bridges for sub-mA electric current measurements, as described in [31]. Obtained oscillograms are shown in Fig. 9. As observed, sensitivities of 0.8 Hz/mA and 0.68 Hz/μA are obtained which are excellent numbers for these purposes.

5.5 *Arrays*

Arrays of sensors are required for specific applications such as non-destructive evaluation/testing (NDE/NDT) [32, 33], bio-technology systems [34–36] or other magnetic imaging requirements [37, 38]. In general, the access to each individual element involves two electrical/physical connections resulting in a total of $2 \times [N \times M]$ connections. In these particular conditions, read out interfaces for such arrays are a matter of concern [39, 40], usually involving analogue multiplexers and shared amplifiers [41].

5.6 *Compatibility with CMOS Technology*

Non Volatile Electronics (NVE) was the first company in merging both technologies by using a dedicated 1.5 m BiCMOS technology [42]. Later, Han et al. used chips made by 0.25 m NSC (National Semiconductor Corporation) BiCMOS technology [43], by applying a post-process that employed reactive ion etching for via opening through the passivation, so allowing access to the buried metal layers. Then, by combining the design rules for CMOS chips with the techniques for GMR device microfabrication allows the full integration of these sensors with the required electronics (e.g., bias and conditioning circuits, signal processing, memory elements, etc.). Recent achievements regarding the monolithic integration of GMR structures onto standard CMOS circuitry is summarized in Fig. 10. The fabrication of spin valve based magnetic field sensing devices directly onto processed chips

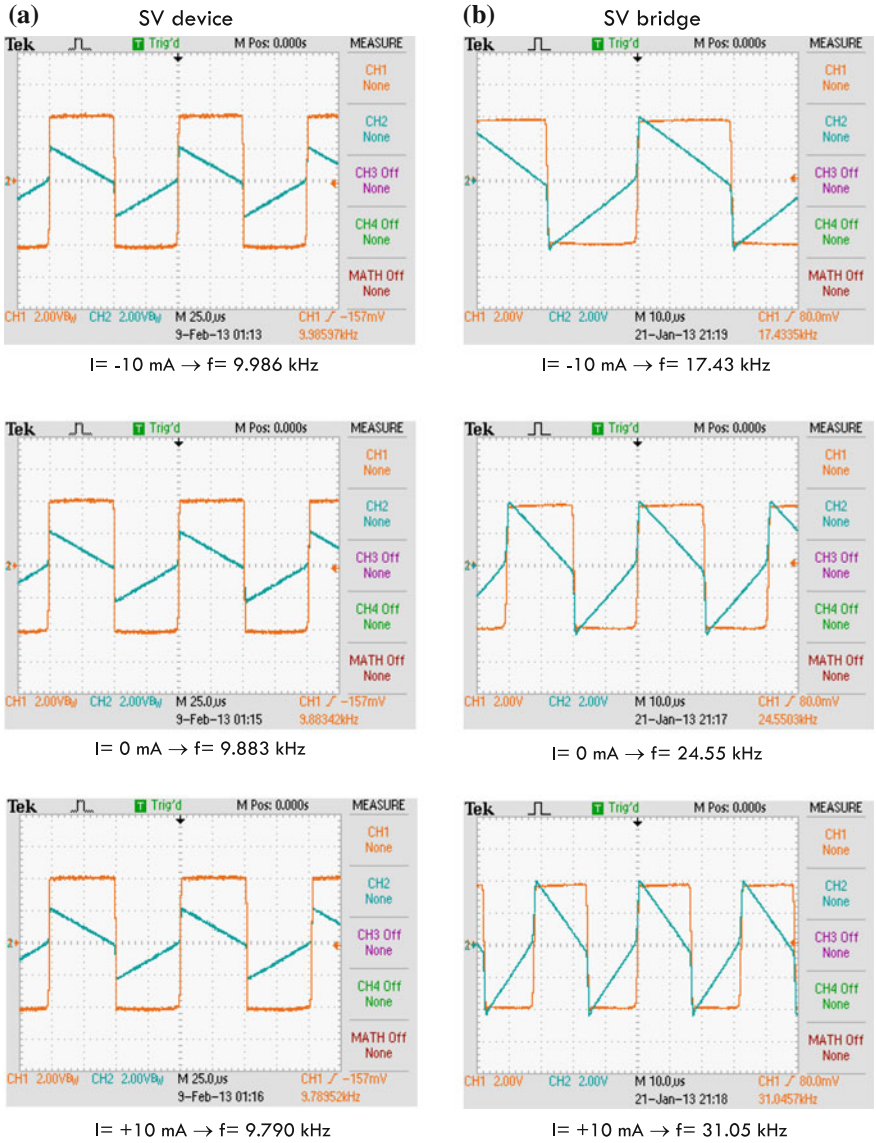

Fig. 9 Experimental oscillograms: **a** from *R*-to-*t* circuit and single GMR devices (Fig. 8c), **b** from *V*-to-*f* circuit and GMR Wheatstone bridges (Fig. 8d)

(from non-dedicated CMOS standard technologies) is described in [44] (see Fig. 10a). Functional devices are successfully developed with an standard 0.35 μm AMS technology and with a non commercial CNM 2.5 μm technology (see Fig. 10b). Due to its extended use, the AMS 0.35 μm process has also recently used for integrated current sensing at the integrated circuit level [45, 46] (see Fig. 10c).

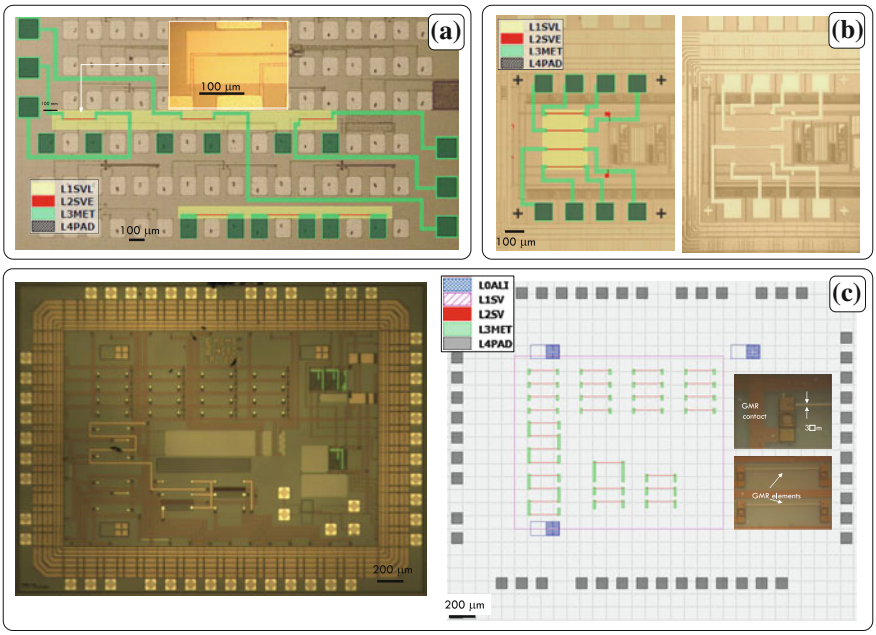

Fig. 10 Real monolithic integration of GMR structures onto pre-processed CMOS chips: **a** wafers from CNM25 non-commercial technology [44], **b** non-dedicated AMS 0.35 µm technology [44], **c** specifically designed AMS 0.35 µm chip for sub-mA current sensing [46]

6 Commercially Available Sensors

GMR is a relatively novel technology. At this moment, up to our knowledge, only few companies (NVE, Infineon and Sensitec) have released GMR linear sensors to the market, beyond the preliminary application on read heads. Other companies include anisotropic magnetoresistance (AMR) based sensors to their portfolio (Honeywell, Zetex, Sypris, Philips and ADI).

NVE

NVE is the world leader company in analog GMR sensing technology. It has a complete catalog [47] with sensors with different magnetic field range applications. Focusing on analog applications, their devices are unipolar (not able to detect sign, see Fig. 11a) and they are based on half bridges (two opposite shielded magnetoresistors) with magnetic flux concentrators. Sensitivities range from 5 to 10 mV/V/mT, with linear ranges from ± 0.1 to $\pm$ 7 mT and an input resistance of about 5 kΩ. They have described a good number of successful applications such as general magnetometry, electric current sensing, magnetic media detection and currency detection and validation.

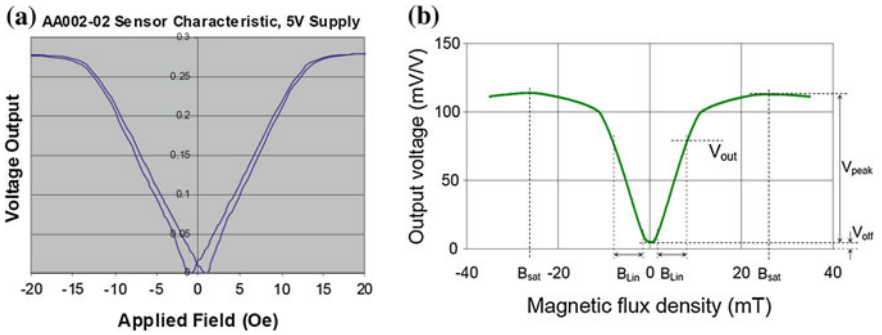

Fig. 11 Output characteristic of two representative GMR commercial sensors: **a** AA002-02 from NVE (reprinted from [47]), **b** GF705 from Sensitec (reprinted from [49])

Infineon

Infineon has developed a line of sensors mainly focusing on the automotive market, with angle sensors and encoders. They release ICs including the associated electronics. A detailed explanation of the functionality can be found in [48].

Sensitec

Sensitec has recently developed GMR sensors for general magnetic field sensing and magnetic encoding also based on unipolar half bridges (see Fig. 11b). Sensitivity is in the order of 10 mV/V/mT with linear range from ±1 to ± 8 mT and input resistance about 5 kΩ.

It is also interesting to compare the noise figure of GMR sensor against those of standard AMR and Hall based, in order to highlight their detectivity level. Such a comparison is made in Fig. 12.

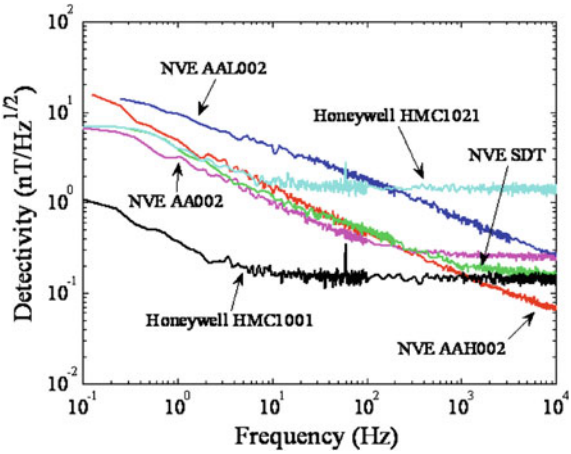

Fig. 12 Comparison of noise performance among commercially available magnetoresistive sensors (reprinted with permission from [50])

7 Successful Applications

7.1 General Magnetometry

The most of the applications developed with GMR magnetic field sensing is related to the measurement of the Earth's magnetic field perturbations produced by specifically considered ferreous body. This way, a position detecting scheme is always present.

For example, it is possible to use GMR sensors to locally measure the small magnetic perturbations caused by the iron of the car's body over the Earth's magnetic field. Moreover, if we use GMR gradient type sensors, the output signal is only dependent on the magnitude of the magnetic field variation, and no additional external magnetic field compensation is required. This way, a voltage 'signature' is obtained from the differential output of such a sensor when a car is running close to it. Within this scheme, it is easy to incorporate another sensor, placed to a well known distance in order to also measure the car speed. This proposal has been successfully developed by Pelegrí et al. [51].

The same physical principle can be directly translated to the measurement of vibrations in industrial machines. The small magnetic variations over the Earth's field produced by the vibration of the ferromagnetic pieces in industrial installations can be converted into resistance variations by the use of GMR magnetic field gradient devices. By using three sensors with the appropriated XYZ arrangement, a complete description of the vibration can be obtained. A prototype was developed by PelegrÍ et al. [52] and successfully tested with a drilling machine.

For linear magnetic position, in addition to the measurement of the Earth's field variations produced by magnetic materials, we can also use, if possible, permanent magnets associated to the moving part of the system. This way, the measurement of the absolute magnetic field is considered. Arana et al. [6] reported on the design of a high sensitivity linear position sensor using granular GMR devices. Sensitivities above 10 mV/V/mm are demonstrated by the utilization of Nd-Fe-B (0.4 T) magnets.

Angle and circular position detectors are also demanded by the industry: automotive applications, rotational machinery, etc. This kind of sensors are usually designed as contact-less systems in which a magnetic sensor (GMR in our case) detects the relative angular position of a rotationally moving magnet. This is the case presented in [53, 54]. In the first case the authors focus on their specifically designed sensor, based on a granular MR. Because of the independence on the magnetic field direction, this technology is optimal for cylindrical symmetry problems. When a NdFeB is used, sensitivities about 0.25 mV/V/° are achieved.

The conservative aerospace sector traditionally used old and well experimented components in its developments. The utilization of brand new technologies in commercial of the shelf (COTS) for space missions is nowadays only in the nearly stage. COTS are cheaper, faster in delivering and with wider reliability. Michelena et al. [55–57] introduce the possibility of using GMR commercial sensors in space

applications. GMR sensors have not been flown yet but INTA, the Spanish National Institute of Aerospace Technology is working on the adaptation of a miniaturized GMR three axis sensor (HMC2003, from Honeywell) to the attitude control system in the frame of the OPTOS project, which is a $10 \times 10 \times 10\,\text{cm}^3$ Picosat devoted to be technological test bed. The circuitry consist of conditioning and biasing electronics blocks.

7.2 Current Sensing

Electrical current can be indirectly monitored with the measurement of the generated magnetic field by means of GMR sensors. In this way, we can achieve a measurement that is sensitive, isolated and from dc up to the bandwidth of the sensors, theoretically in the range of GHz.

In the medium to high current range, a specific full bridge spin valve sensor for industrial applications is designed, characterized, implemented and tested in [58]. After soldering it onto a PCB strap, it is able to monitor currents up to 10 A. An

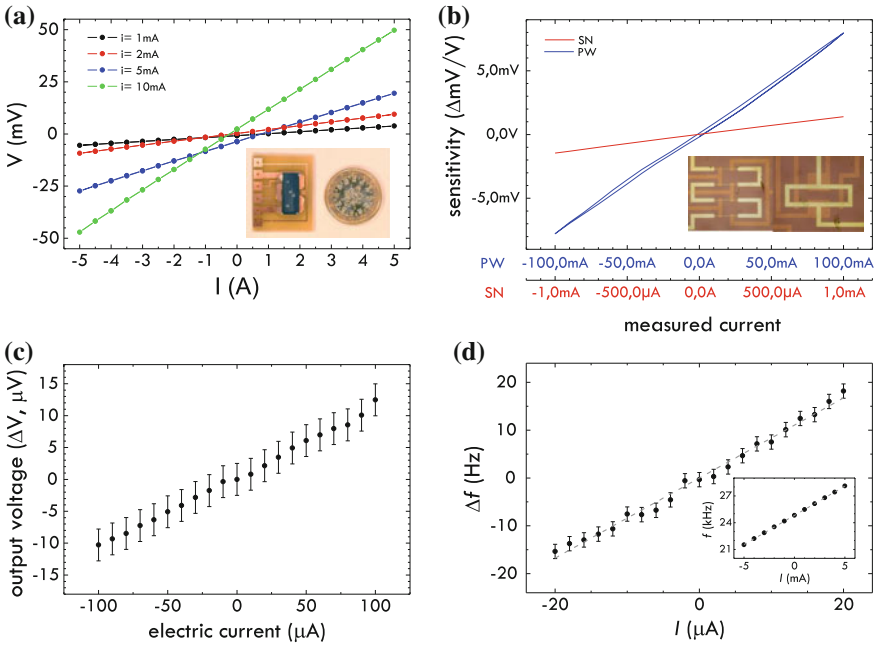

Fig. 13 Electric current sensing with GMR devices: **a** medium to high currents with an hybrid PCB-IC technology [9], **b** integrated low current measurement [22], **c** sub-mA monolithic integrated current measurement in AMS 0.35 µm chips, **d** detection improvement with the help of *V*-to-*f* schemes [31]

improved design is presented in [9] (see Fig. 13a), where a meandered strap is designed in order to give the sensor a better performance regarding voltage offset, thermal drifts and immunity against external magnetic fields. Regarding specific applications, GMR sensors have been successfully used in differential current meters [59], switching regulators [60], electrical power measurement [61] and battery management [62].

GMR based sensors have also been successfully applied to low current measurement, in different scenarios [63], in particular some compatible with CMOS technology. In this sense, we have also demonstrated the applicability of spin-valve structures [11] and bridges [22] (see Fig. 13b) to the measurement of such level electrical currents. The detectivity of such sensors can be improved by including *R*-to-*t* *V*-to-*f* schemes in the measuring process [31] (see Fig. 13c). In addition, electrical analog isolators were also designed with a basis of GMR structures [64]. Finally, the potentiality of these devices as milliwattmeters has been also demonstrated [65].

7.3 Biological

GMR sensors have been proposed for different bioapplications suchs as molecular recognition [66], bacteria analysis [67], microfluidic systems [68], hyperthermia treatments [69] or neural magnetic field detection [70].

With the rapid development of microfabrication techniques, together with the finding of compatible devices, the concept of Lab On a Chip has become more and more important in the last years. Portable devices have been recently developed which are capable of driving a fluid trough microchannels close to a detecting region, with additional conditioning and acquiring electronics. The usual scheme is the detection of the magnetic fringe field of a magnetically labeled biomolecule interaction with a complementary biomolecule bound to a magnetic field sensor. In this context, magnetoelectronics has emerged as a promising new platform technology for biosensor and biochip development [66].

8 Conclusions

GMR technology has demonstrated its maturity in its relatively short existence. It gained its popularity in the hard disks market and its success has open new doors. At this moment, only three companies develop general purpose GMR based magnetometers. But specific GMR sensors are nowadays successfully designed for *ad hoc* applications in the fields of the bio-technology, microelectronics or automotive, among others. Their intrinsic properties regarding high sensitivity, small size and compatibility with CMOS electronics allow us to be optimistic on the next future.

Acknowledgments At the personal level, we should give thanks to E. Figueras, J. Madrenas and A. Yúfera for their kindness regarding standard IC's. Also thanks to A. Roldán and J. B. Roldán for their help in developing electrical models. The authors are permanently grateful for the very fruitful collaborations with the INESC-MN. Part of the work has been carried out under projects: HP2003/0123 (*Ministry of Science and Technology, Spain*), GV05/150 (*Valencian Regional Government*), ENE2008-06588-C04-04 (*Ministry of Science and Innovation, Spain and European Regional Development Fund*), UV-INV-AE11-40892 (*Universitat de València*) and NGG-229 (2010).

References

1. M.N. Baibich, J.M. Broto, A. Fert, F.N. Vandau, F. Petroff, P. Eitenne, G. Creuzet, A. Friederich, J. Chazelas, Giant magnetoresistance of (001)Fe/(001)Cr magnetic superlattices. Phys. Rev. Lett. **61**(21), 2472–2475 (1988)
2. G. Binasch, P. Grunberg, F. Saurenbach, W. Zinn, Enhanced magnetoresistance in layered magnetic-structures with antiferromagnetic interlayer exchange. Phys Rev B **39**(7), 4828–4830 (1989)
3. S.M. Thompson, The discovery, development and future of gmr: the nobel prize 2007. J. Phys. D Appl. Phys. **41**(9), 093001 (2008)
4. U. Hartman. (Ed.), *Magnetic Multilayers and Giant Magnetoresistance: Fundamentals and Industrial Applications*. Surface Sciences (Springer, Berlin, 1999)
5. E Hirota, H Sakakima, K Inomata, *Giant Magnetoresistance Devices*. *Surface Sciences* (Springer, Berlin, 2002)
6. S. Arana, N. Arana, R. Gracia, E. Castaño, High sensitivity linear position sensor developed using granular Ag-Co giant magnetoresistances. *Sens. Actuators A—Phys* 116–121 (2005)
7. C. Reig, M. Cardoso, S.E. Mukhopadhyay, *Giant Magnetoresistance (GMR) Sensors. From Basis to State-of-the-Art Applications*. Smart Sensors, Measurement and Instrumentation (Springer, Berlin, 2013)
8. P.P. Freitas, R. Ferreira, S. Cardoso, F. Cardoso, Magnetoresistive sensors. J. Phys-Condens Matter **19**(16) 21 (2007)
9. C. Reig, D. Ramírez, F. Silva, J. Bernardo, P. Freitas, Design, fabrication, and analysis of a spin-valve based current sensor. Sens Actuators A-Phys **115**(2–3), 259–266 (2004)
10. A. Veloso, P.P. Freitas, P. Wei, N.P. Barradas, J.C. Soares, B. Almeida, J.B. Sousa, Magnetoresistance enhancement in specular, bottom-pinned, $Mn_{83}Ir_{17}$ spin valves with nano-oxide layers. Appl. Phys. Lett. **77**(7), 1020–1022 (2000)
11. C. Reig, D. Ramírez, H.H. Li, P.P. Freitas, Low-current sensing with specular spin valve structures. IEE Proc-Circ Devices Syst **152**(4), 307–311 (2005)
12. V. Peña, Z. Sefrioui, D. Arias, C. Leon, J. Santamaria, J.L. Martinez, S.G.E. te Velthuis, A. Hoffmann, Giant magnetoresistance in ferromagnet/superconductor superlattices. Phys Rev Lett **94**(5) (2005)
13. D. Pullini, D. Busquets, A. Ruotolo, G. Innocenti, V. Amigó, Insights into pulsed electrodeposition of gmr multilayered nanowires. J. Magn. Magn. Mater. **316**(2), E242–E245 (2007)
14. D. Leitao, R. Macedo, A. Silva, D. Hoang, D. MacLaren, S. McVitie, S. Cardoso, P. Freitas, Optimization of exposure parameters for lift-off process of sub-100 features using a negative tone electron beam resist, in *Nanotechnology (IEEE-NANO), 2012 12th IEEE Conference on* (2012), pp. 1–6
15. D.C. Leitao, J.P. Amaral, S. Cardoso, C. Reig, *Giant magnetoresistance (GMR) sensors. From basis to state-of-the-art applications, ch. Microfabrication techniques*. Smart Sensors, Measurement and Instrumentation [7] (2013), pp. 31–46

16. Z. Marinho, S. Cardoso, R. Chaves, R. Ferreira, L.V. Melo, P.P. Freitas, Three dimensional magnetic flux concentrators with improved efficiency for magnetoresistive sensors, J. Appl. Phys. **109**(7) (2011)
17. R.C. Jaeger, *Introduction to microelectronic fabrication*. Modular series on solid state devices (Addison-Wesley, USA, 1988)
18. J. Johnson, Thermal agitation of electricity in conductors. Nature **119**, 50–51 (Jan–Jun 1927)
19. H. Nyquist, Thermal agitation of electric charge in conductors. Phys Rev, **32**, 110–113 (Jul 1928)
20. F.N. Hooge, 1/f noise. Physica B & C **83**(1), 14–23 (1976)
21. C. Fermon, M. Pannetier-Lecoeur, *Giant magnetoresistance (GMR) sensors. From basis to state-of-the-art applications, ch. Noise in GMR and TMR sensors*. In Smart Sensors, Measurement and Instrumentation [7] (2013)
22. M. Cubells-Beltrán, C. Reig, D. Ramírez, S. Cardoso, P. Freitas, Full Wheatstone bridge spin-valve based sensors for IC currents monitoring. IEEE Sens. J. **9**(12), 1756–1762 (2009)
23. P.P. Freitas, S. Cardoso, R. Ferreira, V.C. Martins, A. Guedes, F.A. Cardoso, J. Loureiro, R. Macedo, R.C. Chaves, J. Amaral, Optimization and integration of magnetoresistive sensors. Spin **01**(01), 71–91 (2011)
24. J. Gakkestad, P. Ohlckers, L. Halbo, Compensation of sensitivity shift in piezoresistive pressure sensors using linear voltage excitation. Sens. Actuators A-Phys **49**(1–2), 11–15 (1995)
25. D.R. Muñoz, J.S. Moreno, S.C. Berga, E.C. Montero, C.R. Escrivà, A.E.N. Anton, Temperature compensation of Wheatstone bridge magnetoresistive sensors based on generalized impedance converter with input reference current. Rev. Sci. Instrum. **77**(10), 6 (2006)
26. P. Freitas, F. Silva, N. Oliveira, L. Melo, L. Costa, N. Almeida, Spin valve sensors. Sens. Actuators, A **81**(1–3), 2–8 (2000)
27. A. De Marcellis, G. Ferri, A. D'Amico, C. Di Natale, E. Martinelli, A fully-analog lock-in amplifier with automatic phase alignment for accurate measurements of ppb gas concentrations. Sens. J. IEEE **12**, 1377–1383 (2012)
28. G.T. Ong, P.K. Chan, A power-aware chopper-stabilized instrumentation amplifier for resistive wheatstone bridge sensors. Instrum. Measure. IEEE Transac. **63**, 2253–2263 (2014)
29. C. Reig, M. Cubells-Beltrán, D. Ramírez, *Giant Magnetoresistance: New Research*, *GMR Based Electrical Current Sensors* (Nova Science Publishers, New York, 2009)
30. M. Vopalensky, P. Ripka, J. Kubik, M. Tondra, Improved GMR sensor biasing design. Sens. Actuators A-Phys. **110**(1–3), 254–258 (2004)
31. A. De Marcellis, M.-D. Cubells-Beltrán, C. Reig, J. Madrenas, B. Zadov, E. Paperno, S. Cardoso, P. Freitas, Quasi-digital front-ends for current measurement in integrated circuits with giant magnetoresistance technology. Circ. Devices Syst., IET, **8**, 291–300 (July 2014)
32. W.S. Singh, B.P.C. Rao, S. Thirunavukkarasu, T. Jayakumar, Flexible GMR sensor array for magnetic flux leakage testing of steel track ropes. *J. Sens.* (2012)
33. O. Postolache, A.L. Ribeiro, H. Geirinhas Ramos, GMR array uniform eddy current probe for defect detection in conductive specimens, *Measurement* **46**, 4369–4378 (Dec 2013)
34. D.A. Hall, R.S. Gaster, T. Lin, S.J. Osterfeld, S. Han, B. Murmann, S.X. Wang, GMR biosensor arrays: a system perspective. Biosens Bioelectron. **25**, 2051–2057 (15 May 2010)
35. P. Campiglio, L. Caruso, E. Paul, A. Demonti, L. Azizi-Rogeau, L. Parkkonen, C. Fermon, M. Pannetier-Lecoeur, GMR-based sensors arrays for biomagnetic source imaging applications. IEEE Transac. Magnet. **48**, 3501–3504 (Nov 2012)
36. D.A. Hall, R.S. Gaster, K.A.A. Makinwa, S.X. Wang, B. Murmann, A 256 pixel magnetoresistive biosensor microarray in 0.18 μm CMOS. IEEE J. Solid-State Circ. **48**, 1290–1301 (May 2013)
37. J. Kim, J. Lee, J. Jun, M. Le, C. Cho, Integration of hall and giant magnetoresistive sensor arrays for real-time 2-D visualization of magnetic field vectors. IEEE Transac. Magnet. **48**, 3708–3711 (Nov 2012)

38. G.Y. Tian, A. Al-Qubaa, J. Wilson, Design of an electromagnetic imaging system for weapon detection based on GMR sensor arrays. Sens. Actuators A-Phys. **174**, 75–84 (Feb 2012)
39. H. Liu, Y.F. Zhang, Y.W. Liu, M.H. Jin, Measurement errors in the scanning of resistive sensor arrays. Sens. Actuators A: Phys. **163**(1), 198–204 (2010)
40. R. Saxena, N. Saini, R. Bhan, Analysis of crosstalk in networked arrays of resistive sensors. Sens. J. IEEE **11**, 920–924 (2011)
41. R. Saxena, R. Bhan, A. Aggrawal, A new discrete circuit for readout of resistive sensor arrays. Sens. Actuators, A **149**(1), 93–99 (2009)
42. J. Brown, A universal low-field magnetic field sensor using GMR resistors on a semicustom BiCMOS array, ed. by G. Cameron, M. Hassoun, A. Jerdee, C. Melvin. *Proceedings of the 39th Midwest Symposium on Circuits and Systems* (1996), pp. 123–126
43. S.-J. Han, L. Xu, H. Yu, R.J. Wilson, R.L. White, N. Pourmand, S.X. Wang, CMOS integrated DNA Microarray based on GMR sensors, in *2006 International Electron Devices Meeting*, International Electron Devices Meeting (2006), pp. 451–454
44. M.-D. Cubells-Beltrán, C. Reig, A.D. Marcellis, E. Figueras, A. Yúfera, B. Zadov, E. Paperno, S. Cardoso, P. Freitas, Monolithic integration of giant magnetoresistance (gmr) devices onto standard processed CMOS dies. Microelectron. J. **45**(6), 702–707 (2014)
45. F. Rothan, C. Condemine, B. Delaet, O. Redon, A. Giraud, A low power 16-channel fully integrated gmr-based current sensor, in *ESSCIRC (ESSCIRC), 2012 Proceedings of the* (2012), pp. 245–248
46. A. de Marcellis, C. Reig, M. Cubells, J. Madrenas, F. Cardoso, S. Cardoso, P. Freitas, Giant magnetoresistance (gmr) sensors for 0.35 μm cmos technology sub-ma current sensing. Proc. IEEE Sens. **2014**, 444–447 (2014)
47. NVE Corporation, GMR sensor catalog, (2012)
48. K. Kapser, M. Weinberger, W. Granig, P. Slama, *Giant Magnetoresistance (GMR) Sensors. From Basis to State-of-the-Art Applications*, *ch. GMR Sensors in Automotive Applications*. In Smart Sensors, Measurement and Instrumentation [7] (2013)
49. Sensitec, Gf705 magnetoresistive magnetic field sensor (2014)
50. N.A. Stutzke, S.E. Russek, D.P. Pappas, M. Tondra, Low-frequency noise measurements on commercial magnetoresistive magnetic field sensors. J. Appl. Phys. **97**(10) (2005)
51. J.P. Sebastiá, J.A. Lluch, J.R.L. Vizcano, Signal conditioning for GMR magnetic sensors applied to traffic speed monitoring. Sens. Actuators A-Phys. **137**(2), 230–235 (2007)
52. J.P. Sebastiá, J.A. Lluch, J.R.L. Vizcano, J.S. Bellon, Vibration detector based on gmr sensors. IEEE Trans. Instrum. Meas. **58**(3), 707–712 (2009)
53. S. Arana, E. Castaño, F.J. Gracia, High temperature circular position sensor based on a giant magnetoresistance nanogranular ag_xco_{1-x} alloy. IEEE Sens. J. **4**(2), 221–225 (2004)
54. A.J. López-Martn, A. Carlosena, Performance tradeoffs of three novel gmr contactless angle detectors. IEEE Sens. J. **9**(3), 191–198 (2009)
55. M.D. Michelena, R.P. del Real, H. Guerrero, Magnetic technologies for space: Cots sensors for flight applications and magnetic testing facilities for payloads. Sens. Lett. **5**(1), 207–211 (2007)
56. M.D. Michelena, W. Oelschlagel, I. Arruego, R.P. del Real, J.A.D. Mateos, J.M. Merayo, Magnetic giant magnetoresistance commercial off the shelf for space applications. J. Appl. Phys. **103**(7), 07E912 (2008)
57. M. Diaz-Michelena, Small magnetic sensors for space applications. Sensors **9**(4), 2271–2288 (2009)
58. J.P. Sebastiá, D.R. Munoz, P.J.P. de Freitas, W.J. Ku, A novel spin-valve bridge sensor for current sensing. IEEE Trans. Instrum. Meas. **53**(3), 877–880 (2004)
59. J. Pelegrí-Sebastiá, D. Ramírez-Muñoz, Safety device uses GMR sensor. EDN **48**(15), 84–86 (2003)
60. J. Pelegrí, D. Ramírez, P.P. Freitas, Spin-valve current sensor for industrial applications. Sens. Actuators A-Phys. **105**(2), 132–136 (2003)

61. D.R. Muñoz, D.M. Pérez, J.S. Moreno, S.C. Berga, E.C. Montero, Design and experimental verification of a smart sensor to measure the energy and power consumption in a one-phase ac line. Measurement **42**(3), 412–419 (2009)
62. D. Ramírez, J. Pelegrí, GMR sensors manage batteries. Edn **44**(18), 138 (1999)
63. M. Pannetier-Lecoeur, C. Fermon, A. de Vismes, E. Kerr, L. Vieux-Rochaz, Low noise magnetoresistive sensors for current measurement and compasses. J. Magn. Magn. Mater. **316** (2), E246–E248 (2007)
64. C. Reig, M.-D. Cubells-Beltrán, D. Ramírez, S. Cardoso, P. Freitas, Electrical isolators based on tunneling magnetoresistance technology. IEEE Trans. Magn. **44**(11), 4011–4014 (2008)
65. A. Roldán, C. Reig, M.-D. Cubells-Beltrán, J. Roldán, D. Ramírez, S. Cardoso, P. Freitas, Analytical compact modeling of GMR based current sensors: Application to power measurement at the IC level. Solid-State Electron. **54**, 1606–1612 (2010)
66. D.L. Graham, H.A. Ferreira, P.P. Freitas, Magnetoresistive-based biosensors and biochips. Trends Biotechnol. **22**(9), 455–462 (2004)
67. M. Mujika, S. Arana, E. Castaño, M. Tijero, R. Vilares, J.M. Ruano-López, A. Cruz, L. Sainz, J. Berganza, Microsystem for the immunomagnetic detection of escherichia coli o157: H7. Phys. Status Solidi A **205**(6), 1478–1483 (2008)
68. H. Ferreira, D. Graham, P. Parracho, V. Soares, P.P. Freitas, Flow velocity measurement in microchannels using magnetoresistive chips. Magnet. IEEE Transac. **40**, 2652–2654 (2004)
69. S. Mukhopadhyay, K. Chomsuwan, C. Gooneratne, S. Yamada, A novel needle-type sv-gmr sensor for biomedical applications. Sens. J. IEEE **7**, 401–408 (2007)
70. J. Amaral, S. Cardoso, P. Freitas, A. Sebastiao, Toward a system to measure action potential on mice brain slices with local magnetoresistive probes. J. Appl. Phys. **109**, 07B308–07B308–3 (Apr 2011)

MEMS Lorentz Force Magnetometers

Agustín Leobardo Herrera-May, Francisco López-Huerta and Luz Antonio Aguilera-Cortés

Abstract Lorentz force magnetometers based on microelectromechanical systems (MEMS) have several advantages such as small size, low power consumption, high sensitivity, wide dynamic range, high resolution, and low cost batch fabrication. These magnetometers have potential applications in biomedicine, navigation systems, telecommunications, automotive industry, space satellites, and non-destructive testing. This chapter includes the development of MEMS magnetometers composed by resonant structures that use the Lorentz force and different signal processing techniques. In addition, it presents the operation principle, sensing techniques, fabrication processes, applications, and challenges of MEMS magnetometers. Future applications will consider the integration of magnetometers with different devices (e.g., accelerometers, gyroscopes, energy harvesting and temperature sensors) on a single chip.

1 Introduction

The miniaturization has enabled the fabrication of different elements on the same chip: sensors, actuators, electronics, communication, computation, signal processing and control [1]. This chip can be developed using the batch production of micro-

A.L. Herrera-May (✉)
Micro and Nanotechnology Research Center, Universidad Veracruzana, Calzada Ruiz Cortines 455, 94294 Boca Del Rio, VER, Mexico
e-mail: leherrera@uv.mx

F. López-Huerta
Engineering Faculty, Universidad Veracruzana, Calzada Ruiz Cortines 455, 94294 Boca Del Rio, VER, Mexico
e-mail: frlopez@uv.mx

L.A. Aguilera-Cortés
Depto. Ingeniería Mecánica, DICIS, Universidad de Guanajuato, Carretera Salamanca-Valle de Santiago 3.5 + 1.8 Km, 36885 Salamanca GTO, Mexico
e-mail: aguilera@ugto.mx

A. Grosz et al. (eds.), *High Sensitivity Magnetometers*, Smart Sensors, Measurement and Instrumentation 19, DOI 10.1007/978-3-319-34070-8_9

fabrication processes, which can reduce its cost. The miniaturization is key to produce chips with important characteristics such as multiple functions, small size, low-energy consumption, and high performance. For instance, the recent computing systems are much more powerful and faster than those available 20 years ago. They include more features, are significantly cheaper, and have far less power consumption. Miniaturization has achieved faster devices with considerable cost/performance advantages and the integration of mechanical and fluidic parts with electronics. Thus, these devices can increase their functionality, resolution and sensibility.

1.1 MEMS

Microelectromechanical systems (MEMS) have allowed the development of devices composed by electrical and mechanical components with size in the micrometer-scale, which can include signal acquisition, signal processing, actuation, and control [2]. These devices offer several advantages such as small size, reduced power consumption, high sensitivity, and low cost batch fabrication. Recently, several MEMS devices have been fabricated such as micromirrors, accelerometers, gyroscopes, magnetometers, pressure sensors, micropumps, and microgrippers [3–10]. These devices could be employed in biomedical and chemical analyses, automobile and military industries, telecommunications, consumer electronic, and navigation. Figure 1 depicts SEM image of two MEMS magnetometers designed by researchers from Micro and Nanotechnology Research Center (MICRONA-UV) into collaboration with Microelectronics Institute of Barcelona (IMB-CNM, CSIC).

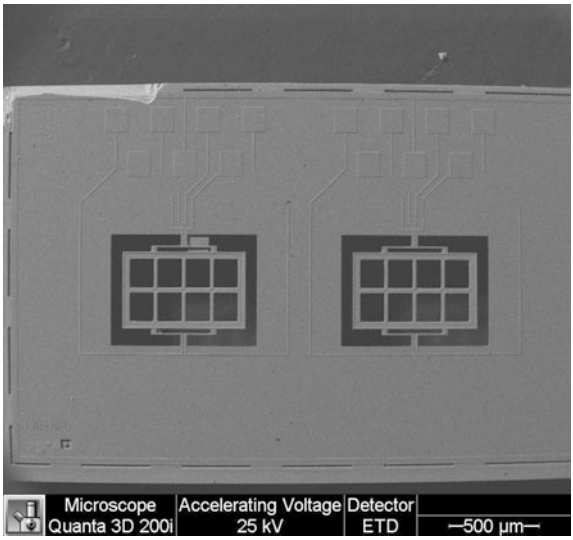

Fig. 1 SEM image of two magnetometers based on resonant silicon structures and piezoresistive sensing. These magnetometers are designed by researchers from MICRONA-UV and IMB-CNM (CSIC)

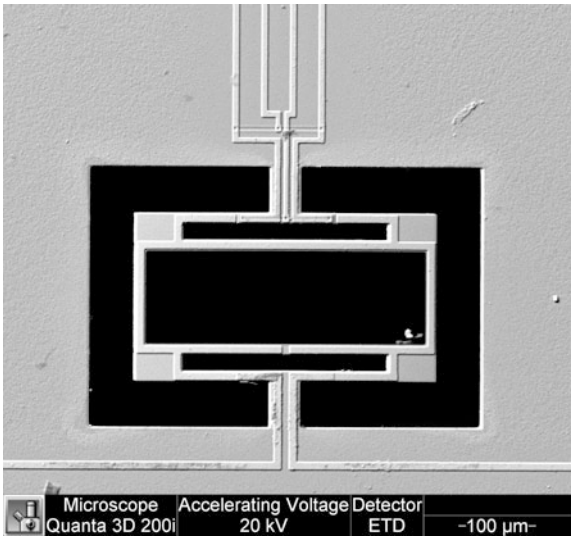

Fig. 2 SEM image of a MEMS magnetometer with piezoresistive sensing, which is developed by researchers from MICRONA-UV and IMB-CNM (CSIC)

The classification of MEMS considers three groups: micromechanical structures, actuators, and sensors [2]. Micromechanical structures can include beams, plates, and microchannels. Actuators convert magnetic or electrical input signals to motions (e.g., resonant structures, micropumps, microgrippers, and microswitches). Sensors detect chemical and physical signals, which are transformed to electrical signals. Figure 2 depicts SEM image of a magnetometer with piezoresistive sensing, which has a resonant silicon structure and a Wheatstone bridge with four p-type piezoresistors. This magnetometer is fabricated by researchers from MICRONA-UV and IMB-CNM (CSIC).

Fabrication of MEMS devices with their microelectronics on a single chip allows integrated devices. They combine microelectromechanical structures, sensing elements, and signal conditioning. These devices will permit new applications, incorporating the advantages of MEMS and microelectronics. The integration of MEMS devices with signal conditioning systems on a single chip can active the design of different devices to monitor several chemical and physical variables. For example, multiaxis MEMS accelerometers and gyroscopes may be applied in smartphones to control the screen orientation.

1.2 Fabrication Processes

MEMS devices can be fabricated using surface and bulk micromachining techniques. These techniques take advantage of both mechanical and electrical properties of the silicon. Silicon mechanical properties have a higher strength than the steel and a minimum mechanical hysteresis. In addition, silicon electrical properties have allowed it to be the most common material of integrated circuits.

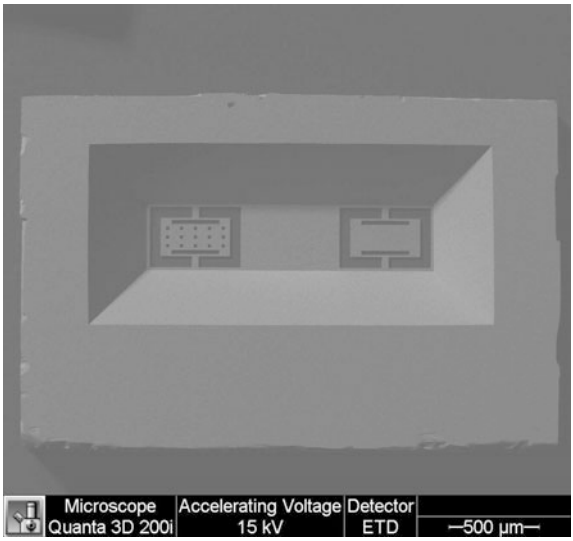

Fig. 3 SEM image of two resonant silicon structures (*backside view*) that are fabricated using bulk micromachining. These magnetometers are designed by researchers from MICRONA-UV and IMB-CNM (CSIC)

Bulk micromachining selectively etches a silicon substrate to fabricate three-dimensional microstructures. In this micromachining process, a great amount of material is removed from silicon wafer to develop beams, membranes, holes, microchannels, and other structures types (see Fig. 3). Etching techniques, during the MEMS fabrication, eliminate materials in desired areas through physical or chemical processes, which define the geometry shape of the MEMS components. Usually chemical etching is referred as wet etching and the physical etching is named as dry or plasma etching. Chemical etching considers solutions with diluted chemicals to dissolve substrates. For example, potassium peroxide (KOH) is employed to etch silicon dioxide (SiO_2), silicon nitride (Si_3N_4), and polycrystalline silicon. Plasma etching generates a stream of positive-charge-carrying ions of a substance with a large number of electrons, which is diluted with inert carrier gas such as argon [11]. It is achieved using a high-voltage electric charge or radiofrequency (RF) sources. This micromachining technology is based on sculpting features in the bulk of the silicon substrate by orientation-independent (isotropic) or orientation-dependent (anisotropic) wet or dry etchants. Wet etching provides higher degree of selectivity than the dry etching [12]. For these etching processes, the etch-stop is related with the crystal orientation or dopant concentration of silicon wafer as well as etchant protection masks, which are not selective to the used etching type. In this technology is key the etching type employed to fabricate the microstructures.

Generally, bulk micromachining take advantages of materials such as silicon, silicon carbide (SiC), gallium arsenide (GaAs), indium phosphide (InP), germanium (Ge), and glass. An etching protection mask covers a part of the material substrate, which is used to protect it of chemical etchants. However, the other part of the silicon substrate without etching protection mask is dissolved by the etchants. Moreover, the chemical etching may undercut a silicon part located under the protective mask. Etching process of the silicon substrate can be isotropic or

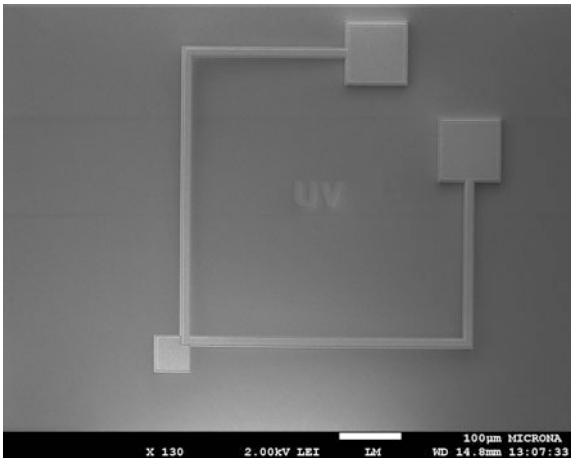

Fig. 4 SEM image of a magnetometer composed by a polysilicon resonator, a micromirror, and an aluminum loop. It is designed by researchers from MICRONA-UV and fabricated using the Sandia Ultra-planar Multi-level MEMS technology (SUMMiT V) process

anisotropic. Isotropic etching attacks in all directions the silicon substrate, which is called orientation-independent etching. This etching type depends of the temperature and has difficult to control the lateral etching of the substrate. On the other hand, anisotropic etching achieves defined well geometry shapes of microstructures due to crystallographic planes of the substrate.

Surface micromachining is based on patterning layers deposited on the silicon surface or any other substrate. It lets the integration of MEMS devices with microelectronics on the same substrate. The thickness of the structural layer is determined by the thickness of the deposited layer. This micromachining process can deposit layers on silicon substrate using the low-pressure chemical vapor deposition (LPCVD) technique. Polysilicon is the most common structural material for surface micromachining. Sacrificial layers (e.g., SiO_2 or phosphorus silicon glass) define the space between the structural layers and substrate, which are removed with wet etching. Thus, the structural layers are suspended (see Fig. 4). In the wet etching the surface tension force may pull the structural layers, causing permanent stiction. Structural layers can be polysilicon, Si_3N_4, polymide, titanium, and tungsten, which can have thickness from 2 to 5 μm. These layers require high temperature treatment to relief their internal stresses generated during the surface micromachining. This fabrication process is much more complex than bulk micromachining.

1.3 Sensing Techniques

MEMS devices can detect different physical, biological or chemical phenomena through piezoresistive, capacitive, or piezoelectric sensing techniques. The selection suitable of a sensing technique for monitoring chemical or physical signal depends of signal dynamic range, environmental parameters, packaging, and required accuracy. Environmental parameters include operating pressure and

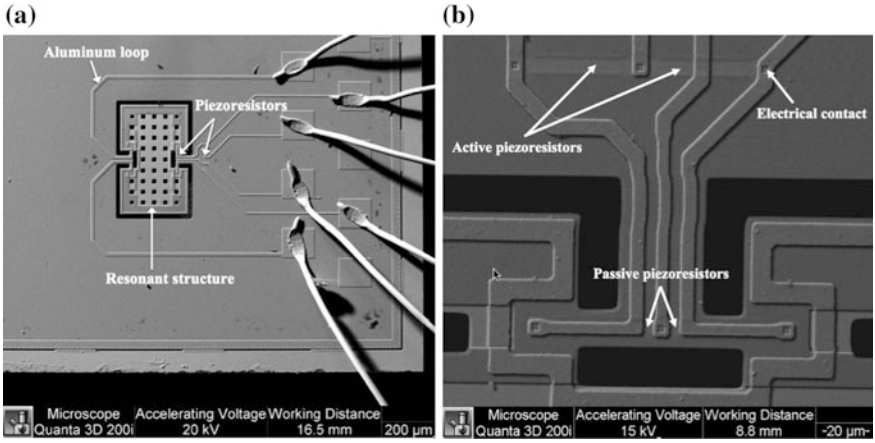

Fig. 5 SEM image of a MEMS magnetometer with piezoresistive sensing. **a** Resonant silicon structure and aluminum loop; **b** four piezoresistors of a Wheatstone bridge [13]. Reprinted with permission from Herrera-May et al., Microelectron. Eng., 142, 12–21, 2015. Copyright © 2015, Elsevier B.V

temperature, moisture, and chemical exposure. In addition, other factors can affect the choice of the sensing technique such as signal processing, data display, device impedance, supply voltage, operating life, frequency response, and calibration.

Piezoresistive sensing is based on the resistance shift of a material when it is mechanically stressed. It can use a Wheatstone bridge of four piezoresistors to convert the variation of piezoresistors resistance to an output voltage shift, as shown in Fig. 5a, b. This sensing technique has a high dependence with respect to piezoresistor doping level and type, as well as operating temperature change. Piezoresistive sensing generates voltage offset in the electrical response of the MEMS device. Other variable resistive elements can be included to adjust the zero-offset level and calibrate the sensitivity, as well as provide temperature compensation. In addition, a temperature dependence of full-scale span (i.e., difference between full-scale output and offset) could be controlled applying suitable doping levels.

Capacitive sensing uses the capacitance variation between electrodes with plates or beams shapes. They provide fixed and moving electrodes that are relatively straightforward to fabricate. This technique must consider interdigitated capacitors and effects of the fringing fields. It is less noisy that piezoresistive sensing but its values of capacitance are extremely small. It can use charge amplifiers, charge balance technique, ac bridge impedance measurements, and several oscillator configurations.

Optical sensing relies on modulating the properties of an optical frequency electromagnetic wave. A MEMS device can module a property of the electromagnetic wave such as intensity, phase, wavelength, frequency, spatial position, and polarization.

Piezoelectric sensing employs piezoelectric materials to generate an electrical signal when they are mechanically deformed. MEMS devices with piezoelectric

elements can produce an output voltage when they are strained. Piezoelectric material as lead zirconate titanate (PZT) is a common material for MEMS devices. Piezoelectric sensing is inexpensive and it does not require a supply voltage. However, piezoelectric materials can lose their piezoelectric properties with temperatures close to their Curie points. In addition, piezoelectric coefficients of these materials depend the temperature change.

1.4 Packaging Process

Packaging process is key for establishing the reliability of MEMS devices. The package offers protection from environmental parameters such as moisture, liquid or gaseous chemicals. MEMS devices can use ball-grid array (BGA) and land-grid array (LGA) packages. Furthermore, surface-mount technology (SMT) can provide wafer-level packages (WLPs), stacked die, wafer-level chip-scale packages (WLCSPs), and 3-D packaging. The cost of a MEMS device can increase about 35–60 % due to the packaging, assembly, test, and calibration steps, as well as the application-specific integrated circuit (ASIC) [14]. After of fabrication process, the MEMS devices are separated into individual die from the wafer by sawing or scribe-and-break techniques. These dice are placed in carriers with automatic pick-and-place machines to move the dice from the carrier to the package, where device die is bonded to a package, as shown in Fig. 6. Next, wire bonds connect the electrical contacts (pads) of the die surface with those of the package, as shown in Fig. 7. It allows the electrical connections between the device and external components.

The design of a MEMS device packaging must take into account the device-specific function and the sensing technique, as well as the thermal stress produced during the packaging process. This thermal stress alters the device sensitivity and resolution. The device packaging can be affected by the characteristic

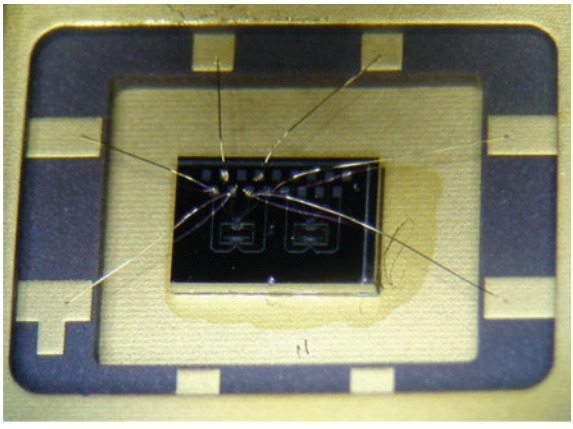

Fig. 6 Microphotography of a packaged MEMS magnetometer, which is fabricated by researchers from MICRONA-UV and IMB-CNM (CSIC)

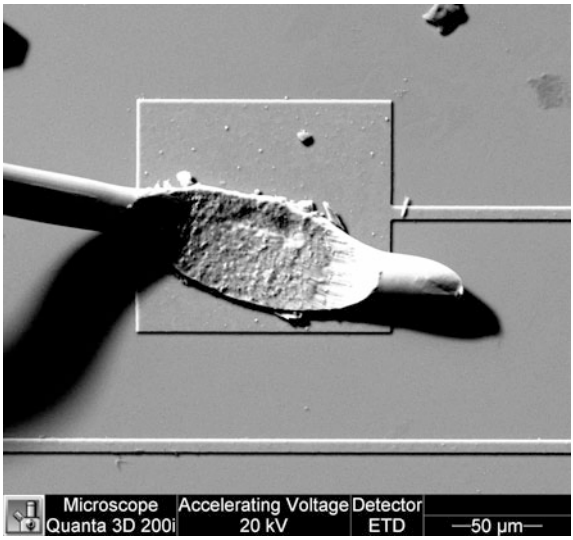

Fig. 7 SEM image of an electrical contact of a gold wire with a MEMS device pad. It is developed by researchers from MICRONA-UV and IMB-CNM (CSIC)

following: wafer thickness and wafer stack, dimensions, integration level, stress sensitivity, environmental sensitivity, heat generation, heat sensitivity, and light sensitivity [10].

1.5 Reliability

MEMS devices require reliability tests to verify their performance under different environmental and operating conditions. These tests can involve operational life, temperature cycling, mechanical shock, humidity variations, high temperature, and vibrations. The lifetime reliability of MEMS devices can be obtained through accelerated life and mechanical integrity testing. For these devices, several failure mechanisms occur during the fabrication, packaging, and signal conditioning processes.

2 Lorentz Force Magnetometers

MEMS-based Lorentz force magnetometers are an alternative for monitoring magnetic field with important advantages such as small size, low power consumption, high sensitivity, good resolution, wide dynamic range, and low cost by using batch fabrication. These magnetometers are small and lightweight compared

to SQUIDs devices, search coil sensors, and fiber optic sensors. They could be commercially competitive with respect to anisotropic magnetoresistive (AMR) and giant magnetoresistive (GMR) sensors, and Hall-effect devices. However, MEMS magnetometers need more reliability studies to ensure a safe performance under different environmental conditions.

2.1 Operation Principle

MEMS Lorentz force magnetometers can operate with silicon-based structures, which interact with an external magnetic field and an electrical current to generate a Lorentz force on the structures. This force is perpendicular to the direction of both magnetic field and electrical current. It causes a deformation of the magnetometer structure that can be measured by using a capacitive, piezoresistive, or optical sensing technique. In order to increase the sensitivity of the magnetometer is recommended to operate its structure at resonance. For this, electrical current is applied with a frequency equal to the resonant frequency of the magnetometer structure. This structure at resonance can increase the magnetometer sensitivity by a parameter equal to its quality factor. Thus, the magnetic field signal can be converted in electrical or optical signal. Figure 8 shows the operation principle of a Lorentz force magnetometer, in which the Lorentz force is obtained as:

$$F_L = I_e B_x L_y \tag{1}$$

with

$$I_e = \sqrt{2} I_{RMS} \sin(\omega t) \tag{2}$$

where L_y is the width of the perforated plate, t is the time, and I_{RMS} and ω are the root-mean-square (RMS) and circular frequency of the sinusoidal electrical current (I_e), respectively.

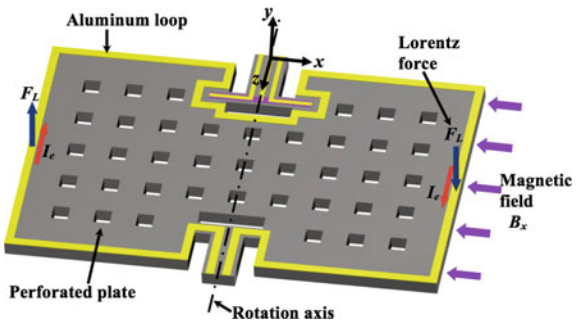

Fig. 8 Schematic view of the operation principle of a MEMS-based Lorentz force magnetometer [13]. Reprinted with permission from Herrera-May et al., Microelectron. Eng., 142, 12–21, 2015. Copyright © 2015, Elsevier B.V

Lorentz force causes a deflection of the magnetometer structure and longitudinal strain (ε_l) of two active piezoresistors (tensile in one, compressive in the other). This strain increases when the magnetometer structure oscillates at resonance. This strain changes the initial resistance (R_i) of each active piezoresistor:

$$\Delta R_i = \pi_l E \varepsilon_l R_i \tag{3}$$

where ΔR_i is the resistance variation of the piezoresistor, E is the Young's modulus of the piezoresistor material and π_l is the longitudinal piezoresistive coefficient.

The resistance variation of the two piezoresistors alters the output voltage (V_{out}) of the Wheatstone bridge. It can be calculated as

$$V_{out} = \frac{1}{2} \pi_l E \varepsilon_l R_i V_{in} \tag{4}$$

where V_{in} is the bias voltage of the Wheatstone bridge.

The magnetometer sensitivity (S) can be determined as the ratio of the output voltage shift (ΔV_{out}) to the range of the magnetic field (ΔB_x) applied in parallel direction to the magnetometer length:

$$S = \frac{\Delta V_{out}}{\Delta B_x} \tag{5}$$

2.2 Materials

The performance of MEMS magnetometers strongly depends of the functional and structural materials. These magnetometers can have single-crystal silicon (SCS) or polysilicon as materials due to their important electrical and mechanical properties. In addition, different thin films materials can be used in MEMS magnetometers. Although, they have properties related with their fabrication process and post-process such as deposition conditions, annealing, deposition apparatus, and film thickness.

Accurate material properties of MEMS magnetometers should be known to predict their performance. Material properties can be measured using microfabricated test structures on the same wafer. For instance, test structures are used to detect Young's modulus, Poisson ratio, fracture stress, fracture toughness, fatigue, thermal conductivity, and specific heat measurement [15].

2.3 Simulation and Design Tools

Design stage of MEMS devices incorporate computer-aided simulation tools with the following advantages:

1. Prediction of devices performance related with different operation conditions, materials, and geometrical dimensions.
2. Syntheses to define optimal operation conditions, dimensions and materials of the devices.
3. Possibility to solve complex partial differential equations related with the devices performance.
4. Feasibility to develop robust and rapid design software tools that help designers to reduce the design time of devices.

Simulations tools are useful to predict the optimal design of MEMS magnetometers. It could help to designers to minimize the cost, size, weight, and losses, as well as maximize the sensibility and resolution of devices.

2.4 Damping Mechanisms

The performance of MEMS devices based on resonant structures is affected by damping mechanisms. The three main damping sources regard the energy lost to surrounding fluid, energy internally dissipated in the material, and vibrating energy dissipated through the support type of the devices. These damping mechanisms modify the quality factor (Q) of resonant structures, which is defined as the ratio of the total energy stored in the device structure to the energy lost per cycle.

Quality factor (Q_f) related with the energy lost to surrounding fluid is affected by the fluid type, structure size and vibration mode, and fluid pressure. It significantly increases when the fluid pressure decreases to values close to vacuum pressure [16, 17].

Thermoelastic damping implicates internal energy dissipation in the structure material. This damping involves a quality factor (Q_i) that depends of the oscillating temperature gradient of resonant structure and the materials thermal properties. It has a maximum magnitude for pressures near to vacuum [18].

Support damping can be defined as the vibration energy dissipated by its transmission through the structure supports. The quality factor (Q_s) associated with the support damping depends of support type of the resonant structure, vibration mode, and dimensions of the structure [19].

Total quality factor (Q_T) of a resonant structure is approximated as:

$$\frac{1}{Q_T} = \frac{1}{Q_f} + \frac{1}{Q_i} + \frac{1}{Q_s} \tag{6}$$

2.5 Classifications

MEMS magnetometers can be classified considering their sensing techniques such as capacitive, piezoresistive or optical. These techniques can convert a magnetic signal into an electrical or optical signal. They use signal conditioning systems integrated by electronic or optics components. Figure 9a, b depicts a schematic view of a Lorentz force based magnetometer with piezoresistive sensing [3]. Magnetometers with piezoresistive sensing have a simple signal processing and low cost fabrication. However, they require compensation circuits to reduce the effect of the temperature shifts on the magnetometers performance.

Generally, capacitive sensing is employed in magnetometers fabricated with surface micromachining, which allows the reduction of size and cost of magnetometers. This technique is impacted by parasitic capacitances, which are minimized through monolithic integration of magnetometers with the signal conditioning systems. Figure 10a, b shows a schematic view of a Lorentz force based magnetometer with capacitive sensing [3]. It incorporates a resonant plate with two torsional beams, an aluminum loop, and electrodes.

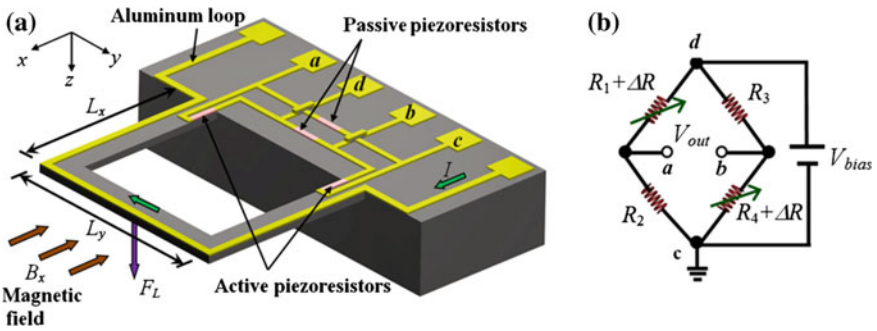

Fig. 9 **a** Schematic view of a Lorentz force based magnetometer with piezoresistive readout and **b** its Wheatstone bridge of four piezoresistors [3]. Reprinted with permission from Herrera-May et al., Sensors, 9, 7785–7813, 2009. Copyright © 2009, MDPI AG

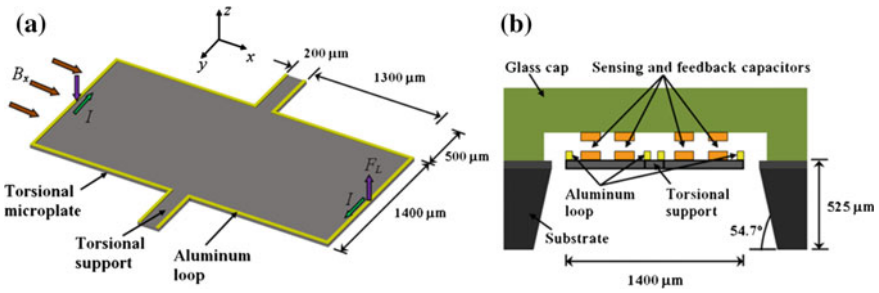

Fig. 10 **a** Schematic view of a Lorentz force based magnetometer composed by a resonant plate and **b** its capacitive readout system [3]. Reprinted with permission from Herrera-May et al., Sensors, 9, 7785–7813, 2009. Copyright © 2009, MDPI AG

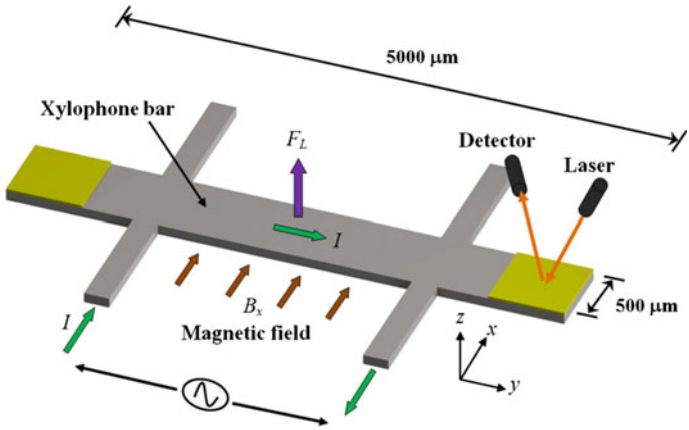

Fig. 11 Schematic view of a Lorentz force based magnetometer with resonant structure and optical sensing [3]. Reprinted with permission from Herrera-May et al., Sensors, 9, 7785–7813, 2009. Copyright © 2009, MDPI AG

Optical sensing allows a decrease of the electronic components and weight of the magnetometers. It has immunity to electromagnetic interference (EMI). A Lorentz force based magnetometer with a resonant structure and an optical readout system can measure external magnetic field through the displacements of its resonator, as shown in Fig. 11.

3 Transduction Techniques

This section presents the description of several MEMS magnetometers based on Lorentz force with different sensing techniques. It involves the main performance characteristics of the magnetometers.

3.1 Piezoresistive Sensing

Herrera-May et al. [20] designed a magnetometer formed by a silicon plate (400 × 150 × 15 μm), an aluminum loop, and a Wheatstone bridge with four p-type piezoresistors (see Fig. 12). It has a simple resonant structure fabricated using bulk micromachining. This plate operates at resonance (136.52 kHz) with a bending vibration mode, which rises its sensitivity to 403 mV T^{-1}. This magnetometer has a high quality factor of 842 at atmospheric pressure and a low power consumption about 10 mW. It uses a piezoresistive sensing, which has a non-linear electrical response with a high offset (close to 4 mV) under an external magnetic field. It registered a theoretical noise voltage of 57.48 nV $Hz^{-1/2}$, including the thermal noise, 1/*f* noise, and amplifier noise.

Later, Herrera-May et al. [21] developed a magnetometer based on a resonant structure composed by a silicon-beams rectangular loop (700 × 400 × 5 μm), an aluminum coil, and a piezoresistive sensing technique (see Fig. 13). It operates in bending vibration mode with a resonant frequency of 22.99 kHz at atmospheric pressure. Furthermore, it has a simple structure fabricated using bulk micromachining. This magnetometer has several advantages, including linear response, a

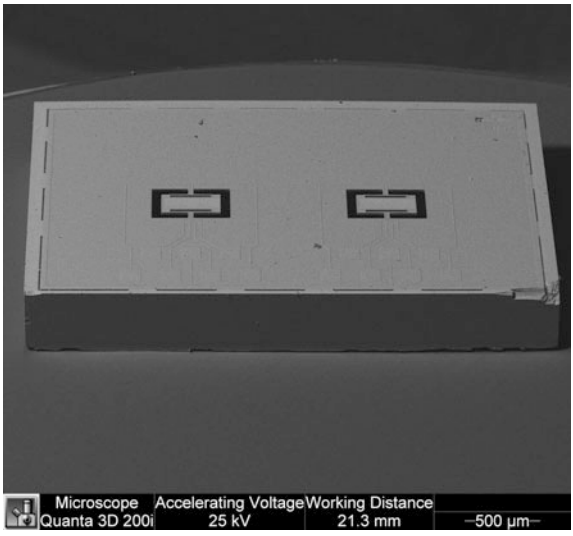

Fig. 12 SEM image of two MEMS magnetometers developed by Herrera-May et al. [20]. It was designed by researchers from MICRONA-UV and IMB-CNM (CSIC)

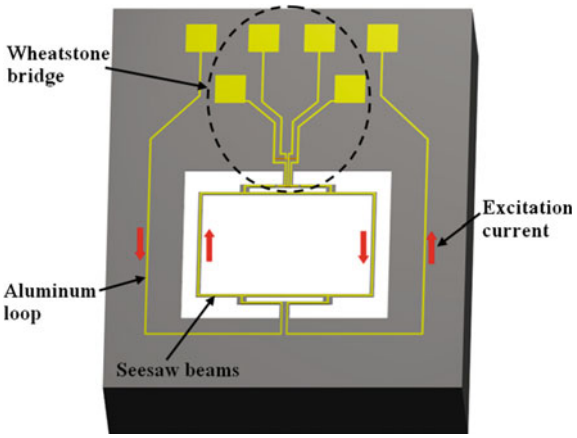

Fig. 13 3D schematic view of a magnetometer design developed by Herrera-May et al. [21]. Reprinted with permission from Herrera-May et al., Sens. Actuators A, 165, 399–409, (2011). Copyright © 2011, Elsevier B.V

quality factor of 96.6, a power consumption close to 16 mV, and a sensitivity of 1.94 V T^{-1}. In addition, it registered a theoretical noise voltage of 83.60 nV $Hz^{-1/2}$. Also, its electrical response registered a high offset due to residual stresses generated during the fabrication process and the Joule effect on the structure caused by the excitation electrical current.

Dominguez-Nicolas et al. [22] fabricated a magnetometer with a signal conditioning system and virtual instrumentation for industrial applications. This signal conditioning system is implemented on a printed circuit board (PCB). The magnetometer has a resonant silicon structure (700 × 600 × 5 μm) integrated by transversal and longitudinal beams, an aluminum loop, and a Wheatstone bridge with four p-type piezoresistors. This structure works in its first bending resonant frequency (14.38 kHz) and has a sensitivity of 4 V T^{-1}. With the signal conditioning system, the output signal of the magnetometer is digitally processed and converted in an industrial standard 4–20 mA output. This output signal has a linear behavior for small magnetic field.

3.2 Capacitive Sensing

Brugger and Paul [23] reported a magnetometer composed by a pair of planar coils and a silicon resonant structure (25 μm thick) with an amorphous magnetic concentrator, which is suspended by four straight flexural springs. It is fabricated with bulk micromachining using a silicon-on-insulator (SOI) substrate. The magnetometer has an electrostatically driven micromachined resonator, which uses capacitive detection. The stiffness and fundamental resonant frequency of the magnetometer is altered by an external magnetic field parallel to the magnetic concentrator. Thus, this resonant frequency shift is related with the applied magnetic field. For a coil current of 80 mA and a pressure of 10^{-5} mbar, the magnetometer reaches a sensitivity of 1.0 MHz T^{-1}, a resolution of 400 nT, and a high

quality factor close to 2400. This magnetometer does not need complex feedback and modulation electronics. However, it requires a post-fabrication process to collocate the magnetic concentrator on the resonant structure as well as a vacuum packaging. Large external mechanical vibrations can affect the magnetometer performance.

Li et al. [24] developed a magnetometer with a resonant polysilicon structure (15 μm thick) for monitoring both out-of-plane and in-plane magnetic field components. It requires capacitive sensing to detect the in-plane and out-of-plane motions of the resonant structure. The magnetometer is fabricated through standard surface micromachining process. It has low power consumption (0.58 mW) as well as sensitivities and resolutions for the out-of-plane and in-plane field of 12.98 V T^{-1}, 0.78 V T^{-1}, 135 nT $Hz^{-1/2}$, and 445 nT $Hz^{-1/2}$, respectively. Although, it needs vacuum (1 mbar) packaging and presents a residual motion induced by the electrostatic force, which causes an offset of the output voltage.

Wu et al. [25] designed a magnetometer with a square silicon plate (1000 × 1000 × 46 μm) and a planar induction coil (0.4 μm thick). It is fabricated using cavity-SOI process. It involves capacitive driving and electromagnetic induction to detect the external magnetic field. This silicon plate operates at resonance with a square-extensional (SE) vibration mode. The induction coil located on silicon plate has motion through magnetic field when the plate oscillates at resonance. The magnetometer has a sensitivity of 3 mV T^{-1} and a large output voltage offset (∼1.9 mV). A vacuum packaging is required to increase the magnetometer sensitivity.

Langfelder et al. [26] presented a magnetic field sensor formed by capacitive polysilicon plates with high aspect ratio that could have potential applications in inertial measurement units (IMUs). It has a compact structure with a sensitivity of 150 V T^{-1} at 250 μA of peak driving current. This sensor requires vacuum packaging (1 mbar) and has a non-linear electrical response.

3.3 Optical Sensing

Keplinger et al. [27, 28] designed two magnetometers with U-shaped silicon cantilevers (1100 × 100 × 10 μm) with an optical detection system (see Fig. 14). These magnetometers are appropriate to detect magnetic field from 10 mT up 50 T in electromagnetically noisy environments. They require an almost perfect vertical front side of the cantilevers. Temperature shifts can alter the fundamental resonant frequencies of the cantilevers, modifying the deflections and output signals of the magnetometers.

Wickenden et al. [29] developed a magnetometer formed by a polysilicon xylophone microbar (500 × 50 × 2 μm), as shown in Fig. 15. It converts the magnetic input signal into an oscillating motion of the xylophone microbar. This motion can be detected by an optical readout system based on a laser diode beam

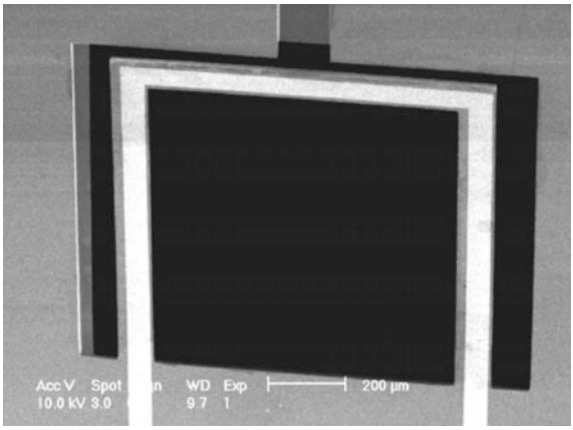

Fig. 14 SEM image of a magnetometer integrated by a resonant silicon structure with optical sensing [28]. The resonant-structure position is measured using an optical fiber. Reprinted with permission from Keplinger et al., Sens. Actuators A, 110, 112–118, 2004. Copyright © 2004, Elsevier B.V

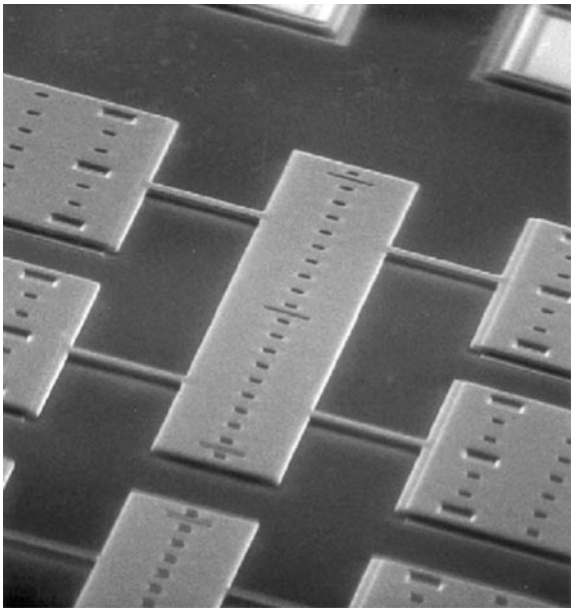

Fig. 15 SEM image of a magnetometer composed by a polysilicon xylophone bar resonator [29]. Reprinted with permission from Wickenden et al., Act. Astronaut., 52, 421–425, 2003. Copyright © 2003, Elsevier B.V

and a position sensitive detector. The magnetometer has a resonant frequency of 78.15 kHz, a quality factor close to 7000 at 4.7 Pa, ac current of 22 μA, a thermal noise of 100 pT A $Hz^{1/2}$, and a resolution close to nanoteslas. In addition, the microsensors with optical sensing have immunity to EMI. Although, it has a linear response up to 150 μT and its performance changes due to variations of pressure and temperature. Magnetometers with optical readout systems can reduce their electronic circuitries and weights.

Table 1 Main characteristics of several MEMS magnetometers

Magnetometer	Sensing technique	Resonant frequency (kHz)	Quality factor	Size (resonant structure) (μm × μm)	Sensitivity
Herrera-May et al. [20]	Piezoresistive	136.52	842	400 × 150	0.403 V T^{-1}
Herrera-May et al. [21]	Piezoresistive	22.99	96.6	700 × 400	1.94 V T^{-1}
Dominguez-Nicolas et al. [22]	Piezoresistive	14.38	93	700 × 600	4.0 V T^{-1}
Brugger and Paul [23]	Capacitive	2.20	2400	2000 × 2000	1.45 MHz T^{-1}
Li et al. [24]	Capacitive	46.96	10000	1000 × 2000	12.98 V T^{-1}
Wu et al. [25]	Capacitive	4329	3700	1000 × 1000	3×10^{-3} V T^{-1}
Langfelder et al. [26]	Capacitive	28.3	328	89 × 868	150 V T^{-1}
Keplinger et al. [27, 28]	Optical	5.0	200	1100 × 1000	*
Wickenden et al. [29]	Optical	78.15	7000	500 × 50	*

*Data not available in the literature

3.4 *Comparisons*

Generally, MEMS magnetometers have important advantages such as small size, lightweight, low power consumption, low cost, high sensitivity, wide dynamic range, and easy signal conditioning. Table 1 shows the main characteristics of several MEMS magnetometers, which operate with Lorentz force. They could be used for potential applications such as telecommunications, industrial, military, biomedical, and consumer electronic products.

4 Challenges and Future Applications

MEMS magnetometers have important characteristics for future commercial markets. However, these magnetometers present several challenges such as the decrease of their output response offset, noise, temperature and humidity dependence, as well as have high reliability. In addition, researches of the magnetometers reliability are needed to study their performance under different environment and operation conditions. Future magnetometers will require be integrated with others devices on a single chip, which will allow the develop of multifunctional sensors for

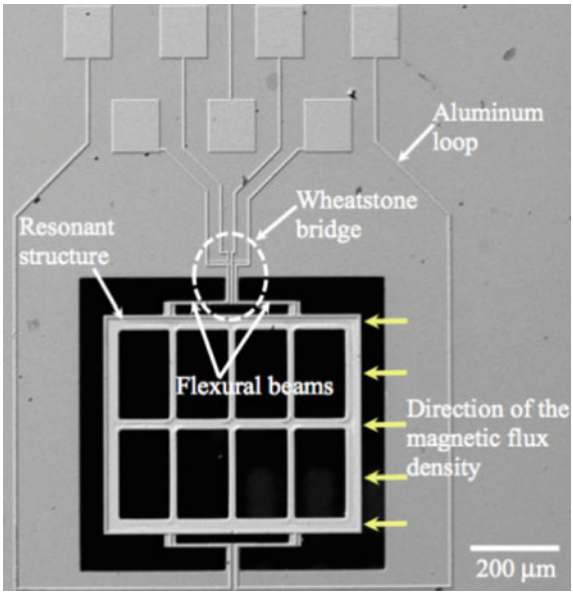

Fig. 16 SEM image of a MEMS magnetometer used for biomedical applications [30]. Reprinted with permission from Dominguez-Nicolás et al., Int. J. Med. Sci., 10, 1445–1450, 2013. Copyright © 2013, Ivyspring International Publisher

monitoring different chemical or physical signals such as gases, magnetic field, acceleration, pressure, and temperature.

A respiratory magnetogram had been developed using MEMS magnetometer (see Fig. 16), which can detect strong magnetic flux density during the respiratory activity of rats [30]. Figure 17a, b depicts the electromyogram and magnetogram of the thoracic cavity of a rat during its respiration [30]. These measurements could be useful in clinical diagnostics for monitoring the health of some organs of the thoracic cavity. Unhealthy organs could have variations of their magnetic flux density with respect to those obtained of healthy organs. For this biomedical application is necessary digital signal processing by virtual instrumentation of MEMS magnetometers [31].

MEMS magnetometers (see Figs. 18 and 19) could be employed to detect cracks and flaws of ferromagnetic materials through non-destructive testing (NDT) such as eddy current inspection and magnetic memory method (MMM) [32–35]. Eddy current technique requires the interaction between a magnetic field source and a ferromagnetic material, which induces eddy currents in the material. Small cracks of the material can be detected for monitoring changes of magnetic field generated by the eddy currents. MMM takes advantage of residual magnetic field of ferromagnetic materials, which can be generated during their fabrication processes or heat treatments. Cracks and geometrical defects of ferromagnetic materials cause variations of magnetic field that can be monitored through MEMS magnetometers.

Inertial measurement units (IMUs) can contain silicon magnetometers, accelerometers, and gyroscopes [26, 36]. These devices could be fabricated on a single chip to reduce the electronic noise and power consumption. IMUs have

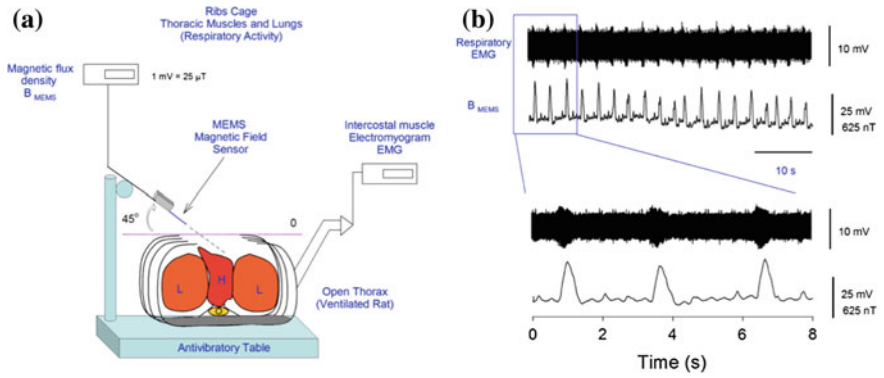

Fig. 17 **a** Diagram of experimental arrangement of a MEMS magnetometer used to measure the respiratory and cardiac activity of a rat. **b** Electromyogram of the thoracic muscles and magnetic flux density, which are detected during the respiratory activity of a rat [30]. Reprinted with permission from Dominguez-Nicolás et al., Int. J. Med. Sci., 10, 1445–1450, 2013. Copyright © 2013, Ivyspring International Publiser

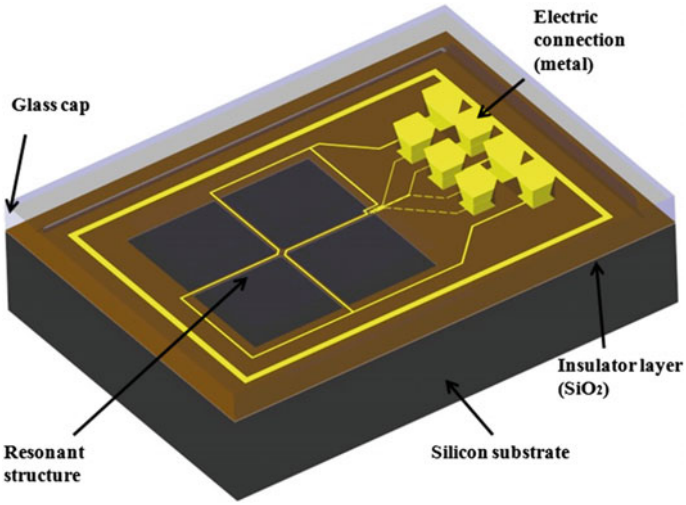

Fig. 18 Design a MEMS magnetometer with piezoresistive sensing with potential application for non-destructive testing (NDT) using the magnetic memory method [32]. Reprinted with permission from Acevedo-Mijangos et al., Microsyst. Technol., 19, 1897–1912, 2013. Copyright © 2013, Springer International Publishing AG

potential applications such as civil and military aviation, trains, space satellites, ships, consumer electronics, and unmanned operated vehicles [37–39]. Figure 20a–c shows a torsional MEMS magnetometer for monitoring in-plane magnetic field, which could be part of IMUs [36]. It operates with the Lorentz force and uses capacitive sensing. It has an area of 282 × 1095 μm, a packaged at nominal

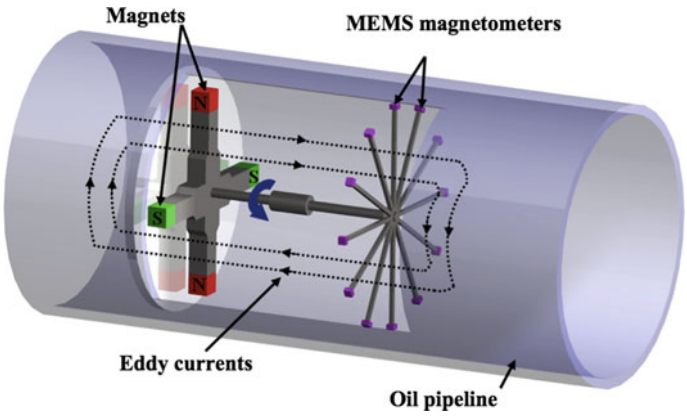

Fig. 19 Inspection system design for monitoring cracks in oil pipeline [34]. It requires eddy currents testing and MEMS magnetometers. Reprinted with permission from Herrera-May et al., Microsensors, Chap. 3, 65–84, 2011. Copyright © 2011, InTech

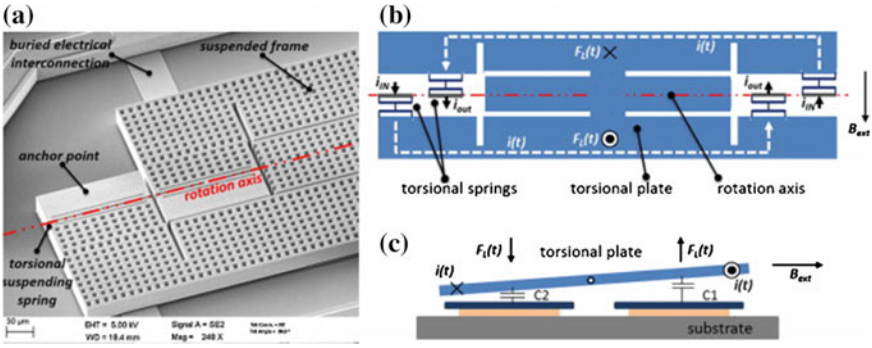

Fig. 20 SEM image of a torsional MEMS magnetometer for IMUs, fabricated using surface micromachining. **a** The magnetometer performance is schematized by the top view **b** and the cross-section **c** [36]. Reprinted with permission from Laghi et al., Sens. Actuat. A, 229, 218–226, 2015. Copyright © 2015, Elsevier B.V

pressure of 0.35 mbar, a resonant frequency of 19.95 kHz, a quality factor of 2500, and a sensitivity of 850 V T^{-1}.

Micro-, nano- or pico-satellites require low mass, small size and low power consumption magnetometers for their space missions. It can be overcome using magnetometers based on polysilicon-xylophone bars that operate at resonance with capacitive sensing [40, 41].

Electronic stability program (EPS) keeps the automotive dynamically stable in critical situations such as hard braking and slippery surfaces. EPS systems require data related with steering-wheel angle, yaw rate, lateral accelerations, and wheel speed. They could be measured through MEMS magnetometers, accelerometers,

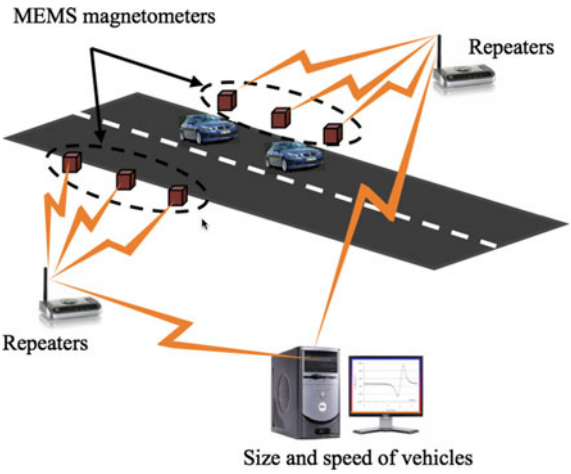

Fig. 21 Schematic diagram of a traffic detection system achieved with MEMS magnetometers [34]. Reprinted with permission from Herrera-May et al., Microsensors, Chap. 3, 65–84, 2011. Copyright © 2011, InTech

gyroscopes, and pressure devices. In addition, magnetometers could be applied in a traffic detection system to detect the speed and size of vehicles, as shown in Fig. 21. This system could be composed by two magnetometers (with a constant separation distance) located in parallel beside the road. Magnetometers will detect the change of the Earth's magnetic field caused by the vehicles motion that will be preceded to A/D converter and digital data processing system. The magnetic field shift will depend of the vehicles' speed and size, which will be detected by the magnetometers in different times (t_1 and t_2). Next, the vehicle speed will be calculated through the ratio of the magnetometers separation distance to the time difference $t_1 - t_2$. In addition, this system with an intelligent signal control could be used to decrease traffic congestion on roads.

5 Conclusions

MEMS technology has allowed the development of magnetometers composed by resonant silicon structures that exploit the Lorentz force. These MEMS magnetometers can be an important option with respect to conventional magnetometers due to their small size, low power consumption, wide dynamic range, high sensitivity and high resolution, and low cost by using batch fabrication. In addition, they could have future commercial markets, including biomedicine, telecommunications, aerospace, and automotive sector. Nevertheless, magnetometers reliability studies are needed to predict their performance under different environment and operation conditions. In addition, monolithic fabrication can be used to develop MEMS magnetometers with low electronic noise.

Acknowledgments This work was partially supported by Sandia National Laboratory's University Alliance Program, FORDECYT-CONACYT through grant 115976, and projects PRODEP "Estudio de Dispositivos Electrónicos y Electromecánicos con Potencial Aplicación en Fisiología y Optoelectrónica" and "Sistema Electrónico de Medición de Campo Magnético Residual de Estructuras Ferromagnéticas". The authors would like to thank Dr. Eduard Figueras of IMB-CNM (CSIC) for his collaboration into the fabrication of MEMS magnetometers and B.S. Fernando Bravo-Barrera of LAPEM for his assistance with the SEM images.

References

1. G.K. Ananthasuresh, K.J. Vinoy, S. Gopalakrishnan, K.N. Bhat, V.K. Aatre, *Micro and Smart Systems Technology and Modeling* (Wiley, Danvers, 2012)
2. S.D. Senturia, *Microsystem Design* (Kluwer Academic Publishers, New York, 2002)
3. A.L. Herrera-May, L.A. Aguilera-Cortés, P.J. García-Ramírez, E. Manjarrez, Resonant magnetic field sensor based on MEMS technology. Sensors **9**, 7785–7813 (2009)
4. O. Solgaard, A.A. Godil, R.T. Howe, L.P. Lee, Y.-A. Peter, H. Zappe, Optical MEMS: from micromirrors to complex systems. J. Microelectromech. Syst. **23**, 517–538 (2014)
5. D. Yamane, T. Konishi, T. Matsushima, K. Machida, H. Toshiyoshi, K. Masu, Design of sub-1 g microelectromechanical systems accelerometers. Appl. Phy. Lett. **104**, 074102Ç (2014)
6. Z. Deyhim, Z. Yousefi, H.B. Ghavifekr, E.N. Aghdam, A high sensitive and robust controllable MEMS gyroscope with inherently linear control force using a high performance 2-DOF oscillator. Microsyst. Technol. **21**, 227–237 (2015)
7. A.L. Herrera-May, J.A. Tapia, S.M. Domínguez-Nicolás, R. Juarez-Aguirre, E.A. Gutierrez-D, A. Flores, E. Figueras, E. Manjarrez, Improved detection of magnetic signals by a MEMS sensor using stochastic resonance. PLoS ONE **9**, e109534 (2014)
8. S. Kulwant, J. Robin, V. Soney, J. Akhtar, Fabrication of electron beam physical vapor deposited polysilicon piezoresistive MEMS pressure sensor. Sens. Actuators A **223**, 151–158 (2015)
9. Y. Liu, P. Song, J. Liu, D.J.H. Tng, R. Hu, H. Chen, Y. Hu, C.H. Tan, J. Wang, J. Liu, L. Ye, K.-T. Yong, An in-vivo evaluation of a MEMS drug delivery device using Kunming mice model. Biomed. Microdevices **17**, 6 (2015)
10. W. Zhenlu, S. Xuejin, C. Xiaoyang, Design, modeling, and characterization of a MEMS electrothermal microgripper. Microsyst. Technol. **21**, 2307–2314 (2015)
11. H. Tai-Ran, *MEMS & Microsystems. Design and Manufacture* (McGraw Hill, New York, 2002)
12. S. Sedky, *Post-processing Techniques for Integrated MEMS* (Artech House, Norwood, 2006)
13. A.L. Herrera-May, M. Lara-Castro, F. López-Huerta, P. Gkotsis, J.-P. Raskin, E. Figueras, A MEMS-based magnetic field sensor with simple resonant structure and linear electrical response. Microelectron. Eng. **142**, 12–21 (2015)
14. "MEMS Packaging," Yole Développement report. http://www.i-micronews.com/mems-sensors-report/product/mems-packaging.html
15. O. Tabata, T. Tsuchiya, MEMS and NEMS Simulation, in *MEMS: A Practical Guide to Design, Analysis, and Applications*, ed. by J.G. Korvink, O. Paul (William Andrew Inc, New York, 2006), pp. 53–186
16. F.R. Bloom, S. Bouwstra, M. Elwenspoek, J.H.J. Fluitman, Dependence of the quality factor of micromachined silicon beam resonators on pressure and geometry. J. Vac. Sci. Technol. B **10**, 19–26 (1992)
17. A.L. Herrera-May, L.A. Aguilera-Cortés, L. García-González, E. Figueras-Costa, Mechanical behavior of a novel resonant microstructure for magnetic applications considering the squeeze-film damping. Microsyst. Technol. **15**, 259–268 (2009)

18. R. Lifshit, M.L. Roukes, Thermoelastic damping in micro-and nanomechanical systems. Phys. Rev. B **61**, 5600–5609 (2000)
19. Z. Hao, A. Erbil, F. Ayazi, An analytical model for support loss in micromachined beam resonators with in-plane flexural vibrations. Sens. Actuators A **109**, 156–164 (2003)
20. A.L. Herrera-May, P.J. García-Ramírez, L.A. Aguilera-Cortés, J. Martínez-Castillo, A. Sauceda-Carvajal, L. García-González, E. Figueras-Costa, A resonant magnetic field microsensor with high quality factor at atmospheric pressure. J. Micromech. Microeng. **19**, 15016 (2009)
21. A.L. Herrera-May, P.J. García-Ramírez, L.A. Aguilera-Cortés, E. Figueras, J. Martínez-Castillo, E. Manjarrez, A. Sauceda, L. García- González, R. Juárez-Aguirre, Mechanical design and characterization of a resonant magnetic field microsensor with linear response and high resolution. Sens. Actuators A **165**, 299–409 (2011)
22. S.M. Dominguez-Nicolas, R. Juarez-Aguirre, P.J. Garcia-Ramirez, A.L. Herrera-May, Signal conditioning system with a 4–20 mA output for a resonant magnetic field sensor based on MEMS technology. IEEE Sens. J. **12**, 935–942 (2012)
23. S. Brugger, O. Paul, Field-concentrator-based resonant magnetic sensor with integrated planar coils. J. Microelectromech. Syst. **18**, 1432–1443 (2009)
24. M. Li, V.T. Rouf, M.J. Thompson, D.A. Horsley, Three-axis Lorentz-force magnetic sensor for electronic compass applications. J. Microelectromech. Syst. **21**, 1002–1010 (2012)
25. G. Wu, D. Xu, B. Xiong, D. Feng, Y. Wang, Resonant magnetic field sensor with capacitive driving and electromagnetic induction sensing. IEEE Electron Devices Lett. **34**, 459–461 (2013)
26. G. Langfelder, C. Buffa, A. Frangi, A. Tocchio, E. Lasalandra, A. Longoni, Z-axis magnetometers for MEMS inertial measurement units using an industrial process. IEEE Trans. Industr. Electron. **60**, 3983–3990 (2013)
27. F. Keplinger, S. Kvasnica, H. Hauser, R. Grössinger, Optical readouts of cantilever bending designed for high magnetic field application. IEEE Trans. Magn. **39**, 3304–3306 (2003)
28. F. Keplinger, S. Kvasnica, A. Jachimowicz, F. Kohl, J. Steurer, H. Hauser, Lorentz force based magnetic field sensor with optical readout. Sens. Actuators A **110**, 112–118 (2004)
29. D.K. Wickenden, J.L. Champion, R. Osiander, R.B. Givens, J.L. Lamb, J.A. Miragliotta, D.A. Oursler, T.J. Kistenmacher, Micromachined polysilicon resonating xylophone bar magnetometer. Acta Astronaut. **52**, 421–425 (2003)
30. S.M. Domínguez-Nicolás, R. Juárez-Aguirre, A.L. Herrera-May, P.J. García-Ramírez, E. Figueras, E. Gutierrez, J.A. Tapia, A. Trejo, E. Manjarrez, Respiratory magnetogram detected with a MEMS device. Int. J. Med. Sci. **10**, 1445–1450 (2013)
31. R. Juárez-Aguirre, S.M. Domínguez-Nicolás, E. Manjarrez, J.A. Tapia, E. Figueras, H. Vázquez-Leal, L.A. Aguilera-Cortés, A.L. Herrera-May, Digital signal processing by virtual instrumentation of a MEMS magnetic field sensor for biomedical applications. Sensors **13**, 15068–15084 (2013)
32. J. Acevedo-Mijangos, C. Soler-Balcázar, H. Vazquez-Leal, J. Martínez-Castillo, A.L. Herrera-May, Design and modeling of a novel microsensor to detect magnetic fields in two orthogonal directions. Microsyst. Technol. **19**, 1897–1912 (2013)
33. A. Dubov, A. Dubov, S. Kolokolnikov, Application of the metal magnetic memory method for detection of defects at the initial stage of their development for prevention of failures of power engineering welded steel structures and steam turbine parts. Weld World **58**, 225–236 (2014)
34. A.L. Herrera-May, L.A. Aguilera-Cortés, P.J. García-Ramírez, N.B. Mota-Carrillo, W.Y. Padrón-Hernández, E. Figueras, Development of Resonant Magnetic Field Microsensors: Challenges and Future Applications, in *Microsensors*, ed. by I. Minin (InTech, Croatia, 2011), pp. 65–84
35. M. Lara-Castro, A.L. Herrera-May, R. Juarez-Aguirre, F. López-Huerta, C.A. Ceron-Alvarez, I.E. Cortes-Mestizo, E.A. Morales-Gonzalez, H. Vazquez-Leal, S.M. Dominguez-Nicolas, Portable signal conditioning system of a MEMS magnetic field sensor for industrial applications. Microsyst. Technol. (2016). doi:10.1007/s00542-016-2816-4

36. G. Laghi, S. Dellea, A. Longoni, P. Minotti, A. Tocchio, S. Zerbini, G. Lagfelder, Torsional MEMS magnetometer operated off-resonance for in-plane magnetic field detection. Sens. Actuators A **229**, 218–226 (2015)
37. C.M.N. Brigante, N. Abbate, A. Basile, A.C. Faulisi, S. Sessa, Towards miniaturization of a MEMS-based wearable motion capture system. IEEE Trans. Industr. Electron. **58**, 3234–3241 (2011)
38. S.P. Won, F. Golnaraghi, W.W. Melek, A fastening tool tracking system using an IMUand a position sensor with Kalman filters and a fuzzy expert system. IEEE Trans. Industr. Electron. **56**, 1782–1792 (2009)
39. R.N. Dean, A. Luque, Applications of microelectromechanical systems in industrial processes and services. IEEE Trans. Industr. Electron. **56**, 913–925 (2009)
40. H. Lamy, V. Rochus, I. Niyonzima, P. Rochus, A xylophone bar magnetometer for micro/pico satellites. Acta Astronaut. **67**, 793–809 (2010)
41. S. Ranvier, V. Rochus, S. Druart, H. Lamy, P. Rochus, L.A. Francis, Detection methods for MEMS-Based xylophone bar magnetometer for pico satellites. J. Mech. Eng. Autom. **1**, 342–350 (2011)

Superconducting Quantum Interference Device (SQUID) Magnetometers

Matthias Schmelz and Ronny Stolz

Abstract Direct Current Superconducting QUantum Interference Devices (dc SQUIDs) are sensors for the detection of magnetic flux or any physical quantity that can be transformed into magnetic flux. They consist of a superconducting loop interrupted by two resistively shunted Josephson tunnel junctions. Typically operated at 4.2 K, they exhibit magnetic flux noise levels of the order of 1 $\mu\Phi_0/\mathrm{Hz}^{1/2}$, corresponding to a noise energy of 10^{-32} $\mathrm{J/Hz}^{1/2}$. They can be used for example as magnetometers, magnetic gradiometers, current sensors and voltmeters, susceptometers or (rf) amplifier. With their large bandwidth and flat frequency response ranging from dc to GHz, they are excellent suited for a wide variety of applications, such as e.g. biomagnetism and geophysical exploration to the detection of gravity waves and magnetic resonance.

1 Introduction

SQUIDs are today's most sensitive devices for the detection of magnetic flux Φ. They convert magnetic flux or any physical property that can be transformed into magnetic flux, for example magnetic flux density B, into e.g. a voltage across the device. The operation of SQUIDs is based on two physical phenomena: flux quantization in a closed superconducting loop in units of the flux quantum $\Phi_0 = h/2e = 2.07 \times 10^{-15}$ Tm^2, and Josephson tunneling.

Superconductivity represents a thermodynamic state—existing below a critical temperature T_C—in which e.g. current is carried by pairs of electrons with opposite momentum and spin, so-called Cooper pairs. For metallic low-temperature superconductors (LTS), like the most widely used Nb, T_C is usually below 10 K. Low

M. Schmelz (✉) · R. Stolz
Leibniz Institute of Photonic Technology, Albert-Einstein-Straße 9,
07745 Jena, Germany
e-mail: matthias.schmelz@ipht-jena.de

R. Stolz
e-mail: ronny.stolz@ipht-jena.de

A. Grosz et al. (eds.), *High Sensitivity Magnetometers*, Smart Sensors,
Measurement and Instrumentation 19, DOI 10.1007/978-3-319-34070-8_10

operation temperatures permit very sensitive measurements but require the use of cryogenics. Although high-temperature superconductors (HTS) have relaxed demands on the cooling system, we will restrict this overview to LTS devices due to their lower intrinsic noise, higher reliability and the potential for an industrial-like fabrication process. The general considerations remain the same for HTS devices. Among the variety of SQUID types, we will focus on dc SQUIDs, since they typically feature superior noise performance compared with rf SQUIDs and are therefore of main significance nowadays.

In this chapter we will give an overview on SQUIDs, their operation principle and design guidelines. We will describe fabrication techniques and comment on associated SQUID electronics. Due to the limited space available, the emphasis is on the understanding of such sensors in view of their practical applicability. For an in-depth view on superconductivity and on its various effects, we refer to the excellent textbooks available [1, 2]. Moreover, a number of books deal in much greater detail with various research topics we can just briefly touch, and offer a detailed view on theory as well as on the application of these devices [3–6].

In Sect. 2 we will briefly review Josephson tunnel junctions as the most important part of SQUIDs and describe basic effects and relations. In Sect. 3 we will delineate how these devices are fabricated and operated. We comment on their sensitivity limitations and how different types of SQUIDs are tailored to the envisaged application. Section 4 review results achieved with state-of-the-art devices aimed for a number of the mentioned applications, and in Sect. 5 we provide some concluding remarks and an outlook.

2 SQUID Fundamentals

The dc SQUID, as first proposed by Jaklevic et al. in 1964 [7], consists of a superconducting loop with inductance L_{SQ} interrupted by two Josephson junctions. Before discussing the operation principle of SQUIDs, we will briefly review Josephson tunnel junctions and related basic effects.

2.1 Josephson Junctions

As described earlier, the current in a superconductor is carried by so-called Cooper pairs. Since these pairs have zero spin, they follow boson statistics. As a consequence, they all condense in the same quantum state and can be described by a collective superconducting wave function $\Psi = \Psi_0 \cdot \exp(i\phi)$, with $\phi(x,t)$ being the time and space dependent phase and $n_S = |\Psi|^2$ the Cooper pair density.

If two superconductors are weakly connected, Cooper pairs can exchange between them. There are different types of how these weak links or junctions can be arranged. Probably the most important type and the one we will focus on is the

so-called SIS Josephson tunnel junction, where a thin insulating barrier (I) is placed between two superconductors (S). The current through the Josephson junction is described by the first Josephson equation $I_C = I_{C,0} \sin(\varphi)$, with $\varphi = \phi_1 - \phi_2$ being the phase difference across the junction [8]. Here $I_{C,0}$ is the junction's maximum critical current which is determined by the thickness of the insulating barrier t_{ox}, the junction area A_{JJ} and the operation temperature T.

When the maximum critical current is exceeded, the phase difference across the junction will evolve over time and a dc voltage across the junction appears. It is described by the second Josephson equation [8]

$$\frac{\partial \varphi}{\partial t} = \frac{2\mathrm{e}}{\hbar} \cdot V_{DC} = \frac{2\pi}{\Phi_0} \cdot V_{DC}, \tag{1}$$

where $\hbar = 1.055 \times 10^{-34}$ Js is the reduced Planck's constant. Please note that subsequently V represents the time averaged dc voltage over the junction. In fact the Josephson current oscillates with the Josephson frequency $2\pi V_{DC}/\Phi_0$, when biased with $I > I_{C,0}$.

A typical current-voltage characteristic of an undamped Josephson junction exhibits a hysteresis, as shown in Fig. 1 (left). A measure for this hysteresis is the McCumber parameter [9, 10]

$$\beta_C = \frac{2\pi I_C R^2 C_{JJ}}{\Phi_0}. \tag{2}$$

In order to avoid the hysteresis and therefore to obtain a single valued characteristic depicted in the right panel of Fig. 1, an additional shunt resistor R_S is usually placed across the junction to damp its dynamics, which is fulfilled for the condition $\beta_C < 1$. The dynamics of Josephson junctions are typically described in the

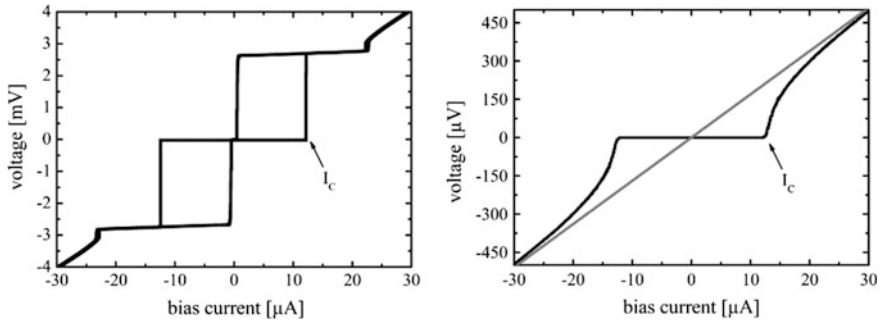

Fig. 1 (*Left*) Current-voltage characteristics of an undamped and (*Right*) of a damped (shunted) Josephson tunnel junction. The critical current of the junction I_C is about 10 μA, as indicated. For large bias currents, the characteristic of the shunted junction converges into an ohmic behavior, given by the shunt resistor value

so-called RCSJ (resistively and capacitively shunted junction) model. Therein a real Josephson junction is composed of an ideal one with additional resistance R and capacitance C_{JJ} in parallel, describing the tunneling of normal electrons in the voltage state and the displacement current over the capacitance between the two superconducting electrodes, respectively.

Due to finite thermal energy at temperatures $T > 0$, the I-V characteristic of a non-hysteretic junction is noise-rounded for currents of about I_C, as can be seen in Fig. 1 (right). The ratio between thermal energy $k_B T$ and Josephson coupling energy $E_J = I_C \Phi_0 / 2\pi$ describes the strength of noise-rounding due to thermal noise of the shunt resistor [11, 12] and is known as the noise parameter

$$\Gamma = \frac{k_B T}{E_J} = \frac{2\pi k_B T}{I_C \Phi_0} \tag{3}$$

Here, k_B is Boltzmann's constant. In LTS dc SQUIDs the influence due to thermal noise-rounding is typically neglected for $\Gamma < 0.05$.

2.2 dc SQUIDs

2.2.1 Operation Principle

As Cooper pairs can be described by a single valued wave function, the phase difference $\Delta\phi$ along an arbitrary closed path $\vec{l}$ inside a superconductor has to be a multiple of 2π. Accordingly, the magnetic flux Φ inside a superconductor can only take integer values of the magnetic flux quantum Φ_0. The externally applied flux Φ_{ext} to a superconducting loop is therefore compensated in units of Φ_0 by an appropriate self-induced flux $\Phi = L_{SQ} \cdot I_{Circ}$ due to a circulating shielding current I_{Circ} in the loop.

For the subsequent discussion, let us assume two identical junctions, each with critical current I_C, which are arranged symmetrically in the SQUID loop, as illustrated in Fig. 2. If the SQUID is biased with a constant current $I_B \geq 2I_C$, the bias current is equally divided between the two branches. As an external flux Φ_{ext} leads to a circulating current to fulfil the flux quantization in the loop, the bias current in a SQUID is redistributed in dependence of the external magnetic flux. For $\Phi_{ext} = n\Phi_0$ no circulating screening current flows and the critical current of the SQUID is just $I = 2I_C$, whereas $\Phi_{ext} \neq n\Phi_0$ leads to a suppression of the critical current of the SQUID. The critical current of a SQUID—or in case of a constant current bias the voltage across the SQUID—hence modulates between the two extremal values $\Phi_{ext} = n\Phi_0$ and $\Phi_{ext} = n\Phi_0/2$ and has a periodic dependence on Φ_{ext} as shown in Fig. 3. A measure for the suppression of the critical current of the SQUID is the dimensionless screening parameter

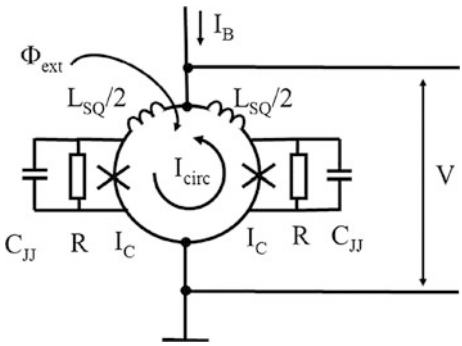

Fig. 2 Schematic of a dc SQUID with two Josephson junctions with SQUID inductance L_{SQ}, critical currents I_C, junction capacitance C_{JJ}, and resistance R. The external flux Φ_{ext}, coupled to the SQUID loop, results in a circulating screening current I_{circ}, which modulates the measured voltage V across the SQUID

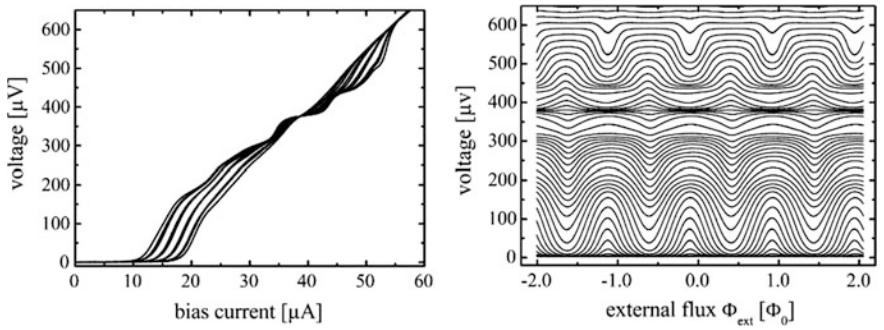

Fig. 3 (*Left*) Measured *I-V* characteristics of a SQUID for Φ_{ext} ranging between $\Phi_{ext} = n\Phi_0$ and $\Phi_{ext} = (2n + 1)\Phi_0/2$ and (*Right*) corresponding set of flux-voltage characteristics for bias currents from 0 μA to 55 μA in steps of 1μA. The flux-voltage characteristics represent the projection of the current-voltage characteristics for modulating external flux Φ_{ext}. The kinks in the current-voltage characteristics are due to resonances occurring in the SQUID, as will be discussed later

$$\beta_L = \frac{2L_{SQ}I_C}{\Phi_0}. \tag{4}$$

For $\beta_L \ll 1$ the current swing ΔI approaches $2I_C$, whereas for $\beta_L \gg 1$ it reduces to zero.

The SQUID may be operated with constant current (so-called current bias) or constant voltage (voltage bias). In current bias mode it is typically operated on the steep part of the flux-voltage characteristics, where the transfer coefficient $V_\Phi = \partial V/\partial\Phi$ is maximum. In the small signal limit ($\Phi_{ext} \ll \Phi_0$) it therefore converts an external magnetic flux Φ_{ext}, or other physical quantities that can be transformed into

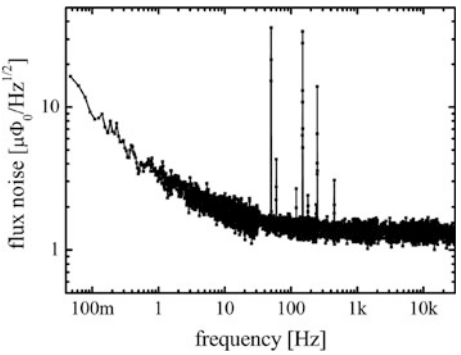

Fig. 4 Typical flux noise spectrum of a dc SQUID measured at 4.2 K. The SQUID has an inductance of L_{SQ} = 180 pH and a normal resistance of $R \approx 10\ \Omega$. The equivalent white flux noise accounts to 1.3 $\mu\Phi_0/\mathrm{Hz}^{1/2}$

magnetic flux, into a voltage across the SQUID. Since the external flux typically exceeds the small signal limit, the SQUID is usually operated in a so-called flux-locked-loop (FLL) feedback circuit, which will be discussed in the subsequent Sect. 2.3.

2.2.2 Noise in dc SQUIDs—White and 1/f Noise

The noise in SQUIDs has two contributions: a frequency independent white and a colored noise, which increases at low frequencies. The colored part of the spectrum is called 1/f noise, too. A representative spectrum of flux noise[1] is shown in Fig. 4. At 4.2 K typically Nyquist noise of the shunt resistors is the dominant source of white noise. It has been shown [13] that for optimum conditions ($\beta_C = \beta_L \approx 1$) the power spectral density of voltage noise is given by

$$S_V(f) \approx 16 k_B T R, \tag{5}$$

which is equivalent to a flux noise with spectral density

$$S_\Phi(f) = S_V / V_\Phi^2 = 16 k_B T L_{SQ}^2 / R. \tag{6}$$

Here, the approximation $V_\Phi = R/L_{SQ}$ for the transfer coefficient is used. Please note, that the measured noise is roughly four times the Nyquist noise due to mixing down effects in the SQUID.

In order to compare SQUIDs with different inductances L_{SQ}, one usually refers to the equivalent energy resolution $\varepsilon = S_\Phi / 2L_{SQ}$—the energy of the signal equal to the intrinsic noise energy in the unit bandwidth. For the optimum conditions above

[1]The equivalent flux noise $S_\Phi^{1/2}$ is given by the measured voltage noise $S_V^{1/2}$ and the transfer function V_Φ as $S_\Phi^{1/2} = S_V^{1/2} / V_\Phi$.

one can rewrite these relations as a function of the SQUID inductance L_{SQ} and junction capacitance C_{JJ} as

$$\sqrt{S_\Phi(f)} = 4 \cdot L_{SQ}^{3/4} C_{JJ}^{1/4} \cdot \sqrt{2k_B T} \text{ and} \tag{7}$$

$$\varepsilon(f) = 16 k_B T \sqrt{L_{SQ} C_{JJ}}. \tag{8}$$

where we have set $\beta_C = \beta_L = 1$.

Typically, the white flux noise of LTS dc SQUIDs operated at 4.2 K is of the order of 10^{-6} $\Phi_0/\text{Hz}^{1/2}$ and the energy resolution amounts to 10^{-32} $\text{J/Hz}^{1/2}$, corresponding to several h, with h being Planck's constant. For temperatures of about 0.3 K a noise energy of about 2 ħ has been achieved for SQUIDs with $L_{SQ} \approx 100$ pH [14]. For such a SQUID inductance the condition $\beta_L = 1$ results in a junction's critical current of about $I_C \approx 10$ μA, which is a typical value for low noise SQUIDs.

It is obvious from the relation above that the energy resolution can be improved by reducing the SQUID inductance, the working temperature and the junction capacitance.

However, for practically applicable sensors the coupling to an external signal imposes a lower limit for the SQUID inductance. The effective flux capture area of e.g. a square washer SQUID scales with the linear dimension of the washer hole, which in turn is proportional to L_{SQ}. Hence, there is a tradeoff between a small inductance for a high energy resolution and a large inductance for a sufficiently effective area and therefore for adequate coupling to external signals

The working temperature of LTS dc SQUIDs is typically fixed—either at 4.2 K or even lower temperatures, determined by the measurement task and available cooling devices. To further enhance the SQUID performance in terms of noise, the total junction capacitance C_{JJ} and hence the junction size needs to be reduced, which is typically limited by the used fabrication process. Furthermore, small area junctions can take advantage of their low capacitance only if careful attention is also been paid on the immediate surroundings of the junctions. An undesired parasitic capacitance $C_{JJ,p}$ due to a nearby overlap of superconducting electrodes may affect or even dominate the performance of superconducting devices. This requirement will be discussed in more detail in Sect. 3.

In addition to the white noise discussed above, below a certain frequency f_C, known as the 1/f corner, the noise increases with $1/f^\alpha$, where α ranges between 0.5 and 1.0. At f_C the contribution of white noise equals the contribution of 1/f noise and may be below 1 Hz. Several sources of low-frequency noise in dc SQUIDs have been identified so far. According to [15] one can distinguish between fluctuations in critical currents of the Josephson junctions and flux noise.

It is generally accepted that critical current fluctuations originate in a random trapping and release of electrons in defect states in the junction barrier. Therefore the barrier height and in this way the critical current of the Josephson junction is locally changed, which leads to a random telegraph noise. The superposition of

many of these fluctuations, each with its own characteristic lifetime, leads to a $1/f$ dependence of the power spectral density of the flux noise S_Φ [16]. As we will see in Sect. 2.3, the influence of critical current fluctuations can be reduced or even eliminated by use of an adequate electronic readout scheme.

The second source of noise, so-called flux noise, arises from the movement of trapped vortices—small non-superconducting regions inside the superconductor—in the SQUID washer. The affinity to trap flux in superconducting structures can be expressed by calculating Gibbs free energy [17–19]. According to these estimations, a small linewidth of the superconductor is usually favorable to prevent vortex trapping in the superconductor during cool-down in an ambient magnetic field. By reducing the linewidth w of superconducting structures to below $w \approx (\Phi_0/B)^{1/2}$ this kind of flux noise can in principle be eliminated. For a magnetic flux density $B \approx 50$ μT this results in $w < 6$ μm.

More recently another source of low-frequency flux noise has been identified, but up to now there is no comprehensive understanding of this phenomenon. During the last years several possible candidates to explain the microscopic origin of this low-frequency flux noise have been discussed. For example Koch et al. [20] suggested that spins of unpaired electrons on the surface of the superconductor, hopping on and off defect states due to thermal activation, may produce such a signature. In this case, the direction of the spins would be locked as long as the electrons are trapped, thus contributing a random magnetic signal. The superposition of many uncorrelated changes of spin direction would thereafter sum up to the observed $1/f$ power spectrum.

As the power spectral density of flux noise scales with V_Φ, this contribution vanishes in working points with $\partial V/\partial \Phi = 0$, whereas critical current fluctuations do not. This allows for an independent estimation and optimization for the contributions of critical current and magnetic flux noise. Although the question about the origin of this kind of flux-noise is still an unsolved puzzle, it seems that the quality of the superconducting film and its interface to e.g. the substrate play an important role for the amount of this $1/f$ flux noise and one may expect considerable improvements in the future.

2.2.3 Practical Devices

As already discussed, a dc SQUID consists of a superconducting loop with inductance L_{SQ} interrupted by two Josephson junctions. Nowadays SQUIDs are typically fabricated in thin film technology, rather than the bulk material SQUIDs that were used in the beginning. In Sect. 3 we will discuss the main steps for the fabrication of modern highly sensitive devices.

Let us now consider one of the simplest designs: the square washer SQUID. Therein the SQUID inductance is shaped as a washer with inner and outer dimensions d and D, as shown in Fig. 5 (left).

Although these “bare” or uncoupled SQUIDs, as no external signal other than the flux threading the hole is coupled to the SQUID, have small inductances given

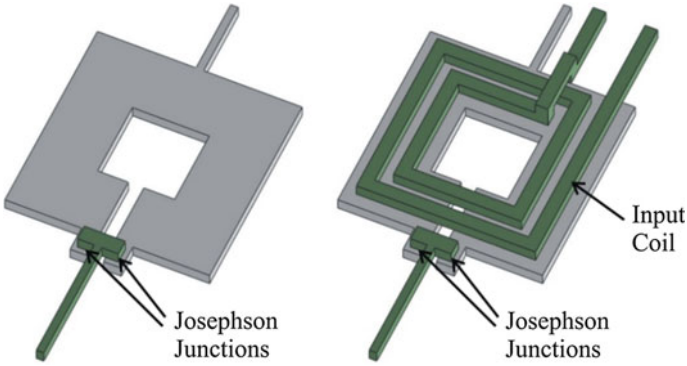

Fig. 5 (*Left*) Model of an uncoupled and (*Right*) of a coupled square washer SQUID. The SQUID inductance is shaped as a square washer with a hole in the center and a slit. The Josephson junctions are located at the outer edge of the slit, as indicated. The coupled SQUID exhibits an input coil on top of the SQUID washer

by $L_{SQ} \approx \mu_0 d$, they exhibit a very small effective flux capture area of about $A_{eff} = \partial\Phi/\partial B = dD$ [21] and therefore poor magnetic field noise

$$\sqrt{S_B(f)} = \sqrt{S_\Phi(f)}/A_{eff}. \tag{9}$$

They are favorable for applications where a good spatial resolution is needed, like in SQUID microscopy or miniature susceptometers [22].

To increase the effective area of these devices without changing their inductance one can simply increase the outer dimension D of the washer, and make use of the flux-focusing effect due to perfect diamagnetism in superconductors. Although this method has successfully been applied especially in high-temperature superconductor devices, the increased linewidth w of the superconductor may deteriorate the low-frequency performance due to trapped flux.

A more effective approach is to place a multi-turn thin film input coil on top of the SQUID washer to ensure a tight inductive coupling between both, as illustrated in Fig. 5 (right). These two layers are separated from each other by an insulating layer. Now a separate pickup loop with much larger effective area can be connected to this input coil to improve the magnetic field resolution. In addition to the input coil, a second coil is typically integrated on top of the SQUID washer in order to couple a feedback signal to the SQUID, as will be discussed in Sect. 2.3.

By integrating a thin-film input coil, SQUIDs can be implemented not only as SQUID magnetometer, but also as sensors for any physical quantity that can be transformed into magnetic flux. Magnetic gradiometers, current sensors and voltmeters, susceptometers, (rf) amplifier or displacement sensors are possible implementations. SQUIDs are therefore very versatile and their applications range from biomagnetism [23, 24] and geophysical exploration [25, 26] to magnetic resonance imaging [27]. Typical sensitivities of SQUIDs for some of these application

Table 1 Typical sensitivities of SQUID sensors

Measurement	Sensitivity
Magnetic field	10^{-15} T/Hz$^{1/2}$
Current	10^{-13} A/Hz$^{1/2}$
Voltage	10^{-14} V/Hz$^{1/2}$
Resistance	10^{-12} Ω
Magnetic moment	10^{-10} emu

scenarios are listed in Table 1. In Sect. 4 we will provide more information on some state-of-the art devices.

As discussed in Sect. 2.2, for the comparison of SQUIDs with different inductances L_{SQ}, one usually refers to the equivalent energy resolution ε. As this describes the energy resolution of an uncoupled SQUID, in practice the so-called coupled energy resolution ε_C is used, which is given by

$$\varepsilon_c = \varepsilon / k_{in}^2 \tag{10}$$

with k_{in} being the coupling constant between the input coil inductance L_{in} and the SQUID loop inductance L_{SQ}. It is determined via the mutual inductance M_{in} between the input coil and the SQUID

$$M_{in} = k_{in} \sqrt{L_{SQ} L_{in}}. \tag{11}$$

According to the definition of ε, the coupled energy resolution ε_C corresponds to the minimum energy that can be detected in the input coil per unit bandwidth. Depending on the intended application and accordingly L_{in}, present SQUIDs exhibit coupled energy resolutions of below 100 h.

The design of coupled SQUIDs on the base of washer SQUIDs is rather straightforward and can easily be carried out based on experimentally proven expressions [28, 29]: The SQUID inductance is thus given by

$$L_{SQ} = L_h + L_s + L_j \tag{12}$$

Here L_h is the inductance of the washer hole, L_s the inductance of the slit and L_j the inductance associated with the Josephson junctions (which typically can be neglected). The inductance of the washer hole is

$$L_h = \alpha \mu_0 d \tag{13}$$

with $\alpha = 1.25$ for square washer, $\alpha = 1.05$ for an octagonal washer and $\alpha = 1$ for a circular washer. The slit inductance can be approximated by

$$L_s = 0.3\,\mathrm{pH}/\mu\mathrm{m}. \tag{14}$$

The mutual inductance between the SQUID and an integrated multi-turn input coil on top of the SQUID washer is given by

$$M_{in} \approx nL_{SQ}. \tag{15}$$

The inductance of the input coil can be expressed as

$$L_{in} \approx n^2 L_{SQ}. \tag{16}$$

The input coil inductance should be matched to the inductance of the pickup circuit for optimum coupling. In case of a SQUID magnetometer the pickup loop is typically a thin film or wire wound loop with inductance L_p, as shown in Fig. 6.

The shape of the pickup circuit has to be adapted to the measurement task, as shown for planar and axial first order gradiometers in Fig. 6.

In practical devices, however, deviations from the ideal behavior may appear, as e.g. stray capacitances between the SQUID washer and the input coil can lead to resonances in the flux-voltage characteristics and may therefore strongly deteriorate the device performance. In consequence, a careful design optimization procedure is typically required for such tightly coupled SQUIDs. Detailed information on this topic can be found e.g. in [30, 31].

Although the coupled energy resolution is a good method to compare SQUIDs with different inductances, the figure of merit for e.g. a magnetometer is the magnetic field noise $S_B^{1/2}$. It has been shown that the magnetic field resolution and hence the magnetic field noise $S_B^{1/2}$ can be improved by increasing the pickup loop area while maintaining $L_{in} \approx L_p$. In Ref. [32] the approximation for the white noise level of $S_B^{1/2}$ vs. the radius r_p of the pickup loop is given as

$$\sqrt{S_B} \approx \frac{2\sqrt{\mu_0 \epsilon}}{r_p^{3/2}}. \tag{17}$$

For a circular pickup loop area with $r_p = 15$ mm and $\varepsilon = 10^{-32}$ Js this results in $S_B^{1/2} \approx 100 \times 10^{-16}$ T/Hz$^{1/2}$ = 0.1 fT/Hz$^{1/2}$.

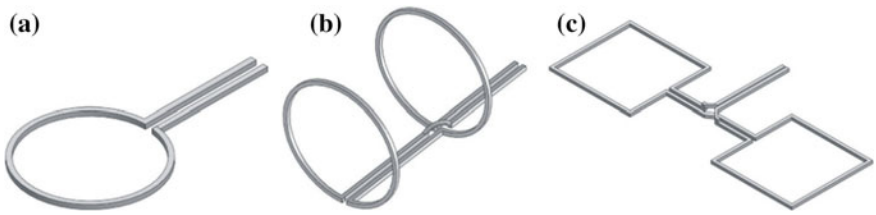

Fig. 6 Common pickup loop configurations: **a** represents a magnetometer, **b** a first order axial gradiometer and **c** a first order planar gradiometer. The two ends of the pickup loops are connected to an integrated input coil on top of the SQUID washer

It is worth to note at this point that although the SQUID sensor by itself may exhibit such an excellent noise performance, the overall noise performance of the SQUID system may be impaired by e.g. noise of the readout circuit as well as the environment as for example by noise arising from the dewar.

Another way to increase the effective area of the magnetometer while maintaining the SQUID inductance at a tolerable level is to divide the superconducting pickup loop into a number of separate loops connected in parallel in order to reduce the total SQUID inductance. In these so-called multiloop magnetometers, as described in detail in [33–36], the SQUID itself typically acts as the sensitive area, whereas the so-called Ketchen-type SQUID is inductively coupled to an antenna as discussed above. Due to inevitable losses owing to the used flux transformer in inductively coupled SQUIDs, the multiloop magnetometer allows for the best field resolution for a given chip area, as for instance described for first order gradiometers in [37].

However, transformer-coupled SQUIDs offer the possibility to include thin-film low-pass filters in the design to increase their robustness—especially for electromagnetically unshielded operation. As an example, Fig. 7 depicts the inner part of a transformer-coupled SQUID with the Josephson junctions [38]. The SQUID itself is shaped in form of a clover leaf with the input coil on top. The layout of the SQUID as a first order gradiometer results in its insensitivity to homogenous ambient field and it may thus be operated as a current sensor.

2.3 SQUID Electronics

As introduced above, the SQUID itself acts as a very sensitive magnetic flux-to-voltage transducer with nonlinear periodic flux-to-voltage characteristic (Fig. 3). In order to obtain a linear dependence of the voltage across the SQUID

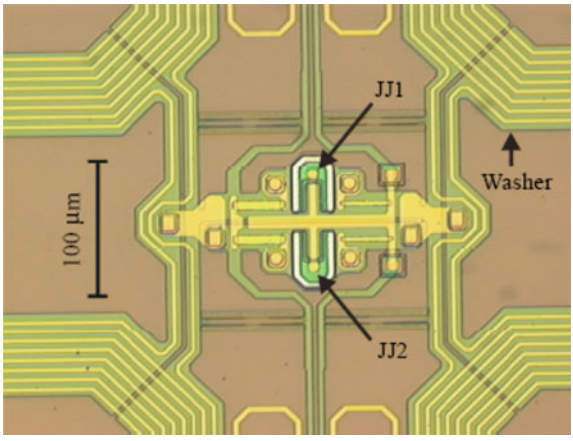

Fig. 7 Microphotograph of the central part of a transformer-coupled SQUID current sensor with the two Josephson junctions indicated as JJ1 and JJ2. The *yellow lines* on top of the SQUID washers represent the input coil. Reprinted from Reference [38], reproduced with permission of IOP Publishing Ltd

from the flux threading the SQUID loop, the SQUID is operated in a feedback loop called flux-locked loop (FLL).

2.3.1 Flux Locked Loop

There are two main FLL schemes [39]: flux-modulation and directly coupled readout.

Due to its ability for the design of compact readout circuits, which are suitable for the use in multi-channel systems with a sufficiently large bandwidth and dynamic range as well as lower power consumption, the directly coupled SQUID electronics is typically used nowadays. We will therefore restrict the discussion to this type of FLL, although the basic concept holds for both.

Before going into details of the directly coupled readout, it should be mentioned that with the flux-modulation readout scheme the preamplifier low-frequency noise and in-phase critical current fluctuations of the Josephson junctions are suppressed. As critical current fluctuations in state-of-the-art LTS tunnel junctions are generally very weak, this is not a major concern for most applications. There are as well readout options like bias reversal [15, 40], which allow suppressing in-phase and out-of-phase critical current fluctuations in both readout schemes.

The directly coupled readout scheme is schematically shown in Fig. 8. The voltage across the SQUID due to a changing signal flux Φ_{Sig} is amplified, integrated and fed back to the SQUID as a feedback flux Φ_{Fb} via a feedback resistor R_{Fb} and a mutual inductance M_{Fb}.

The FLL therefore keeps the flux inside the SQUID constant and the output voltage, the voltage across the feedback resistor, becomes linearly dependent on the applied signal Φ_{Sig} with a strongly increased linear working range.

Besides the linearization, the main purpose of the electronics is to read out the voltage across the SQUID without compromising the low voltage noise level of the SQUID. The influence of the read-out electronics on the total measured flux noise $S_{\Phi,t}^{1/2}$ can be expressed as [39]

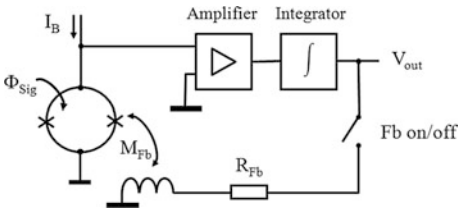

Fig. 8 Schematics of a directly coupled SQUID electronics. R_{Fb} and M_{Fb} denote the feedback resistor and mutual inductance between feedback coil and SQUID, respectively. In feedback mode the output voltage V_{out} is linearly dependent on the external signal flux Φ_{Sig}

$$\sqrt{S_{\Phi,t}} = \sqrt{\left(\sqrt{S_{\Phi,SQ}}\right)^2 + \left(\frac{\sqrt{S_{V,Amp}}}{V_\Phi}\right)^2 + \left(\sqrt{\frac{S_{I,Amp} \cdot R_{dyn}}{V_\Phi}}\right)^2}. \quad (18)$$

Here $S_{\Phi,SQ}^{1/2}$ is the intrinsic flux noise of the SQUID, $S_{V,Amp}^{1/2}$ and $S_{I,Amp}^{1/2}$ are the preamplifier input voltage and current noise, respectively. R_{dyn} denotes the dynamic SQUID resistance in the working point.

Typical input voltage and input current noise of state-of-the-art SQUID electronics are about 0.35 nV/Hz$^{1/2}$ and (2–6) pA/Hz$^{1/2}$ [41, 42]. For currently available dc SQUIDs the usable voltage swing and transfer function can typically vary between (30–150) μV and (100–500) μV/Φ_0, respectively. The dynamic resistance of such SQUIDs is usually between 5 and 50 Ω. As a result, the contribution of the room-temperature SQUID electronics can amount up to (1 − 5) μΦ_0/Hz$^{1/2}$ and may thus considerably contribute to the total measured flux noise. In part two of this section we will comment on possible noise-reduction techniques.

Note that the expression above does not account for the noise contribution due to thermal noise in the feedback resistor, given by $S_I^{1/2} = (4k_B T/R_{Fb})^{1/2}$. This current noise converts into flux noise in the SQUID via the mutual inductance M_{Fb}. Especially in SQUID systems requiring a large dynamic range, for example for unshielded operation within the Earth's magnetic field, this noise, however, may become important or even dominant.

Since SQUIDs are vector magnetometers, a rotation in the Earth's field results in a field difference[2] of up to 130 μT. Thus a SQUID magnetometer system with magnetic field noise of for example 10 fT/Hz$^{1/2}$ would require a dynamic range of the order of 200 dB which is larger than 30 Bit.[3] Even if the SQUID electronics would allow such an operational range, current analogue to digital converters (ADC) are nowadays still limited to about 24 Bit.

Besides the dynamic range, another important parameter correlated with the dynamic behavior of the FLL is the system slew rate [39, 41] given by

$$\dot{\Phi}_{\max} = \left|\frac{\partial \Phi_{Fb}}{\partial t}\right| = 2\pi \cdot f_{GBP} \cdot \delta V \cdot \frac{M_{Fb}}{R_{Fb}}. \quad (19)$$

It describes the maximum signal change in a certain time interval that the electronics is able to follow. Here f_{GBP} is the gain-bandwidth product, a fixed value for a specific amplifier configuration and δV describes the usable voltage swing of the SQUID. Accordingly, a high system slew-rate demands a large δV and a small feedback resistor value, which however may limit the system noise. The

[2]Depending on the location on Earth and taking into account only the crustal contribution of the Earth's magnetic field.

[3]In a 1 Hz bandwidth, the dynamic range can be calculated as $DR = 20 * \log$ (130μT/10fT/Hz$^{1/2}$*crest factor). Taking a crest factor of 4 this results in $DR = 190$ dB > 30 Bit.

configuration of the feedback circuit is therefore always a tradeoff between low system noise and high dynamic range and slew rate.

2.3.2 Noise-Reduction Techniques

As pointed out before, the noise contribution of the electronics may become dominant even with state-of-the-art SQUID electronics. It is obvious that increasing the transfer function V_Φ results in a reduction of this contribution.

In order to raise V_Φ of the SQUID, a readout scheme known as additional positive feedback (APF) was proposed by Drung et al. [43]. It consists of a resistor R_{APF} with an inductor L_{APF} in series, which are connected in parallel to the SQUID, as shown in Fig. 9. The incorporated inductor L_{APF} is magnetically coupled to the SQUID. In a working point on the positive slope of the flux-voltage characteristics a small signal $\delta\Phi$ will produce a positive voltage δV. Accordingly, the current through the APF coil will increase and will thus enlarge the SQUID voltage further. As a result, the flux-voltage characteristic is steepened at the positive slope, whereas the negative slope will be decreased, as illustrated in Fig. 9.

This L_{APF}-R_{APF} circuit acts as a small signal preamplifier and the transfer function V_Φ will be increased on the positive slope of the flux-voltage characteristics. The effect of the input voltage noise of the preamplifier is therefore reduced. This enhancement in V_Φ comes along with a reduction in the usable voltage swing of the SQUID and it reduces the linear flux working range Φ_{lin}. It is thus unfavorable for systems needing a large slew rate [39]. In such a configuration R_{APF} will as well contribute to the total measured noise.

Another way to decrease the contribution of the room temperature SQUID electronics is to use a second SQUID as a low noise preamplifier [44]. Figure 10 illustrates such a two-stage setup. Here, the SQUID to be measured (SQ_1) is typically operated in voltage bias mode ($R_C \ll R_{dyn}$) and the current modulation due to

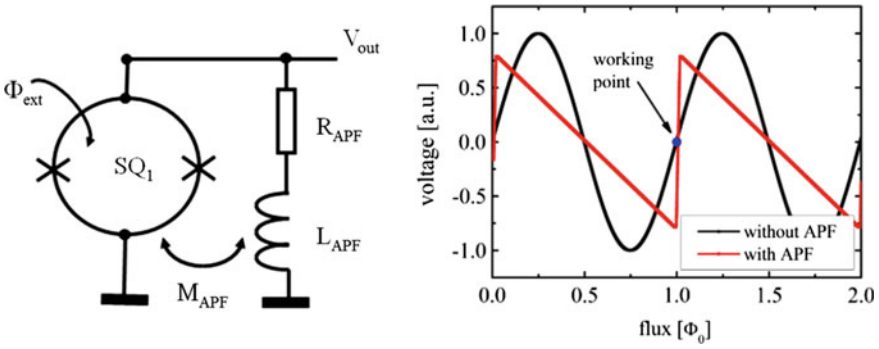

Fig. 9 Schematics of the additional positive feedback (APF) circuit. The flux-voltage characteristic with APF is steepened at the positive slope compared to the characteristics without APF. Note that the usable voltage swing across the SQUID decreases for APF

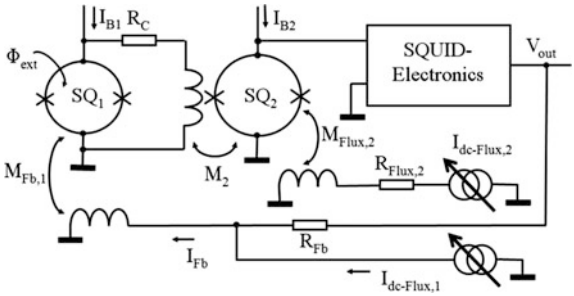

Fig. 10 Schematics of a two-stage measurement setup. The current modulation of SQUID SQ_1 due to an external signal flux Φ_{ext} is sensed in an amplifier SQUID SQ_2. Feedback may be applied to the first stage SQUID (as shown in the figure) or to SQUID SQ_2, when operated as a voltmeter

an external signal is sensed in an amplifier SQUID SQ_2. An appropriate choice of the mutual input coil inductance M_2 of the amplifier SQUID sets the flux gain $G_\Phi = (\partial\Phi_2/\partial\Phi_1)$ between the two SQUID stages to a sufficient level. The overall noise of the two-stage configuration using a directly coupled SQUID electronics amounts to [39]

$$\sqrt{S_\Phi} = \sqrt{\left(\sqrt{S_{\Phi,1}}\right)^2 + \frac{1}{G_\Phi^2}\left[\left(\sqrt{S_{\Phi,2}}\right)^2 + \left(\frac{\sqrt{S_{V,Amp}}}{V_{\Phi,2}}\right)^2 + \left(\sqrt{\frac{S_{I,Amp}\cdot R_{dyn,2}}{V_{\Phi,2}}}\right)^2\right]}. \tag{20}$$

The subscripts 1 and 2 denote SQUID SQ_1 and SQ_2 respectively.

Obviously, a large flux gain allows neglecting the contribution of the amplifier SQUID and the FLL. Especially in cases where the front-end SQUID SQ_1 is operated at a very low temperature $T \ll 4.2$ K, the two-stage configuration is often the only way to make use of the low level of SQUID noise. However, in such a configuration the linear flux-range and thus the system slew rate are reduced.

To increase the voltage signal and thus the transfer function without affecting the linear flux range, a so-called series SQUID array with many identical SQUIDs connected in series can be used. If the deviation in the critical currents of the SQUIDs is low enough and provided that the same flux is coupled to all SQUIDs in the array, the voltage modulations of the individual SQUIDs coherently sum up to a single SQUID-like characteristic. For a series array of N SQUIDs the transfer function and flux noise are given by

$$V_{\Phi,Array} = N \cdot V_{\Phi,SQ} \text{ and} \tag{21}$$

$$\sqrt{S_{\Phi,Array}(f)} = \sqrt{S_{\Phi,SQ}(f)}/\sqrt{N}. \tag{22}$$

Obviously, the flux noise of a SQUID array can become considerably smaller than for a single SQUID. The direct use of series SQUID arrays as a current sensor coupled to a pickup loop with the purpose of measuring the flux induced screening current is, however, not feasible, as inevitable inaccuracies in the lithography and hence small variations in SQUID geometries lead to amplitude modulation of the flux-voltage characteristics for large flux bias values. Trapped flux in the individual SQUIDs of the array may as well cause distortions in the flux-voltage characteristics.

SQUID arrays are therefore often used as amplifier SQUIDs in a two-stage configuration as discussed above. As the flux noise scales with $N^{1/2}$, even a moderate number N of SQUIDs and a low flux gain may be sufficient for most applications. In Refs. [45, 46] the use of series SQUID arrays as readout devices for SQUIDs has been shown. They achieved output voltages in the mV range and bandwidths of more than 100 MHz.

Instead of a series array, which provides a periodic flux-voltage characteristic, a series connection of intentionally different SQUIDs with an appropriate distribution of SQUID inductances show only one pronounced minimum [47, 48]. These devices are known as superconducting quantum interference filter (SQIF). Although this scheme shows somewhat higher noise than series SQUID arrays with the same number of individual SQUIDs, it may be advantageous for some applications since locking to multiple working points in the amplifier SQUID in FLL mode is not possible.

Let us conclude this section with a more general comment: nowadays SQUID electronics have become mature and offer low noise and large bandwidth combined with low thermal drift, low power consumption and small size, allowing to operate SQUID systems even in remote areas. They are typically computer controlled with an automated setup of SQUID working points and there even exist user-friendly one-button solutions. The current trend is towards a higher speed and bandwidth or the integration of preamplifier stages (also SQUID based) at 4.2 K to avoid the delay times due to signal propagation in the connecting wires between room-temperature and the cryogenic bath.

3 SQUID Fabrication

The fabrication of LTS SQUIDs is based on sophisticated thin-film techniques similar to their use in semiconductor industry. SQUID sensors are fabricated on wafers, which are then diced into chips with dimensions of several mm^2 size depending e.g. on the necessary pickup area for the envisaged application. Quartz, silicon or oxidized silicon wafers sized 4 inch or larger are typically used as substrates. Therefore, hundreds of SQUIDs can be fabricated in one run.

In this section we will comment on basic thin-film techniques used for the fabrication of LTS SQUIDs and we will highlight the most important step, the junction fabrication. More detailed information can e.g. be found in [49].

3.1 Lithography and Thin-Film Techniques

Nowadays superconducting thin film materials for LTS SQUIDs are mainly Nb and Al. In the beginning usually Pb or Pb alloys have been used (as well as electrode material for the junction fabrication), but the limited long term stability and problems associated with thermal cycling have led to the "all-refractory" process used today.

To fabricate thin superconducting films, various deposition techniques such as thermal or e-beam evaporation, molecular beam epitaxy, plasma and ion beam sputtering can be used. Due to the high melting temperature of Nb, sputtering is de facto the standard. This is typically done in ultra-high vacuum, as impurities may dramatically change the superconducting thin-film properties.

A careful optimization of the deposition and patterning process of superconducting films with respect to their influence on e.g. minimum film stress, superconducting properties or the shape of the structured edges is essential. Steep edges of superconducting films are usually favorable, as they are less susceptible to flux trapping. In multilayer processes, moreover, special attention has to be paid to avoid residues or fence structures associated with the patterning of the films as they may lead to shortcuts in or failure of the devices. Higher integrated multilayer processes like the Josephson junction based rapid single flux quantum (RSFQ) logic [50, 51] try to overcome difficulties associated with an increased number of superconducting layers and therefore potential step height or surface topography problems by planarization of isolation layers (typically with chemical mechanical polishing). As the design of SQUIDs is usually less complex than RSFQ circuits, planarization is in generally not performed in SQUID fabrication nowadays, but it may be implemented in future.

The patterning of the thin films is either done by lift-off or by etching. For lift-off, the photoresist is applied to the substrate prior to the thin film deposition. When the thin film is patterned via etching, the photoresist is placed on top of the thin film. In both cases the resist acts as a mask for the structure to be defined. For lift-off the resist is removed in an (ultrasonic) solvent bath so that the film on top of the resist is removed as well. The etch process is typically done by dry etching such as plasma or reactive ion-beam etching. Wet etching may as well be used, but is not that attractive due to the isotropic etch behavior. To avoid over-etching of the underlying film, one can either use an end-point detector or make use of thin natural etch stops like an Al layer for a fluorine based etch process.

In general, elevated temperatures should be avoided (especially when the trilayer to form the Josephson junctions is already deposited on the wafer), as this increases e.g. the diffusion of hydrogen into the thin film or may change the barrier characteristics [52, 53].

The typical film thickness is in the range of 50 to about 300 nm. The linewidth of superconducting structures such as patterned multi-turn input coils on top of the SQUID washer may be as small as 1 μm or even less. The resist thickness depends

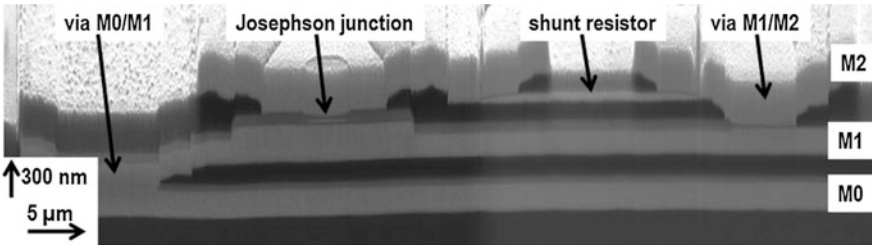

Fig. 11 Scanning electron microscope image of the cross-section of a shunted Nb–AlO_x–Nb Josephson junction. The sample was prepared by focused ion beam etching. M0, M1 and M2 indicate the different Nb wiring layers. The *vias* are interconnects between these layers. Reprinted from Reference [54], reproduced with permission of Elsevier

on the lithography method and the lateral dimension of the desired thin film structure and may vary between several hundred nm to about 2 µm.

Depending on the design complexity, the fabrication of LTS SQUIDs includes at least 2 superconducting layers, one for the SQUID washer and one for the input and feedback coils, and (several) isolation layers. Figure 11 shows a scanning electron microscope image of a cross-section of a shunted Josephson junction together with the appropriate Nb wiring layers used in the Fluxonics foundry RSFQ process [54].

3.2 Junction Fabrication

Nowadays SIS Josephson junctions are typically based on a sandwich of an in situ deposited Nb–AlO_x–Nb trilayer. There are other material systems like e.g. Nb–SiN_x–Nb but they do not exhibit such a good junction quality, reproducibility, low junction capacitance, and low level of critical current fluctuations. Detailed information on other material systems used in the past can be found in [49, 55].

Today, most fabrication technologies are based on the so-called SNAP process (selective niobium anodization process) [56] or its numerous variations. In 1983 Gurvitch introduced the use of Nb–AlO_x–Nb Josephson junctions [57]. This material combination has led to superior junction characteristics and became soon the most important junction fabrication process. Up to now it is the standard even for very complex RSFQ circuits for digital applications and it allows the reliable fabrication of up to tens of thousands Josephson junctions on a single chip [50].

The junction fabrication starts with the deposition of a trilayer consisting of a Nb base electrode, a thin Al layer (which is partly oxidized during the trilayer deposition) and another Nb layer as counter electrode. The in situ deposition of the trilayer is essential for clean interfaces between these layers. The AlO_x is formed by exposing the sputtered Al to pure oxygen atmosphere for a certain time. The thickness of the AlO_x layer t_{ox}—given by the product of oxygen partial pressure and exposure time—determines the junction's critical current density j_C, which is

exponentially dependent on t_{ox}. For SQUIDs j_C is in the range of (0.1–2) kA/cm^2 depending on the desired junction's critical current and size. The typical film thickness is (50–300) nm for Nb layers and about 10 nm for Al. The thin Al layer is used to level out the surface roughness of the underlying Nb layer and allows a low junction capacitance due to the much lower dielectric constant ε_r of AlO_x compared to NbO_x.

In the SNAP process the junction area is defined by anodizing the upper electrode of the trilayer. During anodization the desired junction area is covered by a small resist dot. In this so-called window-type process the typical minimum junction size is several μm^2. Since the anodization solution creeps partly under the photoresist, small junctions are less reproducible or even defective.

For electrical connection of the junction a Nb layer is deposited on top of the counter electrode. Finally a shunt resistor is placed close to the junction to damp its dynamics and to fulfil the condition $\beta_C \leq 1$. Usually Pd, AuPd, Ti, or Mo is used as shunt material. Figure 12 (left) shows a scanning electron microscope image of such a window-type junction with dimensions of (3 × 3) μm^2.

The specific capacitance of a Nb–AlO_x–Nb Josephson junction (it forms a parallel-plate capacitor) is about 45–60 fF/μm^2, depending on the barrier thickness and therefore on the critical current density [58]. Due to the overlap of superconducting layers around the junction (e.g. to compensate inevitable alignment errors between different layers), a parasitic capacitance is formed, which adds to the junction capacitance. The influence of this effect becomes even more pronounced as the junction size is reduced.

As discussed in Sect. 2.2, a small total junction capacitance is favorable since it will improve the performance in terms of energy resolution and voltage swing of the SQUID. To reduce or even avoid parasitic capacitance, several fabrication technologies have been reported. One possible approach is the so-called cross-type technology [59], in which the junction is defined by the overlap of two narrow

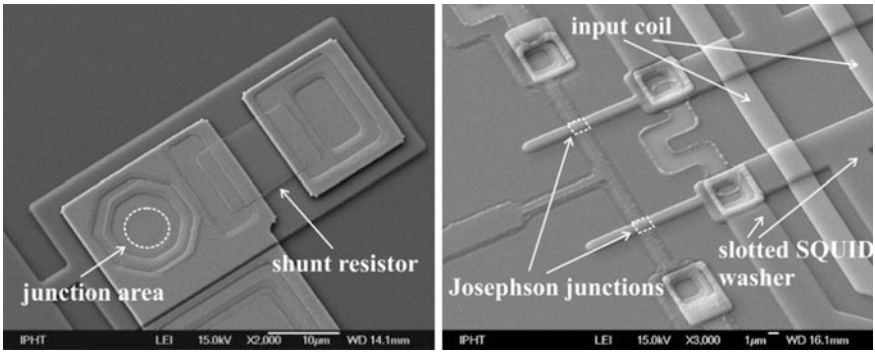

Fig. 12 (*Left*) Scanning electron microscope (SEM) image of a Josephson junction fabricated in the window-type technology and (*Right*) SEM image of a SQUID fabricated in the cross-type junction technology. In this technology the junction size is considerable reduced and parasitic capacitances due to the overlap of superconducting layers around the junction is avoided

perpendicular strips. Figure 12 (right) shows a SEM image of the central SQUID part with the Josephson junctions as indicated. The lower strip is the entire Nb–AlO_x–Nb trilayer, which is patterned with the width corresponding to the desired linear dimension of the junction. The second perpendicular strip of Nb is deposited on top of the trilayer and acts as a mask for patterning the Nb counter electrode from the trilayer. Due to the self-alignment of the process, no parasitic capacitance is formed. In [59], high quality Josephson tunnel junctions with dimensions of $(0.6 \times 0.6)\ \mu m^2$ have been reported. Due to the narrow linewidth design of the junctions, flux trapping is avoided and these devices can be cooled in the Earth's magnetic field without restrictions [60].

The current trend in superconducting fabrication technology is the further decrease in junction capacitance and accordingly a downsizing of the Josephson junctions, while maintaining a high fabrication yield and low parameter spread over the entire wafer.

4 State-of-the-Art Devices

As discussed above, SQUIDs can be used not only as magnetometers, but also as sensors for any physical property that can be transformed into magnetic flux. In this section we will show results achieved with state-of-the-art devices aimed for a number of applications.

4.1 SQUID Magnetometer

For a SQUID magnetometer the figure of merit is the equivalent magnetic field noise $S_B^{1/2} = S_\Phi^{1/2}/A_{eff}$. As we have seen, for optimized SQUID parameter β_L and β_C of about unity, the flux noise $S_\Phi^{1/2}$ can be expressed as a function of the design dependent parameters SQUID inductance L_{SQ} and junction capacitance C_{JJ}. For the smallest junction size in the used fabrication process, the optimization with respect to low $S_B^{1/2}$ can be carried out by minimizing the ratio L_{SQ}/A_{eff}. It describes how effective a given SQUID inductance—which determines the magnitude of white flux noise—is transformed into an effective area.

As already discussed above, multiloop magnetometers allow for the best field resolution for a given chip area. Excellent results have been achieved, yielding in magnetic field noise levels of below 1 $fT/Hz^{1/2}$ in the white noise region [36, 61]. Figure 13 (left) shows a field noise spectrum of a device with an outer pickup coil dimension of 12 mm. The devices show a typical white field noise of about 0.3 $fT/Hz^{1/2}$.

SQUID magnetometers may also be realized by connecting a thin-film or wire wound pickup coil to the input coil of a current sensor SQUID. As discussed in Sect. 2.2, the magnetic field noise can be improved by increasing the pickup loop

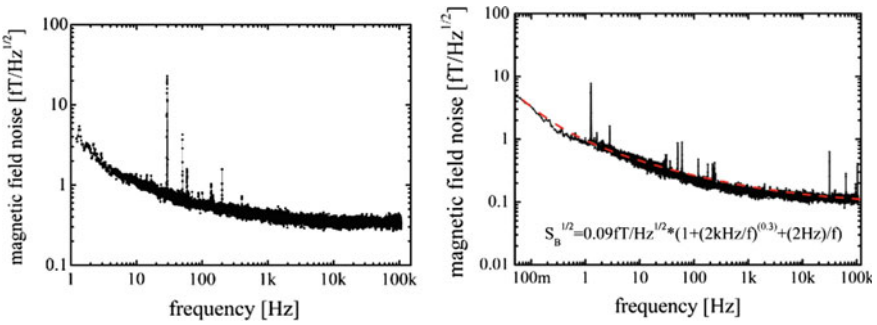

Fig. 13 (*Left*) Field noise spectra of an integrated multiloop magnetometer SQUID with an outer pickup coil dimension of 12 mm and (*Right*) of a magnetometer composed of a SQUID current sensor and an all thin-film pickup coil with dimensions of (29 × 33) mm^2. The *left figure* is reprinted from Reference [61], reproduced with permission of IOP Publishing Ltd

area, while maintaining $L_{in} \approx L_p$. Limitations of this approach are e.g. due to the inner cryostat dimensions or noise arising from impurities in the dewar walls or the used superinsulation around the dewar. The SQUID system should moreover feature a sufficiently large dynamic range for the intended application.

Figure 13 (right) shows a magnetic field noise spectrum of a SQUID magnetometer composed of a highly sensitive SQUID current sensor connected to a thin-film pickup coil with dimensions of (29 × 33) mm^2. The device exhibits a white field noise level of about 0.1 fT/Hz$^{1/2}$, showing excellent agreement with the rough approximations in Sect. 2.2. It is worth to note that $S_B^{1/2}$ is still below 1 fT/Hz$^{1/2}$ at 1 Hz.

Both spectra in Fig. 13 show a shallow increase of the noise starting at frequencies of about 10 kHz, which is caused by magnetic flux noise as discussed in Sect. 2.2. If this source of noise is identified, further noise improvement in the frequency range 1 Hz < f < 10 kHz may be expected. At frequencies below about 1 Hz, noise arising from critical current fluctuations in the Josephson junctions became dominant, as can be seen in Fig. 13 (right).

Beside the superior noise performance of the devices, which is usually measured inside a high-permeable and superconducting shielding, the performance of the SQUID system in unshielded operation is of particular importance. In e.g. [62] the noise of a SQUID system cooled and operated in the Earth's magnetic field has been investigated. The system noise is estimated by correlating the signal of two identical SQUID systems aligned in parallel to cancel out natural geophysical noise. Figure 14 (left) shows the spectrum from raw data of these two systems. As could be seen, there is an excellent correlation between the channels in parallel, allowing to use the discussed correlation techniques.

Figure 14 (right) shows the estimated intrinsic noise by cross-correlation in the frequency domain. The according white system noise is about (1.2–1.5) fT/Hz$^{1/2}$ for the three orthogonal channels. The estimated low-frequency noise may not represent the intrinsic system noise due to a small misalignment between the two

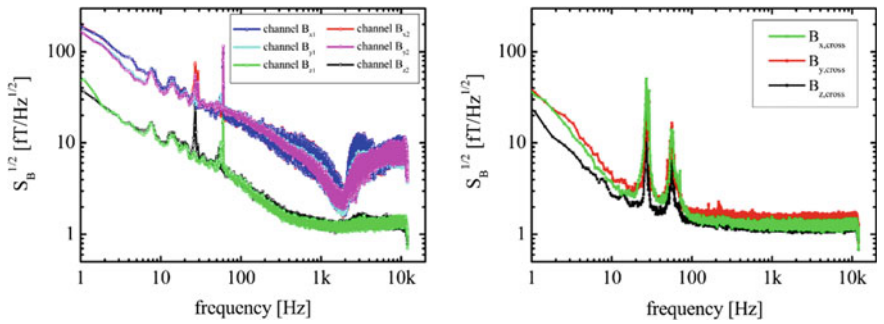

Fig. 14 (*Left*) Spectra of two highly sensitive SQUID systems, each comprising three orthogonal SQUIDs. Unshielded measurement was performed simultaneously NW of Delta, Utah, USA. (*Right*) Estimated intrinsic SQUID system noise obtained by a cross-correlation technique in the frequency domain from the raw data as shown *left*. Reprinted from Reference [62], reproduced with permission of IOP Publishing Ltd

systems and probably due to noise induced by motion of the system in the Earth's magnetic field.

4.2 Gradiometer

As we have discussed in Sect. 2.3, the mobile operation of such highly sensitive SQUID magnetometers in the Earth's magnetic field would require a dynamic range exceeding 30 Bit, well beyond the capability of current electronics and AD converter. If the pickup loop is configured as a gradiometer with two or more coils of opposite winding arranged at a certain baseline, distant (noise) sources do not produce a signal in the input coil since they produce spatially very homogeneous fields. Signals from a nearby sample, however, produce a spatially inhomogeneous field at the gradiometric pickup loop, leading to a signal current in the loop, which will be detected by an inductively coupled SQUID current sensor [63].

The quality of the gradiometer is usually denoted as the balancing, that is the gradiometer response to a homogenous magnetic field. For an ideal gradiometer there is no response, as the effective areas of opposite windings of the input coil are equal. As inaccuracies in e.g. the lithography cannot be avoided, real devices exhibit (small) parasitic areas to a homogenous magnetic field. Thus, in a gradiometer system all components of the magnetic field are usually measured simultaneously to allow for a compensation of the residual imbalance.

There are in principle two classes of gradiometers: electronic and intrinsic gradiometers. In electronic gradiometers, the FLL output voltages of two SQUID magnetometers separated by a certain baseline are subtracted. However, the sensitivity of such SQUIDs, and therefore of the gradiometer, is typically low due to dynamic range issues as discussed for magnetometers operating in the Earth's

magnetic field. To reduce the dynamic range requirements, these two magnetometers may be operated within a global feedback scheme [64].

Intrinsic gradiometers directly measure the difference of magnetic fields threading two pickup-loops. Typically a serial connection of two pickup loops, which are arranged in a figure of eight, is used. The pickup loop may consist of a thin film or be wire wounded, and is connected to the input coil of a SQUID current sensor. In this case the SQUID should be arranged as a second order gradiometer to solely measure the flux induced by the screening current in the pickup loop.

Depending on the component of the magnetic field gradient tensor $G_{i,j} = \{\partial B_i / \partial x_j\}$ (with $i,x_j \in \{x, y, z\}$) that should be measured, either planar or axial type gradiometers are used. Planar type gradiometers are often integrated all thin-film devices, as this allows for better balancing, which is ideally limited just by lithography alignment errors. In their axial counterparts usually a wire wound pickup coil is used.

With an appropriate balance of the gradiometer, they allow for a mobile operation within the Earth's magnetic field, without exceeding the dynamic range of current feedback circuits. Thus, they enable to measure the complete magnetic gradient tensor with high sensitivity. Sophisticated inversion algorithms may thus enable the detection and probably a localization of the signal source.

Figure 15 shows a noise spectrum of a planar integrated all thin-film SQUID gradiometer. The gradiometer has a baseline of 40 mm and a gradiometric pickup loop shaped in a figure of eight with a size of the two loops of each (20 × 20) mm^2. The white noise amounts to 18 $fT/mHz^{1/2}$. These integrated devices show a balance of about 1×10^4. Using the simultaneously acquired magnetic field components to compensate for the measured parasitic areas, a balance of up to 1×10^7 has been achieved [65].

4.3 Current Sensors

For SQUID based current sensors typically an integrated superconducting input coil is placed on top of the SQUID washer. The input coil is inductively coupled to the

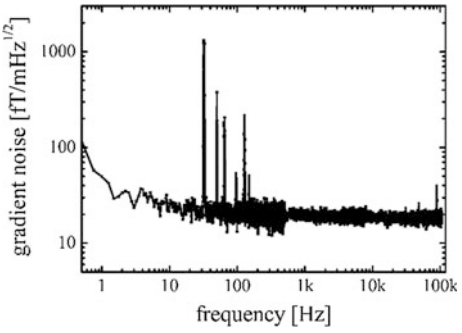

Fig. 15 Noise spectrum of a planar SQUID gradiometer measured inside a magnetic shielding. The gradiometer baseline is 40 mm and the size of the two pickup loops is (20 × 20) mm^2 each. The measured white gradient noise is 18 $fT/mHz^{1/2}$

SQUID loop, so that a current in this coil produces a magnetic flux inside the loop. It therefore can be used as a current sensor with inductive input impedance.

Tight coupling of the input coil allows for a good current resolution $S_I^{1/2} = S_\Phi^{1/2}/M_{in}$. Since the mutual input inductance M_{in} is proportional to the SQUID inductance and the number of turns on the SQUID washer, many turns need to be integrated depending on the required current resolution. Limitations arise from the minimum linewidth and distance between adjacent windings given by the fabrication process. Moreover, the superconducting properties of the input coil need to be preserved: the superconducting thin film needs sufficient edge coverage so that the signal current does not exceed the critical current of the thin film.

However, tight coupling of an integrated input coil may lead to strong resonances in the flux-voltage characteristics and demands for a throughout sensor optimization, as discussed in Sect. 2.2. Another possibility to effectively couple an input coil with a few μH to a SQUID with an inductance of about 100 pH or less is to make use of a double-transformer coupling scheme [66]. Here, an additional intermediate flux transformer is used, which may be a thin-film variant, which may as well be located on a separate chip or a wire wound transformer typically used e.g. for cryogenic current comparators [67].

In [68] a wire wound current comparator having 10,000 turns in the primary coil is reported, achieving a current resolution of 4 fA/Hz$^{1/2}$ in the white noise region. Integrated thin-film devices are in most cases preferable to their bulky wire wound counterparts and recently white noise levels of about 110 fA/Hz$^{1/2}$ [69], 25 fA/Hz$^{1/2}$ [70] and 3 fA/Hz$^{1/2}$ [71] have been achieved.

Figure 16 shows the noise spectrum of the device described in [71]. The white current noise amounts to 3 fA/Hz$^{1/2}$. It consists of a SQUID chip with dimensions of (2.5 × 2.5) mm^2 and separate flux-transformer chips of (12.5 × 12.5) mm^2. With the measured input inductance of 9.5 mH the energy resolution can be estimated to about 65 h.

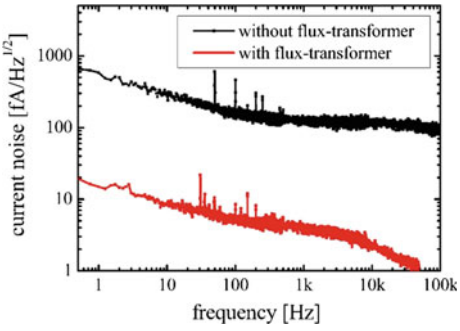

Fig. 16 Noise spectra of the SQUID current sensor with and without the transformer normalized to the input current. The white noise amounts to 3 fA/Hz$^{1/2}$ and 110 fA/Hz$^{1/2}$ with and without transformer, respectively. Reprinted from Reference [71], reproduced with permission of IOP Publishing Ltd

4.4 Further Applications and Trends

4.4.1 Miniature and Nano-SQUIDs

In contrast to SQUID magnetometers, which are usually aimed for a low magnetic field noise, miniature or even nanometer sized SQUIDs or SQUIDs with pickup loops in this dimension are optimized for a good spatial resolution and low noise. They may be used for SQUID microscopy [22] or as miniature SQUID susceptometers [14].

Current research focuses e.g. on the application of such sensors for the investigation of small spin systems and the detection of single electron spin-flips [72–74].

In order to improve the spin sensitivity $S_\mu^{1/2} = S_\Phi^{1/2}/\Phi_\mu$ of such SQUIDs (here S_μ and S_Φ are the noise spectral power density normalized to the magnetic moment and flux, respectively), one needs to reduce their physical dimensions, thereby reducing the equivalent flux noise spectral density S_Φ via the decrease in total SQUID inductance L_{SQ}, as well as increasing the coupling Φ_μ between a particle with magnetic moment μ to the SQUID [14, 75].

Miniaturized SQUIDs are usually realized using constriction type junctions, where a small hole is patterned into a thin superconducting strip either by electron beam or focused ion beam lithography [76–79]. In [80] a nano-SQUID has been realized by depositing a SQUID loop on the apex of a hollow quartz tube pulled into a very sharp pipette. For Pb based devices white flux noise levels of down to 50 $n\Phi_0/Hz^{1/2}$ have been reported.

The above presented cross-type Josephson tunnel junctions allow for the implementation of SIS junctions that are preferred compared to their SNS (superconductor-normal conductor-superconductor) counterparts [81]. Their small junction capacitance results in a remarkable reduction of white flux noise levels. Figure 17 shows a scanning electron micrograph of a device with an inner loop dimension of 1.5 μm. The right panel of Fig. 17 shows the flux noise spectrum of a device with 0.5 μm loop dimension. From the measured white flux noise of about 70 $n\Phi_0/Hz^{1/2}$ a spin sensitivity of $S\mu^{1/2} < 7\mu_B/Hz^{1/2}$ has been estimated [82].

4.4.2 Emerging SQUID Concepts

To overcome the problems associated with the dynamic range of SQUID systems and limited resolution of current AD converters, several SQUID concepts have been introduced, with e.g. digital feedback loops operated either at room temperature [83, 84] or integrated on the sensor chip [85, 86]. These so-called digital SQUIDs are usually based on a critical current comparator in a superconducting pickup loop. Here, the screening current due to an external flux threading the pickup loop is

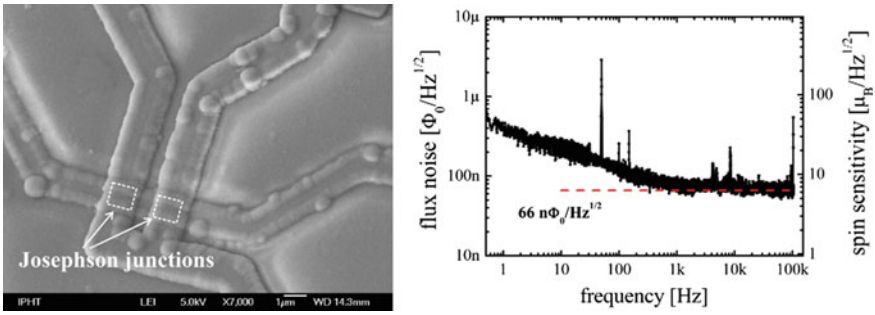

Fig. 17 (*Left*) Scanning electron micrograph of a miniaturized SQUID with an inner loop dimension of 1.5 μm based on cross-type Josephson junctions. (*Right*) Flux noise spectrum of a nanoSQUID with 0.5 μm loop dimension. The equivalent white flux noise corresponds to 66 $n\Phi_0/Hz^{1/2}$. The spin sensitivity (right hand axis) was calculated according to $S_\mu^{1/2} = S_\Phi^{1/2}/\Phi_\mu$, with the estimated coupling $\Phi_\mu = 10.5\ n\Phi_0/\mu_B$. Reprinted from Reference [82], reproduced with permission of IOP Publishing Ltd

superimposed to the bias current of e.g. a hysteretic single Josephson junction. If the sum of both exceeds the junctions critical current, it switches to the voltage state. Applying an ac-bias allows to reset the hysteretic junction and further enables the up and down-counting of the flux in the loop. The single junction may be replaced by a magnetically coupled SQUID to increase the current sensitivity and to avoid a direct feedback to the pickup loop.

The integration of on-chip Josephson junction logic like RSFQ avoids the time delay due to signal propagation to the room-temperature electronics and enables data pre-processing. Thus, large bandwidths of several 100 MHz and large system slew-rates may become possible. First prototypes of such SQUIDs have been fabricated, but the reliable low-noise operation has to be proven in practical applications. However, the on-chip integration is accompanied by a strong increase in circuit complexity and thus greater demands on the fabrication process.

In [87], another operation principle has been introduced to overcome the dynamic range limitation of current SQUID systems. In this configuration, a cascade of coplanar SQUIDs, which exhibit effective areas differing by several orders of magnitude, are arranged on a single chip. Assuming a homogenous magnetic field over the chip area, the information is thus split into several channels, which are digitized individually. Information is composed by post-processing of the data. Figure 18 illustrates the cascade principle. The correct branch of the sensitive SQUID is determined by a reference SQUID which operates in its own feedback loop. The sensitivity of the SQUID system is given by the most sensitive SQUID in the cascade. In [87] an overall dynamic range of 190 dB has been reported. The presented SQUID system, moreover, enables the absolute measurement of the vector components of the Earth's magnetic field.

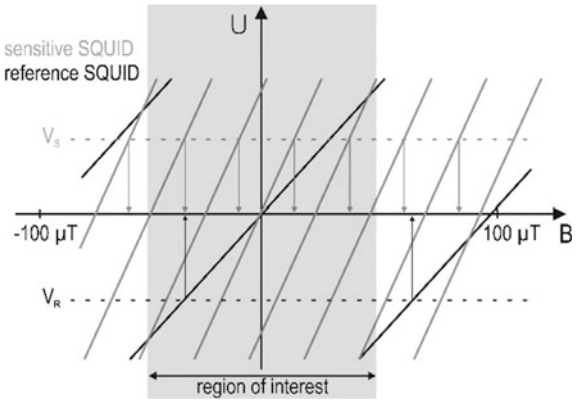

Fig. 18 Working principle of the SQUID cascade setup: In the region of interest, the reference SQUID exhibits a unique operating point. The output voltage of this reference SQUID V_R then indicates the possible working range of the sensitive SQUID, which determines the overall system sensitivity. Reprinted from Reference [87], reproduced with permission of IOP Publishing Ltd

5 Concluding Remarks and Outlook

SQUIDs are today's most sensitive devices for the detection of magnetic flux with energy resolutions approaching the quantum limit. They have a wide and flat frequency response ranging from dc to several GHz. SQUIDs can be used as sensors for any physical quantity that can be transformed into magnetic flux, such as current, voltage, magnetization and susceptibility, displacement as well as temperature and others. They are therefore very versatile and can address a large variety of applications.

To exploit the superior sensitivity of LTS dc SQUIDs, however, a low operation temperature, of 4.2 K and below is mandatory. The need for cryogenics is a significant barrier to the widespread application of SQUIDs since both the operator's convenience and the system costs are impaired. In this context we would like to recall the comment of Harold Weinstock given at a NATO Advanced Study Institute in 1990: "Never use a SQUID when a simpler, cheaper device will do the job."

Fortunately, during the last years, general demand has advanced the development of cryocoolers which are now commercially available in a variety of models. However, to use these mechanical coolers, the measurement chamber is typically magnetically shielded, to attenuate magnetic and vibrational noise from the cryocooler. If these noise sources can be reduced considerably at reasonable expenses, a variety of potential markets may be opened.

The fabrication of LTS SQUIDs based on Nb–AlO_x–Nb Josephson junctions is already a mature technology and allows the reliable fabrication of up to tens of thousands Josephson junctions on a single chip. Current technology development is

mainly towards a further decrease in junction capacitance and accordingly a downsizing of the Josephson junctions, as well as yield and parameter spread optimization. This will result in a strong sensitivity increase of SQUIDs. Moreover, small linewidth devices enable the operation in ambient magnetic fields. Revealing the origin of magnetic flux noise may further improve the sensitivity of modern SQUIDs.

During the last years, SQUID electronics have been developed towards low noise and large bandwidth together with low thermal drift, low power consumption and small size. User-friendly solutions that can be operated even by non-professional personal are available. Current research focuses towards a higher speed and further increased bandwidth and the integration of preamplifier stages at 4.2 K. A significant increase in dynamic performance—a key issue especially for highly sensitive unshielded mobile operation—may be expected.

Acknowledgements The authors highly acknowledge Dr. S. Anders for careful proofreading and many stimulating discussions.

References

1. M. Tinkham, *Introduction to Superconductivity* (Dover Publications, USA, 1996)
2. W. Buckel, R. Kleiner, *Superconductivity* (Wiley-VCH, Weinheim, 2008)
3. H. Weinstock, *Squid Sensors: Fundamentals, Fabrication, and Applications* (Kluwer Academic Publishers, Dordrecht, 1996)
4. J. Clarke, A.I. Braginski, *The SQUID Handbook: Fundamentals and Technology of SQUIDs and SQUID Systems* (Wiley-VCH, Weinheim, 2004)
5. J. Clarke, A.I. Braginski, *The SQUID Handbook: Applications of SQUIDs and SQUID Systems* (Wiley-VCH, Weinheim, 2006)
6. P. Seidel, *Applied Superconductivity: Handbook on Devices and Applications* (Wiley, Hoboken, 2015)
7. R. Jaklevic, J. Lambe, A. Silver, J. Mercereau, Quantum interference effects in Josephson tunneling. Phys. Rev. Lett. **12**, 159–160 (1964)
8. B.D. Josephson, Possible new effects in superconductive tunneling. Phys. Lett. **1**, 251–253 (1962)
9. D.E. McCumber, Effect of ac impedance on dc voltage-current characteristics of superconductor weak-link junctions. J. Appl. Phys. **39**, 3113–3118 (1968)
10. W.C. Stewart, Current-voltage characteristics of Josephson junctions. Appl. Phys. Lett. **12**, 277–280 (1968)
11. C.M. Falco, W.H. Parker, S.E. Trullinger, P.K. Hansma, Effect of thermal noise on current-voltage characteristics of Josephson junctions. Phys. Rev. B. **10**, 1865–1873 (1974)
12. R.F. Voss, Noise characteristics of an ideal shunted Josephson junction. J. Low Temp. Phys. **42**, 151–163 (1981)
13. C.D. Tesche, J. Clarke, dc SQUID: noise and optimization. J. Low Temp. Phys. **29**, 301–331 (1977)
14. M.B. Ketchen, D.D. Awschalom, W.J. Gallagher, A.W. Kleinsasser, R.L. Sandstrom, J.R. Rozen, B. Bumble, Design, fabrication, and performance of integrated miniature SQUID susceptometers. Trans. Magn. IEEE **25**, 1212–1215 (1989)
15. R.H. Koch, J. Clarke, W.M. Goubau, J.M. Martinis, C.M. Pegrum, D.J. Harlingen, Flicker (1/f) noise in tunnel junction dc SQUIDS. J. Low Temp. Phys. **51**, 207–224 (1983)

16. S. Machlup, Noise in semiconductors—spectrum of a two-parameter random signal. J. Appl. Phys. **25**, 341–343 (1954)
17. M.A. Washington, T.A. Fulton, Observation of flux trapping threshold in narrow superconducting thin films. Appl. Phys. Lett. **40**, 848–850 (1982)
18. G. Stan, S. Field, J.M. Martinis, Critical field for complete vortex expulsion from narrow superconducting strips. Phys. Rev. Lett. **92**, 097003 (2004)
19. K. Kuit, J. Kirtley, W. van der Veur, C. Molenaar, F. Roesthuis, A. Troeman, J. Clem, H. Hilgenkamp, H. Rogalla, J. Flokstra, Vortex trapping and expulsion in thin-film $YBa_2Cu_3O_{7-\delta}$ strips. Phys. Rev. B. **77**, 134504 (2008)
20. R.H. Koch, D. DiVincenzo, J. Clarke, Model for 1/f flux noise in SQUIDs and qubits. Phys. Rev. Lett. **98**, 267003 (2007)
21. M.B. Ketchen, W.J. Gallagher, A.W. Kleinsasser, S. Murphy and J.R. Clem, in *dc SQUID Flux Focused,* ed by H.D. Hahlbohm, H. Lübbig. SQUID '85—Superconducting Quantum Interference Devices and their Applications (De Gruyter, 1986), pp. 865–871
22. J.R. Kirtley, Fundamental studies of superconductors using scanning magnetic imaging. Rep. Prog. Phys. **73**, 126501 (2010)
23. J. Vrba, J. Nenonen, L. Trahms, in *Biomagnetism*, ed by J. Clarke, A.I. Braginski. The SQUID Handbook: Applications of SQUIDs and SQUID Systems (Wiley-VCH, Weinheim, 2006), pp. 269–389
24. H. Nowak, in *SQUIDs in Biomagnetism*, ed by P. Seidel. Applied Superconductivity: Handbook on Devices and Applications (Wiley, Hoboken, 2015), pp. 992–1019
25. T.R. Clem, C.P. Foley, M.N. Keene, in *SQUIDs for Geophysical Survey and Magnetic Anomaly Detection*, ed by J. Clarke, A.I. Braginski. The SQUID Handbook: Applications of SQUIDs and SQUID Systems (Wiley-VCH, Weinheim, 2006), pp. 481–543
26. R. Stolz, in *Geophysical Exploration*, ed by P. Seidel. Applied Superconductivity: Handbook on Devices and Applications (Wiley, Hoboken, 2015), pp. 1020–1041
27. R. Kraus, M. Espy, P. Magnelind, P. Volegov, *Ultra-Low Field Nuclear Magnetic Resonance: A New MRI Regime* (Oxford University Press, USA, 2014)
28. J.M. Jaycox, M.B. Ketchen, Planar coupling scheme for ultra low noise dc SQUIDs. Trans. Magn. IEEE **17**, 400–403 (1981)
29. M.B. Ketchen, Integrated thin-film dc SQUID sensors. Trans. Magn. IEEE **23**, 1650–1657 (1987)
30. J. Knuutila, M. Kajola, H. Seppä, R. Mutikainen, J. Salmi, Design, optimization, and construction of a dc SQUID with complete flux transformer circuits. J. Low Temp. Phys. **71**, 369–392 (1988)
31. R. Cantor, in *dc SQUIDS: Design, optimization and practical applications*, ed by H. Weinstock. Squid Sensors: Fundamentals, Fabrication, and Applications (Kluwer Academic Publishers, Dordrecht/Boston/London, 1996), pp. 179–233
32. J. Clarke, in *SQUID fundamentals*, ed by H. Weinstock. SQUID Sensors: Fundamentals, Fabrication and Applications (Kluwer Academic Publishers, Dordrecht/Boston/London, 1996), pp. 1–62
33. J.E. Zimmerman, Sensitivity enhancement of superconducting quantum interference devices through use of fractional-turn loops. J. Appl. Phys. **42**, 4483–4487 (1971)
34. F. Dettmann, W. Richter, G. Albrecht, W. Zahn, A monolithic thin film dc-SQUID. Physica Status Solidi (a). **51**, K185–K188 (1979)
35. P. Carelli, V. Foglietti, Behavior of a multiloop dc superconducting quantum interference device. J. Appl. Phys. **53**, 7592–7598 (1982)
36. D. Drung, S. Knappe, H. Koch, Theory for the multiloop dc superconducting quantum interference device magnetometer and experimental verification. J. Appl. Phys. **77**, 4088–4098 (1995)
37. V. Zakosarenko, L. Warzemann, J. Schambach, K. Blüthner, K.H. Berthel, G. Kirsch, P. Weber, R. Stolz, Integrated LTS gradiometer SQUID systems for unshielded measurements in a disturbed environment. Supercond. Sci. Technol. **9**, A112–A115 (1996)

38. R. Stolz, L. Fritzsch, H.G. Meyer, LTS SQUID sensor with a new configuration. Supercond. Sci. Technol. **12**, 806–808 (1999)
39. D. Drung, in *Advanced SQUID read-out electronics*, ed by H. Weinstock. SQUID Sensors: Fundamentals, Fabrication and Applications (Kluwer Academic Publishers, Dordrecht/Boston/London, 1996), pp. 63–116
40. D. Drung, Low-frequency noise in low-Tc multiloop magnetometers with additional positive feedback. Appl. Phys. Lett. **67**, 1474–1476 (1995)
41. N. Oukhanski, R. Stolz, H.G. Meyer, High slew rate, ultrastable direct-coupled readout for dc superconducting quantum interference devices. Appl. Phys. Lett. **89**, 063502 (2006)
42. D. Drung, C. Hinnrichs, H.-J. Barthelmess, Low-noise ultra-high-speed dc SQUID readout electronics. Supercond. Sci. Technol. **19**, S235–S241 (2006)
43. D. Drung, R. Cantor, M. Peters, H.J. Scheer, H. Koch, Low-noise high-speed dc superconducting quantum interference device magnetometer with simplified feedback electronics. Appl. Phys. Lett. **57**, 406–408 (1990)
44. V. Foglietti, Double dc SQUID for flux-locked-loop operation. Appl. Phys. Lett. **59**, 476–478 (1991)
45. R.P. Welty, J.M. Martinis, Two-stage integrated SQUID amplifier with series array output. IEEE Trans. Appl. Supercond. **3**, 2605–2608 (1993)
46. M.E. Huber, P.A. Neil, R.G. Benson, D.A. Burns, A.F. Corey, C.S. Flynn, Y. Kitaygorodskaya, O. Massihzadeh, J.M. Martinis, G.C. Hilton, dc SQUID series array amplifiers with 120 MHz bandwidth. IEEE Trans. Appl. Supercond. **11**, 1251–1256 (2001)
47. J. Oppenländer, C. Häussler, N. Schopohl, Non Phi0 periodic macroscopic quantum interference in one-dimensional parallel Josephson junction arrays with unconventional grating structure. Phys. Rev. B. **63**, 024511 (2000)
48. C. Häussler, J. Oppenländer, N. Schopohl, Nonperiodic flux to voltage conversion of series arrays of dc superconducting quantum interference devices. J. Appl. Phys. **89**, 1875 (2001)
49. R. Cantor, F. Ludwig, in *SQUID Fabrication Technology*, ed by J. Clarke, A.I. Braginski. The SQUID Handbook vol. 1: Fundamentals and Technology of SQUIDs and SQUID systems (Wiley-VCH, Weinheim, 2004), pp. 93–126
50. H. Hayakawa, N. Yoshikawa, S. Yorozu, A. Fujimaki, Superconducting digital electronics. Proc. IEEE **92**, 1549–1563 (2004)
51. K.K. Likharev, Superconductor digital electronics. Physica C **482**, 6–18 (2012)
52. J.V. Gates, M.A. Washington, M. Gurvitch, Critical current uniformity and stability of Nb/Al–oxide–Nb Josephson junctions. J. Appl. Phys. **55**, 1419 (1984)
53. T. Lehnert, D. Billon, C. Grassl, K.H. Gundlach, Thermal annealing properties of Nb–Al/AlOx–Nb tunnel junctions. J. Appl. Phys. **72**, 3165 (1992)
54. S. Anders, M.G. Blamire, F.I. Buchholz, D.G. Crété, R. Cristiano, P. Febvre, L. Fritzsch, A. Herr, E. Il'ichev, J. Kohlmann, J. Kunert, H.G. Meyer, J. Niemeyer, T. Ortlepp, H. Rogalla, T. Schurig, M. Siegel, R. Stolz, E. Tarte, et al. European roadmap on superconductive electronics—status and perspectives. Physica C: Superconductivity. **470**, 2079–2126 (2010)
55. H.G. Meyer, L. Fritzsch, S. Anders, M. Schmelz, J. Kunert, G. Oelsner, in *LTS Josephson Junctions and Circuits*, ed by P. Seidel. Applied Superconductivity: Handbook on Devices and Applications (Wiley, Hoboken, 2015), pp. 281–297
56. H. Kroger, L.N. Smith, D.W. Jillie, Selective niobium anodization process for fabricating Josephson tunnel junctions. Appl. Phys. Lett. **39**, 280–282 (1981)
57. M. Gurvitch, M.A. Washington, H.A. Huggins, High quality refractory Josephson tunnel junctions utilizing thin aluminum layers. Appl. Phys. Lett. **42**, 472–474 (1983)
58. M. Maezawa, M. Aoyagi, H. Nakagawa, I. Kurosawa, S. Takada, Specific capacitance of $Nb/AlO_x/Nb$ Josephson junctions with critical current densities in the range of 0.1—18 kA/cm^2. Appl. Phys. Lett. **66**, 2134–2136 (1995)
59. S. Anders, M. Schmelz, L. Fritzsch, R. Stolz, V. Zakosarenko, T. Schönau, H.G. Meyer, Sub-micrometer-sized, cross-type Nb–AlOx–Nb tunnel junctions with low parasitic capacitance. Supercond. Sci. Technol. **22**, 064012 (2009)

60. M. Schmelz, R. Stolz, V. Zakosarenko, S. Anders, L. Fritzsch, M. Schubert, H.G. Meyer, SQUIDs based on submicrometer-sized Josephson tunnel junctions fabricated in a cross-type technology. Supercond. Sci. Technol. **24**, 015005 (2011)
61. M. Schmelz, R. Stolz, V. Zakosarenko, T. Schönau, S. Anders, L. Fritzsch, M. Mück, H.G. Meyer, Field-stable SQUID magnetometer with sub-fT $Hz^{-1/2}$ resolution based on sub-micrometer cross-type Josephson tunnel junctions. Supercond. Sci. Technol. **24**, 065009 (2011)
62. A. Chwala, J. Kingman, R. Stolz, M. Schmelz, V. Zakosarenko, S. Linzen, F. Bauer, M. Starkloff, M. Meyer, H.G. Meyer, Noise characterization of highly sensitive SQUID magnetometer systems in unshielded environments. Supercond. Sci. Technol. **26**, 035017 (2013)
63. J. Vrba, in *SQUID Gradiometers in Real Environment*, ed by H. Weinstock. Squid Sensors: Fundamentals, Fabrication, and Applications (Kluwer Academic Publishers, Dordrecht/Boston/London, 1996), pp. 117–178
64. K.P. Humphrey, T.J. Horton, M.N. Keene, Detection of mobile targets from a moving platform using an actively shielded, adaptively balanced SQUID gradiometer. IEEE Trans. Appl. Supercond. **15**, 753–756 (2005)
65. R. Stolz, *Supraleitende Quanten-interferenzdetektor-Gradiometer-Systeme für den geophysikalischen Einsatz* (University Jena, Jena, 2006)
66. B. Muhlfelder, W. Johnson, M.W. Cromar, Double transformer coupling to a very low noise SQUID. IEEE Trans. Magn. **19**, 303–307 (1983)
67. I.K. Harvey, A precise low temperature dc ratio transformer. Rev. Sci. Instrum. **43**, 1626–1629 (1972)
68. F. Gay, F. Piquemal, G. Geneves, Ultralow noise current amplifier based on a cryogenic current comparator. Rev. Sci. Instrum. **71**, 4592–4595 (2000)
69. C. Granata, A. Vettoliere, M. Russo, An ultralow noise current amplifier based on superconducting quantum interference device for high sensitivity applications. Rev. Sci. Instrum. **82**, 013901 (2011)
70. J. Luomahaara, M. Kiviranta, J. Hassel, A large winding-ratio planar transformer with an optimized geometry for SQUID ammeter. Supercond. Sci. Technol. **25**, 035006 (2012)
71. V. Zakosarenko, M. Schmelz, R. Stolz, T. Schönau, L. Fritzsch, S. Anders, H.G. Meyer, Femtoammeter on the base of SQUID with thin-film flux transformer. Supercond. Sci. Technol. **25**, 095014 (2012)
72. W. Wernsdorfer, in *Classical and Quantum Magnetization Reversal Studied in Nanometer-Sized Particles and Clusters*. Advances in Chemical Physics (Wiley, Hoboken, 2001), pp. 99–190
73. W. Wernsdorfer, Molecular magnets: a long-lasting phase. Nat. Mater. **6**, 174–176 (2007)
74. P. Bushev, D. Bothner, J. Nagel, M. Kemmler, K.B. Konovalenko, A. Lörincz, K. Ilin, M. Siegel, D. Koelle, R. Kleiner, F. Schmidt-Kaler, Trapped electron coupled to superconducting devices. Eu Phys. J. D. **63**, 9–16 (2011)
75. M. Schmelz, R. Stolz, V. Zakosarenko, S. Anders, L. Fritzsch, H. Roth, H.G. Meyer, Highly sensitive miniature SQUID magnetometer fabricated with cross-type Josephson tunnel junctions. Physica C **476**, 77–80 (2012)
76. K. Hasselbach, C. Veauvy, D. Mailly, MicroSQUID magnetometry and magnetic imaging. Physica C **332**, 140–147 (2000)
77. S.K.H. Lam, D.L. Tilbrook, Development of a niobium nanosuperconducting quantum interference device for the detection of small spin populations. Appl. Phys. Lett. **82**, 1078 (2003)
78. A.G.P. Troeman, H. Derking, B. Borger, J. Pleikies, D. Veldhuis, H. Hilgenkamp, NanoSQUIDs based on niobium constrictions. Nano Lett. **7**, 2152–2156 (2007)
79. L. Hao, J.C. Macfarlane, J.C. Gallop, D. Cox, J. Beyer, D. Drung, T. Schurig, Measurement and noise performance of nano-superconducting-quantum-interference devices fabricated by focused ion beam. Appl. Phys. Lett. **92**, 192507 (2008)

80. D. Vasyukov, Y. Anahory, L. Embon, D. Halbertal, J. Cuppens, L. Neeman, A. Finkler, Y. Segev, Y. Myasoedov, M.L. Rappaport, M.E. Huber, E. Zeldov, A scanning superconducting quantum interference device with single electron spin sensitivity. Nat Nano. **8**, 639–644 (2013)
81. J. Nagel, O.F. Kieler, T. Weimann, R. Wölbing, J. Kohlmann, A.B. Zorin, R. Kleiner, D. Koelle, M. Kemmler, Superconducting quantum interference devices with submicron Nb/HfTi/Nb junctions for investigation of small magnetic particles. Appl. Phys. Lett. **99**, 032506 (2011)
82. M. Schmelz, Y. Matsui, R. Stolz, V. Zakosarenko, T. Schönau, S. Anders, S. Linzen, H. Itozaki, H.G. Meyer, Investigation of all niobium nano-SQUIDs based on sub-micrometer cross-type Josephson junctions. Supercond. Sci. Technol. **28**, 015004 (2015)
83. D. Drung, Digital feedback loops for dc SQUIDs. Cryogenics **26**, 623–627 (1986)
84. H. Matz, D. Drung, E. Crocoll, R. Herwig, E. Kramer, M. Neuhaus, W. Jutzi, Integrated magnetometer with a digital output. Trans. Magn. IEEE **27**, 2979–2982 (1991)
85. N. Fujimaki, K. Gotoh, T. Imamura, S. Hasuo, Thermal-noise-limited performance in single-chip superconducting quantum interference devices. J. Appl. Phys. **71**, 6182 (1992)
86. T. Reich, P. Febvre, T. Ortlepp, F.H. Uhlmann, J. Kunert, R. Stolz, H.G. Meyer, Experimental study of a hybrid single flux quantum digital superconducting quantum interference device magnetometer. J. Appl. Phys. **104**, 024509 (2008)
87. T. Schönau, M. Schmelz, V. Zakosarenko, R. Stolz, M. Meyer, S. Anders, L. Fritzsch, H.G. Meyer, SQUID-based setup for the absolute measurement of the Earth's magnetic field. Supercond. Sci. Technol. **26**, 035013 (2013)

Cavity Optomechanical Magnetometers

Warwick P. Bowen and Changqiu Yu

Abstract This chapter introduces a new form of magnetometer which combines precision cavity optomechanical measurement with magnetostrictive material response. Such magnetometers can be fabricated on-chip and function both at room temperature and in earths magnetic field. Firstly, we derive the fundamental limit to sensitivity due to the thermomechanical fluctuations of the system, showing that sensitivity exceeding the current state-of-the-art is in-principle possible. We then show that bandwidths in the megahertz range are feasible. Then, we discuss the experimental implementation of these magnetometers, with demonstrated sensitivity at the level of 200 picotesla and tens of micrometer resolution. Finally, we compare both theory and experiments to the state-of-the-art. The sensitivity of current devices is less than a factor of 100 away from the best similarly sized cryogenic SQUID magnetometers, while theory suggests that sensitivity over an order of magnitude superior to those devices is possible.

1 Introduction

Cavity optomechanical magnetometers are a new form of room temperature magnetometer that leverages developments in the fabrication of high quality optical cavities and high quality mechanical resonators. They are based on the magnetostrictive effect whereby magnetic field induce deformation in a bulk material. Magnetometers based on magnetostriction have existed for some time [1–3].

W.P. Bowen (✉) · C. Yu
Australian Centre for Engineered Quantum Systems,
University of Queensland, Brisbane, QLD 4072, Australia
e-mail: w.bowen@uq.edu.au

C. Yu
e-mail: cq.yu.five@gmail.com

C. Yu
National Key Laboratory of Tunable Laser Technology,
Harbin Institute of Technology, Harbin 150080, China

A. Grosz et al. (eds.), *High Sensitivity Magnetometers*, Smart Sensors,
Measurement and Instrumentation 19, DOI 10.1007/978-3-319-34070-8_11

However, prior to the enhanced read-out sensitivity provided by cavity optomechanics, they operated far from the fundamental limit introduced by thermomechanical noise. Recently, in Refs. [4, 5], operation at the thermomechanical noise limit has been achieved using microtoroidal optomechanical systems integrated on a chip and functionalized with a magnetostrictive material. Current devices operate close to the state-of-the art in magnetic field sensitivity for room temperature magnetometers of similar size [6], have dynamic range extending past the Earth's magnetic field, require only microwatts of optical power, and have bandwidth in the range of kilohertz, substantially exceeding other state-of-the-art room temperature magnetometers [7]. Theoretical modeling indicates that sensitivity exceeding even cryogenic superconducting quantum interference device (SQUID) magnetometers should be possible in future devices [7], opening up a range of potential applications in medical diagnosis [8], geosurvey [9], fundamental science [10], and other areas [11, 12].

The book chapter aims to introduce the reader to the basic concepts of cavity optomechanical magnetometry, and outline the current state of development of such magnetometers. It introduces the fundamental thermomechanical noise floor due to the fluctuation-dissipation theorem and the measurement noise floor including quantum back-action though this regime is not relevant to current devices. It then derives the bandwidth of cavity optomechanical magnetometry, predicting that megahertz-range bandwidth should be possible in future devices. It then discussed recent experimental progress, and compares existing devices and theory to the literature.

2 Stress Induced Deformation of a Material

The deformation, or strain, induced in a material due to an applied stress is well studied, particularly in mechanical engineering. In general, such deformations can be quite complex and are described by the stress tensor **T**. Furthermore, nonlinearities are often exhibited, particularly when the level of deformation becomes comparable to one of the physical dimensions of the material. The *duffing nonlinearity* is a classic example of the nonlinear response of a material, resulting in buckling of a beam under sufficient stress [13]. While this full range of possible deformation characteristics can influence the behavior of optomechanical magnetometers, for simplicity here we limit ourselves for the most part to a uniform linear normal strain ε in response to a uniform normal stress σ on a material.

The normal stress on a material is defined as force F per unit area A

$$\sigma = \frac{F}{A}. \tag{1}$$

Upon applying such a stress, the material undergoes linear expansion x in the direction of the stress, with the strain defined as

$$\varepsilon = \frac{x}{L} = \frac{\sigma}{E}, \tag{2}$$

where L is the total length of the material in the direction of the applied stress, and E is Young's modulus. It is this change in length x that encodes information about the applied force.

2.1 Magnetostrictive Stress

Optomechanical magnetometers utilize magnetostrictive materials, for which the application of a magnetic field induces a stress and consequential expansion, as described above. As is the case for all stresses, generally this stress is given by a tensor, the magnetostrictive stress tensor. However, again for simplicity, here we limit ourselves to the basic case where the stress is homogeneous and uniaxial. The stress induced by a magnetic field B in a material can then be simply related to the magnetic field via

$$\sigma_B = \alpha_B B, \tag{3}$$

where α_B is a magnetostrictive coefficient whose value varies widely between materials. Of all commercially available materials, Terfenol-D offers the largest magnetostrictive coefficient at room temperature. Terfenol-D is an alloy of dysprosium, iron and terbium that was first developed by the U.S. Naval Ordinance Laboratory for the purpose of magnetostrictive actuation[1]. Its magnetostrictive coefficient can vary by more than an order-of-magnitude depending on the method of fabrication and treatment [14]. A typical value and the value we use throughout this chapter is $\alpha_B = 5 \times 10^8$ N T^{-1} m^{-2} [15].

3 Thermomechanical Noise Floor of Deformation-Based Magnetometry

It should now be understood that the signal in an optomechanical magnetometers as described above is the magnetostrictive deformation of the material in response to a magnetic field. This signal competes with noise, both intrinsic to the material and in the measurement apparatus. The noise within the material arises from the fact that it is at finite temperature, and therefore thermally excited. Each degree-of-freedom in the material experiences a Markovian Brownian noise force $F_T(t)$ from its environment. In thermal equilibrium the fluctuation-dissipation theorem relates the magnitude of

[1]The name "Terfenol" derives from terbium, iron (Fe) and the the abbreviation NOL for the Naval Ordinance Laboratory.

this thermal force noise to the strength of coupling to the environment. Specifically, the thermal force power spectral density $S_T(\omega)$ experienced by a degree-of-freedom is related to the rate Γ at which energy dissipates from it into the environment by [16]

$$S_T(\omega) \equiv \int_{-\infty}^{\infty} e^{i\omega\tau} \langle F_T(\tau) F_T(0) \rangle d\tau = 2m\Gamma k_B T, \tag{4}$$

where the first expression here is, of course, just an autocorrelation with $\langle \ldots \rangle$ denoting the average, m is the effective mass of the degree-of-freedom, to be defined more precisely later on, and as usual $k_B = 1.38 \times 10^{-23}$ m^2 kg s^{-2} K^{-1} is Boltzmann's constant. Note that we have taken the classical limit where $k_B T \gg \hbar\Omega$, and do so throughout. This is the appropriate limit for room temperature optomechanical magnetometers. Note also that here the right-hand-side is independent of frequency ω, i.e. the thermal forcing is white with magnitude independent of frequency. The fluctuation-dissipation theorem must hold to ensure that, in thermal equilibrium, each degree of freedom in an object has an average energy of $k_B T$ as required by thermodynamics.

Using the fluctuation-dissipation theorem along with Eqs. (1) and (3), we immediately arrive at the thermomechanical noise floor of all linear deformation based magnetic field sensors

$$B_{\min,T} = \frac{S_T^{1/2}}{A\alpha_B} = \frac{\sqrt{2m\Gamma k_B T}}{A\alpha_B} = \frac{1}{\alpha_B}\sqrt{2\rho\left(\frac{L}{A}\right)\Gamma k_B T} \tag{5}$$

where we have assumed that the entire material structure has the same magnetostrictive coefficient, and in the final expression we have further assumed that the full mass of the structure participates in the deformation (i.e. $m = \rho LA$) with ρ being the density of the material. This expression tells us a few interesting things. Firstly, in the thermomechanical noise limited regime, to achieve high sensitivity we require a low dissipation mechanical mode (low Γ). Secondly, for a fixed aspect ratio (i.e. a constant ratio $\sqrt{L/A}$), $L/A \propto V^{-1/3}$ so that the sensitivity improves with increasing device size as $V^{-1/6}$. This can be understood to arise from the fact that the thermal force is spatially uncorrelated, while the signal force is—at least in this model—constant across the full structure. Therefore, as the size of the structure increases the total signal force increases proportionately, while the total thermal force averaged over the material increases more slowly. Finally, note that, since the thermomechanical force is independent of frequency, the thermomechanical limit to magnetic field sensitivity is also independent of frequency.

Taking a density of $\rho = 2000$ kg m^{-3}, diameter of $L = 50\,\mu$m, cross-sectional area of $A = 50\,\mu\text{m} \times 1\,\mu$m, and dissipation rate of $\Gamma = 10$ kHz, roughly consistent with the experiments reported in Ref. [4], where the magnetometer consisted of a microtoroidal optical resonator; we find $B_{\min,T} \approx 0.8$ pT Hz$^{-1/2}$, consistent with the prediction from that paper. Even better thermomechanical noise performance could be achieved in geometries in which the dimension of expansion L is made smaller. The

thermomechanical noise limit of two cavity optomechanical magnetometer geometries is shown by the theory lines in Fig. 9, assuming perfect overlap between the magnetostrictive deformation and the magnetometer spatial mode shape and the density and dissipation rates used above. In the solid black curve, the aspect ratio of the magnetometer is held fixed at $L : W : D = 50 : 50 : 1$ (roughly the aspect ratio in Ref. [4]), where A is defined as $W \times D$, and W (or equivalently L) defines the spatial resolution. In the solid red curve the length L along the direction of magnetostrictive expansion is held fixed at $L = 1\ \mu\text{m}$, with $\sqrt{A} = W = D$ defining the spatial resolution. Both curves were calculated using Eq. (5). As can be seen in Fig. 9, this theoretical sensitivity is substantially better than comparably sized sensors that currently exist.

From this basic discussion the essential effect of thermal fluctuations from the environment on the performance of deformation-based magnetometers should now be evident. To achieve the precision limit introduced by thermomechanical noise, however, it is necessary that the system is not limited by measurement noise. The effect of measurement noise is the topic of the next section.

4 Measurement Precision Limit to Magnetic Field Sensitivity

In optomechanical magnetometers the mechanical response to an applied magnetic stress is generally enhanced by utilizing high quality mechanical resonances in the magnetometer structure. As we will see later, this is reasonable so long as the structure is well modeled as an elastic medium. Generally the structure will contain multiple mechanical resonances, each with different characteristics including dissipation rate, resonance frequency, effective mass, and strength of coupling to the magnetostrictive strain. While it is relatively straightforward to include multiple resonances when modeling magnetostrictive magnetometers, the essentially physics is clearly evidenced in the simple case where only one mechanical resonance contributes substantially to the dynamics of the system in the frequency range of interest. We take that case here, in which case the material can be thought of as a simple harmonic oscillator.

The dynamics of the position x of a simple harmonic oscillator experiencing both a thermal and a magnetic force can be described by the equation of motion

$$m\ddot{x} + m\Gamma\dot{x} + kx = F_T + F_B, \tag{6}$$

where F_B is the net force applied by the magnetic field, and $k = m\Omega^2$ is the spring constant of the oscillator with Ω its resonance frequency. Here, m is the mass of the oscillator, or the *effective mass* for more complicated oscillators such as vibrational modes in elastic structures as we will see later. It is important to note that here F_B is not, in general, given simply by $F_B = A\alpha_B B$ as one would expect from Eqs. (1) and (3). In our earlier discussion we considered a uniform static magnetostrictive expansion. Here, we are instead dealing with a mechanical eigenmode of some

complex structures. In this case F_B depends critically on the spatial overlap between the magnetostrictive stress and the mode shape.

Equation (6) can be easily solved in the frequency domain by taking a Fourier transform, yielding

$$x(\omega) = \chi(\omega)(F_T(\omega) + F_B(\omega)), \tag{7}$$

where $\chi(\omega)$ is the mechanical susceptibility given by the complex Lorenzian function

$$\chi(\omega) = \frac{1}{m(\omega^2 - \Omega^2 + i\Gamma\omega)}, \tag{8}$$

and we have used the Fourier transform relation $\mathscr{F}\{\dot{f}(t)\} = i\omega f(\omega)$.

A measurement of the position of the oscillator x, achieved for example by a resonantly enhanced optical field or through capacitive coupling to an electronic circuit, will always have some uncertainty. Including this uncertainty, the detected photocurrent can be written as

$$i(\omega) = x(\omega) + N(\omega) \tag{9}$$

$$= \chi(\omega)(F_T(\omega) + F_B(\omega)) + N(\omega) \tag{10}$$

$$= \chi(\omega)(F_T(\omega) + c_{\text{eff}}B(\omega)) + N(\omega) \tag{11}$$

where $N(\omega)$ represents the measurement noise, and we have assumed the photocurrent has been calibrated such that $\langle i \rangle = \langle x \rangle$. Here, we have also introduced a coefficient c_{eff} that quantifies how well the signal magnetic field is translated into a force applied upon the oscillator, i.e. $F_B = c_{\text{eff}}B$. In general, this coefficient will depend on how well the spatial profile of the magnetic field induced stress matches the modeshape of the mechanical oscillator, as discussed later. In the simple case where the overlap is perfect, it can be shown from Eqs. (1) and (3) that $c_{\text{eff}} = \alpha_B A$.

Rearranging Eq. (11) for the magnetic field, we find that

$$B(\omega) = B_{\text{est}}(\omega) - \frac{1}{c_{\text{eff}}}\left(\underbrace{\frac{N(\omega)}{\chi(\omega)}}_{\text{measurement noise}} + \underbrace{F_T(\omega)}_{\text{thermal noise}} \right), \tag{12}$$

where

$$B_{\text{est}}(\omega) = \frac{i(\omega)}{c_{\text{eff}}\chi(\omega)} \tag{13}$$

is the estimate of the applied magnetic field based on the measured photocurrent and known response of the mechanical oscillator. We observe that, while the

thermal noise is flat, as we found earlier, since the mechanical susceptibility is sharply peaked at the mechanical resonance frequency the measurement noise is minimized at that frequency. This can be understood since the thermal force and magnetic force are both enhanced by the mechanical resonance, while the measurement noise is not.

The precision of the measurement can then be found simply as

$$B_{\min}(\omega) = \left\langle \left(B(\omega) - B_{\text{est}}(\omega)\right)^{1/2} \right\rangle \tag{14}$$

$$= \frac{1}{c_{\text{eff}}} \left(\frac{S_N(\omega)}{|\chi(\omega)|^2} + S_T(\omega) \right)^{1/2} \tag{15}$$

$$= \frac{1}{c_{\text{eff}}} \left(\frac{S_N(\omega)}{|\chi(\omega)|^2} + 2m\Gamma k_B T \right)^{1/2}, \tag{16}$$

where $S_N(\omega)$ is the measurement noise power spectral density, the thermomechanical force power spectral density $S_T(\omega)$ is given in Eq. (4), and since the thermomechanical and measurement noise are uncorrelated with each other, the cross-terms have averaged to zero. This is plotted as a function of frequency ω for a range of measurement strengths in Fig. 1, assuming that S_N is spectrally flat. This assumption is generally very reasonable in cavity optomechanical sensors, since the

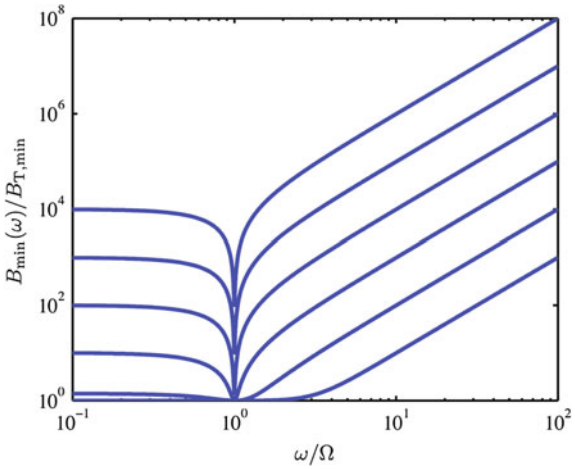

Fig. 1 Magnetic field sensitivity as a function of measurement frequency for various measurement strengths. *Vertical axis* minimum detectable magnetic field strength normalized to the thermomechanical noise limit ($B_{\text{T,min}} = \sqrt{2m\Gamma k_B T}/c_{\text{eff}}$). From the top to bottom traces $B_{\text{N,min}}/B_{\text{T,min}} = \{100, 10, 1, 0.1, 0.01, 0.001\}$, where $B_{\text{N,min}} = S_N(\Omega)^{1/2}/|\chi(\Omega)|c_{\text{eff}}$ is the minimum field strength that would be detectable on the mechanical resonance if there was no thermomechanical noise. For this plot we chose a mechanical quality factor $Q = \Omega/\omega = 100$

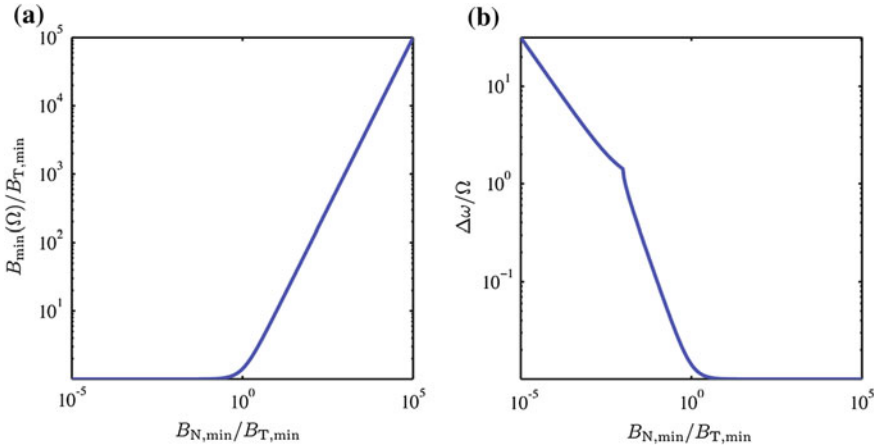

Fig. 2 On-resonance magnetic field sensitivity and sensing bandwidth as a function of measurement strength. **a** Minimum detectable on-resonance ($\omega = \Omega$) magnetic field normalized to the thermomechanical noise limit ($B_{\mathrm{T,min}} = \sqrt{2m\Gamma k_B T}/c_{\mathrm{eff}}$). **b** Bandwidth of magnetic field sensing normalized to the mechanical resonance frequency. The result in **a** is independent of mechanical quality factor, while for **b** we chose a mechanical quality factor $Q = \Omega/\omega = 100$

cavity line width κ which determines the shape of the measurement noise spectrum, as we will see later, is usually in the range of megahertz to gigahertz while the mechanical decay rate is in the range of hertz to kilohertz.

As can be seen from Fig. 1 when the measurement strength is insufficient to resolve the thermal motion of the resonator, the precision is sharply peaked near the mechanical resonance frequency Ω, and has an inverse-Lorenzian lineshape. On the other hand, when the measurement strength is sufficient to resolve the thermal motion, the precision approaches the thermomechanical noise limit at the mechanical resonance frequency and starts to broaden out. Eventually, the thermomechanical noise floor is reached at all frequencies in the range $\omega = 0$ to Ω, with the measurement precision being flat across this range.

The on-resonance magnetic field sensitivity is plotted against measurement strength in Fig. 2a, showing the improving sensitivity as the measurement accuracy approaches the thermomechanical noise floor, and plateau at the thermomechanical noise floor once it exceeds this level.

4.1 Bandwidth of Deformation-Based Magnetometry

From Eq. (16) it is possible to derive an analytic expression for the bandwidth of a magnetostrictive-deformation based magnetometers, under the assumption, again, that the measurement noise floor S_N is white. Here, we define the bandwidth as the width of the spectral region over which $B_{\min}(\omega)$ is within $\sqrt{2}$ (or a factor of two in

power) of the optimum value at $B_{\min}(\Omega)$. Substituting $B_{\min}(\omega) = \sqrt{2}B_{\min}(\Omega)$ into Eq. (16) and solving, we find two solutions given by

$$\left(\frac{\omega_{3\,\mathrm{dB}}^{\pm}}{\Omega}\right)^2 = 1 - \frac{1}{2Q^2} \pm \frac{1}{Q}\left[\frac{1}{4Q^2} + 1 + \frac{2k_B T}{\Gamma k S_N}\right]^{1/2}, \tag{17}$$

where $Q = \Omega/\Gamma$ is the mechanical quality factor, and as usual $k = m\Omega^2$ is the mechanical spring constant. The higher frequency solution is always real. However, for sufficiently high measurement strength the lower frequency solution becomes imaginary. This occurs when the measurement strength is sufficient to resolve the thermomechanical noise on the oscillator at dc ($\omega = 0$). We can therefore define the bandwidth $\Delta\omega$ of the sensor as

$$\Delta\omega = \omega_{3\,\mathrm{dB}}^{+} - \mathrm{real}\left\{\omega_{3\,\mathrm{dB}}^{-}\right\}. \tag{18}$$

The bandwidth is plotted as a function of measurement strength in Fig. 2b. As can be seen, when the measurement strength is insufficient to resolve the thermomechanical noise, the bandwidth is roughly constant and equal to the mechanical dissipation rate Γ. Once the measurement strength is sufficient to resolve the thermomechanical noise the bandwidth increases roughly linearly with measurement strength [2]. A clear kink in the curve is apparent. This kink occurs at the measurement strength for which the thermomechanical noise is resolved at dc. Above the kink, the bandwidth increases more slowly with measurement strength, specifically as its square-root.

Figure 2b highlights one striking difference between optomechanical magnetometers and other precision room temperature magnetometers such as nitrogen-vacancy (NV) and atomic magnetometers. In those cases, the bandwidth is typically limited to the kilohertz range, due to the necessity for relatively complicated control pulse sequences. With sufficient measurement strength, an optomechanical magnetometer based, for example, on a 5 MHz mechanical resonance could achieve megahertz bandwidth, or even greater.

5 Cavity Optomechanical Force and Field Sensing

In the previous section we saw the importance of accurate measurement of the mechanical motion to achieve both high precision and high bandwidth in magnetostrictive deformation-based magnetometers. This motivates the use of both optical fields and an optical cavity—and therefore cavity optomechanics (see Fig. 3). Optical measurements of mechanical motion are routinely achieved. The basic

[2] If we define the measurement strength as the inverse of the on-resonance measurement accuracy $B_{\mathrm{N},min.}$

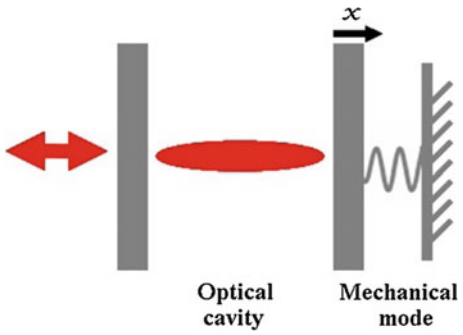

Fig. 3 A generic cavity optomechanical system consisting of a Fabry-Perot type cavity with one mirror attached to a spring

concept is to reflect the field from the mechanical oscillator. Motion of the oscillator then imparts phase shifts on the field which can be measured using an appropriate phase referenced detection technique, such as homodyne or heterodyne detection. Compared to electrical read-out which is constrained by thermal Johnson noise, optical fields offer performance constrained only by the quantum shot noise of the field[3], while the essential effect of an optical cavity is to recycling photons many times and thereby amplifying the phase shift incurred upon them.

When a mechanical oscillator is placed within an optical cavity, the intra-cavity phase shifts due to its motion couple into shifts of the optical resonance frequency Ω_c. A cavity optomechanical system can therefore be described by the Hamiltonian (see for example Ref. [17])

$$H = \hbar(\Omega_c + Gx)n + \frac{p^2}{2m} + \frac{kx^2}{2}, \tag{19}$$

where n is the intra-cavity photon number, p is the momentum of the mechanical resonator, and G is the *optomechanical coupling strength* in units of hertz-per-meter —that is, it quantifies the shift in the optical resonance frequency due to a given displacement of the mechanical oscillator.

While we do not derive the expression here, from Eq. (19) and using input-output theory for optical fields in Ref. [18], it is possible to show that the total noise power spectral density of a measurement of the position of a mechanical oscillator within an optical cavity from phase measurement of the field leaving the cavity is [17]

$$S_N(\omega) = S_{\text{imp}}(\omega) + \frac{\hbar^2|\chi(\omega)|^2}{\eta}\frac{1}{S_{\text{imp}}(\omega)} \tag{20}$$

where we have assumed the incident laser is shot noise limited. Here $S_{\text{imp}}(\omega)$ is the measurement imprecision power spectral density, while the second term in the expression is quantum back-action noise. This term arises from shot noise fluctuations

[3]They can even exceed this limit utilising quantum correlations between photons.

of the intracavity field that drive the mechanical oscillator introducing additional noise to its motion. From the perspective of quantum mechanics, it is necessary to prevent a continuous measurement of a mechanical oscillator simultaneously providing more information about its position and momentum than is allowed by the Heisenberg uncertainty principle. This explains why the term gets larger as the imprecision noise $S_{\mathrm{imp}}(\omega)$ decreases. While quantum back-action is fundamentally interesting and limits the ultimate performance of cavity optomechanical magnetometers, current magnetometers operate well inside the regime where it is negligible compared to the imprecision noise $S_{\mathrm{imp}}(\omega)$. Henceforth, we neglect it. We would note, that several recent fundamental experiments on the optomechanical interaction have entered the regime where back-action noise is significant [19, 20]. It is therefore not implausible that it may play a role in future cavity optomechanical magnetometers.

For on-resonance driving of optical cavity the imprecision noise is [17]

$$S_{\mathrm{imp}}(\omega) = \frac{\kappa}{16\eta n G^2}\left[1 + 4\left(\frac{\omega}{\kappa}\right)^2\right], \tag{21}$$

with η being the total detection efficiency of the light, and κ the optical decay rate of the cavity. Notice from this expression that at frequencies well beneath the optical decay rate ($\omega \ll \kappa$) the measurement noise is spectrally flat, as we approximated in the previous section. At higher frequencies, the measurement noise increases since the cavity is no longer resonant for the signal.

Taking one specific and relevant example, for a microtoroidal resonator the optical decay rate is typically around $\kappa/2\pi = 50$ MHz, for an incident optical power of 10 μW the intracavity photon number is then approximately $n \approx 10^6$. The optomechanical coupling strength for a radial breathing mode which expands isotropically in the radial direction is generally in the range of $G = 100$ GHz/nm [21]. Inserting these parameters into Eq. (21) and taking $\omega \ll \kappa$ and $\eta = 1$ we arrive at a measurement noise of $S_{\mathrm{imp}}(\omega) \approx 3 \times 10^{-38}$ m^2 Hz^{-1}. In other words, it is in principle possible to resolve changes in the circumference of a microtoroidal optical resonator at the level of 10^{-19} m in a one second measurement duration.

As a result of this rather remarkable precision one might expect that microtoroid based force and magnetic field sensors would—at least near the frequency of the radial breathing mode—easily be able to resolve the thermal noise driving the mode. This turns out to be true. Substituting the same values as we have used previously into Eq. (16) and using a typical radial breathing mode mass m = 1 pg, frequency $\Omega/2\pi = 20$ MHz, and dissipation rate $\Gamma/2\pi = 10$ kHz, it is possible to show that the contribution to the minimum resolvable magnetic field from the measurement noise is some four orders of magnitude smaller than the contribution from the thermal force noise. Consequently, an optical cavity of the quality of a microtoroid would not be required when using a 1 pg mechanical resonator if the only objective of the cavity was to improve the minimum resolvable magnetic field at the mechanical resonance frequency, so long as the incident optical power was not constrained to sub-nanowatt levels. However, as we found earlier, as the size of

the resonator increases the level of thermomechanical fluctuations decreases. High quality optical cavities therefore provide a route to achieve the thermomechanical noise limit for larger, more sensitive, magnetometers. Furthermore, as discussed in the previous section, improved measurement accuracy also results in improved bandwidth. Indeed, assuming that the measurement noise is white, Eq. (18) returns a bandwidth of approximately $3\Omega = 2\pi \times 60$ Mrad/s, with thermomechanical noise limited performance over the full range from $\omega = 0$ to 3Ω. Of course, we found from Eq. (21) that the noise floor is not flat, and degrades at frequencies above $\omega = \kappa$. Never-the-less, microtoroid based optomechanical magnetometers have the potential for bandwidth well into the megahertz range.

6 Continuum Mechanics of Bulk Mechanical Resonators

6.1 Elastic Wave Equation

As can be well understood by ringing a wine glass or hitting a tuning fork, bulk materials are capable of sustaining resonant mechanical oscillations, with the restoring force provided by the elasticity of the material. Similarly to the case for electromagnetic fields, this behavior is described by a wave equation. As briefly mentioned earlier, mechanical systems have nonlinear behavior, such as buckling, that in principle should be included in a full wave equation. However, in many circumstances, and indeed usually, the amplitude of the wave motion is sufficiently small that nonlinearities may be safely neglected. This results in the *elastic wave equation* [22]

$$\rho\,\ddot{\mathbf{u}}(\mathbf{r},t) = (\lambda+\mu)\nabla(\nabla\cdot\mathbf{u}(\mathbf{r},t)) + \mu\nabla^2\mathbf{u}(\mathbf{r},t) + \mathbf{f}(\mathbf{r},t), \tag{22}$$

where, as illustrated in Fig. 4, the vector field $u(\mathbf{r},t)$ defines the displacement of an infinitesimally small cubic volume element at initial position $\mathbf{r}$ and time t, $\mathbf{f}(\mathbf{r},t)$ is the mechanical body force density in newtons per unit volume due some applied force, and λ and μ are the Lamé-constants

$$\lambda = \frac{\sigma E}{(1+\sigma)(1-2\sigma)} \tag{23}$$

$$\mu = \frac{E}{2(1+\sigma)} \tag{24}$$

with σ and E being Poissons ratio and Young's modulus, respectively. Young's modulus is a measure of the stiffness of a material, quantifying its axial compression upon application of a strain ε; while Poissons ratio is defined as the ratio of fractional perpendicular expansion to axial compression. For our specific problem of optomechanical magnetometry, the body force $\mathbf{f}(\mathbf{r},t)$ is determined by the signal magnetic field at each point in the material. In general, and in analogy to

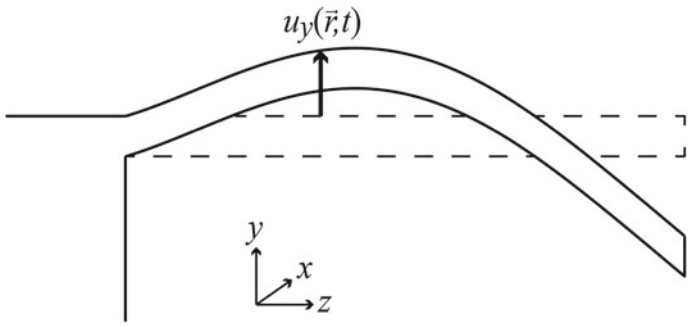

Fig. 4 Illustration of a Euler-Bernoulli cantilever, showing the y-component of the displacement vector $u(\mathbf{r}, t)$

electromagnetism, once the boundary conditions appropriate to the geometry of the material are introduced, this wave equation can be solved to determine the eigenmodes and their resonance frequencies.

6.2 Solving the Wave Equation by Separation of Variables

Separation of variables is a common approach used to solve wave equations. Here, as usual, we proceed by postulating solutions to the elastic wave equation of Eq. (22) that consist of products of independent spatial and temporal mode-functions

$$\mathbf{u}(\mathbf{r}, t) = \boldsymbol{\psi}_q(\mathbf{r}) u_q(t) \tag{25}$$

$$\mathbf{f}(\mathbf{r}, t) = \boldsymbol{\psi}_q(\mathbf{r}) f_q(t), \tag{26}$$

where $u_q(t)$ and $f_q(t)$ are the time dependent oscillation amplitude and body force amplitude experienced by eigenmode q, respectively; and $\boldsymbol{\psi}_q(\mathbf{r})$ is the eigenmodes position dependent modeshape function. The modeshape function normalisation is arbitrary, but chosen by convention here such that

$$\max\{|\boldsymbol{\psi}_q(\mathbf{r})|^2\} = 1 \tag{27}$$

which results in physically reasonable mode effective masses. The mechanical eigenmodes form an orthogonal basis, such that for $p \neq q$, $\int_V \boldsymbol{\psi}_p(\mathbf{r}) \cdot \boldsymbol{\psi}_q(\mathbf{r}) d^3r = 0$, where V is the total volume of the oscillator. Using this, it is straightforward to show that $f_q(t)$ may be uniquely determined from the body force as

$$f_q(t) = \int dV\, \boldsymbol{\psi}_q^*(\mathbf{r}) \cdot \mathbf{f}(\mathbf{r}, t). \tag{28}$$

Substituting Eq. (25) into Eq. (22) yields the new equation of motion

$$\ddot{u_q}(t) = \left[\frac{(\lambda+\mu)\nabla(\nabla\cdot\boldsymbol{\psi}_q(\mathbf{r})) + \mu\nabla^2\boldsymbol{\psi}_q(\mathbf{r})}{\rho\boldsymbol{\psi}_q(\mathbf{r})}\right] u_q(t) + \frac{f_q(t)}{\rho}. \tag{29}$$

Notice that the term in square brackets is independent of time t, while all other terms in the equation are independent of position $\mathbf{r}$. Consequently, the term in square brackets must be a constant. By inspection, we can observe that this term plays the role of a restoring force on the mechanical displacement u_q. For the equation of motion be stable, it must be negative, opposing the displacement. With the benefit of hindsight we define it to equal $-\Omega_q^2$; resulting in the separated spatial and temporal equations of motion

$$(\lambda+\mu)\nabla(\nabla\cdot\boldsymbol{\psi}_q(\mathbf{r})) + \mu\nabla^2\boldsymbol{\psi}_q(\mathbf{r}) = -\rho\Omega_q^2\boldsymbol{\psi}_q(\mathbf{r}) \tag{30}$$

$$m_q\,\ddot{u_q}(t) + k_q u_q(t) = F_q(t), \tag{31}$$

where $k_q = m_q\Omega_q^2$ is the usual oscillator spring constant and

$$F_q(t) = m_q f_q(t)/\rho \tag{32}$$

is the force in newtons experienced by eigenmode q, with m_q introduced as the modes effective mass. Solving Eq. (30) then yields the spatial modeshape function $\boldsymbol{\psi}_q(\mathbf{r})$ and frequency Ω_q of mode q; while Eq. (31) indictates that the mode will behave as a simple harmonic oscillator. This is a direct and somewhat unsurprising consequence of limiting our analysis to the linear elastic wave equation which accounts for the linear elastic behavior of the medium.

The coefficient c_{eff} relevant to magnetostrictive magnetometry can be determined for each mechanical eigenmode q from Eq. (32) using the known body force applied by the magnetostrictive stress. If the magnetic field B is uniform across the sensor, then $c_{q,\text{eff}} = F_q/B$.

While in the preceding sections we have derived approximate analytical expressions for the mode-functions and eigenfrequencies of mechanical resonances in some highly symmetry geometries; generally Eq. (30) is not amenable to analytical solutions, and numerical methods, such as the finite-difference time domain method (FDTD) or finite element method (FEM), are instead used to determine the eigenfrequencies, eigenmodes, dissipation rates, and effective masses of a given structure.

6.3 Determining the Effective Mass of Mechanical Eigenmodes

The characteristic shape of each eigenmode of mechanical oscillation $\boldsymbol{\psi}_q(\mathbf{r})$ determines a unique effective mass. The effective mass can be found by determining the change in elastic potential energy for a given amplitude of material deformation.

The elastic potential energy is given generally by [23]

$$U = \frac{1}{2}\int_V dV\left[\sigma_x\varepsilon_x + \sigma_y\varepsilon_y + \sigma_z\varepsilon_z + \tau_{xy}\gamma_{xy} + \tau_{yz}\gamma_{yz} + \tau_{zx}\gamma_{zx}\right], \tag{33}$$

where the integral is performed over the total volume V of the oscillator; σ_i and τ_{ij} are normal and shear stresses, respectively, commonly written in the matrix form

$$\sigma = \begin{pmatrix} \sigma_{xx} & \sigma_{xy} & \sigma_{xz} \\ \sigma_{yx} & \sigma_{yy} & \sigma_{yz} \\ \sigma_{zx} & \sigma_{zy} & \sigma_{zz} \end{pmatrix} = \begin{pmatrix} \sigma_x & \tau_{xy} & \tau_{xz} \\ \tau_{yx} & \sigma_y & \tau_{yz} \\ \tau_{zx} & \tau_{zy} & \sigma_z \end{pmatrix}. \tag{34}$$

ε_i and γ_{ij} are, respectively, the normal strain, and engineering shear strain; defined as

$$\varepsilon_i = \frac{\partial u_i(\mathbf{r},t)}{\partial i} \tag{35}$$

$$\gamma_{ij} = \frac{1}{2}\left(\frac{\partial u_i(\mathbf{r},t)}{\partial j} + \frac{\partial u_j(\mathbf{r},t)}{\partial i}\right), \tag{36}$$

where $u_i(\mathbf{r},t)$ is the ith component of $\mathbf{u}(\mathbf{r},t)$. The normal and engineering shear strain are also commonly written in matrix form

$$\varepsilon = \begin{pmatrix} \varepsilon_{xx} & \varepsilon_{xy} & \varepsilon_{xz} \\ \varepsilon_{yx} & \varepsilon_{yy} & \varepsilon_{yz} \\ \varepsilon_{zx} & \varepsilon_{zy} & \varepsilon_{zz} \end{pmatrix} = \begin{pmatrix} \varepsilon_x & \gamma_{xy} & \gamma_{xz} \\ \gamma_{yx} & \varepsilon_y & \gamma_{yz} \\ \gamma_{zx} & \gamma_{zy} & \varepsilon_z \end{pmatrix}. \tag{37}$$

For the linear elastic materials typically used for micromechanical oscillators, each stress component is linearly related to every strain component via the generalized Hooke's Law

$$\sigma_{ij} = C_{ijkl}\varepsilon_{kl} \tag{38}$$

expressed here in tensor notation for compactness, where C_{ijkl} is a fourth-order elasticity tensor that depends only on material properties. This relationship, combined with the definitions of normal and shear strain in Eqs. (35) allow the elastic potential energy due to deformation of the mechanical oscillator to be determined,

in general, from Eq. (33). However, significant simplification is possible if the oscillator is formed from an isotropic material, with the generalized Hooke's Law then given by [23]

$$\sigma_{ij} = 2\mu\varepsilon_{ij} + \lambda\varepsilon_{kk}\delta_{ij}. \tag{39}$$

Substituting this expression into Eq. (33) we find

$$U = \frac{1}{2}\int_V dV\left[\lambda\left(\varepsilon_x + \varepsilon_y + \varepsilon_z\right)^2 + 2\mu\left(\varepsilon_x^2 + \varepsilon_y^2 + \varepsilon_z^2\right) + 2\mu\left(\gamma_{xy}^2 + \gamma_{yz}^2 + \gamma_{zx}^2\right)\right]. \tag{40}$$

The mechanical potential energy of the eigenmode q is given by

$$U_q = \frac{1}{2}k_q u_q^2(t) = \frac{1}{2}m_q\,\Omega_q^2 u_q^2(t), \tag{41}$$

where k_q is the spring constant of the mode. This allows us to relate the elastic potential energy due to mechanical deformation in eigenmode q to the effective mass of the mode m_q. Substituting the spatial and temporal dynamics of eigenmode q into Eq. (35) for the normal and shear strain (i.e. setting $u_i(\mathbf{r},t) = u_q(t)\psi_{q,i}(\mathbf{r})$), and using Eq. (40) we find

$$\begin{aligned} m_q &= \frac{2U_q}{\Omega_q^2 u_q^2(t)} \\ &= \frac{1}{\Omega_q^2}\int_V dV\left[\left[\lambda\left(\nabla\cdot\boldsymbol{\psi}_q(\mathbf{r})\right)^2\right.\right. \\ &\quad \left.\left. + 2\mu\left(\frac{\partial\psi_{q,x}}{\partial x}\right)^2 + \left(\frac{\partial\psi_{q,y}}{\partial y}\right)^2 + \left(\frac{\partial\psi_{q,z}}{\partial z}\right)^2\right] \right. \\ &\quad \left. + \frac{\mu}{2}\left|\left(-\frac{\partial}{\partial x},\frac{\partial}{\partial y},\frac{\partial}{\partial z}\right)\times\left(\psi_{q,x}(\mathbf{r}),-\psi_{q,y}(\mathbf{r}),\psi_{q,z}(\mathbf{r})\right)\right|^2. \right. \end{aligned} \tag{42}$$

This expression allows the effective mass of the eigenmodes of a mechanical oscillator to be determined from their modeshape and material properties.

7 Microtoroid-Based Cavity Optomechanical Magnetometers

To date, the only reported cavity optomechanical magnetometers have been based on microtoroial cavities fabricated on a silicon chip (see Fig. 5). In this section we summarize the results obtained with such devices.

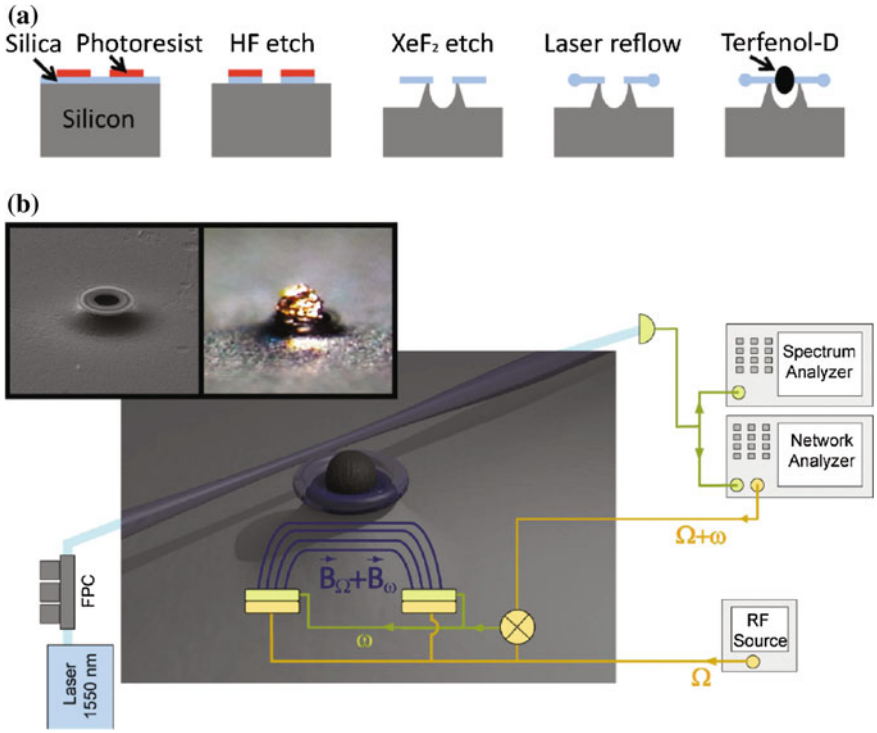

Fig. 5 **a** Magnetometer fabrication process. **b** Experimental setup. *FPC* Fiber polarization controller. *Insets* Scanning electron micrograph of sensor prior to Terfenol-D deposition and optical micrograph of final sensor. Reproduced with permission from Ref. [5], copyright 2014 WILEY-VCH Verlag GmbH & Co. KGaA, Weinheim

7.1 Fabrication

The fabrication process used in Ref. [5] to produce microtoroid-based cavity optomechanical magnetometers is shown in Fig. 5a. The essential concept is to produce a microtoroid with a hole within its core, and embed a magnetostrictive material within that hole. The process begins with a silicon wafer with a 2 μm silica oxide layer. Standard photolithography techniques are used to define a ring of photoresist. Then the hydrofluoric (HF) acid is utilized to remove the uncovered silica, with the remaining photoresist then removed by consecutively using acetone, isopropyl alcohol and deionized water. After this, a xenon difluoride (XeF_2) gas phase etch is used to isotropically under-etch the silicon beneath the silica ring, creating an undercut silicon support pedestal in the shape of a ring with a central void. The silica disk is then reflowed using a 10.6 μm CO_2 laser to form a smooth torus. Finally a particle of Terfenol-D with suitable size is deposited inside the central void and fixed by epoxy. The finished device reported in Ref. [5] had optical

quality factor above 10^6, and exhibited several mechanical modes with quality factor $Q \approx 40$ ranging in frequency from 1 to 40 MHz. While both the optical and mechanical quality factors were relatively low compared to state-of-the-art microtoroids [24, 25], as discussed previously, while ultrahigh quality is necessary to achieve megahertz sensing bandwidths, it is not required to reach the thermomechanical noise limit of such devices. As shown in Fig. 7b, the thermomechanical noise floor is reached with the devices of Ref. [5] in several narrow frequency windows around mechanical resonance frequencies. By contrast, electronic noise typically constrains electrically read-out magnetometers to operate orders-of-magnitude away from this limit.

7.2 Measurement Apparatus

To characterize the sensitivity of optomechanical magnetometers, and ultimately to use them in applications, it is necessary to be able to efficiently couple light into them and then measure the response of the device to the magnetic field, encoded on the output optical field. The schematic of the setup used in Ref. [5] is shown in Fig. 5b. Light from a shot noise limited 1550 nm tunable fiber laser goes through a polarization controller to a tapered optical fiber. The tapered fiber allows evanescent coupling into the microtoroidal optical cavity. The laser frequency is locked on the half maximum of an optical resonance by thermal locking. The strain applied to the resonator induced by the magnetostrictive medium shifts the optical resonance frequency, thus modulating the amplitude of the transmitted light. This transmitted field is detected on an InGaAs photodiode, with 50 μW of off-resonant light sufficient at the detector to observe the thermomechanical noise of mechanical resonances with good signal-to-noise. A spatially uniform radio frequency magnetic field was generated by a pair of solenoids on either side of the device. The magnetic field was calibrated by flowing a known dc current through the coils and measuring the resulting magnetic field using a Hall probe, and using the known frequency response of the coils.

7.3 Sensitivity and Dynamical Range in Linear Mode of Operation

The magnetic field sensitivity as a function of the signal frequency can be determined by a combination of network and spectral analysis of the measured photocurrent [4]. Spectrum analysis gives the background laser and mechanical thermal noise. By applying a known amplitude magnetic field across the sensor at a reference frequency ω_{ref}, the spectral analysis also allows calibration of the magnetic field sensitivity at that frequency via the relationship

$$B_{\min}(\omega_{\text{ref}}) = B_{\text{ref}}/\sqrt{SNR \cdot \text{BW}}, \tag{43}$$

where B_{ref} is the amplitude of the applied field, BW is the resolution bandwidth of the spectrum analyzer, and SNR is the signal-to-noise-ratio of the observed response at ω_{ref} on the spectrum analyzer (see signal spike at 9.7 MHz in Fig. 7b). Network analysis provides the system response to the applied magnetic field as a function of frequency, which allows the magnetic field sensitivity to be quantified via the relationship

$$B_{\min}(\omega) = \sqrt{\frac{S(\omega)N(\omega_{\text{ref}})}{S(\omega_{\text{ref}})N(\omega)}} B_{\min}(\omega_{\text{ref}}), \tag{44}$$

where here $S(\omega)$ and $N(\omega)$ are, respectively, the measured power spectral density and network response.

The sensitivity of magnetostrictive magnetometers is a strong function of the dc magnetic field across the device. This can be understood since the process of magnetostriction involves the realignment of magnetic domains within the material in the direction of the applied field. If there is no dc field, then the domains have no net alignment. The dc field acts to along the domains, with the alignment eventually saturating once all of the domains are polarized in the direction of the field. Measurements of the expansion of the material as a function of applied field therefore show a characterizing sigmoid shape, symmetric about zero field. In the linear mode of operation we have discussed thus far, the magnetostrictive coefficient, and therefore magnetic field sensitivity, is maximized at the (non-zero) dc bias field which maximizes the expansion of the material in the presence of a small additional signal field. The dependence of the magnetostrictive coefficient on applied dc field and optimal magnetostrictive coefficient are shown schematically in Fig. 6.

In the experiments of Ref. [5] a permanent magnet was used to generate the dc bias field. Optimizing the position of the permanent magnet, gave the optimal magnetic field sensitivity as a function of frequency shown in the red curve of Fig. 7a. The peak sensitivity was 200 pT $\text{Hz}^{-1/2}$ at 17 MHz roughly where the radial breathing mode was located for this device, and extends over a bandwidth of hundreds of kilohertz. The megahertz bandwidths predicted earlier are precluded here due, primarily, to the relatively low optical quality factor of the device. The

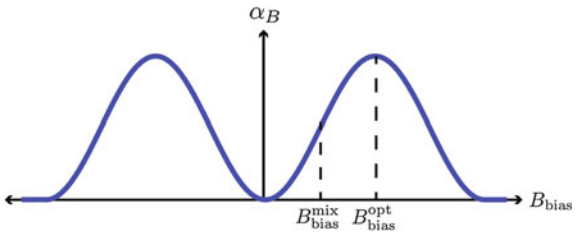

Fig. 6 Illustration of magnetostrictive coefficient as a function of dc bias field amplitude, showing the optimal bias fields for both standard magnetometry and magnetometry based on RF mix-up

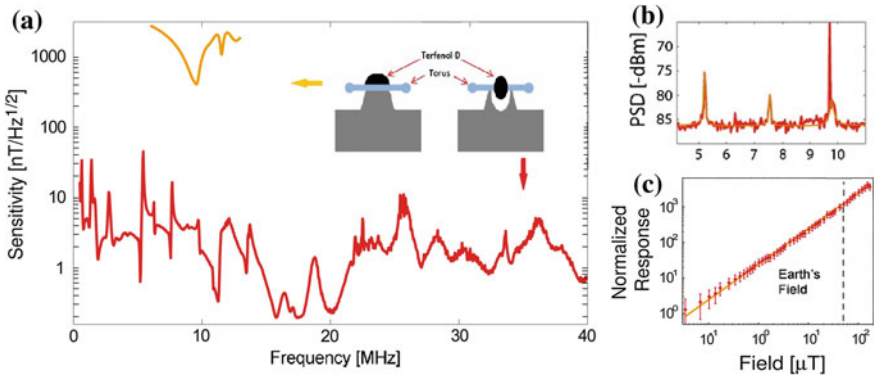

Fig. 7 **a** Sensitivity in linear mode of operation for different structure of the cavity optomechanical magnetometers. *Inset* structures of the cavity optomechanical magnetometers. **b** Power spectral density (PSD) with 1 μT magnetic field excitation at 9.70 MHz. Resolution bandwidth: 10 kHz. *Orange curve* fit including Lorentzian line-shapes of three mechanical resonances at frequencies 5.2, 7.6, and 9.7 MHz. **c** Response as a function of signal field strength with 100 Hz resolution bandwidth, copyright 2014 WILEY-VCH Verlag GmbH & Co. KGaA, Weinheim

results of Ref. [5] are compared to a cavity optomechanical magnetometer produced by affixing terfenol-D directly to the top of a regular microtoroidal resonator that did not have a central hole etched out of the pedestal in Fig. 7a (orange curve). As can be seen, the improved overlap between the body force generated by magnetostriction and the mechanical modes of the device yielded substantial enhancements in both sensitivity and bandwidth.

As shown in Fig. 7c, the response of the magnetometer of Ref. [5] is linear over the full measurement range from 200 pT $Hz^{-1/2}$ to 150 μT $Hz^{-1/2}$, showing no signs of nonlinear behavior over the full range of fields tested. A dynamic range than extends to field magnitudes larger than the Earth's field, as demonstrated here, is unusual for precision magnetometers, and enables unshielded sensing to be performed.

7.4 *Low Frequency Measurements Using Nonlinear Mix-Up*

One of the limitations of optical measurement techniques, quite generally, is an extreme sensitivity to acoustic vibrations and other sources of low frequency noise. In the magnetometer discussed above (and reported in Ref. [5]) this limited the frequencies at which precision magnetic field sensing could be performed to frequencies above around 1 MHz. Low frequency sensitivity is critically important for

many applications including geosurveys and many biological imaging and measurement techniques.

The nonlinear dependence of the expansion of magnetostrictive materials on applied field shown in Fig. 6 suggests an alternative approach to magnetostrictive magnetometry that could allow precision measurements of low frequency fields without exposure to low frequency optical noise sources. The essential idea is that the nonlinear response can be used to mix-up low frequency magnetic field signals into sidebands in the measured photocurrent around a coherent applied radio frequency magnetic field [26]. Here, rather than operating as a dc bias field that maximizes the magnetostrictive coefficient, as in the previous section, one wishes to operate at a bias field that maximizes the change in magnetostrictive coefficient in the presence of a small signal. In this case, low frequency magnetic fields will modify the response of the magnetometer to the coherent radio frequency drive.

Nonlinear mix-up was first observed in a cavity optomechanical magnetometer in Ref. [5]. Figure 8a shows the modulation sidebands that were observed due to a 500 Hz low frequency signal on the signal produced at 5.22 MHz from a strong radio frequency drive. A similar combination of network and spectral analysis allowed the minimum detectable field to be determined for this configuration as a function of frequency, with $B_{\min}(\omega) \approx 130$ nT Hz$^{-1/2}$ over a range of signal frequencies from 2 Hz to 1 kHz. As discussed above, the ability to observe magnetic fields within hertz to kilohertz frequency range is important for many applications. Evidently, nonlinear mix-up provides access to this range of frequencies. However this comes at the cost of—with the implementation of Ref. [5] a degradation in sensitivity of some three orders of magnitude.

One interesting and unexpected observation from the work of Ref. [5] was the appearance of, not only sidebands due to the nonlinear mix-up but also, at sufficiently high signal field amplitude, the appearance of a frequency comb of higher order sidebands as shown in Fig. 8b, c. The authors of Ref. [5] developed a simple nonlinear model to explain this phenomena by recognizing that the nonlinear response of the magnetostrictive energy to mechanical deformation also effects the motion of the mechanical resonances of the structure, specifically introducing a nonlinear term to their dynamics. The equation of motion of the mechanical resonance can then be expressed to second order in x as [5]

$$\ddot{x} + \Gamma\dot{x} + \Omega^2 x + \chi_B x^2 = (c_0 - c_1 x - c_2 x^2)B \tag{45}$$

where χ_B is a nonlinear coefficient introduced by the magnetostriction, while c_0, c_1, and c_2 are the zeroth, first, and second order magnetostrictive coefficients. A model using this equation of motion reasonably well reproduces the experimental results (see Fig. 8e).

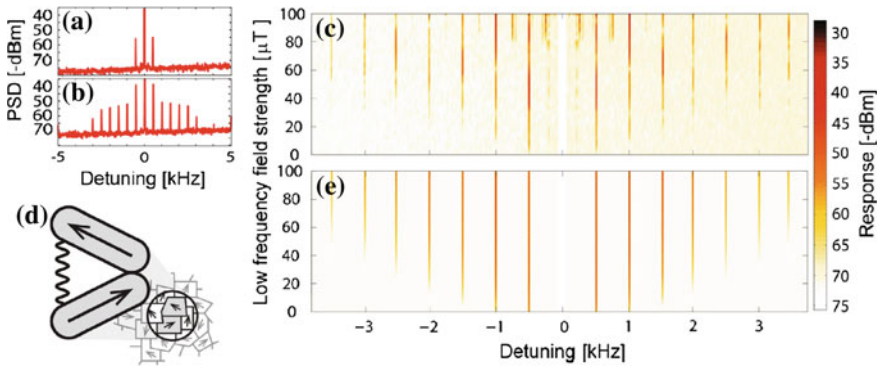

Fig. 8 Nonlinear mix-up based optomechanical magnetometry. **a** Response around the mix-up frequency of 5.22 MHz to a low frequency signal at 500 Hz with amplitude of 1 μT. **b** Response to a signal of 22 μT, a comb of sidebands is present. **c** Pseudocolor plot of the sensors response as a function of signal strength and detuning from the mix-up frequency. **d** Schematic of magnetic dipole interactions in Terfenol-D. **e** Modelled pseudocolor plot of the sensors response as a function of signal strength and detuning. Reproduced with permission from Ref. [5], copyright 2014 WILEY-VCH Verlag GmbH & Co. KGaA, Weinheim

8 Comparison with the State-of-the-Art

As clearly espoused by this book, magnetometers have a wide range of applications, which depend in different ways on a set of parameters including spatial resolution, sensitivity, and operating requirements. The sensitivity and volume are two critical and competing parameters that indictate how small a magnetic field may be detected and over what spatial extent. Figure 9 plots these parameters for several recently developed magnetometers.

In a cryogenic environment, ultra-low field magnetometry is dominated by the SQUID, which can achieve sensitivities of up to 1 fT $Hz^{-1/2}$ [9], enabling the detection of single magnetic flux quanta. However, cryogenic cooling requirements increase operational costs and preclude many applications [27]. At room temperature, atomic magnetometers have achieved record sensitivities down to 160 aT $Hz^{-1/2}$ [28], but with comparatively poor dynamic range and bandwidth [29, 30]. Furthermore, their spatial resolution is generally constrained to the millimeter-scale.

NV diamond magnetometers overcome the size limitation of atomic and SQUID magnetometers, and have achieved record spatial resolutions of as low as tens of nanometers, with a sensitivity of several nT $Hz^{-1/2}$ [31]. Their bandwidth (from a few Hz to a few hundred Hz) and dynamic range are subject to similar limitations to atomic magnetometers. Recently, larger micron-scale NV magnetometers have been developed. By using ensembles of NVs these magnetometers achieve improved precision, with the best reported precision being 1 pT $Hz^{-1/2}$ for a 60 μm diameter magnetometer [32]. NV magnetometers are attractive for many reasons,

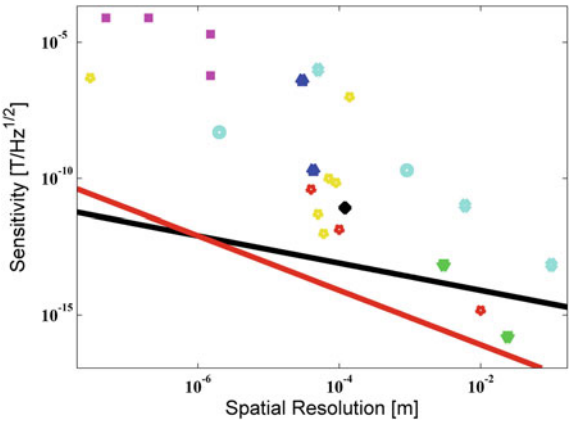

Fig. 9 Sensitivity versus spatial resolution of some modern state-of-the-art magnetic field sensors. Shown are spin-exchange-relaxation-free (*SERF*) magnetometers (*green downtriangles*) [28–30, 33], SQUIDs (*red pentagram*) [34–36], Hall-sensors (*magneta crosses*) [37, 38], NV-center based magnetometers (*yellow pentagram*) [6, 32, 39–42]. Bose-Einstein Condensate (*BEC*) magnetometer (*black crosses*) [43]. Magnetostrictive sensors (*cyan circles and diamonds*) can be found in various sizes and have sensitivity generally lying above modern sensors of comparable size [1, 2, 44]. Cavity optomechanics allows their sensitivity to be greatly enhanced (*blue uptriangles*) [4, 5], as described in this chapter. *Black and red lines* thermomechanical noise limit of magnetostrictive magnetometers discussed in Sect. 3. This figure is partly based on Ref. [45]

including the possibility to integrate them conveniently with biological samples, both using intracellular diamond nanoparticles and using NVs embedded in a diamond substrate for the specimen.

Electronically and interferometrically read-out magnetostrictive magnetometers exist in a broad range of sizes, ranging from microscopic Terfenol-D coated micro-cantilevers to fiber interferometers with sensitivities of fT $Hz^{-1/2}$ and sizes of several centimeters [1, 2, 44]. They have the advantages of room temperature operation, high dynamic range, and integrability. However, until the cavity optomechanical magnetometers of Refs. [4, 5], the sensitivity of these magnetometers was constrained well above the thermomechanical noise limit. The sensitivity achieved in Refs. [4, 5] is around a factor of 100 away from the best NV and cryogenic SQUID magnetometers at similar size; while the hundred kilohertz bandwidth and dynamic range is substantially superior to existing state-of-the-art NV magnetometers. The ability to use reasonably standard fabrication methods to produce these magnetometers, as well as fiber or waveguide couple them to light, and the microwatt power requirements are further advantages.

It is expected that with further advances in fabrication, the theoretical limit to noise performance shown in Fig. 9 could be approached. This provides the prospect of the sensitivity of cavity optomechanical magnetometers surpassing all currently existing magnetometers.

9 Conclusion

In conclusion, cavity optomechanical magnetometers offer an alternative approach to ultra sensitive room temperature magnetometry, that provides magnetic field sensitivity comparable to, and in theory exceeding, the state-of-the-art, kilohertz to megahertz bandwidths, and dynamic range extending past the Earth's magnetic field. Such magnetometers require only microwatts of optical power, with potential for sub-nanowatt power levels, and can be integrated on a silicon chip. These properties may enable new applications such as medical diagnosis on microscale samples [46], and direct measurement of the dynamics of strongly interacting spin systems such as semiconductors [47], superconductors [48], and spinor condensates [49]. With further improvements in sensitivity, these devices could extend the use of microscale magnetometers to areas including magnetic mapping of a single neuron grown on-chip [50] and low-field magnetic resonance imaging [51], allowing portable high-resolution imaging at room temperature with low power and cost.

References

1. F. Bucholtz et al., High frequency fibre optic magnetometer with 70 fT $Hz^{-1/2}$ resolution. Electron. Lett. **25**(25), 1719–1720 (1989)
2. R. Osiander et al., A microelectromechanical-based magnetostrictive magnetometer. Appl. Phys. Lett. **69**(19), 2930 (1996)
3. Y. Hui et al., High resolution magnetometer based on a high frequency magnetoelectric MEMS-CMOS oscillator. J Microelectromech S **24**, 1 (2015)
4. S. Forstner et al., Cavity optomechanical magnetometer. Phys. Rev. Lett. **108**, 120801 (2012)
5. S. Forstner et al., Ultrasensitive optical magnetometry. Adv. Mater. **26**, 6348 (2014)
6. D.L. Sage et al., Efficient photon detection from color centers in a diamond optical waveguide. Phys. Rev. B Rapid **85**, 121202(R) (2012)
7. S. Forstner et al., Sensitivity of cavity optomechanical field sensors. Proc SPIE **8439**, 84390U (2012)
8. L.P. Ichkitidze et al., Magnetic field sensors in medical diagnostics. Biomed. Eng. **48**(6), 305–309 (2015)
9. A. Edelstein, Advances in magnetometry. J. Phys.: Condens. Matter **19**, 165217 (2007)
10. A. Laraoui et al., Diamond nitrogen-vacancy center as a probe of random fluctuations in a nuclear spin ensemble. Phys. Rev. B **84**, 104301 (2011)
11. D. Rühmer et al., Vector fluxgate magnetometer for high operation temperatures up to 250 °C. Sens. Actuat. A-Phys. **228**(1), 118–124 (2015)
12. H. Can, U. Topal, Design of ring core fluxgate magnetometer as attitude control sensor for low and high orbit satellites. J. Supercond. Nov. Magn. **28**(3), 1093–1096 (2015)
13. I. Kovacic, M.J. Brennan, *The Duffing Equation: Nonlinear Oscillators and Their Behavior* (Wiley, London, 2011)
14. M.B. Moffett et al., Characterization of Terfenol-D for magnetostrictive transducers. J. Acoust. Sec. Am. **89**(3), 1448–1455 (1991)
15. G. Engdahl, *Handbook of Gieant Magnetostrictive Materials* (Academic Press, San Diego, 2000)

16. A. Schliesser et al., Resolved-sideband cooling and position measurement of a micromechanical oscillator close to the Heisenberg uncertainty limit. Nat. Phys. **5**, 509–514 (2009)
17. W.P. Bowen, G.J. Milburn, *Quantum Optomechanics* (CRC Press, Taylor & Francis Publishing, London, 2015)
18. C.W. Gardiner, M.J. Collett, Input and output in damped quantum systems: quantum stochastic differential equations and the master equation. Phys. Rev. A **31**, 3761 (1985)
19. T.P. Purdy et al., Observation of radiation pressure shot noise on a macroscopic object. Science **339**(6121), 801–804 (2013)
20. S. Schreppler et al., Optically measuring force near the standard quantum limit. Science **344** (6191), 1486–1489 (2014)
21. L. Ding et al., High frequency GaAs nano-optomechanical disk resonator. Phys. Rev. Lett. **105**, 263903 (2010)
22. L.D. Landau, E.M. Lifshitz, *Theory of Elasticity*, 2nd edn. (Pergamon Press, New York, 1970)
23. M.H. Saad, *Elasticity: Theory, Applications, and Numerics,* 3nd edn. (Academic Press, New York, 2014)
24. D.K. Armani et al., Ultra-high-Q toroid microcavity on a chip. Nature **421**, 925–928 (2003)
25. T.J. Kippenberg et al., Analysis of radiation-pressure induced mechanical oscillation of an optical microcavity. Phys. Rev. Lett. **95**, 033901 (2005)
26. D.M. Dagenais et al., Elimination of residual signals and reduction of noise in a low-frequency magnetic fiber sensor. Appl. Phys. Lett. **53**, 1474 (1988)
27. M. Sawicki et al., Sensitive SQUID magnetometry for studying nanomagnetism. Semicond. Sci. Technol. **26**(6), 064006 (2011)
28. H.B. Dang et al., Ultrahigh sensitivity magnetic field and magnetization measurements with an atomic magnetometer. Appl. Phys. Lett. **97**, 151110 (2010)
29. M.V. Romalis, H.B. Dang, Atomic magnetometers for materials characterization. Mater. Today **14**(6), 258–262 (2011)
30. D. Budker, M. Romalis, Optical magnetometry. Nat. Phys. **3**, 227–234 (2007)
31. G. Balasubramanian et al., Ultralong spin coherence time in isotopically engineered diamond. Nat. Mater. **8**, 383–387 (2009)
32. T. Wolf et al., A subpicotesla diamond magnetometer. arXiv:1411.6553 [quant-ph] (2014)
33. V. Shah et al., Subpicotesla atomic magnetometry with a microfabricated vapour cell. Nat. Photon. **1**, 649–652 (2007)
34. J.R. Kirtley et al., High-resolution scanning SQUID microscope. Appl. Phys. Lett. **66**(9), 1138–1140 (1995)
35. F. Baudenbacher et al., Monolithic low-transition-temperature superconducting magnetometers for high resolution imaging magnetic fields of room temperature samples. Appl. Phys. Lett. **82**(20), 3487–3489 (2003)
36. M.I. Faley et al., A new generation of the HTS multilayer dc-SQUID magnetometers and gradiometers. J. Phys: Conf. Ser. **43**(1), 1199–1202 (2006)
37. A. Sandhu et al., Nano and micro Hall-effect sensors for room-temperature scanning hall probe microscopy. Microelectron. Eng. **73–74**, 524–528 (2004)
38. A. Sandhu et al., 50 nm hall sensors for room temperature scanning hall probe microscopy. Jpn. J. Appl. Phys. **43**(2), 777–778 (2004)
39. J.R. Maze et al., Nanoscale magnetic sensing with an individual electronic spin in diamond. Nature **455**(2), 644–648 (2008)
40. L.M. Pham et al., Magnetic field imaging with nitrogen-vacancy ensembles. New J. Phys. **13**, 045021 (2011)
41. K. Jensen et al., Cavity-enhanced room-temperature magnetometry using absorption by nitrogen-vacancy centers in diamond. Phys. Rev. Lett. **112**, 160802 (2014)
42. V.M. Acosta et al., Broadband magnetometry by infrared-absorption detection of nitrogen-vacancy ensembles in diamond. Appl. Phys. Lett. **97**(17), 174104 (2010)
43. M. Vengalattore et al., High-resolution magnetometry with a Spinor Bose-Einstein condensate. Phys. Rev. Lett. **98**(20), 200801 (2007)

44. D. Shuxiang et al., Ultrahigh magnetic field sensitivity in laminates of TERFENOL-D and Pb $(Mg_{1/3}Nb_{2/3})O_3$-$PbTiO_3$ crystals. Appl. Phys. Lett. **83**(11), 2265 (2003)
45. S. Forstner et al., Sensitivity and performance of cavity optomechanical field sensors. Photonic Sens. **2**(3), 259–270 (2012)
46. V. Demas, T.J. Lowery, Magnetic resonance for in vitro medical diagnostics: superparamagnetic nanoparticle-based magnetic relaxation switches. New J. Phys. **13**, 025005 (2011)
47. S. Steinert et al., Magnetic spin imaging under ambient conditions with sub-cellular resolution. Nat. Commun. **4**, 1607 (2013)
48. L.S. Bouchard et al., Detection of the Meissner effect with a diamond magnetometer. New J. Phys. **13**, 025017 (2011)
49. M.S. Chang et al., Observation of Spinor dynamics in optically trapped Rb_{87} Bose-Einstein condensates. Phys. Rev. Lett. **92**, 140403 (2004)
50. K.B. Blagoev et al., Modelling the magnetic signature of neuronal tissue. Neuroimage **37**, 137–148 (2007)
51. M.P. Ledbetter et al., Near-zero-field nuclear magnetic resonance. Phys. Rev. Lett. **107**(10), 107601 (2011)

Planar Magnetometers

Asif I. Zia and Subhas C. Mukhopadhyay

Abstract The increasing demand of miniaturization, low power consumption, compactness and portability of the equipment has urged the sensors' size to be the only selection criterion for a magnetometer. Applications, such as magnetic micro-beads, micromagnetic scanning, non-destructive testing and medical applications like magnetic drug delivery dictate the requirement of magnetic sensors that are smaller in size and own single side measurement capability. To cater those needs, it is utmost important to explore and apply new principles governing nano-scale science and state-of-the-art fabrication technology. This chapter showcases the recent advances in magnetic field planar sensors that could be used to measure magnetic field with the privilege of non-destructive measurements and single side access to the sample.

1 Introduction

Magnetometers are defined as sensitive electronic readout instruments, equipped with specialized sensors that are used either to measure the magnetization of magnetic materials or measure the strength and direction of magnetic fields at a given point in space. The magnetic-field sensors are the core devices that operate on many physical, electronic, electrical and optical principles including magnetic induction, Lorentz force, Faraday rotation, Hall Effect, and magneto-optical effects. Contemporary techniques applied for magnetic sensing exploit wider areas in the fields of physics and material science. Recent progress in precise control of feature

A.I. Zia (✉) · S.C. Mukhopadhyay
School of Engineering and Advanced Technology, Massey University,
Palmerston North 4442, New Zealand
e-mail: a.i.zia@me.com

S.C. Mukhopadhyay
e-mail: s.c.mukhopadhyay@massey.ac.nz

A.I. Zia
Department of Physics, COMSATS University, Park Road, Islamabad, Pakistan

A. Grosz et al. (eds.), *High Sensitivity Magnetometers*, Smart Sensors,
Measurement and Instrumentation 19, DOI 10.1007/978-3-319-34070-8_12

size using hi-tech lithography techniques in semiconductor industry has paved the way to the successful fabrication of thick and thin film magnetic sensors and related transducers. State-of-the-art modern micromachining techniques have facilitated new types of solid-state microelectromechanical systems (MEMS) that provide versatile solutions to many problems normally associated with similar structures at larger scales. These systems are capable enough to replace bulky three dimensional systems with planar miniature systems. The reduction in fabrication cost in turn leads to a wide range of high precision magnetic sensor types. These include planar induction coil, fluxgate, SQUID, Hall-effect, anisotropic magneto-resistance (AMR), giant magneto-resistance (GMR), magnetic tunnel junctions, giant magneto-impedance, magnetostrictive composites, magnetodiode, magnetotransistor, fiber optic, magneto-optic, optically pumped, nuclear precession, and MEMS based magnetic sensors. This chapter reviews and discusses the advancements in miniaturization and transformation of bulky magnetic sensors into smart sensing devices. Applications of planar meander and mesh coils based magnetic sensors would also be discussed in due course.

2 Background

A magnetic sensor interprets magnetic field into electrical signals; therefore the general principle of operation of a magnetic transducer is either based on alternating current or direct current applications. Figure 1 shows a family tree of magnetic

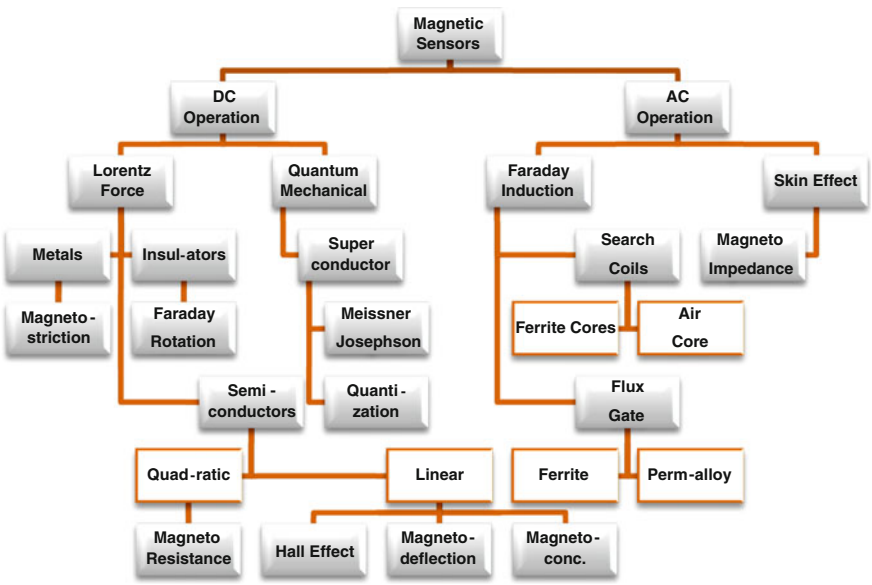

Fig. 1 Family tree of magnetic sensor materials and effects

sensors and materials segregated on the basis of type of exposed excitation and the consequent galvanomagnetic effects produced. The most fundamental of all galvanomagnetic effects is the Hall Effect that is responsible for the generation of an electric field orthogonal to the magnetic induction vector when a direct current flows through a conductor in the direction perpendicular to both. In case of current flowing through a superconducting material the galvanomagnetic effect observed at the Josephson junctions is termed as quantum mechanical galvanomagnetic effect that has become the foundation for realization of highly sensitive SQUID (superconducting quantum interference device) sensors and magnetometers [1].

3 Mathematical Model Based Physical Principles of Operation

Following discussion gives a brief account of some physical principles used to develop planar magnetic sensors and magnetometers operating on direct current technology.

Under the action of Lorentz force and Coulomb force, the phenomena of charge-carrier transport in conducting or superconducting material gives rise to the galvano-magnetic effects governed by the following relation.

$$F = eE + e[v \times B] \tag{1}$$

where 'e' denotes the carrier charge (for electrons $e = -q$, and for holes $e = +q$ and $q = 1.6 \times 10^{-19}$ °C), E denotes the electric field, $\boldsymbol{v}$ the carrier velocity and B the magnetic induction. For non-degenerate semiconducting materials exposed to the transverse electrical and magnetic fields (i.e. $E \cdot B = 0$), the current transport equation in terms of total current density 'J' is given by [2]:

$$J = J_0 + \mu_H [J_0 \times B] \tag{2}$$

where J_o is the carrier charge density due to electric field with a carrier concentration gradient ∇n given in (3). The transport coefficients μH (the Hall mobility which has the sign of the corresponding charge-carrier), σ (the conductivity), and D (the diffusion coefficient) are determined by the carrier scattering processes and generally depend on electric and magnetic fields.

$$J_0 = \sigma E - eD \nabla \mathrm{n} \tag{3}$$

Both the Hall and the magneto-resistive effects can be derived from the solutions of Eq. (2) subject to the application of appropriate boundary conditions [3].

3.1 Hall Effect and Magneto Resistivity in Semiconductors

Consider a special case of carrier transport in a very long narrow strip of an extrinsic and homogeneous ($\nabla n = 0$) semiconductor material along x-axis that is exposed to a magnetic field of known magnetic flux density along y-axis $B = (0, B_y, 0)$. If the strip is exposed to an external electric field $E_x = (E_x, 0, 0)$, a current I will flow through it with current density $J = (J_x, 0, 0)$. Since $J_z = 0$, an internal transverse electric field $\boldsymbol{E}_H$ known as the Hall field must build up in order to counteract the Lorentz force, that can be determined from Eq. (2) by substituting $E = E_x + E_H$, under the condition that the transverse current density vanishes, i.e. $E_H = (0, 0, E_z)$ and $E_z = -\mu_H B E_x$. The appearance of Hall field gives rise to a measurable transverse voltage called Hall voltage V_H that can be calculated as (ignore–sign):

$$V_H = \mu_H E_x B w = R_H J_x B w \tag{4}$$

where w is the strip width. $R_H = \mu_H/\sigma = r/en$ is called the Hall coefficient and r *is* the Hall scattering factor of carriers with n carrier density. In semiconducting materials low carrier density results into a large Hall coefficient; therefore, Eq. (4) explains the superiority of semiconductors over conductors. The deflection of the resultant electric field occurs due to the generation of the Hall Field, that is evaluated in terms of Hall angle measured with respect to the applied external field. Where $\tan \theta_H = E_z/E_x = -\mu_H B$.

A rotation in the electric field lines by θ_L called Lorentz deflection angle is described by a ratio in Eq. (5). It is observed when a short strip of wide cross-sectional area is exposed to the external electric field $E_x = (E_x, 0, 0)$.

$$\frac{J_z}{J_x} = \mu_H B = \tan \theta_L \tag{5}$$

The consequent current density leads to a lateral component J_z that is responsible for longer drift path of the carriers giving rise to geometric magneto-resistance effect mathematically expressed by Eq. (6) [2].

$$\frac{\rho_B - \rho_o}{\rho_o} = (\mu_H B)^2 \tag{6}$$

where ρ_0 represents the electrical resistivity at $B = 0$, and ρ_B the increased resistivity due to the presence of the magnetic field. Equation (6) provides the relative change in resistivity. Due to low carrier mobility, intrinsic silicon does not display considerable amount of magneto-resistivity effect. Magnetic sensors based on this effect require high-mobility narrow band-gap III–V compounds such as Indium Antimonide or Indium Arsenide semiconductors [4].

3.2 Anisotropic Magneto-Resistance

Anisotropic magneto-resistance is an intrinsic property observed in ferromagnetic transition metals and alloys. Permalloy is an alloy containing about 80 % nickel and 20 % iron, exhibit anisotropic magneto-resistance. The magnetization vector determines the direction of current flow in these materials; therefore, when exposed to an external magnetic field the resultant magnetization vector rotates the current path, by an angle θ [5]. The specific resistivity of the sample as a function of θ, $\rho(\theta)$, is given by Eq. (7):

$$\rho(\theta) = \rho_{\perp} + \left(\rho_{||} - \rho_{\perp}\right) \cos^2 \theta = \rho_{\perp} + \Delta\rho \cos^2 \theta \tag{7}$$

where $\rho\|$ is the resistivity of the sample when current flow is parallel to magnetization vector i.e. $\theta = 0$, $\rho\perp$ the resistivity of the sample when current flow is perpendicular to magnetization vector $\theta = 90°$. The magneto-resistive effect $(\Delta\rho/\rho_o)$ is the ratio of change in resistivity to the resistivity at $\theta = 0$. The advances in thin-film deposition technology have paved the way to use anisotropic magneto-resistance effect in magnetic sensor applications [6].

3.3 Flux Quantization-Meissner Effect

The constancy of magnetic flux consequent to flux quantization inside a superconducting closed loop is known as Meissner effect. The magnetic sensors using superconducting materials and applying Meissner effect to measure magnetic field are commonly known as SQUID magnetometers. A closed superconducting loop when placed in an external magnetic field induces a shielding current, known as the super-current I_s, that circulates around the inner surface of the ring such that the total magnetic flux, Φ_i, inside the ring is quantised. Equation (8) provides the magnitude of the quantized flux in terms of self-inductance L of the superconducting closed loop, induced current I_s and external field flux Φ_e.

$$\phi_i = m\phi_o = LI_s + \phi_e \tag{8}$$

where $\Phi_0 = 2.07 \times 10^{-15}$ Wb is the flux quantum and m a multiple integer. Any variation in the external flux is responded by the superconducting loop by an equal but opposite flux as long as the super-current I_s stays within a critical limit of the current value termed as I_c. The current I_s through the superconducting loop is measured using Josephson junctions that provided means to development of highly sensitive SQUID magnetometer.

Alternating current based magnetic sensing uses the physical principles of classical electrodynamics. Planar magnetic sensors like search-coil sensors, fluxgate

sensors and magneto impedance and giant magneto-impedance sensors have been developed using Faraday's law of induction and electromagnetic theories. For ac excitation the voltage V is related to the resulting current I via complex impedance Z which is a function of skin-depth δ that depends on the angular frequency ω and magnetic permeability of the material. Equation (9) and (10) describe the mathematical interpretation of V and I.

$$V = Z(\delta)I \tag{9}$$

$$I = I_o \exp(i\omega t) \tag{10}$$

where I_o is the amplitude

4 Planar Integrated Micro Hall Sensor

Hall Effect is the most applied physical phenomenon for the magnetic sensors [7]. The Hall sensitivity of silicon ranges from 10 to 1000 G or 10^6–10^8 nT and the sensitivity of Hall sensors is typically 1 mV/mT for a 1 mA current. Hall Effect devices have achieved a high number of low cost position sensing applications. They are lightweight planar devices and consume power between 0.1 and 0.2 W and can operate safely over a wide temperature range. Hall Effect sensors can measure either a constant or a varying field with an upper frequency limit at about 1 MHz. For higher sensitivity applications thin-film of Indium Antimonide (InSb) with a typical sensitivity 5 mV/mT and Indium Arsenide (InAs) with a typical sensitivity of 2 mV/mT are used [8]. InAs exhibits better temperature stability of the Hall voltage in comparison to Silicon and InSb. InAs Hall effect sensors can operate in a range of −40 to +150 °C which declares them the best candidates for automotive applications [9]. A promising Hall sensor was made using silicon-on-insulator (SOI) technology: 1μT/√Hz@1 Hz noise was achieved for an 80-μm wide, 50-nm thick sensor [10]. Two-dimensional quantum-well multilayer heterostructures based on GaAs are promising for low-noise Hall sensors: 100nT/√Hz@1 Hz noise was achieved with external spinning-current electronics, which was further improved threefold by using leakage-free switches [11].

Figure 2 shows an off-the-shelf planar InSb Hall sensor. The InSb thin-film Hall sensor is sandwiched between two ferrite pieces with an integrated ferrite concentrator (Asahi Kasei, BW series). The figure shows the FEM simulated flux lines and a micro-photograph of the device [8].

A new microsystem based on the non-invasive Hall principle was published recently. The system owned the ability to detect magnetic microstructures [12]. The micro-Hall plate had an active area of only 2.4 μm × 2.4 μm that is embedded in the microsystem fabricated by applying CMOS technology. The microsystem exhibited a magnetic field resolution of 300 nT/√Hz at 1 Hz. A two-dimensional

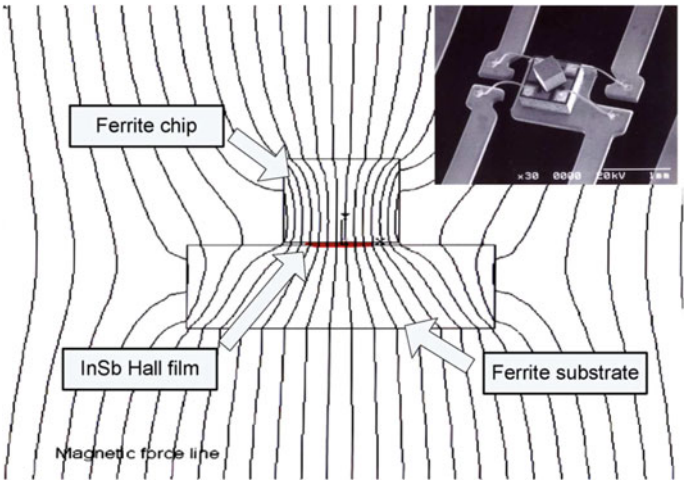

Fig. 2 Magnetic force lines of field concentrators for a thin-film Hall sensor (FEM simulation [8])

magnetic scanner was developed to demonstrate the performances of the developed microsystem [12]. The microsystem displayed its ability to compensate the temperature dependence of the sensor and the magnetic circuit enclosing the sensor by embedding the sensor on a planar CMOS chip with dimensions 2600 µm by 900 µm.

The micro-Hall plate sensor is placed in the peripheral corner of the silicon chip as depicted in Fig. 3. The bonding connections are placed on the opposite side of the chip far away from the Hall sensor to minimize the noise. Such planar design allows non-invasive single side access of the Hall sensitive area to the surface required to be magnetically characterized.

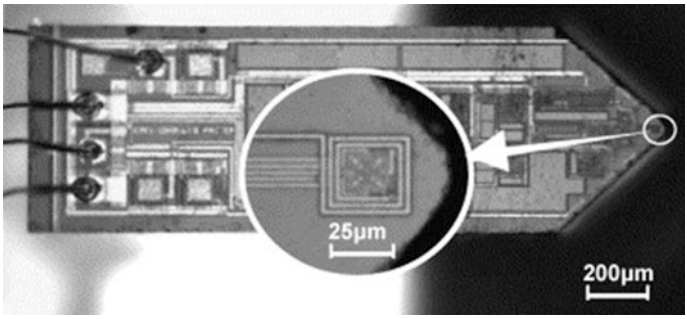

Fig. 3 Photograph of the integrated micro-Hall probe. The micro-Hall plate sensor is placed in the peripheral corner of the silicon chip. Chip dimensions are 2600 µm × 900 µm [12]

5 Planar Anisotropic Magneto-Resistance (AMR) Sensors

Permalloy is probably the most common material for AMR sensors due to its relatively larger magneto-resistance. The other merit points of using Permalloy as AMR sensor are its characteristics compatibility with the applied fabrication techniques employed to make silicon integrated circuits such as a zero coefficient of magnetostriction and ease of thin film deposition [5]. A planar AMR integrated sensor comprises of a bridge configuration of four Permalloy resistors. The fabrication is normally achieved by sputtering process that deposits the bridge in form of thin film on a silicon substrate. A potential difference develops between the two paths of current if there is a mismatch of resistance between the two paths. Longer current path designs ensure high bridge resistance consequently reducing the power requirement of the AMR sensor [8]. A precise resistance match is required for all four bridge resistors in order to avoid any offset potential difference to appear across the two paths of current flow in the absence of test magnetic field. Special design and fabrication methodologies are adopted to reduce the offset potential difference appearing from mismatches in the four resistors.

Figure 4 [13] shows an image of planar design for AMR chip sensor with four Resistor Bridge. Two meander coils are fabricated in order to provide feedback field and a set/reset field.

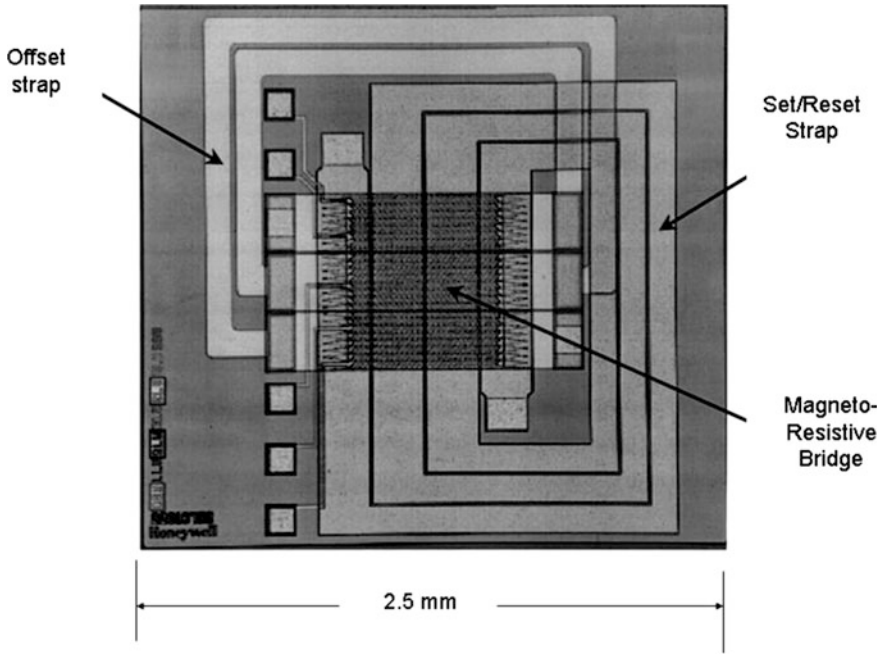

Fig. 4 Planar design configuration of an AMR sensor displaying four resistors bridge, and two coils, (i) for set/reset field pulses and, (ii) for feedback field [13]

The recent fabrication advancement in semiconductor fabrication industry has made it viable to fabricate the magnetometer readout electronics and additional temperature-compensating circuitry on the same chip. To achieve linearity between changes in resistance corresponding to change in the magnetic field, the biasing of the bridge is applied to rotate the direction of magnetization. A thin film of cobalt is sputter-coated over the resistors to provide shorting paths on the Permalloy strip. On magnetizing cobalt, magnetic field causes the current to direct at an angle of 45 relative to the direction of magnetization that appears as a barber pole [4].

The AMR planar sensors have a sensitivity range of 10^{-2} to 50 G or 10^{3} to 5×10^{6} nT with open-loop readout electronics [13]. For limited bandwidths and applying closed-loop feedback readout electronic methods, a minimum detectable field of 0.1 nT can be achieved.

AMR sensors based magnetometers own an outstanding capability to measure magnetic field strength over an extremely wide dynamic range from 0 Hz to nearly 1 GHz. These sensors are lightweight, miniaturized in size and require merely up to 0.5 mW of power. The operating temperatures normally are between 55 and 200 °C [14].

6 Planar Fluxgate Magnetic Sensors

A recent publication presented a novel class of miniature fluxgate magnetometers fabricated on a printed circuit board (PCB) substrate and electrically connected to each other similar to the current "flip chip" concept in semiconductor package. The proposed sensor was soldered together by reversely flipping a 5 cm × 3 cm PCB substrate to the other identical one which included dual magnetic cores, planar pick-up coils, and 3-D excitation coils constructed by planar Cu interconnections patterned on PCB substrates [15]. Schematic of the proposed flip-chip micro-fluxgate sensor is shown in Fig. 5.

The main components and the final assembly of the "flip chip" fluxgate sensor are shown schematically in Fig. 6.

The sensor's operation has been characterized by employing the improved second-harmonic detection technique that enabled linear *V-B* correlation and responsivity verification. Additionally, the double magnitude of responsivity measured at very low frequency (1 Hz) magnetic fields had been experimentally demonstrated. The maximum responsivity of 593 V/T at 50 kHz of excitation frequency with the second harmonic wave of excitation was concluded; however, the minimum magnetic field noise was found to be 0.05nT/$\sqrt{\text{Hz}}$ @ 1 Hz for the mentioned excitation potential [15].

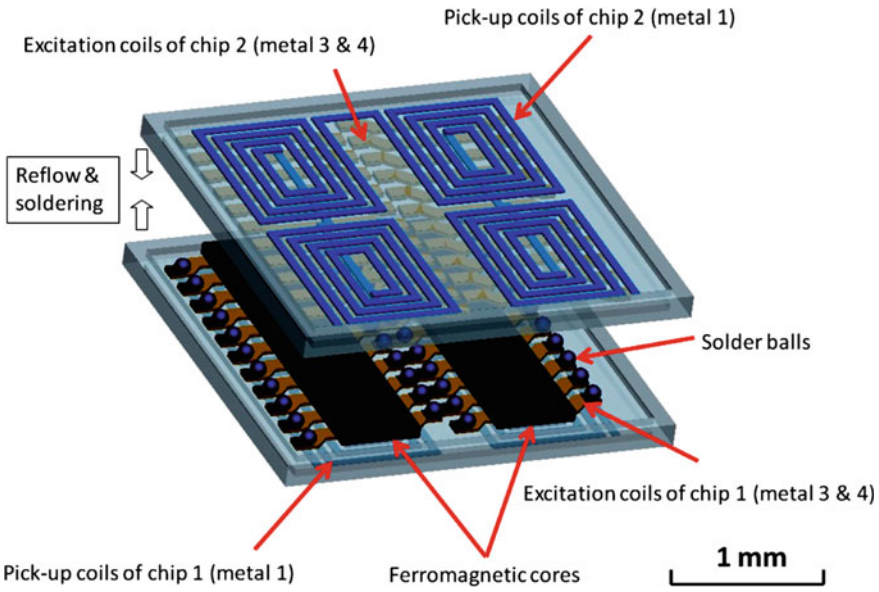

Fig. 5 Shematic of the proposed flip-chip micro-fluxgate sensor [15]

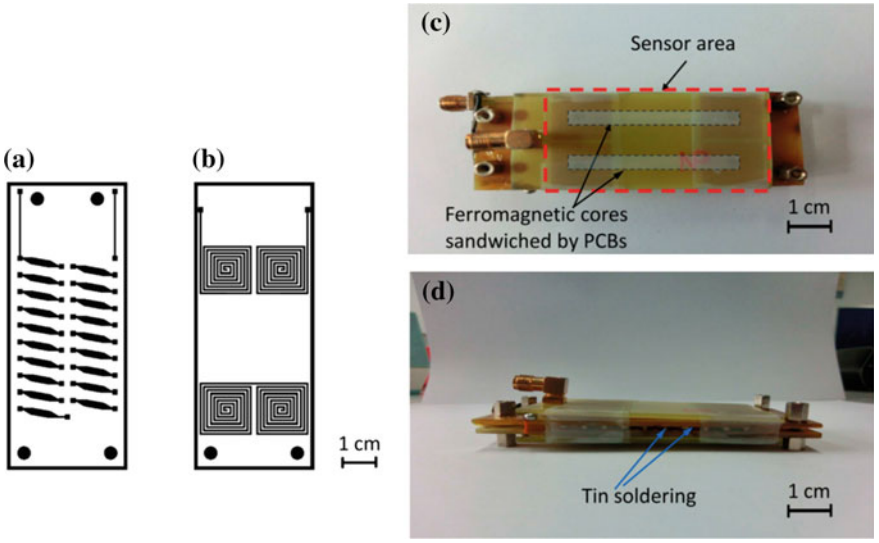

Fig. 6 **a** Cu patterns of the excitation coil on PCB substrate (*front side*); **b** Cu patterns of the pick-up coil on PCB substrate (*back side*); **c** top view and **d** side view of the completed "flip-chip" fluxgate sensor [15]

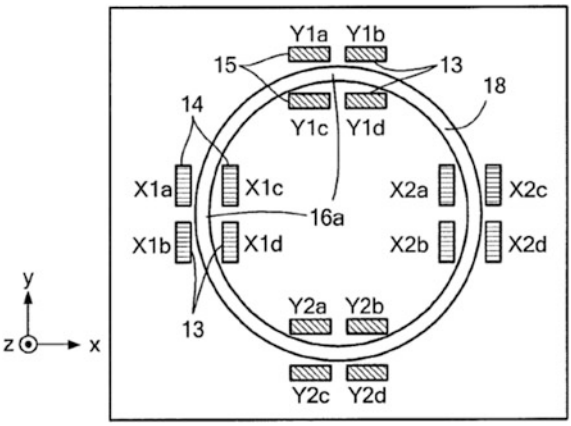

Fig. 7 View of the three axis planar magnetic field sensor with ring shaped magnetic concentrator [16]

7 Planar Three-Axes GMR Magnetometer

A planar three axis sensor has been patented in October 2013 for sensing magnetic flux along three mutually orthogonal axes. The proposed magnetometer can be used for three dimensional magnetic sensing and other magnetic field sensing applications. The sensing units operate to sense X and Y axis magnetic flux signals in the device XY-plane, While Z axis sensitivity has been achieved by use of a continuous ring shaped or octagonal magnetic concentrator that has been adapted to transform the Z axis magnetic flux signal into magnetic flux signals into the XY-plane

Referring to Fig. 7, magnetometer layout in accordance with the presented design shows a continuous, ring-shaped magnetic concentrator. The magnetic concentrator is formed of a ferromagnetic material having high permeability and low coercive force. The GMR and/or TGMR units 14 and 15 (Fig. 7) on each side of the magnetic concentrator are structurally identical. The units 14 and 15 are disposed on opposite sides of concentrator. A set/reset coil arrangement had been used for initiating, setting, and resetting the magnetization directions of the free layer and the magnetic concentrator. With multiple groups of sensing units for the XZ plane and multiple groups of sensing units for the YZ plane, it was made possible to acquire a differential signal for Z from one of the sensing units and a composite signal for X or Y from another sensing units [16].

8 Planar Induction Coil Sensors

Induction coil sensors commonly called search coil and pickup coil sensors are the oldest and well-researched types of magnetic sensors operating on alternating current technology. The transfer function governing the magnetic sensing $V = f(B)$ results from the fundamental Faraday's law of induction. The transfer impedance is defined as the ratio of the induced voltage across the sensing coil to the

current of the exciting coil. The exciting winding carries time varying (high-frequency) magnetic field to inspect non-conducting magnetic media in which no eddy-currents are induced, as well as to inspect conducting media, such as metal, in which eddy currents are induced [17]. The planar type configuration being flexible is suitable for curved surfaces and can be used for the inspection of cooling pipes used in nuclear power station and also the aircraft's surface etc.

Many research papers have been reported for the determination of near-surface material properties using the measured frequency-dependent impedance of a small right cylindrical air-core coil placed next to the metal surface and driven by an alternating current [18–22]. Usually the electromagnetic properties of the test material, including its defects, are inferred from the changes in the coil impedance caused by the presence of the test material [23, 24]. The normalized values of resistive component, R_n, and the reactive component, X_n are used and are given by,

$$R_n = \frac{R_m - R_o}{R_o} \quad and \quad X_n = \frac{X_m}{X_o} \tag{11}$$

where R_m, and X_m, are the real and imaginary components of the impedance when the sensor is coupled to the material and R_o and X_o are the corresponding air, or uncoupled values. The experimental results indicate that the shapes of the normalized impedance diagrams of ferrite pot core eddy current sensors are independent of sensors design parameters, lift-off, and material resistivity [18].

Planar type meander coils have been used for the evaluation of near-surface properties and are reported in [25, 26]. The aim is to extend the modelling technique to planar mesh type sensors and to investigate the feasibility of applying it to estimate the near-surface material properties and the quality inspection of structural health and crack determination [27], electroplated materials [17], fat contents in dairy products [28], saxophone reeds [29] and nitrate contamination in potable water [30].

8.1 Configuration of Planar Induction Coil Sensors

There are two types of planar electromagnetic sensors commonly used for performance evaluation of material properties for non-destructive evaluation and single side access of the magnetic material under test. The type of test material dictates the sensor-type chosen for the particular application. Figure 8a, b show the configuration of meander and mesh type planar induction coil sensors. The meander and mesh sensors consist of two planar coils; an excitation coil (meander type) and a sensing coil (mesh type) with mesh planar coil placed on top of meander coil with insulation sandwiched between the two planar configurations. The meander coil is energised by a high-frequency sinusoidal perturbation that induces an electromagnetic field in the test material. The material-induced field interacts with the

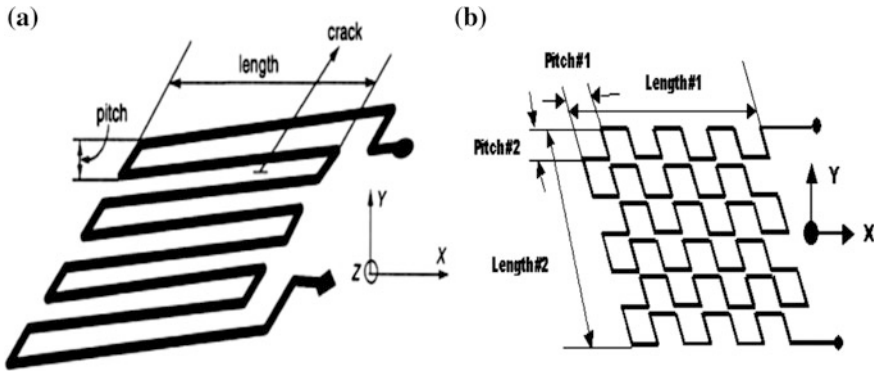

Fig. 8 Configuration of planar electromagnetic sensors. **a** Meander type. **b** Mesh type [29]

applied field and the resultant field is picked up by the planar mesh coil placed above the exciting coil.

The meander and the mesh planar configurations are separated by a polyimide film of 50 μm thickness. To improve the magnetic flux penetration in the test-material, a magnetic plate of N_iZ_n is placed on top of the sensing coil. The size of the sensor depends on the number of pitches used in it. The optimum pitch size depends on the application. The size used in this application is 27 × 27 mm, with a pitch size of 3.25 mm. The sensitivity of the meander-type sensor varies with its orientation with respect to the test-material. Hence, in some applications the mesh

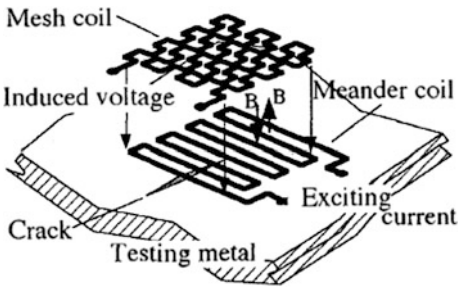

Fig. 9 Configuration of meander/mesh coupled eddy current testing probe [27]

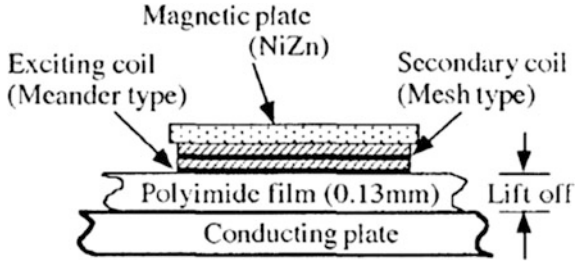

Fig. 10 Cross section of the planar eddy current test probe (ETC) [27]

type is more appropriate. The structural configuration of these sensors is shown Fig. 9. Figure 10 shows the cross-sectional view of the sensor applied for crack determination in a metallic plate.

8.2 *Finite Element Modelling of Mesh and Meander Coils*

The electromagnetic field distribution of mesh and meander configurations of planar sensors was analysed with the help of finite-element analysis tools. Comsol Multiphysics FEM software was used to deduce the critical parameters in addition to magnetic field distributions for the designed planar sensors. Figures 11 and 12 show the screen-shots of the magnetic field distribution across meander and mesh-type planar sensors, respectively.

The software uses mathematical models and Maxwell's equations to deduce important numerical parameters for the simulated design of the magnetic sensor. Based on provided boundary conditions and calculated parameters the software plots the expected magnetic field distribution around the sensors. It was observed that the magnetic flux lines enter the horizontal plane (*Z*-axis) perpendicularly and come out for both sensors. The distribution affects only one axis (parallel to horizontal plane) for the meander type, whereas for the mesh type, the distribution affects both axes of the horizontal plane.

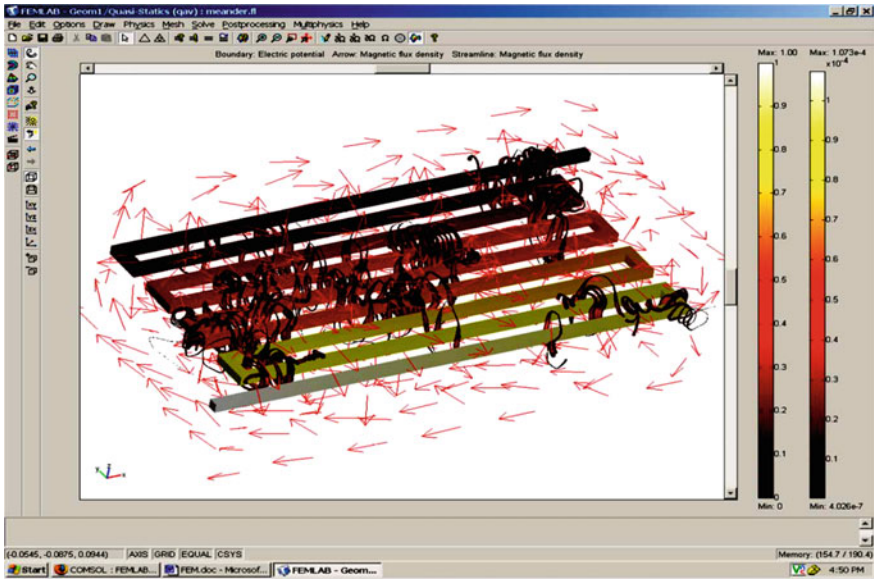

Fig. 11 Magnetic field distribution for meander planar sensor mathematically deduced by COMSOL FEM software [29]

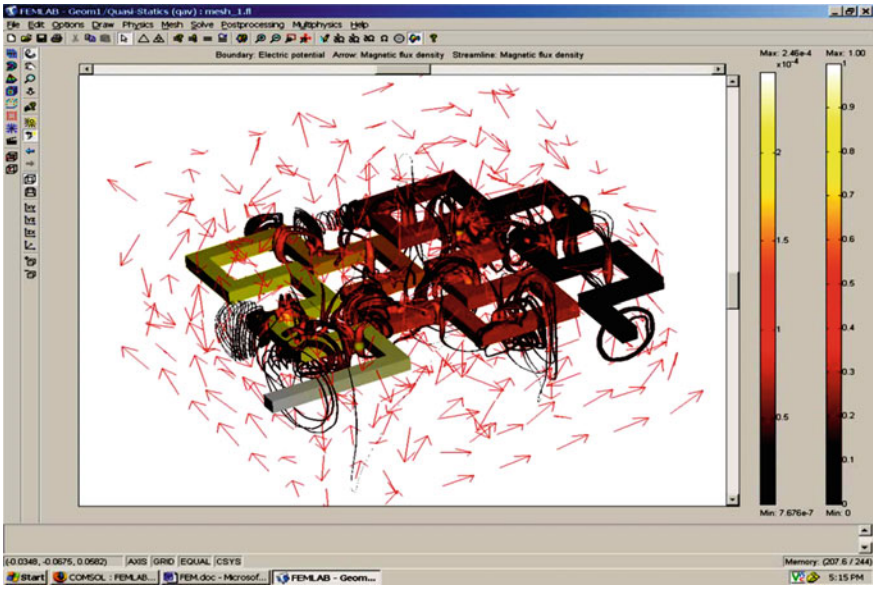

Fig. 12 Magnetic field distribution for meander planar sensor mathematically deduced by COMSOL FEM software [29]

8.3 Planar Meander and Mesh Sensors' Fabrication

All sensors were designed using the Altium Designer 6.0. The FR4 substrate sensors were fabricated at Massey University using standard PCB printing technology. The design was laser-printed on transparency film. The photo-resist board was used. The conducting layers of the board are typically made of thin copper foil. The film together with the board was exposed to the UV light. This process will impress and burn the desired sensor design onto the board. The photo-resist board was then placed in a tank filled with developer. Then, the board was immersed into a special chemical for etching process to remove the unwanted copper, leaving only the desired copper trace. The sensors were cut into a suitable design for testing [31, 32].

9 Applications of Meander-Mesh Planar Sensors

9.1 Defect Imaging by Planar ECT Probe

Advanced planar type eddy current testing probe (ETC) had been developed for detecting cracks/defects in metallic objects. The key idea for this probe is the induction of eddy currents inside a conductive plate on application of alternating

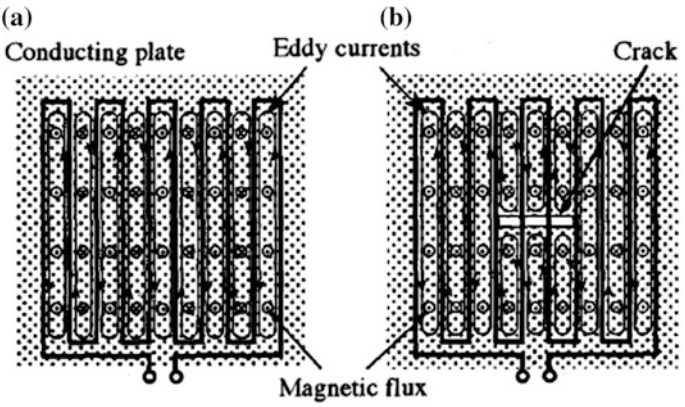

Fig. 13 Distribution of induced magnetic flux and eddy currents [27]

magnetic field produced by the meander coil. The mesh coil is a two-dimension pick up coil that senses a localized magnetic field generated by rotating currents in the conductive plate. With no defects the magnetic fields produce regular patterns and thus eddy currents have the direction at each pitch as shown in Fig. 13a. In other case, the distribution of eddy currents has localized patterns if defects exist as shown in Fig. 13b.

Imaging technology can further expand the use of ECTs by enhancing the resolution and sensitivity of the visual record.

9.2 Saxophone Reed Inspection

Planar mesh-meander induction sensor was employed for non-destructive evaluation (NDE) of saxophone reeds. Reeds were rated on the following parameters: ease of attack, ease of sustenance, and tone quality in the low, middle, and high ranges of the instrument, as well as a score for volume. Figure 14 shows the types of saxophone reeds evaluated for the said parameters using planar mesh-meander planar electromagnetic system. Figure 15 displays the FR4 substrate based fabricated sensors for the mentioned application.

The frequency response obtained as a test of 8 different reeds show that the reeds with better tone quality behaved as resonant circuits with a peak obtained at 579 MHz as shown in the phase-shift vs frequency plot in Fig. 16.

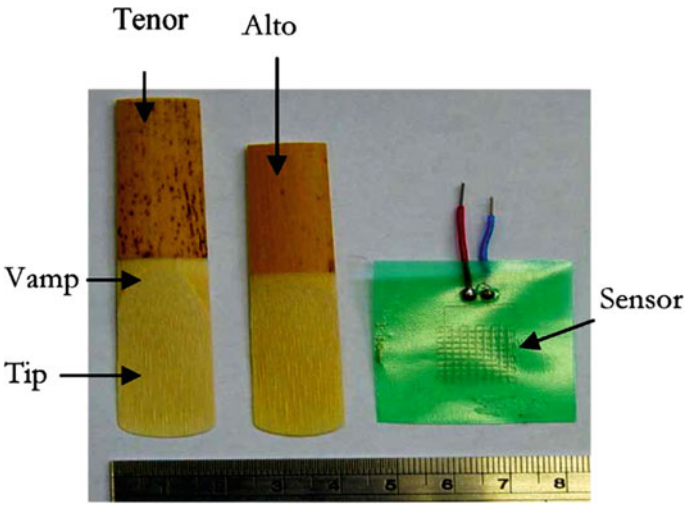

Fig. 14 A tenor and an alto saxophone reeds [29]

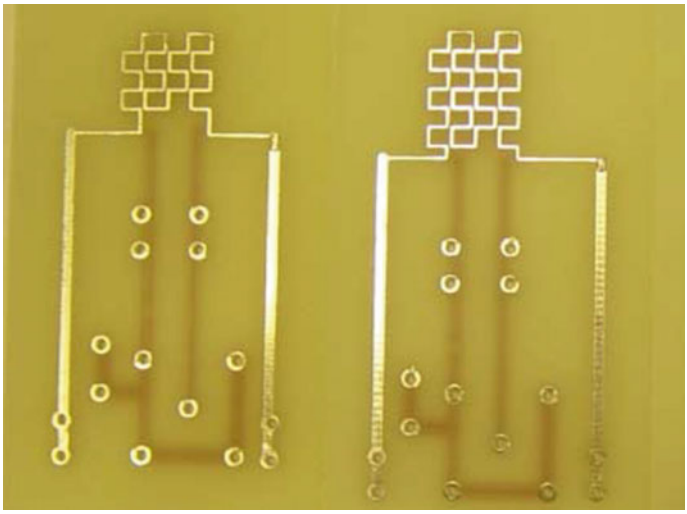

Fig. 15 FR4 substrate mesh sensor [29]

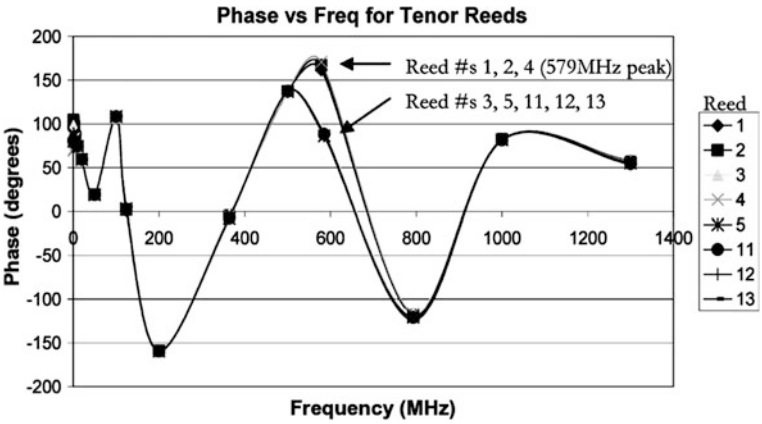

Fig. 16 Frequency response of tested reeds [29]

9.3 Planar Meander Sensors in Robotics

Pairs of meander coils were tested against angular displacements in a robotic foot, and results showed that the sensor gives correct information about displacement regardless how the foot touches the ground with its whole area. A planar meander-type sensor, where variation of input inductance serves as a measure of displacement, could be used as a ground reaction force (GRF) sensor to provide dynamic balance for legged locomotion. This inductive displacement sensor is constructed to detect normal, as well as tangential component of the force [33]. Figure 17 shows schematics of single-link actuated robotic foot and Fig. 18 shows the position of planar meander coil induction sensors in the robotic foot.

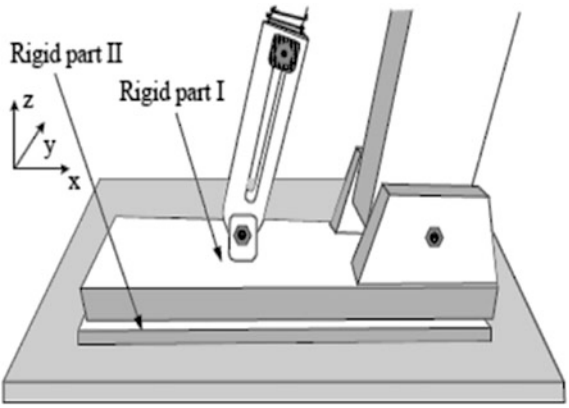

Fig. 17 Single-link robotic foot [33]

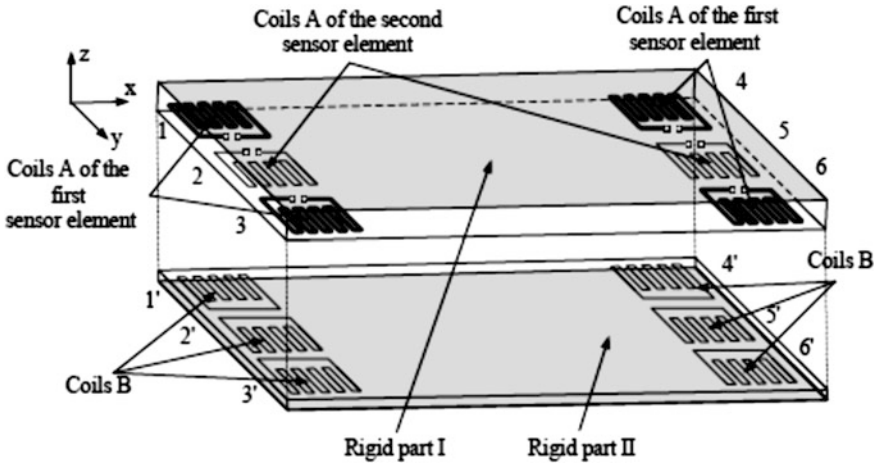

Fig. 18 Meander coil positioning in the foot [33]

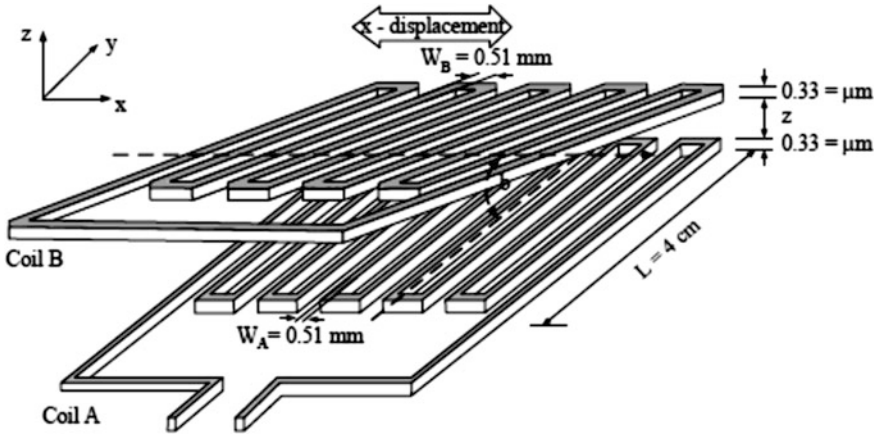

Fig. 19 Rotation of meander coil B about x-axis

Two most common cases were analyzed: when coil B rotates around x-axis for angle b (shown in Fig. 19) and around y-axis.

Impedance Analyzer HP4194A was used in the research to measure the inductive outcome from the meander sensing elements for different angles and distances between coils at the frequency of 1 MHz. The case results for x-axis rotations (i.e. for maximal angle β_{max} at particular distance), as shown in Fig. 20, for normal and tangential displacement. Calculated deviation between characteristics for maximal angle ($\beta = \beta_{max}$) and for the case when coils are parallel ($\beta = 0$) is

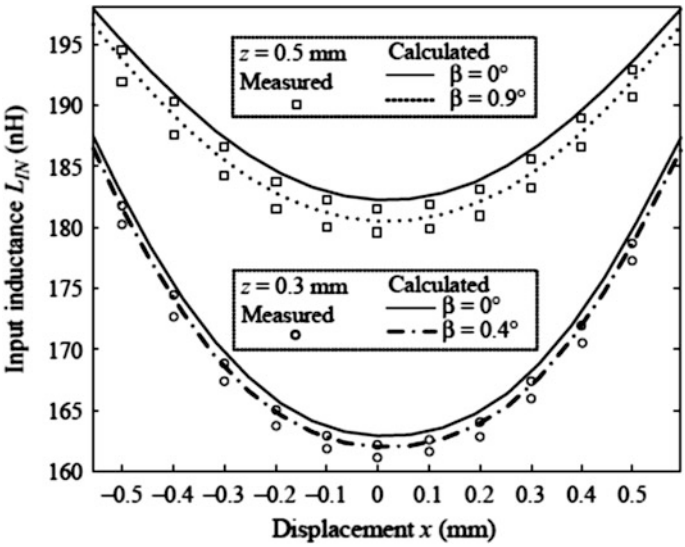

Fig. 20 Measured and calculated values of input inductance LIN when coil B rotates around x-axis [33]

shown in Fig. 20. Results reveal that these deviations are negligible concluding that the planar meander induction sensors provide the dependable information about the foot displacement, regardless how it touches the ground exposing the complete foot area to ground [33].

10 Conclusions

We have tried to showcase the recent advances in magnetic field planar sensors that could be used to measure magnetic field enjoying the privilege of non-destructive measurements and single side access to the sample. A trade-off between the sensor's size and its parameters measurement capability has always been accepted so far. With the increasing demand of miniaturization, low power consumption, compactness and portability of magnetometers, sensor size is often the only selection criterion. Applications, such as magnetic micro-beads, micro-magnetic scanning, non-destructive testing and medical applications like magnetic drug delivery urge the need of magnetic sensors that are smaller in size and own single side measurement capability. To cater those needs, it is utmost important to explore and apply new principles governing nano-scale science and technology.

References

1. A. Mahdi, L. Panina, D. Mapps, Some new horizons in magnetic sensing: high-T c SQUIDs, GMR and GMI materials. Sens. Actuators, A **105**, 271–285 (2003)
2. S.M. Sze, *Semiconductor Sensors* (Wiley, New York, 1994)
3. P. Ripka, Sensors based on bulk soft magnetic materials: advances and challenges. J. Magn. Magn. Mater. **320**, 2466–2473 (2008)
4. A. Ozbay, E. Nowak, A. Edelstein, G. Fischer, C. Nordman, S.F. Cheng, Magnetic-field dependence of the noise in a magnetoresistive sensor having MEMS flux concentrators. Trans. Magn. IEEE **42**, 3306–3308 (2006)
5. W. Lee, M. Toney, D. Mauri, High magnetoresistance in sputtered permalloy thin films through growth on seed layers of (Ni 0.81 Fe 0.19) 1-x Cr x. Trans. Magn. IEEE **36**, 381–385 (2000)
6. P. Ciureanu, S. Middelhoek, *Thin film resistive sensors* (CRC Press, Boca Raton, 1992)
7. R.S. Popovic, *Hall effect devices* (CRC Press, Boca Raton, 2003)
8. P. Ripka, M. Janošek, *Advances in magnetic field sensors* (2010)
9. C. Lei, R. Wang, Y. Zhou, Z. Zhou, MEMS micro fluxgate sensors with mutual vertical excitation coils and detection coils. Microsyst. Technol. **15**, 969–972 (2009)
10. Y. Haddab, V. Mosser, M. Lysowec, J. Suski, L. Demeus, C. Renaux, D. Flandre, in *Low-noise SOI Hall devices*, *SPIE's First International Symposium on Fluctuations and Noise* (2003), pp. 196–203
11. A. Kerlain, V. Mosser, Low frequency noise suppression in III-V Hall magnetic microsystems with integrated switches. Sens. Lett. **5**, 192–195 (2007)
12. P. Kejik, G. Boero, M. Demierre, R. Popovic, An integrated micro-hall probe for scanning magnetic microscopy. Sens. Actuators, A **129**, 212–215 (2006)
13. J. Lenz, A.S. Edelstein, Magnetic sensors and their applications. Sens. J. IEEE **6**, 631–649 (2006)
14. A. Bertoldi, D. Bassi, L. Ricci, D. Covi, S. Varas, Magnetoresistive magnetometer with improved bandwidth and response characteristics. Rev. Sci. Instrum. **76**, 065106-065106-6 (2005)
15. C.-C. Lu, J. Huang, P.-K. Chiu, S.-L. Chiu, J.-T. Jeng, High-sensitivity low-noise miniature fluxgate magnetometers using a flip chip conceptual design. Sensors **14**, 13815–13829 (2014)
16. Y. Cai, J. Qiu, L. Jiang, Planar three-axis magnetometer (2013)
17. S. Mukhopadhyay, Development of a novel planar mesh type micro-magnetic sensor for the quality inspection of electroplated materials. Sens. 2002 Proc. IEEE **2002**, 741–746 (2002)
18. S. Vernon, The universal impedance diagram of the ferrite pot core eddy current transducer. Trans. Magn. IEEE **25**, 2639–2645 (1989)
19. J. Bowler, H. Sabbagh, L. Sabbagh, The reduced impedance function for cup-core eddy-current probes. Trans. Magn. IEEE **25**, 2646–2649 (1989)
20. J.C. Moulder, E. Uzal, J.H. Rose, Thickness and conductivity of metallic layers from eddy current measurements. Rev. Sci. Instrum. **63**, 3455–3465 (1992)
21. S.C. Mukhopadhyay, S. Yamada, M. Iwahara, Investigation of near-surface material properties using planar type meander coil. JSAEM Stud. Appl. Electromagnet. Mech. **11**, 61–69 (2001)
22. S.C. Mukhopadhyay, Planar electromagnetic sensors: characterization, applications and experimental results (Planare elektromagnetische Sensoren: Charakterisierung, Anwendungen und experimentelle Ergebnisse). Tm-Technisches Messen **74**, 290–297 (2007)
23. S. Mukhopadhyay, C. Gooneratne, G.S. Gupta, S. Yamada, Characterization and comparative evaluation of novel planar electromagnetic sensors. Trans. Magn. IEEE **41**, 3658–3660 (2005)
24. N.J. Goldfine, K.G. Rhoads, K.E. Walrath, D.C. Clark, *Method for characterizing coating and substrates*. Google Patents, (2002)
25. N.J. Goldfine, Conformable, meandering winding magnetometer (MWM) for flaw and materials characterization in ferrous and nonferrous metals. Am. Soc. Mech. Eng. Press. Vessels Pip. Div. (Publication) PVP **352**, 39–43 (1997)

26. N.J. Goldfine, Magnetometers for improved materials characterization in aerospace applications. Mater. Eval. **51**, 396–405 (1993)
27. S. Yamada, M. Katou, M. Iwahara, F.P. Dawson, Defect images by planar ECT probe of Meander-Mesh coils. Trans. Magn. IEEE **32**, 4956–4958 (1996)
28. S.C. Mukhopadhyay, C.P. Gooneratne, G.S. Gupta, S.N. Demidenko, A low-cost sensing system for quality monitoring of dairy products. IEEE Trans. Instrum. Meas. **55**, 1331–1338 (2006)
29. S.C. Mukhopadhyay, G.S. Gupta, J.D. Woolley, S.N. Demidenko, Saxophone reed inspection employing planar electromagnetic sensors. IEEE Trans. Instrum. Meas. **56**, 2492–2503 (2007)
30. M.A.M. Yunus, S.C. Mukhopadhyay, Novel planar electromagnetic sensors for detection of nitrates and contamination in natural water sources. IEEE Sens. J **11**, 1440–1447 (2011)
31. A.R.M. Syaifudin, P. Yu, S. Mukhopadhyay, M.J. Haji-Sheikh, J. Vanderford, *Performance evaluation of a new novel planar interdigital sensors* (2010), pp. 731–736
32. M.A.M. Yunus, G.R. Mendez, S.C. Mukhopadhyay, Development of a low cost system for nitrate and contamination detections in natural water supply based on a planar electromagnetic sensor. Instrum. Measur. Technol. Conf. (I2MTC), 2011 IEEE **2011**, 1–6 (2011)
33. S.M. Djuric, L.F. Nagy, M.S. Damnjanovic, N.M. Djuric, L.D. Zivanov, A novel application of planar-type meander sensors. Microelectron. Int. **28**, 41–49 (2011)

Magnetic Resonance Based Atomic Magnetometers

Antoine Weis, Georg Bison and Zoran D. Grujić

Abstract The chapter gives a comprehensive account of the theory of atomic magnetometers deploying optically detected magnetic resonance (ODMR) in spin-polarized atomic ensembles, and of the practical realization of such magnetometers. We address single laser beam experiments throughout, but give explicit hints on how the results can be extended to pump-probe configurations. After a general introduction and the presentation of a classification of atomic magnetometer principles, we address the three major processes, viz., polarization creation, atom-field interaction, and optical detection that occur in the subclass of magnetic resonance-based magnetometers. The time-independent signals on which so-called Hanle magnetometers built are also reviewed for both spin-oriented and spin-aligned media. In the extended central part we derive an algebraic master expression (valid for all ODMR magnetometers) that expresses the signal, i.e., the detected time-dependent light power in terms of all system parameters. We then give explicit algebraic results for the absolute signals observed in the so-called M_z- and M_x-configurations for various geometries with arbitrary relative orientations of the static field, the oscillating field and the light propagation direction. Although the chapter's main focus is on magnetic resonance processes driven by oscillating magnetic fields (we treat both spin-oriented and spin-aligned media), we also address magnetometers in which the magnetic resonance is driven by amplitude-, frequency-, or polarization-modulated light. The final section of the chapter gives a detailed account of the physical realization of an M_x-magnetometer array and the electronics used for its operation. We demonstrate that the observed resonance signals have the predicted spectral shapes and illustrate procedures for optimizing the magnetometric sensitivity.

A. Weis (✉) · Z.D. Grujić
Physics Department, University of Fribourg, 1700 Fribourg, Switzerland
e-mail: antoine.weis@unifr.ch

G. Bison
Paul Scherrer Institut, 5232 Villigen, Switzerland
e-mail: georg.bison@psi.ch

A. Grosz et al. (eds.), *High Sensitivity Magnetometers*, Smart Sensors, Measurement and Instrumentation 19, DOI 10.1007/978-3-319-34070-8_13

1 Introduction

Atomic magnetometers detect changes of a specific property of light that has resonantly interacted with an atomic gas or vapor exposed to the magnetic field, $\mathbf{B}_0$, of interest.[1] Most commonly, the influence of $\mathbf{B}_0$ on the atomic medium is inferred from a measurement of the power P of a light beam transmitted through the medium. Alternative detection methods involve measuring the change of polarization of the transmitted beam or recording the light-induced fluorescence power (or polarization).

Atomic magnetometers rely on resonant magneto-optical effects, the wealth of whose variants and applications was comprehensively reviewed in 2002 [1]. Atomic magnetometers are also referred to as 'optical magnetometers' (OM), since the magnetometric information is encoded into optical signals, or as 'optically pumped magnetometers' (OPM), since optical pumping is an essential feature of the magnetometers' operation. The magnetometers based on magnetic resonance that are addressed in this chapter are also known as 'radio-optical' or 'double resonance (DR)' magnetometers, where the latter name is derived from the fact that both the optical excitation/detection and the magnetic resonance process are driven resonantly. Because of the deployed optical detection such magnetometers are also referred to as 'ODMR' (optically detected magnetic resonance) magnetometers, where a distinction has been made between 'DROM' and 'DRAM' (double resonance orientation/alignment-based magnetometer) variants, depending on whether they are operated by circularly-polarized light (creating basically only spin orientation) or linearly polarized light (creating spin alignment).

The 2007 review by Budker and Romalis [2] and a recent (2013) textbook on optical magnetometry [3] give a broad overview of various atomic magnetometers principles and methods, practical implementations, performance and applications, and the present chapter, is in many aspects complementary to information presented in Chaps. 4 and 6 of [3].

Any optical property of an atomic medium that is influenced by a magnetic field can, in principle, be used to build an atomic magnetometer. The atom-field interaction is governed by the Zeeman effect, parametrized in terms of the Larmor frequency ω_L, where $\hbar\omega_L$ represents the energy splitting of adjacent magnetic sublevels. Extraction of the magnetometric information relies on the (gyromagnetic) relation

$$\omega_L = 2\pi\nu_L = \frac{g_F\mu_B}{\hbar}|\mathbf{B}_0| \equiv \gamma_F|\mathbf{B}_0|, \tag{1}$$

between the field of interest $\mathbf{B}_0$ and the Larmor frequency, where γ_F is the (atom specific) gyromagnetic ratio.

[1] Free spin precession magnetometers discussed in Chap. 16 form an exception from this general rule.

Signals in magneto-optical experiments can be expressed in terms of a dimensionless parameter $\nu_L/\Delta\nu$, where the frequency $\Delta\nu$ represents the characteristic width of the resonance occuring in the considered experiment. For instance, in linear magneto-optical experiments in a room temperature atomic vapor, one has $\Delta\nu = \Delta\nu_D$, where the Doppler width $\Delta\nu_D$ is typically a few hundred MHz. When dealing with trapped cold atoms, $\Delta\nu = \Delta\nu_{\text{opt}}$, where the natural linewidth $\Delta\nu_{\text{opt}}$, representing the decoherence rate of the optical dipole moment, is on the order of MHz in alkali atoms.

Ultrahigh sensitivity atomic magnetometers build on spin-polarized atomic media, in which $2\pi\Delta\nu = \gamma_2$ represents the spin coherence decay rate. Such experiments are nonlinear in the sense that the (optically) resonant light is used, on one hand, to create the spin polarization, and, on the other hand, to probe its evolution under the influence of the magnetic field. When the pump and probe processes occur within a light beam of diameter d traversing a vacuum-alkali vapor cell, the coherence time is determined by the ballistic transit (at average velocity $\bar{v}$) through the light field, yielding $\Delta\nu = \bar{v}/2\pi d$ values in the few kHz range. Suppressing the ballistic flight by imposing a diffusive motion to the atoms through the addition of an inert buffer gas, reduces $\Delta\nu$ to the tens of Hz range, while coating the walls of an alkali vacuum cell with paraffin or silane that reduces depolarization during wall collisions leads to $\Delta\nu$ in the Hz range. The 8 orders of magnitude in reduction of $\Delta\nu$, when going from linear magneto-optical spectroscopy to nonlinear spin-polarization spectroscopy in coated cells goes in pair with a corresponding increase of the magnetometric sensitivity.

As a back-of-the-envelope estimation of the sensitivity limit in the latter case we consider a $\Delta\nu = 3.5$ Hz wide magneto-optical resonance, which, for Cs corresponds to the change of Larmor frequency produced by a 1 nT field. When recorded with a signal/noise ratio of 10^5, the line center, i.e., the magnetic field can be determined with a precision of $\approx 1\ \text{nT}/10^5 = 10$ fT.

We add a statement made by E. B. Alexandrov (author of the chapter on M_x and M_z magnetometers in [3]) in a private conversation with the authors many years ago: "There is no best magnetometer, but there is a best suited magnetometer for every application", and expand this statement as follows: Sensitivity (ability to detect field changes) is only one characteristic property of a given magnetometer. Accuracy (ability to infer the absolute field value), e.g., is a property that has not been given much attention in the atomic magnetometers community.[2] Other questions that a full characterization of a magnetometer has to address are (non-exhaustive list): (a) How does the magnetometer's sensitivity compare to its accuracy? (b) Does it measure quasi-static or oscillating fields? (c) For what range of field strengths can it be used (dynamic range)? (d) How fast does it react to a sudden field change (measurement bandwidth)? (e) Can it be turned into a portable device? (f) Is it meant to monitor a laboratory field whose magnitude and

[2]Here also the ^{3}He magnetometers described by W. Heil elsewhere in this book are a most notable exception.

orientation are *known* a priori? (g) Which field direction maximizes its sensitivity, what are its orientational dead zones? (h) Does the device suffer from heading errors, i.e., are its field readings dependent on the field orientation? (i) Does the method allow the easy deployment of the device in a multi-sensor array? (j) Can the magnetometer be operated in harsh (vacuum, airborne, space-borne, underwater) conditions? (k) Does the device's stability allow long-time (hours/days) measurements?

1.1 Classification of Atomic Magnetometer Principles

Before describing the scope of this chapter we attempt a classification of the various types of atomic magnetometers that have emerged in the past two decades, following the use of laser radiation for the magnetometer operation.

- **Type 1: Hanle magnetometers**: These magnetometers are also known as 'zero-field ground state level crossing magnetometers' (introduced by Lehmann and Cohen-Tannoudji in 1964 [4]), since they rely on the resonant modification of the atomic spin polarization, when the magnetic field $\mathbf{B}_0$ to which the atoms are exposed is scanned through $\mathbf{B}_0 = 0$. This modification can be detected by either monitoring the transmission of the light beam that has produced the spin polarization, or the transmission of a second light beam (probe beam) that propagates at another direction (preferably under 90°) through the medium. In the two-beam variant, one may also record the change of (light) polarization of the probe beam. When the medium is spin-oriented, probing may be achieved by recording the paramagnetic rotation (often erroneously referred to as Faraday rotation) using a balanced polarimeter that allows suppressing technical noise. Since the light polarization is affected by the medium's index of refraction, its recording needs a light beam whose frequency is detuned from the atomic resonance frequency.
  The atomic magnetometers that have come to be known as 'SERF' (spin-exchage relaxation free) magnetometers (cf. Chap. 15) are in fact Hanle magnetometers, where SERF refers to a property of the magnetic medium, rather than to the field recording method proper. This unfortunate designation becomes even more confusing when considering that recently optical methods have been demonstrated (see discussion in Sect. 7) that allow a suppression of spin exchange relaxation collisions in magnetic resonance-based [5] and light modulation based magnetometers (cf. Chap. 14).
  A general theory of Hanle line shapes under excitation (and probing) with both circularly and linearly polarized laser radiation was presented by Castagna and Weis [6] (erratum [7]), and Breschi and Weis [8], respectively.
  The equations derived in the latter references show that the operation of Hanle magnetometers requires an extremely homogeneous near-zero magnetic field, which limits the fields of their applications. Although Hanle magnetometers

under SERF conditions have proven to break the 1 fT/$\sqrt{\text{Hz}}$ sensitivity limit [9], their absolute accuracy is rather limited.

- **Type 2: Magnetic resonance magnetometers**: These magnetometers in which resonant light interaction is combined with a resonant magnetic resonance interaction can be given the general name of ODMR (optically detected magnetic resonance) magnetometers. The detailed discussion of their underlying physics and their concrete implementation are in the focus of the present chapter. Albeit not being the most sensitive type of atomic magnetometers, they are robust, easy to implement devices that reach sensitivities in the one-digit fT/$\sqrt{\text{Hz}}$ range and a typical absolute accuracy in the pT range.
- **Type 3: Light modulation magnetometers**: The coherent coupling of magnetic sublevels that underlies magnetic resonance cannot only be achieved by a periodically varying magnetic field, but also by a periodically modulated property (amplitude, frequency, polarization) of the optical field that is resonantly coupled to the atoms. The modeling of magnetometers based on light modulation bears many resemblances with ODMR magnetometers, which has motivated us to include the corresponding modeling here.
- **Type 4: Free spin precession magnetometers**: In the free spin precession (FSP) magnetometer, the sample is spin polarized by cw pumping or, preferably, by pulsed optical pumping in a transverse magnetic field, after which the polarization freely precesses (while decaying) around the field. Alternatively, pumping can be achieved in a longitudinal field, and the free spin precession initiated by a $\pi/2$ pulse. The free spin precession is monitored by a probe beam of reduced intensity, and the field value is inferred from the oscillatory frequency during the decay. Recently we have demonstrated that a shot-noise limited sensitivity below 100 fT/$\sqrt{\text{Hz}}$ can be achieved by a Cs FSP magnetometer [10]. FSP signals obtained with linearly-polarized light were recently shown to yield vector information on the magnetic field [11].
  In case the spin precession cannot be read out by optical means, it may be observed using an auxiliary magnetometer, such as commonly used for detecting the free spin precession of nuclear spin polarized ^{3}He (cf. Chap. 16). SQUIDs are traditionally used for this readout [12], but it was shown already in 1969 [13] that an alkali vapor magnetometer can be deployed for the same purpose. Recently we have demonstrated a ^{3}He FSP magnetometer read out by the simultaneous recording of 8 Cs double resonance magnetometers [14].

In the above classification we have not included magnetometers based on the use of coherent bi- or polychromatic light fields. Such magnetometers are referred to in the literature as 'CPT (coherent population trapping)', 'dark state', 'bright state', 'Λ-resonance', etc., magnetometers. In essence, the underlying physics is closely related to the light modulation magnetometers because of the close resemblance of the optical field's Fourier spectrum in both cases. To our knowledge, no review of this class of magnetometers has been published so far (for a restricted review of CPT magnetometer applications see, e.g. [15]), and we shall not address such magnetometers here.

1.2 Note on Scalar Versus Vector Magnetometers

We note that the magnetic resonance based magnetometers addressed here are all *scalar magnetometers*, meaning that the detected power P is a function of the field modulus $|\mathbf{B}_0| = (B_x^2 + B_y^2 + B_z^2)^{1/2}$ only. However, a scalar magnetometer, when operated in a an offset field $\mathbf{B}_0 = B_0\hat{\mathbf{z}}$ can be used to detect a single vector component of a much weaker field $\delta\mathbf{B}$ with components $(\delta B_x, \delta B_y, \delta B_z)$: Since the magnetometer measures the field modulus, one has

$$B_{\mathrm{tot}} = |\mathbf{B}_{\mathrm{tot}}| = |\mathbf{B}_0 + \delta\mathbf{B}| \approx B_0 + \delta B_z + \mathcal{O}(\delta B_i^2), \tag{2}$$

so that—to first order in small quantities—the magnetometer detects effectively only one vector component of δB_z of $\delta\mathbf{B}$.

1.3 Scope of This Chapter

The present chapter deals with atomic magnetometer variants in which the interaction of the magnetic field with spin-polarized atoms is resonantly enhanced by specific magnetic resonance (MR) processes. MR is conventionally—but not solely—achieved by a weak oscillating magnetic field, which ensures that the detected optical signal is resonantly enhanced when that oscillation frequency matches the atomic Larmor frequency, itself proportional to $|\mathbf{B}_0|$. We will focus on the theory of so-called M_x magnetometers, which are the most widely spread variant of ODMR (optically detected magnetic resonance) magnetometers and develop a general theoretical framework for calculating the detected optical signals. This model allows us to derive the MR lineshapes and their dependence on detector parameters, (amplitude and orientation of the oscillating field, laser power as well as the dimensions, density and relaxation rates of the atomic medium) and the properties (magnitude and spatial orientation) of the detected magnetic field.

In Sect. 2 we will discuss how the detected laser power depends on the degree and orientation of the atomic spin polarization. Section 3 discusses the steady-state spin polarization resulting from the interaction of the atoms with the static and oscillating fields, culminating in a general master expression describing the ODMR signals in arbitrary field geometries. In Sect. 4 we will apply the general expressions to specific M_x magnetometer variants, of which the so-called M_z magnetometer is a particular case. In Sect. 5 we will briefly address the less well explored ODMR magnetometers building on tensor spin polarization (alignment). In Sect. 6 we will address lineshapes encountered in magnetometers where the magnetic resonance transitions between magnetic sublevels are resonantly driven by a modulation of specific light parameters (amplitude, frequency, or polarization), rather than by an oscillating magnetic field. Finally, Sect. 7 gives an extensive discussion of the experimental implementation of M_x magnetometers, including details on the control and data acquisition electronics, the performance and their deployment in sensor arrays.

2 Principles of Atomic Magnetometry

The physics underlying atomic magnetometers is the interplay of (i) the spin polarization creation process, (ii) the steady-state polarization resulting from the torque exerted by $\mathbf{B}_0$ on the polarization and relaxation processes, and (iii) the optical detection of the altered spin polarization.

2.1 (i) Polarization Creation by Optical Pumping

Atomic spin polarization is created in the atomic medium by optical pumping, the physics of which is discussed by Cohen-Tannoudji and Kastler [16], with more details given by Happer [17].

The left graph of Fig. 1 shows an initially unpolarized ensemble of spin $1/2$ atoms having equal populations in their magnetic sublevels $|1/2, m\rangle$. In alkali atoms—to which we restrict the discussion of this chapter—the hyperfine structure of the ground state is resolved when excited by single mode laser radiation, and the corresponding sublevels will be labeled by $|F, m\rangle \equiv |n^2S_{1/2}; F, m\rangle$. Several absorption/re-emission processes of photons from a polarized light beam that is resonant with an atomic transition, lead to a non-isotropic distribution of magnetic sublevel populations p_m (middle graph). As a consequence, the absorbing sublevel is emptied, leading to a reduced light absorption. The right graph shows that the magnetic resonance transitions (addressed in Sect. 3) induce a coherent oscillation between the sublevel populations, thereby leading to a periodic revival of the absorption, detected as probe light modulation.[3]

The induced anisotropy (sublevel population imbalance) reflects the (mirror inversion and rotational) symmetry of the light's polarization and can be visualized by methods introduced in Ref. [18]. Figure 2 represents an isotropic unpolarized medium (graph a) as well as the anisotropies created by optical pumping with circularly-(graphs b, b′) and linearly-polarized (graph c) light.

The medium's spin-polarization is conveniently described in terms of its irreducible spherical multipole moments $m_{k,q}$ with $0 \leq k \leq 2F$ and $-1 \leq q \leq +1$ [1, 19]. As noted by Happer [17], the optical properties of the medium, when probed by light driving an electric dipole transition depend only on specific orientation ($m_{1,q}$) and alignment ($m_{2,q}$) multipole moments, a fact which greatly simplifies the mathematical modeling of a polarized medium's interaction with light. The relevant multipole moments created by pumping with *circularly-polarized* light are $m_{1,0} \propto S_z \equiv S_0$ and $m_{2,0} \propto A_{zz} \equiv A_0$, where S_0 and A_0, defined by

[3]The non-absorbing state $|1/2, +1/2\rangle$ is called a 'dark' state since atoms in that state do not fluoresce, while the $|1/2, -1/2\rangle$ state is a 'bright' state. In this sense the oscillatory time-dependence of the magnetometer principles discussed below in this chapter can be understood as resulting from coherent oscillations between dark and bright states.

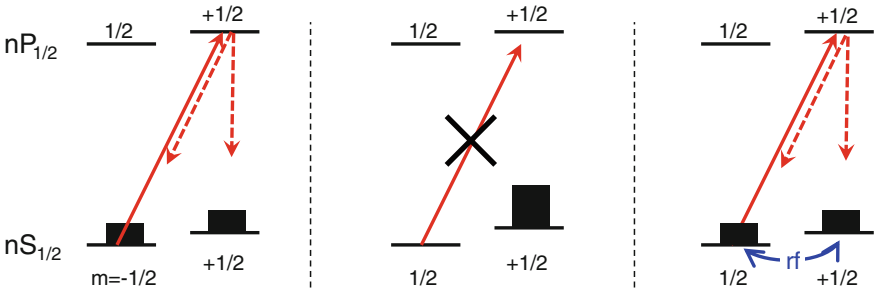

Fig. 1 Details of the creation of spin polarization (shown as population imbalance) by optical pumping on a D_1 transition—here shown without hyperfine structure. The magnetic resonance interaction with the rf field induces an oscillation of the sublevel populations

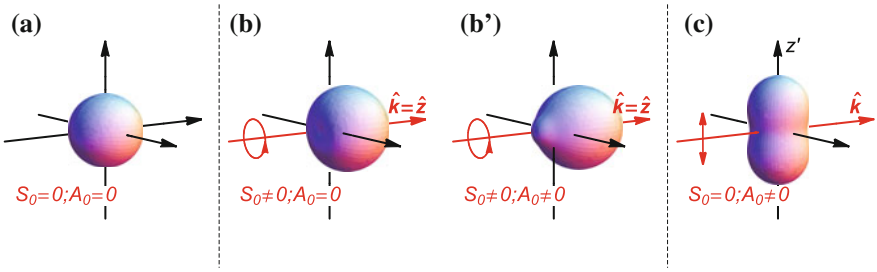

Fig. 2 Multipole moment representation of unpolarized medium (**a**), of medium having longitudinal ($\|\mathbf{k}$) orientation $S_z = S_0$ only (**b**), having longitudinal orientation S_0 and alignment $A_{zz} = A_0$ (**b'**) prepared by pumping with circularly-polarized light, and medium having transverse alignment A_0' (**c**), prepared by linearly-polarized light. The shown surfaces represent the probability of finding the medium in the stretched state $|F, m = F\rangle$ when making a measurement with the quantization axis along a specific spatial direction

$$S_0 = \langle \mathbb{F}_z \rangle = \sum_{m=-F}^{F} p_m \, m \tag{3}$$

and

$$A_0 = \langle 3\mathbb{F}_z^2 - \mathbb{F}^2 \rangle = \sum_{m=-F}^{F} p_m \left[3m^2 - F(F+1) \right], \tag{4}$$

are the Cartesian equivalents of the spherical moments. For pumping with *linearly-polarized* light, the produced alignment A_0' is given by the same expression as Eq. 4 with populations $p_{m'}$ referred to a quantization axis z' parallel to the light polarization (Fig. 2c).

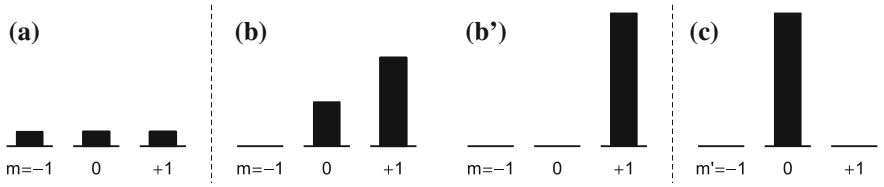

Fig. 3 Population distributions—shown here for $F = 1$—of Zeeman levels reflecting the multipole moments of Fig. 2. **a** unpolarized medium, **b** medium with orientation along **k**, **b**′: medium with orientation and alignment along **k**, and **c**: medium with transverse alignment. Note that in case **c** the quantization axis is orthogonal to **k**

In Fig. 3 we represent the magnetic sublevel populations that yield multipole moments similar to the ones shown in Fig. 2. For simplicity, we show these populations for the particular case $F = 1$, which has only orientation and alignment multipoles.

Polarization build-up

The signals in optically-pumped magnetometers are proportional to the spin polarization S_0 (and/or A_0) achieved by optical pumping. When optical pumping is achieved by optical transitions between atomic ground and excited states small angular momenta, such as on $F = 1/2 \rightarrow F' = 1/2$ or $F = 1 \rightarrow F' = 0$ transitions, the equilibrium spin polarization is given by

$$S_0 = S_\infty \frac{\gamma_{\text{pump}}}{\gamma_{\text{pump}} + \gamma} = S_\infty \frac{G_{\text{op}}}{G_{\text{op}} + 1} \quad \text{with} \quad G_{\text{op}} = \frac{\gamma_{\text{pump}}}{\gamma} = \frac{P_0}{P_{\text{sat}}}, \tag{5}$$

where γ_{pump} is the optical pumping rate, γ the spin relaxation rate, and S_∞ the maximal spin polarization achieved for $\gamma_{\text{pump}} \gg \gamma$. We refer to G_{op} as the (dimensionless) optical pumping saturation parameter. It is proportional to the laser power P_0, P_{sat} being a scaling power.

We note that Eq. 5 is no longer valid in systems with larger angular momenta. However, its low power limit, viz., $S_0 \approx S_\infty P/P_{\text{sat}}$ still remains generally valid.

2.2 (ii) Atom-Field Interaction

For polarized atoms with ground state angular momentum F, the atom-field interaction strength is characterized by the Larmor frequency

$$\omega_L = \frac{g_F \mu_B}{\hbar} |\mathbf{B}_0| \equiv \gamma_F |\mathbf{B}_0|, \tag{6}$$

where g_F and γ_F are the Landé factor and the gyromagnetic ratio of the ground state, respectively. The index F is the quantum number associated with the total atomic angular momentum $\mathbf{F} = \mathbf{J} + \mathbf{I}$, with $\mathbf{J} = \mathbf{L} + \mathbf{S}$, where J, L, I, and S are the total electronic angular momentum, the orbital angular momentum, and the nuclear and electronic spin angular momentum quantum numbers, respectively.

The Larmor frequency is the frequency at which the atomic spin polarization precesses due to the torque exerted by the field on the magnetization associated with the spin polarization. In a quantum picture, the Larmor frequency corresponds to the energy separation (measured in angular frequency units) between adjacent Zeeman sublevels $|F, m_F\rangle$.

We note that the power of magnetic resonance-based magnetometers lies in the fact that they allow for a direct measurement of the Larmor frequency, and hence of the magnetic field, with an accuracy, that is, in principle, only limited by the accuracy with which the proportionality constant γ_F is known.

2.3 (iii) Optical Detection

The magnetic field induced alterations of the spin polarization alter the optical properties of the atomic medium, the latter affecting themselves the properties of a probe light beam traversing the atomic medium. Below we restrict the discussion to the case where the probe beam is identical with the pump beam. The magnetometric information may thus be extracted from either

(a) the power of the probe beam traversing the medium,
(b) the polarization of the probe beam traversing the medium,
(c) the intensity of fluorescence induced by the probe beam,
(d) the Stokes parameters of the induced fluorescence, or
(e) the power (polarization) of retro-reflected probe beam.

The explicit expressions derived below will exclusively deal with case (a) of the above list, and can be easily extended to case (b). We note that cases (c)...(e) are little explored in atomic magnetometry, and quote Ref. [20] as an example for case (c) and Refs. [21, 22] for case (e).

Light transmission through unpolarized medium: The power of a light beam of frequency ω_{opt} (nearly resonant with an atomic absorption line of frequency ω_{atom}) that is transmitted by an unpolarized atomic medium of length L is given by the Lambert-Beer law

$$P = P_0 \exp\left[-\kappa_0^{\text{unpol}} L \mathcal{L}(\omega_{\text{opt}} - \omega_{\text{atom}})\right], \tag{7}$$

where P_0 is the incident power and $\mathcal{L}$ the optical absorption line shape function, with typically a Voigt, Doppler, or Lorentzian profile, normalized such that $\mathcal{L}(0) = 1$. The peak absorption cross section $\kappa_0^{\text{unpol}} = \kappa(\omega_{\text{opt}} = \omega_{\text{atom}})$ represents

the absorption coefficient of the *unpolarized medium* when the light frequency ω_{opt} is tuned to the atomic resonance frequency $\omega_{\text{atom}} = (E_{nL_J,F} - E_{n'L'_{J'}F'})/\hbar \equiv \omega_{F,F'}$. For resonant light traversing an optically thin ($\kappa_0^{\text{unpol}} L \ll 1$) unpolarized medium, Eq. 7 reduces to

$$P \approx P_0 - P_0\, \kappa_0^{\text{unpol}} L. \tag{8}$$

We assume that the magnetometer operates on an absorption line corresponding to a resolved hyperfine transition $nL_J, F \rightarrow n'L'_{J'}F'$. This situation is commonly encountered in laser-operated alkali vapor magnetometers working on the D_1 ($nS_{1/2}, F \rightarrow nP_{1/2}, F'$) or D_2 ($nS_{1/2}, F \rightarrow nP_{3/2}, F'$) transitions.

Light transmission through spin-polarized medium: When the atomic medium is spin-polarized, the absorption coefficient has to be modified according to

$$\kappa_0^{\text{unpol}} \rightarrow \kappa_0^{\text{unpol}} \left[1 - \alpha^{(1)}_{F,F'}\, S_z - \alpha^{(2)}_{F,F'}\, A_{zz}\right] \tag{9}$$

for *circularly*-polarized light, and

$$\kappa_0^{\text{unpol}} \rightarrow \kappa_0^{\text{unpol}} \left[1 - \alpha^{(2)}_{F,F'}\, A'_{z'z'}\right] \tag{10}$$

for *linearly*-polarized light, respectively.[4] In these equations the parameters $\alpha^{(k)}_{F,F'}$ are multipole analyzing powers (notation, based on corresponding notation in nuclear physics) that depend—via the angular momentum quantum numbers F, F'—on the atomic transition with which the light is resonant. Explicit algebraic expressions for these parameters shall be published elsewhere [23]. The absorption coefficient of a spin-polarized medium traversed by resonant light is thus fully described by the three polarization components S_z, A_{zz} and $A_{z'z'}$. These parameters describe the steady-state orientation and alignment towards which the initial polarization components $(S_z^0, A_{zz}^0, A_{z'z'}^0)$ evolve under the action of the magnetic field.

2.4 The Magnetometer Signal

For a *circularly-polarized* light beam, the results of this section can be summarized as follows: Optical pumping polarizes the medium by creating spin orientation and spin alignment. The latter evolve under the action of the magnetic field and relaxation, yielding steady-state values $S_z(\mathbf{B}_0)$ and $A_{zz}(\mathbf{B}_0)$. This evolution may occur in a passive manner in the static field of interest, or may be actively driven by

[4]Note that S_z and A_{zz} in Eq. 9 refer to a quantization axis along the **k**-vector, while the quantization axis defining $A'_{z'z'}$ in Eq. 10 is along the light polarization as shown in Fig. 2.

an additional oscillating magnetic field (or a modulation of a light beam parameter, such as power, frequency, or polarization). For an optically thin medium, the detected power is given by

$$P(\mathbf{B}_0) \approx P_0 - P_0\,\kappa_0^{\text{unpol}} L\Big[1 - \alpha^{(1)}_{F,F'} S_z(\mathbf{B}_0) - \alpha^{(2)}_{F,F'} A_{zz}(\mathbf{B}_0)\Big]. \tag{11}$$

When actively driven, such as in the ODMR magnetometer described in the next section, the orientation $S_z(\mathbf{B}_0)$ and alignment $A_{zz}(\mathbf{B}_0)$ become time-dependent. This dependence allows the extraction of the specific terms containing the magnetometric information using phase-sensitive (lock-in) detection. We note that Eq. 11 applies to the case of a single light beam which acts both as circularly-polarized pump and probe beam propagating along the quantization axis z. When using a probe beam with a different propagation direction and/or a different polarization, the orientation and alignment in Eq. 11 have to be replaced by the components $S_i(\mathbf{B}_0)$ and $A_{jk}(\mathbf{B}_0)$, to which the probe beam is sensitive.

The Hanle magnetometer

As an example for a passively operated magnetometer we give explicit expressions for the steady-sate orientation and alignment occurring in a Hanle magnetometer operated with a single circularly-polarized light beam. In such a magnetometer the atoms are exposed to a static field with components B_x, B_y, B_z only, and the steady-state orientation in Eq. 11 is given by [6]

$$\frac{S_z(B_x, B_y, B_z)}{S_0} = \frac{1 + x_\parallel^2}{1 + x_\parallel^2 + x_\perp^2}, \tag{12}$$

while the steady-state alignment is given by (adapting results from [8])

$$\frac{A_{zz}(B_x, B_y, B_z)}{A_0} = \frac{1}{4} + \frac{3}{4}\frac{1 + 8x_\parallel^2 + 16x_\parallel^4}{1 + 4x_\parallel^2 + 4x_\perp^2} - 3\frac{1 + x_\parallel^2 + x_\parallel^4}{1 + x_\parallel^2 + x_\perp^2}, \tag{13}$$

with

$$x_\parallel = \frac{\gamma_F B_z}{\gamma} \quad \text{and} \quad x_\perp = \frac{\gamma_F \sqrt{B_x^2 + B_y^2}}{\gamma}, \tag{14}$$

where S_0 and A_0 denote the longitudinal orientation and alignment created by the optical pumping process, and where we have set all relaxation rates equal to γ.

Note that in Eq. 12 the quantization axis z intervening in the definition of $x_\parallel$ is along $\mathbf{k}$, while in Eq. 13 the quantization axis refers to the direction of linear polarization that is perpendicular to $\mathbf{k}$.

The Hanle magnetometer signals thus manifest themselves as resonances when one of the field components B_i is scanned through zero. The amplitudes and widths

of these resonances depend on the magnitude of the field components that are not scanned as discussed in Refs. [6, 8], a fact that makes the precision calibration of such magnetometers on an absolute scale difficult. As stated earlier, the so-called SERF magnetometers (discussed in Chap. 15) are in fact ground state Hanle magnetometers.

In the following sections we will discuss the signals occurring in actively driven magnetometers.

3 Optically Detected Magnetic Resonance (ODMR)

3.1 Magnetic Resonance

Magnetic resonance, MR, is a generic name for processes that affect the spatial orientation and/or the magnitude of a medium's spin polarization in a resonant manner by the interaction with a time-periodic perturbation. In the most widely used implementation of MR, this perturbation is provided by an oscillating (or rotating) magnetic field $\mathbf{B}_{\rm rf}(t)$. The process is resonantly enhanced when the frequency, $\omega_{\rm rf}$, of the perturbation is tuned near a characteristic frequency of the system, such as the Larmor frequency, ω_L, induced by an external magnetic field (case of interest here).[5]

When the polarized medium is described by its spin density operator

$$\mathbb{p} = \sum_{k,q} m_{k,q}\, \mathbb{T}^k_q\,, \tag{15}$$

parametrized in terms of the polarization multipole moments, $m_{k,q}$ (the $\mathbb{T}^k_q$ are irreducible spherical tensor operators [19]), the MR process is modeled by solutions of $\mathbb{p}$'s equation of motion (Liouville equation)

$$\mathrm{i}\hbar\,\dot{\mathbb{p}} = [\mathbb{H}, \mathbb{p}] \;+\; \text{relaxation terms}, \tag{16}$$

where $\mathbb{H}$ is the atom-field interaction Hamiltonian. Inserting Eq. 15 into 16 yields equations of motion for the multipole moments.

When the interaction with the field is linear in B_0, i.e., when $\mathbb{H} = -\mathbb{\mu}\cdot\mathbf{B}_0$, the commutator in Eq. 16 of $\mathbb{H}$ with an operator $\mathbb{T}^k_q$ of given rank k yields a linear combination of operators with the same rank [24]. As a consequence the equations of motion for each set of multipoles $m_{k,q=-k\cdots+k}$ of given k are decoupled and thus reduce—for each rank k—to a set of $2k+1$ equations coupling the corresponding $2k+1$ multipoles labeled by q (see also [24]). For the vector multipole moments $m_{1,q}$, the three corresponding equations are known as Bloch equations. These are commonly expressed in terms of the three Cartesian vector components S_i as

[5]Magnetic resonance transitions can also be driven between atomic fine or hyperfine structure components, in which case the characteristic frequencies, $\omega_{\rm fs} = \Delta E_{\rm fs}/\hbar$ and $\omega_{\rm hfs} = \Delta E_{\rm hfs}/\hbar$, respectively, are determined by internal magnetic fields.

$$\dot{\mathbf{S}} = \mathbf{S} \times (\gamma_F \mathbf{B}_{\text{tot}}) + \text{relaxation terms}, \tag{17}$$

where $\mathbf{B}_{\text{tot}} = \mathbf{B}_0 + \mathbf{B}_{\text{rf}}(t)$ is the total magnetic field vector. The components of the Cartesian orientation vector (Bloch vector) $\mathbf{S}$ are related to the corresponding multipole moments by

$$m_{1,\pm 1} \propto \mp \frac{S_x \pm iS_y}{\sqrt{2}} \quad \text{and} \quad m_{1,0} \propto S_z, \tag{18}$$

with an F-dependent proportionality factor (given, e.g., in Ref. [19]).

Equation 17 cannot be solved algebraically for a linearly oscillating rf field that we parametrize as $\mathbf{B}_{\text{rf}}(t) = 2\mathbf{B}_1 \sin \omega_{\text{rf}} t$, and one makes use of the so-called rotating wave approximation for obtaining algebraic solutions.

3.2 Rotating Wave Approximation

Any component of $\mathbf{B}_{\text{rf}}(t)$ along $\mathbf{B}_0$ does not induce magnetic resonance, and we thus consider only the component

$$\widetilde{\mathbf{B}}_{\text{rf}}(t) = 2\widetilde{\mathbf{B}}_1 \sin \omega_{\text{rf}} t = \frac{\widetilde{\mathbf{\Omega}}}{\gamma_F} \sin \omega_{\text{rf}} t \tag{19}$$

of $\mathbf{B}_{\text{rf}}(t)$ that is orthogonal to $\mathbf{B}_0$ (Fig. 4a). We refer to $\tilde{\mathbf{B}}_{\text{rf}}$ as the 'effective rf field'.

This linearly oscillating field is then decomposed into two rotating components (each of amplitude $\widetilde{\mathbf{B}}_1$), one that co-rotates with the atomic spin polarization at frequency ω_{rf} around $\mathbf{B}_0$ (Fig. 4b), and a counter-rotating component that is neglected[6] (rotating wave approximation). In a next step one considers a coordinate frame $(x'y'z')$ that co-rotates with the spin polarization around $\mathbf{B}_0$ ($\|\hat{z}'$), so that $\widetilde{\mathbf{B}}_1$ in that frame becomes a static field in the $x'y'$-plane (Fig. 4c). The transformation into the rotating frame leads to the appearance of a fictitious magnetic field $\mathbf{B}_f = -\omega_{\text{rf}}/\gamma_F \hat{z}'$, so that the total field (in the rotating frame) $\mathbf{B}'_{\text{tot}}$ has components $(B_1, 0, B_0 - \omega_{\text{rf}}/\gamma_F)$. This field can be expressed in terms of frequencies using $\widetilde{\mathbf{\Omega}}' = \gamma_F \mathbf{B}'_{\text{tot}}$, where the components of the total effective Rabi vector $\widetilde{\mathbf{\Omega}}$ are $(\widetilde{\Omega}_{x'}, \widetilde{\Omega}_{y'}, -\delta\omega)$. In the last expression we have introduced the detuning $\delta\omega = \omega_{\text{rf}} - \omega_L$ of the rf frequency from the Larmor frequency, and the Rabi frequencies $\widetilde{\Omega}_{x'} = \gamma_F \widetilde{\mathbf{B}}_{1,x'}$ and $\widetilde{\Omega}_{y'} = \gamma_F \widetilde{\mathbf{B}}_{1,y'}$.

[6]The neglected component induces a systematic red shift $\Delta\omega_L$ (Bloch-Siegert shift) of the magnetic resonance frequency ω_L that is on the order of $\Delta\omega_L \sim \gamma^2/\omega_L$. where γ is the polarization relaxation rate.

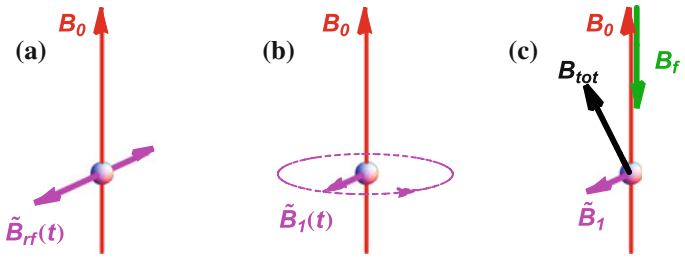

Fig. 4 Rotating wave approximation. **a** Only the oscillating field $(\widetilde{\mathbf{B}}_{\mathrm{rf}}(t) = 2\widetilde{\mathbf{B}}_1 \cos \omega_{\mathrm{rf}} t$ orthogonal to $\mathbf{B}_0$ drives the magnetic resonance; **b** The linearly oscillating field is decomposed into counter-rotating components, each of amplitude $\widetilde{B}_1$, of which only one is retained; **c** In a reference frame rotating around $\mathbf{B}_0$ at frequency ω_{rf}, the rf field becomes static, and an additional fictitious magnetic field $\mathbf{B}_f$ appears

The components of the polarization vector $\mathbf{S}'$ in the rotating frame are usually denoted by (u, v, w), whose equations of motion, derived from Eq. 17, read

$$\dot{u} = -\delta\omega v - \widetilde{\Omega}_{y'} w - \gamma_2 (u - u^{eq}) \tag{20}$$

$$\dot{v} = +\widetilde{\Omega}_{x'} w + \delta\omega u - \gamma_2 (v - v^{eq}) \tag{21}$$

$$\dot{w} = +\widetilde{\Omega}_{y'} u - \widetilde{\Omega}_{x'} v - \gamma_1 (w - w^{eq}), \tag{22}$$

where γ_1/γ_2 are the longitudinal/transverse relaxation rates respectively. The quantities u^{eq}, v^{eq} and w^{eq} represent the steady-state ($\dot{u} = \dot{v} = \dot{w} \equiv 0$) equilibrium values that u, v, and w assume in the absence of any magnetic fields ($\widetilde{\mathbf{\Omega}} = \mathbf{0}$).

In the absence of all magnetic fields, the light beam (in the laboratory frame) produces a spin polarization $\mathbf{S}_0 = S_0 \mathbf{k}/|\mathbf{k}|$ along the light propagation direction. In the rotating frame, the $\mathbf{k}$-vector rotates around $\mathbf{B}_0$ (Fig. 5). It is therefore reasonable to assume that

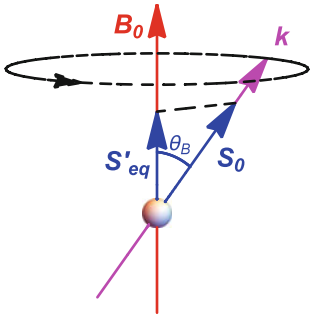

Fig. 5 In the rotating frame, the equilibrium spin polarization $\mathbf{S}'_{eq}$ is the projection of $\mathbf{S}_0$ onto $\mathbf{B}_0$

$$\mathbf{S}'_{eq} = \{u^{eq}, v^{eq}, w^{eq}\} \equiv \{0, 0, S_0 \cos\theta_B\}, \tag{23}$$

where $S_0 \cos\theta_B = \mathbf{S}_0 \cdot \mathbf{B}_0/|\mathbf{B}_0|$ is the component of the polarization $\mathbf{S}_0$ produced by the laser along the magnetic field. This assumption is valid in the (low power) limit, in which the rate γ_p (pumping rate) at which spin polarization is produced by optical pumping is $\ll \omega_L$.

With the above assumptions one can derive the steady-state solutions by setting $\dot{\mathbf{S}}' = \mathbf{0}$ and solving the ensuing three algebraic equations, yielding $\mathbf{S}'_{ss}$, i.e., the steady-state polarization vector in the rotating frame. Its components are given by

$$u_{ss} = \frac{-\delta\omega\,\widetilde{\Omega}_{x'} + \gamma\widetilde{\Omega}_{y'}}{\delta\omega^2 + \gamma^2 + \widetilde{\Omega}^2_{x'} + \widetilde{\Omega}^2_{y'}} S_0 \cos\theta_B \tag{24}$$

$$v_{ss} = \frac{-\delta\omega\widetilde{\Omega}_{y'} - \gamma\widetilde{\Omega}_{x'}}{\delta\omega^2 + \gamma^2 + \widetilde{\Omega}^2_{x'} + \widetilde{\Omega}^2_{y'}} S_0 \cos\theta_B \tag{25}$$

$$w_{ss} = \frac{\delta\omega^2 + \gamma^2}{\delta\omega^2 + \gamma^2 + \widetilde{\Omega}^2_{x'} + \widetilde{\Omega}^2_{y'}} S_0 \cos\theta_B. \tag{26}$$

The general modeling of a magnetic resonance based magnetometer with a given geometry will consist in transforming the specific vectors of that system into the rotating frame, finding the solutions in the rotating frame, and then transforming back to the laboratory frame, in which the specific experimental observables can then be derived.

3.3 General Geometry of Single-Beam ODMR Magnetometer

Figure 6 shows the general geometry of a magnetometer based on optically detected magnetic resonance (ODMR). We assume that a single circularly-polarized light beam, propagating along $\mathbf{k}\|\hat{z}$, acts as pump- and readout-beam. Without loss of generality, we assume that the oscillating field in the lab frame lies in the x-z plane, making an angle θ_{rf} with the $\mathbf{k}$-vector, i.e., that $\mathbf{B}_{rf}(t)$ has components $2(\sin\theta_{rf}, 0, \cos\theta_{rf})\Omega/\gamma_F$, where $2\Omega/\gamma_F = 2B_1$ is the amplitude of $\mathbf{B}_{rf}(t)$. The direction $\widehat{\mathbf{B}}_0$ of the magnetic field of interest is defined by the spherical coordinates θ_B and φ_B.

In order to apply the results derived in the previous paragraph, we have to determine the components $\widetilde{\Omega}_{x'}$ and $\widetilde{\Omega}_{y'}$ of the effective rf field in the rotating frame. The rf field in that frame is given by $\mathbf{B}'_{rf} = R_z(+\omega_{rf}t)R_y(-\theta_B)R_z(-\varphi_B)\mathbf{B}_{rf}$, and the component orthogonal to $\mathbf{B}_0$ that rotates at angular velocity ω_{rf} around $\mathbf{B}_0$ is

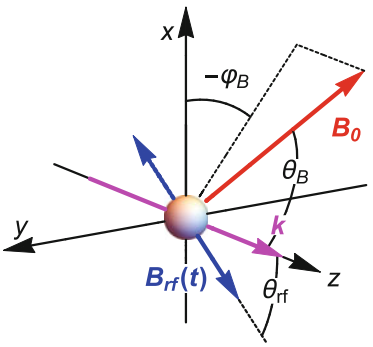

Fig. 6 General geometry of an ODMR magnetometer. The rf field is chosen to lie in the x-z plane. Further details given in the text

$$\widetilde{\mathbf{B}}_1 = \frac{1}{2}\left[\mathbf{B}'_{\rm rf} - (\mathbf{B}'_{\rm rf}\cdot\mathbf{B}_0)\frac{\mathbf{B}_0}{|\mathbf{B}_0|^2}\right], \tag{27}$$

where the factor $1/2$ reflects the rotating wave approximation, i.e., the dropping of the counter-rotating component rotating at $-2\omega_{\rm rf}$. With these transformations the components of the effective Rabi vector $\widetilde{\mathbf{\Omega}}$ (with norm $\widetilde{\Omega} = |\widetilde{\Omega}|$) are given by

$$\widetilde{\Omega}_{x'} = \widetilde{\Omega}\ \sin\varphi_B \sin\theta_{\rm rf} \quad \text{and} \quad \widetilde{\Omega}_{y'} = -\widetilde{\Omega}\sin\theta_B\cos\theta_{\rm rf} - \widetilde{\Omega}\cos\theta_B\cos\varphi_B\sin\theta_{\rm rf}. \tag{28}$$

These expressions can be inserted into Eqs. 24–26 to obtain general algebraic expressions for the components of the steady-state polarization vector $\mathbf{S}'_{\rm ss}$ in the rotating frame.

Next, the rotating frame solutions can be transformed back to the laboratory frame. For this, one first leaves the rotating frame by applying a time-dependent rotation (at frequency $+\omega_{\rm rf}$) around the z'-axis, yielding $\mathbf{S}'(t) = R_z(-\omega_{\rm rf}\,t)\mathbf{S}'_{\rm ss}$. One then transforms $\mathbf{S}'(t)$ back to laboratory coordinates via the rotation $\mathbf{S}(t) = R_z(\varphi_B)R_y(\theta_B)\mathbf{S}'(t)$ that brings $\mathbf{B}_0$ to $\mathbf{k}$. For circularly-polarized light only the component of $\mathbf{S}(t)$ along the $\mathbf{k}$-vector, given by $S_k(t) = \mathbf{S}(t)\cdot\mathbf{k}/|\mathbf{k}|$, affects the absorption coefficient.[7] Performing the above transformations one finds

$$S_k(t) = S_{\rm DC} + S_{\rm IP}\ \sin\omega_{\rm rf}t + S_{\rm QU}\cos\omega_{\rm rf}t, \tag{29}$$

with

$$S_{\rm DC} = w_{\rm ss}\cos\theta_B, \quad S_{\rm IP} = -v_{\rm ss}\sin\theta_B, \quad \text{and} \quad S_{\rm QU} = -u_{\rm ss}\sin\theta_B. \tag{30}$$

[7]The results given below are easily extended to magnetometers using a probe beam that propagates along a direction $\mathbf{k}_{\rm probe} \neq \mathbf{k}_{\rm pump}$. For this one has to project $\mathbf{S}(t)$ onto the probe beam by $S_{\rm probe}(t) = \mathbf{S}(t)\cdot\mathbf{k}_{\rm probe}/|\mathbf{k}_{\rm probe}|$ and replace in the subsequent equations $S_k(t)$ by $S_{\rm probe}(t)$.

The polarization along the **k**-vector thus has a time-independent contribution S_{DC}, and time-dependent contributions that oscillate in-phase (S_{IP}) and in quadrature (S_{QU}) with the rf field.

3.4 Optically Detected Magnetic Resonance

The effect of the altered steady-state spin polarization $S_k(t)$ on the transmitted power of a circularly-polarized light beam is obtained by replacing S_z in Eq. 11 by expressions 29 and 30, yielding a general expression of the form

$$P(t) = P_{\mathrm{DC}} + P_{\mathrm{IP}} \sin \omega_{\mathrm{rf}} t + P_{\mathrm{QU}} \cos \omega_{\mathrm{rf}} t, \tag{31}$$

with

$$P_{\mathrm{DC}} = P_0 - P_0 \kappa_0^{\mathrm{unpol}} L + P_0 \kappa_0^{\mathrm{unpol}} L \alpha_{F,F'}^{(1)} w_{\mathrm{ss}} \cos \theta_B \tag{32}$$

$$P_{\mathrm{IP}} = -P_0 \kappa_0^{\mathrm{unpol}} L \alpha_{F,F'}^{(1)} v_{\mathrm{ss}} \sin \theta_B \tag{33}$$

$$P_{\mathrm{QU}} = -P_0 \kappa_0^{\mathrm{unpol}} L \alpha_{F,F'}^{(1)} u_{\mathrm{ss}} \sin \theta_B. \tag{34}$$

Equation 31 can be written alternatively as

$$P(t) = P_{\mathrm{DC}} + P_{\mathrm{R}} \sin(\omega_{\mathrm{rf}} t + \phi), \tag{35}$$

with

$$P_{\mathrm{R}} = P_0 \kappa_0^{\mathrm{unpol}} L \alpha_{F,F'}^{(1)} \sin \theta_B \sqrt{u_{\mathrm{ss}}^2 + v_{\mathrm{ss}}^2} \tag{36}$$

and

$$\tan \phi = \frac{P_{\mathrm{QU}}}{P_{\mathrm{IP}}} = \frac{S_{\mathrm{QU}}}{S_{\mathrm{IP}}} = \frac{u_{\mathrm{ss}}}{v_{\mathrm{ss}}}. \tag{37}$$

Equation 31—together with the explicit expressions for $S_{\mathrm{DC}}, S_{\mathrm{IP}}, S_{\mathrm{QU}}, S_{\mathrm{IP}}$ and ϕ derived in the next section—represents the master equation describing ODMR magnetometer signals in terms of the detected light power.

We note that in the above derivation we have dropped the alignment (A_{zz}) term of Eq. 11, whose contribution is often negligible on $F \rightarrow F - 1$ hyperfine components of the alkali D_1 line [25], and whose effect on magnetometer performance has never been addressed to the best of our knowledge.

4 Theory of Orientation-Based Magnetometers

In this section we will focus on magnetometers building on vector polarization (orientation) produced by optical pumping with a *circularly-polarized* light beam (pump beam) propagating along $\mathbf{k}\|\hat{z}$, thus producing, in absence of external fields a spin polarization $(0, 0, S_z)$ in lab frame coordinates. The magnitude and orientation of this spin polarization is altered by the joint action of the field of interest $\mathbf{B}_0$, the rf field $\mathbf{B}_{\mathrm{rf}}$, and relaxation as discussed in the previous section. A second (circularly polarized) light beam (probe beam) detects a specific component of the altered spin polarization. For practical reasons, e.g., in order to simplify the sensor hardware in the case of multi-sensor arrays (Sect. 7.7), or in the case of portable magnetometers, one often uses a single beam that serves both as pump and probe beam. Below we shall address such single beam layouts only.

4.1 M_z and M_x Classification

As discussed in Sect. 3.2, the equilibrium vector polarization (orientation) $\mathbf{S}'_{eq}$ produced by a circularly-polarized pump beam propagating along $\mathbf{k}_{\mathrm{pump}}$ is oriented along $\mathbf{B}_0\|\hat{z}$. The atomic magnetometer literature (Chap. 4 in [3]) refers to a configuration in which the z-component of the spin polarization is detected by a probe beam $\mathbf{k}_{\mathrm{probe}}\|\hat{z}$ as M_z-magnetometer (left graph of Fig. 7). Since the pump and probe beams carry identical polarization and propagate along the same direction, they represent in fact the same single beam. Any arrangement in which a polarization component orthogonal to $\mathbf{B}_0$ (say the x-component) is detected, is referred to as M_x-magnetometer (middle graph of Fig. 7). A 'pure' M_x magnetometer would require two distinct beams. However, it may be realized—as shown in the right graph of Fig. 7—by a single beam, that reads out simultaneously the x- and z-components of the steady-state polarization.

This classification is somewhat artificial in situations, in which one does not know a priori the relative orientation of $\mathbf{B}_0$ with respect to $\mathbf{k}_{\mathrm{probe}}$. Hereafter, we shall nonetheless retain the established concepts of M_x- and M_z-magnetometers.

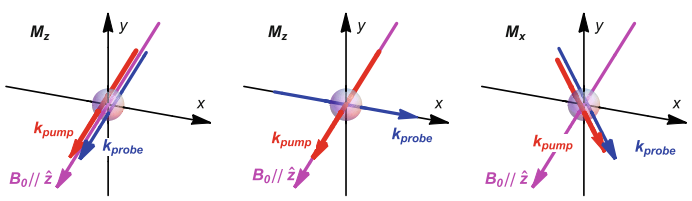

Fig. 7 Magnetometer geometries classified as M_z (*left*) and M_x (*middle*, *right*). For the discussion in this section all light beams are assumed to be circularly polarized

4.2 The M_x Magnetometer

We address the general case of an M_x-magnetometer whose sensor proper consists of an alkali vapor, contained in a spherical cell that is traversed by a single, circularly-polarized light beam whose frequency is tuned to an atomic absorption line. The light beam is assumed to propagate along $\mathbf{k} = k\hat{z}$, while the atoms are exposed to an oscillatory magnetic field $\mathbf{B}_{\mathrm{rf}}(t)$, the two vectors define the magnetometer's geometry, and hence the orientational dependence of its sensitivity. It is useful to distinguish two subclasses, viz., magnetometers in which the rf field is arranged to be parallel to $\mathbf{k}$ or perpendicular to $\mathbf{k}$. These two particular cases are important since sensor heads obeying the conditions $\hat{\mathbf{k}} \cdot \widehat{\mathbf{B}}_{\mathrm{rf}} = 1$ and $\hat{\mathbf{k}} \cdot \widehat{\mathbf{B}}_{\mathrm{rf}} = 0$ can be easily realized by precision machining.

M_x magnetometer with $\mathbf{B}_{\mathrm{rf}} \| \mathbf{k}$

Figure 8 shows the geometrical layout of an M_x magnetometer designed such that the rf field $\mathbf{B}_{\mathrm{rf}}(t)$ is parallel to the light propagation direction $\mathbf{k}$. Because of the cylindrical symmetry of the sensor, the magnetic field orientation in this geometry is characterized by the single angle θ_B. The effective rf field in the lab frame $\widetilde{\Omega}(\theta_{\mathrm{rf}} = 0)$, given by Eq. 28, has components $= (0, -\widetilde{\Omega} \sin\theta_B, 0)$, and the magnetometer signals (Eqs. 24–28) turn out to be

$$\begin{aligned} S_{\mathrm{IP}} &= S_0 \frac{\gamma \widetilde{\Omega} \sin\theta_B}{(\omega_{\mathrm{rf}} - \omega_L)^2 + \gamma^2 + \widetilde{\Omega}^2 \sin^2\theta_B} \cos\theta_B \sin\theta_B \\ &= S_0 \frac{1}{x^2 + 1 + \widetilde{G}_{\mathrm{rf}}} \sqrt{\widetilde{G}_{\mathrm{rf}}} \cos\theta_B \sin\theta_B \end{aligned} \tag{38}$$

$$\begin{aligned} S_{\mathrm{QU}} &= -S_0 \frac{(\omega_{\mathrm{rf}} - \omega_L)\widetilde{\Omega} \sin\theta_B}{(\omega_{\mathrm{rf}} - \omega_L)^2 + \gamma^2 + \widetilde{\Omega}^2 \sin^2\theta_B} \cos\theta_B \sin\theta_B \\ &= -S_0 \frac{x}{x^2 + 1 + \widetilde{G}_{\mathrm{rf}}} \sqrt{\widetilde{G}_{\mathrm{rf}}} \cos\theta_B \sin\theta_B, \end{aligned} \tag{39}$$

and

$$S_{\mathrm{R}} = S_0 \frac{\sqrt{x^2 + 1}}{x^2 + 1 + \widetilde{G}_{\mathrm{rf}}} \sqrt{\widetilde{G}_{\mathrm{rf}}} \, |\cos\theta_B \sin\theta_B| \tag{40}$$

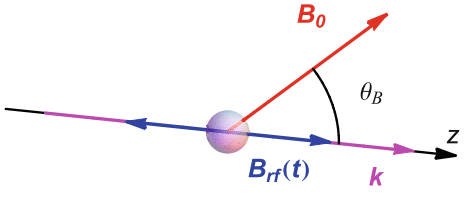

Fig. 8 M_x magnetometer in the $\mathbf{B}_{\mathrm{rf}} \| \mathbf{k}$ geometry

$$\tan\phi = \frac{S_{\mathrm{QU}}}{S_{\mathrm{IP}}} = -x. \tag{41}$$

Dimensionless parameters: In the above equations we have introduced a dimensionless 'detuning parameter' x, defined as

$$x = \frac{\omega_{\mathrm{rf}} - \omega_L}{\gamma} = \frac{\delta\omega}{\gamma} \tag{42}$$

and a dimensionless 'effective rf saturation parameter' $\widetilde{G}_{\mathrm{rf}}$, defined as

$$\widetilde{G}_{\mathrm{rf}} = \frac{\widetilde{\Omega}^2}{\gamma^2}\sin^2\theta_B = G_{\mathrm{rf}}\ \sin^2\theta_B, \tag{43}$$

where the Rabi frequency is related to the half-amplitude of the oscillating field by $\Omega = \gamma_F B_1$. In order to simplify the expressions, we have set $\gamma_1 = \gamma_2 \equiv \gamma$, an approximation that is well obeyed in paraffin-coated alkali vapor cells [7, 26], while in buffer gas cells the coherence relaxation rate γ_2 may be substantially larger than γ_1. When dropping the $\gamma_2 = \gamma_1$ assumption, Eqs. 38–41 become more complicated, but the detuning and saturation parameters are given by the simple relations

$$x = \frac{\delta\omega}{\gamma_2} \quad \text{and} \quad G_{\mathrm{rf}} = \frac{\Omega^2}{\gamma_1\gamma_2}. \tag{44}$$

Optical power broadening: The process of optical pumping affects the intrinsic relaxation rates γ_i, and one can show that—to lowest order in $G_{\mathrm{op}} \propto P_0$ (introduced in Sect. 2.1)—this effect can be taken into account by substituting in the above

$$\gamma_i \Rightarrow \Gamma_i = \gamma_i + \gamma_{\mathrm{pump}}. \tag{45}$$

Rewriting the signals in a universal form: We recall that the signals $S_{\mathrm{IP}}, S_{\mathrm{QU}}, S_{\mathrm{R}}$, and ϕ above relate to a parametrization of the time-dependent polarization according to

$$S_k(t) = S_{\mathrm{R}}\ \sin(\omega_{\mathrm{rf}}t + \phi) = S_{\mathrm{IP}}\ \sin\omega_{\mathrm{rf}}t + S_{\mathrm{QU}}\cos\omega_{\mathrm{rf}}t. \tag{46}$$

Equations (38)–(41) are specific for M_x-magnetometers having $\mathbf{B}_{\mathrm{rf}} \| \mathbf{k}$. However, as we will see below, magnetometers that do not obey the last relation can also be brought to the same universal form of Eqs. (38)–(41) by introducing a suitable phase shift ϕ_0, such that

$$\phi = \phi_0 - \arctan x. \tag{47}$$

Note that in the above case $\phi_0 = 0$. Defining $\tilde{\phi} = \phi - \phi_0$, one can show—after some algebra—that the time-dependent detected spin polarization can be expressed, for all types of M_x magnetometers, as

$$S_k(t) = \widetilde{S}_{\mathrm{IP}} \sin(\omega_{\mathrm{rf}} t + \phi_0) + \widetilde{S}_{\mathrm{QU}} \cos(\omega_{\mathrm{rf}} t + \phi_0), \tag{48}$$

with

$$\widetilde{S}_{\mathrm{IP}} = S_0 \frac{1}{x^2 + 1 + \widetilde{G}_{\mathrm{rf}}} \sqrt{\widetilde{G}_{\mathrm{rf}}} \, |\cos\theta_B \sin\theta_B| \tag{49}$$

$$\widetilde{S}_{\mathrm{QU}} = -S_0 \frac{x}{x^2 + 1 + \widetilde{G}_{\mathrm{rf}}} \sqrt{\widetilde{G}_{\mathrm{rf}}} \, |\cos\theta_B \sin\theta_B| \tag{50}$$

$$\widetilde{S}_{\mathrm{R}} = S_{\mathrm{R}} = S_0 \frac{\sqrt{x^2 + 1}}{x^2 + 1 + \widetilde{G}_{\mathrm{rf}}} \sqrt{\widetilde{G}_{\mathrm{rf}}} \, |\cos\theta_B \sin\theta_B| \tag{51}$$

$$\tan\tilde{\phi} = \tan(\phi - \phi_0) = -x, \quad \text{where} \quad \phi_0 = 0 \ \text{ for the } B_{\mathrm{rf}} \| \mathbf{k} \text{ case.} \tag{52}$$

We shall refer to the latter expressions as the 'standard universal form' of the M_x magnetometers signals. As we shall see below, this standard form is universal in the sense that all M_x magnetometer signals can be expressed in this form, irrespective of the orientation of $\mathbf{B}_0$ and $\mathbf{B}_{\mathrm{rf}}$. The distinctive feature of the standard form of the M_x signal is that the on-resonance phase vanishes, i.e., $\tilde{\phi}(x = 0) = 0$, and has a negative slope, i.e., $d\phi/dx|_{x=0} < 0$.

Line shapes of the $\mathbf{B_{rf}} \parallel \mathbf{k}$ magnetometer: Fig. 9 shows the detuning dependence of the standard signals $\widetilde{S}_{\mathrm{IP}}, \widetilde{S}_{\mathrm{QU}}, S_{\mathrm{R}}$, and $\tilde{\phi} = \phi - \phi_0$ given by Eqs. 49–52 for various values of the effective rf saturation parameter $\widetilde{G}_{\mathrm{rf}}$.

The in-phase/quadrature signals are dispersive/absorptive Lorentzians, respectively, with rf power broadened linewidths given by

$$\Delta x_{\mathrm{FWHM}} = 2\sqrt{1 + \widetilde{G}_{\mathrm{rf}}} \Rightarrow \Delta\omega_{\mathrm{FWHM}} = 2\gamma \sqrt{1 + \left(\frac{\Omega}{\gamma}\right)^2 \sin^2\theta_B}. \tag{53}$$

For $\widetilde{G}_{\mathrm{rf}} \ll 1$, the S_{R}-signal is a single absorptive line that has twice the width of the S_{QU}-signal, while for larger amplitudes it splits into two lines.

Phase signal of the $\mathbf{B_{rf}} \| \mathbf{k}$ magnetometer: The arctan-function (Eq. 41) describing the phase is not affected by rf power broadening, but depends—by virtue of Eq. 45—on laser power. This remarkable fact, together with the linear dependence on the magnetic field magnitude near $x = 0$, makes this signal an ideal discriminator function for operating a feedback loop that keeps the rf frequency, ω_{rf}, actively locked to the Larmor frequency, ω_L (more details given in Sect. 7). Furthermore, Eq. 52 shows that the phase is independent of the magnetic field

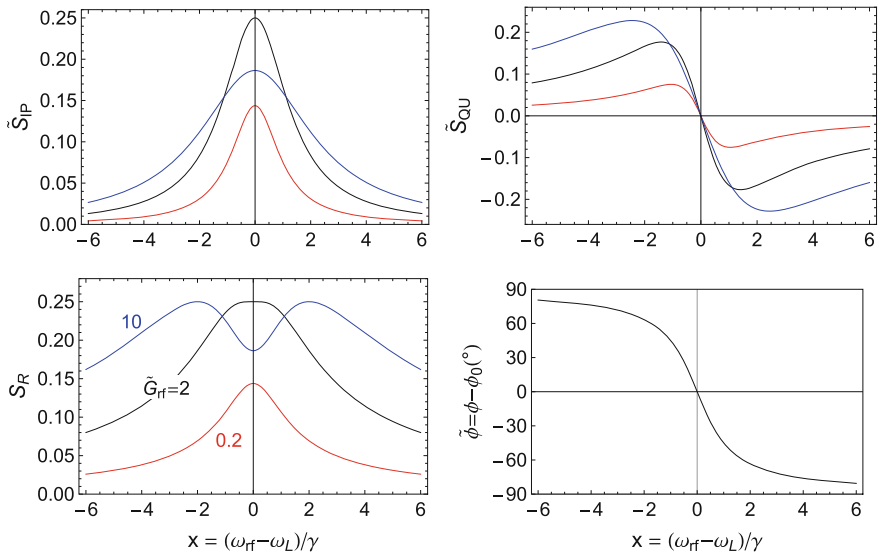

Fig. 9 Universal lineshape functions of M_x magnetometers: Dependence of the signals $\widetilde{S}_{IP}, \widetilde{S}_{QU}, S_R$, and $\tilde{\phi}$ given by 49–52 on the rf frequency ω_{rf}. The graphs are shown for effective rf saturation parameters $\widetilde{G}_{rf}$ = 0.2 (*red*), 2 (*black*) and 10 (*blue*). For the $\mathbf{B}_{rf}\|\mathbf{k}$ case discussed in this paragraph one has $\widetilde{G}_{rf} = G_{rf}\ \sin^2\theta_B$ and $\phi_0 = 0$

orientation (characterized by θ_B), which makes the $\mathbf{B}_{rf}\|\mathbf{k}$ variant of the M_x magnetometer a *true scalar magnetometer*.

Nyquist plot: Nyquist plots (shown in Fig. 10) are an alternative way for representing the universal $\widetilde{S}_{IP}(x)$ and $\widetilde{S}_{QU}(x)$ signals that also visualize the $S_R(x)$ and $\tilde{\phi}(x)$ dependencies. For each given $\widetilde{G}_{rf}$ value the corresponding curve represents the x-dependence of the $(\widetilde{S}_{QU}, \widetilde{S}_{IP})$ values. When the detuning x is varied from $-\infty$ to $+\infty$, the curves evolve from the origin back to the origin in the sense indicated by the arrow on the $\widetilde{G}_{rf} = 0.1$ curve, where red dots mark specific values of

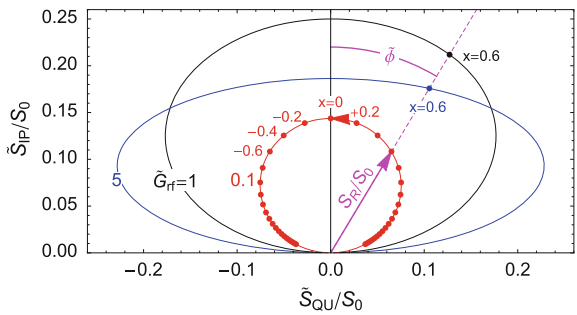

Fig. 10 Nyquist representation of the universal M_x-signals for $\widetilde{G}_{rf} = 0.1, 1, 5$

$x = (\omega_{\rm rf} - \omega_L)/\gamma$. One easily sees from Eqs. 49 and 50 that for $\widetilde{G}_{\rm rf} \ll 1$ the Nyquist curves are circles with radii $\sqrt{\widetilde{G}_{\rm rf}}\,|\sin\theta_B \cos\theta_B|$.

The Nyquist plots are experimentally useful representations that may serve to adjust the reference phase of the lock-in demodulator (see Sect. 7), to uncover spurious oscillatory signals in the photocurrent induced by (inductive or capacitive) electronic pickup of the oscillating magnetic field, or to assess line broadening by inhomogeneous fields, as discussed in Ref. [27].

Angular dependence of the $\mathbf{B_{rf}}\|\mathbf{k}$ magnetometer: There are two ways to look at the angular dependence of the $\mathbf{B_{rf}}\|\mathbf{k}$ magnetometer. On one hand, the equations derived above yield for the on-resonance value of the R-signal

$$S_{\rm R}(x=0) = S_0\,|\cos\theta_B|\sin^2\theta_B\,\frac{\sqrt{G_{\rm rf}}}{1+G_{\rm rf}\sin^2\theta_B}. \tag{54}$$

a function that depends both on $G_{\rm rf}$ and θ_B, and reaches an absolute maximum for $G_{\rm rf} = 2$ and $\theta_B = \pi/4$, as shown in the left graph of Fig. 11. The solid line represents values $G_{\rm rf}^{\rm opt}$ and $\theta_B^{\rm opt}$ that yield a maximal signal for given values of θ_B and $G_{\rm rf}$, respectively. The white dot represents the combination of parameters for which the (absolutely) largest signal occurs. The middle graph shows $G_{\rm rf}$-dependence of the R signal at $\theta_B = \pi/4$, which reaches a maximum for $G_{\rm rf} = 2$.

On the other hand, one may optimize, for each given field orientation θ_B the on-resonance R-signal by varying the rf amplitude $\Omega \propto \sqrt{G_{\rm rf}} \propto \sqrt{\widetilde{G}_{\rm rf}}$. Under optimized rf conditions the angular dependence becomes independent of the rf amplitude as shown in the right graph of Fig. 11. reaching a maximum for $\widetilde{G}_{\rm rf} = 1$.

Figure 12 shows the angular dependence of the $S_{\rm R}$ signal for different rf saturation amplitudes. The dashed lines represent vertical cuts through the left graph of Fig. 11, while the solid line represents the universal angular dependence obtained under optimized $G_{\rm rf}$ conditions. For $G_{\rm rf} \ll 1$, the angular dependence of the $S_{\rm R}$

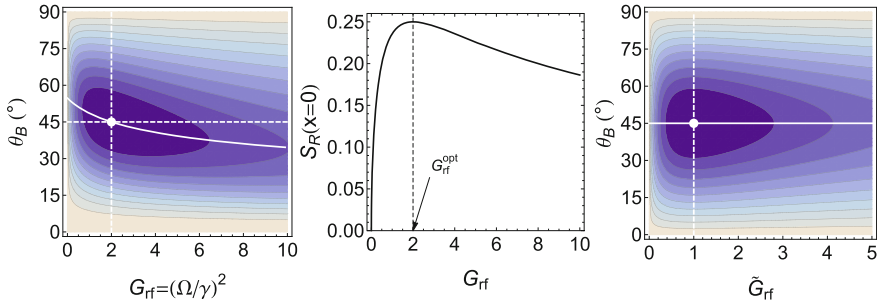

Fig. 11 *Left* Contour plot of the on-resonance R-signal $S_{\rm R}$ $(x = 0)$ in the $\mathbf{B}_{\rm rf}\|\mathbf{k}$ geometry as a function of $G_{\rm rf}$ and θ_B. *Middle* Cut through the *left graph* along the *horizontal dashed line* $(\theta_B = \pi/4)$, showing that the maximum R signal occurs for $G_{\rm rf} = 2$, corresponding to $\widetilde{G}_{\rm rf} = 1$ on the *right graph*. *Right* Same plot as left graph as function of θ_B and effective rf power $\widetilde{G}_{\rm rf}$. In this universal representation the maximum signal is found at $\theta_B = 45°$

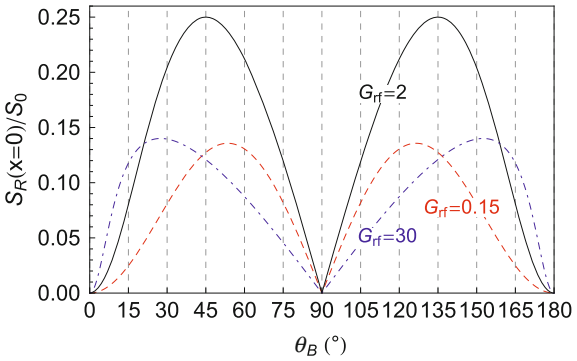

Fig. 12 $\mathbf{B}_{rf} \| \mathbf{k}$ geometry: Angular dependence of the S_R signal amplitudes for various values of G_{rf}

signal is given by $\cos\theta_B \sin^2\theta_B$, a function that reaches a maximum value for $\theta_B = 54.74°$, while for $G_{rf} \gg 1$ the peak asymptotically evolves towards $\theta_B = 180°$. For an rf power that maximizes $S_R(0)$, i.e., for $G_{rf} = 2$ (equivalent to $\widetilde{G}_{rf} = 1$) the angular dependence peaks at $\theta_B = 45°$ (solid black line).

M_x magnetometer with $\mathbf{B}_{rf} \perp \mathbf{k}$

Figure 13 shows the geometrical layout of an M_x magnetometer designed such that the rf field $\mathbf{B}_{rf}(t)$ is orthogonal to the light propagation direction $\mathbf{k}$.

In this case the magnetometer has no longer a rotational symmetry and the magnetic field orientation has to be specified by the two spherical coordinate angles θ_B and φ_B as shown in the figure. In this geometry the effective rf field in the lab frame $\Omega(\theta_{rf} = \pi/2)$, given by Eq. 28 has components $(-\sin\varphi_B, -\cos\theta_B\cos\varphi_B, 0)\Omega$, and the magnetometer signals are given by

$$S_{IP} = S_0 \frac{x\cos\theta_B\cos\varphi_B + \sin\varphi_B}{x^2 + 1 + \widetilde{G}_{rf}} \sqrt{G_{rf}}\cos\theta_B \sin\theta_B \tag{55}$$

$$S_{QU} = S_0 \frac{\cos\theta_B\cos\varphi_B - x\sin\varphi_B}{x^2 + 1 + \widetilde{G}_{rf}} \sqrt{G_{rf}}\cos\theta_B \sin\theta_B \tag{56}$$

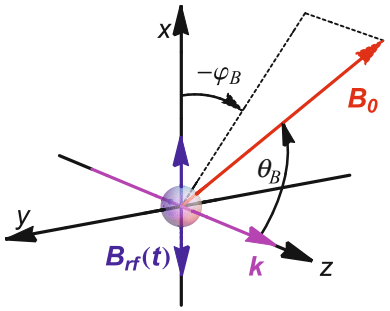

Fig. 13 M_x magnetometer in the $\mathbf{B}_{rf} \perp \mathbf{k}$ geometry

$$S_{\mathrm{R}} = S_0 \frac{\sqrt{x^2+1}}{x^2+1+\widetilde{G}_{\mathrm{rf}}} \sqrt{\widetilde{G}_{\mathrm{rf}}}\,|\cos\theta_B \sin\theta_B| \tag{57}$$

$$\tan\phi = \frac{\cos\theta_B \cos\varphi_B - x\sin\varphi_B}{x\cos\theta_B \cos\varphi_B + \sin\varphi_B}, \tag{58}$$

where $\widetilde{G}_{\mathrm{rf}} = G_{\mathrm{rf}} g(\theta_B, \varphi_B)$ with

$$g(\theta_B, \varphi_B) = \cos^2\theta_B \cos^2\varphi_B + \sin^2\varphi_B = \cos^2\theta_B + \sin^2\theta_B \sin^2\varphi_B. \tag{59}$$

As in the $\mathbf{B}_{\mathrm{rf}} \| \mathbf{k}$ case, the phase given by Eq. 58 does not depend on the rf saturation parameter G_{rf}, but we note that it does depend on the field orientation. We also note the 'asymmetric' appearance of G_{rf} and $\widetilde{G}_{\mathrm{rf}}$ in Eqs. 55–57.

Rewriting the signals in the standard universal form: The bulky expressions for the in-phase and quadrature signals can be transformed to the standard universal form, introduced for the $\mathbf{B}_{\mathrm{rf}} \| \mathbf{k}$ case in Sect. 4.2. After some algebra one can show that the time dependent polarization can be expressed by the same universal expressions as 48–51, viz.,

$$S_k(t) = \widetilde{S}_{\mathrm{IP}} \sin(\omega_{\mathrm{rf}} t + \phi_0) + \widetilde{S}_{\mathrm{QU}} \cos(\omega_{\mathrm{rf}} t + \phi_0), \tag{60}$$

where

$$\widetilde{S}_{\mathrm{IP}} = S_0 \frac{1}{x^2+1+\widetilde{G}_{\mathrm{rf}}} \sqrt{\widetilde{G}_{\mathrm{rf}}}\,|\cos\theta_B \sin\theta_B| \tag{61}$$

$$\widetilde{S}_{\mathrm{QU}} = -S_0 \frac{x}{x^2+1+\widetilde{G}_{\mathrm{rf}}} \sqrt{\widetilde{G}_{\mathrm{rf}}}\,|\cos\theta_B \sin\theta_B| \tag{62}$$

$$\widetilde{S}_{\mathrm{R}} = S_{\mathrm{R}} = S_0 \frac{\sqrt{x^2+1}}{x^2+1+\widetilde{G}_{\mathrm{rf}}} \sqrt{\widetilde{G}_{\mathrm{rf}}}\,|\cos\theta_B \sin\theta_B| \tag{63}$$

$$\phi = \phi_0 - \arctan x, \tag{64}$$

with

$$\tan\phi_0 = \cos\theta_B \cot\varphi_B. \tag{65}$$

On-resonance phase: The on-resonance offset phase $\phi_0 = \tilde{\phi}\,(x = 0)$ deserves special attention. Figure 14 shows the θ_B versus φ_B dependence of ϕ_0. The red lines in the figure show that for $\theta_B = 90°$ the phase has no φ_B-dependence, and conversely, that for $\varphi_B = 90°$ the phase has no θ_B-dependence. These two special cases are equivalent to the magnetic field $\mathbf{B}_0$ lying in the x-y plane and in the x-z plane, respectively (cf. Fig. 13). The blue lines on the edges of the graph show

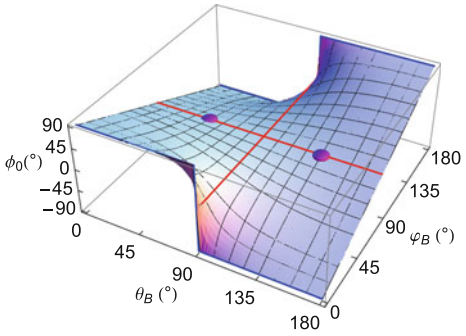

Fig. 14 $\mathbf{B}_{\rm rf}\perp\mathbf{k}$ geometry: $\theta_B - \varphi_B$ dependence of the on-resonance phase ϕ_0. The *red* and *blue lines* indicate specific planes in which the phase is independent (up to a sign) of the field orientation, while the *magenta dots* refer to the field orientation yielding a maximal S_R signal

that for $\varphi_B = 0°$ or 180° ($\mathbf{B}_0$ in the x-z plane), the phase has no θ_B-dependence, except for a phase jump by 180° that corresponds to a sign change of the $S_{\rm QU}$ signal. For magnetic fields that do not lie in either of the three coordinate planes, the phase thus depends on the field orientation. The signal amplitudes depend on θ_B, φ_B and $G_{\rm rf}$, which makes the discussion difficult.

Particular case $\mathbf{B}_{\rm rf}\perp\mathbf{k}$ and $\mathbf{B}_{\rm rf}\perp\mathbf{B}_0$: The particular case in which one 'forces' $\mathbf{B}_{\rm rf}$ to be perpendicular to $\mathbf{B}_0$ has been addressed earlier [27, 28]. In the frame of the model presented here it corresponds to the $\mathbf{B}_{\rm rf}\perp\mathbf{k}$ magnetometer with $\varphi_B = \pi/2$, in which case the orientational dependence reduces to a pure θ_B-dependence, and the general Eqs. 55–58 reduce to

$$S_{\rm IP} = S_0 \frac{1}{x^2 + 1 + G_{\rm rf}} \sqrt{G_{\rm rf}} \cos\theta_B \sin\theta_B \tag{66}$$

$$S_{\rm QU} = -S_0 \frac{x}{x^2 + 1 + G_{\rm rf}} \sqrt{G_{\rm rf}} \cos\theta_B \sin\theta_B \tag{67}$$

$$S_{\rm R} = S_0 \frac{\sqrt{x^2+1}}{x^2 + 1 + G_{\rm rf}} \sqrt{G_{\rm rf}} \,|\cos\theta_B \sin\theta_B| \tag{68}$$

$$\phi = -\arctan x. \tag{69}$$

We note that the signals of this particular case are identical with the 'standard universal' lineshape functions without the need for introducing an offset phase.

4.3 M_z Magnetometer

Figure 15 shows the geometrical layout of a so-called M_z magnetometer in which the magnetic field $\mathbf{B}_0$ is along the $\mathbf{k}$ vector of the light, while the rf field $\mathbf{B}_{\rm rf}$ is orthogonal to $\mathbf{k}$. One readily sees that this represents the particular case ($\theta_B = 0$) of the $\mathbf{B}_{\rm rf}\perp\mathbf{k}$ variant of the M_x geometry, for which the signals are given by

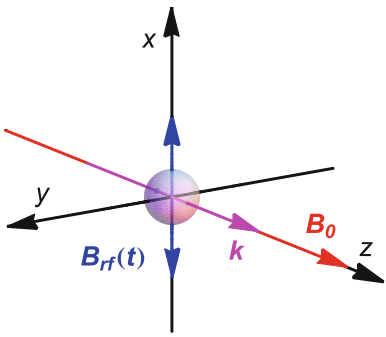

Fig. 15 Geometry of the M_z magnetometer

$$S_{\mathrm{IP}}^{M_z} = S_{\mathrm{QU}}^{M_z} = 0 \quad \text{and} \quad S_{\mathrm{DC}}^{M_z} = S_0\left(1 - \frac{G_{\mathrm{rf}}}{x^2 + 1 + G_{\mathrm{rf}}}\right). \tag{70}$$

The specific feature of the M_z magnetometer is the absence of time-dependent signals, a feature that may, e.g., be used for the precise parallel alignment of a laser beam with a magnetic field. We also note that $\widetilde{G}_{\mathrm{rf}} = G_{\mathrm{rf}}$ for the M_z geometry.

4.4 Time-Independent Signals in the M_x Geometry

The signals in the M_x geometry discussed earlier also have time-independent contributions S_{DC}, whose measurement does not require a lock-in amplifier. For all geometries these dc signals read:

$$S_{\mathrm{DC}} = S_0\left(1 - \frac{\widetilde{G}_{\mathrm{rf}}}{x^2 + 1 + \widetilde{G}_{\mathrm{rf}}}\right)\cos^2\theta_B, \tag{71}$$

with $\widetilde{G}_{\mathrm{rf}} = G_{\mathrm{rf}} f(\theta_B, \varphi_B)$, where $f(\theta_B, \varphi_B)$ is given by Eq. 74 below. All dc signals are thus downward-pointing Lorentzians with $\widetilde{G}_{\mathrm{rf}}$-dependent widths and amplitudes that are superposed on an orientation dependent background, as shown in Fig. 16.

4.5 Master Expressions for All M_x Magnetometer Signals

In the preceding paragraphs we have discussed all possible geometrical variants of the M_x magnetometer. Inspection of the results reveals that they all feature the following common basic signal structures:

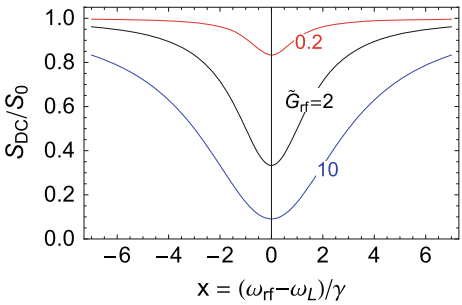

Fig. 16 Time-independent (dc) signals S_{DC} that have a universal unique representation in all M_x geometries. All signals scale as $\cos^2\theta_B$ with the field orientation

- The **phase signal** in all geometries can be expressed as

$$\tilde{\phi} = -\arctan x = -\arctan\frac{\delta\omega}{\gamma} = -\arctan\frac{\omega_{rf}-\omega_L}{\gamma}, \tag{72}$$

with $\tilde{\phi} = \phi - \phi_0$, where $\tilde{\phi}$ is the phase between $\mathbf{B}_{rf}(t)$ and the detected light power P(t), and where the offset phase ϕ_0 depends on the specific orientations of $\widehat{\mathbf{B}}_{rf}$ and $\widehat{\mathbf{B}}_0$ with respect to $\hat{\mathbf{k}}$. From an experimental point of view, the offset phase ϕ_0 is irrelevant, since it has in any case[8] to be determined experimentally and compensated for by subtracting a suitable reference phase in the phase-sensitive amplifier used in experiments.

- The $\mathbf{S}_R$ **signal** in all geometries can be written as

$$S_R = S_0\frac{\sqrt{x^2+1}}{x^2+1+\widetilde{G}_{rf}}\sqrt{\widetilde{G}_{rf}}\,|\cos\theta_B\sin\theta_B|, \tag{73}$$

where $\widetilde{G}_{rf} = G_{rf}f(\theta_B,\varphi_B)$ is an 'effective' rf saturation parameter that depends on the relative orientation of $\widehat{\mathbf{B}}_{rf}$ and $\widehat{\mathbf{B}}_0$, and is given by

$$f(\theta_B,\varphi_B) = \begin{cases} \cos^2\theta_B + \sin^2\theta_B\sin^2\varphi_B & \text{in the } \mathbf{B}_{rf}\perp\mathbf{k} \text{ geometry} \\ \sin^2\theta_B & \text{in the } \mathbf{B}_{rf}\|\mathbf{k} \text{ geometry.} \end{cases} \tag{74}$$

This function is also—from an experimental point of view—irrelevant, since in any case one optimizes the current I_{rf} through the rf coil in order to maximize the on-resonance R-signal

$$S_R\,(x=0) \propto \frac{\sqrt{\widetilde{G}_{rf}}}{1+\widetilde{G}_{rf}} = \frac{I_{rf}/I_c}{1+(I_{rf}/I_c)^2}, \tag{75}$$

[8]Besides its dependence on the field orientation, the phase offset ϕ_0 may be affected by additional phase shifts arising, e.g., from complex impedances in the coil driving and photo-detector circuits, or geometrical alignment uncertainties of the rf coils.

where I_c is a coil-specific calibration constant. The latter function peaks for $I_{\mathrm{rf}} = I_c$, equivalent to $\widetilde{G}_{\mathrm{rf}} = 1$.

- The **angular dependence** of the amplitude of all signals is proportional to $\sin 2\theta_B$, thus yielding a maximal signal for $\theta_B = \pi/4$.
- The expressions 72 and 73 for ϕ and S_{R} contain all the lineshape information and can be used to derive the **in-phase** and **quadrature** signals:

$$S_{\mathrm{IP}} = S_0 \frac{1}{x^2 + 1 + \widetilde{G}_{\mathrm{rf}}} \sqrt{\widetilde{G}_{\mathrm{rf}}} \, |\cos\theta_B \sin\theta_B| \tag{76}$$

$$S_{\mathrm{QU}} = -S_0 \frac{x}{x^2 + 1 + \widetilde{G}_{\mathrm{rf}}} \sqrt{\widetilde{G}_{\mathrm{rf}}} \, |\cos\theta_B \sin\theta_B|. \tag{77}$$

- As a final result, the **in-phase and quadrature components of the detected light power** are obtained by inserting the last expressions into Eqs. 33 and 34, yielding

$$P_{\mathrm{IP}} = \widetilde{P} \frac{1}{x^2 + 1 + \widetilde{G}_{\mathrm{rf}}} \sqrt{\widetilde{G}_{\mathrm{rf}}} \, |\cos\theta_B \sin\theta_B| \tag{78}$$

$$P_{\mathrm{QU}} = -\widetilde{P} \frac{x}{x^2 + 1 + \widetilde{G}_{\mathrm{rf}}} \sqrt{\widetilde{G}_{\mathrm{rf}}} \, |\cos\theta_B \sin\theta_B| \tag{79}$$

$$P_{\mathrm{R}} = \widetilde{P} \frac{\sqrt{1 + x^2}}{x^2 + 1 + \widetilde{G}_{\mathrm{rf}}} \sqrt{\widetilde{G}_{\mathrm{rf}}} \, |\cos\theta_B \sin\theta_B|, \tag{80}$$

where

$$\widetilde{P} = S_0 P_0 \kappa_0^{\mathrm{unpol}} L \alpha_{F,F'}^{(1)} \tag{81}$$

is, in principle, also a mere experimental calibration factor, but whose representation in terms of physical system parameters is useful for discussing the sensitivity, the limitations and possible improvements of M_x magnetometers.

5 Theory of Alignment-Based Magnetometers

The magnetometers discussed so far are all based on vector polarization (orientation) created (and probed) by the use of resonant *circularly-polarized* light. Although circularly polarized light also produces an alignment (tensor polarization)

along the direction **k** of light propagation, that contribution has been neglected so far in theoretical treatments. This is justified by the fact that the alignment contribution is negligibly small on the alkali's $nS_{1/2}, F \rightarrow nP_{1/2}, F-1$ (D_1) hyperfine component of the D_1 transition that is most efficient for laser-based magnetometry.

In this section we address magnetic resonance processes in atomic media in which tensor spin polarization (alignment) is created (and probed) by *linearly-polarized* light (Fig. 2). Alignment-based double resonance magnetometers (DRAM) are less well studied in the atomic magnetometry context than orientation-based (DROM) devices. The reason for this is as follows: Since their invention, and until the boost that atomic magnetometry has received in the past two decades by the use of laser radiation, atomic magnetometers were mainly driven by resonance radiation from lamps running a discharge in a gas of the chemical element used in the magnetometer sensor. The Doppler (and/or buffer gas pressure) broadening of the resonance lines emitted by the lamp do not allow resolving the hyperfine structure of the sensor medium, so that the D_1 transition excited by the lamp rather reads $nS_{1/2} \rightarrow nP_{1/2}$. Disregarding again the alignment along **k** that light of any spectral width or degree and type of polarization produces linearly polarized lamp radiation will not produce any transverse alignment since a medium with angular moment $J = 1/2$ cannot be aligned, i.e., cannot have a second rank tensor property, such as an $m_{2,q} \propto \langle 6S_{1/2}|T_q^{(2)}|6P_{1/2}\rangle \equiv 0$, where $T_q^{(2)}$ denotes the set of second rank irreducible tensor operators [19]. For the same reason linearly-polarized light may not achieve significant optical pumping in alkali vapor cells containing buffer gas at a pressure that broadens the optical lines such that the transition's hyperfine structure is no longer resolved.

On the other hand, optical pumping with linearly-polarized laser radiation, tuned to a specific hyperfine transition of an atomic resonance line in a vacuum cell (with or without anti-relaxation wall coatings), will produce an alignment that is parallel to the light polarization, i.e., orthogonal to **k** (Fig. 2). Any static magnetic field $\mathbf{B}_0$ that is not parallel to the laser polarization will lead to a precession of the produced alignment. That precession can be resonantly driven by an oscillating (or rotating) field $\mathbf{B}_{\mathrm{rf}}$ that is orthogonal to $\mathbf{B}_0$. This forms the basis of the alignment-based double resonance (DRAM) magnetometer.

In Ref. [29] we have derived algebraic expressions for the lineshapes and orientational dependencies of the signals encountered in DRAM magnetometers. The method is similar to the one presented in detail for DROM magnetometers in the preceding section, the main difference being that the three Bloch equations for the orientation components $m_{1,q}$ have to be replaced by the five corresponding equations describing the dynamics of the five alignment components $m_{2,q}$. Note that a generalization of the Bloch equations to spin $F = 1$ systems was first given by Fano in 1964 [30], while explicit equations for the (relaxing) multipole moment precession in systems with arbitrary spin F is given, e.g., in Refs. [24, 31].

Figure 17 shows the geometry of a DRAM magnetometer. The magnetometer's orientation is described by the direction $\boldsymbol{\varepsilon}$ of the light's linear polarization, since $\boldsymbol{\varepsilon}$ is a rotational symmetry axis of the produced (and probed) alignment (cf. Fig. 2). The

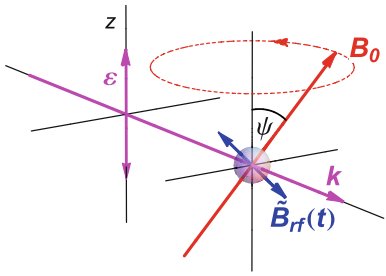

Fig. 17 Geometrical layout of DRAM (alignment-based magnetic resonance) magnetometer. We show only the effective component of the rf field that is perpendicular to $\mathbf{B}_0$

orientational dependence for the detection of a specific magnetic field $\mathbf{B}_0$ is thus fully characterized by the angle ψ between $\mathbf{B}_0$ and $\boldsymbol{\varepsilon}$. As in the case of the DROM magnetometer, components of the rf field $\mathbf{B}_{\mathrm{rf}}$ along the field will not induce magnetic resonance transitions, so that we show only the effective rf field $\widetilde{\mathbf{B}}_{\mathrm{rf}}$ in Fig. 17.

The essential results of the derivation presented in Ref. [29] are the following: The detected light power

$$P(t) = P_{\mathrm{DC}} + P_{\mathrm{IP}}^{\omega_{\mathrm{rf}}} \cos \omega_{\mathrm{rf}} t + P_{\mathrm{QU}}^{\omega_{\mathrm{rf}}} \sin \omega_{\mathrm{rf}} t + P_{\mathrm{IP}}^{2\omega_{\mathrm{rf}}} \cos 2\omega_{\mathrm{rf}} t + P_{\mathrm{QU}}^{2\omega_{\mathrm{rf}}} \cos 2\omega_{\mathrm{rf}} t \quad (82)$$

has a time-independent contribution (not addressed here) and contains terms that oscillate in-phase and in quadrature with the rf drive and its second harmonic, the latter arising from the spin polarization's second rank tensor nature. The in-phase and quadrature signal amplitudes are given by

$$P_{\mathrm{IP}}^{\omega_{\mathrm{rf}}} = \widetilde{P} \frac{4x^2 + 1 + \widetilde{G}_{\mathrm{rf}}}{(x^2 + 1 + \widetilde{G}_{\mathrm{rf}})(4x^2 + 1 + 4\widetilde{G}_{\mathrm{rf}})} \sqrt{G_{\mathrm{rf}}} h_{\omega_{\mathrm{rf}}}(\psi) \quad (83)$$

$$P_{\mathrm{QU}}^{\omega_{\mathrm{rf}}} = \widetilde{P} \frac{x(4x^2 + 1 - 2\widetilde{G}_{\mathrm{rf}})}{(x^2 + 1 + \widetilde{G}_{\mathrm{rf}})(4x^2 + 1 + 4G_{\mathrm{rf}})} \sqrt{\widetilde{G}_{\mathrm{rf}}} h_{\omega_{\mathrm{rf}}}(\psi) \quad (84)$$

and

$$P_{\mathrm{IP}}^{2\omega_{\mathrm{rf}}} = -\widetilde{P} \frac{2x^2 - 1 - \widetilde{G}_{\mathrm{rf}}}{(x^2 + 1 + \widetilde{G}_{\mathrm{rf}})(4x^2 + 1 + 4\widetilde{G}_{\mathrm{rf}})} \widetilde{G}_{\mathrm{rf}} h_{2\omega_{\mathrm{rf}}}(\psi) \quad (85)$$

$$P_{\mathrm{QU}}^{2\omega_{\mathrm{rf}}} = \widetilde{P} \frac{3x}{(x^2 + 1 + \widetilde{G}_{\mathrm{rf}})(4x^2 + 1 + 4\widetilde{G}_{\mathrm{rf}})} \widetilde{G}_{\mathrm{rf}} h_{2\omega_{\mathrm{rf}}}(\psi), \quad (86)$$

respectively, where x is the dimensionless detuning introduced in Sect. 3.2, and where $\widetilde{P}$ is an experimental calibration constant. Figures 18 and 19 show the relevant line shapes when the detected power is demodulated at ω_{rf} and $2\omega_{\mathrm{rf}}$, respectively. As a general feature we note that for large rf saturation parameters, the

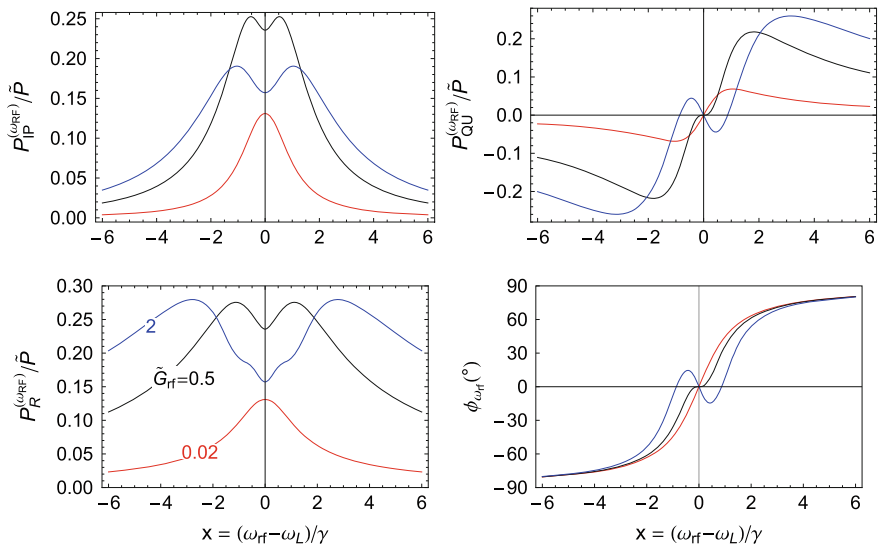

Fig. 18 DRAM magnetometer lineshapes for $P(t)$ demodulated at ω_{rf}

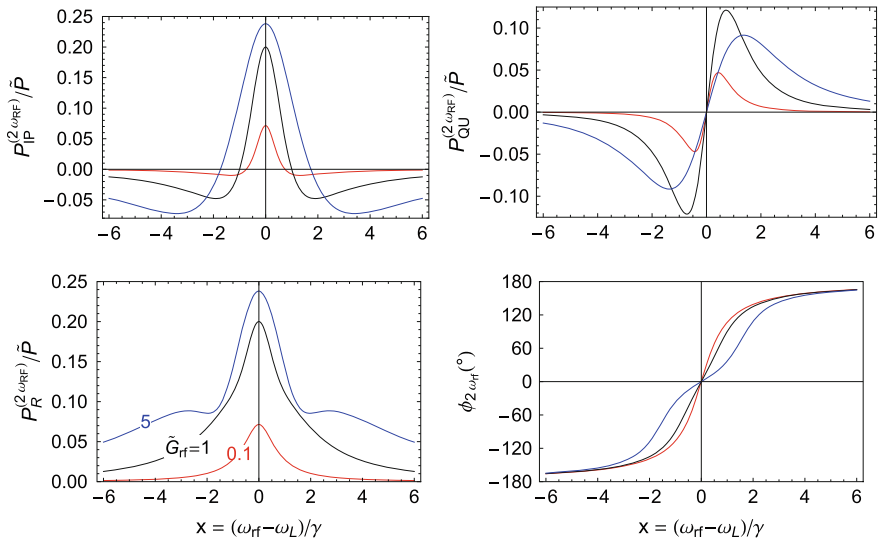

Fig. 19 DRAM magnetometer lineshapes for $P(t)$ demodulated at $2\omega_{rf}$

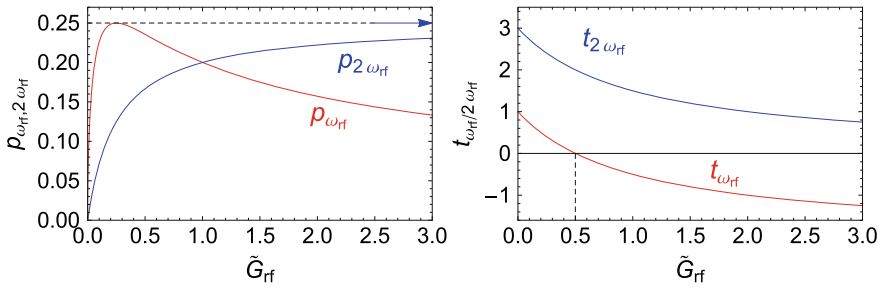

Fig. 20 $\widetilde{G}_{rf}$ dependence of the on-resonance R signals (*left*) and phase slopes (*right*). The *arrow* on the *left graph* indicates the asymptotic value of $p_{2\omega_{rf}}$ for $\widetilde{G}_{rf} \to \infty$

lineshapes are more complex than the ones derived for DROM magnetometers. The phase in the two demodulation channels is given by $\tan \phi_{\omega_{rf},2\omega_{rf}} = P_{QU}^{\omega_{rf},2\omega_{rf}} / P_{IP}^{\omega_{rf},2\omega_{rf}}$.

The normalized on-resonance R signals $P_R = \sqrt{P_{IP}^2 + P_{QU}^2}$ read

$$p_{\omega_{rf}} \equiv \frac{P_R^{\omega_{rf}}}{\widetilde{P}h_{\omega_{rf}}(\psi)} = \frac{\sqrt{\widetilde{G}_{rf}}}{1+4\widetilde{G}_{rf}} \quad \text{and} \quad p_{2\omega_{rf}} \equiv \frac{P_R^{2\omega_{rf}}}{\widetilde{P}h_{2\omega_{rf}}(\psi)} = \frac{\widetilde{G}_{rf}}{1+4\widetilde{G}_{rf}}, \tag{87}$$

and are shown in the left graph of Fig. 20. The $p_{\omega_{rf}}$ signal peaks at a value of 1/4 for $G_{rf} = 1/4$, while the $p_{\omega_{rf}}$ signal reaches the same value asymptotically.

A distinct feature of the DRAM signals is the dependence of the signal phase on G_{rf}, and in particular the fact that the on-resonance phase slope

$$t_{\omega_{rf},2\omega_{rf}} \equiv \left. \frac{d\phi_{\omega_{rf},2\omega_{rf}}}{dx} \right|_{x=0} \tag{88}$$

changes sign above $\widetilde{G}_{rf} = 0.5$, as evidenced by the right graph in Fig. 20. We also note that $t_{2\omega_{rf}} = t_{\omega_{rf}} + 2$ for all values of $\widetilde{G}_{rf}$.

In Eqs. 83–86 the angular dependence functions are given by

$$h_{\omega_{rf}}(\psi) = \frac{3}{2} \sin\psi \cos\psi (3\cos^2\psi - 1) \tag{89}$$

$$h_{2\omega_{rf}}(\psi) = \frac{3}{4} \sin^2\psi (1 - 3\cos^2\psi), \tag{90}$$

where ψ is the angle between $\boldsymbol{\varepsilon}$ and $\mathbf{B}_0$ (Fig. 17).

Experiments using alignment-based ODMR

The lineshapes, saturation behaviour, and angular dependences of the alignment-based double resonance (DRAM) signals described above were experimentally verified in our Fribourg laboratory [32]. All properties were found to be

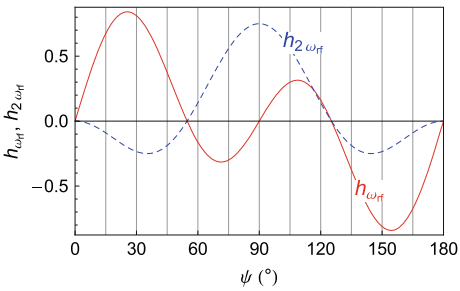

Fig. 21 Orientational dependence of the in-phase and quadrature DRAM signals oscillating at ω_{rf} (*red*, *solid line*) and $2\omega_{rf}$ (*blue*, *dashed*), respectively

perfectly well reproduced by the theoretical signals described above. In the same paper we used the excellent agreement between experimental and theoretical lineshapes to infer the three relevant alignment relaxation rates. In a subsequent study [33], we have optimized the DRAM operation parameters in view of optimizing the DRAM's magnetometric sensitivities. We have performed a quantitative comparison between orientation (DROM)- and alignment (DRAM)-based Cs magnetometers by also varying the Cs number density. We were able to demonstrate a sub-30 fT/$\sqrt{\text{Hz}}$ sensitivity for the DRAM operation that is, however, a factor of ~ 3 worse than the best DROM (i.e., M_x) mode of operation in the same cell. As a side-product the latter study allowed us to infer the collisional disalignment cross-sections.

We note that the alignment-based (DRAM) double resonance magnetometers have other orientational dead-zones than the orientation-based (DROM) magnetometers, a fact that can, in principle be used to infer vector information from magnetometer signals obtained with light of circular and linear polarizations. To our knowledge this access to vector information has never been brought to a practical application in a magnetic resonance-based magnetometer.

6 Light Modulation Based Magnetometers

In their seminal paper Bell and Bloom [34] have shown in 1961 that magnetic resonance transitions can be driven in the atomic ground state by chopping the intensity of a circularly polarized resonant light beam exposed to a transverse field (left graph in Fig. 22). The atomic spin polarization **S** precesses at frequency ω_L. When the on/off-modulation of the light power at frequency[9] ω_{mod} is synchronized with the Larmor precession, the transmitted light power is resonantly enhanced. Modulating the light frequency from on-resonance to off-resonance values (FM-modulation), or modulating the light helicity from σ_+ to σ_- (SM

[9]We note that the modulation frequency ω_{mod} used in this section plays an equivalent role than the rf frequency ω_{rf} in the 'true' magnetic resonance magnetometrs discussed in the previous sections.

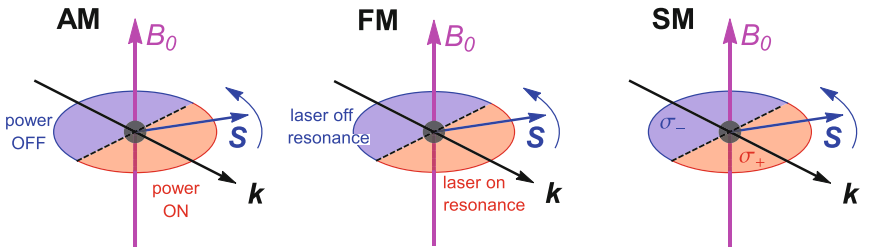

Fig. 22 Principle of polarization build-up with amplitude(AM)-, frequency(FM)-, and polarization (SM)-modulated light: In AM (FM), the pumping light is on (on resonance) and optical pumping occurs while the precessing spin polarization is in the forward direction with respect to **k** (*red half disks*), and no pumping occurs during the second half-period (*blue half-disks*). In SM, on the other hand, pumping occurs both in the forward and backward directions, and one speaks of 'push-pull' pumping

modulation[10]) are alternative ways to realize such modulation resonances (middle and right graph of Fig. 22).

The underlying mechanism can be understood as follows: In the AM and FM schemes the spin polarization is increased by optical pumping during the polarization's motion through the red-shaded areas, while no pumping occurs in the blue-shaded region. In the SM scheme pumping occurs in both regions, in the red region by σ_+ polarized light and in the blue region by σ_--polarized light. Because of this property, SM-pumping is also referred to as 'push-pull pumping' [35].

In 2013 Grujić and Weis [25] have presented a general lineshape theory for the rich structure of the spectra occurring in AM-, FM-, and SM-modulated magnetic resonance experiments. Figure 23 shows the square-wave modulation functions $\xi(t)$ with duty cycle η for the three cases discussed here.

In AM and FM experiments, the cos-Fourier coefficients of $\xi(t)$ are given by

$$g_0 = \eta \quad \text{and} \quad g_{m\neq 0} = \frac{1}{\pi}\frac{\sin(m\pi\eta)}{m}, \tag{91}$$

while for polarization modulation (SM) the g_m read

$$g_0 = 2\eta - 1 \quad \text{and} \quad g_{m\neq 0} = \frac{2}{\pi}\frac{\sin(m\pi\eta)}{m}. \tag{92}$$

[10]For polarization modulation we use the acronym SM—meaning Stokes (parameter) modulation—since the acronym *PM* might be mistaken with the standing acronym for phase modulation.

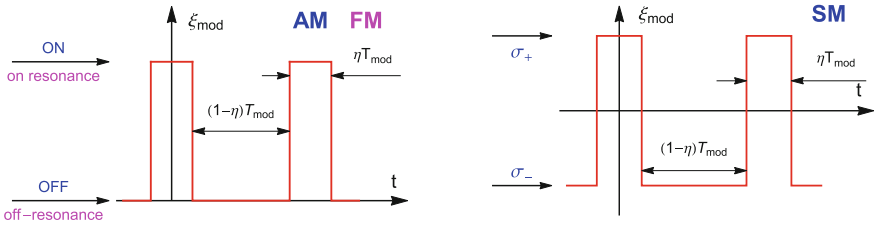

Fig. 23 Modulation function $\xi(t)$ with which a given property of the light beam is modulated. *Left* AM and FM scheme; *Right* SM scheme

For each type of experiment (TOE = AM, FM, SM), the detected power has the structure

$$P^{\mathrm{TOE}}(t) = P^{\mathrm{TOE}}_{\mathrm{DC}} + \sqrt{2}\sum_{q=1}^{\infty} P^{\mathrm{TOE}}_{\mathrm{IP},q}\cos(q\,\omega_{\mathrm{mod}}t) + \sqrt{2}\sum_{q=1}^{\infty} P^{\mathrm{TOE}}_{\mathrm{QU},q}\sin(q\omega_{\mathrm{mod}}t), \quad (93)$$

with time-independent (dc) components ($P^{\mathrm{TOE}}_{\mathrm{DC}}$) as well as components that oscillate in-phase ($P^{\mathrm{TOE}}_{\mathrm{IP},q}$) and in quadrature ($P^{\mathrm{TOE}}_{\mathrm{QU},q}$) with the modulation frequency and harmonics, $q\omega_{\mathrm{mod}}$, thereof.

6.1 DC Signals

The results derived in [25] yield—in the low-power limit—for the time-independent transmission ($P^{\mathrm{TOE}}_{\mathrm{DC}}/P_0$) in each type of experiment

$$\frac{P^{\mathrm{AM}}_{\mathrm{DC}}}{P_0} = (1-\kappa_0 L)g_0 + \beta P_0 \sum_{m=-\infty}^{+\infty} g_m^2 \mathcal{A}_m(\omega_L) \quad (94)$$

$$\frac{P^{\mathrm{FM}}_{\mathrm{DC}}}{P_0} = 1-\kappa_0 L g_0 + \beta P_0 \sum_{m=-\infty}^{+\infty} g_m^2 \mathcal{A}_m(\omega_L) \quad (95)$$

$$\frac{P^{\mathrm{SM}}_{\mathrm{DC}}}{P_0} = 1-\kappa_0 L + \beta P_0 \sum_{m=-\infty}^{+\infty} g_m^2 \mathcal{A}_m(\omega_L), \quad (96)$$

with $\beta = \alpha^{(1)}_{F,F'}\kappa_0 L\, S_\infty/P_{\mathrm{sat}}$, where $\alpha^{(1)}_{F,F'}$ and $S_\infty, P_{\mathrm{sat}}$ have been introduced in Sects. 2.3, and 2.1, respectively.

6.2 In-Phase and Quadrature Signals

In the same low-power limit, the in-phase transmission signals read

$$\frac{P_{\mathrm{IP},q}^{\mathrm{AM}}}{P_0} = \sqrt{2}(1-\kappa_0 L)\, g_q + \sqrt{2}\,\beta P_0 \sum_{m=-\infty}^{+\infty} g_m (g_{q-m} + g_{q+m})\, \mathcal{A}_m(\omega_L) \tag{97}$$

$$\frac{P_{\mathrm{IP},q}^{\mathrm{FM}}}{P_0} = -\sqrt{2}\kappa_0 L\, g_q + \sqrt{2}\,\beta P_0 \sum_{m=-\infty}^{+\infty} g_m (g_{q-m} + \mathrm{g}_{q+m})\, \mathcal{A}_m(\omega_L) \tag{98}$$

$$\frac{P_{\mathrm{IP},q}^{\mathrm{SM}}}{P_0} = \sqrt{2}\beta P_0 \sum_{m=-\infty}^{+\infty} g_m (g_{q-m} + g_{q+m})\, \mathcal{A}_m(\omega_L), \tag{99}$$

while the quadrature signals are given by

$$\frac{P_{\mathrm{QU},q}^{\mathrm{AM}}}{P_0} = \sqrt{2}\beta P_0 \sum_{m=-\infty}^{+\infty} g_m (g_{q-m} - g_{q+m}) \mathcal{D}_m(\omega_L) \tag{100}$$

$$\frac{P_{\mathrm{QU},q}^{\mathrm{FM}}}{P_0} = \sqrt{2}\beta P_0 \sum_{m=-\infty}^{+\infty} g_m (g_{q-m} - g_{q+m}) \mathcal{D}_m(\omega_L) \tag{101}$$

$$\frac{P_{\mathrm{QU},q}^{\mathrm{SM}}}{P_0} = \sqrt{2}\beta P_0 \sum_{m=-\infty}^{+\infty} g_m (g_{q-m} - g_{q+m}) \mathcal{D}_m(\omega_L), \tag{102}$$

respectively. The absorptive and dispersive lineshape functions are given by

$$\mathcal{D}_m(\omega_L) = \frac{m x_{\mathrm{mod}} - x_L}{(m x_{\mathrm{mod}} - x_L)^2 + 1} \quad \text{and} \quad \mathcal{A}_m(\omega_L) = \frac{1}{(m x_{\mathrm{mod}} - x_L)^2 + 1}, \tag{103}$$

with $x_{\mathrm{mod}} = \omega_{\mathrm{mod}}/\gamma$ and $x_L = \omega_L/\gamma$.

Figure 24 shows the spectra of $P_{\mathrm{DC}}, P_{\mathrm{IP}}$ and P_{QU} given by the expressions above for the AM (left column), FM (middle column) and SM (right column) modulation schemes, respectively. For each type of experiment the figure shows—from top to bottom—the (dc) spectra recorded without demodulation of the photocurrent, the in-phase (IP) components when the photocurrent is demodulated at ω_{mod} ($q = 1$) and $2\omega_{\mathrm{mod}}$ ($q = 2$), respectively, and the quadrature (QU) components demodulated at ω_{mod} ($q = 1$) and $2\omega_{\mathrm{mod}}$ ($q = 2$), respectively. Resonances occur in zero field and for Larmor frequencies given by overtones of the modulation frequency, i.e., $\omega_L = n\omega_{\mathrm{mod}}$.

The relative magnitudes of the resonances in the AM and FM spectra are identical. However, they are superposed on different magnetic field independent offset levels that depend on $\kappa_0^{\mathrm{unpol}} L$ and which may be a source of additional noise

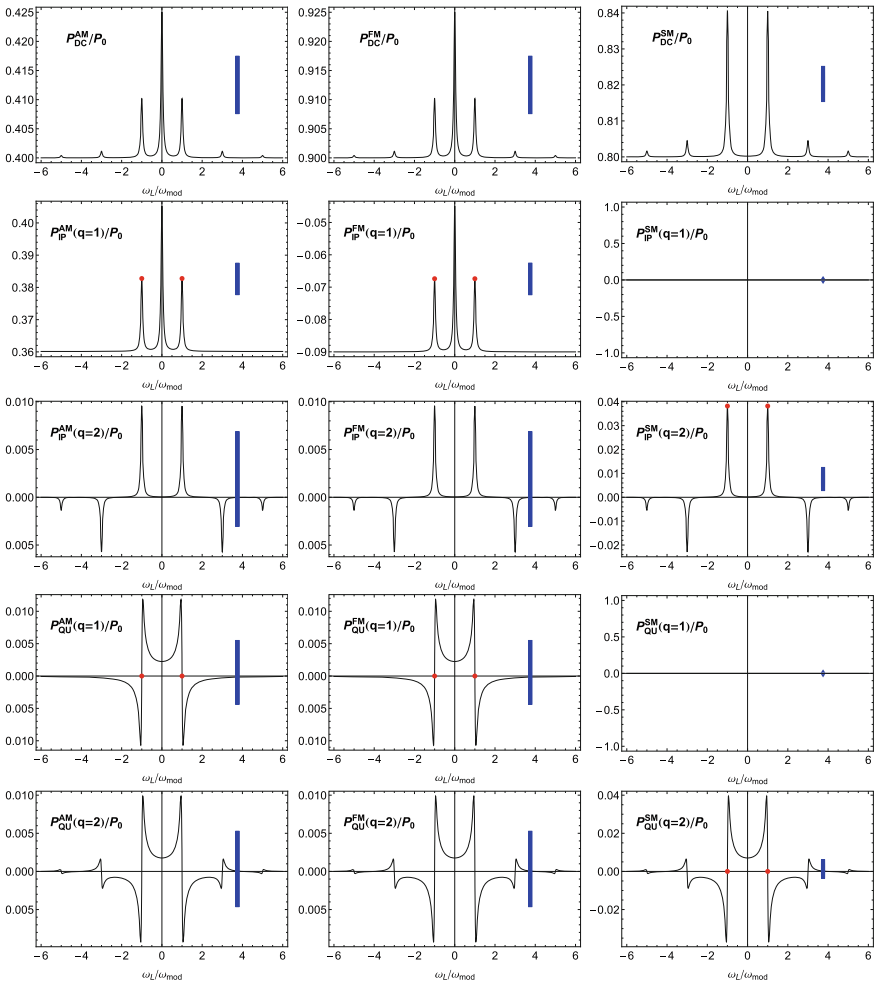

Fig. 24 Magnetic resonance line shapes induced by amplitude-modulated (AM, *left*), frequency-modulated (FM, *middle*), and polarization-modulated (SM, *right*) light with 50 % duty cycle ($\eta = 0.5$). Numerical values obtained with $\kappa_0^{\text{unpol}} L = 0.2, \beta = 0.5, P_0 = P_{\text{sat}}$, and a resonance quality factor $Q = \omega_L/\gamma$ of 20. The *dots* indicate the strongest signals for each type of modulation. The *vertical bars* all have the same absolute magnitude, helping to compare relative signal amplitudes

in experiments. For a better judgment of the relative magnitudes of all signals in the figure we have added the vertical (blue) bars in the graphs, which all have an absolute length of 0.01 units.

The SM spectra produced by polarization modulated light show different features, which are due to the bipolar nature of their modulation function, compared to the unipolar AM/FM modulation functions Fig. 23. The most noticeable feature of

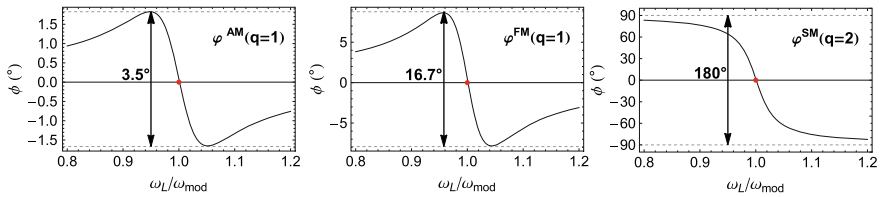

Fig. 25 Signal phase, defined by $\tan\phi = P_{\mathrm{QU}}^{\mathrm{TOE}}/P_{\mathrm{IP}}^{\mathrm{TOE}}$, of the different modulation schemes (from left to right $TOE = AM, FM, SM$). Functions calculated with the same parameter values of $\kappa_0^{\mathrm{unpol}}L$, β, and P_0/P_{sat} as in Fig. 24

the SM spectra is that the in-phase components are background-free and do not show up when the signals are demodulated at the fundamental of the modulation frequency ω_{mod}.

The red dots on the IP spectra mark the largest amplitude resonances that occur —for all spectra—at $\omega_L/\omega_{\mathrm{mod}} = \pm 1$. We note that the resonance amplitudes in the SM spectra are twice larger in the SM than in the AM/FM spectra, a consequence of the push-pull nature of the optical pumping with polarization-modulated light.

The quadrature spectra show resonances at the same positions as the in-phase signals. However, their relative magnitudes differ from those of the in-phase signals because of the minus sign in the g_m-dependent amplitudes of Eqs. 97–99 compared to the plus sign in corresponding Eqs. 100–102.

The background offset in the AM and FM spectra has a severe consequence on the signal phase, defined by $\tan\phi = P_{\mathrm{QU}}^{\mathrm{TOE}}/P_{\mathrm{IP}}^{\mathrm{TOE}}$. Figure 25 shows the detuning dependences of the phase in the three modulation schemes in the vicinity of the strongest resonances (marked by red dots in Fig. 24). Because of the background in the AM and FM signals, the total phase swing (with the selected experimental parameters) is only 3.5° and 16.7°, respectively, while the SM signal shows a full phase swing of 180°, as for M_x-magnetometers. As a consequence, the discriminator signal $d\phi/d\omega_{\mathrm{rf}}$ is less well suited for driving magnetometer building on AM and FM with a phase feedback loop. Since polarization modulation (SM) produces background-free signals that are twice larger than the AM/FM signals, and because of its larger discriminator choice, it has—among the three discussed schemes—the largest potential for feedback-operated (single beam) magnetometry.

Experiments using light modulation techniques

Amplitude modulation (AM): Grujić and Weis have verified [25] that the experimental in-phase and quadrature lineshapes obtained with amplitude-modulated (AM) light are indeed well described by Eqs. 97 and 100 for $q = 1\ldots6$, the $q = 1, 2$ cases of which being shown above in the left column of Fig. 24. Demodulation signals with $q = 1$ were presented earlier by Schultze et al. [36]. The work described in the latter two references was based on a single light beam. The ultimate magnetometric sensitivity with an AM-based magnetometer is

obtained with a dual (pump/probe) scheme (see Chap. 14 for more details on this variant). Note that all quoted work used circularly-polarized pump light.

Frequency modulation (FM): Frequency modulation has been used for realizing single beam magnetometers with linearly polarized light and polarimetric detection [37, 38] yielding a demonstrated sub-10 fT/$\sqrt{\text{Hz}}$ sensitivity.

Polarization modulation (SM): Fescenko et al. have studied the dc signals obtained with σ_+/σ_- polarization-modulated light [39], the polarization modulation equivalent of Bell and Bloom's seminal work [34] on amplitude modulation. It was shown that the signals are well described by the above model function (Eq. 94) for any duty cycle η of the polarization modulation function. Breschi et al. have studied the P_{IP} and P_{QU} resonance lineshapes in the SM scheme for arbitrary modulation duty cycles η using phase sensitive detection. They found good agreement [40] with the lineshapes predicted by Eqs. 99 and 102. The same authors have built a push-pull magnetometer [35] based on circular polarization-modulated light using active feedback of the phase signal, similar to the method described in Sect. 7 for the M_x magnetometer. They could demonstrate a sub-20 fT/$\sqrt{\text{Hz}}$ sensitivity with this scheme with a single light beam in a paraffin-coated room-temperature Cs vapor cell. More recently Bevilacqua and Breschi [41] have modeled and studied in the same apparatus SM spectra by modulating the orientation of a linearly-polarized laser beam by 90°. The claim is made that this modulation scheme is free of orientational dead zones.

7 Practical Implementation of ODMR Magnetometers

The performance of an ODMR magnetometer in terms of its magnetometric sensitivity depends on many details of its practical implementation. In this section we will present details on the experimental realization of a specific ODMR magnetometer, addressing hardware, signal acquisition and processing electronics. We will focus on the $\mathbf{B}_{\text{rf}} \| \mathbf{k}$ variant of the M_x magnetometer as described in Sect. 4.2 using the general form of the ODMR signals from Sect. 4.5. We note, however, that the concepts discussed here can be used in a similar way to optimize any other ODMR-based magnetometer.

7.1 Experimental Setup

Figure 26 shows a typical experimental setup for an M_x ODMR magnetometer. The light is generated by a single mode diode laser and transmitted to the magnetometer head by an optical fiber. A fraction of the light is supplied to a spectroscopy system that actively stabilizes the light frequency in resonance to the desired atomic

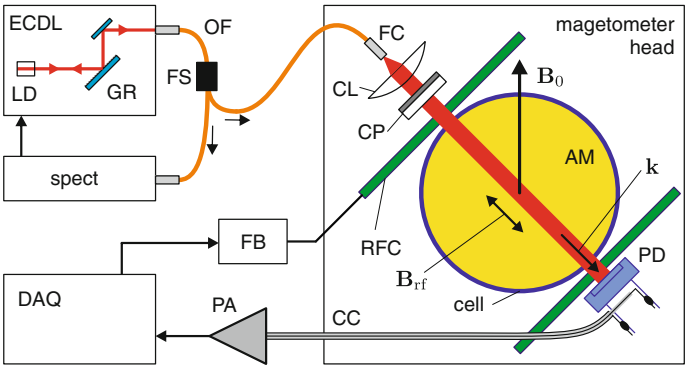

Fig. 26 Schematic of an experimental M_x magnetometer (not to scale). The light from a single mode diode laser (here shown as extended cavity laser, ECDL, with laser diode, LD, and grating, GR) is carried by an optical fiber (OF) to the magnetometer head. A fiber splitter (FS) supplies light to the spectroscopy setup (spect) used to stabilize the laser frequency. In the magnetometer head a lens (CL) forms a collimated beam which is polarized by a circular polarizer (CP). The light traversing the cell containing the atomic medium (AM) is detected by a photodiode (PD) converting its power to a photocurrent that is carried by a coaxial cable (CC) to the pre-amplifier (PA). Note the details on how the CC is connected to the PD in order to minimize electrical pick-up by inductive coupling. The AM is exposed to an rf field $\mathbf{B}_{rf} \| \mathbf{k}$ produced by rf-coils (RFC). The field of interest $\mathbf{B}_0$ oriented at $|\theta_B| = \pi/4$ with respect to $\mathbf{k}$ maximizes the signal. The data acquisition (DAQ) system samples and processes the the signal from the PA and generates the feedback signal (FB) for magnetometer operation. Details of DAQ and FB shown in Fig. 33

transition.[11] In the sensor head the light interacts with the atoms contained in a glass cell. Prior to entering the cell the laser beam is collimated and polarized. For the standard M_x magnetometer a circular light polarization is ensured by a combination of linear polarizer and quarter-wave plate. The light power P transmitted through the cell is detected by a photodiode. The combination of optical fiber output and collimation lens defines the light propagation direction and ensures that the light is efficiently transmitted to the photodiode. All components in the sensor head must be non-magnetic to prevent local magnetic fields and gradients produced by magnetized components from reducing the spin coherence time, thereby degrading magnetometer sensitivity. It may be a challenging task to find truly non-magnetic components. For example, the gold-plated contacts in many standard electronic components are usually applied over a thin layer of nickel. Another source of magnetic contamination can be pigments in plastics (in particular black pigments that are often based on iron oxide). We successfully used polycarbonate for mechanical parts which is relatively strong, easily machinable, non-magnetic and vacuum compatible.

[11] In alkali atoms the $F \rightarrow F - 1$ hyperfine component of the $|n^2S_{1/2}\rangle \rightarrow |n^2P_{1/2}\rangle$ transition yields the largest signals.

7.2 *Magnetometer Sensitivity*

As discussed in Sect. 4.5, the magnetometric information of interest is encoded in the frequency, $f_{\rm rf} = \omega_{\rm rf}/2\pi$, the amplitude, $P_{\rm R}$, and the phase ϕ of the light power $P(t)$ detected by the photodiode. $P_{\rm R}$ and ϕ show resonant behavior if $\omega_{\rm rf}$ is chosen close to $\omega_{\rm L}$. Taking optical power broadening (Eq. 45) into account, Eqs. 72 and 73 yield

$$P_{\rm R} = \widetilde{P}\frac{\sqrt{\delta\omega^2 + \Gamma^2}\,\widetilde{\Omega}}{\delta\omega^2 + \Gamma^2 + \widetilde{\Omega}^2}\,|\sin\theta_B \cos\theta_B| \tag{104}$$

$$\tilde{\phi} = \phi_0 - \arctan\frac{\delta\omega}{\Gamma}, \tag{105}$$

with $\delta\omega = \omega_{\rm rf} - \omega_L$. The orientational dependence $\sin\theta_B \cos\theta_B$ takes the value 1/2 at the optimum sensitivity conditions $\theta_B = \pi/4$ or $3\pi/4$.

Figure 27 shows measurements of the magnetic resonance line-shapes. The phase-signal $\tilde{\phi}(\omega_{\rm rf})$ is unique among the plotted signals, since its shape is not affected by the driving rf amplitude (no rf power broadening). It is also independent

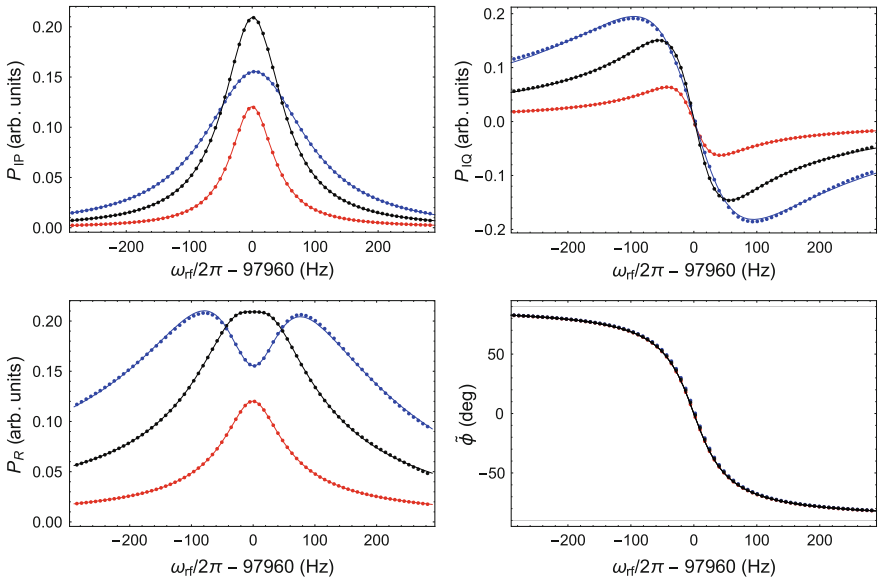

Fig. 27 Experimental magnetic resonance line shapes for different rf saturation parameters corresponding to Fig. 9. The *points* represent the measured dependence of the signals $P_{\rm IP}, P_{\rm QU}, P_{\rm R}$, and $\tilde{\phi}$ on frequency $\omega_{\rm rf}$. The *solid lines* are fits of the theoretical models given by Eqs. 78–80 and 72. The graphs are shown for effective rf saturation parameters $\widetilde{G}_{\rm rf}$ = 0.2 (*red*), 2 (*black*) and 10 (*blue*)

of the overall signal amplitude $\widetilde{P}$ (Sect. 4.5). For that reason we use the amplitude and phase representation of $P(t)$ since it decouples important influence factors in the sensitivity optimization process.

Signals from an M_x magnetometer are usually recorded by photodiodes that convert the photon flux into a photocurrent I (flux of photo-electrons) that is proportional to the light power, i.e., the sum of all photon energies detected per unit time. The quantum efficiency (QE) of a photodiode represents the ratio of photo-electrons produced per second to the number of incident photons per second ($\dot{N}_e = QE\,\dot{N}_\gamma$). Commercial Si PIN photodiodes [42] achieve radiant sensitivities

$$\eta = \frac{I}{P} = \frac{e\,\lambda}{h\,c}\,QE \approx \frac{1242}{\lambda\,(\mathrm{nm})}\,QE, \tag{106}$$

on the order of 0.6 μA/μW that correspond to $QE = 97\ldots83\,\%$ in the wavelength range $\lambda = 770\ldots894$ that is relevant for alkali ODMR magnetometers. Given the almost perfect conversion from photons to photoelectrons we will discuss magnetometer performance in terms of photocurrent.

The on-resonance ($\delta\omega = 0$) signal amplitude of the photocurrent I_R reads

$$I_\mathrm{R} = \widetilde{I}\,\frac{\Gamma\,\widetilde{\Omega}}{\Gamma^2 + \widetilde{\Omega}^2} \quad \text{with } \widetilde{I} = \eta\widetilde{P} = \eta S_0 P_0 \kappa_0^{\mathrm{unpol}} L \alpha^{(1)}_{F,F'}. \tag{107}$$

The absorption coefficient $\kappa_0^{\mathrm{unpol}} = n\sigma_0^{\mathrm{unpol}}$ is proportional to the atom number density n and the on-resonance light absorption cross-section $\sigma_0^{\mathrm{unpol}}$. The current amplitude $\widetilde{I}$, which is usually determined experimentally, contains further factors like the sample length L and the photosensitivity η of the photodiode.

For an M_x magnetometer the sensitivity to changes in the magnetic field can be easily estimated in the free running mode in which ω_rf has a fixed value close to resonance, e.i. $|\omega_\mathrm{rf} - \omega_L| \ll \Gamma$. In the free running mode, phase changes $\Delta\phi$ are proportional to magnetic field changes

$$\Delta\phi = \Delta B \left.\frac{d\phi}{dB}\right|_{\delta\omega=0} = \Delta B\,\frac{\gamma_F}{\Gamma}. \tag{108}$$

This expression can be used to convert statistical phase errors to equivalent magnetic field errors that quantify the statistical sensitivity of the magnetometer. Conversely, the same expression can be used to convert systematic phase uncertainties (phase shifts) to systematic field estimation errors.

Statistical errors of a quantity $x(t)$ are most commonly quantified using the standard deviation σ_x of the spectral noise density $\rho_x(f)$, defined by the variance

$$\sigma_x^2 = \int_0^{f_{\rm bw}} \rho_x^2(f) df. \tag{109}$$

Here $f_{\rm bw}$ is the signal bandwidth. For signals sampled at a rate $f_{\rm SR}$ it represents the detection bandwidth given by the Nyquist frequency $f_N = f_{\rm SR}/2$. If the spectral density does not depend on frequency (white noise), Eq. 109 simplifies to $\sigma_x = \rho\sqrt{f_{\rm bw}}$. In order to avoid complications arising from the dependence of σ_x^2 on $f_{\rm bw}$, we use the noise density ρ_x to quantify the magnetometer sensitivity. From Eq. 108 it follows that

$$\rho_B = \frac{\Gamma}{\gamma_F}\rho_\phi, \tag{110}$$

the unit of ρ_B and ρ_ϕ being T/Hz$^{1/2}$ and rad/Hz$^{1/2}$, respectively. Their numerical values are equal to the standard deviation for a bandwidth of 1 Hz, which is equivalent to an integration time of 0.5 s.

Figure 28 shows the definition of the phase ϕ and the amplitude $I_{\rm R}$ that describe the Fourier component of the photocurrent $I(t)$ at the frequency $f_{\rm rf}$. The peak amplitude $I_{\rm R}$ that is used throughout this section is related to the root-mean-square (RMS) amplitude by $I_{\rm R}^{\rm RMS} = I_{\rm R}/\sqrt{2}$. The process of extracting parameters like amplitude and phase from a time series of sampled current values $I_i = T(t_i)$ is called estimation [43]. In the estimation process statistical fluctuations of I propagate to fluctuations of ϕ and $I_{\rm R}$. Using estimation theory it can be shown [44] that the noise density of an ideal phase estimator is given by

$$\rho_\phi = \frac{\sqrt{2}\rho_I}{I_{\rm R}} = \frac{\rho_I}{I_{\rm R}^{\rm RMS}}. \tag{111}$$

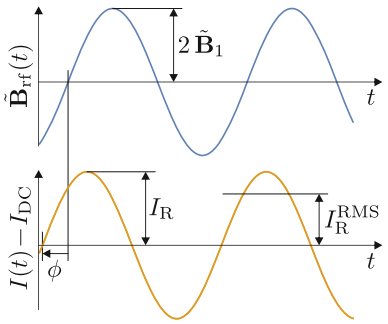

Fig. 28 The detected photocurrent $I(t) = I_{\rm DC} + I_{\rm R}\sin(\omega_{\rm rf}t + \phi)$, is defined by its dc-component $I_{\rm DC}$, its amplitude $I_{\rm R}$ and its phase ϕ with respect to the driving magnetic field $\widetilde{\mathbf{B}}_{\rm rf}(t)$. The plot shows a positive phase shift $\phi > 0$ of $I(t)$ with respect to $\widetilde{\mathbf{B}}_{\rm rf}(t)$

Using Eqs. 108 and 111 the statistical magnetometer sensitivity thus reads

$$\rho_B = \frac{\sqrt{2}\,\rho_I\,\Gamma}{I_R \gamma_F} = \sqrt{2}\rho_I \frac{\Gamma^2 + \widetilde{\Omega}^2}{\widetilde{I}\gamma_F\,\widetilde{\Omega}}. \tag{112}$$

The following sections discuss how an efficient implementation achieves the best sensitivity ρ_B under given constraints imposed by technical and economical considerations.

7.3 Noise in the Optical Detection Process

The fundamental noise in the detection process is the electron shot-noise caused by the statistical generation of discrete electron-hole pairs in the photodiode. The photocurrent shot-noise density $\rho_I^{(\mathrm{sn})}$ represents a lower bound for the current noise density, i.e.,

$$\rho_I \geq \rho_I^{(\mathrm{sn})} = \sqrt{2eI_{\mathrm{DC}}},$$

where I_{DC} is the dc photocurrent which is proportional to the detected power P_{DC} (see Eq. 31). Since $\rho_I^{(\mathrm{sn})} \propto \sqrt{P_{\mathrm{DC}}}$, an increase of the light power P_{DC} will result in a better signal to noise density ratio if the signal increases with P_{DC} faster than $\sqrt{P_{\mathrm{DC}}}$, which is usually the case in the low power limit.

In addition to the fundamental shot-noise, technical noise sources will in general contribute to the detected photocurrent noise. Technical noise sources affecting ρ_P, and hence ρ_I directly are:

- At low frequencies f, the power emitted by laser diodes has a power spectral density $\rho^2 \propto 1/f$ (flicker noise, pink noise) caused by processes in the laser diode as well as noise in the laser driving electronics. An active power stabilization can reduce this contribution.
- The effect of mechanical vibrations on the light transmission system may induce noise in the detection system. As an example we consider light transport by an optical multi-mode fiber. While the injected light is in general linearly polarized, the multiple transverse modes propagating in the fiber along different paths lead to a strong, albeit not perfect depolarization of the exiting light. Changes in the path lengths may be caused by small mechanical fiber motions induced by sound and/or vibrations. As a result, the emerging light's polarization may change in degree and orientation, which implies—after the linear polarizer—intensity fluctuations. Remedies for this are a rigid mounting of the fiber and an efficient polarization scrambler consisting in coiling up the fiber in multiple loops. Large fiber diameters (e.g. 400–800 μm) also help to suppress the fluctuations since the power distributes to a large number of transverse and

polarization modes which all contribute to the transmitted power and thus partly average out fluctuations of individual modes. For that reason single-mode fibers do not prevent this effect at all since the single transverse mode in the fiber still has two polarization modes. Polarization-maintaining single-mode fibers, however, strongly suppress the fluctuations since the two polarization modes of the core do not couple. Since polarization-maintaining single-mode fibers are an order of magnitude more expensive than large-diameter fibers they are currently not an economical solution for sensor arrays.

- Frequency noise in the laser is usually caused by changes of the effective length of the laser cavity (see Fig. 26) which is influenced by many parameters. Those include mechanical vibrations (sound), changes in the refractive index of the medium (air) in the cavity induced, e.g., by pressure changes, and injection current- or temperature-induced changes of laser diode's refractive index. Frequency noise can be converted to amplitude noise through the laser frequency-dependent atomic absorption (FM-AM noise conversion). Passive frequency stability is achieved by a rigid and sealed laser cavity design, while active schemes, such as the 'photocurrent subtraction' method [45] may further suppress such noise contributions.

The technical noise contributions scale linearly with P_{DC} and thus dominate the noise spectrum for sufficiently large laser powers. Figure 29 shows the typical $1/f$ spectral dependence often encountered in those noise contributions.

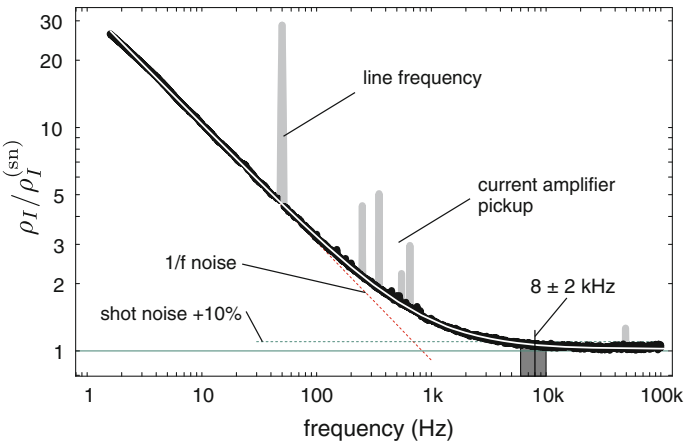

Fig. 29 Noise spectral density (normalized to the theoretical shot-noise density $\rho_I^{(\mathrm{sn})}$) of the light power emitted by a diode laser, producing a photocurrent I_{DC} of 1.8 μA in a photodiode. The (*thick*) *black curve* represents measured data that was transformed using a Hann-windowed fast Fourier transform (FFT). Many FFT spectra were averaged to reduce the scatter and facilitate the comparison with the model function $\rho(f) = \sqrt{\rho_A^2/f + \rho_B^2}$ shown as (*thin*) *white curve*. The *gray peaks* are pickup by the current pre-amplifier and were ignored in the fit. The low frequency part of the signal is dominated by technical noise with a $\rho^2 \propto 1/f$ frequency dependence. For frequencies above 4 kHz the noise is within 10 % of shot-noise. The *gray band* represents the noise components that would pass a lock-in amplifier with an 8 kHz reference frequency and a 2 kHz filter bandwidth

A different class of noise contributions, that do not depend on laser power, are caused by processes that influence the photocurrent on its transmission from the photodiode to the processing electronics. In the circuit that carries the photocurrent an additional ('pick-up') current can be induced by inductive and/or capacitive coupling. Inductively coupled noise is typically observed at the line frequency and its odd harmonics (Fig. 29). Also the oscillating magnetic field used to drive the magnetic resonance in the atomic medium can couple to the photocurrent. The latter contributions are easy to distinguish from light-induced noise since they do not disappear when blocking the laser beam. Minimizing enclosed areas (pick-up loops) in the coupling of the photodiode to the coaxial cable, such as shown in Fig. 26 reduces this noise contribution.

7.4 Optimization of Linewidth and Signal Amplitude

In a well-optimized ODMR setup the noise should be close to the photoelectron shot-noise $\rho_I^{(\mathrm{sn})}$ and thus depend only on the detected light power P_{DC}. The amplitude $\widetilde{I}$ in Eq. 112 and the magnetic resonance linewidth Γ, however, depend on many parameters that shall be discussed in this section.

It is generally desirable to operate ODMR magnetometers with linewidths as narrow as possible since statistical (Eq. 112) and many systematic errors (Eqs. 120 and 121) scale with Γ. The minimal linewidth achievable in a given ODMR setup is limited by processes that cause atomic spin relaxation. Those processes include collisions of the alkali atoms with the walls of the glass-cell and with other atoms or molecules. In order to prevent spin relaxation during wall collisions, the rate at which such collisions occur can be significantly decreased by a buffer gas in which the alkali atoms undergo a diffusive motion that slows down their wall collision rate. However, when the buffer gas density is too high, buffer gas collisions will depolarize the alkali atoms, so that there is—for each atom and buffer gas species—an optimal buffer gas pressure [46]. Under optimal buffer gas conditions the atoms may interact during several ms with the magnetic resonance driving rf field, thereby leading to a corresponding reduction of the magnetic resonance linewidth. Since the volume that each atom explores during its spin coherence time is much smaller than the cell, signal/noise can be increased by illuminating a large fraction of the cell, thereby increasing the total number of atoms contributing to the signal. However, buffer gas cells put tighter constraints on the magnetic field homogeneity since the magnetic resonance line will experience an inhomogeneous broadening in presence of a magnetic field gradient. The narrow linewidths due to the atomic confinement can therefore only be observed when the spatial field variation ΔB_0 over the illuminated volume is smaller than the magnetic resonance linewidth ($\gamma_F \Delta B_0 < \Gamma$). A further point has to be noted when dealing with buffer gas cells. Under buffer gas conditions that minimize the magnetic resonance linewidth, the (natural) optical linewidth of the pumping/probing transition is usually strongly broadened with a

corresponding decrease of the optical peak absorption coefficient κ_0 that determines the magnetometric sensitivity. As a consequence, buffer gas magnetometers require in general a larger laser power than vacuum cells in order to make up for the latter signal loss.

A second method to prevent spin relaxation during wall collisions are wall coatings that shorten the time atoms spend close to the wall. Such repellant coatings are typically made of paraffins [26] or silanes (see, e.g., Chap. 11 in [3]) and can reduce the probability for spin relaxation per wall collision from 1 to below 10^{-3}. Anti-spin-relaxation coated cells typically do not contain any buffer gas which allows the atoms to explore the whole cell volume at their thermal velocity. It is not desirable that atoms collide with the droplet of solid/liquid alkali metal since the metal surface efficiently depolarizes the atoms. For that reason the bulk metal is contained in a side-arm that is connected to the main cell volume by a capillary (Fig. 37). The ballistic motion of the alkali atoms in coated vacuum cells leads to a reduction in gradient induced line broadening since every atom explores the whole cell volume and effectively averages out odd magnetic field gradients (motional narrowing [47]). For that reason coated vacuum cells are to be preferred if the presence of magnetic field gradients can not be excluded.

The achievable linewidth is a function of temperature since the density n and velocity of the atoms are strongly temperature dependent. The signal amplitude also depends, via n, on temperature. Both dependencies are difficult to model precisely and require an experimental optimization [27]. In general, atomic media contained in a small volume require higher optimum temperatures than large volume media. For spin anti-relaxation coated Cs cells of 30 mm diameter the optimum operation temperature is close to room temperature [26].

Optimum rf-power: The magnetometer noise density ρ_B is minimized for $\widetilde{\Omega} = \Gamma$, for which Eq. 112 reduces to

$$\rho_B = 2\sqrt{2}\rho_I \frac{\Gamma}{\gamma_F \widetilde{I}}. \tag{113}$$

Experimentally, this optimum (cf. Fig. 30) is easy to find in the free running mode with ω_{rf} set to ω_{L}. The rf-amplitude that achieves the largest on-resonance amplitude (Eq. 107) is the optimal choice. This is a simple one-dimensional optimization problem which can be easily automatized. In the following optimization steps we assume that the rf-amplitude is always optimized.

Optimum laser power: Many parameters that determine the sensitivity ρ_B (Eq. 113) depend on the dc laser power P_0 incident on the atomic medium which is related to the dc power P detected by the photodiode (Eq. 7). The signal amplitude $\widetilde{I}$ is proportional to P_0 and the equilibrium spin polarization S_0 created by optical pumping (see Eqs. 5 and 107 and discussion in Sect. 2.1)

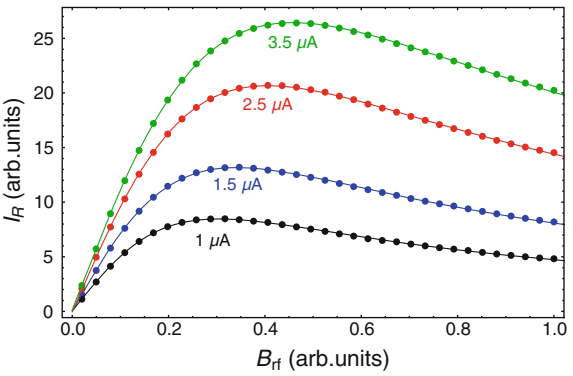

Fig. 30 Experimental magnetic resonance amplitudes I_R (with ω_{rf} set to ω_L) as a function of rf-amplitude B_{rf} for different dc photocurrents

$$\widetilde{I} \propto P_0 S_0 \propto P_0 \frac{G_{op}}{G_{op}+1} = P_0 \frac{P_0/P_{sat}}{P_0/P_{sat}+1}.$$

Here P_{sat} is the saturation power of the optical pumping process which has to be determined experimentally [26]. The laser power further influences the relaxation rate by optical power broadening (see Eq. 45)

$$\Gamma = \gamma + \gamma_p = \gamma\,(1+\gamma_p/\gamma) = \gamma\,(1+P_0/P_{sat}) = \gamma\,(1+G_{op}). \tag{114}$$

Finally, the noise—in the case of shot noise limited operation—scales[12] as $\rho_I \propto \sqrt{P_0}$. Combining the mentioned effects yields the following expression for the scaling off the sensitivity (Eq. 113) with respect to laser power

$$\rho_B \propto \rho_I \Gamma \widetilde{I}^{-1} \propto \sqrt{P_0}\frac{(1+P_0/P_{sat})^2}{P_0^2/P_{sat}} \propto \frac{(1+G_{op})}{G_{op}^{3/2}}.$$

The last expression is minimized for $G_{op} = 3$ which means that the optimal power broadens the resonance by a factor 4, according to Eq. 114. Figure 31 shows how the sensitivity degrades with respect to the optimal sensitivity ρ_B^{opt} at $G_{op} = 3$. We note that this simplified derivation of the optimal laser power does not take all possible effects into account. For example the loss of spin polarization due to hyperfine pumping causes an additional reduction of $\widetilde{I}$ for larger laser powers and thus a smaller optimal power. Those processes depend on the atoms' level structure and the used hyperfine transition and are thus best optimized experimentally. We usually start with a laser power that doubles the magnetic resonance width ($G_{op} = 1$) and then increase the power until the optimum is reached.

[12]Here we used the proportionality between P_0 and P_{DC} to write the scaling of the noise with respect to P_0.

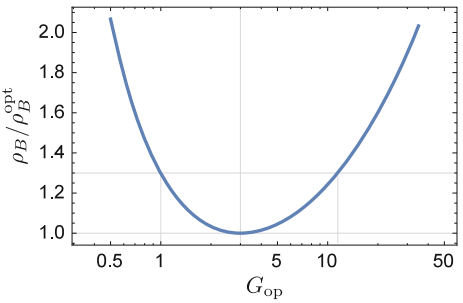

Fig. 31 Magnetometer sensitivity ρ_B relative to the optimized sensitivity ρ_B^{opt} as a function of the optical pumping saturation parameter G_{op}. A sensitivity within 30 % of the optimum is achieved for $1 < G_{\mathrm{op}} < 11.5$

7.5 Signal Acquisition and Feedback Control Electronics

The role of the acquisition and control electronics is to record the photodiode signal and to process it in order to generate the oscillatory signal sent to the rf coils for driving the magnetic resonance.

Self-oscillation mode: The simplest way of operating the M_x magnetometer is the so-called 'self-oscillating' scheme, described in detail by Bloom in 1962 [48] (more recent developments are addressed by Alexandrov and Vershoskiy [3]). In this scheme, the ac part of the photocurrent—after suitable amplification and phase-shifting—is directly used to drive the rf coils, leading to a spontaneous oscillation of the system at a frequency close to the Larmor frequency. An automatic gain control system (AGC) stabilizes the amplitude of the coil current. The magnetic field modulus is inferred by sending an—eventually band-pass filtered—copy of the generated signal to a frequency counter. Traditionally analog circuits were used to generate the oscillation directly by amplifying and phase shifting the measured signal. As shown in Ref. [48], the self-oscillating magnetometer has a quasi-instantaneous response to field changes, i.e., a bandwidth that is limited only by delays in the analog processing electronics. Such delays can be caused by the settling time $\tau \approx 2Q/\omega_{\mathrm{rf}}$ of analog phase shifters and bandpass-filters with quality factor Q.

Using a commercial lock-in amplifier: In order to achieve the ideal magnetometer sensitivity given by Eq. 112 an ideal phase estimator (Eq. 111) is needed. Commercially available digital dual-phase lock-in amplifiers [49–51] approximate ideal phase estimators for a wide range of signals—including ODMR magnetometers.

Figure 32a shows a lock-in amplifier (LIA) connected to a magnetometer head. The reference output $\mathrm{ref}_{\mathrm{out}}$ is a pure sinusoidal wave that is phase-locked to the reference input. It is used to generate the rf-field B_{rf} that drives the magnetic resonance in the magnetometer, thus defining ω_{rf}. The reference phase ϕ_{ref} can be set such that the phase output ϕ_{out} measures the signal $\tilde{\phi}$ (for details refer to Eq. 117 and Fig. 35). As discussed earlier, the phase signal can be used to measure the magnetic field directly. Alternatively, it can be used to control ω_{rf} in a feedback loop. The outputs of modern digital LIA are typically available as scaled analog

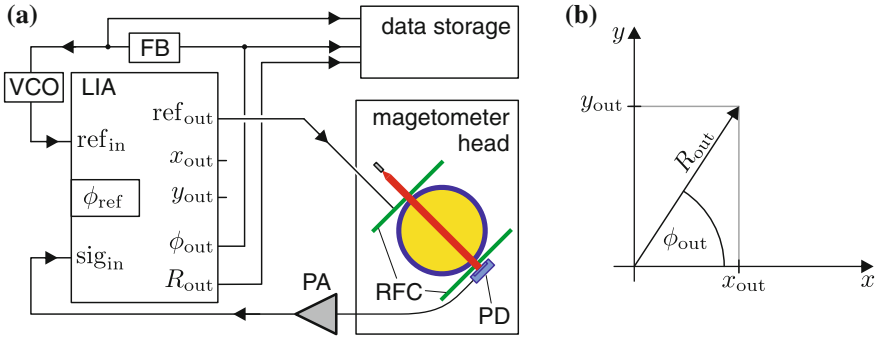

Fig. 32 **a** Schematic connections of the magnetometer head to a lock-in amplifier (LIA) that detects the phase of the preamplified (PA) photodiode (PD) signal. The feedback controller (FB) provides the LIA reference frequency via a voltage controlled oscillator (VCO). The oscillating magnetic field in the magnetometer head is generated by the rf-coils (RFC) which are driven by the reference output of the LIA. **b** The output signals of the LIA represent a 2D vector which can either be represented by the angle ϕ_{out} and the radius R_{out} or its x and y components. These signals are proportional to $\tilde{\phi}, R, \tilde{S}_{\text{IP}}$ and $\tilde{S}_{\text{QU}}$ of the magnetometer's theoretical model (Sect. 4)

voltages and in digital form. The implementation of the feedback control using the analog signals is straightforward with an analog feedback controller and a voltage controlled oscillator (VCO). Internally all digital lock-in amplifiers use digital signal processing schemes very similar to the one discussed in the following section.

Using digital signal processing: For operating multi-sensor magnetometer arrays, one cannot rely on commercial lock-in amplifiers for obvious cost reasons. For this reason we have opted for our own development of a lock-in approach based on digital signal processing (DSP). This approach allows full control of all demodulation and feedback processes and can be easily scaled to a practically unlimited number of channels. As for the LIA, the goal of the DSP scheme is to implement a digital representation of the universal phase signal $\tilde{\phi}$ that can be either used as a direct measure for the magnetic field (free-running mode) or as input for a feedback algorithm. Figure 33 shows a typical DSP scheme that processes the photocurrent $I(t)$ from the magnetometer head sampled by an analog-to-digital converter (ADC). The digital representation of $I(t)$ is modelled as $I(t) = I_R \sin(\omega_{\text{rf}} t + \phi_{\text{in}})$ with an amplitude I_R corresponding to Eqs. 105 and 107. In addition to the phase, parametrized in the theoretical modeling section (Eq. 52) as $\phi = \tilde{\phi} + \phi_0$, the experimental signal treatment has to take technical phase shifts ϕ_{tec} into account by setting

$$\phi_{\text{in}} = \tilde{\phi} + \phi_0 + \phi_{\text{tec}}. \tag{115}$$

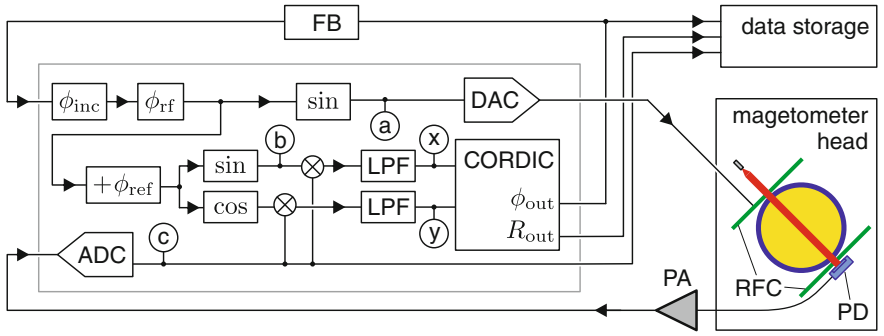

Fig. 33 Digital signal processing scheme. The photocurrent from the photodiode (PD) is amplified by a pre-amplifier (PA) and digitized by an analog to digital converter (ADC) with a sampling rate $f_{sr} = 1/\Delta t$. In each sampling cycle the phase increment $\phi_{inc} = \omega_{rf}/\Delta t$ is added to the rf-phase $\phi_{rf} = \omega_{rf} t$. A digital to analog converter (DAC) supplies the driving rf signal (a) which is given by $\sin \phi_{rf} = \sin \omega_{rf} t$ to the rf coil (RFC). Phase shifted reference oscillations are generated in further sin and cos units which yield $(b) = \sin(\omega_{rf} t + \phi_{ref})$. The reference oscillations are mixed with the ADC samples (c) and fed to low pass filters (LPF). A CORDIC unit [52] converts the resulting in-phase (x) and quadrature (y) signals to output phase ϕ_{out} and amplitude R_{out}. A feedback algorithm (FB) can be used to control ϕ_{inc}

The digital representation of $I(t)$ is labeled (c) in Fig. 33. When a sufficiently high converter resolution is used (typically 16 or 24 bit $\Delta\Sigma$-ADC are used), the noise density of the sampled signal is limited by the physical processes discussed in Sect. 7.3. This is best verified in experiment by a Fourier transform of the sampled signal, which should result in a spectrum like the one shown in Fig. 29 when the driving rf field is not applied to the atoms. When the rf field is applied, the corresponding modulation in the photocurrent appears as a prominent peak (carrier at f_{rf}) as Fig. 34 shows. The pedestal (green curve) under the peak is caused by the modulation of the carrier's phase due to fluctuations of the magnetic field. The raw ADC data (c) is streamed to the data storage in Fig. 33 for such a noise test. During normal magnetometer operation it is not necessary to record the raw ADC samples.

The digital lock-in DSP algorithm can be implemented as a microprocessor program [53, 54] or in an field programmable gate array (FPGA) [55, 56]. In both cases, the algorithm should be executed in synchronicity with the ADC's sampling rate $f_{SR} = 1/\Delta t$. At each ADC conversion cycle the rf-phase ϕ_{rf} is incremented by $\phi_{inc} = \omega_{rf}/\Delta t$. When ϕ is represented as an n bit integer variable, scaled such that $2^n \equiv 2\pi$, the integer addition overflow produces the correct phase wrapping. Using this representation, arbitrary (constant or time dependent) phase offsets can be simply added to a phase variable.[13]

The rf signal driving the ODMR process (signal a in Fig. 33) is generated by a digital-to-analog converter (DAC) and supplied to the magnetometer head. The

[13]Lookup table based implementations of the sin and cos functions [55] profit from this representation since the two most significant bits of ϕ correspond to its quadrant.

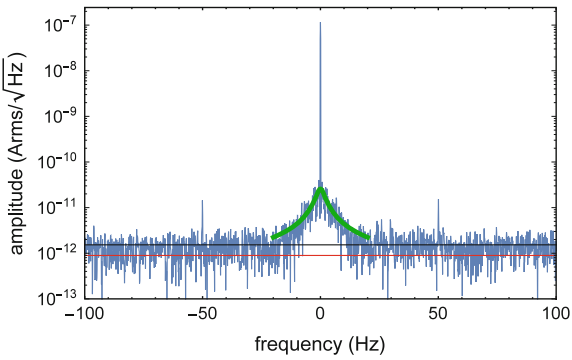

Fig. 34 Noise density of the sampled photocurrent as a function of frequency offset from the carrier at $f_{\mathrm{rf}} = 8.3\,\mathrm{kHz}$. The pedestal around the carrier frequency (*green curve*) is caused by the modulation of the carriers phase due to fluctuating magnetic fields. Further modulation sidebands at $\pm 50\,\mathrm{Hz}$ are caused by magnetic fields oscillating at line frequency. Apart from the modulation, the noise drops to $\rho_I = 1.3\,\mathrm{pA/Hz^{1/2}}$ (*black line*) which is 1.7 times above shot-noise (*red line*)

reference oscillations $R_S = 2\sin(\omega_{\mathrm{rf}}t + \phi_{\mathrm{ref}})$ (signal ⓑ in Fig. 33) and $R_C = 2\cos(\omega_{\mathrm{rf}}t + \phi_{\mathrm{ref}})$ are generated using the same rf-phase after adding the constant phase offset ϕ_{ref}. The sampled input signal $I(t)$ (signal ⓒ in Fig. 33) is mixed (multiplied) with the reference oscillations yielding

$$\begin{aligned} I(t)R_S &= I_R \sin(\omega_{\mathrm{rf}}t + \phi_{\mathrm{in}})\, 2\sin(\omega_{\mathrm{rf}}t + \phi_{\mathrm{ref}}) \\ &= I_R \cos(\phi_{\mathrm{in}} - \phi_{\mathrm{ref}}) - I_R \cos(2\omega t + \phi_{\mathrm{in}} + \phi_{\mathrm{ref}}) \\ I(t)R_C &= I_R \sin(\omega_{\mathrm{rf}}t + \phi_{\mathrm{in}})\, 2\cos(\omega_{\mathrm{rf}}t + \phi_{\mathrm{ref}}) \\ &= I_R \sin(\phi_{\mathrm{in}} - \phi_{\mathrm{ref}}) + I_R \sin(2\omega t + \phi_{\mathrm{in}} + \phi_{\mathrm{ref}}). \end{aligned} \tag{116}$$

The components oscillating with $2\omega t$ are removed by the digital low-pass filters (LPF in Fig. 33). The frequency components of the input signal $I(t)$ that significantly contribute to the signal after the LPF lie in a frequency band from $f - f_{\mathrm{LPF}}$ to $f + f_{\mathrm{LPF}}$. Only those frequency components are mixed down to a frequency passing the LPF. Close to optimum noise performance can be expected when the noise density in this frequency band is close to shot-noise. This is best verified with a Fourier spectrum computed from the raw data sampled by the ADC (signal c in Fig. 33). Figure 29 shows an example of such a spectrum and the noise in a frequency band $\pm f_{\mathrm{LPF}} = \pm 2$ kHz around f = 8 kHz. Note that a large fraction of the $1/f$ noise is suppressed by the LPF since $f_{\mathrm{LPF}} \ll f$.

The remaining signals after the low-pass filters, can be interpreted as the projections of a two-dimensional vector onto the coordinate axes. Figure 32b shows the components $x_{\mathrm{out}} = R_{\mathrm{out}} \cos\phi_{\mathrm{out}}$ and $y_{\mathrm{out}} = R_{\mathrm{out}} \sin\phi_{\mathrm{out}}$ which correspond to the in-phase and quadrature signals in the Nyquist plot of Fig. 10. The quantities R_{out} and ϕ_{out} can be extracted from x_{out} and y_{out} in a computationally efficient way

using the CORDIC algorithm [52] which does not contribute additional noise when implemented with a sufficient bit depth [57]. A comparison of x_{out} and y_{out} with Eqs. 116 shows that the extracted amplitude is $R_{\text{out}} = I_R$ and the phase is $\phi_{\text{out}} = \phi_{\text{in}} - \phi_{\text{ref}}$. Using the phase definition of Eq. 115, the measured phase thus reads

$$\phi_{\text{out}} = \tilde{\phi} + \phi_0 + \phi_{\text{tec}} - \phi_{\text{ref}}. \tag{117}$$

The output phase is equal to the desired universal phase signal ($\phi_{\text{out}} = \tilde{\phi}$) when the reference phase obeys $\phi_{\text{ref}} \stackrel{!}{=} \phi_0 + \phi_{\text{tec}}$, thereby compensating the total phase resulting from the magnetic resonance process and technical phase shifts. Under this condition the reference oscillation R_S will be in phase with $I(t)$ when $\omega_{\text{rf}} = \omega_L$.

Figure 35 shows an experimental recording of the phase ϕ_{out} as a function of ω_{rf}. A least squares fit was used to extract the phase offset which was then used to set the reference phase ϕ_{ref}. After this phase calibration procedure the measured phase follows the general phase curve $\phi_{\text{out}} = \tilde{\phi}$ and its near-resonant linear approximation is given by

$$\phi_{\text{out}}(\omega, |B|) \approx \frac{\gamma_F |B| - \omega_{\text{rf}}}{\Gamma}. \tag{118}$$

In the free running mode of operation with a fixed value of ω_{rf} the phase signal in Eq. 118 can be used to detect small deviations of the field modulus with respect to a field value that corresponds to ω_{rf}. However, the free running mode has a quite limited dynamic range of $\Delta B \ll \Gamma/\gamma_F$. For an effective linewidth of $\Gamma = 2\pi \times 5.4\,\text{Hz}$ (Fig. 35) and the Cs gyromagnetic ratio $\gamma_{\text{F}} \approx 3.5$ Hz/nT the condition is $\Delta B = 1.5$ nT.

Extending the dynamic range by active feedback: The dynamic range can be significantly increased by using active feedback. The goal of the feedback system is to keep the generated rf frequency ω_{rf} in resonance with ω_{L}. Depending on the application several different feedback methods can be deployed which change either

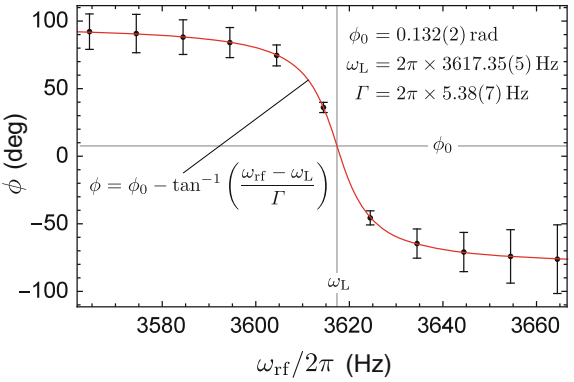

Fig. 35 Measured signal phase (*black dots*) of a Cs magnetometer as a function of ω_{rf}. The error bars are scaled up by a factor of 50. Each point was recorded after a waiting time that allowed the phase to settle completely. The values in the figure are results from a least square fit of the given fit model (*red curve*)

ω_{rf} (rf-feedback) or ω_{L} (magnetic feedback). There are two commonly used techniques for rf-fedback. The original implementation is the self oscillating scheme mentioned above which can be implemented using analog electronics only.

The rf feedback scheme using a lock-in amplifier is shown in Fig. 32 and a fully digital version in Fig. 33. The rf frequency, ω_{rf}, is controlled by the feedback system (FB) either with the VCO or numerically by changing the phase increment register ϕ_{inc}. The feedback system uses the measured phase ϕ_{out} as input error signal and aims at maintaining the condition $\phi_{\mathrm{out}} = 0$. Typical feedback algorithms include the PI and the PID schemes described in [58] and can be implemented in digital or analog form. In the rf-feedback mode the measured quantity is ω_{rf} which is numerically available in the phase increment register ϕ_{inc} and can be easily forwarded to a suitable recording device. In this scheme the magnetic field modulus is estimated as $|B| = \omega_{\mathrm{rf}}/\gamma_F$.

This estimation is correct if the feedback algorithm can always achieve the condition $\phi_{\mathrm{out}} = 0$ and if this condition also corresponds to $\omega_{\mathrm{rf}} = \omega_{\mathrm{L}}$. Some feedback algorithms need a non-zero error input in order to generate a non-zero output (e.g. simple proportional feedback). Integrators in the feedback algorithm suppress that error and a recording of ϕ_{out} can be used for an offline correction of remaining feedback errors. In the following discussion we assume that the feedback loop always achieves $\phi_{\mathrm{out}} = 0$.

This leaves the assumption $\omega_{\mathrm{rf}} = \omega_{\mathrm{L}}$ as a potential source of error. According to Eq. 118 one has

$$\phi_{\mathrm{out}}(\omega_{\mathrm{rf}}, |B|) = -\frac{\omega_{\mathrm{rf}} - \omega_{\mathrm{L}}}{\Gamma} + \delta\phi \stackrel{!}{=} 0. \tag{119}$$

Any uncompensated phase shift $\delta\phi$ yields a locking point $\omega_{\mathrm{rf}} = \omega_{\mathrm{L}} + \delta\phi\Gamma$ and thus leads to a systematic measurement error δB given by

$$\delta B = \frac{\delta\phi\Gamma}{\gamma_F}. \tag{120}$$

In order to verify that such phase offsets are compensated, periodic phase calibrations need to be performed. Since the phase shifts can be frequency dependent, phase calibrations at different frequencies and more elaborate compensation schemes may be necessary to achieve accurate measurements over a large range of Larmor frequencies.

Magnetic field feedback works in much the same way as rf-feedback except that ω_{L} is adjusted such as to balance Eq. 119. The feedback algorithm controls ω_{L} by generating an additional magnetic field that counteracts the field changes to be measured. If the feedback field is generated by a coil the measured quantity of the magnetometer is the coil current I_{FB}. Magnetic feedback has the same dynamic range extending effect as rf feedback and in addition keeps the resonance frequency constant. Thus the phase response has to be calibrated for one frequency only.

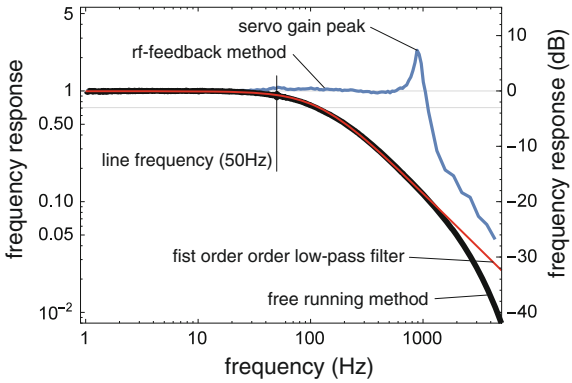

Fig. 36 Measured response of the magnetometer to a small magnetic field oscillation as a function of oscillation frequency. The response in the free-running mode (*black curve*) is well approximated by a first order low-pass filter (*red curve*). The response in the rf-feedback mode (*blue curve*) shows the typical 'servo-bump' often encountered in feedback control. The deviation between the *black* and the *red curve* at frequencies above 2 kHz is caused by the low-pass filter of the lock-in amplifier

Bandwidth: In the free running mode with a fixed ω_{rf} the measurement bandwidth is given by the delay time after which the measured quantity (ϕ_{out}) reacts to a change in the magnetic field. After a magnetic field step ΔB (see Eq. 108) the new phase value ϕ_n is reached in an exponential manner $\phi(t) = \phi_n - \Delta\phi\exp(-t/\tau)$. The time constant τ cannot be shorter than the spin coherence time $T_c = \Gamma^{-1}$ since the atoms effectively integrate the magnetic field during T_c. The atoms thus act as a first-order low-pass filter with a cutoff (−3 dB) frequency of $f_c = \Gamma/(2\pi)$ as shown in Fig. 36. Since the magnetometer noise density (Eq. 113) is proportional to Γ, high resolution and high bandwidth cannot be easily achieved simultaneously.

In addition to an extension of the dynamic range, the feedback stabilization of the magnetic resonance condition $\omega_{\mathrm{rf}} = \omega_{\mathrm{L}}$ also increases the measurement bandwidth. When the phase starts to deviate from 0 following a field change, the feedback algorithm starts to change ω_{rf} long before the phase has settled to the value it would have reached in a free running mode of operation. A feedback algorithm with a high gain can set ω_{rf} to the new resonance frequency in a fraction of the spin coherence time. In this situation the phase never settles at a value different than 0 since it is always immediately corrected. The bandwidth of the feedback is limited by the low-pass filter (LPF) used in the DSP scheme and thus has to be much smaller than the Larmor frequency.

Figure 36 compares the frequency response of the free-running mode of operation to the one achieved with rf-feedback. The useful bandwidth (characterized, e.g., by the −3 dB points) is approximately one order of magnitude larger in the feedback mode. The gain peak in the feedback response leads to an amplification of the corresponding frequency components between 600 and 1000 Hz which can be corrected in an off-line data processing step. The peak-gain and the usable

bandwidth will decrease for smaller feedback gains. If the feedback gain is increased the peak will quickly diverge and cause an unstable feedback loop operation.

7.6 Heading Errors in Feedback-Locked M_x Magnetometers

M_x magnetometers are subject to two types of heading errors, also called orientational errors. Heading errors (HE) denote systematic readout errors that manifest themselves as a change of the magnetometer reading, i.e., the Larmor frequency when the orientation of $\mathbf{B}_0$ (supposed to be of constant magnitude $|\mathbf{B}_0|$) changes with respect to the magnetometer orientation, characterized by $\mathbf{k}$ and $\mathbf{B}_{\mathrm{rf}}$.

One type of HE originates from the nonlinear Zeeman effect due to the Breit-Rabi interaction in the alkali ground state. This type of HE is discussed in Chap. 5 of [3] for the self-oscillating mode of operation (Sect. 7.5) of the M_x magnetometer, but applies as well to the active feedback-locked mode of operation, discussed above. This effect makes, e.g., Cs M_x magnetometers unsuitable for the accurate measurement of the Earth's magnetic field ($B_0 \approx 40\,\mu\mathrm{T}$). Here we discuss another HE that occurs in the $\mathbf{B}_{\mathrm{rf}} \perp \mathbf{B}_0$ variant of the M_x magnetometer.

Projection phase error: In the $\mathbf{B}_{\mathrm{rf}} \parallel \mathbf{k}$ variant of the M_x magnetometer the phase ϕ, given by Eq. 41, does not depend on θ_B nor φ_B, which makes this variant of the magnetometer a *true scalar magnetometer* in which the lock-point depends—via $\omega_L = \gamma_F |\mathbf{B}_0|$—on the field modulus only, and not on the field orientation.

In the $\mathbf{B}_{\mathbf{rf}} \perp \mathbf{k}$ variant of the magnetometer, on the other hand, one encounters a quite different situation, since the phase offset ϕ_0 is a function of θ_B and φ_B (see Eq. 65 and Fig. 14). For a more detailed description we assume that the magnetometer is operated in an orientation (marked by the magenta dots in Fig. 14) that yields a maximal S_{R} signal. Under these conditions the offset phase is ϕ_0 ($\theta_B = \pi/4, \varphi_B = \pi/2) = 0$ and we assume that technical phase shifts are perfectly compensated. When the polar orientation θ_B of the magnetic field is rotated (at constant field amplitude B_0) by an arbitrary amount $\delta\theta_B$ away from the optimal orientation $\theta_B = \pi/4$, the offset phase ϕ_0 will not change, as evidenced by the red line in Fig. 14. In consequence, the magnetometers oscillation frequency will not be changed by the feedback, and the magnetometer reading thus not affected.

A change of the azimuthal orientation $\delta\varphi_B$, on the other hand, will induce a phase shift $\delta\phi$ that leads, according to Eq. 120 to a systematic field estimation error δB of

$$\delta B = \frac{\delta\phi\Gamma}{\gamma_F} = \frac{\Gamma}{\gamma_F}\delta\varphi_B \frac{d\phi_0}{d\varphi_B}\bigg|_{\theta_B=\frac{\pi}{4},\varphi_B=\frac{\pi}{2}} = \frac{\Gamma}{\gamma_F}\frac{\delta\varphi_B}{\sqrt{2}} \tag{121}$$

We refer to this heading error as *projection phase error*. As a numerical example, consider the resonance curve shown in Fig. 35 with a linewidth Γ of $2\pi \times 5.4\,\text{Hz}$, for which a $\delta\varphi_B$ orientation change of 1 mrad implies a HE of $|\delta B|$ of ≈ 1 pT. Such a systematic error is more than 2 orders of magnitude larger than the typical sensitivity of the same magnetometer, which is able to detect field changes below 10 fT.

7.7 Realization of a Sensor Array

Arrays of magnetic field sensors are used to measure the spatial distribution of magnetic fields. For geomagnetic field exploration, e.g., one deploys sensor arrays with an inter-sensor spacing that is significantly larger than the individual sensor size, so that the sensors operate independently of each other. For sensor separations that are comparable to the sensor size, individual sensors may mutually interact, thus requiring more elaborate feedback schemes. Applications like the recording of magneto-cardiograms (MCG) or magneto-encephalograms (MEG), i.e., the mapping of the magnetic fields generated by the human heart [60] or the human brain [61] require such sensor arrays with closely packed sensors. A spatial resolution on the order of 30 mm is necessary to resolve the spatial structure of the MCG recorded above the chest of a patient.

Figure 37 shows a design of sensor modules deployed in a large 2-dimensional array. The typical single laser beam M_x magnetometers facilitate a mechanical design with a high integration density. The sensor modules are placed in dedicated openings in a stack of printed circuit boards (main PCB) that serve as mechanical support, defining the common sensor plane. The PCBs have the advantage of providing relatively rigid structures, on which conductors with precision geometries can be printed for realizing various coils. By stacking two or three sensor planes one can easily build first or second order gradiometers. In this way we have realized arrays carrying 25 [60] or 57 [59] individual sensor modules. The following description applies to the sensor modules of the latter publication.

A sensor module proper consists of an optical module (containing a channel for the fiber ferrule, a lens, and a linear polarizer), the glass cell containing the Cs vapor, and a photodiode. These components are mechanically supported by a plastic holder that is sandwiched between two thin PCB (pd PCB) which also support the Cs cell and the photodiode. The PCB has printed circuits that conduct the photocurrent to a position where an electrical connector can be conveniently placed. A multi-mode fiber, which is terminated with a non-magnetic fiber coupler, guides the light to the optical module. The fiber coupler consists of a ceramic ferrule that holds the end of the multimode fiber with 400 μm core diameter. The ferrule is connected to the fiber protection gasket by a plastic tube and pressed to the precision-machined optical module by a swivel nut. All components of the fiber coupler are custom-made since non-magnetic couplers are not commercially available. The light from the fiber is collimated by a 6 mm focal length lens.

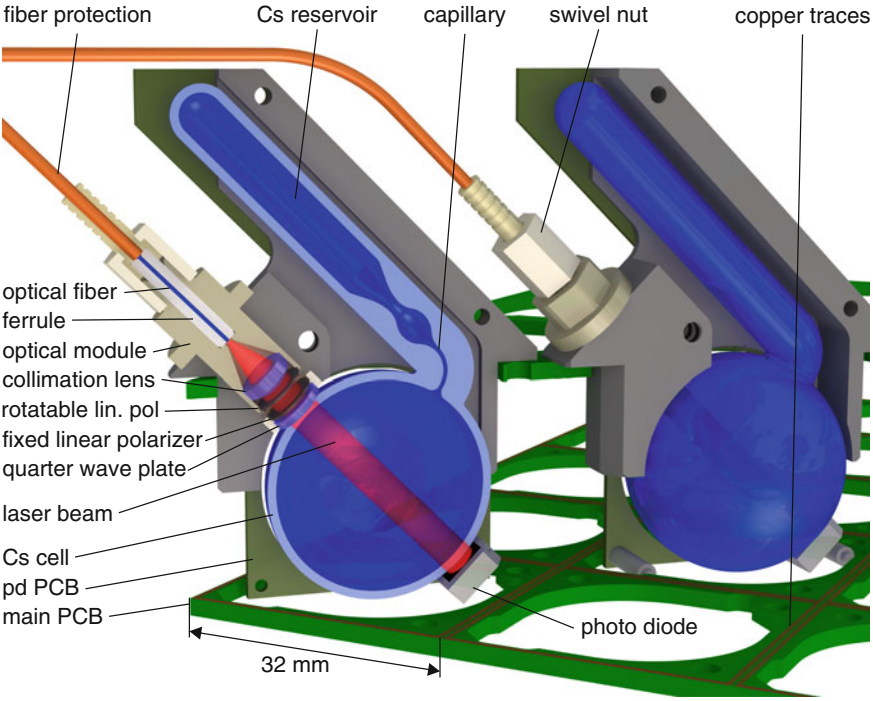

Fig. 37 Cut view of a part of the sensor array used for cardio-magnetic mapping in Ref. [59]. The transparent glass parts are tinted blue for better visibility

Collimation is not perfect, since the fiber has a rather large core diameter, and the lens is rather used to image the fiber end onto the photodiode that is located ≈32 mm away from the lens. The last optical element in the optical module is a dichroic linear polarizer for adjusting the light power transmitted to the Cs cell.

The circular polarizer consists of a second linear polarizer and a quarter-wave plate that are glued to a mounting ring after careful adjustment of their relative orientation. The circular polarizer assembly is fixed with respect to the Cs cell.

In each module, the power entering the Cs cell can be adjusted by rotating the optical module (containing, as mentioned, a linear polarizer) with respect to the the circular polarizer. We use dichroic (colorPol IR 905) polarizers from Codixx [62] that are available in quadratic and circular shapes that have an extinction ratio of >1000 at 894 nm.

The power of the laser beam transmitted through the Cs cell is detected by a non-magnetic photodiode mounted on the pd PCB. We used a Hamamatsu (model S6775) Si-PIN photodiode [63] which is sensitive, inexpensive, has a relatively large photosensitive area and is almost completely non-magnetic. The outer diameter of the Cs cell is 27 mm which is the largest cell size we could accommodate in an array with 32 mm sensor spacing. For the array described in Ref. [60]

Cs cells with an outer diameter of 30 mm, spaced by 50 mm were used. Each sensor module can be easily removed from the array after disconnecting its optical fiber, the fiber of one neighboring module and the photocurrent-carrying cable. This ease of sensor placement and replacement is a significant advantage with respect to SQUID sensors (commonly used for MCG measurements), which require complicated technical procedures for sensor replacement because of the required cryogenic environment.

The main PCB contributes to the simple sensor replacement since it carries conductors for all necessary coils. Those include a large coil that provides the rf magnetic field to all sensors as well as coils for magnetic field feedback individual to each sensor. All coils are optimized for best field homogeneity over the cell volumes and are distributed over four surfaces (only two are shown in Fig. 37). The magnetic feedback induces a certain cross-talk since the feedback coil of a given sensor also changes the field at the neighboring sensors. This cross talk on the order of 10% does not prevent a stable feedback operation and can be corrected for in the off-line data analysis [60].

8 Summary and Conclusions

We have presented a detailed account of the theory underlying double resonance magnetometers building on magnetic resonance processes in atoms. We have focused on 'true' magnetic resonance processes driven by oscillating magnetic fields (treating both spin-oriented and spin-aligned media), and discussed as well magnetic resonance building on light modulation techniques. Among all discussed methods the so-called M_x magnetometer has the longest history. In its simplest implementation involving a single light beam and the detection of transmitted light power it has proven to be a very robust and easy-to-realize, relatively inexpensive device. The M_x magnetometer has been applied in a broad range of fields spanning geomagnetic prospection, biomedical imaging and field control in fundamental physics experiments. In paraffin-coated cells the M_x-magnetometer operation requires only a few μW of resonance light, so that any mW delivering commercial diode laser can easily operate arrays of several dozen of sensors. A discussion of more recent developments of M_x-magnetometers involving variants using polarimetric detection, spatially separated pump-probe extensions, miniaturization to chip-scale and ultra-thin cell sensors, and bichromatic excitation go beyond the scope of this chapter, but are addressed in Chaps. 14, 15, 16, 17, and 18 of this book. We note, however, that the fundamentals derived here can be applied to model most of these extensions.

References

1. D. Budker, W. Gawlik, D.F. Kimball, S.M. Rochester, V.V. Yashchuk, A. Weis, Resonant nonlinear magneto-optical effects in atoms. Rev. Mod. Phys. **74**, 1153–1201 (2002)
2. D. Budker, M. Romalis, Optical magnetometry. Nat. Phys. **3**(4), 227–234 (2007)
3. D. Budker, D.F. Jackson Kimball (ed.), *Optical Magnetometry* (Cambridge University Press, Cambridge, 2013)
4. J.C. Lehmann, C. Cohen-Tannoudji, Pompage optique en champ magnétique faible. CR Acad. Sci. Paris **258**, 4463 (1964)
5. T. Scholtes, V. Schultze, R. IJsselsteijn, S. Woetzel, H.-G. Meyer, Light-narrowed optically pumped M_x magnetometer with a miniaturized Cs cell. Phys. Rev. A **84**, 043416 (2011)
6. N. Castagna, A. Weis, Measurement of longitudinal and transverse spin relaxation rates using the ground-state Hanle effect. Phys. Rev. A **84**, 053421 (2012). (**85**:059907, November 2011. Erratum)
7. N. Castagna, A. Weis, Erratum: Measurement of longitudinal and transverse spin relaxation rates using the ground-state Hanle effect. Phys. Rev. A **85,** 059907 (2012) ([Phys. Rev. A 84, 053421 (2011)])
8. E. Breschi, A. Weis, Ground-state Hanle effect based on atomic alignment. Phys. Rev. A **86** (5), 053427 (2012)
9. I.K. Kominis, T.W. Kornack, J.C. Allred, M.V. Romalis, A subfemtotesla multichannel atomic magnetometer. Nature **422**(6932), 596–599 (2003)
10. Z.D. Grujić, P.A. Koss, G. Bison, A. Weis, A sensitive and accurate atomic magnetometer based on free spin precession. Eur. Phys. J. D **69**, 1–10 (2015)
11. L. Lenci, A. Auyuanet, S. Barreiro, P. Valente, A. Lezama, H. Failache, Vectorial atomic magnetometer based on coherent transients of laser absorption in Rb vapor. Phys. Rev. A **89** (4), 043836 (2014)
12. A. Nikiel, P. Blümler, W. Heil, M. Hehn, S. Karpuk, A. Maul, E. Otten, L.M. Schreiber, M. Terekhov, Ultrasensitive ^{3}He magnetometer for measurements of high magnetic fields. Eur. Phys. J. D **68**(11), 1–12 (2014)
13. C. Cohen-Tannoudji, J. Duppont-Roc, S. Haroche, F. Laloë, Detection of the static magnetic field produced by the oriented nuclei of optically pumped He-3 gas. Phys. Rev. Lett. **22**(15), 758 (1969)
14. H.C. Koch, G. Bison, Z.D. Grujić, W. Heil, M. Kasprzak, P. Knowles, A. Kraft, A. Pazgalev, A. Schnabel, J. Voigt, A. Weis, Design and performance of an absolute ^{3}He/Cs magnetometer. Eur. Phys. J. D **69**, 1–12 (2015)
15. L. Moi, S. Cartaleva, Sensitive magnetometers based on dark states. Europhys. News **43**(6), 2427 (2012)
16. C. Cohen-Tannoudji, A. Kastler, Optical pumping. Rev. Mod. Phys. **5**, 1–81 (1966)
17. W. Happer, Optical pumping. Rev. Mod. Phys. **44**(2), 169–249 (1972)
18. S.M. Rochester, D. Budker, Atomic polarization visualized. Am. J. Phys. **69**(4), 450 (2001)
19. K. Blum, *Density matrix theory and applications* (Plenum Press, Berlin, 1996)
20. I. Fescenko, A. Weis, Imaging magnetic scalar potentials by laser-induced fluorescence from bright and dark atoms. J. Phys. D Appl. Phys. **47**(23), 235001 (2014)
21. A. Weis, V.A. Sautenkov, T.W. Hänsch, Observation of ground-state Zeeman coherences in the selective reflection from cesium vapor. Phys. Rev. A **45**(11), 7991 (1992)
22. B. Gross, N. Papageorgiou, V. Sautenkov, A. Weis, Velocity selective optical pumping and dark resonances in selective reflection spectroscopy. Phys. Rev. A **55**(4), 2973 (1997)
23. A. Weis. unpublished
24. G. Bevilacqua, E. Breschi, A. Weis, Steady-state solutions for atomic multipole moments in an arbitrarily oriented static magnetic field. Phys. Rev. **89**(3), 033406 (2014)
25. Z.D. Grujić, A. Weis, Atomic magnetic resonance induced by amplitude-, frequency-, or polarization-modulated light. Phys. Rev. A **88**, 012508 (2013)

26. N. Castagna, G. Bison, G. Di Domenico, A. Hofer, P. Knowles, C. Macchione, H. Saudan, A. Weis, A large sample study of spin relaxation and magnetometric sensitivity of paraffin-coated Cs vapor cells. Appl. Phys. B Lasers Opt. **96**, 763–772 (2009)
27. G. Bison, R. Wynands, A. Weis, Optimization and performance of an optical cardiomagnetometer. J. Opt. Soc. Am. B **22**(1), 77–87 (2005)
28. S. Groeger, G. Bison, J.-L. Schenker, R. Wynands, A. Weis, A high-sensitivity laser-pumped M_x magnetometer. Eur. Phys. J. D **38**, 239–247 (2006)
29. A. Weis, G. Bison, A.S. Pazgalev, Theory of double resonance magnetometers based on atomic alignment. Phys. Rev. A **74**, 033401 (2006)
30. U. Fano, Precession equation of a spinning particle in nonuniform fields. Phys. Rev. **133**(3B), B828 (1964)
31. H.-J. Stöckmann, D. Dubbers, Generalized spin precession equations. New J. Phys. **16**(5), 053050 (2014)
32. G. Di Domenico, G. Bison, S. Groeger, P. Knowles, A.S. Pazgalev, M. Rebetez, H. Saudan, A. Weis, Experimental study of laser-detected magnetic resonance based on atomic alignment. Phys. Rev. A, **74**(6), 063415 (2006)
33. G. Di Domenico, H. Saudan, G. Bison, P. Knowles, A. Weis, Sensitivity of double-resonance alignment magnetometers. Phys. Rev. A **76**(2), 023407 (2007)
34. W.E. Bell, A.L. Bloom, Optically driven spin precession. Phys. Rev. Lett. **6**, 280–281 (1961)
35. E. Breschi, Z.D. Grujić, P. Knowles, A. Weis, A high-sensitivity push-pull magnetometer. Appl. Phys. Lett. **104**(2), 023501 (2014)
36. V. Schultze, R. IJsselsteijn, T. Scholtes, S. Woetzel, H.-G. Meyer, Characteristics and performance of an intensity-modulated optically pumped magnetometer in comparison to the classical M_x magnetometer. Opt. Express **20**(13), 14201–14212 (2012)
37. V. Acosta, M.P. Ledbetter, S.M. Rochester, D. Budker, D.F. Jackson Kimball, D.C. Hovde, W. Gawlik, S. Pustelny, J. Zachorowski, V.V. Yashchuk, Nonlinear magneto-optical rotation with frequency-modulated light in the geophysical field range. Phys. Rev. A **73**(5), 053404 (2006)
38. D.F. Jackson Kimball, L.R. Jacome, S. Guttikonda, E.J. Bahr, L.F. Chan, Magnetometric sensitivity optimization for nonlinear optical rotation with frequency-modulated light: Rubidium D_2 line. J. Appl. Phys. **106**(6), 063113 (2009)
39. I. Fescenko, P. Knowles, A. Weis, E. Breschi, A Bell-Bloom experiment with polarization-modulated light of arbitrary duty cycle. Opt. Express **21**(13), 15121–15130 (2013)
40. E. Breschi, Z.D. Gruijć, P. Knowles, A. Weis, Magneto-optical spectroscopy with polarization-modulated light. Phys. Rev. A **88**(2),022506 (2013)
41. G. Bevilacqua, E. Breschi, Magneto-optic spectroscopy with linearly polarized modulated light: theory and experiment. Phys. Rev. A **89**(6), 062507 (2014)
42. M. Bass, in *Handbook of Optics: Fundamentals, techniques, and design*. Number Bd. 1. Handbook of Optics (McGraw-Hill, New York, 1994)
43. S.M. Kay, *Fundamentals of Statistical Signal Processing: Estimation Theory* (Prentice-Hall Inc, Upper Saddle River, 1993)
44. D.C. Rife, R. Boorstyn, Single tone parameter estimation from discrete-time observations. Inf. Theor. IEEE Trans. **20**(5), 591–598 (1974)
45. V. Schultze, R. IJsselsteijn, H.-G. Meyer, Noise reduction in optically pumped magnetometer assemblies. Appl. Phys. B **100**(4), 717–724 (2010)
46. A. Corney, *Atomic and laser spectroscopy* (Clarendon Press, Oxford, 1978)
47. A. Abragam, *The principles of nuclear magnetic resonance* (Clarendon, Oxford, 1961)
48. A.L. Bloom, Principles of operation of the rubidium vapor magnetometer. Appl. Opt. **1**, 61 (1962)
49. Stanford Research Systems. www.thinksrs.com
50. Signal Recovery. www.signalrecovery.com
51. Zurich Instruments AG. www.zhinst.com

52. J.E. Volder, The CORDIC trigonometric computing technique. IRE Trans. Electron. Comput. EC **8**(3), 330–334 (1959)
53. J. Gaspar, S.F. Chen, A. Gordillo, M. Hepp, P. Ferreyra, C. Marqués, Digital lock in amplifier: study, design and development with a digital signal processor. Microprocess. Microsyst. **28**(4), 157–162 (2004)
54. Stanford Research Systems, *User's Manual, Model SR830 DSP Lock-In Amplifier* (2011)
55. A. Restelli, R. Abbiati, A. Geraci, Digital field programmable gate array-based lock-in amplifier for high-performance photon counting applications. Rev. Sci. Instrum. **76**(9), 093112 (2005)
56. J.-J. Vandenbussche, P. Lee, J. Peuteman, On the accuracy of digital phase sensitive detectors implemented in FPGA technology. IEEE Trans. Instrum. Measur. **63**(8), 1926–1936 (2014)
57. Y. Hu, The quantization effects of the CORDIC algorithm. IEEE Trans. Sig. Process. **40** (4),834–844 (1992)
58. K.J. Åström, T. Hägglund, *PID Controllers: Theory, Design, and Tuning*, 2 edn. (Instrument Society of America, Research Triangle Park, NC, 1995)
59. G. Lembke, S.N. Erné, H. Nowak, B. Menhorn, A. Pasquarelli, G. Bison, Optical multichannel room temperature magnetic field imaging system for clinical application. Biomed. Opt. Express **5**(3), 876–881 (2014)
60. G. Bison, N. Castagna, A. Hofer, P. Knowles, J.-L. Schenker, M. Kasprzak, H. Saudan, A. Weis, A room temperature 19-channel magnetic field mapping device for cardiac signals. Appl. Phys. Lett. **95**(17), 173701 (2009)
61. H. Xia, A. Ben-Amar Baranga, D. Hoffman, M.V. Romalis, Magnetoencephalography with an atomic magnetometer. Appl. Phys. Lett. **89**, 211104 (2006)
62. CODIXX AG. www.codixx.de
63. Hamamatsu Photonics. *Si PIN Photodiodes, S6775 series datasheet* (2014)

Nonlinear Magneto-Optical Rotation Magnetometers

Wojciech Gawlik and Szymon Pustelny

Abstract Nonlinear magneto-optical rotation (NMOR) is the nonlinear contribution to the overall magneto-optical rotation (Faraday) signal. It yields signals that are dependent on the light and magnetic-field intensities. The later dependence enables precision magnetometry of very weak fields (relaxation-rate limited). The effect may also be investigated with the modulated light (frequency and/or amplitude modulation) to allow accurate measurements of non-zero magnetic fields. The main advantages of the NMOR magnetometry are: technical simplicity, high accuracy and wide dynamic range.

1 Introduction

Magneto-optical rotation is a magneto-optical effect, consisting in the rotation of a polarization plane of linearly polarized light during its propagation through a medium subject to an external magnetic field. The polarization rotation was discovered by M. Faraday in 1845, during his studies of propagation of light through solids [1]. Half a century later, D. Macaluso and O. Corbino investigated the Faraday effect in gases [2, 3]. Their investigations revealed a strong resonance behavior of polarization rotation on the wavelength of propagating light. This discovery was eventually recognized by calling the resonant version of the Faraday effect the Macaluso-Corbino effect [4].

Figure 1 illustrates a principle of the magneto-optical rotation experiment. Resonant, linearly polarized light is used to illuminate a magneto-optically active medium subject to a longitudinal magnetic field $\boldsymbol{B}$. Rotation of the polarization plane $\varphi(B)$ allows measurement of the magnitude of the field.

The Faraday effect results from the magnetic-field induced circular birefringence of a medium (magnetic-field-induced difference in refractive indices n_- and n_+ of

W. Gawlik (✉) · S. Pustelny
M. Smoluchowski Institute of Physics of the Jagiellonian University,
ul. Łojasiewicza 11, 30-348 Kraków, Poland
e-mail: gawlik@uj.edu.pl

S. Pustelny
e-mail: pustelny@uj.edu.pl

A. Grosz et al. (eds.), *High Sensitivity Magnetometers*, Smart Sensors,
Measurement and Instrumentation 19, DOI 10.1007/978-3-319-34070-8_14

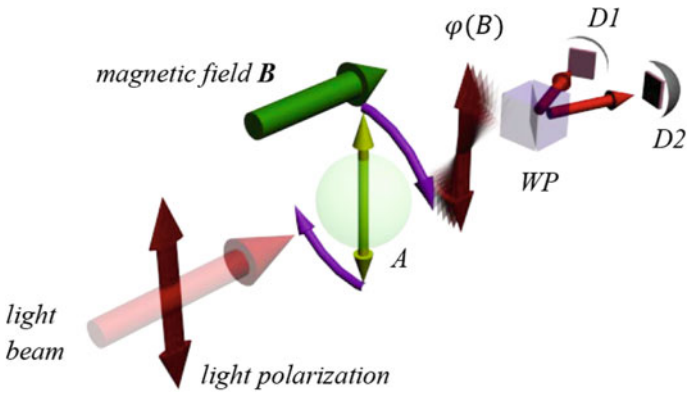

Fig. 1 Schematic of magneto-optical rotation experiment. Resonant, linearly polarized light beam illuminates a magneto-optically active medium (A) subject to a longitudinal magnetic field $\boldsymbol{B}$. Magnetic-field induced rotation of the polarization plane $\varphi(B)$ is measured by a polarimeter composed of a polarizer (WP) and two photodetectors

left- and right-hand circularly polarized light, respectively). The effect links a specific optical property of a material, the Verdet constant V [5], with the magnitude B of the magnetic field $\boldsymbol{B}$ aligned along the light beam. For weak light intensity, i.e. in a linear regime of light-matter interaction, the dependence of polarization rotation on the magnetic field is characterized with a simple proportionality relation [1].

$$\varphi = VLB, \tag{1}$$

where L is the path length of light in the medium. This dependence enables quantification of the magnetic field by the detection of polarization rotation.

Equation (1) shows that magnetometric capabilities of the Faraday effect are determined by the Verdet constant. In solid-state materials, large Verdet constants are observed, for example, in magnetic garnets. In particular, terbium gallium garnet reveals the highest ever-reported Verdet constant of roughly 100 rad/(T m) at 600 nm. Large Verdet constants are also observed in glasses containing high concentrations of lead and bismuth. Unfortunately, the choice of appropriate materials with high Verdet constants and low absorption is rather limited. Therefore, magnetometric sensitivity of a sensor is often increased by prolongation of light propagation length. A specific solution following this approach consists in application of optical fibers containing ferromagnetic dopants [6].

In gases, the situation is different than in solids. Atomic or molecular gases illuminated with off-resonance light typically reveal very small Verdet constants. Therefore, it is very difficult to get measurable rotation signals without application of multipass cells [7, 8] or optical cavities [9]. However, the strong dependence of the Verdet constant on the wavelength results in significant increase in magneto-optical rotation for resonant light, enabling observation of sizeable magneto-optical signals. The transformation between the Macaluso-Corbino and

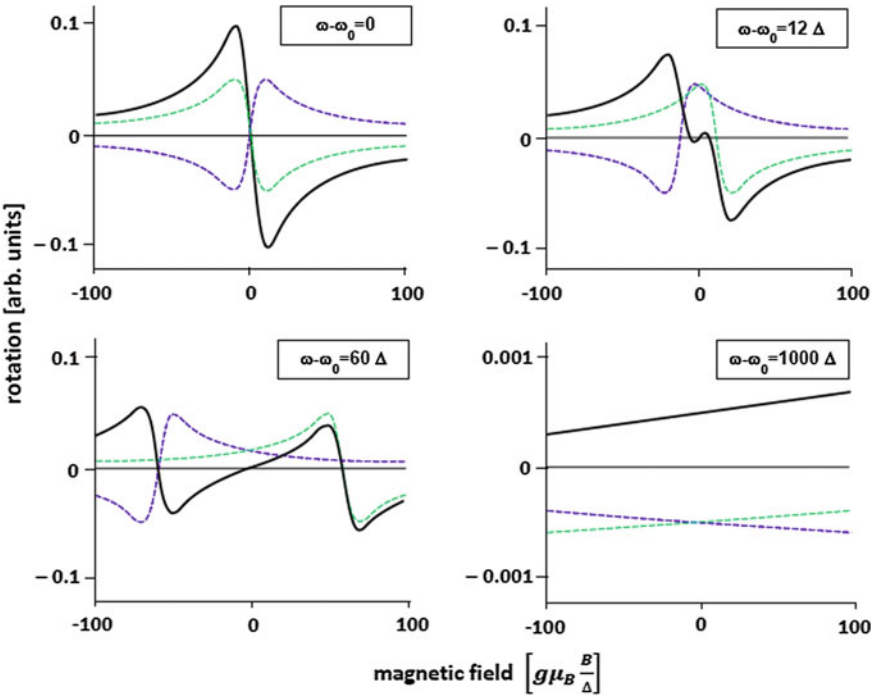

Fig. 2 Transition between the Macaluso-Corbino effect (the resonant Faraday effect) and the Faraday effect (strong detuning). The plots show the magnetic-field dependence of the refractive indices for the left- (*dashed green lines*) and right-handed (*dashed blue lines*) components of the linearly polarized light. Their difference (*solid line*) determines the overall polarization rotation φ. Various panels correspond to different detunings $\omega - \omega_0$. Increasing detuning results in: (i) inversion of sign of the polarization rotation $\varphi(B)$ curve near $B = 0$; (ii) lowering of the rotation amplitude (note the expansion of the vertical scale by factor of 100 in the last plot); (iii) broadening of the linear dependence of φ on B. Magnetic field is expressed in relative units $g\mu_B B/\Delta$, where g is the Lande factor, μ_B is the Bohr magneton, and $\Delta = 10$ is the transition linewidth

Faraday effect is schematically presented in Fig. 2. The figure depicts the refractive indices n_- and n_+ of the left- and right-hand polarization components of linearly polarized light, as well as their difference, determining the polarization rotation φ, as functions of the magnitude of longitudinal magnetic field B

$$\varphi = \frac{\omega}{2}(n_+ - n_-)L, \tag{2}$$

where we used natural units $c = \hbar = 1$. The panels corresponding to various detunings $\omega - \omega_0$, where ω is the frequency of light and ω_0 is the transition frequency, demonstrate the change of the rotation amplitude from the on-resonance excitation (the Macaluso-Corbino effect) to the off-resonance excitation (the Faraday effect). Together with the amplitude reduction, the panels demonstrate

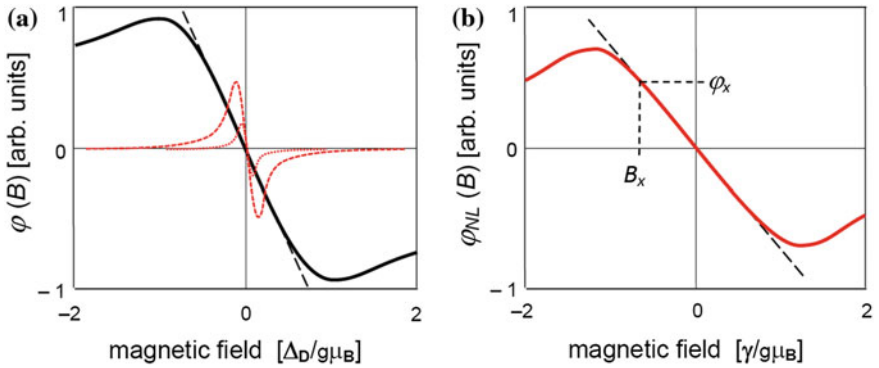

Fig. 3 **a** Schematic illustration of polarization rotation as a function of the magnitude of longitudinal magnetic field, $\varphi(B)$ in the Macaluso-Corbino effect, recorded in a typical inhomogeneously broadened medium (*solid line*). The central part of this dependence, where $\varphi(B)$ exhibits linear dependence (*dashed line*), can be used for determination of the magnetic field. Contribution of the nonlinear rotation adds an intensity-dependent, narrow feature, $\varphi_{NL}(B)$, to the linear rotation (*dotted* and *broken lines* depict contributions for two different light intensities affected by power-broadening). **b** Thanks to the linear dependence of the central part of the narrow $\varphi_{NL}(B)$ contribution associated with the nonlinear Faraday effect, precision determination of the magnetic field B is possible from the measurement of the rotation angle φ. Note the horizontal scale difference between (**a**) and (**b**) which reflects the difference between the Doppler width Δ_D and relaxation rate γ of the ground-state coherence

widening of the magnetic-field range where relation (1) can be applied for measurement of the magnetic field.

Despite the difference in the dependence of the magneto-optical rotation on the magnetic field in the Faraday and Macaluso-Corbino effects, in each case there is a finite magnetic-field range around $B = 0$, which, according to Eq. (1), reveals a linear dependence on the field (broken line in Fig. 3a). Such linearity is very convenient for magnetometry, the polarization rotation provides information about the magnitude of the field B and the steepness of the dependence $(d\varphi/dB|_{B=0})$ determines sensitivity of weak-field measurements (Sect. 3.1). For low light power, the rotation amplitude and the linearity range are limited by the linewidth of the transition light acts on. In solids, where the linewidths may be as large as tens of nanometers, the linearity range is large, but for sensors based on atomic/molecular gases the typical width is on the order of a Doppler width Δ_D (on the order of a gigahertz), which corresponds to the measurement range significantly smaller than one tesla ($\Delta B \lesssim 0.1\,\mathrm{T}$). Consequently, for such sensors the deviations from the linear dependence are observed already at moderate magnetic fields. When the magnetic-field splitting of the resonance line exceeds the linewidth, the rotation decreases and, more importantly, cannot be unambiguously attributed to a specific value of a magnetic field.

The development of techniques of optical pumping [10] and sensitive methods of radio-frequency spectroscopy [11, 12] in 1950–1960 triggered a substantial progress in optical magnetometry (see other chapters of this book). However, it was the advent of tunable lasers that boosted the development of the techniques based

on magneto-optical rotation. One of early studies of the Macaluso-Corbino effect with laser light was performed in the forward-scattering geometry, where transmission of light through a magneto-optically active medium placed between two crossed polarizers was detected (the signal in the arrangement is given by $S \propto I_0 \sin^2 \varphi(B)$, where I_0 is the intensity of light) [13]. The authors of Ref. [13] discovered that when the light intensity is not very low, the polarization-rotation dependence differs, in its central part (around $B \approx 0$), from the standard low-intensity signal $\varphi_L(B)$ (Fig. 3). In particular, a narrow structure arises with the amplitude depending on the light intensity, which reveals nonlinear character of the effect. The nonlinear contribution of the overall magneto-optical rotation signal is denoted as $\varphi_{NL}(B)$ and the related effect is called nonlinear magneto-optical rotation (NMOR). It should be stressed that the range where this feature appears is not subject to Doppler broadening but is determined by the relaxation rate of the atomic/molecular ground state that is coupled with light. Since the rate is orders of magnitude smaller than the Doppler width, even with somewhat smaller rotation amplitude than in the linear effect, the steepness of the polarization-rotation is much larger than in the linear effect ($d\varphi_{NL}/dB \gg d\varphi_L/dB$). Consequently, the sensitivity of NMOR to the magnetic field is much higher than in its linear counterpart. This enhancement can be exploited for magnetometry, as shown in Fig. 3b, albeit in a correspondingly narrower magnetic-field range. Section 2.2 describes the measurements without compromising on the field range.

2 Physical Grounds of Nonlinear Magneto-Optical Rotation (NMOR)

2.1 DC Light

There are several effects that contribute to NMOR signals. The underlying effects behind the phenomenon are associated with redistribution of atomic populations by velocity-selective optical pumping (the Bennet effect [14]) and atomic polarization of a ground state (redistribution of atomic population of the state and generation of coherence between its Zeeman sublevels) [4, 15, 16]. Some of these contributions can be distinguished in the magnetic-field domain as they typically give rise to optical rotation that peaks at different magnetic fields, leading to a group of dispersive features nested around $B = 0$. In general, the width of the narrowest feature is determined by the ground-state coherence relaxation rate γ, which is inversely proportional to the transverse relaxation time T_2.

To understand the basic principles of this relation and limitations of traditional[1] (dc) NMOR for the detection of weak magnetic fields, it is instructive to consider a simple $J = 1 \rightarrow J' = 0$ atomic system resonantly coupled by linearly-polarized

[1]Using unmodulated light.

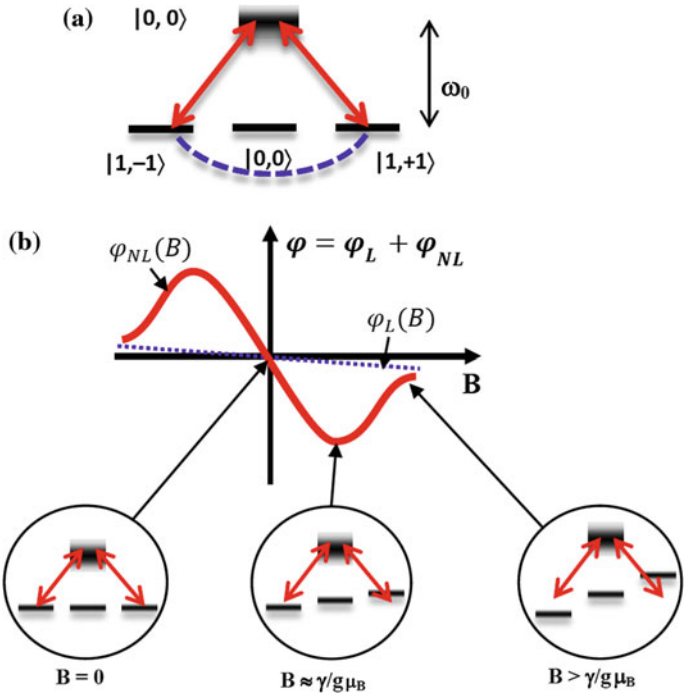

Fig. 4 Schematic illustration of the creation of the coherence contribution to NMOR. **a** Linearly-polarized light creates Raman coupling of the ground-state sublevels $|1, \pm 1\rangle$ via the excited state $|0, 0\rangle$ (ground-state coherence marked by *blue dashed line*). **b** atomic coherence between states $m_J = \pm 1$ (not shown in *insets*) is responsible for the additional contribution $\varphi_{NL}(B)$ to the overall rotation (*red line*) which is narrower than the contribution of the linear polarization rotation $\varphi_L(B)$ (*dotted line*). The *insets* represent the creation of the coherence for three characteristic values of the magnetic field intensity, $B = 0$, $B \approx \gamma/(g\mu_B)$, and $B > \gamma/(g\mu_B)$

light. If the light propagates along the quantization axis z, its linear polarization is a superposition of two circular polarizations σ^+ and σ^-, which excite transitions according to specific selection rules (the σ^+-polarized light excites transitions with $m_{J'} - m_J = 1$, where m_J and $m_{J'}$ are the magnetic quantum numbers of a ground and excited state, respectively, and the σ^--polarized light excites transition with $m_{J'} - m_J = -1$). Thereby, in the $J = 1 \rightarrow J' = 0$ system, the light coherently couples the $|1, \pm 1\rangle$[2] ground-state sublevels with the $|0, 0\rangle$ excited-state sublevels, generating the superposition of ground-state sublevels with $\Delta m = 2$ (represented in Fig. 4a by a dashed line). In zero magnetic field, the ground-state sublevels are degenerate, thus the light-established coherence has maximal amplitude but the coherence is stationary (the same energy of the sublevels ensures absence of the coherence evolution).

[2]We label the states as $|J, m_J\rangle$.

Despite the maximal amplitude of the coherence, a perfect symmetry in the propagation of σ^+ and σ^- components of light at $B = 0$ ensures absence of the phase shift between the beams and hence no polarization rotation, $\varphi(0) = 0$. For non-zero fields, $B \neq 0$, the Zeeman sublevels are split (sublevel energy shift is given by $E_Z^m = m\omega_L$, where $\omega_L = g\mu_B B$ is the Larmor frequency). Consequently, the superposition becomes nonstationary, i.e., its phase oscillates with a frequency $2\omega_L$.[3] Competition between generation of the coherence and its precession reduces the amplitude of the net coherence and changes its phase depending on the magnetic-field. Although the amplitude of the light-generated coherence at $B \neq 0$ is smaller than that established at $B = 0$, the different phase shift of the two circular components of light leads to non-zero polarization rotation. The polarization-rotation angle depends on the amplitude of the coherence, determined, for example, by light intensity and tuning, but also by the magnetic field. For instance, for $|B| < \gamma/(g\mu_B)$ the rotation linearly depends on the magnetic field, reaching its extreme value for $|B| = \gamma/(g\mu_B)$ and deteriorating for stronger fields. This is due to the further decrease of the amplitude of generated coherence. Figure 4b schematically shows the characteristic features of the NMOR signal along with the corresponding physical system.

While the first manifestation of NMOR was in the forward-scattering experiment, the recorded NMOR signals even though of subnatural width (narrower than the relaxation rate of the excited state) were still relatively broad (hundred-nanotesla range). In 1998, D. Budker and coworkers investigated NMOR, demonstrating signals with a width of roughly 10^{-10} T [17]. These signals allow for a magnetic-field sensitivity of 10^{-15} T/Hz$^{1/2}$ detectable in a dynamic field range of roughly 10^{-10} T. While this is one of the highest sensitivity ever demonstrated, the narrow dynamic range is one of the largest problem of the technique.

2.2 Modulated Light

A significant step in alleviating the limitation of the dynamic range to fields close to $B = 0$, was the application of modulated light for synchronous pumping of atoms. This idea goes back to the seminal work of Bell and Bloom [18] who discovered that modulation of light enables generation of dynamic (time varying) spin polarization of a medium. Specifically, the authors showed that intensity modulation of circularly-polarized light with frequency ω_m allows observation of a resonance in light absorption; the reduced absorption is observed if the modulation frequency coincides with the Larmor frequency, $\omega_m = \omega_L$. Synchronous optical pumping, which the Bell-Bloom experiment is an example of, can be also realized with linearly polarized light. To understand NMOR when modulated light is used, it is instructive to consider the system in the frame rotating with the modulation

[3] In general, the evolution frequency ω_{coh} is given by $\omega_{coh} = \Delta m \omega_L$.

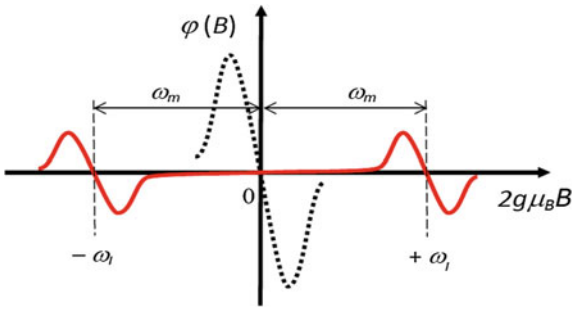

Fig. 5 Modulation of pumping creates dynamic/modulated NMOR signals allowing measurements of nonzero magnetic fields. The measurement accuracy of the stronger, nonzero fields is close to what dc NMOR offers in the low-field region (depicted by the *black dotted line*) yet thanks to the modulation of the pumping rate the measurements may be extended to higher fields. When the modulated rotation signal is retrieved by a lock-in detector, the signal consists only of the two side components centered at $\pm\omega_m/(2\,g\mu_B)$ (*red solid line*)

frequency ω_m. Since modulated light can be decomposed into two counter-rotating components, $\pm\omega_m$, for a given magnetic field, one of the components rotates with the frequency close to the spin-precision frequency (coherence-evolution frequency), while the other is strongly off-resonant and hence its contribution to coherence generation is negligible. As described above, in NMOR the coherence evolution frequency is given by $2\omega_L$, thus for the frame rotating with $\omega_m \approx 2\omega_L$, NMOR with modulated light is equivalent to dc NMOR. Figure 5 illustrates how the existence of two counter-rotating components of modulated light results in resonant generation of the ground-state coherence when

$$B = \pm\frac{\omega_m}{2g\mu_B}. \tag{3}$$

The relaxation rate of the coherence generated with modulated light is determined by the ground-state coherence relaxation rate γ, similarly as in the dc case. Hence, in the first order, the zero-field NMOR signal and the signal with modulated light have same widths. As the modulation frequency can be varied, the position of the high-field NMOR resonance can be precisely controlled (Eq. 3). This opens the possibility to detect stronger magnetic fields and extend the dynamic range to the fields exceeding the Earth's magnetic field. It should be noted, however, that at stronger fields, the high-field NMOR signal deteriorates due to the nonlinear Zeeman effect [19], alignment-to-orientation conversion [20], nonlinearities of the magnetic field, etc. This deterioration sets a practical limit on the dynamic range of NMOR with modulated light.

In principle, any quantity that affects the light-atom interaction can be used as a source of modulation in synchronous pumping. In the case of magnetometers based on magneto-optical rotation, two techniques are used most often: the frequency modulation (FM NMOR) and amplitude (or intensity) modulation (AMOR) [21].

A thorough analysis of methods based on other modulation schemes has been recently published by Weis et al. [22, 23].

2.2.1 FM NMOR

The FM NMOR technique employs frequency-modulated (FM) light with its electric field depending on time as [24]

$$E = E_0 \cos(\omega(t)t) = E_0 \cos\left(\omega^{(0)} + \Delta\omega \cos\omega_m t\right)t \tag{4}$$

where $\omega^{(0)}$ is the carrier frequency and $\Delta\omega$ is the modulation amplitude. The described modulation of the light-beam modulates the pumping rate of atoms (Fig. 6a shows the concept of FM optical pumping using the $F = 2 \rightarrow F'$ transitions of the rubidium D_1 line , i.e. a system often used in NMOR). If ω_m is resonant with twice the Larmor frequency, $\omega_m = 2\omega_L$ (Eq. 3), atoms are synchronously pumped, maximum dynamic polarization is induced and modulated component of the polarization rotation reaches its maximum, i.e., the FM NMOR resonance is observed.

Figure 6b shows a typical FM NMOR signal measured versus the modulation frequency for a given magnetic field ($B \approx 1.8$ μT). The NMOR signal was measured with an unmodulated light beam whose polarization rotation was detected with a lock-in amplifier operating at the first harmonic of the modulation frequency (see Sect. 4.2.1 for more details). The two curves correspond to the two component of the signal: the dispersive in-phase component (solid blue line) and the quadrature component (dashed red line). For a given set of parameters, the amplitude of the

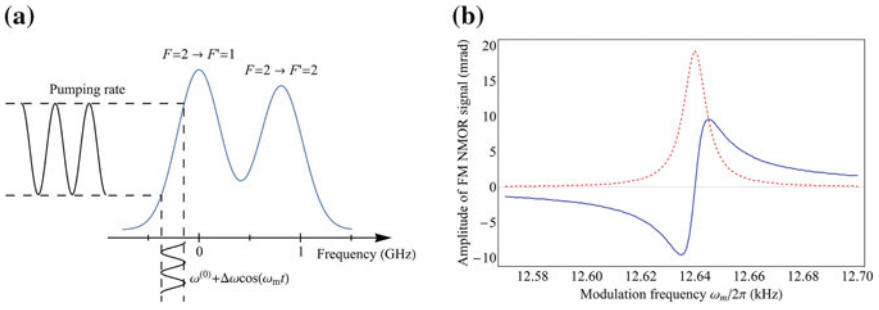

Fig. 6 **a** Schematic of the mechanism of modulation of pumping rate using FM light. The plot shows a case of light tuned to the $F = 2 \rightarrow F'$ transitions of the Doppler-broadened rubidium D_1 line (often used for NMOR magnetometry) with frequency modulated on a slope of a Doppler broadened transition. The scheme depicts how the frequency modulation of light (horizontal modulation) leads to the modulation of the pumping rate of atoms. **b** The in-phase and quadrature components of a typical FM NMOR signal measured in rubidium vapor contained in paraffin-coated cell. The signal was recorded for light intensity of roughly 1 mW/cm^2 tuned to the low-frequency slope of the $F = 2 \rightarrow F' = 1$ transition of the rubidium D_1 line with $\Delta\omega \approx 2\pi \times 100\,\mathrm{s}^{-1}$

recorded signal is equal to about 20 mrad, while its width is about 30 Hz (measured peak-to-peak).

Figure 6b illustrates that the FM NMOR resonance occurs at nonzero magnetic field. When the field changes, the resonance position can be retrieved by corresponding change of the modulation frequency ω_m, which enables magnetometry beyond the $B \approx 0$ limit of dc NMOR.

2.2.2 AMOR

The AMOR technique employs modulation of the amplitude (AM) of the light field used for the experiment. For detection of the modulation signal the same procedure as in the case of FM NMOR is used, with lock-in detection of the time-dependent rotation detected at the harmonic of the modulation frequency [25].

An example of AMOR signal is shown in Fig. 7. Similarly as for FM NMOR, a strong resonance is observed when light modulation frequency coincides with twice the Larmor frequency. The signal was measured in the same cell as the signal presented in Fig. 6, however, different tuning, average light intensity and magnetic field lead to slightly broader resonance of larger amplitude occurring at $\omega_m \approx 29.3$ kHz.

All modulators used for AMOR technique modulate the light intensity I,

$$I(t) = \frac{I_0}{2}(1 + \mathrm{A}\,\cos\omega_m t), \tag{5}$$

where A is the modulation amplitude. That simple modulation technique yields very conveniently detection signals. The theoretical analysis, however, addresses the

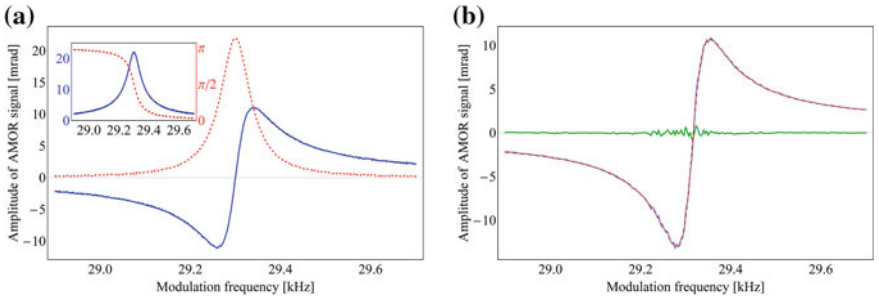

Fig. 7 **a** Typical AMOR signal measured in-phase (*solid blue*) and quadrature (*dashed red*) with the modulation frequency at its first harmonic. *Inset* shows the corresponding amplitude (*solid blue*) and phase (*dashed red*) of the AMOR signal. **b** In-phase AMOR signal (*solid blue*) overlaid with the fit to the dispersive Lorentz function (*dashed red*) and the data-fitting difference signal (*solid green*). The AMOR signal was recorded in paraffin-coated cell with sinusoidally modulated light (100 % modulation depth), average light intensity of 1 mW/cm^2, and light tuned to the center of the $F = 2 \rightarrow F' = 1$ transition of the rubidium D_1

electric field amplitude, rather than the light intensity. For the 100 % modulation, $A \approx 1$, in which case the relation for the amplitude of light field ($E = \sqrt{I}$) yields

$$E(t) = \frac{E_0}{2}\left[\cos\left(\omega - \frac{\omega_m}{2}\right)t + \cos\left(\omega + \frac{\omega_m}{2}\right)t\right]. \tag{6}$$

As will be discussed in more details later in this chapter, FM NMOR method is very easily applicable thanks to the possibility of using diode lasers where FM can be easily accomplished by modulating the diode-laser current. At the same time, however, current modulation is associated with modulation of the light intensity, so a pure FM modulation becomes difficult or even impossible. In such cases the AM technique is more recommended.

3 Characteristics of Optical Magnetometers

3.1 Sensitivity

3.1.1 Fundamental Limits on the Sensitivity

One of the most important parameters of a magnetometer is its sensitivity. In optical magnetometers, the fundamental limit on the sensitivity stems from the quantum nature of objects involved in magnetic-field sensing as well as coupling between them. Since the contributions from the atoms, photons, and atom-photon interaction are independent, the fundamentally sensitivity limited δB_f may be written as

$$\delta B_f = \sqrt{\delta B_{at}^2 + \delta B_{ph}^2 + \delta B_{ba}^2}, \tag{7}$$

where δB_{at} is the sensitivity limit due to the atoms, δB_{ph} is the photon-limited sensitivity, and δB_{ba} is the limit due to the action of the probing light onto the atoms.

The atomic limit on the sensitivity originates from the Heisenberg uncertainty principle on spin projections

$$\delta F_i^2 \delta F_j^2 \geq \frac{\left|\left\langle \left[F_i, F_j\right]\right\rangle\right|^2}{4} = \frac{\langle F_k \rangle^2}{4}, \tag{8}$$

where $F_{i,j,k}$ are three components of the spin $\boldsymbol{F}$ and [,] denotes the commutator. For the coherent spin states [26], inequality (8) is saturated and the projection-noise-limited magnetic-field sensitivity δB_{at} may be written as [27]

$$\delta B_{at} = \frac{1}{g\mu_B}\sqrt{\frac{1}{N_{at} T_2 \tau}}, \tag{9}$$

where N_{at} is the total number of atoms involved in light-atom interaction, T_2 is the transverse relaxation time (the spin-coherence lifetime), and τ is the duration of the measurement. According to Eq. (9), the sensitivity depends on the number of atoms N_{at}, the relaxation time T_2, and the measurement time τ. This dependence reveals potential strategies for improving the sensitivity, which consist in improving the measurement time or increasing the $N_{at}T_2$ product. The limitation of the first approach is a finite bandwidth required in many measurements or necessity of providing good temporal stability of such parameters as magnetic field or light intensity/frequency. The second approach requires increasing the number of atoms involved in the field detection (achievable, for example, by rising atoms' density n_{at} via vapor temperature) or by increasing the transverse relaxation time T_2. In typical NMOR magnetometers, where magneto-optically-active vapors are contained in volumes smaller than 10 cm^3, the magnetic-field sensing is performed at room or slightly alleviated temperatures (typically lower than 60 °C). This condition is set by the desire to operate with media of optical depths on the order of unity, which optimizes the spin-polarization process (optical pumping) and hence the sensing performance on NMOR magnetometer. In particular, at higher depths/concentrations, such processes as radiation trapping [28] and spin-exchange collisions [29] become important sources of relaxation, limiting the sensitivity of NMOR magnetometer. Therefore, to further increase the sensitivity, one needs to prolong the transverse relaxation time T_2. In NMOR magnetometers, T_2 is limited by light-matter effective-interaction time. In evacuated vapor cells, this time is determined by the (effective) time of flight of atoms across the light beam [30, 31] but it can be prolonged either by coating cell walls with a special anti-relaxation layer or by introduction of a buffer gas into the cell. While putting the special (e.g. paraffin) layer on the walls may prevent atoms from depolarizing collisions with the wall, introduction of the buffer (typically noble) gas into the cell slows down the diffusion of atoms toward the walls (the collisions between alkali and buffer-gas atoms preserve, to the first order, the ground-state polarization). These two approaches enable to prolong the relaxation time T_2: up to 10 ms in the buffer-gas cells [32] and over 60 s in the paraffin-coated cells [33]. Although the difference between the times seems to imply the application of anti-relaxation coating, there are additional differences between the approaches that may favor application of a buffer gas (e.g., the ability to operate at higher temperature, spatial sensitivity of the field detection, etc.).

The second contribution to the fundamental limit of the magnetic-field sensitivity is related with the nature of photons. Photons, as quantum particles, obey the Poissonian statistics, which states that their flux per unit time fluctuates over time around its mean value $\bar{N}_{ph}$ with the amplitude $\bar{N}_{ph}^{1/2}$. Consequently, the intensity and polarization of light can be determined with a finite precision given by $\left(\bar{N}_{pr}\tau\right)^{-1/2}$, where $\bar{N}_{pr}$ is the number of probe-light photons. This sets a limit on the precision of spin-state determination and hence the sensitivity of magnetic-field measurements. To alleviate this problem, one can operate with higher probe-light intensities, where

the signal-to-noise ratio increases[4] and hence does the magnetic-field sensitivity. With such increased intensity it was possible to reach the shot-noise limit over a wide magnetic-field range from 5 to 75 μT with AMOR magnetometer [34]. It should be noted, however, that for more intense probe light, optical pumping with probe becomes an important process. Thus, to reduce this effect, one may detune the probe beam from the transition. In that case, the photon shot-noise limited sensitivity δB_{ph} improves due to the increase in $\bar{N}_{pr}$, while the medium is still weakly affected (absorption on an isolated transition scales as $1/\Delta^2$, while dispersion as $1/\Delta$, where Δ is detuning).

The final contribution limiting the magnetic-field sensitivity arises from the back-action of probe light onto the atoms. This contribution originates from the ac Stark shift, the effect, consisting in the modification of Zeeman-sublevel energies by an electric field of light. This modification leads to the change of spins' precession frequency, mimicking the change of the external magnetic field. Thereby, the fundamental fluctuations in light intensity may contribute to the uncertainty of the spin-state determination and hence limit the sensitivity. Consequently, reduction of the back action becomes an important issue in optical magnetometry. Several approaches to reduce the back action have been reported in the literature [34–37]. Among them, a popular strategy based on detuning of the probe light from an optical transition seems particularly appealing [38]; for large detunings, the Stark shift scales inversely proportional to the square of the detuning, thus operation under such conditions allows one to significantly reduce the back-action contribution to the sensitivity. By an appropriate choice of a magneto-optically active medium and an appropriate choice of operation conditions (gas temperature, transverse relaxation limiting techniques, pump- and probe-light intensities and detunings, etc.), the fundamental limit on the sensitivity of NMOR magnetometer can reach or even surpass 1 fT/Hz$^{1/2}$. In particular, the low-field NMOR magnetometer discussed in Ref. [39] reveals the fundamental sensitivity of 0.16 fT/Hz$^{1/2}$, while its high-field counterpart, exploiting intensity-modulated light, had a sensitivity on the order of 10 fT/Hz$^{1/2}$ [40, 41].

3.1.2 Technical Limits on the Sensitivity

While three contributions described above set the fundamental limit on the sensitivity of NMOR magnetometers, practical devices are typically characterized with worse performance. The sensitivity deterioration stems from non-ideal conditions under which the devices are being operated. In real world, technical factors increase the noise, which impairs the sensitivity of the magnetometer.

[4]Neglecting optical pumping of atoms by the probe light, the NMOR-signal amplitude scales linearly with the number of probe-light photons (the signal is $S = I_{pr} \sin^2 \varphi$), while the noise/uncertainty is proportional $\sqrt{I_{pr}}$.

A particular source of technical noise in optical magnetometers are fluctuations in light-propagation conditions. In real systems, vibrations of optical elements and air turbulences change phase, intensity, and spatial profile of light interacting with the magneto-optically-active medium. This may affect the light-matter coupling and/or efficiency of light detection. Thermally-induced drifts of optical or mechanical properties of components used in the magnetometers may also affect the interaction between light and matter and hence contribute to the noise. Another source of noise is electronics, which may contribute to the sensitivity loss via photodetector dark current, electromagnetic (e.g., ac) pickups, or thermal instabilities of electronic equipment. In contrast to the fundamental noise, however, most of these contributions is frequency dependent. Figure 8 shows a typical noise spectrum of the NMOR magnetometer. As seen, the spectrum reveals a $1/f$-dependence with clearly visible harmonics of the ac line (50 and 100 Hz). Such characteristics suggest approaches aiming at reduction of the technical-noise. Specifically, operating the device at higher frequencies reduces the technical-noise contribution. This may be achieved either by modulation of the probe light and its phase-sensitive detection (see Sect. 4.2.1) or by operation of the device in non-zero magnetic fields. The later approach may only be achieved with the devices of sufficiently broad dynamic ranges (Sect. 5). It should be noted, however, that while the contributions from technical noise may be small, they will always impart the performance of NMOR magnetometers.

Independently of the technical-noise contribution, the NMOR magnetometer can also suffer from the magnetic noise present in the detection region of the magnetometer. While, strictly speaking, magnetic-field instability is not "the intrinsic noise" of the magnetometer, it is a factor determining the magnetometric performance of the device (uncontrollable magnetic-field fluctuations may significantly hamper the magnetometer ability to detect small changes of the field).

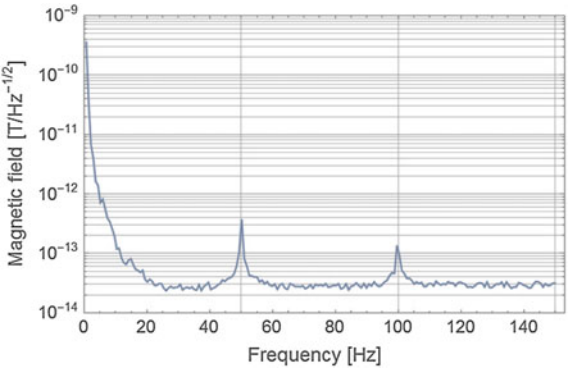

Fig. 8 Noise spectrum of the NMOR magnetometer operating at $B \approx 0$. The spectra reveal a $1/f$-dependence with clearly visible noise peaks at the harmonics of the ac line (50 Hz). In the presented case, the fundamental noise limit is roughly an order of magnitude smaller than the noise floor recorded with the spectra. The difference arises most likely due to the fluctuations of the detected magnetic field

To address this problem, various approaches may be undertaken. One group of the approaches is based on shielding (passive or active) of the external magnetic fields, which enables detection of the field in quieter magnetic-field environment. The passive shielding is typically realized inside magnetic enclosures made of high permeability materials [42]. Particular examples of such enclosures are multilayer mumetal magnetic shields, which typically offer shielding factors at the level larger than 10^4 (depending on the number of layers, geometry, size, etc.). Alternatively, one can use a set of magnetic-field coils to compensate the external fields. This technique enables active compensation of field's drifts as well as fluctuations of the external magnetic fields. To realize such active compensation, an error signal providing a measure of the compensation, is required. Such signal is often provided by non-optical sensors (e.g., flux-gate magnetometers or magneto-resistive sensors), which offer worse magnetic performance (particularly, less sensitive) but are easier to be handled.

An alternative technique of reducing environmental magnetic noise is based on the so-called magnetic gradiometer [43]. In such mode, readouts of two magnetometers placed in series with a source of measured weak magnetic field are being subtracted. As the background field exhibits relatively high spatial uniformity[5] and the magnetic field from the weak source is characterized with a strong distance dependence (r^{-q}, where $q \geq 1$), the separation of the two magnetometers (typically comparable to the source dimensions) ensures that the readout of one of the magnetometers is dominated by the weak source. The difference signal allows reduction of the environmental noise and more accurate measurement of the magnetic field produced by the weak source. Typically, the noise in the gradiometer mode can be reduced by more than an order of magnitude [44].

3.1.3 Sensitivity of Optical Magnetometer

From the practical standpoint, the sensitivity of the NMOR magnetometer is determined by the signal-to-noise ratio (SNR) of the measured NMOR signal; to determine the ability to detect weak magnetic fields, one first needs to determine the slope of the NMOR resonance as a function of the magnetic field and then recalculate the noise into the amplitude of rotation into magnetic-field-determination uncertainty

$$\delta B_{pr} = \frac{\delta\varphi}{\delta B}\frac{N}{S}, \tag{10}$$

where $\delta\varphi/\delta B$ is the slope of the NMOR resonance in its central part. This dependence determines the experimentally detected sensitivity of the magnetic-field

[5]It is typically assumed that the background field is produced by distant sources, so that change of the magnetic field between two magnetometers is negligible.

measurement achieved for a specific set of experimental parameters, including light intensity, tuning, lock-in time constant, etc. To some extent, the optimum conditions depend on one another, but also on environmental conditions (e.g., magnetic-field noise). For this reason, the practical optimization of the sensitivity of the magnetometer requires careful choice of the parameters.

3.2 Bandwidth

Bandwidth is another important characteristic of the optical magnetometer. For a typical optical magnetometer, the response of the magnetometer to small magnetic-field changes is equivalent to a response of a first-order low-pass filter with the time constant T_2 [45]. In turn, for $T_2 < \tau$, the magnetometer bandwidth is determined by $(2\pi T_2)^{-1/2}$, while for shorter measurement times $(T_2 > \tau)$, the bandwidth is given by $(2\pi T_2)^{-1}$. Therefore, to increase the bandwidth one may increase light intensity, vapor temperature or introduce the inhomogeneous magnetic field, which all may shorten the relaxation time T_2. It should be stressed, however, that due to the dependence of the sensitivity and bandwidth on the same parameter T_2, its adjustment needs to be a compromise between sensitivity and bandwidth.

3.3 Dynamic Range

In traditional NMOR magnetometers, i.e., the magnetometers exploiting CW light (Sect. 2.1), not only the sensitivity and bandwidth, but also the dynamic range ΔB_{CW} is limited by the transverse relaxation time T_2, $\Delta B_{CW} = 1/(g\mu_B \pi T_2)$. As shown in Fig. 3, this stems from the dispersive shape of the zero-field NMOR signal, which reveals a linear dependence on the magnetic field only within the range from $-\Delta B_{CW}/2$ to $\Delta B_{CW}/2$. Fields stronger than $|B| > \Delta B_{CW}/2$ cannot be distinguished from the weaker ones (see Fig. 3).

As noted in Sect. 2, to expand the dynamic range of the NMOR magnetometer, one may use modulated light. In that case, the range is not limited by the width of the NMOR signal because the position of the high-field NMOR resonance follows the magnetic field and can be adjusted by changing the modulation frequency (Eq. 3). To the first order, the dynamic range ΔB_{mod} of the modulated NMOR magnetometers is unlimited. In practice, however, the strongest fields measurable with the magnetometers rarely exceed the Earth's magnetic field. This originates from the fact that higher-order effects (e.g., nonlinear Zeeman effect [19], alignment-to-orientation

conversion [20]) diminish the amplitude of NMOR resonance. Also, it is much harder to provide good spatial homogeneity of stronger fields.[6]

3.4 Operation Modes

There are two modes of detection of stronger magnetic fields using NMOR magnetometers. In the first, so-called passive mode, magnetic field is detected by demodulating the magnetometer's output signal (polarization rotation) at the modulation frequency. This allows extraction of the amplitude and phase of the signal. Since in resonance (e.g., for $\omega_m = 2\omega_L$), two characteristics of the signal take specific values (maximum rotation and 90° phase shift), application of a feedback loop controlling the modulation frequency and tracking the resonance position enables measurement of the magnetic field. The phase-sensitive detection allows strong noise suppression (better SNR) and hence more precise tracking of the magnetic field in a broad dynamic range.

Alternatively to the passive mode, the magnetometer can be operated in the self-oscillating mode. In such an arrangement, the magnetometer's output signal is filtered and amplified and then used to modulate light. The dependence of the signal on the modulation frequency (Eq. 3) ensures that from the whole noise spectrum of the signal the system promotes only a specific modulation frequency, i.e., the resonance frequency $(\omega_m = 2\omega_L)$. Moreover, since there is no delay in the response of the spin precession to a magnetic-field change, the system instantaneously adjusts modulation frequency so that $\omega_m = 2\omega_L$. In such a way, the system automatically tracks magnetic-field changes and the modulation frequency provides information about the magnetic field. Moreover, in the self-oscillation mode the width of the NMOR signal may be narrower. This is due to the fact that in the self-oscillating mode the fluctuating magnetic field appears as sidebands to the main frequency determined $2\omega_L$ and can be easily filtered out, while in the passive mode they lead to the broadening of the resonance.

3.5 Scalar/Vector Sensor

In general, NMOR magnetometers are scalar sensors, i.e., they are sensitive to magnitude of the magnetic field. However, a scalar magnetometer can be easily converted into a vector magnetometer by introducing modulation of the magnetic field in three transverse direction at distinct modulation frequencies. Detection of the signal at those frequencies provides information about the magnetic field

[6]The magnetic-field inhomogeneity causes broadening of the observed NMOR resonance and hence deterioration of the magnetometric sensitivity of the device.

components in various directions. Alternatively, the measurement of the field direction may be obtained by the detection of the rotation signal at two frequencies: ω_L and $2\omega_L$. As shown in Ref. [46], the amplitudes of the signals measured at those frequencies depend on the direction of the magnetic field such that their ratio provides information about the direction of the field in the plane perpendicular to the polarization of the incident (probe) light.

3.6 Power Consumption

A particular advantage of optical magnetometers with respect to widespread SQUID magnetometers, that is, the devices of comparable sensitivity, is their low power consumption. In NMOR magnetometers, heating of atomic vapor cell is the most important contribution to the overall energy budget of the system. Modern lasers, particularly, vertical cavity surface emitting lasers (VCSELs), and electronic systems have low power consumption. Consequently, the whole system, without the heating, can be characterized with power demands smaller than 10 W.

4 NMOR Magnetometer Setup

Figure 9 shows a generic setup of a high-field NMOR magnetometer. The system consists of two main parts: optoelectronic part, which contains all light processing and sensing elements and electronic part that contains all elements used in electrical-signal processing.

4.1 Optics and Optoelectronics

The aim of the optoelectronic part of the system is to: (1) generate light with appropriate properties (intensity, wavelength, polarization, temporal characteristics, etc.), (2) couple the light with atomic vapor to effectively optically pump the medium, and (3) characterize the polarization state of the probe light. Below, we describe the means to achieve these aims in more details.

4.1.1 Light Sources

In all NMOR magnetometers, diode lasers are used. From the point of view of optical magnetometry, the diode lasers offer several advantages: tunability, narrow linewidth (<10 MHz for a single-mode laser), and sufficient light power ($\sim$100 μW) of the emitted light. The lasers are also characterized with small sizes,

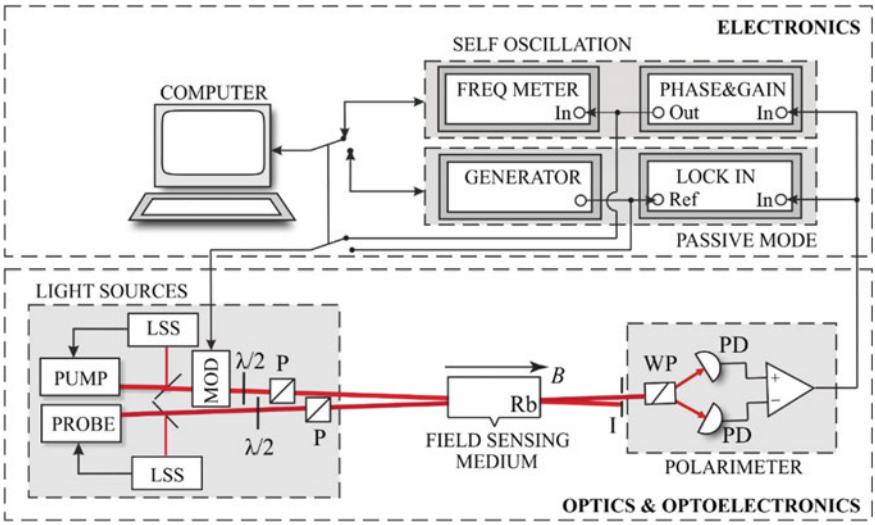

Fig. 9 Generic scheme of the NMOR magnetometer. The upper part represents the electronic part of the system. It contains elements required for operation in the self-oscillation mode (phase shifter, amplifier, frequency meter), as well as elements for the passive mode (lock-in amplifier, generator) along with the computer controlling the whole experiment. The lower part is the optoelectronic part of the system. It contains two lasers (pump and probe), light-wavelength control and stabilization systems (LSS), a light modulator (MOD) placed in the pumping-beam path, vapor cell filled with a magneto-optically-active medium (e.g., Rb), and a polarimeter to detect the polarization state of light. Additionally the system contains a set of optical elements: P and WP stand for polarizers (WP is the Wollastone prism specifically used in the system), PD denotes the photodiodes, $\lambda/2$ is the half-wave plate

low power consumption, good reliability, and possibility of integration with optoelectronic components.

In the context of NMOR magnetometry, applied light needs to be tuned to a specific transition in magneto-optically active medium. In the case of alkali vapor, typically used in optical magnetometers, the light is tuned to the strongest D_1 or D_2 spectral lines (e.g., rubidium D_1—795 nm, rubidium D_2—780 nm, cesium D_1—894 nm, cesium D_2—852 nm, potassium—770 nm). This tuning needs to be performed with subpicometer precision. Moreover, due to the dependence of the NMOR signal on the wavelength, the wavelength needs to be stabilized over time with even better stability. This aim can be achieved with several techniques, e.g. absorption spectroscopy or magnetically induced dichroism or birefringence.

Another crucial characteristic required for the NMOR magnetometry of stronger fields is the modulation of light. With diode lasers, FM light can be generated by varying the laser current. This can be easily realized within a bandwidth of 0–1 MHz, which corresponds to the magnetic-field range spanning from ultra-weak to geophysical (or stronger) fields. The FM light may be also generated with external elements, e.g., electro-optical phase shifters. Application of AM light in NMOR

typically requires a use of external modulators.[7] Simplistic approach consists in mechanical chopping of the light beam. This approach, however, has serious drawbacks like: (1) narrow bandwidth of the light modulation and limited precision of frequency control, and (2) limited capabilities of the pulse shaping. Therefore, other approaches are used for AM modulation. One of them employs application of the acousto-optical modulators (AOMs). By varying the amplitude of radio-frequency signal driving the AOM, one may modulate the efficiency of the light diffraction. This enables modulation of light intensity in broad dynamic range and arbitrary shaping of light pulses. The drawback of the AOMs, however, is the power required for their operation (typically on the order of 10 W). To avoid this problem, waveguide-based modulators may be used. Such devices are based on a Mach-Zehnder interferometers with electro-optical modulators incorporated into interferometer arms. By changing the phase of interfering beams one can modulate the intensity of light. The advantages of such modulators are their flexibility in shaping of pulse characteristics and low power consumption. Additionally, the devices offer good integrability with other electronic components.

The last group of elements used for tailoring the light parameters in NMOR magnetometers are passive optical elements. In each system, such elements as mirrors, wave plates, polarizers, optical fibers are being used to direct light beam, control its polarization and intensity.

4.1.2 Field-Sensing Medium

In NMOR magnetometers, alkali-metal vapors are most commonly used as magneto-optically-active medium. Their main advantages are simple electronic structure, enabling manipulation of a single spin, excitability of spectral lines with available light sources (diode lasers), high vapor pressures at not-too-high temperatures. The vapors are contained in glass cells (typically made of Pyrex) of sizes ranging between 0.01 and 1000 cm^3 (with $\sim$1-cm^3 being a typical size of the vapor cell). The cells are often heated to several tens of Celsius, providing the vapor optical depth on the order of unity. The vapor heating, to enhance the NMOR-signal amplitude, is typically performed using electric heaters (typically doubly twisted wire producing very low magnetic field) or with hot water/air. To prolong the effective interaction time of light and atoms, the glass cell is filled with additional buffer gas, e.g., neon, xenon, or molecular nitrogen, or its walls are coated with special anti-relaxation layer (Sect. 3.1.1). The typical relaxation times in the vapor cells used in optical magnetometers are on the order of 10 ms.

[7]While, in general, intensity of light can be modulated by varying the diode-laser current, such modulation requires changing the current in a broad range. The current modulation would also introduce frequency modulation of light in a range strongly exceeding the width of optical transition light operates at. This disables the possibility of decoupling of one modulation type from the other but also complicates the stabilization of (mean) wavelength of light, introducing instabilities of the recorded NMOR signals.

4.1.3 Polarimeter

To measure the magnetic field, the polarization rotation needs to be precisely determined. In most NMOR magnetometers, the detection of light polarization is performed using a balanced polarimeter. The polarimeter consists of a crystal polarizer, e.g., Wollaston prism, and two photodiodes monitoring light intensities directed in respective channels of the polarizer. Orientation of the polarizer axis by 45° with respect to the incident light polarization and detection of the difference of two photocurrents of the photodiodes provide direct measure of polarization rotation

$$\begin{aligned} S \propto I_1 - I_2 &= I_0 \sin^2[45^\circ + \varphi(t)] - I_0 \sin^2[45^\circ - \varphi(t)] \\ &= I_0 \sin[2\varphi(t)] \approx 2I_0\varphi(t), \end{aligned} \tag{11}$$

where $I_{1,2}$ are the intensities of light directed in respective channels of the polarimeter and I_0 is the intensity of light illuminating the polarizer. Based on Eq. (11), one can conclude that higher probe-light intensity allows for larger NMOR signals. Moreover, as discussed in Sect. 3.1.1, higher probe intensity allows reduction of the shot-noise. It should be noted, however, that larger I_0 more significantly affects evolution of the medium (optical pumping with the probe), which results in deterioration of the polarization rotation $\varphi(t)$.

Alternatively to the polarimeter detection, the polarization rotation can be measured with a single polarizer, slightly tilted with respect to the axis of incoming polarimeter

$$S \propto I_1 = I_0 \sin^2[\varphi_0 + \varphi(t)], \tag{12}$$

where φ_0 is the small uncrossing angle relative to the initial light polarization before the atomic sample. Tilting of the polarizer allows one to differentiate between rotation in opposite direction.[8] While the second solution is easier to implement, the detected signal is, for small angle proportional to the uncrossing angle, constant component proportional to φ_0^2, but also linearly and quadratically proportional to the magneto-optical rotation $\varphi(t)$.

4.2 Electronics

To detect magnetic field, the photodiode signal needs to be processed. In NMOR magnetometers, this task can be realized in two ways: detection of the amplitude of

[8]If $\varphi_0 = 0$, than $S \propto I_1 = I_0 \sin^2 \varphi(t)$. Thus, the signals for rotations in opposite directions are indistinguishable and the modulation of light polarization at $2\omega_L$ observed in the high-field NMOR results in the signal modulation at $4\omega_L$.

NMOR signal demodulated at the first harmonic of the modulation frequency (passive mode) or by the measurement of the frequency of the detected signal (self-oscillating mode).

4.2.1 Amplitude and Phase Detection

In the passive mode (see discussion in Sect. 3.4), the photodiode signal is fed into a lock-in amplifier. The amplifier demodulates the signal at a specific (typically first) harmonic of the light modulation frequency ω_m. This allows one to determine the amplitude and phase of the signal and track its characteristics in resonance (e.g., $\omega_m = 2\omega_L$). The tracking is realized using a software algorithm, implemented on a computer controlling the reference generator, or by hardware, where adjustment of the modulation frequency is realized by, for example, phase-locked loop (PLL) and voltage controlled oscillator (VCO). In typical fields measurements, the lock-in integration time is larger than the transverse relaxation time T_2, which enables strong suppression of the noise and more precise determination of the resonance position.

4.2.2 Frequency Detection

Alternatively to the amplitude and phase detection in the passive mode, the time-dependent photodiode difference signal may be used to drive the light modulation in the self-oscillation mode. In this mode, the polarimeter output signal is first filtered, then phase shifted, and amplified. The processed signal is then feed into the modulation port of the light-source system. If the phase between the driving signal and the output signal is shifted by 90°, this solution allows for automatic tracking of all magnetic-field changes. In this mode, the magnitude of the magnetic field is determined by the detection of the frequency of the modulation signal.

5 High-Field NMOR Magnetometry

The experimental arrangement discussed in the previous section allows one to build a fully operational NMOR magnetometer. Depending on the parameters of the system, such as light intensity and wavelength, type and shape of modulation, magnetic-field inhomogeneity, etc., the system may offer different performance. Figure 10 shows an exemplary magnetic-field tracking signal obtained with NMOR magnetometer exploiting AM light and rubidium vapor as the field-sensing medium. The system was operated in the self-oscillation mode, where every several tens of seconds the magnetic field was changed significantly (~ 10 μT). As shown, after each step, the system instantly follows magnetic-field changes.

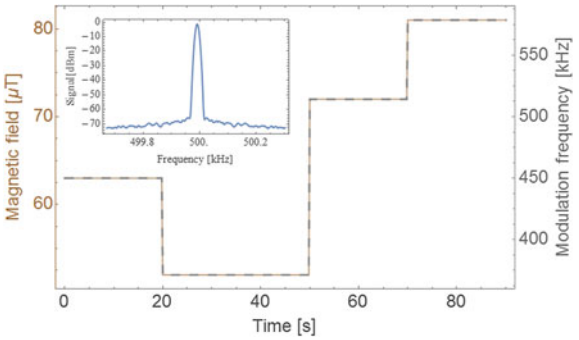

Fig. 10 Magnetic-field tracking signal. The *gray solid line* shows the detected modulation frequency of the self-oscillating system responding to the magnetic field (*dashed brown line*). Every time magnetic field was abruptly changed, the magnetometer momentarily adjusted its modulation frequency to the new resonance conditions. The *inset* shows the spectra of the signal recorded in the self-oscillating magnetometer for given conditions at magnetic field of 18.5 μT

The sensitivity of the measurement can be determined based on the SNR. Inset presents the square-root of the power spectral density of a magnetic field measured in semi-shielded magnetic-field environment (the end-caps at one side of the three-layer cylindrical mumetal magnetic shield were removed). At the spectrum, the strongest peak is observed at $\omega_m = 510$ kHz, which corresponds to the self-oscillating signal at a magnetic field of 18.5 μT ($\omega_L = 255$ kHz). From the Lorentz curve fitting to the peak and the noise floor observed in the spectrum (SNR $\approx$ 3500), we calculated the actual magnetometric sensitivity of the device $\sim$20 fT/Hz$^{1/2}$. This is roughly a factor of 10 larger than the corresponding fundamental sensitivity limit calculated based on Eq. (8). We attribute the deterioration of the sensitivity to a leakage of the uncontrollable magnetic field into the detection area, but also not-fully optimized conditions of the magnetometer operation.

A significant step in practical applications of NMOR magnetometer is its miniaturization. Figure 11 shows a picture of NMOR magnetometric head housing most of the optoelectronic component of the system. The head exists in two incarnations: (i) it is fully fiber coupled, i.e., light is remotely generated and

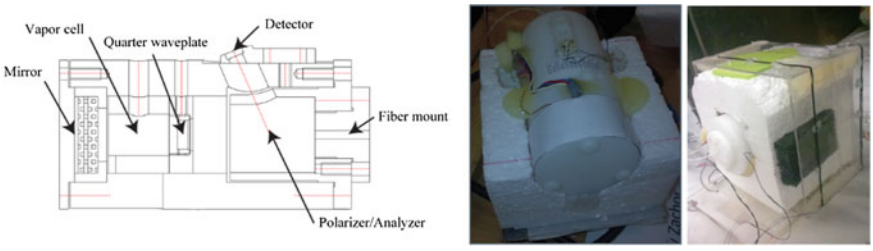

Fig. 11 A sensor head of a magnetometer exploiting AMOR

detected and it is delivered to and from the head through optical fibers and (ii) the diode laser and photodetectors are incorporated in the sensor head. While the first solution offers to remove all the metallic elements from the vicinity of the investigated magnetic-field source, the second is less demanding technical-wise (no need for coupling light into a single-mode polarization-maintaining fibers).

6 Conclusions and Outlook

Optical magnetometers have their roots in early discoveries in optics and magnetism. Progress in laser spectroscopy, optical pumping and understanding of quantum interference led to development of NMOR magnetometers as very useful and reliable instruments. The main advantages of the NMOR magnetometry which made this possible are: technical simplicity, high accuracy and wide dynamic range. The potential of these devices is exploited in ever-increasing area which spans from the basic science to many important practical applications.

References

1. M. Faraday, On the magnetization of light, and the illumination of magnetic lines of force. Philos. Trans. R. Soc. Lond. **1**, 104–123 (1846)
2. D. Macaluso, O. Corbino, Sopra una nuova azione che la luce subisce attraversando alcuni vapori metallici in un campo magnetico. Nuovo Cimento **8**, 257–258 (1898)
3. D. Macaluso, O.M. Corbino, L. Magri, Sulla relazione tra il fenomeno di Zeemann e la rotazione magnetica anomala del piano di polarizzazione della luce. Nuovo Cimento **9**, 384–389 (1899)
4. D. Budker, W. Gawlik, D.F. Kimball, S.M. Rochester, V.V. Yashchuk, A. Weis, Resonant nonlinear magneto-optical effects in atoms. Rev. Mod. Phys. **74**, 1153–1201 (2002)
5. E. Verdet, Recherches sur les proprietes optiques developpees dans les corps transparents par laction du magnetisme. Ann. Chim. Phys. **41**, 370–412 (1854)
6. L. Sun, S. Jiang, J.R. Marciante, Compact all-fiber optical Faraday components using 65-wt%-terbium-doped fiber with a record Verdet constant of-32 rad/(Tm). Opt. Express **18**, 12191–12196 (2010)
7. S. Li, P. Vachaspati, D. Sheng, N. Dural, M.V. Romalis, Optical rotation in excess of 100 rad generated by Rb vapor in a multipass cell. Phys. Rev. A **84**, 061403(R) (2011)
8. D. Sheng, S. Li, N. Dural, M.V. Romalis, Subfemtotesla scalar atomic magnetometry using multipass cells. Phys. Rev. Lett. **110**, 160802 (2013)
9. D. Jacob, M. Vallet, F. Bretenaker, A. Le Floch, R. Le Naour, Small Faraday rotation measurement with a Fabry-Perot cavity. Appl. Phys. Lett. **66**, 3546 (1995)
10. C. Cohen-Tannoudji, A. Kastler, Optical pumping, in *Progress in Optics*, vol V, ed. by E. Wolf, (Elsevier, North Holland, 1966), p. 1
11. G.W. Series, Optical pumping and related topics, in *Quantum Optics*, the 1969 Scottisch Universities Summer School, ed. by S.M. Kay, A. Maitland (Academic Press, London, 1970), p. 395
12. A. Corney, *Atomic and Laser Spectroscopy* (Oxford University Presss, Oxford, 1977)

13. W. Gawlik, J. Kowalski, R. Neumann, F. Träger, Observation of the electric hexadecapole moment of free Na atoms in a forward scattering experiement. Opt. Commun. **12**, 400 (1974)
14. W. Bennett, Hole burning effects in a He-Ne optical maser. Phys. Rev. **126**, 580 (1962)
15. W. Gawlik, S. Pustelny, Nonlinear Faraday effect and its applications, in *New Trends in Quantum Coherence*, ed. by R. Drampyan (Nova, New York, 2009), p. 47
16. D. Budker, D.F. Kimbal Rochester (eds.), *Optical Magnetometry* (Cambridge University Press, Cambridge, 2013)
17. D. Budker, V. Yashchuk, M. Zolotorev, Nonlinear Magneto-optic effects with ultranarrow widths. Phys. Rev. Lett. **81**, 5788 (1998)
18. W.E. Bell, A.L. Bloom, Optically driven spin precession. Phys. Rev. Lett. **6**, 280–281 (1961)
19. S. Pustelny, M. Koczwara, Ł. Cincio, W. Gawlik, Tailoring quantum superpositions with linearly polarized amplitude-modulated light. Phys. Rev. A **83**, 043832 (2011)
20. D. Budker, D.F. Kimball, S.M. Rochester, V.V. Yashchuk, Nonlinear magneto-optical rotation via alignment-to-orientation conversion. Phys. Rev. Lett. **85**, 2088 (2000)
21. D.F. Jackson Kimball, S. Pustelny, V.V. Yashchuk, D. Budker, Optical magnetometry with modulated light, in *Optical magnetometry*, ed. by D. Budker, F.D.J. Kimball (Cambridge University Press, Cambridge, 2013), pp. 104–124
22. Z.D. Grujić, A. Weis, Atomic magnetic resonance induced by amplitude-, frequency-, or polarization-modulated light. Phys. Rev. A **88**, 012508 (2013)
23. E. Breschi, Z.D. Gruijć, P. Knowles, A. Weis, Magneto-optical spectroscopy with polarization-modulated light. Phys. Rev. A **88**, 022506 (2013)
24. Y.P. Malakyan, S.M. Rochester, D. Budker, D.F. Kimball, V.V. Yashchuk, Nonlinear magneto-optical rotation of frequency-modulated light resonant with a low-*J* transition. Phys. Rev. A **69**, 013817 (2004)
25. W. Gawlik, L. Krzemień, S. Pustelny, D. Sangla, J. Zachorowski, M. Graf, A. Sushkov, D. Budker, Nonlinear magneto-optical rotation with amplitude-modulated light. Appl. Phys. Lett. **88**, 131108 (2006)
26. C.C. Gerry, P.L. Knight, *Introductory Quantum Optics* (Cambridge University Press, Cambridge, 2005)
27. M. Auzinsh, M. Auzinsh, D. Budker, D.F. Kimball, S.M. Rochester, J.E. Stalnaker, A.O. Sushkov, V.V. Yashchuk, Phys. Rev. Lett. **93**, 173002 (2004)
28. A.F. Molish, B.P. Oehry, *Radiation Trapping in Atomic Vapours* (Oxford University Press, Oxford, 1998)
29. J.P. Wittke, R.H. Dicke, Phys. Rev. **103**, 620 (1956)
30. W. Gawlik, Nonstationary effects in velocity-selective optical pumping. Phys. Rev. A **34**, 3760 (1986)
31. E. Pfleghaar, J. Wurster, S.I. Kanorsky, A. Weis, Time of flight effects in nonlinear magneto-optical spectroscopy. Opt. Commun. **99**, 303 (1993)
32. M. Erhard, H.-P. Helm, Buffer-gas effects on dark resonances: theory and experiment. Phys. Rev. A **63**, 043813 (2001)
33. M.V. Balabas, T. Karaulanov, M.P. Ledbetter, D. Budker, Polarized alkali-metal vapor with minute-long transverse spin-relaxation time. Phys. Rev. Lett. **105**, 070801 (2010)
34. V.G. Lucivero, P. Anielski, W. Gawlik, M.W. Mitchell, Shot-noise-limited magnetometer with sub-picotesla sensitivity at room temperature. Rev. Sci. Instr. **85**, 113108 (2014)
35. W. Wasilewski, K. Jensen, H. Krauter, J.J. Renema, M.V. Balabas, E.S. Polzik, Phys. Rev. Lett. **104**, 133601 (2010)
36. I. Novikova, A.B. Matsko, V.L. Velichansky, M.O. Scully, G.R. Welch, Phys. Rev. A **63**, 12 (2001)
37. G. Vasilakis, V. Shah, M.V. Romalis, Phys. Rev. Lett. **106**, 143601 (2011)
38. K. Jensen, V.M. Acosta, J.M. Higbie, M.P. Ledbetter, S.M. Rochester, D. Budker, Phys. Rev. A **79**, 023406 (2009)
39. D. Budker, D.F. Kimball, S.M. Rochester, V.V. Yashchuk, M. Zolotorev, Sensitive magnetometry based on nonlinear magneto-optical rotation. Phys. Rev. A **62**, 043403 (2000)

40. S. Pustelny, A. Wojciechowski, M. Gring, M. Kotyrba, J. Zachorowski, W. Gawlik, Magnetometry based on nonlinear magneto-optical rotation with amplitude modulated light. J. Appl. Phys. **103**, 063108 (2008)
41. W. Chalupczak, R.M. Godun, S. Pustelny, W. Gawlik, Room temperature femtotesla radio-frequency atomic magnetometer. Appl. Phys. Lett. **100**, 242401 (2012)
42. V.V. Yashchuk, S.-K. Lee, E. Paperno, Magnetic shielding, in *Optical Magnetometry*, ed. by D. Budker, D.F.J. Kimball (Cambridge University Press, Cambridge, 2013), pp. 104–124
43. S. Xu, S.M. Rochester, V.V. Yashchuk, M.H. Donaldson, D. Budker, Construction and applications of an atomic magnetic gradiometer based on nonlinear magneto-optical rotation. Rev. Sci. Instr. **77**, 083106 (2006)
44. S.J. Smullin, I.M. Savukov, G. Vasilakis, R.K. Ghosh, M.V. Romalis, Low-noise high-density alkali-metal scalar magnetometer. Phys. Rev. A **80**, 033420 (2009)
45. P. Wlodarczyk, S. Pustelny, J. Zachorowski, M. Lipinski, Modeling an optical magnetometer with electronic circuits-analysis and optimization. J. Instr. **7**, P07015 (2012)
46. S. Pustelny, W. Gawlik, S.M. Rochester, D.F. Jackson Kimball, V.V. Yashchuk, D. Budker, Nonlinear magneto-optical rotation with modulated light in tilted magnetic fields. Phys. Rev. A **74**, 063420 (2006)

Spin Exchange Relaxation Free (SERF) Magnetometers

Igor Mykhaylovich Savukov

Abstract A little more than a decade ago spin-exchange relaxation free (SERF) magnetometers set a new record of magnetic field sensitivity surpassing cryogenic SQUIDs. Since then a lot of progress has been made in design, commercialization, and development of novel applications of the SERF magnetometers. In addition, the operation of the SERF magnetometer was extended beyond the SERF regime resulting in the discovery of ultra-high sensitivity high frequency and scalar magnetometers. This chapter will cover some basic principles of SERF and high-density SERF-like magnetometers in the regimes when spin-exchange collisions affect the line-width of the magnetometers. Various topics will be covered: the SERF operation, the role of spin-exchange collisions, fundamental and technical noises in SERF and other high-density magnetometers, light shifts, optical pumping. The formalism of density matrix equations will be briefly described with some illustrations. At some conditions, Bloch equations can also provide adequate treatment of spin dynamics, so this topic is also briefly covered. Some applications, such as magnetoencephalography and magnetic resonance imaging (MRI), of SERF, high-frequency, and scalar magnetometers will be discussed. The number of applications will grow in the future, especially when high-sensitivity SERF magnetometers become commercially available and their operation becomes simple and user-friendly. Finally, it is anticipated that in the near future many applications developed with SQUIDs will be gradually replaced with those based on SERF and other ultra-sensitive atomic magnetometers.

1 Introduction

In this chapter, we will review the most sensitive high-density atomic magnetometers (AM) and some of their multiple possible applications. The most notable feature of these magnetometers is that they exceed fT sensitivity [1] without requirements for

I.M. Savukov (✉)
Los Alamos National Laboratory, Los Alamos, NM, USA
e-mail: isavukov@lanl.gov

A. Grosz et al. (eds.), *High Sensitivity Magnetometers*, Smart Sensors, Measurement and Instrumentation 19, DOI 10.1007/978-3-319-34070-8_15

cryogenic cooling. Currently AMs can compete with SQUIDs in many applications that require the highest possible sensitivity. Magnetoencephalography (MEG) has become the primary target application, since the AMs are the only non-cryogenic alternative to SQUIDs [2–4]. Other applications include ultra-low-field (ULF) MRI [5] and ULF NMR [6, 7], which hold promise to revolutionize magnetic resonance; magneto-cardiography (MCG) [8] and biomagnetism in general. Submarine detection and space magnetic field measurements [9] are important national security applications. AMs provide many advantages because they are both relatively sensitive compared to conventional inexpensive magnetometers, such as fluxgates, and more convenient and less restrictive compared to SQUIDs. For several decades low-Tc SQUIDs had been by far the most sensitive magnetometers at low frequency, but the situation has now changed.

We will focus on discussion of the spin-exchange relaxation-free (SERF) atomic magnetometer [10] and its derivatives including high-density radio-frequency (RF) [6] and scalar magnetometers [11]. Because spin-exchange (SE) cross-section exceeds other relaxation cross-sections by orders of magnitude [10], the SERF magnetometer in which SE effects are eliminated [12] has superior sensitivity, better than $fT/Hz^{1/2}$ [1, 13]. Thus the key to the SERF and SERF-derivative magnetometers is the understanding of SE effects, which are covered in this chapter. Apart from the SE aspect, several properties of SERF and SERF-like magnetometers are important to consider: the high density of atoms and hence high temperature of the atomic cell, the use of buffer gas to prevent collisions with the walls, and the two-beam pump-probe scheme, which can be reduced to a less-sensitive single beam scheme.

1.1 SERF Magnetometers

Spin-exchange-relaxation-free (SERF) magnetometers have the potential for the highest possible sensitivity [1, 10, 13]. To reach the SERF regime and sub fT sensitivity for a cm-size vapor cell, a certain atomic spin density for a given field is required, actually on the order of 10^{14} cm^{-3} as found experimentally. For atomic magnetometers, such densities are considered high, so for this reason they can be referred to as high-density AMs. Any alkali-metal atom can be used, but K, Rb, and Cs are most practical and convenient. K SERF gives the highest sensitivity, but needs the highest operating temperature −180 °C; Cs has the lowest sensitivity and requires the lowest temperature (100–120 °C); Rb occupies the place in between. The high temperature of operation is the main disadvantage of SERF magnetometers, mostly due to issues related to oven design, such as compromise in heating methods and limited choice of non-magnetic, non-conductive materials structurally stable at required temperatures. In this regard constructing ovens for K cells is the most demanding task. Important consideration is the long-term deterioration in cell performance when it is heated to elevated temperatures.

Initially, SERF magnetometers relied on hot air heating [10] to minimize magnetic field noise, and the system consisted of a heating element, a copper or high-temperature plastic tube connected to a source of compressed air, a double-wall oven with vacuum-tube inserts as windows for light. A high-temperature non-metalic oven, together with the tube, was surrounded by a thick layer of thermal insulation. A long tube, the short path of air in the oven, and exhaust of hot air from the oven resulted in excessive heat losses and hence low power efficiency. A bulk of the oven is an additional negative factor. Electrical power for heating was as high as 1 kW, with extra power reserve required for fast heating and accurate temperature control. This heating system was also rigid, suitable mostly for lab applications with a magnetometer positioned inside a shield. So it is not surprising that an alternative was actively sought. Later on, air heating was replaced with electrical heating, which dramatically reduced the oven size and power consumption [14]. But the electrical heating introduced other problems, such as Johnson noise and low duty cycle. To reduce Johnson noise in the AM, the heating element was positioned at some distance from the cell and electrical current was switched off during measurement. In addition to creating noise, the magnetic field from the electrical heater perturbed atomic polarization, and to mitigate this, a high-frequency AC current has been used to which atomic spins do not respond [15]. In spite of the shortcomings, the electric oven design is invaluable in out-of-the-lab applications, where power consumption and portability are at premium and became commonly adopted by many groups. An alternative laser heating method became practically possible in an AM with a small Rb cell [4]. But this type of heating has its own drawbacks when applied to 1-cm cells [16], such as possibility of burning the light-absorbing material used to convert light to heat.

Returning to the discussion of the choice of an optimal alkali-metal atom, one criterion is the fundamental sensitivity or quantum noise. As we will show later, in the SERF regime the fundamental noise depends on the spin destruction (SD) (spin-de-coherence) rate as $R_{SD}^{1/2}$. In the sequence of K, Rb, Cs, which has the spin destruction rates in ratios 1:10:100 [10, 17, 18], the fundamental sensitivities scale as 1:3:10, and even the least sensitive Cs SERF magnetometer is expected to have fundamental noise on the order of 0.1 fT/Hz$^{1/2}$, better than the demonstrated sensitivity level with a potassium cell, 0.16 fT/Hz$^{1/2}$ [13]. The fundamental sensitivity limits currently are well below the demonstrated sensitivities, which are limited by technical noise, and for applications in the presence of magnetic field noise of a few fT, for example due to thermal currents in the magnetic shield, it seems that K, Rb, and Cs are all good choices for AMs. The demonstrated sensitivities is the highest for K [1, 13]; Rb SERF occupies the second place with demonstrated sensitivity of a few fT [3]; Cs SERF comes the last, with demonstrated sensitivity of 40 fT (4 fT photon-shot noise level) [19]. The advantage of low temperature of Cs cell was exploited for the detection of NMR in a microfluidic channel with a Cs SERF based on a microfabricated cell in [20].

Important motivation for developing atomic magnetometers comes from “outdoor” applications, in which portability, low weight, low-power consumption, and

vibration stability are essential. The first SERF magnetometer [1, 10] was implemented on a special non-magnetic optical table with a multi-layer mu-metal shield reducing the ambient magnetic field by a factor of 1 million, and due to the complexity of experimental arrangement and high price, such magnetometers would have only limited use, in the lab with the aim to demonstrate the highest possible sensitivity or in fundamental experiments. For external applications the design had to be simplified and miniaturized, and for successful commercialization, the price also had to be greatly reduced.

With the goal of cost and weight reduction, Kitching's NIST group has been working on the micro-fabrication of miniaturized atomic vapor cells and the integrated laser-electronics packaging, a spin-off project from miniature atomic clock development [14, 21]. They showed that the clock package can be adapted to magnetic field measurements with sensitivity of 50 $pT/Hz^{1/2}$ at 10 Hz. The clocks/magnetometer modules consisted of many layers of various functional components: lasers, filters, lenses, quartz waveplates, ITO heaters, atomic cells, and photodiodes. The components, thin wafers, were stacked on the top of each other to form a compact assembly. Because magnetometers of this type initially were not set up in the SERF configuration, they had fairly poor sensitivity. However, when in a follow-up experiment, a microfabricated atomic cell was tested in the SERF regime, dramatic improvement in sensitivity, almost 1000 times, to the level of 65 $fT/Hz^{1/2}$ was observed [22]. Even higher sensitivity should be possible from the analysis of fundamental quantum noise. One problem with microfabricated cells is that they have significant spin-destruction rate due to diffusion to the walls, so the magnetic resonance is much wider than in a cm-size cells, but in principle this can be compensated by operating the cell at higher than normal temperatures [23].

In parallel at Princeton a cm-scale magnetometer with a small oven and optic setup has been tested to show a high sensitivity on the order of a few $fT/Hz^{1/2}$ [24]. The single-beam fiber-coupled design allowed for not only miniaturization but also flexibility. Indeed, later on, commercial prototypes based on fiber-coupling appeared [4, 25], and now high-sensitivity cm-size atomic magnetometers became commercially available.

The interest in high-density AMs was initially stimulated by high sensitivity in the SERF regime; however, later it was also shown that high-density AMs can be very sensitive outside the SERF regime [6]. For this reason, we combine the overview of SERF and other types of high-density magnetometers in one chapter. The qualitative difference between SERF and non-SERF high-density magnetometers is in the effects of SE collisions on spin de-coherence and sensitivity, so the SE phenomenon will be discussed in some detail.

1.2 Operating High-Density AMs Outside the SERF Regime

Typically the SERF magnetometer is operated with all fields precisely zeroed, and the magnetometer has its frequency sensitivity profile similar to that of the

first-order low-pass filter, with the bandwidth proportional to spin de-coherence rate. When the frequency f of the measured field is outside the bandwidth, the signal falls off as $1/f$ and the sensitivity is mostly lost above a few hundred Hz. The sensitivity can be partially restored if a bias field is applied to "tune" the magnetometer to the frequency of interest [6, 26]. When the resonance frequency exceeds the resonance width, the AM frequency response exhibits a distinct resonance with an additional tail coming from the oppositely rotating field component. At zero field, the contributions from the two resonances double the signal, but with a significant bias field, only one resonance contributes. However, more importantly, the bias field leads to the additional broadening from SE collisions, signifying operation outside the SERF regime. Initially, the SE broadening grows quadratically with the field, but then it slows down and reaches asymptotically some maximum value, which is a non-small fraction of the SE rate. The SE broadening, in addition to the bias field, depends on spin polarization and hence the pumping rate. At a high pumping rate, it is possible to suppress SE broadening with the process known as light narrowing [27]. Pumping, however, leads to additional spin-decoherence, so there is a minimal value of the resonance width, experimentally observed on the order of 100 Hz [6], at the optimal pumping rate, which depends on SE and spin-destruction (SD) rates. Because with frequency laser technical noise decreases and can approach the photon-shot noise limit, of ten nrad level at typical laser power used, it is possible to reach sub fT sensitivity for SE-affected wider magnetic resonances of several hundred Hz [6, 28]. We will discuss RF magnetometer sensitivity and light narrowing in more detail later (e.g. Eqs. 9 and 23).

The RF magnetometer can be converted to a scalar magnetometer if its resonance frequency, which is proportional to a bias magnetic field, is used to measure the field. The only complication is that the coefficient of proportionality, the gyromagnetic factor, is not constant and depends on other parameters. At low frequency it can change by a factor of 1.5 in the case of Rb-87 or K, when field and polarization vary [26]. At a high frequency below the hyperfine frequency, the gyromagnetic factor is almost constant, so the scalar magnetometer can give the absolute value of the field. Near and above the hyperfine frequency, the Zeeman splitting between different levels becomes noticeably unequal leading to distinct multiple magnetic resonances. These resonances can be observed in the Earth's field in atomic cells with low buffer-gas pressure and anti-relaxation coating, when resonance widths are smaller than the splitting. The consequence of multiple resonances is that magnetic field measurements based on resonance frequency will depend on orientation, resulting in the so-called heading error, which limits accuracy to 1–10 nT level. For measurements of the field on the fly, this can be a problem.

2 Principles of Operation and Theory

2.1 The Interaction of Spins with Magnetic Field

A typical high-density atomic magnetometer, such as SERF, contains a heated vapor cell filled with alkali-metal atoms. These atoms have unpaired electron spins which interact with magnetic field. By measuring spin states, one can measure the magnetic field. Quantum-mechanically, the interaction between an atomic spin and a magnetic field is described by the Hamiltonian

$$H = \gamma_e \mathbf{J} \cdot \mathbf{B} + \gamma_N \mathbf{I} \cdot \mathbf{B} + a_{hf} \mathbf{J} \cdot \mathbf{I} \tag{1}$$

Here $\gamma_e = g_J \mu_B/\hbar$, $\gamma_N = g_I \mu_B/\hbar$, μ_B is the Bohr magneton, g_J, g_I are electron's and nuclear g-factors, $\mathbf{J}$ is the total angular momentum of the electron, which is the sum of the electron spin and the orbital momentum, $\mathbf{J} = \mathbf{S} + \mathbf{L}$; $\mathbf{I}$ is the nuclear angular momentum, and a_{hf} is the hyperfine constant. This Hamiltonian is responsible for the splitting of degenerate m-sublevels in magnetic field, called the Zeeman splitting. The solution of Eq. (1) in the case of $\mathbf{J} = \mathbf{S} = 1/2$ is known as Breit-Rabi equation [29]:

$$W(F, M_F) = -\frac{\Delta W}{2(2I+1)} - \frac{\mu_I}{I} B M_F \pm \frac{\Delta W}{2} \sqrt{1 + \frac{4M_F}{2I+1} x + x^2} \tag{2}$$

where $\Delta W = a_{hf}[F_2(F_2+1) - F_1(F_1+1)]/2$ is the hyperfine splitting between $F_2 = I + 1/2$ and $F_1 = I - 1/2$ states at zeros field, $x = (g_J - g_I)\mu_B B/\Delta W$, $g_I = -\mu_I/I\mu_B$. Table 1 gives the list of parameters for different isotopes that can be used in atomic magnetometers. Figure 1 shows a typical dependence of the energy of hyperfine sublevels on applied magnetic field. The transitions between magnetic sublevels $M \rightarrow M \pm 1$ can be induced by time-varying magnetic field that leads to the interaction Hamiltonian $H_{\text{int}} = \gamma_e \mathbf{J} \cdot \mathbf{B}(t) + \gamma_N \mathbf{I} \cdot \mathbf{B}(t)$. The Zeeman resonances often have the Lorentzian shape with the width determined by the spin decoherence rate. Multiple resonances at a low field have almost the same frequency for a given field; however, in a large field the frequency degeneracy is removed, and multiple resonances can be observed. The resonance frequency is the function of the applied dc field and can be used to measure the absolute value of the magnetic field or with higher sensitivity its relative variation.

Table 1 Parameters for calculating Breit-Pauli splitting; μ_N is the nuclear magneton

Alkali-metal atom	I	ΔW (MHz)	μ_I/μ_N
^{39}K	3/2	461.7	+0.39147
^{41}K	3/2	254.0	−0.21487
^{85}Rb	5/2	3036	+1.3527
^{87}Rb	3/2	6835	+2.7506
Cs	7/2	9193	+2.578 8

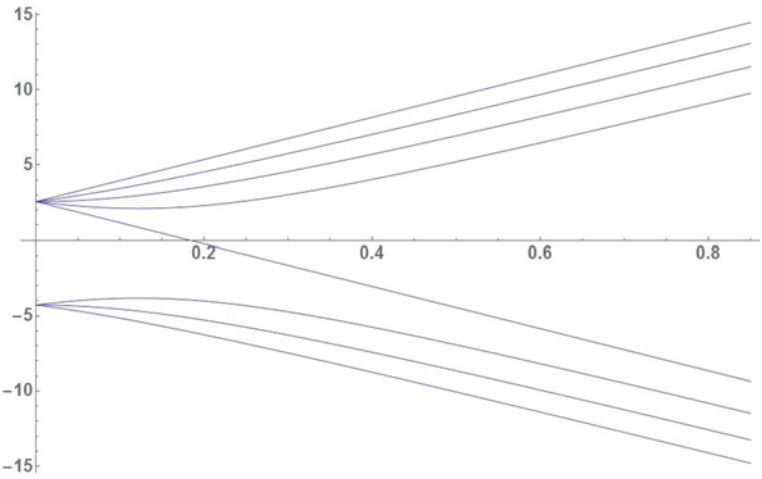

Fig. 1 Zeeman splitting in GHz as a function of magnetic field in T for the case of Rb-87, I = 3/2

2.2 *Light-Spin Interactions*

There are at least two methods for creating significant spin polarization: (i) application of magnetic field and (ii) irradiation of atoms with resonant circularly polarized light [30]. For the first method, to reach high degree of polarization would require prohibitively large fields, not to mention that such fields or coils generating them would interfere with sensitive measurements; thus, the field-polarization method is impractical for use in atomic magnetometers. The second method—*optical pumping*—is not only very efficient but also straightforward to implement. Not surprisingly, all sensitive atomic magnetometers rely on this second method. How does optical pumping work? Intuitively, optical pumping can be understood from the conservation of angular momentum, since with the absorption of a photon, a unit of angular momentum is transferred to the atom. The conservation of angular momentum, on the other hand, is the consequence of the well-known m-selection rules. Using these rules, the pumping efficiency can be predicted if we also consider the balance between various transitions in the atom after it absorbs a photon. In the presence of buffer gas, usually added to the alkali-metal cell of high-density AMs, in a quantity of 1 amg or so, the hyperfine levels are not resolved, and only four levels (Fig. 2) will be necessary to consider: two m-sublevels of the ground state and two m-sublevels of the $p_{1/2}$ excited state. Note that for simplicity and practical relevance we consider here the pumping on the D1 line: Other lines can be used as well, but pumping on the D1 line is most optimal for achieving almost 100 % polarization in optically dense vapor. When a circularly polarized photon is absorbed, an alkali-metal atom undergoes the transition $|ns_{1/2}, -1/2\rangle \rightarrow |np_{1/2}, +1/2\rangle$, which depletes the population of the $-1/2$ ground state. If the atom returned to the same state, no pumping would occur, but because of fast collisions with nitrogen

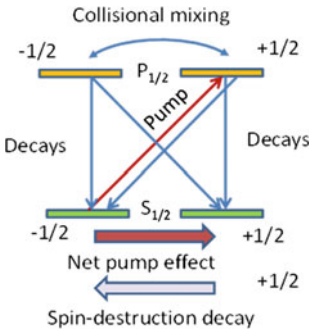

Fig. 2 Diagram for explaining depopulation pumping with a circularly polarized light with a four-level system

molecules (added to improve pumping efficiency) equally repopulating the excited states and following radiative transitions to the both ground states with equal probability, the transfer of population from the −1/2 ground state to the other ground state will be significant. The pumping efficiency, as measured by the ratio of the number of polarized atoms to the number of absorbed photons, is quite high, only somewhat reduced by the decays to the −1/2 ground state. More specifically, when collisional mixing is faster than radiation decay, one absorbed photon would remove one atom from the $m = -1/2$ ground state which then would return with equal probability to either ground states, so the efficiency is one half of the case when the atom would only return to the $m = +1/2$ state.

Optical pumping continuously creates difference in the population of Zeeman sublevels, but the population is also randomly redistributed with some rate, spin-destruction rate, due to various relaxation processes. After many absorption/decay cycles, some equilibrium polarization, often close to 1, is established, $R/(R+R_{SD})$, where R_{SD} is the spin destruction rate and R is the pumping rate.

When spins are polarized, their dynamics can be described by a single average spin. In a magnetic field, it will change its orientation and magnetic field can be detected by measuring one projection of the spin. For this, the rotation (the Faraday effect) of the linear polarization by atomic vapor of the probe beam can be used. The best sensitivity can be achieved when the probe beam is sent at the perpendicular direction to the pump beam.

Optical probing is a highly sensitive method to detect the states of atomic spins based on strong spin-dependent interaction of light with polarized atoms. This is for two reasons. First, interaction of light with atoms is spin-dependent due to the m-selection rules; second, the noise of polarization measurements is very low, limited by the fundamental photon-counting noise of nrad level. Absorption measurements are also possible, but they result in lower sensitivity. One drawback of the absorption method is stronger decoherence of spins by light tuned closer to the absorption resonance.

The absorption and Faraday rotation for a typical density of alkali-metal atoms can be estimated by employing a two-level model, applicable to an atom collisionally broadened in 1 amg of helium or nitrogen, which is a typical pressure in

high-density AMs. In this case, the collisional width exceeds both the Doppler width and the hyperfine splitting; thus the absorption coefficient is:

$$\alpha(v) = ncr_e f \frac{\gamma}{(v - v_0)^2 + \gamma^2} \tag{3}$$

Here n is the density of atoms, c is the speed of light, r_e is the classical electron radius, v is the frequency of light, f is the oscillator strength, and γ is the absorption profile linewidth. The maximum absorption will be in the center, $\alpha(v_0) = ncr_e f/\gamma$. When the potassium cell is filled with He, the linewidth is about 7 GHz (HWHM) or 0.014 nm per 1 amg (1 amg is the density of the gas at normal conditions) [26]. This line width at He density on the order of 1 amg exceeds the hyperfine spitting of ^{39}K (I = 3/2), 462 MHz, and the Doppler width HWHM = 500 MHz. In heavier alkali-metal atoms the hyperfine splitting, which is 3036 MHz in Rb (I = 5/2) and 9192 MHz in Cs (I = 7/2), can become comparable to the buffer gas broadening at 1 atm and more complicated model needs to be used.

In the Faraday detection method, the probe laser is detuned from the resonance, which facilitates the propagation of light through the optically thick medium and reduces the spin destruction by the probe light, which follows the profile of $\alpha(v)$. Linearly polarized light can be decomposed into two circularly polarized components, and because refractive indices n_+ and n_- are not equal due to differences in the population of the m-sublevels (this is when spins are polarized), the plane of polarization of linearly polarized light will be rotated by non-zero angle

$$\theta = \frac{\pi(n_- - n_+)l}{\lambda} \tag{4}$$

Here λ is the wavelength and l is the pathlength. Large rotation of light polarization in optically pumped vapors is due to the strong dependence of the refractive index on atomic spin orientation. It can be derived from Eqs. 3–4 and the Kramers-Kronig relations that the rotation angle by alkali-metal atoms is

$$\theta = \pm\frac{1}{2} l r_e c f n P_x D(v - v_0) \tag{5}$$

where $D(v)$ is Lorentzian dispersion profile, $D(v) = \frac{v}{v^2 + \gamma^2}$. The rotation for D1 and D2 lines are of opposite signs. In most practical cases, only one line needs to be considered.

While optical pumping leads to redistribution of populations, both the pump or probe beams can affect the Zeeman splitting, similarly to magnetic fields. The effect is referred to as light shift. The pump rate R and light shift L are both proportional to the intensity of the circularly polarized light, and they can be found from the expression for the complex optical pumping rate:

$$R + iL = \pi r_e c f \Phi \Lambda(v - v_0) \tag{6}$$

where $\Lambda(v) = \frac{1}{2\pi}\frac{2\gamma + iv}{v^2 + \gamma^2}$ and $\Phi = I/hv$ is the photon flux.

It can be immediately seen that light shift is comparable to the pumping rate when the light is detuned by one linewidth from the absorption maximum. Light shift follows the dispersion Lorentzian, while the pumping rate follows the absorption Lorentzian, with the same coefficient. Divided by gyromagnetic factor, light shift will have units of a magnetic field and it can be included into the Bloch equations or in the density matrix equation as an additional fictitious magnetic field. Its direction coincides with the direction of the laser beam and the sign depends on the sign of circular polarization. Normally, only circularly polarized light creates light shift. When light is linearly polarized, it consists of almost equal number of circularly polarized photons of two signs, with small fluctuation in the difference. The fluctuations lead to so-called light-shift noise [6].

For elliptically polarized light, in general, it can be written that

$$P = \mathbf{s}\, \cos\theta R/(R + R_{SD}) \tag{7}$$

where **s** is the vector which amplitude is equal to the degree of circular polarization and direction is pointing along the pumping beam direction. Scattering of pump light by atoms can lead to pumping in "wrong" directions and the reduction in the polarization. To minimize the scattered light from re-emission, the AM cell is filled with nitrogen buffer gas that effectively quenches excited states faster than the radiation decay.

Since the light intensity and frequency constantly fluctuate and the intensity is not uniform across the AM cell, light shift both adds noise to the AM signal and broadens magnetic resonances similarly as magnetic field gradients. If intensity fluctuations play a dominant role, the light shift effects can be minimized by tuning the laser to the center of the absorption resonance. If frequency fluctuations are more important, then light-shift noise can be minimized by detuning from the center, but in general it is impossible to remove completely light shift noise by changing the wavelength. Light shift produced by linearly polarized probe beam (probe light shift) can also lead to the noise and broadening, not only due to fundamental fluctuations in the number of photons, but also due to imperfections of glass cell windows and other optics that lead to birefringence. By stabilizing wavelength and intensity, the fluctuations in light shift can be reduced, so it is important to use high-quality lasers not only for probing but for pumping as well.

As we mentioned above, alkali-metal atoms have two strong D1 and D2 absorption lines in a convenient wavelength range, but the D1 line is preferable due to higher polarization level that can be achieved in optically dense vapors. One reason for this is that D1 light is less attenuated in optically dense polarized vapors. Actually, the intensity I of the D1 line follows this equation

$$dI/dz = -\alpha(1 - P_z)I \tag{8}$$

and intensity attenuation is substantially reduced when the polarization projection along the propagation direction P_z is close to 1. This is not true for the D2 line. Alternatively, to avoid strong absorption in an optically dense vapor, the pump laser can be tuned off the D1 or D2 resonance. For far enough detuning, the intensity attenuation can become linear with the propagation distance rather than exponential, and this would improve the uniformity of AM sensitivity across the cell, especially if a counter propagating beam is added by, for example, retro-reflecting the beam after it passes the cell. One consequence of detuning is large light shift. It can be minimized by having two frequencies on opposite sides of the center of absorption [28].

For probing, D1 also gives some advantage because of smaller absorption coefficient (note that the absorption reduces the probe beam intensity on the photo-diode and hence shot-noise sensitivity); still, D2 line has been used for probing in some cases for example to combine probe and pump beams in a single beam and separate them after the cell [3].

2.3 Spin-Exchange Collisions

SE collisions between alkali-metal atoms have cross-sections on the order of 10^{-14} cm^2, substantially exceeding the cross-sections of spin-destruction collisions [10]. In case of potassium, which is used in most sensitive SERF magnetometers, the ratio is very large, $\sim 10^4$. SE collisions can limit the sensitivity of AMs. Because alkali-metal atoms have a non-zero nuclear spin, the ground state is split in many sublevels each having its own somewhat independent evolution and interacting with others. For complete analysis, the density-matrix-equations (DME) have to be solved [10, 26] (a short discussion is provided below).

The SERF magnetometer idea is based on the discovery by Happer and Tang [12] that in a small magnetic field the spin-resonance lines at high densities of alkali-metal vapors become very narrow. Happer and Tam [31] derived an analytical expression for the frequency shift and width of magnetic resonances for an arbitrary SE rate in the limiting case of low polarization. This equation predicts zero broadening at large SE rates at zero field, essentially the SERF regime, although low polarization is not optimal for the SERF operation. Another interesting effect—light narrowing of magnetic resonances, or more precisely the reduction of the SE contribution to transverse relaxation rate at high polarization levels—was discovered much later in 1998 by Appelt et al. [27]. The analysis of SE effects at low magnetic field for an arbitrary spin polarization was first performed in [10], where it was shown that SE relaxation is completely eliminated at zero field for arbitrary spin polarization. The density-matrix equations that contain SE collisions, optical pumping, and other terms for complete description of the SERF magnetometer have been formulated in [10, 32]. The numerical solution of this density-matrix equation

for an extensive range of AM parameters, such as SE rate, pumping rate, and magnetic field, has been obtained and compared with experimental measurements to establish a firm basis for the analysis of SERF and other high-density AMs [26].

2.4 *Classification of High-Density AMs (SERF, RF AM, and Scalar RF AM)*

The SERF magnetometer exploits full suppression of otherwise large effects of SE collisions on relaxation for superior sensitivity, especially at the fundamental level. However, the operation in the SERF regime is limited to a low frequency and magnetic field range. By applying a bias field the frequency range can be greatly extended, so it is interesting to consider the operation of the high-density magnetometer beyond the SERF regime, when the bias magnetic field is no longer small. The investigation of the non-SERF regime of "the SERF magnetometer" was conducted in detail in Ref. [26], which resulted later in the discovery that at high frequency an AM can also have fT sensitivity [6].

One characteristic feature in operation outside the SERF regime is that SE collisions start to affect the magnetic resonance of the spins. As we mentioned, SE collisions have much larger cross section than SD collisions, and the broadening due to SE collisions can be on the order of several kHz at typical densities of alkali vapors used in SERF magnetometers, exceeding by orders of magnitude a typical SERF bandwidth of several Hz. Because in the AM the bandwidth and the signal amplitude are inversely related, the bandwidth investigation is central for the analysis of the sensitivity. The bandwidth of high-density magnetometers and the broadening due to SE were investigated in detail [26] experimentally and numerically by solving the DM equation. An example of comparison of simulations with experiment is given in Fig. 3.

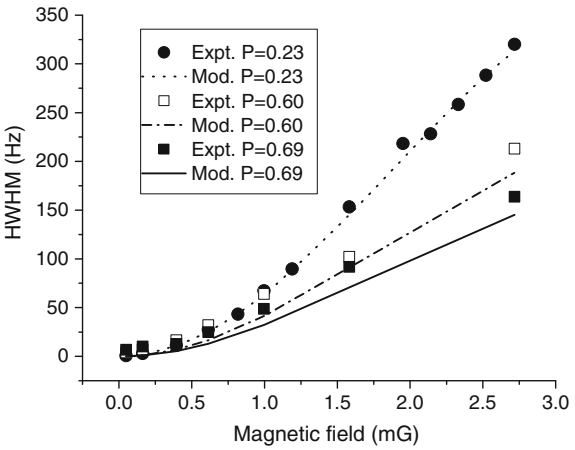

Fig. 3 Broadening of magnetic resonance with the field. Adopted from [26]

In the non-SERF regime, the SE broadening can reach levels of several kHz for typical SERF magnetometer operating temperatures. Good understanding of SE effects is essential for designing sensitive magnetometers at arbitrary frequency. For example, the SE broadening can be suppressed with light narrowing [27]. Light narrowing happens due to the reduction of the SE collisions between oppositely precessing spins of F = I + 1/2 and F = I − 1/2 hyperfine manifolds when the majority of atoms are populated into the stretched state (F = I + 1/2, M = F) by the strong pumping action. Additional detailed explanation is provided in Refs. [6, 26]. Experimentally, light narrowing of more than 10 times was observed, with similar improvement in magnetic field sensitivity. Although SE broadening can be totally suppressed by pumping all atoms into the stretched state, the pump light itself broadens the magnetic resonance, linearly with power, and thus an optimal pumping rate exists that minimizes the resonance width. This is evident from an analytical equation [6] in the limit of polarization close to 1:

$$T_2^{-1} = \frac{R}{4} + \frac{R_{SE}R_{SD}}{R} G(\omega_0, R_{SE}) \tag{9}$$

$$G(\omega_0, R_{SE}) = \mathrm{Re}\left[\frac{R_{SE} + 4i\omega_0^2/\pi v_{HF}}{5R_{SE} + 8i\omega_0^2/\pi v_{HF}}\right] \tag{10}$$

Here ω_0 is the spin precession frequency and v_{HF} is hyperfine frequency. This equation is derived for atoms with I = 3/2. In the case of precession frequency below the MHz range, $T_2^{-1} = \frac{R}{4} + \frac{R_{SE}R_{SD}}{5R}$ and the optimized pumping rate leads to the following minimal bandwidth: $(1/T_2)_{\min} = (R_{SE}R_{SD}/5)^{1/2}$. This width is much smaller than spin-exchange broadening in the no-light-narrowing regime, $R_{SE}/8$, because $R_{SD} \ll R_{SE}$, about 10,000 times in potassium. The light-narrowing factor, which is the ratio of the minimal width for the optimal pumping rate and the maximum width without light narrowing, is $K = (5R_{SE}/R_{SD})^{1/2}/8$. If the SD rate is dominated by K-K collisions, a condition that can be achieved by raising density of alkali-metal atoms, then $K = (5\sigma_{SE}/\sigma_{SD})^{1/2}/8$, where σ_{SE} and σ_{SD} are spin-exchange and spin-destruction cross sections. Potassium has $\sigma_{SE} = 1.8 \times 10^{-14}\,\mathrm{cm}^2$ and $\sigma_{SD} = 1 \times 10^{-18}\,\mathrm{cm}^2$, so the maximum light-narrowing factor $K_{\max} \approx 37$. In practice, such light-narrowing is hard to achieve due to, for example, non-uniformity of the pumping rate across the cell.

The high sensitivity of the RF magnetometer is achieved by bias field magnetic resonance tuning, light narrowing, and technical noise reduction at high frequencies. It turns out that in terms of demonstrated sensitivity the FR AM [6, 28] can be comparable to that of the SERF magnetometer [1, 13], primarily due to the latter technical noise limitations. The fundamental noise of the RF magnetometer has been investigated in Ref. [6]. We discuss this question in a separate section below.

Because the RF magnetometer sensitivity exhibits resonant behavior with resonance frequency being a function of the bias magnetic field, this magnetometer can be converted to a scalar magnetometer by applying an RF modulation field near

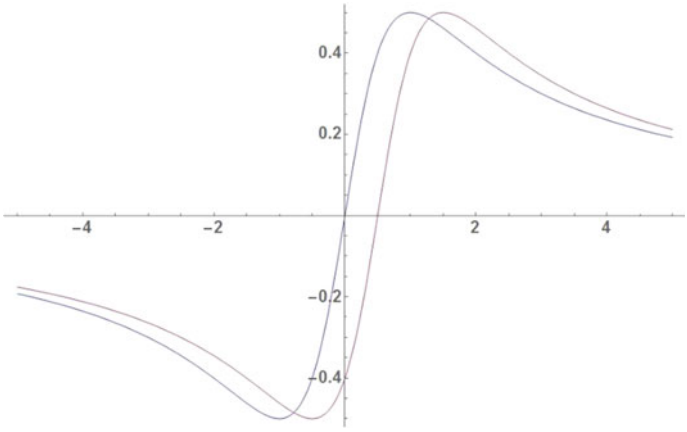

Fig. 4 Conversion of the RF magnetometer out-of-phase signal to the scalar magnetometer signal. Magnetic field shifts the curve and hence the RF signal is sensitive to the field. Arbitrary units are used, with the position of the maximum being on the order of magnetic resonance width

the resonance frequency, $\omega_L = \gamma\sqrt{B_x^2 + B_y^2 + B_z^2}$. Note that the position of magnetic resonance depends on the total field, not its projection. One advantage of the scalar magnetometer is that it can measure magnetic field in the Earth-field environment, without mu-metal shielding or field compensation, unlike the SERF. The resonance frequency is about 350 kHz (I = 3/2 atoms), and small variations in the Earth's field can be readily observed as the shifts in the resonance. The in-phase and out-of-phase lock-in amplifier signals near the magnetic resonance have absorption and dispersion Lorentzian dependencies on frequency. It is convenient to use the dispersion component that gives the maximum slope at the resonance (Fig. 4). Then the signal of the scalar magnetometer is proportional to the deviation of the field from the resonance condition. The lock-in amplifier can be used to demodulate the high-frequency RF magnetometer signal to extract slow-varying quasi-dc field. The sensitivity to the dc field is determined by the slope of the dispersive component. The slope of the RF magnetometer was investigated in Ref. [11]. Because the signal initially grows with the RF field excitation amplitude and then decreases due to SE broadening, optimal excitation amplitude exists. The fundamental limit of the sensitivity of the scalar magnetometer can be derived from that of the RF magnetometer in which the effects of large-excitation amplitude broadening are incorporated. The fundamental noise of the scalar magnetometer is investigated in a separate section.

The principal advantage of the scalar magnetometer is its insensitivity to orientation and possibility to operate in the ambient Earth's field without compensation coils. The scalar magnetometer can also measure the absolute value of the field without calibration by converting frequency to the field using the gyromagnetic constant. Unfortunately, the gyromagnetic constant slightly depends on the field,

polarization, and orientation, which is the consequence of multiple partially overlapping Zeeman resonances. If the nuclear spin were zero, only one resonance would exist and its position would be a function of magnetic field only. In this regard, the He magnetometer has an advantage.

2.5 Dynamics of Atomic Spins

Spins in atomic vapors can have complicated dynamics. Their behavior is affected by magnetic fields, light-atom interactions, atomic-wall and interatomic collisions, and other factors. In the presence of spin-affecting collisions, the Schrödinger equation has to be replaced with the density matrix equations. In SERF and similar high-density magnetometers, only ground-state hyperfine sublevels need to be considered. There are 2F + 1 = (2I + 2) upper and 2I lower hyperfine states with the total number of 4I + 2 states (in the case of I = 3/2, 8). Zeeman splitting at low field is linear and the hyperfine states oscillate with the same frequency in magnetic field (recall that ac magnetic field causes transitions between neighboring M states), although the precession directions of spins of the lower and upper hyperfine states are opposite. Spin exchange collisions strongly affect the evolution of hyperfine sublevels. However, SE collisions conserve the total angular momentum of the colliding pair, and at certain conditions, when AM operates in the SERF regime, SE collisions do not lead to change in the polarization and do not affect the coherence. Qualitative and intuitive considerations are possible, but ultimately to simulate spin dynamics and extract important parameters such as the magnetic resonance width, the density matrix equations need to be solved. The density matrix equations provide accurate description of the system, as long as experimental parameters such as spin density, buffer gas pressure, laser intensities and polarization are specified.

2.5.1 Density Matrix Equations

The behavior of atomic spins in alkali-metal vapors is quantitatively described with the following density matrix (DM) equation [10, 26, 32, 33]:

$$\frac{d\rho}{dt} = a_{hf}\frac{[\mathbf{I}\cdot\mathbf{S},\rho]}{i\hbar} + \mu_B g_S \frac{[\mathbf{B}\cdot\mathbf{S},\rho]}{i\hbar} + \frac{\varphi(1+4\langle\mathbf{S}\rangle\cdot\mathbf{S})-\rho}{T_{SE}} + \frac{\varphi-\rho}{T_{SD}} + R[\varphi(1+2\mathbf{s}\cdot\mathbf{S})-\rho] + D\nabla^2\rho. \tag{11}$$

Here ρ is the density matrix, which has dimension of the number of hyperfine states; $\varphi = \rho/4 + \mathbf{S}\cdot\rho\mathbf{S}$ is the pure nuclear part of the density matrix, $\langle\mathbf{S}\rangle = Tr(\rho\mathbf{S})$, T_{SE} is the spin-exchange collision time, T_{SD} is the spin-destruction time, R is the pumping rate, and $\mathbf{s}$ is the optical pumping vector defined earlier. The first and the second terms describing the hyperfine and Zeeman interactions are

obtained from the Von Neumann equation, $i\hbar\frac{d\rho}{dt} = [H, \rho]$, where H is the Hamiltonian defined in Eq. 1. The rest are spin-exchange, relaxation, optical pumping, and diffusion terms. The solution of the DM equation can be used to explain many observed effects in atomic magnetometers, including the spin precession frequency and decoherence rate in a wide range of experimental conditions. The DM equation is considered the most appropriate theoretical framework, but, unfortunately, in many cases only numerical solutions are possible. Note that the SE term, $\frac{\varphi(1+4\langle\mathbf{S}\rangle\cdot\mathbf{S})-\rho}{T_{SE}}$, is non-linear, and the solution using eigenvalue-finding subroutines is not immediately applicable. Instead, an iterative solution has to be used with appropriate zero-order guess solutions. Under some conditions, the DM equation can be simplified and analytical solutions can be derived. It is also quite useful to separate the expectation value of spin into two parts, averaged over the upper (F = I + 1/2) $\mathbf{S}_{\text{up}}$ and the lower (F = I − 1/2) $\mathbf{S}_{\text{down}}$ hyperfine manifolds of the ground state. At low field, the spins of these manifolds rotate with equal but opposite frequency:

$$\begin{aligned}\frac{d\mathbf{S}_{up}}{dt} &= \gamma\mathbf{B}\times\mathbf{S}_{up}\\ \frac{d\mathbf{S}_{down}}{dt} &= -\gamma\mathbf{B}\times\mathbf{S}_{down}\end{aligned} \tag{12}$$

If the density were small, these two groups would precess independently, but at typical densities of SERF magnetometers, the strong SE interaction affects their dynamics. In the SERF regime, when between SE collisions the spins of the two manifolds do not significantly change orientations, they tend to rotate together, but at slower rate. In non-SERF regime, the spins of the two manifolds start to spread, and after SE realignment, transverse polarization becomes lost. When pumping is strong enough to populate most spins into the stretched state, the RF magnetometer would have much smaller number of atoms in the down manifold, resulting in the reduced spin-decoherence rate from the SE collisions.

When no field excitation is applied, SE collisions lead to establishing the well-known in NMR spin-temperature (ST) distribution:

$$\rho_{ST} = k_n \exp(\boldsymbol{\beta}\mathbf{F}) \tag{13}$$

where $\boldsymbol{\beta}$ is the ST parameter, k_n is the normalization factor, and $\mathbf{F}$ is the total angular momentum vector. This specific matrix is the eigensolution of the DM equation that contains the SE term.

The ST distribution for I = 3/2 is illustrated in Fig. 5. The ST distribution is maintained in the SERF regime in the static and the rotating frame, if the spin precession is induced. Outside the SERF regime, the ST distribution is not valid, but when the deviation from the SE distribution is small, perturbation theory can be effectively used to obtain a solution. The dynamics of spins in the RF AM was analyzed with this approach [6, 26, 33].

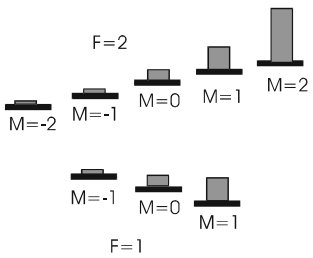

Fig. 5 A typical spin-temperature distribution for the case of I = 3/2

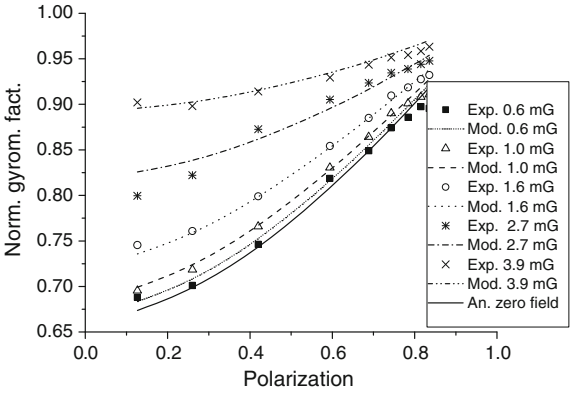

Fig. 6 Dependence of the gyromagnetic factor on spin polarization. Adopted from [26]

The solution of DM in the general case was analyzed and compared against experimental data in [26]. For example, it was found that gyromagnetic factor depends on the field and polarization as shown in Fig. 6. The magnetic resonance width also depends on these parameters (Fig. 3).

2.5.2 Bloch Equation

In the SERF regime, because the spins precess with the same frequency and relax with the same rate, they can be described by a single Bloch equation:

$$\begin{aligned} dS_x/dt &= \gamma S_y B_z - \gamma S_z B_y - S_x/T_2 \\ dS_y/dt &= -\gamma S_x B_z + \gamma S_z B_x - S_y/T_2 \\ dS_z/dt &= \gamma S_x B_y - \gamma S_y B_x + (S_0 - S_z)/T_1 \end{aligned} \tag{14}$$

Here γ is the gyromagnetic ratio of atomic spins, T_1 is the longitudinal relaxation time, and T_2 is the transverse relaxation time. This behavior can be verified by direct solution of the DM equation. Outside the SERF regime but when spins are fully polarized, the behavior of spins can still be described with one Bloch equation. The effect of the spins from the down manifold precessing in the opposite direction can be incorporated into modification of the gyromagnetic factor and relaxation

rates. The rotating frame approximation, which is often used for deriving analytical solutions of the Bloch equation, can be applied, as long as the interaction with the down-manifold spins can be neglected beyond their contributions to the gyromagnetic factor and relaxation constants.

The description of dynamics with the Bloch equation is convenient to exploit the analogy with NMR [34], where it is the basis for the analysis of a multitude of sequences for manipulating nuclear spins. Among topics that can be readily studied by analogy with NMR are: the free-induction decay, spin echo, spin-temperature distribution, motional narrowing, broadening by the RF field and field gradients, validity of rotating wave-approximation, magnetic-resonance imaging. Even when the Bloch equation is not strictly applicable, it can still provide qualitative guidance for many experiments with atomic magnetometers. For example, a small excitation amplitude solution of the DM equation for a given separate resonance is equivalent to a small amplitude solution of the Bloch equation. This becomes evident with the use of complex variables $A_+ = A_x + iA_y$ allowing us to simplify the Bloch equation to this form:

$$dS_+/dt = i\gamma(B_z S_+ - S_z B_+) - S_+/T_2 \tag{15}$$

In the SERF regime, a steady-state solution of the Bloch equation can be used to characterize the dynamics of spins and obtain the magnetometer signal:

$$S_x = S_0 \frac{\gamma B_y T_2 - (\gamma T_2)^2 B_x B_z}{1 + (\gamma T_2)^2 (B_x^2 + B_y^2 + B_z^2)} \tag{16}$$

In this equation, T_2 includes the broadening by the pump beam. The x-component of the spin, which is along the probe beam, gives normally the signal of the SERF magnetometer that has orthogonal pump and probe beams.

2.5.3 Tuning Fields for Maximum Sensitivity

According to Eq. 16 to maximize the sensitivity of the SERF magnetometer all magnetic-field components have to be zeroed. There are several strategies for doing this. In one strategy, the dc AM signal offset is used to zero the By field, then Bx is modulated to zero the Bz field, and Bz is modulated to zero the Bx field. The process is repeated until convergence is achieved. An alternative strategy is to maximize the signal induced by low-frequency By modulation by varying all three components in an arbitrary sequence. This strategy works because the denominator containing the sum of squares of all the components is minimized independently when each component is zeroed. The modulation frequency has to be lower than the bandwidth for the steady-state solution to be valid. If frequency is too high, the signal maximization procedure can result in some residual non-zero field. This is because outside the steady-state regime, the resonance enhancement for a non-zero

bias field would increase the signal. In the presence of noise, using high-frequency magnetometer signal can be useful for approximate zeroing of transverse components.

Apart from giving maximum signal, field zeroing also helps to reduce light-shift noise that can be present due to pump and probe laser frequency and intensity fluctuations. Light shift is equivalent to magnetic field, as we discussed earlier, and the SERF signal will depend on the product of Bx and Lz, where Lz is the light shift along the pump direction. Similarly, the contribution of the probe light shift noise will be proportional to Bz, and it can be removed by zeroing Bz.

When a magnetometer is tuned with a biased field and its operation moves outside the SERF regime, the situation become quite different. First, zeroing all components is replaced with zeroing transverse components only. The AM response to Bx and By fields is the same, and the AM output can be maximized using the modulation of either component. Second, RF AM would have the light-narrowing effect maximized when the total field is along the pump direction, and hence by maximizing the output, the transverse components will be zeroed. Because when the transverse components are smaller than the z component, their effect on frequency is quadratically small, the iterations of maximization by adjusting transverse and then longitudinal components would converge. The pump light-shift noise becomes suppressed when the transverse fields are zeroed, but probe light-shift noise does not. Thus it is important to have a probe laser with a stable amplitude and frequency, also its beam expanded to reduce the light intensity and hence the magnitude of light shift.

Tuning the fields for the scalar magnetometer is not discussed in the literature. To some extent, the scalar magnetometer by definition has to be immune to field orientation. Apparently, if it is based on the RF magnetometer, the performance of the RF magnetometer has to be optimized. However, there could be some additional issues with the scalar magnetometer. Pump light-shift becomes very important to consider and its contribution to the signal cannot be removed by adjusting fields. The probe light shift plays a similar role as in the RF magnetometer.

Finally, the fields in a parallel beam SERF magnetometer [3, 24] can be zeroed as well using the signal maximization strategy discussed above. The steady-state solution for the z component can be similarly derived from the Bloch equation.

2.5.4 Analogy with NMR

Atomic spins obey the Bloch equation under some conditions (SERF regime; strong polarization case) as nuclear spins and direct analogy with NMR exists that can be exploited. The field of NMR is very rich, including applications of many pulse sequences, such as free induction decay (FID), spin-echo, Car-Purcell-Meiboom-Gill (CPMG); this analogy can be used for benefits of both NMR and atomic magnetometry. Some work has been already done, merely scratching the surface, but a lot remains to be explored. To give some flavor of possibilities, below we will discuss magnetic resonance imaging of Rb-87 spins.

2.5.5 Magnetic Resonance Imaging of Rb Atomic Spins

Magnetic resonance imaging (MRI) is an extremely valuable method of imaging based on the precession of spins in a magnetic field. Introduction of MRI for medical diagnostics revolutionized the field. Many applications have been developed over the years. From the analogy between nuclear and alkali-metal spins, which includes a similar resonance response to the RF excitation in a magnetic field, long coherence times, possibility for frequency and phase encoding with constant and pulsed gradients, it is obvious that MRI methods can be used in experiments with atomic spins. Several publications have demonstrated MRI of Rb and Cs spins. Below we will describe in some detail an imaging experiment published in [34].

As in usual MRI, the system contains uniform-field and gradient coils; the uniform field is necessary to specify the spin precession frequency, while gradients are used for frequency and phase encoding. The field strength is much below the field in conventional MRI, but considering much larger polarization of the atomic spins achieved with optical pumping and high-sensitivity of optical detection, the low-field operation should provide sufficient SNR.

A 3D MRI gradient-echo method with one frequency and two phase-encoding gradients was used to image the polarization in the atomic cell. The sequence started with a $\pi/2$ pulse, which excited polarized Rb-87 spins. During the $\pi/2$ pulse all gradients were off to avoid the slice selection or position-dependent phase accumulation. The gradient echo was formed by the reversal of the gradient G_z along the readout direction, which was also the direction of the pump beam. Phase encoding gradients G_y(the y axis approximately coincides with the probe-beam direction) and G_x were applied between the $\pi/2$ pulse and G_z reversal times, $t_{\pi/2}$ and t_{-G_z}.

The resulting image shown in Fig. 7 demonstrates resolution on the order of 1 mm. While in conventional MRI proton spins do not move much across the tissue, in the case of Rb spins, a characteristic diffusion length is comparable to the resolution. To reduce motional artifacts, the sequence timing was shortened to the

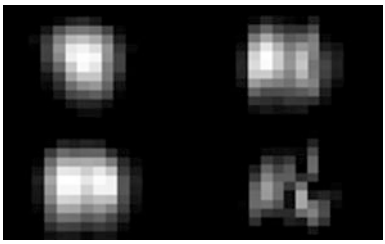

Fig. 7 Rb polarization in an atomic cell. Slices in depth are arranged from top to bottom and left to right in increments of 1.4 mm. In-plane resolution is 1.2 (horizontal) by 0.8 (vertical) mm^2. Resolution in vertical direction is affected by diffusion. The maximum brightness corresponds to polarization of 1. Adopted from [34]

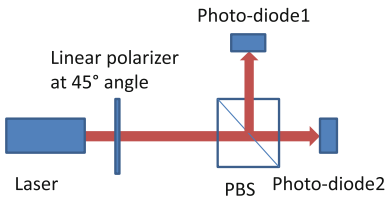

Fig. 8 Polarization detection with a polarizing beam splitter (PBS)

msec scale. One noticeable feature that some areas on the image of the atoms inside the cell are dark, meaning incomplete fill with pump and probe beams of the cell volume. Since the sensitivity depends on active volume, MRI of the magnetometer cell can be a valuable diagnostic tool for checking the beam alignment or for other troubleshooting tasks. More generally, MRI can be a valuable research tool for studying spin dynamics and interactions in the cell.

2.6 Polarization Rotation Measurement Schemes

Optical detection of the atomic spin state is normally based on the measurement of polarization rotation using laser polarimetry. A typical polarimeter consists of a polarizing beam splitter (PBS) and a polarizer rotated at an angle ($\sim 45°$) with respect to the PBS axis (Fig. 8). The intensities of the split beams are $I_0 \cos^2 \theta$ and $I_0 \sin^2 \theta$, where θ is the angle between light polarization and the axis of the beam-splitter cube. When the PBS outputs are accurately balanced, the noise arising from laser intensity fluctuations will be suppressed, in some cases 100 times. The angle rotation can be determined as

$$\delta\theta = \frac{U_1 - U_2}{2(U_1 + U_2)} \approx \frac{\delta U}{4U_1} \tag{17}$$

where U_1 and U_2 are the outputs of the two photo-detectors, usually measured with trans-impedance amplifiers. The noise level is determined by the number of electrons, which is the current divided by the electron charge.

An alternative polarimetry setup contains two crossed polarizers, a polarization modulator inserted between, and a photodiode. The signal is detected as the first harmonics of the modulation frequency. A polarization modulator reduces noise arising from intensity fluctuations in the probe beam and from other causes, which often inversely scale with frequency, 1/f noise. The modulation amplitude of polarization angle is chosen to be a few degrees. Both the beam splitter method and polarization modulation techniques can be used in multi-channel magnetic field measurements.

2.7 Noise Analysis

AM noise in general can be separated into detection system noise and intrinsic spin noise. While many schemes for the detection were demonstrated, usually they are not analyzed in terms of fundamental noise, but rather the experiments are focused on sensitivity demonstrations. Most complete fundamental noise analysis is done in the case of orthogonal beam configurations with the Faraday detection method using a polarizing beam splitter. So this analysis will be discussed in this section in detail.

The sensitivity of probe light polarization measurements is limited by photon shot noise $1/\sqrt{N_{Ph}}$, where N_{Ph} is the number of detected photons. This is because linearly-polarized light can be decomposed into an equal mixture of right and left circularly polarized photons, which numbers fluctuate according to a Poisson distribution. The polarization noise is extremely low, in nrad range, even at moderate laser power of a few mW. At high frequency it can be readily reached, but at low frequency, technical noise often exceeds the photon shot noise.

Apart from this noise, spin-fluctuation noise can also limit the sensitivity. This type of noise occurs due to quantum fluctuations of projections of the spin, which can be estimated from the uncertainty principle. The spin noise scales as $1/\sqrt{N_{Spin}}$, where N_{Spin} is the number of spins in the active volume of the AM. In a typical AM, the fundamental noise is much below 1 fT/Hz$^{1/2}$ and in practical systems, especially at high frequency of operation, the sensitivity is not far off from the fundamental sensitivity.

2.7.1 SERF Sensitivity

High sensitivity of the SERF magnetometer is primarily due to full suppression of SE broadening. The residual magnetic resonance width is determined by spin-destruction rates from interatomic collisions, collisions with the walls, the interaction with the pump and probe beam. In Ref. [19] the fundamental noise of SERF magnetometer has been derived

$$\delta B = \frac{1}{g_S \mu_B P_z \sqrt{nVt}} \sqrt{2\left(R + \Gamma_{pr} + \Gamma_{SD}\right) + \frac{4\left(R + \Gamma_{pr} + \Gamma_{SD}\right)^2}{\Gamma_{pr}(OD)_0}} \tag{18}$$

where Γ_{SD} is the total collisional spin-destruction rate, Γ_{pr} is the spin-destruction rate due to probe beam, $(OD)_0$ is the optical density at the center of the line, n is the density of alkali-metal spins, V is the active volume of the atomic cell. For typical conditions: $V = 1$ cm^3, density $n = 1.7 \times 10^{13}$ cm^{-3}, $(OD)_0 = 12$, $\Gamma_{SD} = 300\,\mathrm{s}^{-1}$, $R = 710\,\mathrm{s}^{-1}$, and $\Gamma_{pr} = 91\,\mathrm{s}^{-1}$, the Cs AM noise is $\delta B = 0.24\,\mathrm{fT/Hz}^{1/2}$. The second term in this expression can be minimized if $(OD)_0$ is increased, for example, by increasing the density:

$$\delta B = \frac{1}{g_S \mu_B P_z \sqrt{nVt}} \sqrt{2(R + \Gamma_{pr} + \Gamma_{SD})} \tag{19}$$

Then the fundamental noise will be limited by the spin projection noise, which can be in turn optimized by adjusting the pump rate to $R = \Gamma_{SD}/2$ and detuning the probe away from resonance: $\delta B = \frac{3\sqrt{3/2}}{g_S \mu_B} \sqrt{\frac{\Gamma_{SD}}{nVt}}$.

This can be further reduced to the expression

$$\delta B = \frac{3\sqrt{3/2}}{g_S \mu_B} \sqrt{\frac{v\sigma_{SD}}{Vt}} \tag{20}$$

that depends only on a fundamental quantity—the spin-destruction cross section. In case of K, the sensitivity level of aT is possible. By scaling sensitivities with $\sigma_{SD}^{1/2}$ for K, Rb, and Cs, we find that the sensitivity along this sequence changes by an order of magnitude, and even in the case of Cs, it is fairly high. At the moment, the actual question is not much what the fundamental sensitivity is but how closely it can be approached. In each specific case, optimization described above can be accomplished in principle by raising the temperature of the cell. However, there is a limit imposed by properties of glasses and oven design. Cs and Rb require much lower temperature than K, so they can approach the fundamental limit closer. Another important question is the detection sensitivity of the field of a magnetic dipole, which arises in applications of micro-magnetic measurements. Because the field from a dipole falls off cubically with the distance and the field sensitivity scales as square root of the volume, smaller cells actually can win. However, the spin-destruction due to diffusion to the walls can become important to consider and different optimization needs to be carried out. In some detail this question was discussed in [22].

2.7.2 RF AM Sensitivity

Outside the SERF regime, the SE broadening can become very large, with magnetic resonance widths exceeding kHz at typical alkali-metal densities used in SERF magnetometers. To improve sensitivity, it is necessary to use light narrowing, Eq. 9. When the Larmor frequency is relatively low, $\omega_0 \ll \nu_{HF}$,

$$T_2^{-1} = \frac{R}{4} + \frac{R_{SE} R_{SD}}{5R} \tag{21}$$

(I = 3/2 case). With optimization of the pumping rate, the minimal linewidth is:

$$(1/T_2)_{\min} = (R_{SE}R_{SD}/5)^{1/2} \tag{22}$$

The ratio of this minimal width to the width at very small pump rate, $R_{SE}/8$, gives the light narrowing coefficient, $K = (5\sigma_{SE}/\sigma_{SD})^{1/2}/8$. In the case of potassium, $\sigma_{SE} = 1.8 \times 10^{-14}\,\mathrm{cm}^2$ and $\sigma_{SD} = 1 \times 10^{-18}\,\mathrm{cm}^2$, so the maximum light-narrowing factor is $K_{\max} \approx 37$.

By tuning to resonance and by optimizing the optical pumping, the response of the RF AM to the ac magnetic field can be greatly increased. Because at high frequency the laser technical noise can be removed, for example by using a polarizing beam splitter, the RF AM can be as sensitive as the SERF magnetometer. Fundamental limits of the SERF might be by several orders better, but the RF magnetometer can approach its fundamental limit closer while SERF will be by far dominated by technical noise. The fundamental noise of the RF magnetometer has been investigated in Ref. [6]. After optimization of various parameters, such as the pumping rate and the probe laser intensity, this noise can be expressed in terms of fundamental quantities of atomic vapors, such as SE and SD cross sections:

$$\delta B_{\min} = \frac{2}{\gamma}\sqrt{\frac{\bar{v}[\sigma_{SE}\sigma_{SD}/5]^{1/2}}{V}\left(1 + \frac{1}{4\sqrt{\eta}}\right)} \tag{23}$$

where $\bar{v}$ is the mean thermal velocity of K-K collisions. For a typical photodiode quantum efficiency $\eta = 50\,\%$ and a cell active volume $V = 1\,\mathrm{cm}^3$ cell, the optimized fundamental magnetic field sensitivity is about 0.1 $\mathrm{fT/Hz^{1/2}}$.

2.7.3 Intermediate Case Between SERF and RF Magnetometer

In the SERF regime the width is determined by spin-destruction rates, while in the high-frequency RF magnetometer, the width is the function of the SE, SD, and R. In the intermediate regime, the width varies smoothly between minimal in the SERF regime and maximum in the RF magnetometer. This intermediate case can be analyzed using equations for spin-projection noise, photon shot noise, and light-shift noise. However, the width is not a simple analytical function of the SE, SD, and R. Instead numerical simulations of DME are required. Intuitively, we can presume that at optimal conditions the sensitivity will be determined by spin-projection noise and hence scale as

$$\delta B = \frac{1}{g_S\mu_B P_z\sqrt{nVt}}\sqrt{2\left(R + \Gamma_{pr} + \Gamma_{SD} + \Gamma_{extra}\right)} \tag{24}$$

where Γ_{extra} is the contribution arising from spin-exchange collisions, which depends on polarization and magnetic field [26].

2.7.4 Large-Field Scalar AM Sensitivity

If we convert the RF magnetometer to a scalar magnetometer by inducing magnetic-field modulation near the magnetic resonance and by measuring the position of the magnetic resonance, the sensitivity after various optimization steps would be limited by [11]

$$\delta B = \frac{0.77}{\gamma}\sqrt{\frac{v\sigma_{SE}(1+\eta^{-1/2})}{V}} \tag{25}$$

It is interesting to note that now the sensitivity does not depend on the spin-destruction cross section, as in the case of RF AM. The reason for that is that by applying modulation we reduce the polarization level, which was essentially close to 1 in the case of RF magnetometer, so the light narrowing effect is suppressed. Because SE cross sections are almost the same for K, Rb, and Cs, it follows that the sensitivity of the scalar magnetometer will be quite similar for all three alkali-metal atoms. Moreover, it might not be necessary to heat the cell to high temperatures, as in case of SERF and RF magnetometers. The sensitivity limit of 0.9 fT/Hz$^{1/2}$ is expected for $\sigma_{SE} = 1.8 \times 10^{-14}$ cm^2 and $\eta = 0.8$. It seems that the only way to improve the sensitivity is to increase the volume.

2.7.5 Parallel-Beam AM Sensitivity

The above three cases were considered for the perpendicular pump-probe configuration. The parallel beam configuration has somewhat different result for sensitivity. The spin-projection noise expression would be similar, although the relaxation rate would be larger due to additional contribution of the SE rate arising from relatively large modulation necessary to achieve optimal sensitivity conditions. Alternatively, we can also consider a case when a static field is applied to tilt spins at some angle φ with respect to the pump-probe beam. This essentially would lead to the situation similar to that when the pump and probe beams are perpendicular, except that polarization will be reduced by $\cos(\varphi)$ and the detection signal by additional $\sin(\varphi)$. If we carry out similar optimization as in the previous example, we might conclude that the ultimate limit would come from spin-projection noise and hence the ultimate sensitivity would be not far off from that in the case of the orthogonal configuration.

3 Design and Implementation of an Atomic Magnetometer

3.1 Two-Beam Atomic Magnetometer Scheme

A typical SERF configuration with two orthogonal beams, which was used in first demonstrations of the SERF magnetometer, is shown in Fig. 9. This configuration is the most optimal in terms of sensitivity and is more intuitive for understanding. In case of the high-density RF AM and its scalar derivative, they were implemented only in the two-beam configuration. Furthermore, the two-beam magnetometers are the ones whose fundamental noise was analyzed in the literature.

In the two-beam scheme (Fig. 9), the pump beam is circularly polarized and orients spins along its propagation direction (usually chosen as the Z direction). The Y component of magnetic field rotates the spins from the Z direction into the probe-beam X-direction, and the X-projection of spins (S_x) is detected with a linearly polarized probe beam, which polarization is rotated by atomic vapor (the Faraday effect). Thus, the signal of the AM is proportional to S_x, so the AM signal can be obtained with Eq. (16) in quasi-static approximation. Faraday rotation behaves as dispersive Lorentzian, and the probe beam is detuned from the center of D1 line to maximize the SNR, which is negatively affected by the absorption and spin-destruction by the probe beam, discussed earlier.

The atomic spins are contained in the atomic cell (see below). The cell is heated to increase the density of alkali-metal vapor to the level of 10^{14} cm^{-3}. The alkali-metal atomic spins are polarized and detected with light with high efficiency. Almost 100 % polarization is achieved with the optical pumping method, as we discussed earlier. The pump laser is usually tuned to D1 line (770 nm K, 794 nm Rb, 894 nm Cs) to maximize efficiency and facilitate beam propagation in optically thick vapor. Although many types of lasers can be used and there is no strict requirement on the laser line width, it is found that mode hops produce very large noise and laser stability is important to consider. Distributed feedback (DFB) lasers available for 770 (need cooling to tune from 773 nm) and 794 nm wavelengths are almost ideal due to their low noise and mode-hop-free operation.

The pump and probe (Faraday detection mode) beams require different wavelengths and polarizations, and the best optimization of the sensitivity can be

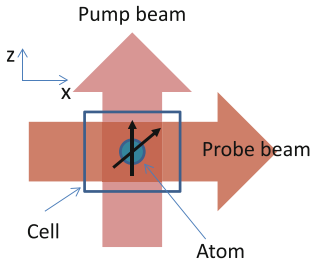

Fig. 9 A typical SERF magnetometer arrangement. Magnetic field is applied perpendicular to the picture plane

achieved with two separate lasers. In principle, it is still possible to reach high sensitivity with a single laser and a single elliptically polarized beam [24], but this is a compromised solution. The spins in this case are tilted by magnetic field to "imitate" the orthogonal configuration, and the tilt can be made to oscillate to reduce 1/f and other technical noises to compensate for the loss of sensitivity in comparison to the more optimal orthogonal configuration. If absorption instead of Faraday rotation is used to detect spins, then the wavelength in the center of the line and the circular polarization will be optimal for the pump and probe beams [4]. The single-laser parallel-beam schemes are ideal for miniaturization of the design and cost reduction.

3.1.1 Atomic Cell

The atomic vapor cell is the key element of an alkali-metal atomic magnetometer. A typical SERF (RF AM or scalar AM) cell contains a small droplet of K, 1 atm of He to slow-down diffusion, and 30 mtorr of N_2. The diffusion slow-down is important to reduce spin destruction from wall collisions. Helium as a buffer gas provides some advantage because it has the smallest spin-destruction rate with alkali-metal atoms [10]; however, other noble gases and nitrogen can be used as well. In small cells were diffusion spin-destruction start to dominate, nitrogen can be a better choice due to its smaller diffusion coefficient. The nitrogen gas is essential to quench excited states to avoid spin depolarization from spontaneously re-emitted photons. In terms of variation of the cell compositions it is important to optimize the overall spin-destruction rate: the diffusion SD scales inversely with the buffer-gas pressure and inversely quadratically with the size, while the relaxation due to alkali-buffer-gas collisions is proportional to the pressure. From point of view of safety and ease of construction, it is sometimes desirable to use buffer gas at about 1 atm. Pressure as high as 12 atm has been used in experiments where it was necessary to achieve uniform polarization [26]; dealing with such high-pressure cells requires caution since they can explode. Research has also recently focused on realizing a SERF magnetometer using antirelaxation coating rather than buffer gas [35].

Another consideration is the glass material of the cell. Special aluminosilicate glass 1720, which minimizes helium diffusion outside the cell and interaction of alkali-metal atoms with the walls, would be ideal. However, this type of glass is expensive and its availability is limited. Alternatively, Pyrex (borosilicate glass) has been successfully used in SERF magnetometer cells, but at high temperature the diffusion of helium through the glass is significant, and the atomic cell may change its properties over time. To avoid the leakage, neon or nitrogen can replace helium as a buffer gas.

Recently, in SERF magnetometry, trends have been toward miniature cells [4, 36], of less than 1 cm. One issue is that it is more difficult to make a miniature cell with windows of optical quality. In addition, diffusion plays a more important role, and to compensate for its spin-destruction effect, a higher temperature and higher

pressure of buffer gas are needed. Nitrogen, with the largest diffusion slowing, provides an advantage over helium. Having one buffer gas also simplifies the filling procedure.

It is interesting to compare the properties of AMs based on different alkali metals. Potassium of natural abundance, 93.3 % of ^{41}K and 6.7 % of ^{39}K, with both isotopes having the nuclear spin of 3/2, at low field will have atomic spins precessing at one frequency and there will be no negative effect from the mixture. At high field, above the Earth's field magnitude, the resonances will be different and can be resolved. Still, because of small percentage of ^{39}K, only one dominant resonance will be of any consequence. For most applications, the use of pure isotopes won't be necessary. Natural Rb, with 72 % of ^{85}Rb(I = 5/2) and 28 % of ^{87}Rb(I = 3/2) is quite different in this regard. At low frequency, because of difference in slowing down factors, 1/(2I + 1), their precession frequencies will be substantially different and at low density or outside of the SERF regime, the two isotopes will lead to two magnetic resonances or broadening when unresolved. The RF magnetometer will have much smaller light-narrowing effect. In the SERF regime, that is at high densities and low field, the SE rate is much higher than the Larmor frequencies of the two atoms, and the spins will precess with the same frequency and SE relaxation will be suppressed, regardless of the presence of more than one isotope. Thus for high-frequency applications, it is necessary to use isotopically refined Rb, while not in the SERF magnetometer. Cs has only one stable isotope, and does not cause any complication of this kind. A SERF magnetometer typically require densities on the order of 10^{14} cm^{-3} and hence heating to relatively high temperatures (180 °C for K, 160 °C for Rb, and 120 °C for Cs). Various issues related to heating were discussed in the introduction.

3.2 Single Beam Design

As we already mentioned, single-beam or parallel beam designs provide advantages for compact arrangement and low cost. If the Faraday effect is used to detect spins, the magnetometer signal will be proportional to the projection of the spin along the beam. Alternatively, if the absorption is used, the signal will similarly depend on S_z, that is the spin projection along the beam, since absorption is $\exp[-\alpha(1-P_z)] \approx 1+\alpha(1-P_z)$. When the magnetic field is small, S_z variation with the field will be quadratically small and the AM response to a small field will be suppressed. However, when a sufficiently large field is applied that rotates spins away from the Z direction at a significant angle, then the magnetometer becomes linearly sensitive to small fields. The steady-state solution for S_z can be obtained similarly as for S_x but the expression is principally different:

$$S_z = S_0 \frac{1 + (\gamma T_2 B_z)^2}{1 + (\gamma T_2)^2 (B_x^2 + B_y^2 + B_z^2)} \tag{26}$$

Now the signal depends quadratically on all field components, and when they are zerod, the magnetometer becomes insensitive to small field variations. The maximum response to B_x will be when $B_y = 0$ and $B_z = 0$, but $B_x = B_{x,0}$, then

$$\delta S_z = -S_0 \frac{2(\gamma T_2)^2 B_{x,0} \delta B_x}{\left[1 + (\gamma T_2)^2 B_{x,0}^2\right]^2} \tag{27}$$

This expression can be optimized with respect to the field offset

$$\delta S_z = -S_0 \frac{3\sqrt{3}}{8} \gamma T_2 \delta B_x \approx -0.64 S_0 \gamma T_2 \delta B_x \tag{28}$$

which is about one and a half times smaller than the response of the orthogonal SERF to the B_y field in Eq. 16. It is possible either to measure field when a constant B_x is applied or when it is modulated. Modulation of $B_{x,0}$ provides an advantage of noise reduction by shifting the detection frequency to the region of low-noise. It was found in [24] that by applying large modulation (T_2 also depends on the field, at small fields quadratically, and spin exchange rate), the magnetometer can be optimized and work at modulation of a few kHz. This further reduces the 1/f noise.

3.3 Micro-Fabricated Atomic Magnetometers

It is instructive to investigate how sensitivity depends on the size of the atomic cell. The fundamental noise scales with the combination of nVT_2, so if volume V is reduced, the sensitivity decreases, but it can be partially compensated with the density n, within some limits. The spin-exchange rate and spin destruction rate due to alkali-alkali collisions depend linearly on the density of alkali-metal atoms, while other rates are density independent, and thus raising the density improves sensitivity until alkali-alkali collisions start to dominate the spin-destruction rate. With the size reduction, the spin-destruction due to diffusion to the walls, which scales inversely with the area, become more important. It can be reduced by using N_2 as a buffer gas, which has a smaller diffusion coefficient than helium, traditionally used in SERF due to its smallest spin-destruction rate with alkalis. Raising buffer-gas pressure is another measure for optimization. On the other hand, small cells require much less power and the whole package can be micro-fabricated to reduce the cost. The analysis of the size-dependent sensitivity is provided in [36].

3.4 Multi-channel Magnetometers

In many applications, such as source localization in MEG and MCG, simultaneous detection of a magnetic field in multiple points is required. Commercial SQUID-based MEG systems have hundreds of channels; the two main problems with these systems are cryogenic operation and high cost. If SQUIDs are replaced with atomic magnetometers, cryogenic requirement will be eliminated, but the price of building hundreds of atomic magnetometers can still be very high. The price can be reduced if various elements of atomic magnetometers are shared. For example, instead of having a separate laser for each magnetometer, laser power can be amplified and distributed among multiple magnetometers, saving the cost for laser electronics and optics, such as optical isolators. Additional savings on optics and atomic cells can be achieved by using a large atomic cell that is imaged with a broad beam [2]. Such sharing is possible because buffer gas restricts the diffusion of atoms to less than cm distances ($\sqrt{D_0 t}$, where D_0 is the diffusion coefficient and t diffusion time), so that multiple regions of a 10-cm cell can independently measure field at as many as hundred points. The only drawback of such a multi-channel system is geometry: in MEG systems for full coverage the sensors have to be inserted in a helmet configuration, which is impossible with one large cell. Still, by positioning such multi-channel large-cell magnetometers at several head locations, more or less complete coverage can be achieved. Demonstration of multi-channel MEG with a large cell was given in Ref. [2]. On the other hand, for MCG applications, a flat geometry is almost ideal, and only one multi-channel AM would be needed.

Applications in MRI also can benefit from multi-channel operation to save the cost. At low frequency, the multi-channel AM can be directly used, but at high frequency a difficult problem exists that NMR and AM fields have to be 400-time different. One solution that would work for anatomical MRI is addition of flux transformers. Multiple flux transformers, which are inductively decoupled, can be used to realize multi-channel parallel imaging [37].

3.5 Design Issues

3.5.1 Lasers

Lasers have been essential to the success of high-sensitivity magnetometers. It is important to have high-quality lasers for both pumping and probing, although in some cases, requirements can be relaxed. The effects of laser instabilities and noise on the AM sensitivity are different in cases of pump and probe lasers. Fluctuations in pump intensity and wavelength can lead to light-shift noise in the pump direction, which is equivalent to fluctuating magnetic field along this direction. This technical noise can easily become dominant source of noise; however, it is possible

suppress it in the SERF magnetometer by zeroing the field along the probe direction if the pump and probe beams are orthogonal. Another way to suppress this noise is to choose a laser wavelength that will minimize light shift fluctuations. As we previously discussed, light shift is proportional to the light intensity and depends on wavelength as a dispersion Lorentzian, crossing zero at the center of the absorption line. Minimum fluctuations in the light shift due to intensity variation will occur when the laser is tuned to the line center, while minimum light shift fluctuations due to wavelength instability will be when the laser is detuned from the center by one line width. Depending on the dominant nature of fluctuations, the pump laser can be tuned accordingly to minimize the light shift noise. When AM is operating in the scalar magnetometer mode, i.e. measuring the z component of the field, the light shift cannot be reduced by zeroing the B_x field (along the probe beam), thus it is highly desirable to use a high-quality pump laser.

The requirement for a probe laser is even more demanding since the probe noise contributes to the magnetometer noise directly. If the probe beam is detuned away from the D1 or D2 line by several linewidths, the effect of wavelength fluctuations is suppressed, and intensity fluctuations can become more important. (Although we note that the analysis of wavelength fluctuation effects was not conducted in the literature.) For this reason, a polarizing beam splitter is used to reduce the effect of intensity fluctuations. When carefully balanced, the polarimeter based on the PBS can suppress the intensity fluctuation 30 times or even more, ideally to the level of photon shot noise. Some asymmetry in the detection channels for the two beams leads to the reduction in noise suppression. So it is important to have high quality lasers to avoid additional technical noise.

It has been found that DFB lasers have very good noise performance. Their noise level with PBS starting with relatively low frequency is close to photon-shot noise limit. Lasers with gratings that are not very rigidly attached generate more noise, and mode hops occur frequently that result in very large noise, requiring adjusting the laser current and temperature. Long-term measurements with such lasers are often problematic. Multi-mode lasers are not generally suitable for high-sensitivity low-frequency magnetometers. However, at high frequency, noise usually approaches photon-shot noise, even in inexpensive lasers. Thus RF magnetometers have less stringent requirements on the lasers. The scalar magnetometer, on the other hand, although its signal is detected at high frequency (in Earth's field, at about 350 kHz), is sensitive to pump beam light shift at low frequency. Thus requirement on the pump laser might be more stringent than for the probe laser.

3.5.2 Fiber-Coupling

Fiber-coupling has been used to reduce price and add flexibility in measurements. It has been found that the light beam generated by a DFB laser after passing through a fiber (for example, a PM fiber) does not have excessive noise. Thus a head of a magnetometer, which contains the cell, can be spatially separated from other supporting equipment as much as 5 m. Both single-beam [3, 4, 24] and two-beam [16]

fiber-coupled designs have been developed. Also DFB lasers have been used that were fiber-coupled removing the need for extra optical components required to inject the light into a single mode fiber [16]. However, feedback from the fiber attached to the laser can lead to instabilities, and substantial increase in noise in the schemes where PBS is not used. Thus it is still preferable to have an external coupler with an optical isolator, despite extra cost and complexity of design.

3.5.3 Commercial Designs

Fiber-coupled designs have been commercialized by Twinleaf and QuSpin companies. The sensitivity on the order of 10 fT/Hz$^{1/2}$ has been demonstrated. The magnetometers are in the process of further development. One direction is to make the magnetometer user-friendly, so the operator does not need to tune fields, lasers, etc. manually. Once the magnetometers become widely available they would strongly compete with SQUIDs in many demanding applications such as MEG.

3.6 Sensitivity Demonstrations

Sensitivity demonstrations are the most important aspect of the research on atomic magnetometers. The first significant milestone was the demonstrations of superior sensitivity by SERF magnetometer [1]. Then various designs of SERF, RF, and scalar magnetometers have been explored with sensitivity demonstrations and analysis. In particular, an RF magnetometer has demonstrated sensitivity of 0.2 fT/Hz$^{1/2}$ adopted for NQR detection [28]. Many groups now were able to achieve fT sensitivity with various designs, which were aimed at specific goals, such as MEG, cost reduction, simplification of design, or micro-fabrication. Fiber-coupled designs are approaching the sensitivity of the original optical table AMs, and there is a potential for further improvement [4, 16]. The highest sensitivity to date in SERF regime was demonstrated by Princeton using vacuum-enclosed optical design [13]. Scalar magnetometers, although less sensitive than SERF magnetometers, have been of great interest to geophysical and military applications, when the magnetometer needs to operate at ambient field. Substantial advantage of scalar magnetometers is their invariance with respect to field rotation, so vibration and orientation instabilities do not lead to large noise. Unfortunately, due to multiple hyperfine structure Zeeman levels, with splitting non-linear in the Earth's field, the magnetometer has its frequency slightly sensitive to field rotation. The demonstration of high sensitivity of a scalar magnetometer based on RF AM was recently given [11]. The analysis showed that this is close to the fundamental limit. However, further improvements were found, using for example multi-pass approach [38].

4 Applications

4.1 Comparison with SQUID

SERF AMs and SQUIDs are the most sensitive magnetometers at low frequencies. Although it is also possible to construct a large coil that can have fT sensitivity, many applications introduce restrictions on weight and size, and at very low frequency, coils become problematic. SQUID technology has been around for decades and matured enough to be readily available from a company; however, SERF, scalar, and especially RF magnetometers are just at the initial stage of technology readiness. From point of view of sensitivity, SERF magnetometers should be able to replace SQUIDs in most applications, but both SERF and SQUIDs have application limits stemming from their physical principles. Non-cryogenic operation of SERF is the main strength of this technology. Supply of expensive liquid helium is limited and requirement for cryogenic infrastructure is restrictive. Apart from this, SQUID systems also require maintenance. Also important is that thermal electrically conductive shields, needed for improving the efficiency of cryogenic cooling, produce excessive noise, degrading the performance of SQUID systems and making practical SERF magnetometers more sensitive.

Unlike SQUIDs, SERF magnetometers are not used with superconducting flux transformers (SFT), which configured as gradiometers in SQUID systems, reject common-mode magnetic noise by several orders of magnitude enabling operation in poorly shielded environments. Alternatively configured as gradiometers from several magnetometers [4] or channels in large-cell multi-channel systems [2], SERF magnetometers do not provide as large common-mode noise suppression. This is due to instability of the magnetometer signals, which depend on many parameters. In the presence of gradients, SERF magnetic resonances are broadened and sensitivity is reduced, while SQUID gradiometers with feedbacks can operate in a relatively large dc field and are insensitive to dc gradients.

In contrast to SQUIDs, the SERF magnetometer also needs to be zeroed to operate with maximum sensitivity. In the Earth's field environment, this can be done with a three-axis Helmholtz coil system, but gradients and magnetic field fluctuations negatively affect the sensitivity [39]. When SERF or RF magnetometers are used for NMR or MRI detection, the AMs need to be decoupled from NMR and MRI fields [5, 40]. SQUIDs decoupled with SFT do not compromise the sensitivity, but using AMs is problematic. Several methods have been developed for this, but each has some issues [5, 40–42].

SERF and SQUID have also different bandwidths (BW). In case of SERF, there is inverse relation between BW and the sensitivity, and SERF magnetometers with fT sensitivity do not have BW exceeding much 100 Hz. SQUIDs, on the other hand, can have response in a very large frequency range. The dc SQUID BW is only restricted by a feedback system that has finite BW. In systems used for ULF-MRI detection, BW has been on the order of several kHz, with sensitivity still in fT range. But the large BW of SQUIDs is their liability, making them sensitive to

noise in the frequency range from dc to microwaves. High-frequency noise can be effectively reduced with Mylar® foil, but this foil produces noise on the order of a few fT, reducing SQUID sensitivity. SERF does not need protection against high-frequency noise. Low frequency noise is important to remove.

In terms of operation temperature, the SERF magnetometer cell is heated above 100 °C while SQUIDs are kept in LHe Dewar (high-Tc variety is less sensitive). In both cases, effective thermal insulation is required to reduce the stand-off distance to the measured object.

Despite various problematic issues with SERF and other atomic magnetometers, the absence of cryogens is the principal benefit that would lead to replacement of SQUIDs in a wide range of applications.

4.2 Biomedical Applications of High-Density AMs

Research on atomic magnetometers is strongly motivated by many current and potential future applications. Among such applications, MEG is probably the most invaluable because no other device than the atomic magnetometer can rival low-Tc SQUIDs in sensitivity at low frequency, in the range of interest to MEG.

4.2.1 MEG Applications of SERF Magnetometers

MEG history starts with the first magnetic recordings of brain activity with a Faraday coil [43], which served as the proof of principle of existence of the brain magnetic field. Shortly after the first demonstration, the sensitivity was dramatically improved with a SQUID magnetometer [44], and tater on, multi-channel systems have been introduced for MEG source localization. After further development, the multi-channel systems became the basis for MEG research and clinical applications. However, the cost of MEG systems that included the price of liquid helium, maintenance, magnetically shielded rooms, and other expenses have been very high, resulting in modest propagation of the MEG method into the clinical practice and research. Some work has been directed toward cost reduction, such as construction of SQUID gradiometers that do not require expensive multi-layer shielded rooms for MEG measurements, but all practical MEG systems have been based on SQUIDs requiring liquid helium supply.

However, MEG systems can be also based on atomic magnetometers to eliminate the need for cryogens. In 2006, the first demonstration was done [2] and it was reasoned that a commercial multi-channel system can be built at a fraction of cost of a multi-channel SQUID system. As we have already discussed it, there are several strategies for cost reduction, including an inexpensive multi-channel operation, possible with a large atomic cell. In addition, because AM do not require a large Dewar, a low cost shield can be designed for subjects in a reclining position consisting of mu-metal cylinders [2]. Unfortunately, the demonstrated design was

not yet suitable for a full-head MEG system that is needed for medical applications. However, the work AM-MEG has been continued. Instead of building SERF magnetometers with large cells, several groups focused on AM-MEG demonstrations with separate AM sensors with the goal in reduction cost per channel. In particular, fiber-coupled sensors were developed that could reach sensitivity of a few fT and these sensors were applied to detect MEG signals [3, 4, 45]. Currently the cost of building hundreds of AM channels is relatively high, but it is hoped that with mass-production development, this cost can be significantly reduced.

4.2.2 Other Applications of SERF and High-Density Magnetometers

Magnetocardiography

Magnetocardiography (MCG) in general requires lower sensitivity than MEG and is another promising direction for applications of SERF and other atomic magnetometers. Since heart anomalies are among leading causes of death, their diagnosis is extremely important, and AM MCG could become an invaluable tool for saving millions of lives. Multi-channel MCG provides information on electrical activity in the heart non-invasively, and hence this modality can be crucial for revealing heart anomalies and the analysis of their localization. With high sensitivity and multi-channel detection capability of SERF, more sensitive diagnostics of heart anomalies can be developed. Already, FDA approval has been obtained for diagnostics of women heart conditions with MEG, and study was conducted that showed that the MCG diagnostics is much more reliable than other methods. Although the clinical trials were conducted with SQUIDs, it is clear that they can be replaced with AMs to relieve the requirement for cryogens. Potentially lower cost of construction of multi-channel system and of maintenance will facilitate wide spread of the AM-based MCG method and make it competitive with inexpensive conventional technology such as ECG. Compared to MEG, MCG application will require only one or two multi-channel magnetometers with large cells: one positioned on the chest area and the other on the back. SQUIDs are held in a Dewar and in general are only positioned above the patient, but better diagnostics can be performed with more complete coverage.

Detection of Magnetic Nano-Particles

Another class of medical applications is based on nano-particle detection. For example, it has been found that magnetic nanoparticles of specific size attached to cancerous cells have a specific magnetization variation after alignment with a strong field. Again SQUIDs were used to pioneer this diagnostic method, but future is quite promising for AMs as well. The main problem is the need to conduct measurements in unshielded environment, but SERF magnetometers are not ideal in this

situation. It would be necessary to set up a gradiometric operation that would cancel fairly large magnetic field noise in ambient clinical environment.

NMR and MRI Applications

High sensitivity of atomic magnetometers can be important for applications in unconventional low- and ultra-low field (ULF) NMR and MRI. One motivation for exploring ULF MRI is that it is not based on bulky and expensive superconducting or permanent magnets and some applications complementary to conventional MRI can be developed. One example of such application is combined MEG and MRI [46] that can reduce the co-registration error. Another class of novel applications can exploit unique properties of ULF MRI such as low cost and portability. In long run, ULF MRI scanners can lead to increased availability of MRI diagnostics around the world. However, obtaining clinically useful images at ULF is fraught with challenges. First, because NMR/MRI is detected with a pick-up coil, which output is the time derivative of the magnetic flux (Faraday's law), SNR is severely compromised at low frequency. Second, the polarization of nuclear spins is very weak in ultra-low field further reducing SNR. To make things worse for a developing technology, conventional MRI has set very high standards of image quality: with high resolution, high SNR, and fast imaging.

To some extent, the compensation for a weak signal in the ULF regime can be made with the pulsed-prepolarization method, in which a much larger field is applied to polarize nuclear spins (e.g. [47]). During the detection stage this field is removed, so it does not affect the ULF or LF signal read-out. However even with prepolarization enhancement, the SNR and resolution are still poor. Some progress has been made with replacement of coils with SQUIDs to improve the sensitivity at low frequency and to realize multi-channel parallel MRI acceleration [46]. This of course brought the problem of cryogenic operation. To amend this, AMs have been proposed to replace SQUIDs.

The most potentially useful AM magnetometer for MRI applications is the high-density RF atomic magnetometer [5]. The RF magnetometer has several useful features: (i) very high sensitivity with fundamental limit about 0.1 fT/Hz$^{1/2}$ for 1 cm^3 cell [6] and demonstrated sensitivity in a large cell 0.2 fT/Hz$^{1/2}$ [28]; (ii) sufficient bandwidth, reaching a kHz range, much larger than that of other AMs; (iii) operation at high frequency where ambient noise is lower; (iv) low cost and finally multi-channel operation [37]. The first demonstration of MRI with AM in the configuration that is suitable for anatomical imaging was done in 2009 [40] and actual anatomical imaging with RF AM was achieved in 2013 [48]. The latest achievements are the demonstration with AM of MRI of the human brain [49] and multi-channel operation [37].

With regard to MRI applications, it is important to remember that while the sensitivity of SQUIDs and AMs is about the same, the AM is highly sensitive to static fields and gradients, while SQUIDs are to a large extent immune to them. The field affects the AM frequency of maximum response—in fact it is applied to tune

the AM to a specific frequency, while the gradients broaden atomic magnetic resonances and reduce sensitivity.

In direct MRI detection, the MRI field and gradients need to be removed at the AM sensor location. The difference in gyromagnetic ratios between protons and K (Rb-87) spins is about 400, so the gradient applied in MRI will broaden the AM BW 400 times, well beyond that required for optimal operation. For these reasons, AMs in general are more problematic for MRI applications than SQUIDs, but solutions for these problems exist.

One strategy for detection MRI signal with AM is to do it remotely [42], with the liquid sample arranged to flow from a pre-polarization region and an encoding region to a detection region. The prepolarization can be done with a strong non-uniform permanent magnet, while the detection region can be isolated from environment noise and external field with a ferromagnetic shield. The main disadvantage of remote detection is that the sample needs to be moved, which is difficult in the case of anatomical imaging. As the result, anatomical imaging has not been demonstrated with this approach.

The second strategy is detection at ultra-low frequency ($\sim$kHz) with the sample placed in a solenoid to separate the NMR and AM fields [41]. Because of ultra-low field, the field separation with a not-ideal solenoid does not lead to artifacts. With additional work on perfecting the solenoid, this approach can be in principle extended to frequencies on the order of 100 kHz [5], but there are other factors that would limit applications: the solenoid has to be long preventing easy access for anatomical imaging; more importantly, imaging gradients are very large and will broaden magnetometer resonance and decrease its sensitivity.

The most currently feasible approach for anatomical imaging with an AM is the detection mediated with a flux transformer (FT) (Fig. 10) [40]. FTs are widely used with SQUID magnetometers, where they are cryogenic and superconducting. The FT consists of two coils, an input coil that generates voltage from the MRI signal, and an output coil, electrically connected to the input coil, that generates magnetic field. Basically FT transfers magnetic field from the MRI region to the detection region. The input coil can be configured as a gradiometer to reduce noise. The output coil is placed near a magnetometer, SQUID or AM. AMs can be in principle used with a cryogenic FT, but the overall advantage of non-cryogenic operation would be lost. We have recently demonstrated MRI using a room-temperature (RT) FT. The room temperature FT brings flexibility in the positioning and simplicity in operation. RT FT removes the dc and attenuates low-frequency components of the field and gradients, solving the problem of decoupling AM and MRI field systems. However, the RT operation comes at the price of additional Johnson noise. Because with frequency the Johnson noise as well as the noise of surrounding metallic parts decreases, the increase in frequency can be a very efficient method for noise reduction.

Additional benefit of the FT-AM detection scheme is the increase in the bandwidth (BW) when the FT is detuned from the AM magnetic resonance (Fig. 11). Larger BWs are needed for high-resolution imaging and for fast multi-pulse imaging methods. This can be illustrated with an example. For a 100-ms acquisition

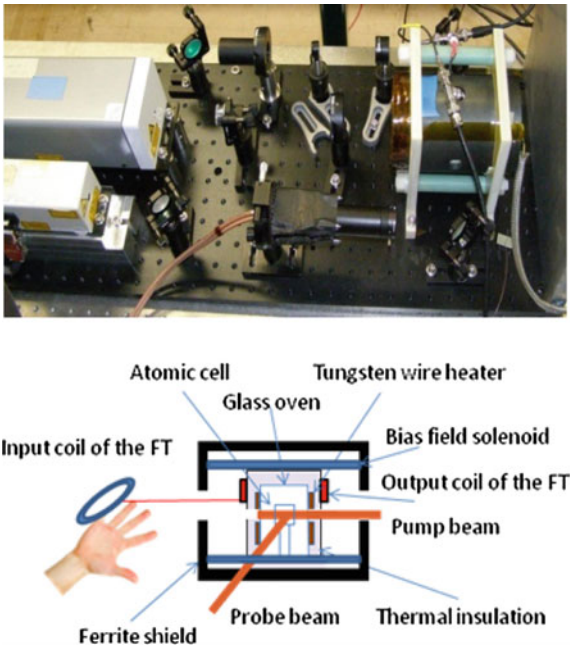

Fig. 10 Atomic magnetometer and flux transformer setup (*top*) and its diagram (*bottom*). Adopted from [37]

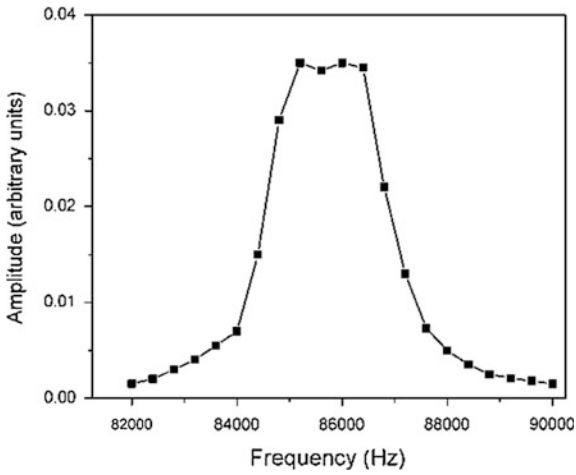

Fig. 11 Illustration of BW enhancement of AM+FT detection method, without loss in sensitivity [48]

time, typically used in ULF MRI, the required BW per pixel is 10 Hz. Fifty-pixel image in the read-out direction translates into 500-Hz BW, and if a Car-Purcell-Meiboom-Gill (CMPG) sequence with 5 pulses per excitation is employed, the BW will be needed as large as 2.5 kHz. A typical RF AM has BW on the order of 200 Hz, so from this estimate it cannot obviously be used for fast sequences, but the FT-AM detector will be suitable.

Other Potential Applications Based on High Sensitivity

There are many other potential applications of AMs which can be developed where high sensitivity is required. For example, AMs can be used in submarine detection, geology, archeology, military applications. Currently, high-sensitivity AMs are becoming commercially available, and this will certainly increase the range their applications.

Fundamental experiments

Some of the most fascinating applications are in the academic world, for example in tests of fundamental symmetries. Here cryogenic operation of SQUIDs is not a big problem, but still AMs have some unique properties that they themselves become the objects of research. An example of such an application is the measurement of electric dipole moments (EDM) of atoms. There are several schemes for EDM experiments. The basic idea is to apply a strong electric field and to measure with high sensitivity a weak magnetic field arising due to EDM. Because the hypothetical atomic EDMs are extremely small, it is necessary to use sensors of highest possible sensitivity. Some schemes are based on unique properties of atomic spins and such experiments cannot be done with arbitrary magnetic sensors. Others do not necessarily need atomic magnetometers, and low-Tc SQUIDs are used as more conventional commercially available sensors. Early EDM experiments and theoretical calculations are reviewed in [50].

Atomic magnetometers, or rather co-magnetometers, were also used in fundamental CPT violation experiments and recently a new limit was set [51, 52].

Basic research in atomic magnetometers

While atomic magnetometers are great for the multitude of their applications, on the basic science side, also there are many activities. Setting new limits or demonstration of new principles and configurations have been one focus of such activities.

5 Conclusions

We have discussed ultra-sensitive atomic magnetometers based on high-density alkali-metal vapors. This chapter covers the principles of the operation of ultra-sensitive magnetometers and their applications. Among applications MEG and ULF MRI have been considered in some detail. Because low-Tc SQIUDs have been known as the most sensitive magnetometers for a long time and are still considered such by many researchers, the important conclusion from this chapter should be that atomic magnetometers can provide similar sensitivity and can be used instead of SQUIDs in many applications.

References

1. I.K. Kominis, T.W. Kornack, J.C. Allred, M.V. Romalis, A subfemtotesla multichannel atomic magnetometer. Nature **422**, 596 (2003)
2. H. Xia, A. Ben-Amar Baranga, D. Hoffman, M.V. Romalis, Magnetoencephalography with an atomic magnetometer. Appl. Phys. Lett. **89**, 211104 (2006)
3. K. Johnson, P.D.D. Schwindt, M. Weisend, Magnetoencephalography with a two-color pump-probe, fiber-coupled atomic magnetometer. Appl. Phys. Lett. **97**, 243703 (2010)
4. V. Shah, R.T. Wakai, A compact, high performance atomic magnetometer for biomedical applications. Phys. Med. Biol. **58**, 8153–8161 (2013)
5. I.M. Savukov, S.J. Seltzer, M.V. Romalis, Detection of NMR signals with a radio-frequency atomic magnetometer. JMR **185**, 214 (2007)
6. I.M. Savukov, S.J. Seltzer, M.V. Romalis, K.L. Sauer, Tunable atomic magnetometer for detection of radio-frequency magnetic fields. Phys. Rev. Lett. **95**, 063004 (2005)
7. E. Harel, L. Schröder, S. Xu, Annu. Rev. Anal. Chem. **1**, 133 (2008)
8. G. Bison, R. Wynands, A. Weis, Opt. Express **11**, 904–909 (2003)
9. B. Patton, A.W. Brown, R. Slocum, E.J. Smith, in *Ch. 15, Space Magnetometry*, ed by D. Budker, D.F.J. Kimball. Optical Magnetometry (Cambridge University Press, Cambridge, 2013), pp. 285–302
10. J. Allred, R. Lyman, T. Kornack, M. Romalis, A high-sensitivity atomic magnetometer unaffected by spin-exchange relaxation. Phys. Rev. Lett. **89**, 130801 (2002)
11. S.J. Smullin, I.M. Savukov, G. Vasilakis, R.K. Ghosh, M.V. Romalis, A low-noise high-density alkali-metal scalar magnetometer. Phys. Rev. A **80**, 033420 (2009)
12. W. Happer, H. Tang, Phys. Rev. Lett. **31**, 273 (1973)
13. H.B. Dang, A.C. Maloof, M.V. Romalis, Ultrahigh sensitivity magnetic field and magnetization measurements with an atomic magnetometer. Appl. Phys. Lett. **97**, 151110 (2010)
14. P.D.D. Schwindt, S. Knappe, V. Shah, L. Hollberg, J. Kitching, Chip-scale atomic magnetometer. Appl. Phys. Lett. **85**, 6409 (2004)
15. T.W. Kornack, S.J. Smullin, S.K. Lee, M.V. Romalis, Appl. Phys. Lett. **90**, 223501 (2007)
16. I. Savukov, T. Karaulanov, M. Boshier, Ultra-sensitive high-density Rb-87 radio-frequency magnetometer. Appl. Phys. Lett. **104**, 023504 (2014)
17. T.G. Walker, W. Happer, Spin-exchange optical pumping of noble-gas nuclei. Rev. Mod. Phys. **69**, 629–642 (1997)
18. S. Kadlecek, L.W. Anderson, T. Walker, Measurement of potassium-potassium spin relaxation cross sections. Nucl. Instrum. Meth. Phys. Res. A **402**, 208–211 (1998)
19. M.P. Ledbetter, I.M. Savukov, V.M. Acosta, D. Budker, M.V. Romalis, Spin-exchange-relaxation-free magnetometry with Cs vapor. Phys. Rev. A **77**, 033408 (2008)
20. M.P. Ledbetter, I.M. Savukov, D. Budker, V. Shah, S. Knappe, J. Kitching, D.J. Michalak, S. Xu, A. Pines, Zero-field remote detection of NMR with a microfabricated atomic magnetometer. Proc. Natl. Acad. Sci. USA **105**, 2286 (2008)
21. S. Knappe, P. D. D. Schwindt, V. Gerginov, V. Shah, L. Liew, J. Moreland, H. G. Robinson, L. Hollberg, J. Kitching, Microfabricated atomic clocks and magnetometers. J. Opt. A Pure Appl. Opt. **8**, S318–S322 (2006)
22. V. Shah, S. Knappe, P.D.D. Schwindt, J. Kitching, Subpicotesla atomic magnetometry with a microfabricated vapour cell. Nat. Photonics **1**(11), 649–652 (2007)
23. W.C. Griffith, S. Knappe, J. Kitching, Opt. Express **18**, 27167 (2010)
24. V. Shah, M.V. Romalis, Spin-exchange relaxation-free magnetometry using elliptically polarized light. Phys. Rev. A **80**, 013416 (2009)
25. Twinleaf, [Online]. Available: http://www.twinleaf.com/
26. I.M. Savukov, M.V. Romalis, Effects of spin-exchange collisions in a high-density alkali-metal vapor in low magnetic fields. Phys. Rev. A **71**(2), 023405 (2005)

27. S. Appelt, A. Ben-Amar Baranga, A.R. Young,. H.W. Young, Light narrowing of rubidium magnetic-resonance lines in high-pressure optical-pumping cells. Phys. Rev. A **59**, 2078–2084 (1999)
28. S.-K. Lee, K. Sauer, S.J. Seltzer, O. Alem, M.V. Romalis, Subfemtotesla radio-frequency atomic magnetometer for detection of nuclear quadrupole resonance. Appl. Phys. Lett. **89**(21), 214106 (2006)
29. G. Breit, I.I. Rabi, Measurement of nuclear spin. Phys. Rev. **38**(11), 2082 (1931)
30. W. Happer, W.A. van Wijngaarden, An optical pumping primer. Hyperfine Interact. **38**(1), 435–470 (1987)
31. W. Happer, A.C. Tam, Effect of rapid spin exchange on the magneticresonance spectrum of alkali vapors. Phys. Rev. A **16**(5), 1877–1891 (1977)
32. W. Happer, Optical pumping. Rev. Mod. Phys. **44**, 169–250 (1972)
33. A. Appelt, B.-A. Baranga, C.J. Erickson, M.V. Romalis, A.R. Young, W. Happer, Theory of spin-exchange optical pumping of 3He and 129Xe. Phys. Rev. A **1412–1439**(2), 58 (1998)
34. I. Savukov, Gradient-echo 3D imaging of Rb polarization in fiber-coupled atomic magnetometer. JMR **256**, 9–13 (2015)
35. S.J. Seltzer, M.V. Romalis, J. Appl. Phys. **106**, 114905 (2009)
36. V. Shah, S. Knappe, P.D.D. Schwindt, J. Kitching, Subpicotesla atomic magnetometry with a microfabricated vapour cell. Nat. Photonics **1**, 649–652 (2007)
37. I. Savukov, T. Karaulanov, Multi-flux-transformer MRI detection with an atomic magnetometer. JMR **249**, 49–52 (2014)
38. D. Sheng, S. Li, N. Dural, M.V. Romalis, Subfemtotesla scalar atomic magnetometry using multipass cells. Phys. Rev. Lett. **110**, 160802 (2013)
39. S.J. Seltzer, M.V. Romalis, Unshielded three-axis vector operation of a spin-exchange-relaxation-free atomic magnetometer. Appl. Phys. Lett. **85**(20), 4804 (2004)
40. I.M. Savukov, V.S. Zotev, P.L. Volegov, M.A. Espy, A.N. Matlashov, J.J. Gomez, R.H. J. Kraus, MRI with an atomic magnetometer suitable for practical imaging applications. JMR **199**, 188–191 (2009)
41. I.M. Savukov, M.V. Romalis, NMR detection with an atomic magnetometer. Phys. Rev. Lett. **94**, 123001 (2005)
42. S. Xu, S. Rochester, V.V. Yashchuk, M. Donaldson, D. Budker, Rev. Sci. Instrum. **77**, 083106 (2006)
43. D. Cohen, Magnetoecephalography: evidence of magnetic field produced by alpha- rhythm current. Science **161**, 784–786 (1968)
44. D. Cohen, Magnetoencephalography: detection of the brain's electrical activity with a superconducting magnetometer. Science **175**, 664–666 (1972)
45. T.H. Sander, J. Preusser, R. Mhaskar, J. Kitching, L. Trahms, S. Knappe, Magnetoencephalography with a chip-scale atomic magnetometer. Biomed. Opt. Express **3**, 981 (2012)
46. V.S. Zotev, A.N. Matlashov, P.L. Volegov, I.M. Savukov, M.A. Espy, J.C. Mosher, J. J. Gomez, R.H.J. Kraus, Microtesla MRI of the human brain combined with MEG. JMR **194**, 115–120 (2008)
47. A. Macovski, S. Conolly, Novel approaches to low-cost MRI. Magn. Reson. Med. **30**(2), 221–230 (2005)
48. I. Savukov, T. Karaulanov, Anatomical MRI with an atomic magnetometer. JMR **231**, 39–45 (2013)
49. I. Savukov, T. Karaulanov, Magnetic-resonance imaging of the human brain with an atomic magnetometer. Appl. Phys. Lett. **103**, 043703 (2013)
50. I.B. Khriplovich, L.S.K. Khriplovich, *CP Violation Without Strangeness: Electric Dipole Moments of Particles, Atoms, and Molecules* (Springer, Berlin, 1997)
51. J.M. Brown, S.J. Smullin, T.W. Kornack, M.V. Romalis, New limit on lorentz-and CPT-violating neutron spin interactions. Phys. Rev. Lett. **105**, 151604 (2010)
52. M. Smiciklas, J.M. Brown, L.W. Cheuk, S.J. Smullin, M.V. Romalis, New test of local lorentz invariance using a 21Ne–Rb–K comagnetometer. Phys. Rev. Lett. **107**, 171604 (2011)

Helium Magnetometers

Werner Heil

Abstract Optically pumped helium (^{4}He, ^{3}He) magnetometers have provided magnetic field data for military, space exploration and geophysical laboratory applications for over five decades. More recently they are increasingly being used for experiments in basic research. The characteristics of He magnetometers that have made them instruments of choice for these varied applications include high sensitivity, high accuracy, simplicity of the resonance line, small heading errors due to light shifts, temperature independence of resonance cells, linear relationship between the magnetic field and the resonance frequency, excellent stability for gradiometer operation and robustness for field and space use . All He magnetometers manufactured from 1960 to 1990 utilized an RF electrodeless discharge He-4 lamp as an optical pumping source of 1083 nm resonance radiation. With the invent of optical fiber lasers at 1083 nm from the 1990s on, laser-pumped He magnetometers are characterized by sensitivities up to two orders of magnitude better than lamp-pumped He magnetometers and are more accurate, smaller, and very stable for use in magnetic gradiometers. A quantum step forward in terms of precision was achieved by utilizing the benefits of free spin precession. For polarized helium-3 the coherent spin precession time T^*_2 can reach up to 100 h at low magnetic fields and even at high magnetic fields (> 0.1 T) nuclear spin precession times of $\sim$5 min have been reported. This opens a new chapter of ultra-high precision magnetometry where the signal readout is accomplished by using SQUIDs, optical pumped alkalimagnetometers or NMR techniques. The following article provides a comprehensive overview on helium magnetometry starting from some historical remarks to the latest developments including future perspectives.

W. Heil (✉)
Johannes Gutenberg University of Mainz, Mainz, Germany
e-mail: wheil@uni-mainz.de

A. Grosz et al. (eds.), *High Sensitivity Magnetometers*, Smart Sensors, Measurement and Instrumentation 19, DOI 10.1007/978-3-319-34070-8_16

1 Introduction

The crucial breakthroughs enabling modern optical magnetometry were the nearly simultaneous development of optical detection of magnetic resonance by Bitter in 1949 [1] and optical pumping (OP) by Kastler in 1950 [2, 3]. Demelt [4] and Bell and Bloom [5] demonstrated that the orientation of atoms (and molecules) can be effectively monitored by observing the transmission of a beam of polarized optical resonance radiation. The general idea of the method is that light that is near-resonant with an optical transition creates long-lived orientation and/or higher-order moments in the atomic ground state, which subsequently undergo Larmor spin precession in the magnetic field. This precession modifies the optical absorptive and dispersive properties of the atoms, and this modification is detected by measuring the light transmitted through the atomic medium.

In many modern optical magnetometers, the techniques used to optically pump and probe atomic polarization are combined with methods to excite transitions between Zeeman and hyperfine levels using either additional radio- or microwave-frequency fields [6] or modulation of the intensity, frequency, or polarization of the light [7]. The idea of the double-resonance technique [8] is that optical pumping by a light beam tuned to resonance with an optical transition, $f = f_0$ is significantly modified when the frequency f_{rf}, e.g., of a radio-frequency field is tuned to the Larmor frequency, $f_{rf} = f_L$. Under proper conditions, absorption/emission of radio-frequency photons is accompanied by absorption/emission of optical photons, which substantially increases the detection efficiency of radio-frequency transition events. The double-resonance method is the basis for the widely used M_x- and M_z-magnetometers, A description of magnetometers based on magnetic resonance phenomena can be found, e.g., in [6].

2 He Magnetometers—Some History

2.1 Optically Pumped He-4 Magnetometers

Helium magnetometers began with the first optical pumping of the metastable level of ^{4}He by Colegrove and Franken [9] and the first helium magnetometer was demonstrated in [10]. As opposed to alkali-atom magnetometers which utilize ground-state polarization, He-4 magnetometers use polarization of the 2^3S_1 metastable state populated by a high-frequency discharge. Otherwise, the optical magnetometry techniques employed in helium magnetometers are similar: optical pumping and probing of atomic spin polarization is used along with double-resonance techniques involving either additional RF fields or frequency/amplitude modulation of the light. The general principle of an M_z-mode He-4 magnetometer is shown in Fig. 1. For the He-4 magnetometer the circular polarizer shown may be replaced by a linear polarizing filter, and the need for an

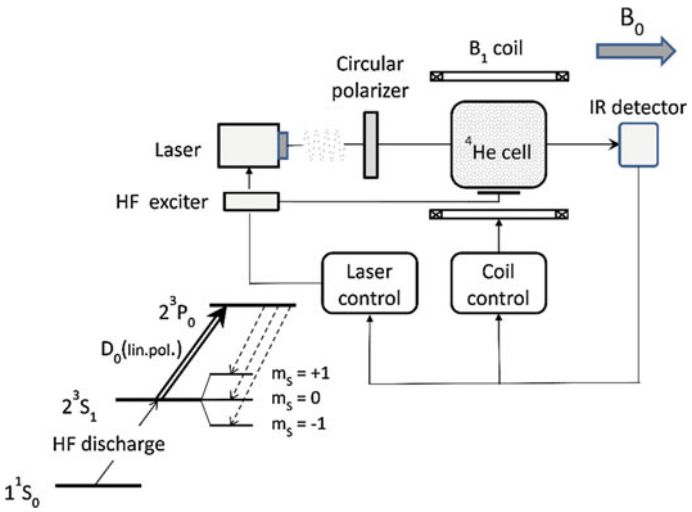

Fig. 1 Schematic block diagram of a double-resonance He-4 magnetometer with single line pumping in magnetic spin states of the ^{4}He 2^3S_1 metastable level (D_0: 2^3S_1 ($m_s = 0$) → 2^3P_0). Details see text

interference filter depends on the actual light source used. Using a laser, e.g., a tunable diode laser operating at 1083 nm [11–14] it can be locked to the single D_0 line, whereas a He-lamp will transmit the D_1 and D_2 lines as well, and requires some filtering in order to minimise absorption transitions at these lines [15]. The sensing element is a cylindrical glass cell containing ^{4}He at a few mbar. A small fraction of the helium is excited by a weak electrodeless HF discharge into the 2^3S_1 metastable state. This excitation introduces unpolarized metastable atoms. The external magnetic field B_o splits the energy into three Zeeman levels, designated $m_S = +1$, $m_S = -1$ and $m_S = 0$, where $\Delta E = h \cdot f_L$ is the energy difference between $m_S = 0$ and $m_S = \pm 1$. The transition from ± 1 to 0 can be induced by a resonance ac-magnetic field $B_1(t) = B_1 \cdot \cos(2\pi \cdot f_L)$. The determination of the Larmor resonance frequency f_L then yields the scalar magnitude of the external field according to:

$$\Delta E = h \cdot f_L = 2 \cdot \mu_e \cdot B_0 \text{ or } f_L = (\gamma_e / 2\pi) \cdot B_0 \tag{1}$$

where the free electron gyromagnetic ratio $\gamma_e/2\pi = (2 \cdot \mu_e/h) = 28.02495266$ [GHz/T], which is the largest conversion factor of any optically pumped magnetometer.

The determination of the frequency f_L is established in the following way: Electrons in the triple metastable 2^3S_1 state are optically excited into the higher 2^3P_0 energy level by a suitably narrow bandwidth IR-light beam. The excited 2^3P_0 atoms spontaneously decay unpreferentially to each Zeeman sublevel of the metastable 2^3S_1 state. Thus the light establishes a longitudinal magnetic polarization of the gas.

The transmitted laser light is monitored with an InGaAs or Si photodiode. Using linear polarized light, the $m_S = 0$ electrons will have a much reduced population, and absorption of the light can not any longer take place. This is line saturation when (almost) all the $m_S = 0$ electrons are removed, and the cell then recovers the full transparency. However, by applying the ac-magnetic resonance field $B_1 \cdot \cos(2\pi \cdot f_L)$ at right angles to the external field, then electrons are induced to go from the $m_S = \pm 1$ states into the $m_S = 0$ state, and $m_S = 0$ electrons again become available for light absorption.

In typical double-resonance, longitudinally monitored magnetometers (M_z-mode) the frequency f_{rf} of the magnetic resonance coils is swept across the Larmor frequency $f_{L.}$ The monitored light is synchronously detected at the fundamental frequency of the B_1 coils, and the center frequency of the modulation is adjusted until the fundamental vanishes from the detected output light, at which point the center frequency of the input modulation equals $f_L = (\gamma_e/2\pi) \cdot B_o$, giving an absolute measurement of the ambient magnetic field.

2.2 Optically Pumped He-3 Nuclear Magnetometer

When using ^{3}He one has the added process of metastability exchange collisions which allows angular momentum transfer from the metastable state to the $1^1S_o(I = 1/2)$ ground state. This mechanism is so effective that the entire ground state attains the same polarization as the 2^3S_1 metastable levels. Colegrove, Schearer and Walters were the first who demonstrated the method of spin-exchange optical pumping of metastable helium atoms to create spin-polarized ^{3}He nuclei [16, 17] which led to the development of the He-3 nuclear magnetometer [18]. The resonance in which one is interested in this case occurs when the nuclear polarization of the ground state is perturbed by the application of an oscillatory magnetic field at the Larmor frequency of the precessing ground state spins. Because of the tight coupling between metastable and ground state atoms, any perturbation on the polarization of the latter is transmitted to the former in a time much shorter than the nuclear Larmor period. The thusly perturbed metastable polarization alters the optical transparency of the cell. The significant difference in ^{3}He is that the nuclear spins do not interact directly with the resonance light beam producing the polarization so that light shifts should be negligibly small. In 2^3S_1 metastable helium the Larmor frequency may be shifted as a function of light intensity, wavelength, metastable density, and ambient field strength, and experimental measurements of these shifts have been made in [19].

With the discharge on to maintain atoms in the metastable state, both the longitudinal relaxation time T_1 and the transverse relaxation time T_2 depend upon the density of the metastable atoms. Typically T_1 is tens of seconds and T_2 is about 1.5 s. T_1 is measured by observing the rate at which the polarization comes to equilibrium. T_2 is the inverse rate at which ground state atoms undergo exchange collisions with atoms in the metastable state. Thus $T_2 = 1/(v \cdot \sigma \cdot n)$, where v is the

relative velocity of the colliding metastable atoms, n is the metastable density, and σ is the cross section for excitation transfer between a normal and a metastable state atom. The line width in the M_x-mode is $\Delta f = 1/(\pi T_2)$ in frequency units. This results in a narrow resonance line ΔB of about $\Delta B = \Delta f/(\gamma_{He}/2\pi) \approx 7$ nT, where $\gamma_{He}/2\pi = -32.43409966(43)$ Hz/μT ($\Delta\gamma_{He}/\gamma_{He} = 1.3 \times 10^{-8}$) is the gyromagnetic ratio of the ^{3}He nucleus [20]. For comparison: The transverse relaxation rate of an experimental He-4 magnetometer is essentially determined by diffusion of metastables to the cell wall, metastable collisions and light broadening and is about $1/T_2 \sim 8 \times 10^3$/s for a variety of cell dimensions and pressures in the range of 0.5–3 mbar [21]. Thus, the width of the magnetic resonance curve here is $\Delta B = 1/(\pi T_2)/(\gamma_e/2\pi) \approx 100$ nT which is more than a factor of 10 bigger than for the He-3 nuclear magnetometer. These examples show the benefits of using a He-3 nuclear magnetometer in particular if an absolute field measurement is required.

In conclusion: Although He optical magnetometers are often less well known to commercial magnetometer customers than alkali vapour magnetometers, lamp-pumped He-4 magnetometers have played significant roles in military and geophysical airborne magnetometry for more than 50 years. Innovations in He magnetometers have occurred at a rapid pace over the last 10 years following the advent of 1083 nm laser pump sources. Single-line laser pumping resulted in an improvement in sensitivity of more than two orders of magnitude over lamp-pumped magnetometers without sacrifices in portability or stability. Robust and stable field units have been demonstrated approaching 40 fT/√Hz sensitivity with excellent accuracy improved by the absence of light shifts. The increasing use of laser-pumped He magnetometers and the decreasing price of 1083 nm lasers is making these instruments more affordable relative to other types of magnetometers for both commercial and military customers.

2.3 *He-3 Nuclear Magnetometers Based on Free Spin Precession*

Already in the He-3 nuclear magnetometer paper of Schearer et al. [18], the authors pointed out the possibility of constructing a free precession device. The ^{3}He nuclear spins are extremely well shielded. In the absence of the discharge, T_1 has been measured as several thousand seconds. And T_2 should be in the same order provided the ground state atomes diffuse throughout the sample cell in a time $\tau_d \ll 1/(\gamma_{He}\Delta B)$, where ΔB is the field inhomogeneity across the bulb (see Sect. 4.2). The expected longer decay times and larger signals offer a several fold improvement in terms of magnetic resonance width (linewidths considerably smaller than 7 nT should be achievable) and absolute magnetic flux measurements. The advantages of using low pressure gaseous ^{3}He are that it can be used over a wide temperature range, including cryogenic temperatures, and, having negligible diamagnetic susceptibility, it has no temperature or sample shape dependence and so does not

change the magnetic flux density being measured except through the action of its container (see Ref. [22] and Sect. 6).

Cohen-Tannoudji et al. [23] were the first who used this new type of very-sensitive low-field magnetometer to detect the static field produced by optically pumped ^{3}He nuclei which precess freely in a spherical sample cell. The detection of the very weak magnetic field they produce is done by ^{87}Rb atoms contained in a second cell placed close to the ^{3}He cell. The ^{87}Rb magnetometer makes use of zero-field level-crossing resonances appearing in the ground state of optically pumped atoms [24]. The plot of the modulation of the magnetic field due to the free precession of ^{3}He nuclear spins (5 mbar, $P_{He} \sim 5$ %) is shown in Fig. 2. The measured transverse nuclear relaxation time is $T_2^* \approx 140$ min (definition of T_2^*, see Sect. 4.2) and the sensitivity of the readout device (^{87}Rb magnetometer) reaches 100 fT in a bandwidth of 0.3 Hz. Furthermore it was demonstrated, that the magnetostatic detection creates no detectable perturbation of the ^{3}He nuclear spins.

Free precession in the Earth's magnetic field ($\sim$50 μT) by optically polarized ^{3}He nuclei has been observed for the first time by Robert E. Slocum and Bela I. Marton in 1974 [25]. The readout here was accomplished by an NMR receiver coil wound coaxially on the cylindrical ^{3}He sample cell. The decay of the free

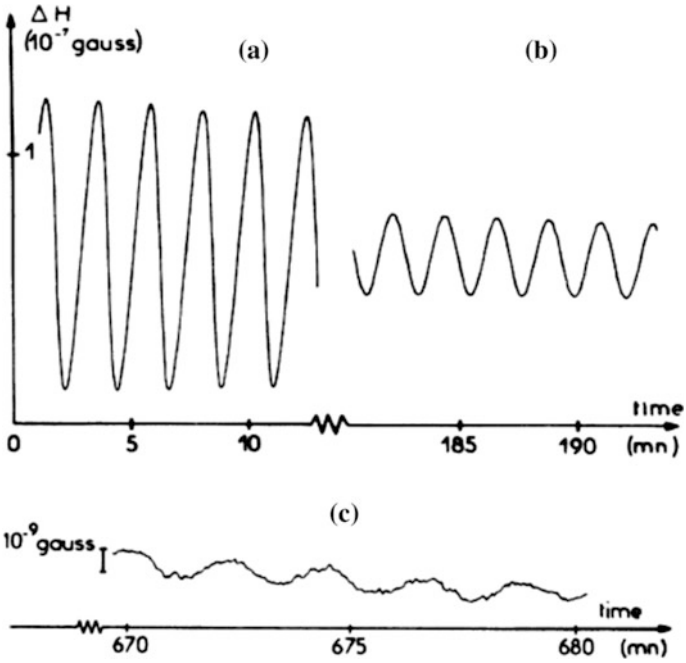

Fig. 2 Recorded free precession of the ^{3}He nuclear spins from Ref. [23], **a** just after optical pumping has been stopped, **b** 3 h later, and **c** 11 h later. On a closer look, a small magnetic drift of $\sim$20 pT can be seen due to the imperfections of the shield providing a mean residual field of $\sim$250 pT

precession signal was dominated by radiation damping ($\sim$10 min) [26], a problem which could partly be solved by Moreau et al. [27] by tuning the resonance frequency of the NMR circuit far away from the Larmor frequency of the precessing ^{3}He spins (weak coupling). The time evolution of the amplitude of the precession signal gave a characteristic relaxation time of $\sim$70 min. In spite of the weak coupling that limits the obtainable signal-to-noise ratio, the Earth's field could be recorded with a precision of $\sim$300 fT thanks to the use of diode lasers resulting in an increased degree of polarization of the ^{3}He nuclear spins.

When laser light with adequate spectral characteristics at 1083 nm is used, MEOP provides very high nuclear polarization (>0.7) with good photon efficiency ($\sim$1 polarized nucleus per absorbed photon) [28]. Given the development of suitable high power fibre lasers [29–31], the only drawback of this method is the limited range of operating pressures of order 0.5–5 mbar [32] for which a suitable plasma can excite metastable atoms. When a higher final pressure is needed, non-relaxing compression of the gas becomes necessary and this introduces demanding requirements on the gas handling and compressing devices. However it has recently been shown that the range of operating pressures can be extended to several tens or hundreds of mbar by performing MEOP in high magnetic fields up to 4.7 T [33].

3 ^{3}He Optical Pumping

3.1 Level Structure of the 2^3S and 2^3P States

We use the notations of Ref. [34] where the structure and energies of the sublevels of the 2^3S and 2^3P states are derived for both isotopes in arbitrary magnetic field. For simplicity we only discuss two experimentally relevant limiting cases: low and high magnetic fields.

Low field—For the sake of completeness, the complete level structure of ^{4}He involved in optical pumping is shown in Fig. 3a. The 2^3P state of ^{4}He has three fine-structure levels with J = 0, 1 and 2, hence nine Zeeman sublevels. There are twice as many Zeeman sublevels for ^{3}He due to its two nuclear spin states: six (A1 to A6) in the 2^3S state and eighteen (B1 to B18) in the 2^3P state that has five fine- and hyperfine-structure levels (see Fig. 2b). In low magnetic field, the F = 3/2 and F = 1/2 hyperfine levels of the 2^3S state of ^{3}He are well resolved and split by 6.74 GHz (Fig. 3b). The magnetic sublevels can be written using the decoupled basis states $|m_S, m_I\rangle$. $A_1 = |-1, -\rangle$ and $A_4 = |1, +\rangle$ are pure states of maximum $|m_F|$ = 3/2 but the other states involve large mixing parameters Θ_- and Θ_+ [34]:

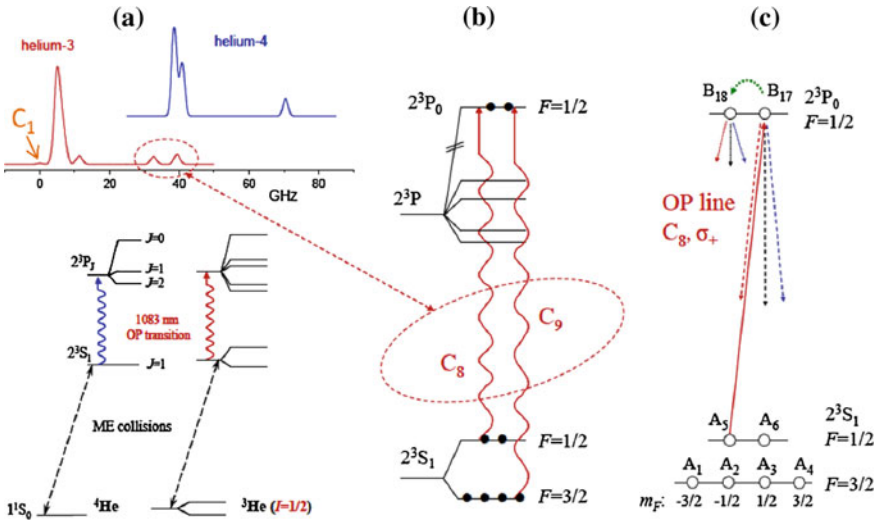

Fig. 3 **a** Fine- and hyperfine-structures of the atomic states of He involved in the MEOP process, for the ^{4}He (*left*) and ^{3}He (*right*) isotopes, in low magnetic field (below a few 10 mT). The resulting spectra of the 1083 nm transition (upper graphs, computed with 300 K Doppler widths and no collisional broadening) extend over ~70 GHz when the isotope shift is considered. Optical transition frequencies are referenced to that of the C1 line at zero field [34]. **b** C8 and C9 lines, which are the most efficient in usual OP conditions, connect the 2^3S_1, F = 1/2 and F = 3/2 levels of ^{3}He, respectively, to the 2^3P_0 level. **c** Example of elementary processes considered in the angular momentum budget for C8 optical pumping. The fluorescence light is emitted almost isotropically due to J-changing collisions in the 2^3P_J-states, proportional to pressure and of order a few 10^7 s^{-1}/mbar [35, 36]. That can result in significant population transfers during the 2^3P state radiative lifetime

$$
\begin{aligned}
A_2 &= \cos\Theta_-|-1,+\rangle + \sin\Theta_-|0,-\rangle \\
A_3 &= \cos\Theta_+|0,+\rangle + \sin\Theta_+|1,-\rangle \\
A_5 &= \cos\Theta_-|0,-\rangle - \sin\Theta_-|-1,+\rangle \\
A_6 &= \cos\Theta_+|1,-\rangle - \sin\Theta_+|0,+\rangle
\end{aligned}
\qquad (2)
$$

Strong and maximal mixing of electronic and nuclear angular momenta occurs at $B_0 \approx 0$, with $\sin^2\Theta_- = 2/3$ and $\sin^2\Theta_+ = 1/3$. The mixing parameters and the sublevel energies, as well as those of the 2^3P_0 sublevels addressed by the C8 and C9 transitions used for ^{3}He MEOP (see Fig. 3b), linearly depend on B_0 for low fields. The corresponding Zeeman line shifts do not exceed 30 MHz/mT and the relative changes in transition intensities do not exceed 0.6 %/mT. Given the Doppler width of the optical transitions (of order 2 GHz fwhm at room temperature for ^{3}He), the OP rate equations are almost field-independent up to several mT. For instance, for the simple low-field case illustrated in Fig. 3c, the C8 line with right-handed circular (σ+) polarization excites atoms from the A5 sublevel (m_F = −1/2) to the B17 sublevel (m_F = 1/2). Radiative decay brings atoms back to the 2^3S state with

well-defined branching ratios from the B17 sublevel (dashed lines in Fig. 3c) and from any other sublevel that may have been indirectly populated by collisions (green arrow and dotted lines in Fig. 3c).

High field—When the Zeeman energy exceeds the fine- and hyperfine-structure energy scales the angular momentum structures of 2^3S and 2^3P levels and the 1083 nm transition are deeply modified. Figure 4 displays the energy of all Zeeman sublevels for $B_0 = 1.5$ T, a field strength commonly met in MRI systems. At this field strength, only a weak state mixing remains in the 2^3S state (Eq. 2 with $\sin\Theta_+ = 0.07128$ and $\sin\Theta_- = 0.07697$). The six Zeeman sublevels of the ^{3}He isotope levels are organized in three pairs of states (Fig. 4a, bottom graph). In each pair the level energy is mostly determined by the common dominant value of m_S while the nuclear spin projections are almost antiparallel. Similarly, hyperfine coupling only weakly mixes levels of different m_I values in the 2^3P state (Fig. 4a, upper graph). As a result, high-field spectra for a given light polarization are thus composed of six main components which appear in two groups: a pair and a quartet, each group being unresolved at room temperature. These features clearly appear on the ^{3}He absorption spectra displayed in Fig. 4b, that are computed at 1.5 T assuming room temperature Doppler widths and no collision broadening. The strong lines in the ^{3}He spectra are labelled $f_n^{\pm}$, where $n = 2$ or 4 refers to the number of unresolved components and $\pm$ to the sign of the circular light polarization.

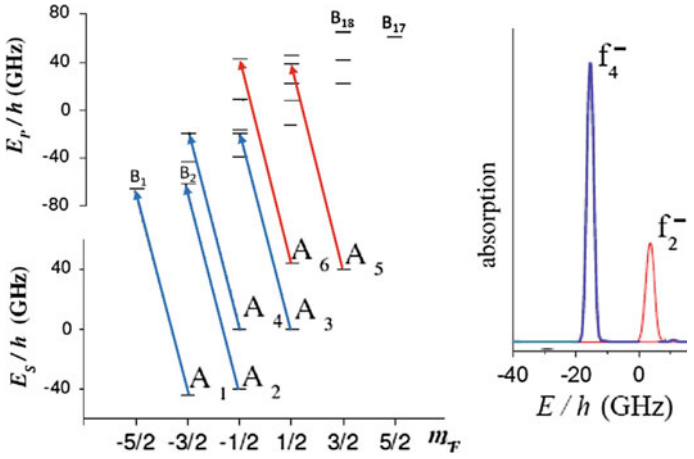

Fig. 4 **a** Energies and magnetic quantum numbers m_F of the ^{3}He sublevels at 1.5 T for the 2^3S (E_S) and 2^3P (E_P) states. The *blue* (*red*) scheme corresponds to the f_4^- (f_2^-) optical pumping configuration. The f_4 (f_2) line consists of four (two) unresolved transitions. The σ^- pumping transitions are displayed. **b** Computed absorption spectra for σ^- light at 1.5 T. f_4^- and f_2^- are the two optical pumping lines used in high field OP. The optical transition frequencies are referenced to that of the C_1 line in zero field (see Fig. 3a (top) and Ref. [34] for more details)

3.2 MEOP Under Non Standard Conditions

MEOP in standard conditions provides in a few seconds high nuclear polarizations (up to 90 % at 0.7 mbar [31]) in a guiding magnetic field up to a few mT. Unfortunately, the achieved nuclear polarization rapidly drops down when the ^{3}He pressure exceeds a few mbar [32, 37]. The hyperfine interaction plays a crucial role in MEOP: (a) it provides the physical mechanism for the polarization transfer during optical pumping from the atomic electrons to the ^{3}He nuclei and (b) it causes nuclear polarization losses by back transfers of nuclear orientation to electronic orientations of higher exited states with $L \neq 0$ in the discharge plasma that is sustained in the gas to populate the metastable state and perform OP. When the operating magnetic field is increased to $B_0 > 0.1$ T, the influence of hyperfine coupling on the nuclear relaxation is strongly reduced, counterbalancing the reduction of population of metastable atoms at higher gas pressures. In contrast, the strong hyperfine coupling in the metastable state still remains effective even at magnetic fields up to 7 T. That's why the MEOP technique can be extended to elevated gas pressures ($\sim$100 mbar) at high magnetic fields.

While this discussion holds for room temperature, the situation changes when decreasing the temperature. Under such conditions, the rate of metastability exchange collisions $(v_{rel} \cdot \sigma_{ME})$ is drastically reduced [38, 39], e.g. by a factor of about 30 by dropping the temperature from 300 to $\approx$4 K as can be seen in Fig. 5. That is why MEOP becomes inefficient and slow. We determined build-up times for the nuclear polarization of ^{3}He in small sample cells (see Fig. 6) at 300 K and 4.7 T in the order of seconds which would increase to 1–2 min at around 4 K without any further optimization. The elevated build-up times at low temperatures, however, should not be a big impairment for the applicability of this magnetometer. MEOP at cryogenic temperatures has been demonstrated in Refs. [40, 41] that allows in situ optical pumping inside the cold bore tube of, e.g., a Penning trap magnet.

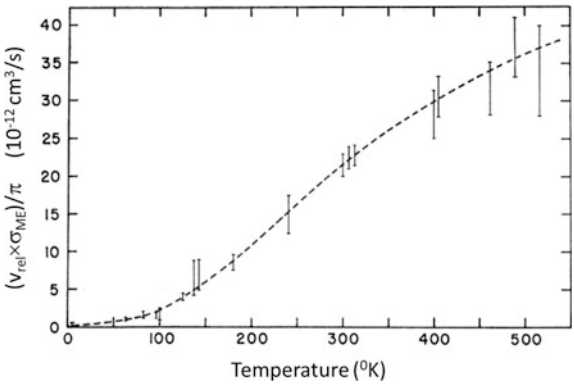

Fig. 5 Temperature dependence of the product of metastability exchange cross section (σ_{ME}) and relative collision velocity (v_{rel}) (from Ref. [38])

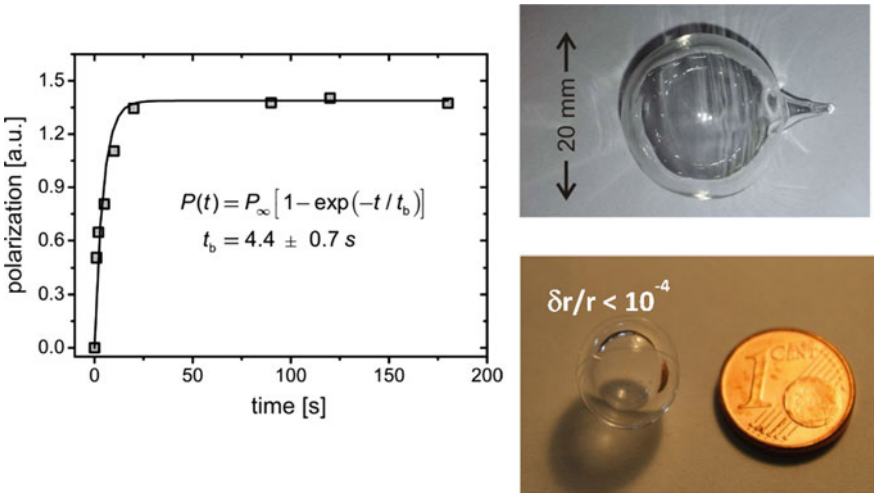

Fig. 6 Build-up of ^{3}He nuclear polarization (a.u.) in spherical Pyrex cell of 20 mm diameter (*top right*) with 2 W optical pumping laser power and strong discharge conditions in a magnetic field of 4.7 T. Sphericity of magnetometer cells (quartz) filled with ^{3}He of ~ 1 mbar could be significantly improved to $\delta r/r < 10^{-4}$ (*bottom right*)

4 Methodology

4.1 Readout of Spin Precession Signal

For the readout of the spin precession signal one can use several sensors like low- and/or high-T_c SQUID gradiometers, Rb(Cs) M_x gradiometers or standard NMR techniques. At low magnetic fields ($B_0 < 50$ μT) it is advantageous to use SQUIDs or alkali-magnetometers to record the free spin precession since they directly measure the temporal change of the ^{3}He magnetization M(t). At magnetic fields exceeding 0.1 T, NMR detection techniques are clearly preferable since they detect the induced field of the precessing sample magnetization being $\sim dM/dt$, i.e., the recorded signal scales with the Larmor frequency and thus with the magnetic field strength. In each case gradiometer arrangements of the respective readout devices is advantageous in order to reduce most of the environmental noise (common mode rejection).

Figure 7 sketches the three scenarios: The oriented nuclear magnetic moments inside a spherical sample cell of radius R give rise to a macroscopic magnetization M_0 that produces a magnetic dipole-like field B_{He} outside of the cell. One readily estimates that the field from a 100 % polarized gas at 1 mbar is on the order of $B_{\mathrm{He,s}} \sim 200$ pT on the outside surface of the cell and then decays like $B_{He} \sim B_{He,s} \cdot (R/r)^3$ with the radial distance r from the center. Taking $N_{\mathrm{SQUID}} \approx 3$ fT/$\sqrt{\mathrm{Hz}}$ for the white system noise measured with low-T_c dc–SQUIDs inside a magnetically

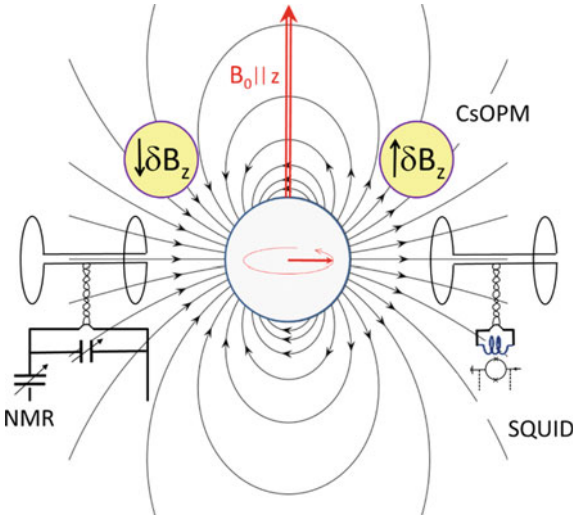

Fig. 7 Schematic layout of the He-3 nuclear magnetometer based on free spin precession. The ^{3}He magnetization in a spherical sample cell produces a dipolar field distribution outside the cell. As readout of the rotating magnetization three types of gradiometer systems are shown: **a** low-T_c SQUIDs, **b** Cs optical pumped magnetometers (CsOPM), and **c** NMR detection. Whereas (**a**) and (**b**) are used at $B_0 < 50$ μT, magnetic measurements via NMR are preferable at high magnetic fields ($B_0 > 0.1$ T). For details see text

shielded room, a first rough estimation shows that a signal-to-noise ratio of $SNR \approx$ 10000:1 at a bandwidth (f_{BW}) of 1 Hz can be reached for SQUID gradiometers positioned close, i.e., $r \approx 2R$ to the sample cell [42]. Using cesium optically pumped magnetometers (CsOPM), operated in the M_x configuration [43], an experimental observed value of $N_{Cs} \approx 30$ fT/$\sqrt{\text{Hz}}$ can be reached that is roughly a factor of two above the shotnoise limit of these devices. This results in an expected SNR of $\sim$500:1 ($f_{BW} = 1$ Hz). Note that the Cs magnetometers used are scalar magnetometers, i.e., they measure the modulus $B(r,t) = \left|\vec{B}_0(r,t) + \vec{B}_{He}(r,t)\right|$ of the total field at their location. Since $B_{He} \ll B_0$, and B_0 is nominally constant in time one has $B \approx B_0 + \vec{B}_0 \cdot \vec{B}_{He}(r,t)$, so that the CsOPMs are, to first order, only sensitive to the component δB_z of the ^{3}He free spin precession field along the applied magnetic field $B_0 || \hat{z}$. A simple calculation shows that—for a given distance r_{Cs}—this time dependent projection has a maximum amplitude when the sensors are located on a double cone with a half-opening angle of $\varphi = 45°$ with respect to B_0. Going to high magnetic fields and using NMR, the polarized ^{3}He sample is usually placed in a receiver coil of quality factor Q which is tuned to be resonant at the larmor frequency f_L. After the nuclear magnetization has been rotated by, e.g., a $\pi/2$-pulse, a voltage is induced in the coil by the rotating nuclear magnetization and the ratio of signal-to-noise voltages is given by [44, 45]

$$SNR = K \cdot \eta \cdot \left(\frac{\mu_0 \cdot Q \cdot (2\pi \cdot f_L) \cdot V_c}{4 \cdot F \cdot kT_c \cdot f_{BW}} \right)^{1/2} \cdot M_0 \tag{3}$$

where K is a numerical factor (~ 1) dependent on the receiving coil geometry, η is the "filling factor", i.e. a measure of the fraction of the coil volume occupied by the sample, μ_0 is the permeability of free space, V_c is the volume of the coil, F is the noise figure of the amplifier, $k_B T_c$ is the thermal energy of the probe, and f_{BW} is the bandwidth of the receiver. Calculations show that $SNR > 1000{:}1$ ($f_{BW} = 1$ Hz) can be easily obtained even if filling factor (η) and/or quality factor (Q) had to be reduced in order to suppress radiation damping. In Fig. 8 is shown the measured precession of the rotating ^{3}He magnetization using the mentioned readout devices. Figure 8a

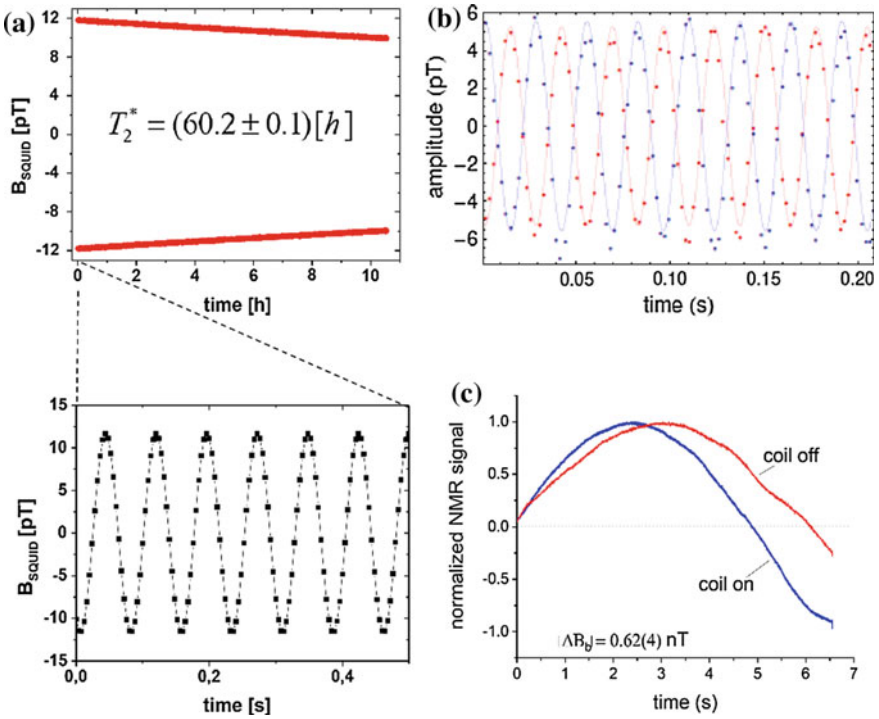

Fig. 8 **a** Free spin-precession signal ($f_L \approx 13$ Hz) of a polarized ^{3}He sample cell, recorded by means of a low-T_c dc-SQUID gradiometer (sampling rate: 250 Hz) [42]. The uncertainty at each data point is ± 34 fT and therefore less than the symbol size. Envelope of the decaying signal amplitude from that a transverse relaxation time of $T_2^* = (60.2 \pm 0.1)$ h can be deduced. **b** Time series of the two CsOPM signals (sampling rate 450 Hz) dephased by π [43]. The frequency is $f_L \approx 37$ Hz ($B_0 \approx 1.14$ μT) and the extracted $SNR_{diff} \approx 140$ (f_{BW} 1 Hz). **c** Measured FID (normalized signal; sampling rate: 620 Hz, $SNR \approx 1800$ @ $f_{BW} = 1$ Hz) of the beat frequency $f_b = f_L - f_R$ with and without preset magnetic field shifts of $\left|\Delta B_b^{set}\right| = 0.6$ nT added to the $B_0 = 1.5$ T field of the MR scanner [46]. The characteristic time constant of the FID could be determined to be $T_2^* \approx 70$ s. For technical reasons only 6.6 s of the FID could be recorded

shows the recorded SQUID gradiometer signal over a time interval of 0.5 s at the beginning of the precession cycle. The signal amplitude reaches $\Delta B_{\mathrm{He,SQ}} \approx 12.5$ pT and the precession frequency is $f_{\mathrm{L}} \approx 13$ Hz ($B_0 \approx 400$ nT). Further shown is the exponential decay of the signal amplitude (envelope) over a period of about 10 h from which one can deduce a transverse relaxation time of $T_2^* = (60.2 \pm 0.1)$ h. The time series of the CSOPM signals ($S_{\mathrm{Cs,I}}$, $S_{\mathrm{Cs,II}}$) dephased by π is shown in Fig. 8b. Both signals carry perturbations from the 50 Hz line frequency. In the differential signal, the 50 Hz perturbation has vanished (common mode rejection), as evidenced by the Fourier spectrum. The (random) noise amplitude spectral densities of the two signals $N_{\mathrm{Cs,I}} = 48$ fT/√Hz and $N_{\mathrm{Cs,II}} = 59$ fT/√Hz add quadratically in the differential signal $N_{\mathrm{Cs,diff}} = \sqrt{N_{Cs,I}^2 + N_{Cs,II}^2} = 76\,\mathrm{fT}/\sqrt{\mathrm{Hz}}$, so the expected SNR_{diff} is given by $SNR_{diff} = \left(S_{Cs,I} + S_{Cs,II}\right)/N_{Cs,diff}$, yielding $SNR_{\mathrm{diff}} \approx 140$ in a bandwidth of 1 Hz. Figure 8c shows the beating of free induction decay (FID) signals against a reference signal $f_{\mathrm{R}} = 48.6$ MHz from the local frequency standard at beat frequencies $f_{\mathrm{b}} = f_{\mathrm{L}} - f_{\mathrm{R}}$ of roughly 0.1 Hz. The NMR signal has been recorded in the homogeneous field of an MR scanner (1.5 T) for the maximum available acquisition time of 6.6 s using the spherical cell shown in Fig. 6 (top right) [46]. The measured T_2^*-time is $T_2^* \approx 70$ s. By help of a Helmholtz coil, the pair of FID signals in Fig. 8c has been split by applying a field of $\left|\Delta B_b^{set}\right| = 0.6$ nT. The beat frequencies of the pair can be roughly evaluated from the swept time intervals for, e.g., 0.5 cycles. Estimating an error of 0.05 s for this reading one evaluates for the pair a frequency difference of $|\Delta f_b| = 0.0210(13)$ Hz $\Rightarrow |\Delta B_b| = 0.62(4)$ nT. Within the error bars these results correspond to the set ΔB-value. This rough and ready evaluation reaches already a sensitivity limit for detecting relative field shifts as a small as $\Delta B/B_0 \approx 3 \times 10^{-11}$ at $B_0 = 1.5\,\mathrm{T}$ ($f_{\mathrm{L}} = 48.6\,\mathrm{MHz}$).

The given realizations for the readout of the precession signal demonstrate that He-3 nuclear magnetometers can be used over a wide dynamic range in magnetic field strengths (nT < B_0 < 10 T) for precise field monitoring. The ^{3}He pressure in all three cases was around $p_{\mathrm{He}} \sim 1$ mbar and the degree of nuclear polarization between $0.3 < P_{\mathrm{He}} < 0.5$. With a signal-to-noise ratio of $SNR > 1000{:}1$ (f_{BW}: 1 Hz) relative field measurements of $\Delta B/B_0 \approx 10^{-11}$ are possible (deduced from Fig. 8c). The T_2^*-times of coherent spin precession can reach days, so continuous field monitoring over several hours is possible in particular at low fields. Even at high magnetic fields (>0.1 T), the T_2^*-times may reach several minutes in sample cells of good sphericity (Fig. 6, bottom right) and radii $R < 0.5$ cm. Quasi continuous field monitoring can also be accomplished there by a tandem of He-3 magnetometers which are alternately operated in optical pump- and free spin precession mode being in opposite phase with each other.

4.2 Concept of Long Nuclear-Spin Phase Coherence Times

The presence of a magnetic field gradient in a sample cell containing spin-polarized ^{3}He gas will cause an increased transverse relaxation rate. The origin of this relaxation mechanism is the loss of phase coherence of the atoms due to the fluctuating magnetic field seen by the atoms as they diffuse throughout the cell (self-diffusion). In the so-called "motional narrowing" regime, where the gas atoms diffuse throughout the sample cell (spherical cell of radius R) in a relative short time $T_D \approx R^2/D \ll 1/(\gamma \Delta B)$, the disturbing influence of the field inhomogeneity ($\Delta B \approx R \cdot \vec{\nabla} B$) on the spin coherence time T_2^* is strongly suppressed. Analytical expressions can be derived for the transverse relaxation rate for spherical and cylindrical sample cells, as reported in references [47, 48], respectively. Subsuming the relaxation rate at the walls, $1/T_{1,\mathrm{wall}}$, and other spin-relaxation modes under the longitudinal relaxation time T_1, the general expression for the transverse relaxation rate $1/T_2^*$ for a spherical sample cell of radius R is

$$\begin{aligned}\frac{1}{T_2^*} &= \frac{1}{T_1} + \frac{1}{T_{2,field}} \\ &= \frac{1}{T_1} + \frac{8R^4\gamma_{He}^2\left|\vec{\nabla}B_{1,z}\right|^2}{175 \cdot D_{He}} + D_{He}\frac{\left|\vec{\nabla}B_{1,x}\right|^2 + \left|\vec{\nabla}B_{1,y}\right|^2}{B_0^2} \\ &\quad \times \sum_n \frac{1}{\left|x_{1n}^2 - 2\right| \cdot \left(1 + x_{1n}^4(\gamma_{He}B_0R^2/D_{He})^{-2}\right)}\end{aligned} \tag{4}$$

with the magnetic holding field B_0 pointing along the z-direction. D_{He} is the diffusion coefficient of the gas D_{He} [cm^2/s] = 1880/p_{He} [mbar] at T = 300 K [49], and x_{1n} (n = 1, 2, 3, …) are the zeros of the derivative $(d/dx)j_1(x) = 0$ of the spherical Bessel function $j_1(x)$. The deviation $\boldsymbol{B}_1(\mathbf{r})$ of the local field from the average homogeneous field $\boldsymbol{B}_0$ was approximated by the uniform gradient field $\boldsymbol{B}_1(\mathbf{r}) = \boldsymbol{r} \cdot \nabla \boldsymbol{B}_1$, with $\nabla \boldsymbol{B}_1$ being a traceless, symmetric second-rank tensor. Equation (4) can be simplified for the low and high field limit using $Y := x_{11}^4 \cdot D_{He}^2/(\gamma_{He}^2 \cdot R^4 \cdot B_0^2) \gg 1$ and $Y \ll 1$, respectively.

$$\begin{aligned}&\frac{1}{T_2^*} = \frac{1}{T_1} + \frac{1}{T_{2,field}} = \frac{1}{T_1} + \frac{4 \cdot R^4 \cdot \gamma_{He}^2}{175 \cdot D_{He}}\left(2\left|\vec{\nabla}B_{1,z}\right|^2 + \left|\vec{\nabla}B_{1,x}\right|^2 + \left|\vec{\nabla}B_{1,y}\right|^2\right) \quad low\,field\,B_0 < 10\,\mu T \\ &\frac{1}{T_2^*} = \frac{1}{T_1} + \frac{8 \cdot R^4 \cdot \gamma_{He}^2}{175 \cdot D_{He}} \cdot \left|\vec{\nabla}B_{1,z}\right|^2 \quad high\,field\,B_0 > 0.1\,T\end{aligned} \tag{5}$$

with R [cm].

The longitudinal relaxation time T_1 of container vessels made from low-relaxation GE180 glass has been systematically investigated in [50–53]. At ^{3}He pressures well below 1 bar as it is the case for all He-3 magnetometer applications,

T_1 is essentially determined by the wall relaxation time $T_{1,\mathrm{wall}}$ which describes the relaxation due to collisions with the inner walls of the container and depends as

$$\frac{1}{T_{1,wall}} = \eta_R \cdot \frac{S}{V} \tag{6}$$

on its surface to volume ratio (S/V). The relaxivity (η_R) is presumed to be a constant for each vessel and related to the interaction between the HP-gas with para- or ferromagnetic centers on top or close to the inner surface. For uncoated GE180 glass cells, the relaxivity is typically $\eta_\mathrm{R} \approx 0.01$ [cm/h], i.e., even for miniaturized sample cells ($R \leq 0.5$ cm) which are used specifically in high-field magnetometry, T_2^* is essentially determined by the field-gradient induced transverse relaxation time $T_{2,field}$ (see Eq. 5). The latter one can reach $T_{2,field} \approx 100$ h in sample cells of $\Phi = 10$ cm, provided the absolute field gradients across the cell are less than $\left|\vec{\nabla}B_{1,j}\right| < 50$ pT/cm that corresponds to a relative field gradient of 5×10^{-5}/cm in a $B_0 = 1$ μT field. Going to high magnetic fields ($B_0 > 0.1$ T), $T_{2,field}$ drops off dramatically! For the same relative field gradient, $T_{2,field}$ and thus T_2^* only reaches $T_2^* \approx 2$ s in a $B_0 = 1.5$ T field for a cell of $R = 0.1$ cm ($p_\mathrm{He} = 1$ mbar). In the example given above ($T_2^* \approx 70$ s, see Fig. 8c), the absolute field gradient was $\left|\vec{\nabla}B_{1,z}\right| \approx 1.5 \times 10^{-7}$ T/cm and $R = 0.9$ cm ($p_\mathrm{He} \sim 1$ mbar) [46].

5 Performance of the Free Precession He-3 Magnetometer

5.1 Sensitivity

The possible achievable accuracy of the frequency and thus magnetic field measurement can be estimated in the following solely statistical way: Assuming the noise is Gaussian distributed, the Cramér-Rao Lower Bound (CRLB) [54] sets the lower limit on the variance σ_f^2 for the frequency estimation of an exponentially damped sinusoidal signal given by

$$\sigma_f^2 \geq \frac{12}{(2\pi)^2 \cdot SNR^2 \cdot f_{BW} \cdot T^3} \cdot C\left(T, T_2^*\right) \tag{7}$$

where f_{BW} is the bandwidth of the acquisition of duration T and $C\left(T, T_2^*\right)$, describes the effect of exponential damping of the signal amplitude with T_2^*. For observation times $T \leq T_2^*$, $C\left(T, T_2^*\right)$ is of order one [42]. The sensitivity δB on the respective magnetic field B_0 seen by the sample spins is derived from Eq. 7 using $f_L = (\gamma_{He}/2\pi) \cdot B_0$. It increases with the observation time, T, according to

$$\delta B \geq \frac{\sqrt{12} \cdot \sqrt{C(T, T_2^*)}}{\gamma_{He} \cdot SNR \cdot \sqrt{f_{BW}} \cdot T^{3/2}} \tag{8}$$

Due to their 2–3 orders of magnitude higher gyromagnetic ratio γ, Eq. 8 suggests the use of magnetometers based on the spin precession of electrons (e.g. He-4 magnetometer) rather than on the spin precession of nuclei. Usually, the relaxation time of electron spins is short ($\sim$ms), while nuclei, such as ^{3}He, display a much longer spin-relaxation time. In practice, the product of $\gamma_{He} \cdot T^{3/2}$ exceeds that of electron spin based magnetometers for $T > 0.1$ s, already. Moreover, at high magnetic fields, where the frequencies of electron spin magnetometers are in the GHz range, elaborated microwave techniques are necessary for excitation and detection. Taking an *SNR* of *SNR* = 1000:1 in a bandwidth of 1 Hz, and $T = T_2^* \approx 1\ min$, a lower limit of $\delta B \approx 40$ fT corresponding to a relative precision in magnetic field measurement of

$$\left(\frac{\delta B}{B}\right)_{\text{CRLB}} \approx 4 \cdot 10^{-14}/B[\text{T}] \tag{9}$$

is expected from Eq. 8. In the following it is discussed how far this CRLB limit in measurement sensitivity is met under realistic conditions, in particular in situations where the magnetic field and with it the signal frequency may vary within the measurement time T by amounts $\delta f \gg \left(\sigma_f\right)_{CRLB}$. Analogue to other experiments with high precision in frequency, the phase $\Phi(t) = \int_0^t f(t')dt'$ is analyzed. For example, the NMR signal is registered as a complex transient, so the phase can be directly calculated (removing phase jumps by standard phase unwrapping algorithms implemented, e.g., in MATLAB, Mathworks USA). The free induction decay of ^{3}He can be described as $S(t) = S_0 \cdot \exp(-i\Phi(t)) \cdot \exp\left(-t/T_2^*\right)$. Then the phase is simply calculated by

$$\Phi(t) = \tan^{-1}\frac{\Re(S(t))}{\Im(S(t))} = \int \gamma_{He} B(t)dt \tag{10}$$

The slope or the first time derivative of Φ(t) is then the magnetic field multiplied by the gyromagnetic ratio. In a similar way the accumulated phases can be extracted from the recorded SQUID/CsOPM signal of the precessing spins (see Fig. 8a, b) discussed in detail, e.g., in Refs. [42, 43]. Now, the signal frequency from the source (in the given example of Fig. 8c, the beat frequency f_b) may vary within the measurement time T by amounts $\delta f_b \gg \sigma_f^{CRLB}$. In this case, one may wish to measure the frequency averaged over the period T represented by

$$\bar{f}_{\text{b}} = \frac{\Delta\phi}{2\pi \cdot T} \tag{11}$$

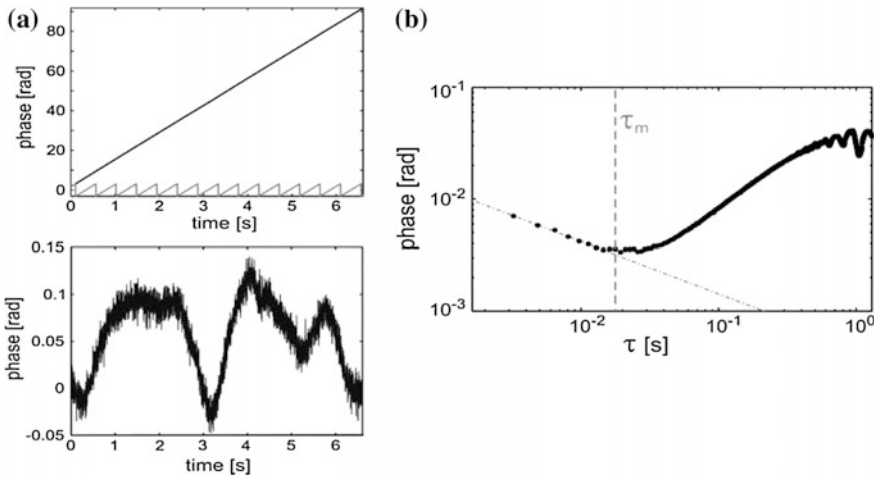

Fig. 9 **a** *Top* Acquired phase data from an FID run at B_0 = 1.5 T. During the acquisition time of T = 6.6 s, the accumulated phase ("unwrapped" data in *black*) amounts to $\Delta\Phi \approx 90$ rad. The number m of phase jumps (2π) is extracted from the arctangent function that gives the wrapped phase variation (sawtooth-like structure in gray, here $m = 15$). *Bottom* Phase residuals after subtraction of Eq. 13 indicate the environmental phase noise induced by field changes of ≤ 0.5 nT. **b** Allan Standard Deviation (ASD) of the phase residuals. For integration times $\tau_m < 20$ ms, the residual phase noise decreases with $\tau^{-1/2}$ as indicated by an according fit (*dashed-dotted line*). Beyond τ_m, the temporal characteristics of external field fluctuations causes the observed increase of non-statistical phase fluctuations

$\Delta\phi$ is the accumulated phase as shown in Fig. 9a (top) which can be expressed as

$$\Delta\phi = 2\pi \cdot m + \phi_F - \phi_I \tag{12}$$

where m is the number of phase jumps (2π) within T and $\phi_{F,I}$ are the respective values of the phase determined at the beginning (I) and at the end (F) of the data train. The task now is to estimate the error on $\phi_{F,I}$ with maximum efficiency. The example given in Fig. 9 shows the acquired phase data from the FID run shown in Fig. 8c (with Helmholtz-coil off: $\Delta B = 0$). At the sensitivity scale of *rad*, a linear functional dependence is the finding. Subtracting the function

$$g(t) = 2\pi \cdot \bar{f}_b \cdot t + \phi_I \tag{13}$$

we obtain the corresponding phase residuals $\varphi(t)$ which vary within ≈150 mrad (Fig. 9a, bottom). The time derivative of which gives the change in Larmor precession frequency or magnetic flux vs. time. From that a maximum field change of about 0.5 nT caused by environmental fluctuations of the magnetic field ("visible wiggles" in Fig. 8c) was estimated for this run.

These phase residuals $\varphi(t)$ are used to estimate the error on $\phi_{F,I}$. Thereby, the Allan Standard Deviation (ASD) method is applied for the analysis of signal noise and drift. The ASD [55] is the most convenient measure to study the temporal

characteristics of frequency fluctuations and to identify the power-law model for the phase-noise spectrum under study. The ASD of the phase-residuals of the FID run shown in Fig. 9, is calculated according to

$$\sigma_{\mathrm{ASD}}(\tau) = \sqrt{\frac{1}{2(N-1)} \sum_{i=1}^{N-1} \left(\bar{\varphi}_{i+1}(\tau) - \bar{\varphi}_i(\tau)\right)^2} \tag{14}$$

where the total acquisition time T is subdivided in N smaller time intervals of the same length τ, so that $N\tau = T$. For each such sub-dataset (i = 1, 2, …, N − 1), the mean phase $\bar{\varphi}(\tau) = \langle \varphi_i(t) \rangle_\tau$ is determined. For white Gaussian noise—one essential requirement the derivation of CRLB is based on—σ_{ASD} coincides with the classical standard deviation and we expect a $\sigma_{\mathrm{ASD}} \sim \tau^{-1/2}$ dependence on the integration time τ. This power-law is also found in our data for short integration times $\tau_{\mathrm{m}} \leq 20$ ms shown by the dashed-dotted line in Fig. 9b, whereas σ_{ASD} increases again for $\tau > \tau_{\mathrm{m}}$ due to the temporal characteristics of external field fluctuations that are the dominant sources of non-statistical phase fluctuations. From the ASD-plot one can extrapolate the respective phase noise σ_0 at the sampling rate $\mathrm{r_{s,0}}$ = 620 Hz corresponding to $\tau = 1/r_{\mathrm{s},0} \approx 1.6$ ms: $\sigma_0 = 9.8$ mrad. This phase noise defines the error on $\phi_{F,I}$. Using Eqs. 11 and 12, the error on the average frequency $\bar{f}_b$ can be extracted to be $\sigma_{\bar{f}_b} = \sqrt{2} \cdot \sigma_0/(2\pi \cdot T) \cong 3.5 \times 10^{-4}$ Hz with $\sigma_{\phi_I} = \sigma_{\phi_F} = \sigma_0$. Finally, by use of $\mathrm{f_b = f_L - f_R}$, we obtain a first hint on the true sensitivity of this magnetometer: The accuracy with which the average Larmor frequency $\bar{f}_L$ and thus the average magnetic field $\bar{B}_0 = 1.5$ T can be determined over the period of T = 6.6 s is given by $\delta B/\bar{B}_0 = \delta f_L/\bar{f}_L \approx \sigma_{\bar{f}_b}/48.6\,[\mathrm{MHz}] \approx 10^{-11}$. Here, we assumed that the frequency f_R of the local oscillator (atomic clock in principle) is free of error.

A more refined analysis on the measurement sensitivity can be done if we determine the value $\bar{\phi}_{I,F}$ from a group of data extending over ΔT at the beginning (I) and at the end (F) of the data train [46]. The ASD-plot in Fig. 9b shows that the "zero-mean Gaussian noise" criterion CRLB is based on can be used for time intervals ΔT up to $\Delta T \approx 20$ ms. Within that time interval the residual phase φ (t) can be set constant, i.e., the phase drift ϕ(t) within ΔT is linear. As discussed in detail in Ref. [46], the relative accuracy to which the average Larmor frequency and thus the average magnetic field can be determined over the total acquisition time T is

$$\frac{\delta B}{\bar{B}_0} = \frac{\sigma_{\bar{f}_b}}{f_R + f_b} \cong \frac{\sigma}{\pi\sqrt{2 \cdot r_s} \cdot T \cdot \sqrt{\Delta T} \cdot f_R} \tag{15}$$

For instance, using values T = 6.6 s, ΔT = 20 ms, $r_{\mathrm{s},0}$ = 620 Hz, $\sigma_0 \approx 10$ mrad, and $f_{\mathrm{R}} = 48.6$ MHz ($\bar{B}_0 = 1.5$ T) this results in

$$\frac{\delta B}{\bar{B}_0} \cong 2 \cdot 10^{-12}. \tag{16}$$

The gain in sensitivity compared to the first estimate was achieved by the factor $\sqrt{N_0} \approx 5$, representing the increased statistical accuracy to estimate the error on $\bar{\phi}_{I,F}$ with N_0 being the number of data points within the time interval ΔT.

5.2 Dynamic Range of Field Monitoring

The data presented were measured at an almost constant magnetic field of $\bar{B}_0 =$ 1.5 T with disturbing influences of the environmental fields being of order nTesla. The legitimate question may arise which dynamic range of field fluctuations can be covered by this magnetometer without significantly affecting its sensitivity. The precise measurement of the accumulated phase as discussed in the previous section presupposes that during data acquisition deviations Δf_L from the mean value $\bar{f}_L \cong f_R$ of the Larmor frequency which are equivalent to the changes Δf_b of the beat frequency after rf mixing with a carrier frequency f_{R}, have to fulfil the Nyquist-Shannon sampling theorem

$$\Delta f_{\mathrm{b}} \leq r_{\mathrm{s}}/2 \equiv f_{\mathrm{Ny}} \tag{17}$$

With $\Delta f_b \leq 25$ mHz, the number which can be deduced from the phase residuals (time derivative) as shown in Fig. 9a, the above requirement is met by far for the chosen sampling rate of $r_{\mathrm{s},0} = 620$ Hz. In principle, the sampling rate (r_{s}) can be noticeably increased in order to extend the dynamic range further. This, however, is associated by an increase of the phase noise (white noise) given by

$$\sigma = \sigma_0 \cdot \sqrt{\frac{r_{\mathrm{s}}}{r_{\mathrm{s},0}}} \tag{18}$$

Since the measurement precision is directly related to the error $\sigma_{\Delta\Phi}$ in the accumulated phase, we take Eq. 12 as starting point and derive

$$\sigma_{\Delta\phi} = \sqrt{\sigma_{\mathrm{I}}^2 + \sigma_{\mathrm{F}}^2 + (2\pi \cdot \Delta m)^2} \tag{19}$$

Besides the phase errors $\sigma_{I,F}$, we also have to consider noise induced phase wraps Δm which get more and more important the larger the dynamic frequency range that must be covered by the magnetometer. Already for $\Delta m = 1$, $\sigma_{\Delta\Phi}$ is dominated by the latter effect since we have $\sigma_{I(F)} \ll 2\pi$. It is the distinction between true or genuine phase wraps (m) and apparent or fake phase wraps (Δm) that have been caused by phase noise that make the practical phase unwrapping such a challenging task. An analysis for the FID signal was done in Ref. [46]:

$\sigma_{\Delta\Phi} \approx 0.16 rad$ for $SNR = 6$. As a result, one can derive the sensitivity to which the field $\bar{B}_0$ averaged over the period T can be measured if we allow for relative field fluctuations of 0.04 %:

$$\frac{\delta B}{\bar{B}_0} \approx \frac{\sigma_{\Delta\Phi}/(2\pi \cdot T)}{\bar{f}_L} \approx 7.8 \times 10^{-10}/\mathrm{T[s]}/\bar{B}_0 \text{ [Tesla]} \tag{20}$$

5.3 Systematics

5.3.1 Readout

The detection of the ^{3}He free spin precession by external magnetometers/sensors provides an *indirect* optical readout that to first order does not perturb the free spin precession. This avoids possible systematic effects as they may occur e.g. in optical alkali magnetometers by the *direct* read-out beams (light shift) or by phase errors in their feedback electronics (M_x-mode). The latter ones change the zero crossing of the dispersive line shape where the feedback system locks to the resonance. On the other hand, the systematic effects affecting the CsOPMs are irrelevant for their use as readouts for the rotating ^{3}He magnetization.

Because CsOPMs are driven magnetometers (M_x-mode), the driving rf-field $B_1(t)$ may introduce a systematic frequency shift (Ramsey-Bloch-Siegert (RBS) shift) in the free precession (Larmor precession) of the ^{3}He nuclear spins. The exact expression for the shift in the Larmor frequency due to a rotating field with amplitude B_1 and frequency f_D ($f_D = (\gamma_{Cs}/2\pi) \cdot B_0$, $\gamma_{Cs}/2\pi = 3.5\,\mathrm{kHz/\mu T}$) is given by [56, 57]

$$\delta f_{RBS} = \pm\left(\sqrt{\Delta f^2 + (\gamma_{He}/2\pi)^2 \cdot B_1^2} - \Delta f\right) \tag{21}$$

with $\Delta f = |f_L - f_D|$. The plus sign applies to $(f_D/f_L) < 1$, the minus sign to $(f_D/f_L) > 1$, respectively. For $\Delta f \gg (\gamma_{He}/2\pi) \cdot B_1$ this expression reduces to

$$\delta f_{RBS} = \pm\frac{(\gamma_{He}/2\pi)^2 \cdot B_1^2}{2 \cdot \Delta f} \tag{22}$$

Taking the geometrical arrangement of the combined Cs/^{3}He magnetometer as described in [43] for studying the ^{3}He free spin precession readout with laser pumped CsOPMs, the Cs rf-coils produce a residual rf-field at the center of the ^{3}He sample cell of about $B_1 \sim 2 \times 10^{-11}$ T. That results in a RBS shift of $|\delta f_{RBS}| \approx 6 \times 10^{-10}$ Hz ($\delta f_{RBS}/f_{L,He} \approx 2 \times 10^{-11}$) for the applied $B_0 \sim 1$ μT field.

Concerning readout by SQUIDs: Traditionally, SQUIDs were operated in a flux-locked loop (FLL) using a flux modulation technique [58]. Since the early

1990 many novel readout concepts were developed which were stimulated in part by the need to simplify the SQUID electronics for biomagnetic multichannel systems [59, 60]. The direct-coupled low-T_c dc-SQUID magnetometers used here achieve a very low noise level using simple FFL electronics *without* flux modulation. Crosstalk problems among the SQUID sensors are practically avoided because of the absence of any ac bias signals. Therefore we do not expect an RBS-shift on the Larmor frequency of the precessing ^{3}He spins.

NMR-readout: When the Larmor frequency f_L of the spin sample is not exact the resonance frequency of the electronic detection circuit, f_c, radiation damping gives rise to an induced frequency shift Δf_{RD}. For flip angle $\alpha < \pi/6$ and $2Q \cdot (f_L - f_c)/f_c \ll 1$, Guéron [61] obtained the expression $\Delta f_{RD} \approx (f_L - f_c) \cdot Q/(\pi f_c \tau_{RD})$. Although this frequency shift is negligibly small in most practical NMR applications, the high resolution $(\Delta f_L/f_L)$ of this magnetometer sets upper limits on the detuning of the resonator with respect to the atomic Zeeman frequency given by

$$(f_L - f_c) < \frac{\pi \cdot \tau_{RD}}{Q} \cdot f_L^2 \cdot \left(\frac{\Delta f_L}{f_L}\right) \tag{23}$$

For $f_L = 48.6\,\text{MHz}$, Q = 280, and $\tau_{RD} = 200\,\text{s}$, we obtain $(f_L - f_c) < 5.3$ kHz, taking $(\Delta f_L/f_L) = 10^{-12}$, for example.

5.3.2 Investigation of Intrinsic Frequency Shifts

In order to investigate the CRLB sensitivity limit of the free precession 3He nuclear magnetometer (see Eq. 7), one has to study its inherent noise sources. In frequency metrology it is customary to represent frequency fluctuations in terms of the Allan standard deviation σ_{ASD} (see Sect. 5.1). A double logarithmic plot of the dependence of σ_{ASD} on the integration time τ is a valuable tool for assigning the origin of the noise processes that limit the performance of an oscillator. In order to determine the magnetometer performance limit, one is generally forced to actively stabilize the magnetic field. Otherwise non-statistical field fluctuations would create noise sources which—a priori—cannot be distinguished from inherent noise sources from the magnetometer itself. A better approach to get rid of the influence of the ambient magnetic field and its temporal fluctuations is to use co-located spin samples, e.g., ^{3}He and ^{129}Xe. In so called ^{3}He/^{129}Xe clock-comparison experiments, the Zeeman-term and thus any dependence on magnetic field fluctuations should drops out for the given combination of Larmor frequencies, i.e.,

$$\Delta f_c = f_{L,He} - (\gamma_{He}/\gamma_{Xe}) \cdot f_{L,Xe} \tag{24}$$

with $(\gamma_{He}/\gamma_{Xe}) = 2.75408159(20)$ [62, 63].

Δf_c or its equivalent, the residual phase $\Delta\Phi_c$, is the relevant quantity to be further analyzed in order to trace properly possible frequency- or phase shifts inherent to the

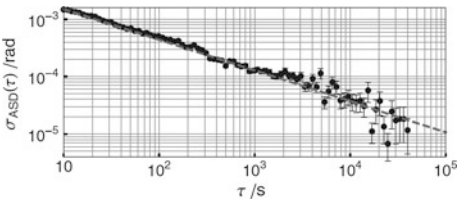

Fig. 10 Allan Standard Deviations (ASD) of the residual phase noise of a single run (^{3}He/^{129}Xe co-magnetometry at $B_0 \approx 0.4$ μT with low-T_c dc-SQUID readout). The total observation time was $T = 90{,}000$ s. With increasing integration times τ the uncertainty in phase decreases as $\propto \tau^{-1/2}$ indicating the presence of white phase noise. Deterministic phase drifts with well defined time-structure have been subtracted from the weighted frequency/phase difference, see text

magnetometer. The behavior of the phase uncertainty in the ASD plot is shown in Fig. 10. Indeed, the observed phase fluctuations decrease as $\propto \tau^{-1/2}$ indicating the presence of white phase noise. After one day (T_d) of coherent spin precession, the uncertainty in the weighted phase difference is $\sigma_{\Delta\Phi_c} \approx 10$ μrad, typically. That corresponds to an uncertainty in the measured frequency of $\sigma_f = \sigma_{\Delta\Phi_c}/(2\pi \cdot T_d) \approx 18$ pHz. These runs have been performed in a $B_0 \approx 0.4$ μT field using low-Tc dc-SQUID gradiometer as readout of the precessing ^{3}He and ^{129}Xe spins. On a closer inspection, the effect of Earth's rotation (i.e., the rotation of the SQUID detectors—and for the other readout devices as well—with respect to the precessing spins) is not compensated by comagnetometry as well as frequency shifts due to the Ramsey-Bloch-Siegert (RBS) shift, i.e., self-shift (ss) and cross-talk (ct) [64]. Thus, the residual phase noise shown in Fig. 10 has been obtained after subtraction of these deterministic phase drifts which have a well defined time structure [42, 64]. For the operation of the He-3 magnetometer, only the rotation of the SQUID detector (Δf_{rot}) with respect to the precessing spins ($f_{L,He}$) and the self-shift $\Delta f^{ss}_{RBS}(t)$, i.e., the coupling of the precessing magnetic moments of the same spin species, have to be considered. The Earth's rotation results in a constant frequency shift given by $\Delta f_{rot} = f_{Earth} \cdot \cos\Theta \cdot \cos\rho$ with $f_{Earth} = 1.16057614(2) \times 10^{-5}$ Hz = $1.16057614(2) \times 10^{-5}$ Hz, the latitude Θ, and the angle ρ between north-south direction and magnetic guiding field. Δf_{rot} is known and the magnetometer readings can be corrected for.

Concerning the RBS self shift we have $f_L \approx f_D$ and thus $\Delta f \ll (\gamma_{He}/2\pi) \cdot B_1$ (see Eq. 21). So the shift $\Delta f^{ss}_{RBS}(t)$ peaks at a value $\delta f^{ss}_{RBS}(t) \propto \gamma_{He} \cdot B_1(t) \propto \exp\left(-t(T^*_{2,He}\right)$ which is proportional to the signal amplitude. The proportionality factor (X_{He}) depends on the shape of the sample cell, the actual field gradients across the cell as well as on the gas pressure and may vary within the range $|X_{He}| \leq 3 \times 10^{-6}$ Hz [42]. As a result we get a systematic error in the absolute frequency measurement of $\left\langle \delta f^{ss}_{RBS}(t) \right\rangle_T < \left(T^*_{2,He} \cdot X_{He}/T\right) \cdot \left(1 - \exp\left(-T/T^*_{2,He}\right)\right)$.

6 Conclusion

The He-3 nuclear magnetometer based on free spin precession can be used for ultra-sensitive measurements and monitoring of magnetic fields ranging from nT < B_0 < 10 T. Its range of application can be extended to cryogenic temperatures, e.g., inside the cold bore tube of a Penning trap magnet. Almost all other substances are solid at these temperatures in which the dipolar interaction between the nuclear spins leads to a dramatic decrease of $T_2^*(<1\,\mathrm{ms})$. The technique of metastabilty optical pumping allows in situ OP both at low and high magnetic fields as well as over the entire temperature range 4 K < T < 300 K of interest. The field of application ranges from fundamental physics to applied research and practical applications like shimming preceduces for permanent and superconducting magnets [65] or gradient monitoring [42, 66]. In the following some peculiarities of the He-3 magnetometer are listed that are considered worth mentioning:

6.1 Fast Response

Besides precise field monitoring, the long time span ($\approx t_2^*$) can be used for feedback control to stabilize a magnetic field. For precise control of magnetic fields, the present state of the art at least at high magnetic fields goes back to the scanning of the resonance curve of the stationary spin resonance signal, e.g., of hydrogen with a variable excitation frequency. High accuracy requires correspondingly small line widths of the resonance. So a long T_2^* is desirable here, too. On the other hand, the stationary resonant amplitude is responsive to a change in the excitation frequency with a settling time of T_2^*. Consequently, this feedback control method is slower, the higher accuracy one aims for. The phase-locked coupling of the free precession signal at a standard frequency, however, avoids this disadvantage. In this respect we have a similar situation as in the M_x-magnetometers which preferably operate at low magnetic fields and where the phase of the oscillating transverse component of the magnetic moment is detected.

6.2 Miniaturization

The free spin precession He-3 nuclear magnetometer can be further miniaturized. That is obviously at high magnetic fields with NMR detection since the size of the magnetometer is essentially given by the size of the spherical sample cell (R). According to Eq. 8, the sensitivity scales $\propto SNR \times \left(T_2^*\right)^{3/2}$. To first order the drop

in *SNR* in going to smaller sample sizes scales like $SNR \sim R^2$ (Eq. 10 of Ref. [45]) and can be compensated by higher gas pressures and/or the use of detection coils with improved filling factors. With the measured SNR_0 of $SNR_0 = 1800$ ($f_{BW} = 1$ Hz) in a sample cell of $R_0 = 1$ cm filled with ^{3}He of $p_0 \sim 1$ mbar (see Fig. 8), we deduce an actual field gradient $\left|\vec{\nabla}B_z\right|_0$ across the cell of $\left|\vec{\nabla}B_z\right|_0 \approx 1.5 \times 10^{-7}$ T/cm using Eq. 5 and taking the measured value of the transverse relaxation time of $T^*_{2,0} = 70$ s. Finally, by demanding the same measurement sensitivity, i.e., $SNR \times \left(T^*_2\right)^{3/2} = SNR_0 \times \left(T^*_{2,0}\right)^{3/2}$, this results in a simple scaling law for (R/R_0) given by $R/R_0 = \left(\sqrt{(p/p_0)}/(R_G)^3\right)^{1/4}$ which is shown in Fig. 11 as a function of $R_G = \left|\vec{\nabla}B_z\right| / \left|\vec{\nabla}B_z\right|_0$ together with the corresponding functional dependences of the ratios SNR/SNR_0 and $(T^*_2)/(T^*_2)_0$, respectively. The ^{3}He pressure taken in this example is $p_{He} = 100$ mbar. As a result: miniaturizing does not strongly affect the performance of the He-3 nuclear magnetometer. For $R \approx 0.5$ mm we still expect an *SNR* of $\sim$200 and a transverse relaxation time of $T^*_2 \sim 200$ s; and the demand on the absolute field gradient is more relaxed with $\left|\vec{\nabla}B_z\right| \approx 5 \times 10^{-6}$ T/cm.

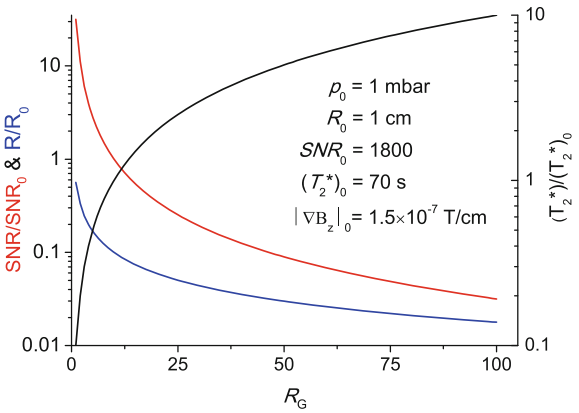

Fig. 11 Performance of a nuclear He-3 magnetometer upon miniaturization (sample size *R*). Plot of the ratios SNR/SNR_0, R/R_0, and $(T^*_2)/(T^*_2)_0$ as a function of $R_G = \left|\vec{\nabla}B_z\right| / \left|\vec{\nabla}B_z\right|_0$. The graphs are based on the assumption $SNR \times \left(T^*_2\right)^{3/2} = SNR_0 \times \left(T^*_{2,0}\right)^{3/2}$, i.e., same measurement sensitivity (Eq. 8). As ^{3}He pressure $p_{He} = 100$ mbar was used

6.3 Absolute Field Measurements

Many experiments in metrology, atomic, nuclear and particle physics, e.g., the muon g-2 experiment [67], require an accurate determination of the spin precession frequency f_p of a free-proton in a magnetic flux density B_0

$$f_p = \left(\frac{\gamma_p'}{2\pi}\right) \cdot B_0 \tag{25}$$

where γ_p' is the free-proton gyromagnetic ratio. The conversion to flux density is then made by using a recommended value for the gyromagnetic ratio of the proton in water referred to a standard temperature of 25°. The usefulness of gaseous ^{3}He as an alternative to water for the measurement of the absolute magnetic flux density by NMR has been discussed already by Flowers et al. [22]. In their paper they suggest that it would be better to attempt a high precision determination of $\mu_h(^3\text{He})/\mu_B$ to provide the universal reference and to use ^{3}He as the primary means of disseminating the tesla. $\mu_h(^3\text{He})$ is the magnetic moment of the ^{3}He nucleus (helion) in ^{3}He. Particular attention has to be paid to the fabrication of a standard cell whose shape is accurately spherical. For small departures from exact sphericity with change δr in the radius r, they find by numerical integration that the fractional shift is approximately linear, with the greatest slope given by

$$\left|\frac{\delta B}{B_0}\right| = 2,4 \times 10^{-7} \cdot \frac{\delta r}{r} \tag{26}$$

With our spherical quartz cells of $\delta r/r < 10^{-4}$ (see Fig. 6), the shift δB is less than 1 part in 10^{-10}.

The direct vicinity of the NMR circuit board or other objects increases the magnetic field inhomogeneity in the coil/sample system and its local surroundings due to a susceptibility mismatch that, according to Eq. 6, may considerably shorten the T_2^*. Therefore, magnetic susceptibility related field inhomogeneities have to be eliminated, too, by taking zero-susceptibility matched matter samples ($\chi_{mag} \approx 0$ ppm) as it is common practice in high resolution NMR spectroscopy [68].

6.4 Large Size Magnetometer Vessels

In the examples given we restricted ourselves on spherical sample cells of sizes $R < 5$ cm. However, the size and the shape of the magnetometer vessels are not a mandatory requirement in particular for low field magnetometry. For example, two flat cylindrical magnetometer vessels ($\Phi \approx 50$ cm, height 5 cm) are used in the neutron electric dipole moment (nEDM) experiment at PSI [69, 70] to cover the entire magnetic flux across the nEDM spectrometer (sandwich type of

arrangement). As readout CsOPM gradiometers are used which are positioned at the edges of each vessel where the highest sensitivity to monitor the ^{3}He nuclear spin precession is reached. A detailed description is given in [69]. It should be noted that T_2^*-times of up to 45 min have been obtained in such big container vessels thanks to the low magnetic field gradients ($\sim$30 pT/cm) of the applied weak uniform magnetic field inside a multi-layer μ-metal shielded room.

References

1. F. Bitter, Phys. Rev. **76**, 833 (1949)
2. A. Kastler, J. Phys. Radium **11**, 255 (1950)
3. A. Kastler, J. Opt. Soc. Am. **47**, 460 (1957)
4. H.G. Demelt, PR **105**, 1924 (1957)
5. W.E. Bell, A.L. Bloom, PR **107**, 1559 (1957)
6. E.B. Alexandrov, A.K. Vershovskii, Mx and Mz magnetometers (chapter 4, 60–84), in *Optical Magnetometry*, eds. D. Budker, D.F. Jackson Kimball (Cambridge University Press, Cambridge, 2013)
7. D.F. Jackson Kimball, S. Pustelny, V.V. Yashchuk, D. Budker, Optical magnetometry with modulated light (chapter 6, 104–125), in *Optical Magnetometry*, eds. D. Budker, D.F. Jackson Kimball (Cambridge University Press, Cambridge, 2013)
8. J. Brossel, A. Kastler, Compt. Rend. Acad. Sci. **229**, 1213 (1949)
9. F.D. Colegrove, P.A. Franken, Phys. Rev. **119**, 680 (1960)
10. A.R. Keyser, J.A. Rice, L.D. Schearer, J. Geophys. Res. **66**, 4163 (1961)
11. B. Chéron, H. Gilles, J. Hamel, O. Moreau, E. Noël, Opt. Commun. **115**, 71 (1995)
12. H. Gilles, J. Hamel, B. Chéron, Rev. Sci. Instrum. **72**, 2253 (2001)
13. R.E. Slocum, E.J. Smith, Contrib. Geophys. Geodesy **31**, 99 (2001)
14. R.E. Slocum, G. Kuhlman, L. Ryan, D. King, in OCEANS'02 MTS/IEEE, eds. by H.W. Anderson, T.W. Donaldson, Vol. 2, (IEEE Press, Biloxi, MS, 2002), p. 945
15. R.E. Slocum, D.D. McGregor, Measurement of the geomagnetic field using parametric resonance in optically pumped He4. IEEE Trans. Mag., MAG **10**, 532–535 (1974)
16. G.K. Walters, F.D. Colegrove, L.D. Schearer, Phys. Rev. Lett. **8**, 439 (1962)
17. F.D. Colegrove, L.D. Schearer, G.K. Walters, Phys. Rev. **132**, 2561 (1963)
18. L.D. Schearer, F.D. Colegrove, G.K. Walters, Rev. Sci. Instr. **34**, 1363 (1963)
19. L.D. Schearer, Phys. Rev. **127**, 512 (1962)
20. P.J. Mohr, B.N. Taylor, D.B. Newell. Codata recommended values of the fundamental physical constants (2014)
21. D.D. McGregor, Rev. Sci. Instr. **58**, 1067 (1987)
22. J.L. Flowers, B.W. Petley, M.G. Richards, Metrologia **30**, 75 (1993)
23. C. Cohen-Tannoudji, J. DuPont-Roc, S. Haroche, F. Laloë, Phys. Rev. Lett. **22**, 758 (1969)
24. J. Dupont-Roc, S. Haroche, C. Cohen-Tannoudji, Phys. Lett. **28A**, 638 (1969)
25. R.E. Slocum, B.I. Marton, IEEE Trans. Magn. **10**, 528 (1974)
26. N. Bloembergen, R.V. Pound, Phys. Rev. **95**, 8 (1954)
27. O. Moreau, B. Charon, H. Gilles, J. Hamel, E. Noël, J. Phys. III France **7**, 99 (1997)
28. P.J. Nacher, M. Leduc, J. de Physique **46**, 2057–2073 (1985)
29. R. Mueller, Physica B **297**, 277–281 (2001)
30. T. Gentile, M. Hayden, M. Barlow, J. Opt. Soc. Am. B **20**, 2068–2074 (2003)
31. G. Tastevin, S. Grot, E. Courtade, S. Bordais, P.J. Nacher, Appl. Phys. B: Lasers Optics **78**, 145–156 (2004)

32. P.J. Nacher, E. Courtade, M. Abboud, A. Sinatra, G. Tastevin, T. Dohnalik, Acta Phys. Pol., B **33**, 2225–2236 (2002)
33. A. Nikiel-Osuchowska, G. Collier, B. Głowacz, T. Pałasz, Z. Olejniczak, W.P. Węglarz, G. Tastevin, P.J. Nacher, T. Dohnalik, Eur. Phys. J. D **67**, 200 (2013)
34. E. Courtade, F. Marion, P.J. Nacher, G. Tastevin, K. Kiersnowski, T. Dohnalik, Eur. Phys. J. D **21**, 25–55 (2002)
35. L.D. Schearer, Phys. Rev. **160**, 76–80 (1967)
36. D. Vrinceanu, S. Kotochigova, H.R. Sadeghpour, Phys. Rev. A **69**, 022714 (2004)
37. T.R. Gentile, R.D. McKeown, Phys. Rev. A **47**, 456 (1993)
38. F.D. Colegrove, L.D. Schearer, G.K. Walters, Phys. Rev. **135**, A353 (1964)
39. W.A. Fitzsimmons, N.F. Lane, G.K. Walters, Phys. Rev. **174**, 193 (1968)
40. R. Barbé, F. Laloë, J. Brossel, Phys. Rev. Lett. **34**, 1488 (1975)
41. M. Himbert, V. Lefevre-Seguin, P.J. Nacher, J. Dupont-Roc, M. Leduc, F. Laloë, J. Phys. Lett. **44**, 523 (1983)
42. C. Gemmel, W. Heil, S. Karpuk, K. Lenz, C. Ludwig, Y. Sobolev, K. Tullney, M. Burghoff, W. Kilian, S. Knappe-Grüneberg, W. Müller, A. Schnabel, F. Seifert, L. Trahms, S. Baeßler, Eur. Phys. J. D **57**, 303–320 (2010)
43. H.-C. Koch, G. Bison, Z.D. Grujić, W. Heil, M. Kasprzak, P. Knowles, A. Kraft, A. Pazgalev, A. Schnabel, J. Voigt, A. Weis, arXiv: 1502.06366v1 (2015)
44. A. Abragam, *The Principles of Nuclear Magnetism* (Clarendon Press, Oxford, 1961), pp. 82–83
45. D.I. Hoult, R.E. Richards, J. Magn. Reson. **24**, 71–85 (1976)
46. A. Nikiel, P. Blümler, W. Heil, M. Hehn, S. Karpuk, A. Maul, E. Otten, L.M. Schreiber, M. Terekhov, Eur. Phys. J. D **68**, 330 (2014)
47. G.D. Cates, S.R. Schaefer, W. Happer, Phys. Rev. A **37**, 2877 (1988)
48. D.D. McGregor, Phys. Rev. A **41**, 2631 (1990)
49. R. Barbé, M. Leduc, F. Laloë, J. Phys. France **35**, 935 (1974)
50. D.R. Rich, T.R. Gentile, T.B. Smith, A.K. Thompson, G.L. Jones, Appl. Phys. Lett. **80**, 2210 (2002)
51. J. Schmiedeskamp, W. Heil, E.W. Otten, R.K. Kremer, A. Simon, J. Zimmer, Part I., Eur. Phys. J. D **38**, 427–438 (2006)
52. A. Deninger, W. Heil, E.W. Otten, M. Wolf, R.K. Kremer, A. Simon, Part II, Eur. Phys. J. D **38**, 439–443 (2006)
53. J. Schmiedeskamp, H.-J. Elmers, W. Heil, E.W. Otten, Y. Sobolev, W. Kilian, H. Rinneberg, T. Sander-Thömmes, F. Seifert, J. Zimmer, Part III., Eur. Phys. J. D **38**, 445–454 (2006)
54. S.M. Kay, *Fundamentals of Statistical Signal Processing: Estimation Theory* (Prentice Hall PTR, Upper Saddle River, 1993)
55. J.A. Barnes et al., IEEE Trans. Instrum. Meas. **20**, 105 (1971)
56. F. Bloch, A. Siegert, Phys. Rev. **57**, 522 (1940)
57. N.F. Ramsey, Phys. Rev. **100**, 1191 (1955)
58. J. Clarke, W.M. Goubau, M.B. Ketchen, J. Low Temp. Phys. **25**, 99 (1976)
59. D. Drung, Supercond. Sci. Technol. **16**, 1320–1336 (2003)
60. M. Burghoff, H. Schleyerbach, D. Drung, L. Trahms, H. Koch, IEEE Trans. Appl. Superconductivity **9**, 4069–4072 (1999)
61. M. Guéron, Magn. Reson. Med. **19**, 31 (1991)
62. M. Pfeffer, O. Lutz, J. Magn. Res. A **108**, 106 (2005)
63. International Council for Science: Committee on Data for Science and Technology (CODATA). www.codata.org. (2007)
64. F. Allmendinger, W. Heil, S. Karpuk, W. Kilian, A. Scharth, U. Schmidt, A. Schnabel, Y. Sobolev, K. Tullney, PRL **112**, 110801 (2014)
65. L.F. Fuks, F.S.C. Huang, C.M. Carter, W.A. Edelstein, B.P. Roemer, J. Magn. Reson. **100**, 229 (1992)
66. C. Barmet, N. de Zanche, B.J. Wilm, K.P. Pruessmann, Magn. Reson. Med. **62**, 269 (2009)
67. G.W. Bennett et al., Phys. Rev. D **73**, 072003 (2006)

68. R. Kc, Y.N. Gowda, D. Djukovic, I.D. Henry, G.H.J. Park, D. Raftery, J. Magn. Reson. **205**, 63 (2010)
69. A. Kraft, H-Ch. Koch, M. Daum, W. Heil, Th Lauer, D. Neumann, A. Pazgalev, Yu. Sobolev, A. Weis, EPJ Tech. Instrum. **1**, 8 (2014)
70. http://supernovae.in2p3.fr/users/jacdz/csin2p3–20131024/report_CSIN2P3_n2EDM.pdf

Microfabricated Optically-Pumped Magnetometers

Ricardo Jiménez-Martínez and Svenja Knappe

Abstract Optical magnetometers (OPMs), implemented by optical interrogation of alkali-atoms contained in a vapor cell, are among the most sensitive detectors for magnetic fields. Due to the fact that weak magnetic fields are ubiquitous in our world, high-sensitive magnetometers are demanded in a wide range of scientific and practical applications. Here we review some of the highly miniaturized OPMs recently developed using silicon microfabrication techniques. This approach opens a number of attractive advantages, besides further miniaturization, such as integration of different sensing technologies within the same silicon platform and cost-efficient manufacturing of a large number of sensors with tight tolerances at potentially low cost.

1 Introduction

Optical magnetometers (OPMs), implemented by optical interrogation of alkali-atoms contained in a vapor cell, are among the most sensitive detectors for magnetic fields [1–3]. Due to the fact that weak magnetic fields are ubiquitous in our world, high-sensitive magnetometers are demanded in a wide range of scientific and practical applications. In addition to sensitivity, the impact of magnetometers in applications outside a laboratory environment is determined by other sensor characteristics such as size, weight, power, and cost. In this regard, the highly miniaturized optical magnetometers developed during the last decade using silicon microfabrica-

R. Jiménez-Martínez
ICFO-Institut de Ciencies Fotoniques, The Barcelona Institute of Science and Technology, 08860 Castelldefels, Barcelona, Spain
e-mail: ricardo.jimenez@icfo.es

S. Knappe (✉)
Time and Frequency Division, National Institute of Standards and Technology, 325 Broadway, Boulder, CO 80305, USA
e-mail: knappe@nist.gov

S. Knappe
University of Colorado, Boulder, CO 80309, USA

A. Grosz et al. (eds.), *High Sensitivity Magnetometers*, Smart Sensors, Measurement and Instrumentation 19, DOI 10.1007/978-3-319-34070-8_17

tion techniques are very attractive. These microfabricated optically-pumped magnetometers (μOPMs) have been implemented with physics package volumes of 0.01 to 1 cm^3, masses of a few grams, and power consumption of less than 200 mW, while still capable of detecting biomagnetic signals [4–6]. Small and highly sensitive OPMs have been developed using standard fabrication techniques, and outstanding progress has been achieved in detecting faint fields, such as those produced by the human body [7–14]. At the same time micromachining of silicon and glass opens a number of attractive advantages, besides further miniaturization, such as integration of different physical sensing technologies within the same silicon platform and cost-efficient manufacturing of a large number of sensors with tight tolerances at potentially low cost. The small size and low power of μOPMs paired with high sensitivity makes them appealing for many resource-constrained applications, such as deployment in small satellites [15] and spacecrafts [16], magnetic anomaly detection (MAD), magnetic resonance imaging (MRI) and nuclear magnetic resonance (NMR) in medicine, biology, and quality control [17, 18], nondestructive testing (NDT) for manufacturing [19], and non-invasive biomagnetic imaging of the brain [20]; in the future, μOPMs could find use in wearable devices for health-care diagnosis [21].

1.1 Principle of Operation

Optical magnetometers are a type of spin-based device that uses optical interrogation of atomic spins to detect magnetic fields in their environment. The working principle can be understood as evolving in three steps (see Fig. 1). First, the atoms

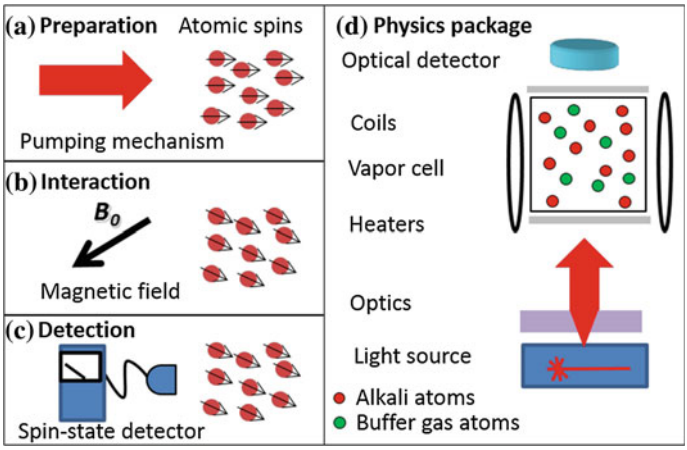

Fig. 1 Spin-based magnetometers work in three steps: spin preparation, spin interaction, and spin detection. **a** Spin preparation is achieved by transferring angular momentum to the spins. **b** In the presence of an external magnetic field the spins precess about the field at a rate proportional to the field magnitude. **c** Detection of the evolution of the spin makes an indirect measurement of the magnetic field. **d** In optical magnetometers, resonant light is used to spin polarize alkali atoms contained in a vapor cell. Spin precession in a magnetic field changes the refractive index of the atomic ensemble, which is detected by monitoring either the absorption or polarization of the transmitted light

are prepared in a well-defined spin state through their interaction with a reservoir of angular momentum. As a result, the atoms become spin polarized. In the second step, the spins interact with magnetic fields in their environment, causing their precession at the Larmor frequency $\omega = \gamma B$, proportional to the absolute value of the field B. In the third step, the state of the spin ensemble is detected. From the measured precession angle and the known gyromagnetic ratio γ of the atoms, the strength of the magnetic field, or one of its components, is estimated.

The devices described here use the spin orientation of ground state alkali atoms in the vapor phase, such as rubidium (Rb), cesium (Cs), and potassium (K). The polarization and detection of the spins are implemented by optical pumping [22]. Through this mechanism resonant or near-resonant light transfers angular momentum to the atoms, resulting in the orientation of their spin. In turn, the atoms can alter the amplitude, phase, or polarization of the light field, which enables readout of the spins (see Fig. 1).

1.2 Chapter Outline

Due to their small volume, μOPMs are fundamentally less sensitive compared to larger OPMs. Section 2 discusses how fundamental sensitivity and power consumption scale with cell size. Section 3 presents the components in the physics package of μOPMs, i.e., light source, vapor cell, heaters, and optical detectors. Section 3 also includes recent work addressing some of the unique challenges in these miniaturized sensors. Different implementations of μOPMs, in both scalar and low-field modes are described in Sect. 4, including the implementation of fiber-coupled OPMs. Section 5 briefly presents multichannel systems. While most of the magnetometers described in this chapter are based on the spin-orientation of alkali atoms, similar devices can be implemented utilizing higher-order atomic-polarization moments, such as spin alignments, using the electronic spin of metastable He-4 atoms, or the spin-orientation of nuclear spins, for example, in xenon gas. Recent work in such magnetometers using microfabricated components is presented in Sect. 6. Finally, in Sect. 7 we present an outlook for future work in this technology.

2 Size-Scaling in OPMs

To explore the possibilities of miniaturized magnetometers, the sensitivity and heating power of an optimized magnetometer was calculated as a function of cell size in Ref. [23]. For a cell of volume l^3 the buffer gas pressure, determined by minimizing spin-relaxation caused by wall and buffer-gas collisions, was optimized. The fundamental sensitivity determined by spin-projection noise, assuming that the

alkali density is optimized so that the spin-relaxation mechanism is dominated by alkali-alkali collisions, is given by

$$\delta B \approx \frac{1}{\gamma}\sqrt{\frac{\bar{v}\sigma_{\mathrm{se/sd}}}{l^3\tau}} \tag{1}$$

where γ is the gyromagnetic ratio of the atoms, $\bar{v}$ corresponds to their mean relative thermal velocity, τ is the measurement time, and $\sigma_{\mathrm{se/sd}}$ is the spin-relaxation cross-section due to spin-exchange or spin-destruction collisions, depending on the dominating decoherence mechanism. Figure 2 reproduces the estimated spin-projection sensitivity given by Eq. (1) for a ^{87}Rb magnetometer, assuming $\bar{v} = 400\,\mathrm{m/s}$, $\sigma_{\mathrm{se}} = 2 \times 10^{-14}\,\mathrm{cm}^2$, and $\sigma_{\mathrm{sd}} = 1.6 \times 10^{-17}\,\mathrm{cm}^2$. As in Ref. [23] we assume no nuclear slow-down of the relaxation rate for simplicity. While Eq. (1) only assumes spin-projection noise, other sources of noise affect the sensitivity, such as photon shot noise and probe light-shift noise. More general analyses considering these noise sources for scalar, radio-frequency (RF), and spin-exchange relaxation-free (SERF) magnetometers have been described in Refs. [24–26], respectively. The authors of these works find that the sensitivities for these three types of magnetometers degrade with smaller sizes as the square root of the cell volume as well.

Figure 2 shows the measured sensitivities, i.e., the noise equivalent magnetic field, of several types of dc magnetometers at frequencies between 10 and 100 Hz as a function of their characteristic size. Here, for "volume" magnetometers of probing volume V, "Characteristic Size" was calculated as $V^{1/3}$, while for "surface" magnetometers of probing surface S as $\sqrt{S}$. Hollow symbols represent sensors that require cryogenics. As a guide to the eye, lines are included that correspond to energy resolutions per unit bandwidth of 1 $\hbar$, 10^3 $\hbar$, and 10^6 $\hbar$. Here, the magnetic field energy resolution is defined as $V\,(\delta B)^2/2\mu_0$, where δB is the noise-equivalent magnetic field, and μ_0 is the magnetic permeability. It can clearly be seen from Fig. 2 that superconducting-quantum interference devices (SQUIDs) and atomic magnetometers have reached sensitivities below 10 fT/Hz$^{1/2}$ with sizes around 1 cm. But there are other sensing technologies such as giant magnetoresistance (GMR) and nitrogen vacancy centers (NVs) that can reach sensitivities in the low picoTeslas.

For many applications, besides sensitivity, power consumption is equally important. The main driver of power consumption is the operating temperature of the cell. Following the analysis of Ref. [23], the temperatures required to reach the optimum alkali density for the spin-projection noise sensitivity, as discussed above, of a ^{87}Rb magnetometer are computed in Fig. 3a. Vapor pressures were taken from Ref. [27] and nitrogen was used as a buffer gas. The power needed to heat the vapor cell to the given temperatures in an ambient temperature of 0 °C is shown in Fig. 3b, assuming the heat losses are dominated by radiation and cell-surfaces have an emissivity of 1. These estimates predict an optimum operating temperature for a ^{87}Rb magnetometer implemented in a 1 mm^3 cell of roughly 70 °C for a spin-exchange limited and 200 °C for a spin-destruction limited magnetometer,

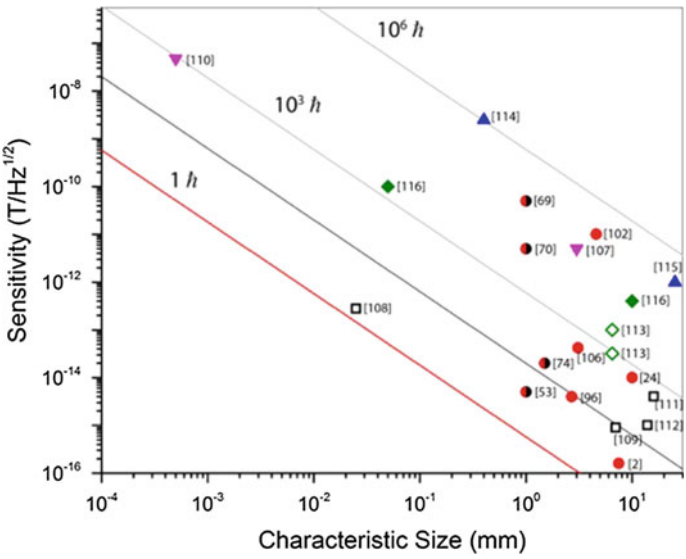

Fig. 2 Sensitivities, i.e., noise equivalent magnetic fields, of dc magnetometers between 10 and 100 Hz as a function of characteristic size. The data points correspond to SQUIDs (*white squares* [108, 109, 111, 112]), alkali OPMs (*red circles* [2, 24, 53, 69, 70, 74, 96, 102, 106]), magnetoresistive and mixed sensors (*green diamonds* [113, 116]), NVs (*pink downwards triangles* [107, 110]), and multiferroic sensors (*blue upwards triangles* [114, 115]). The *hollow symbols* indicate cryogenically-cooled sensors. μOPMs are indicated by *circles* in *red* and *black* [53, 69, 70, 74]. The *red line* represents the spin-projection noise limit of a Rb magnetometer with spin relaxation dominated by spin-destruction collisions, which is very close to an energy resolution of $\hbar$, and the *black line* represents the spin-exchange limited magnetometer sensitivity. The assumptions are very similar to those in Ref. [23]

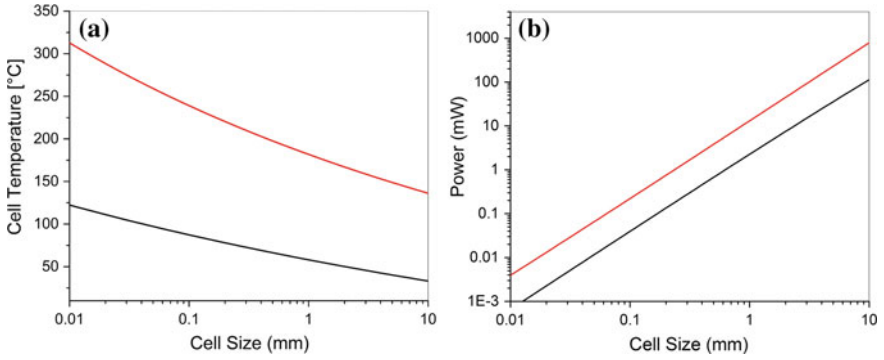

Fig. 3 **a** Cell temperature for an optimized ^{87}Rb magnetometer in the spin-exchange (*black*) and spin-destruction limited regime (*red*), based on the size-scale analysis presented in Ref. [23]. **b** Power required to heat a ^{87}Rb cell to its optimum operating temperature shown in (**a**) assuming the cell as a blackbody radiating in ambient temperature of 0 °C

with corresponding heating power of 1 and 10 mW, respectively. Clearly, miniaturization enables low-power operation.

As described above in our analysis the optimum alkali density corresponds to the density at which spin-relaxation due to alkali-alkali collisions is equal to the intrinsic spin-relaxation of the cell due to wall and buffer-gas collisions, which increases with decreasing cell size. The estimated numbers change slightly, when nuclear slow-down, optical broadening, and practical issues are considered. Spin-projection noise sensitivities are achieved only, when spin-projection noise is observable, which requires on-resonance optical depths larger than one [28]. Likewise, when light transmission is monitored in a single-beam scalar magnetometer, for example, the best performance is reached, when roughly half the light is absorbed.

3 Sensor Design

The general system components of μOPMs are similar to those of their larger counterparts, which are thoroughly described in previous chapters. Scalar and RF magnetometers contain a local oscillator (LO), a physics package, and control electronics. While for Earth-field magnetometers the LO is used to generate the RF signal driving spin precession on resonance at the Larmor frequency, for low-field magnetometers it is used to modulate a parameter in the device without driving spin precession. The physics package contains the spectroscopy, i.e., light source, optics, vapor cell, and optical detectors. The control electronics tune the LO frequency and stabilize and operate LO and physics package. One or multiple lasers can be part of either the physics package or the control electronics.

In the implementation of most microfabricated physics packages, simplicity is favored. For instance, designs comprising fewer components and those that are less prone to optical misalignments are preferred, even if sensitivity is slightly compromised. Physics package designs that use only one laser beam to pump and interrogate the atomic spins simultaneously are preferred, followed by designs that have collinear pump and probe laser beams. In the integration of all components that go into the physics package, two general design directions have been taken: a fully-integrated physics package design and a sensor head interrogated with a remote laser design, where sensor and laser are coupled either through free space [29] or through optical fibers [30]. In this section we describe the separate components of a microfabricated physics package in detail.

3.1 Light Sources

Light, resonant or near-resonant with one of the D-line transitions of the atoms, is used for pumping and probing. Due to their characteristics, e.g., simplicity, single

mode operation, and tunability, monolithic diode lasers such as vertical-cavity surface-emitting lasers (VCSELs), distributed Bragg reflector lasers (DBR), and distributed feedback laser (DFB) are favored for optical pumping in compact and portable devices and have been used in μOPMs. VCSELs have been employed in a number of fully-integrated physics packages. When power consumption has not constrained the designs, DBR and DFB lasers, as well as extended-cavity diode lasers, have been used. They provide narrower linewidths than VCSELs (<1 MHz), and much larger output powers of more than 100 mW, allowing operation of larger arrays of sensors with a single laser [8].

In all-optical magnetometers, such as Bell-Bloom [31], frequency-modulated non-linear magneto-optical rotation (FM-NMOR) [32], or coherent population trapping (CPT) [33] magnetometers, the modulation bandwidth is important. In most cases, modulation sidebands at the Larmor frequency, a higher multiple of the Larmor frequency, or even at the hyperfine frequency are generated by direct modulation of the laser injection current. Some VCSELs and DFB lasers have provided modulation bandwidth of several gigahertz [34].

Diode lasers are precisely tunable by varying their temperature and injection current. Due to the sensitivity of the laser wavelength to variations in these parameters, precision control electronics are often required to keep the lasers on resonance with the atoms. For this purpose, external microfabricated frequency references can be used [35–37] or the laser wavelength can be stabilized to the atomic resonance in the measurement cell itself [35].

Due to the complexity and difficulty of precise control of diode laser parameters, simpler light sources are sometimes desirable. Alkali discharge lamps are attractive light sources with low intensity noise and modest control electronics. A microfabricated Rb discharge lamp has been demonstrated recently [38] (see Fig. 4). This discharge lamp emits a total optical power of 140 μW when coupling less than 20 mW RF power to the discharge cell, with up to 15 and 9 μW on the Rb D2 and D1 lines, respectively. The Rb lamp has been used as a pumping light source in an Mz μOPM [39]. Low-power operation will need to be demonstrated.

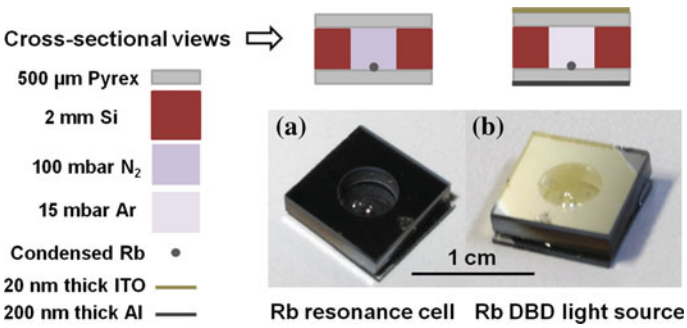

Fig. 4 Photographs of a MEMS cell **(a)** and a MEMS discharge lamp **(b)**, along with the cross-sectional views (*top*) and materials (*left*). (*Source* Ref. [39]; reproduced with permission from AIP)

Requirements for light source technology within the context of small and portable atomic sensors are presented in [40].

3.2 MEMS Vapor Cells

The vapor cell contains the alkali atoms used to detect magnetic fields in the environment. Besides being a hermetic container that does not react with the alkali atoms, the cell has to provide optical access for the interrogating light. It needs to withstand elevated temperatures and thermal cycles. A number of approaches have been implemented to fabricate millimeter-scale vapor cells meeting these requirements, such as those using hollow-core optical fibers [41]. Here, we focus on cells made with techniques used in microelectromechanical systems (MEMS), which is a very scalable approach that enables parallel wafer-level fabrication.

3.2.1 Vapor-Cell Fabrication

The fabrication of MEMS vapor cells typically consists of three steps as described in Fig. 5: the creation of the cell cavity, filling the cavity with alkalis, and the hermetic sealing of the cell. In the first step, cavities are created in a silicon wafer with standard bulk etching techniques, such as wet potassium hydroxide (KOH) etching or dry deep reactive ion etching (DRIE). In both of these methods, the lateral cell geometry is defined through photolithographic patterning. Cavities with lateral dimensions ranging from 300 μm to 5 mm have been etched in silicon wafers with thicknesses between 200 μm and 4.5 mm. Complex geometries with reservoirs and channels can be easily accommodated. In most cases, holes are etched all the way through the silicon wafers, and cell preforms are created by sealing one side of the hole with a glass window. Usually, the cavities are sealed by anodic bonding [42] of the silicon wafer to a glass wafer, although other bonding mechanisms could be used.

3.2.2 Alkali Activation

Alkali atoms can be released in microfabricated vapor cells using methods originally developed for chip-scale atomic clocks [44]. Although differing in their details, these techniques can be grouped into pre-sealing and post-sealing methods.

One pre-sealing method is based on the chemical reaction of barium azide and alkali chloride inside the cell [44, 45]. To keep the etched cavity clean from any residues, the reaction can also occur in an ampoule inside a vacuum chamber [44]. In this case the alkali vapor is then evaporated through a small nozzle of the ampoule into the etched silicon cavity. Then the vacuum chamber is filled with the desired amount and composition of buffer gases, which are used to mitigate wall

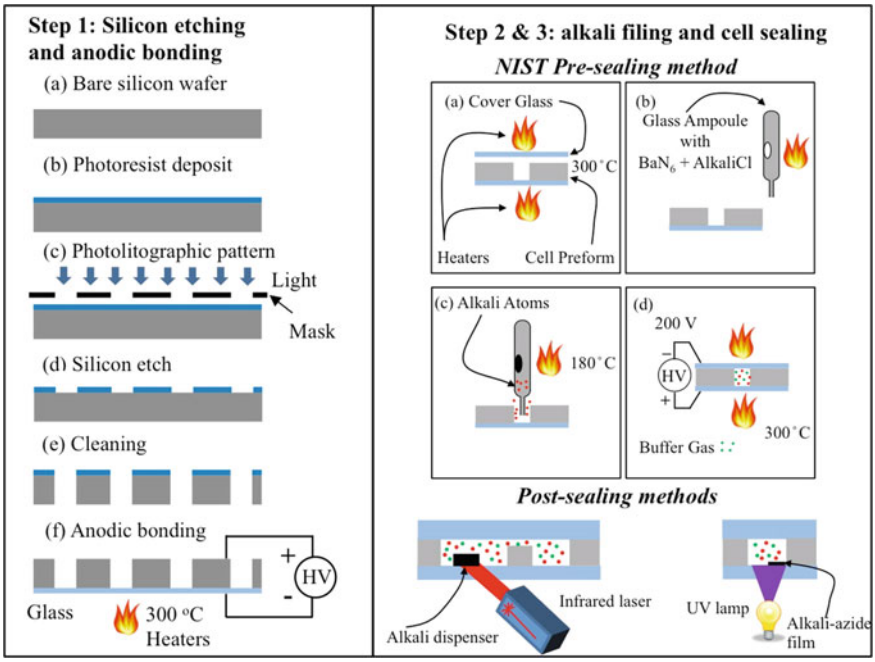

Fig. 5 The three steps of MEMS vapor cell fabrication. *Step 1* silicon etching with bulk etching techniques and anodic bonding of one glass window. *Step 2* alkali filling in a controlled environment. *Step 3* cell sealing

induced relaxation, and the chip is hermetically sealed by anodic bonding to a second glass chip. This method provides clean cells without residues and flexibility in the choice of the alkali atoms and isotope, as well as in the type and amount of buffer gas. However, at the moment, no results have been published that demonstrate parallel wafer-level fabrication of cells with this method.

Post-sealing methods [46, 47] are easier to implement in wafer-level fabrication. Here, alkali atoms are inserted into the cavity as a chemical compound, which is stable in air. The alkali atoms are then released after the cavity has been sealed. One such method is based on the deposition of a thin film of cesium azide (CsN_3) or rubidium azide (RbN_3) inside the cavity [47]. After sealing of the cavity, alkali vapor is produced by the decomposition of the alkali azide initiated by irradiating UV light onto the film or through heat. The nitrogen produced during the decomposition is used as buffer gas. Tight control of the amount of buffer gas has been demonstrated in a small array of cells [48]. Wafer-level cell fabrication has also been demonstrated with this technique using an automatic dispensing system, allowing the fabrication of hundreds of rubidium cells on a single 100 mm diameter wafer [49] (see Fig. 6).

Finally, commercially available alkali dispensers have been used in both pre-sealing [43] and post-sealing approaches [50, 51]. One advantage is that it allows for a simple fabrication process without buffer gas. Here, a small dispenser is

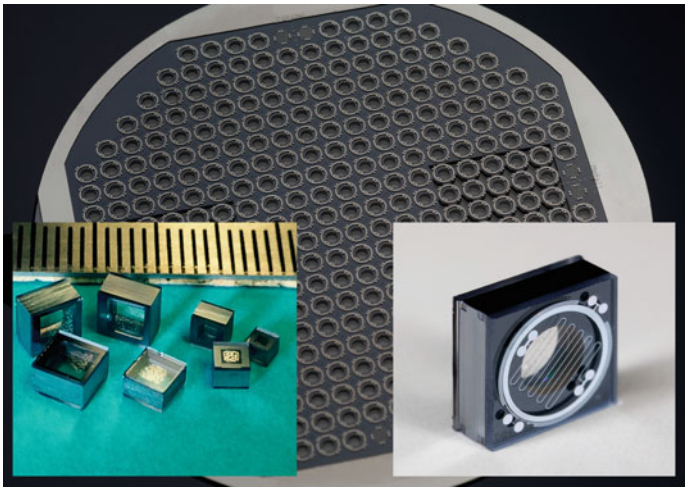

Fig. 6 Photographs of MEMS alkali vapor cells: pre-sealed cells at NIST (*left*) and post-sealed cells with alkali azide at CSEM (*right*). The background shows a photograph of a whole wafer of MEMS cells fabricated in parallel, similar to the one shown on the right. (*Source* (*background and bottom right*) CSEM SA, Switzerland, http://www.csem.ch; reproduced with permission from CSEM SA)

sealed into a cavity under vacuum and alkalis are released by heating the dispenser locally with a laser.

3.3 Advanced Cell Designs

The operation of atomic magnetometers with small vapor cells has some unique challenges that require designs and fabrication techniques more advanced than what has been described so far. Here we briefly describe some of these advanced designs.

Cells with reduced intrinsic magnetic field noise. One particular challenge is the mitigation of magnetic field noise produced by Johnson currents in conductive materials [52]. Due to the close proximity of the walls, noise arising from the silicon cell body can be of concern. The silicon body of a 1 mm^3 cell with a resistivity of 5 Ω cm produces magnetic field noise of 3 $fT/Hz^{1/2}$ at a distance of 1 mm [53]. Furthermore, Rb droplets of 100 μm diameter produce a magnetic field noise of 3 $fT/Hz^{1/2}$ at a distance of 0.5 mm. If the cell walls of a 1 mm^3 cubic cell were coated with a 1 nm thick film of Rb, a noise of 7 $fT/Hz^{1/2}$ would be expected [53]. Alkali droplets condense in the coldest region of the cell. To avoid their Johnson noise from limiting the magnetometer sensitivity, the condensation region should be as far as possible from the probed volume. One possibility, for example, is a cell with two chambers connected by a thin channel (see Fig. 7b). One chamber is kept at a lower temperature, where the alkali atoms condense, while the magnetic

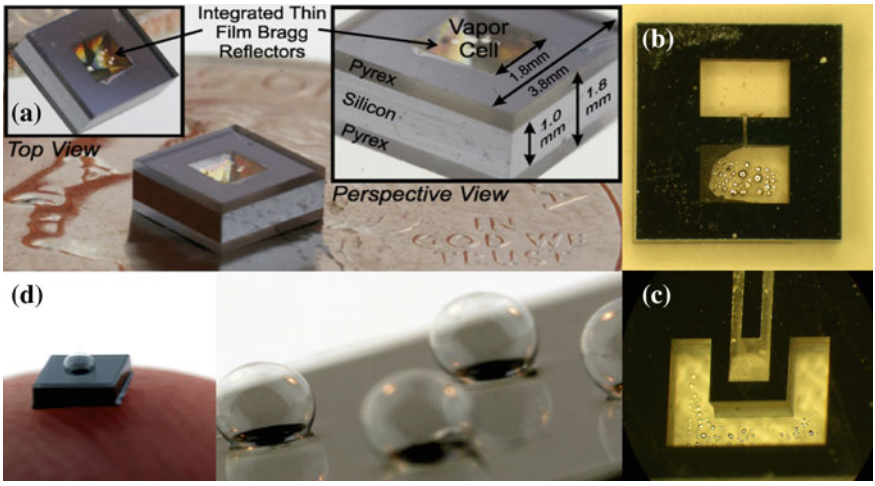

Fig. 7 Photographs of advanced cell designs: **a** cells with internal angles reflectors, **b** cells with reservoirs and **c** more complex shapes for multiple laser beams, and **d** MEMS glass-blown cells. (*Source* (*top*): Ref. [54]; reproduced with permission from Elsevier; (*bottom*): Ref. [56]; reproduced with permission from Elsevier)

field measurements are performed in the second chamber, where alkali droplets are absent. This design also minimizes alkali condensation on the cell window, allowing for unobstructed transmission of light through the cell.

Cells with increased optical access. In standard MEMS cells, optical access is often restricted to one axis by the small aperture of the windows and the use of silicon as sidewall material, which is not transparent to the light interrogating alkali atoms. Some interrogation schemes take advantage of using two non-collinear light beams [3]. While it is possible to rotate the MEMS cell by 45° with respect to the two orthogonal optical axes [23, 53], it does not lend itself to easy integration in the physics package. One cell design addressing this issue exploits the anisotropic etching rates experienced by different crystalline planes of silicon [54] to generate angled walls that reflect incident light to produce two beams crossing inside the vapor cell. KOH etching exposes the $\langle 111 \rangle$ crystalline plane of silicon at 54.7° with respect to the wafer surface and results in very smooth sidewalls. Coating the walls with non-metallic thin film reflectors can increase reflectivity as shown in Ref. [54], where an increase by a factor of three with respect to bare silicon (33 % reflectance at 795 nm) was reported, after depositing alternating layers of amorphous Si and SiO_2. Intrinsic angled reflectors have also been demonstrated with angles of 45° to the silicon surface, by wet etching the silicon wafer in a tetramethylammonium hydroxide (TMAH) solution with a surfactant added [55]. A different approach to improve optical access increases the surfaces of transparent material in the cell by use of spherical microcells fabricated by MEMS glass blowing [56], shown in Fig. 7. The cell is generated by anodic bonding of a Pyrex wafer to a silicon wafer with a cavity in air. When the wafer stack is heated above the softening temperature

of the glass, the air expands and a silicon bubble is formed. The spherical symmetry of these cells is also advantageous in other atomic sensors, such as NMR gyroscopes [57]. Finally, a recent study identifies gallium phosphide as a favorable material to replace silicon in anodically bonded vapor cells [58] since it is transparent to near-infrared light and can be bonded to glass at temperatures below 200 °C.

Low-temperature hermetic sealing of vapor cells. The elevated temperatures, around 300 °C, at which standard MEMS cells are hermetically sealed makes fabrication challenging and can limit the flexibility of the cell design. Thus, lower temperature sealing techniques are desirable. A number of low-temperature bonding techniques have recently been demonstrated [59, 60]. One technique is based on an interface bonding material consisting of lithium-niobate-phosphate glasses engineered to have an alkaline-ion conductivity at room temperature similar to that of borosilicate glass at 250 °C. As a result, it has been possible to perform room-temperature anodic bonding to silicon of thin layers (up to 1 mm thick) of lithium-niobate-phosphate glass, which are patterned onto a borosilicate or silicon wafer [59]. Using this approach, silicon cavities, filled with alkali vapor and nitrogen buffer gas, have been sealed at room temperature. Hermeticity tests show tight seals, measured by the evolution of buffer gas content in a period of months. These phosphate glasses have a coefficient of thermal expansion on the order of 12 ppm/K, which is higher than that of silicon (3 ppm/K). As a result, bonded structures may not withstand elevated temperatures, although cells have successfully operated at 80 °C [59]. Another low-temperature technique is based on thin-film indium thermo-compression bonding and has demonstrated sealing temperatures below 140 °C [60] in microfabricated cells. In this indium-based bonding method, a metallic adhesion layer is used. The extent to which this conductive trace affects the magnetic sensitivity has not been studied yet.

Cells with antirelaxation coating. Antirelaxation coatings represent an attractive alternative to buffer gases for mitigating spin-relaxation caused by wall collisions in miniature cells. In large cells, the most efficient coatings are alkenes and alkanes, allowing more than 10^6 [61] and 10^4 [62] wall collisions of alkali atoms before depolarization, respectively. These films have not been used in microfabricated cells to date, because their melting points, of 30 °C for alkenes and up to 100 °C for alkanes, are below the typical anodic temperatures of 300 °C. Organosilane coatings, such as octadecytrichlorosilane (OTS), can withstand temperatures up to 170 °C in the presence of alkali vapor [63, 64]. The combination of OTS films with low-temperature indium-based sealing techniques [60] has enabled the fabrication of a microfabricated cell with antirelaxation coatings [65]. Hyperfine spectroscopy of Rb atoms in this cell suggests that the atomic polarization survives on average 11 wall collisions [65]. For comparison, the best OTS coatings in centimeter-scale cells support 2000 wall collisions [63]. We also note that alkene coatings deposited into glass cells with microchannels 300 μm × 300 μm in cross section have enabled 5000 collisions of Cs atoms with the channel walls [66]. Based on these results, combined with further improvements and low-temperature anodic bonding, it is expected that MEMS cells with high quality antirelaxation coatings can be fabricated in the future.

3.4 Heating

Different factors have to be considered when designing heaters for μOPMs. Besides reaching the required temperatures, careful thermal design has to ensure that the alkali atoms do not condense on the cell windows and that the heaters do not cause magnetic noise or magnetic offsets. Two heating approaches that have been implemented to date are electrical heating and optical heating, which we consider next.

Electrical heating. In electrical heating approaches, the current flowing through resistive elements in close contact with the cell dissipates energy into heat that is transferred to the interior of the cell. Resistive heaters have been patterned onto glass windows using a variety of materials, such as gold and titanium. Resistive heaters based on silicon-on-sapphire (SOS-CMOS) technology have also been implemented [67], which are particularly attractive for their good thermal conductivity. In all these designs, great care is taken to prevent the magnetic fields produced by the heater currents from affecting the performance of the magnetometer in the form of magnetic interference, noise, and drifts [68]. Often the heater traces are arranged so that magnetic fields from neighboring wires largely cancel each other. Double-layer designs, where two identical wires are patterned on top of each other, allow for current flow in opposite directions, with a thin isolating material of only a few microns thickness. Materials transparent to the light interrogating the alkalis, such as indium tin oxide (ITO), have been used in the form of sheets [69] or laser patterned double layers [70] deposited onto the cell windows. In order to further reduce the effect of magnetic fields, the heater currents can be modulated at a frequency far above the bandwidth of the magnetometer. Finally, nonmagnetic chip resistors have also been used to heat the cells [53, 71].

Optical heating. To completely eliminate magnetic fields produced by electrical currents in resistive heaters, optical heating can be used instead, whereby optical power of a laser is transformed into heat when absorbed by the cell body [72]. In the first demonstration design, heating light at 915 nm was absorbed by the silicon sidewalls of the vapor cell. Since the thermal design was not optimal, alkalis condensed on the cell windows after several hours of operation resulting in the inefficient transmission of light through the cell. In subsequent designs, absorptive filters, transparent to the pumping and probing light, have been attached to the windows of the vapor cell. This allows for a simpler design with collinear heating and pump laser beams. In these designs, half the heating light is absorbed by the filter on the entrance window of the cell, while the rest is absorbed by the filter on the exit window, resulting in an even heat distribution, where the windows remain slightly hotter than the silicon body. The wavelength of the heating laser was chosen close to 1.5 μm, which is outside the detection range of the silicon photodiode used in the device [68].

3.5 Thermal Management

Thermal isolation of the physics package is important not only for efficient heating, which enables low-power consumption, but also to protect the specimens under test from the elevated temperatures of the cell. Thermal isolation of MEMS vapor cells has first been developed for chip-scale atomic clocks by suspending the physics package on a web of strained polyimide inside a vacuum enclosure [73], which reduces conductive heat losses. This design required less than 10 mW of heating power to raise the temperature of a 1 mm^3 vapor cell to 75 °C from ambient conditions. For magnetometers, a similar but non-magnetic hermetic enclosure has been developed [74], based on anodic bonding of glass wafers to each side of a silicon frame, similar to a large MEMS vapor cell (see Fig. 8a). In these magnetometers, optical heating has been used, which relieves the need for electrical feedthroughs into the vacuum package. Experimental tests indicate that below 1 mTorr heating losses due to gas conduction and convection within the enclosure are suppressed (see Fig. 8b). Ideas to further reduce the power consumption have been proposed in Ref. [75], for example, where a series of microfabricated radiation baffles have been added around the cell to reduce radiation in four directions. The baffles were fabricated out of silicon and suspended on a silicon nitride membrane.

3.6 Signal Detection

In alkali-based magnetometers, the spin-state is read optically by monitoring the absorption and phase of a light beam transmitted through the ensemble (see Fig. 9).

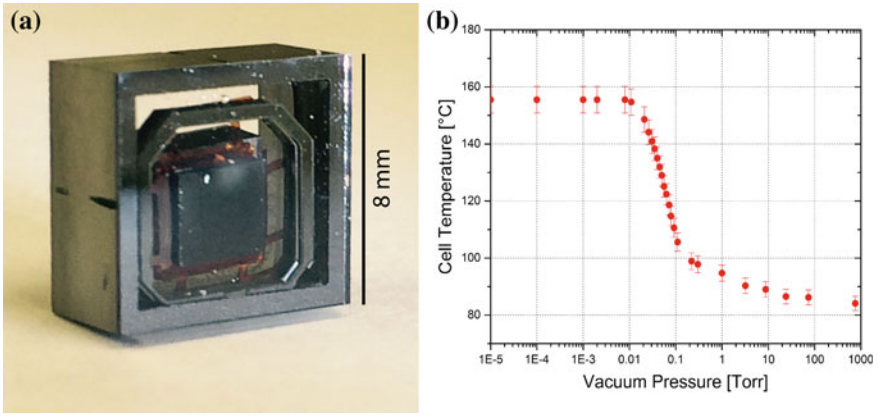

Fig. 8 **a** Photograph of an anodically-bonded vacuum package containing a MEMS vapor cell suspended on a polyimide web, held on a support frame. **b** Temperature of a (1.5 mm^3) MEMS cell as a function of enclosure gas pressure for a constant heating power of 50 mW

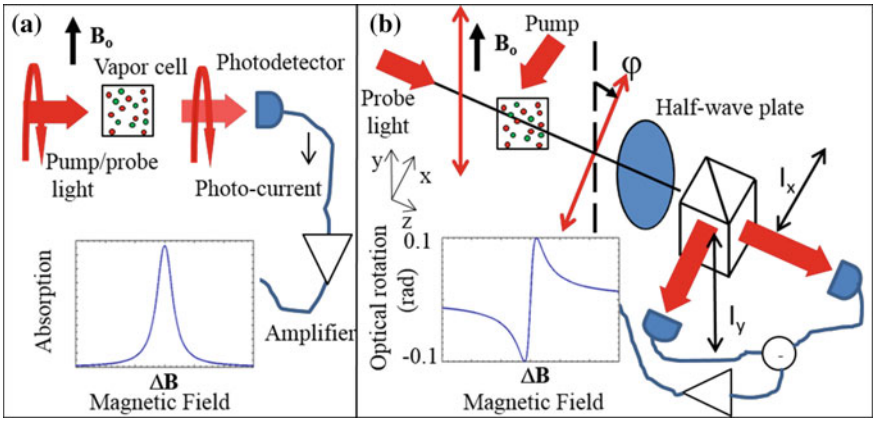

Fig. 9 Detection schemes: **a** Monitoring the transmission of a laser beam through the atomic sample results in a symmetric absorption line as a transverse magnetic field is scanned through resonance. **b** Implementation of a balanced polarimeter can reduce the laser-intensity noise and yields a dispersive resonance line, when the transverse spin polarization is detected

Absorption measurements are performed by monitoring changes in the electrical current generated by the transmitted light impinging on a photodiode. Phase-shift measurements are performed by monitoring the optical rotation of a linearly-polarized off-resonance probe light beam with a balanced polarimeter. Because absorption measurements can be performed by monitoring the transmitted pump light, they allow for a simple detection scheme based on a single light beam for pumping and probing. For this reason most μOPMs have been implemented using absorption measurements. However, compared to other devices based on phase-shift measurement, their performance is reduced in some cases, because pump and probe light parameters cannot be optimized independently and intensity noise is not cancelled.

3.7 Additional Hardware

In addition to the physics package, control electronics and often a local oscillator are required to enable a fully functional atomic magnetometer. In either absorption or phase-shift measurements, a transimpedance amplifier with one or more amplification stages is used to bring the signal at the adequate voltage levels for the given data acquisition and processing electronics of the instrument. Care needs to be taken that the noise added by the electronics does not become a limiting factor [16].

In resonantly driven magnetometers, a local oscillator drives the spin precession. It is locked to the magnetic resonance by means of a phase-sensitive detector and servo control system. Alternatively, in a simpler self-oscillating design, the oscillating field is generated from the photodiode signal in a positive feedback loop [76,

77]. For low-field magnetometers, a local oscillator is used to modulate one parameter, such as the magnetic field [78] or the probe light polarization [1–3], and the probe light is detected using phase-sensitive detection where the local oscillator modulation signal serves as a phase-reference. With this scheme, closed-loop magnetometers have been demonstrated as well [79, 80].

Control electronics are required to stabilize the laser and cell temperatures and an additional feedback loop is used to stabilize the laser frequency onto the optical transition. To date, there have been no publications on μOPMs integrating physics package, local oscillators, and control electronics in a compact system. In this regard, previous work integrating electronics with chip-scale atomic-clocks [81] and nuclear magnetic gyroscopes [82], whose working mechanism is similar to magnetometers, can pave the way for the implementation of a fully-integrated magnetometer system.

4 Implementations

During the past ten years μOPMs have been demonstrated in the laboratory in scalar and low-field configurations. Figure 10 shows the magnetic noise spectral density of some of these microfabricated sensors as well as others implemented with glass-blown cells. In what follows, we briefly review some of the μOPM implementations to date.

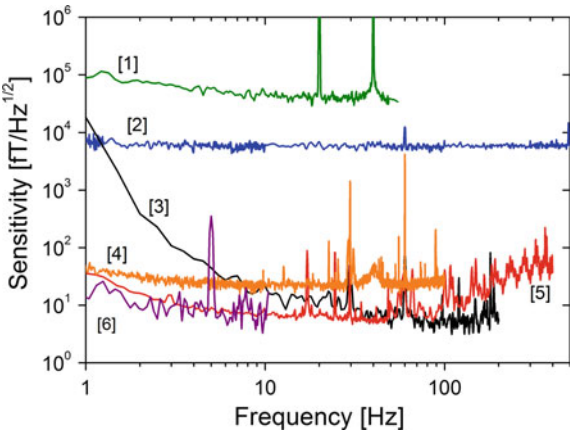

Fig. 10 Sensitivity measured in a variety of small magnetometers discussed below: (*1*, *green*) an integrated microfabricated CPT magnetometer; from Ref. [69], (*2*, *blue*) an integrated microfabricated Mx magnetometer; from Ref. [70], (*3*, *black*) a SERF magnetometer with two orthogonal beams in a microfabricated vapor cell; from Ref. [53], (*4*, *orange*) a fiber-coupled microfabricated zero-field magnetometer; from Ref. [74], (*5*, *red*) a small zero-field integrated gradiometer (from Ref. [96]), (*6*, *purple*) a small zero-field fiber-coupled gradiometer [courtesy of QuSpin Inc.(see footnote 1)]

4.1 Scalar Magnetometers

The first microfabricated magnetometers [69, 70] were implemented in an integrated physics package as that shown in Fig. 11. The first sensor was based on coherent population trapping (CPT) on a magnetically sensitive hyperfine transition of ground state ^{87}Rb atoms [69], while the second one used an RF coil to drive Zeeman resonances in ^{87}Rb atoms in the standard Mx configuration [70]. Sensitivities of 50 pT-Hz$^{-1/2}$ and 5 pT-Hz$^{-1/2}$ were measured in the CPT and Mx magnetometers, respectively, with corresponding linewidths (FWHM) of 13.2 and 1.7 kHz. The ^{87}Rb MEMS vapor cells were 1 mm^3 (CPT) and 2 mm^3 (Mx) in size. Both sensors consumed about 200 mW of electrical power to heat the cell in an ambient of roughly 20 °C. The power consumption was dominated by conductive heat losses from the vapor cell, followed by radiation and convection heat losses [83]. The sensitivity of the Mx magnetometer enabled the recording of magnetic cardiac signals generated by mice [84].

The CPT magnetometer has the appealing feature of generating its magnetic resonance optically. As a result, it does not suffer from problems caused by RF coils such as cross-talk between sensors in array-based applications, or bias errors due to a misalignment between the RF coils axis and the probe light beam in the Mx magnetometer [76]. Since all Zeeman components are resolved in geomagnetic fields, it is less prone to heading errors caused by the non-linear Zeeman shift and omni-directionality has been achieved [85]. On the other hand, the operation of the

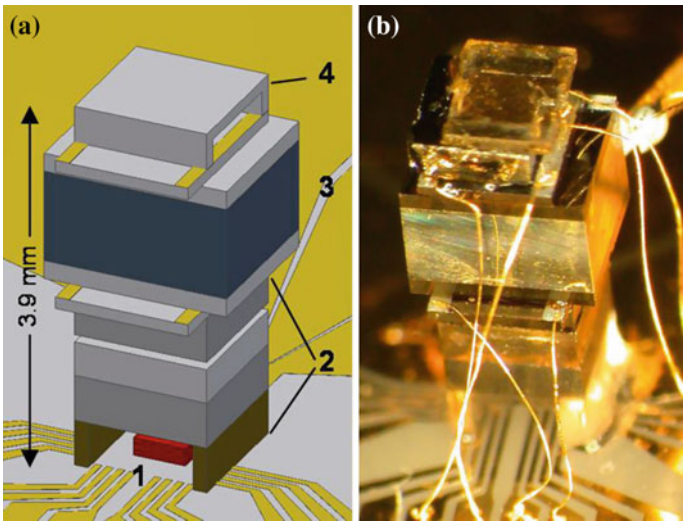

Fig. 11 Schematic **(a)** and photograph **(b)** of a microfabricated physics package of a fully-integrated optically-pumped magnetometer (see Ref. [70]). The components include (1) VCSEL, (2) micro optics, (3) MEMS vapor cell, and (4) photodiode. (*Source* Ref. [70]; reproduced with permission from AIP)

CPT magnetometer is more complex compared to the Mx magnetometer, due to additional hardware and signal processing requirements. It requires a local oscillator in the gigahertz range and is prone to shifts caused by changes in buffer gas pressure. Small space-qualified CPT and Mx magnetometers are being developed for space applications with a major focus on long-term stability and accuracy [67, 86].

A magnetometer that combines the advantages of optical excitation and the simplicity of the Mx magnetometer is the configuration known as Bell-Bloom magnetometer [31]. In this case, the spin precession is driven optically by modulating the optical pumping rate at the Larmor frequency. This can be achieved by modulation of the intensity, polarization, or detuning of the pumping light [76, 87]. Bell-Bloom magnetometers have been implemented with microfabricated vapor cells by either modulating the optical detuning [88] or intensity of the pump beam. Sensitivities on the order of 10 pT-Hz$^{-1/2}$ with bandwidths of 10 kHz have been measured using a 1 mm^3 ^{87}Rb MEMS cell [71], and sensitivities on the order of 0.3 pT-Hz$^{-1/2}$ were measured in Cs MEMS cell of volume 50 mm^3 [89].

4.2 *Low-Field, Spin-Exchange Relaxation-Free Magnetometer*

To date, the most sensitive optical magnetometers operate at large alkali atomic densities and low magnetic fields. These instruments have high signal strength due to high atomic density and a long spin coherence time due to the suppression of spin-exchange broadening, [1, 90]. These magnetometers, often referred to as Spin-Exchange Relaxation-Free (SERF) magnetometers [1], have reached sensitivities below 1 fT-Hz$^{-1/2}$ [2, 3], and have been used by researchers to detect weak magnetic fields from a wide variety of sources, such as the human brain [6, 9, 11, 14], atomic nuclei [91] cancerous cells [92], and for material characterization [93]. The SERF regime is particularly well suited for small magnetometers, where the alkali density must be high to provide sufficient absorption for high signal-to-noise detection of the alkali polarization.

Microfabricated SERF magnetometers have demonstrated magnetic sensitivities of 5 fT-Hz$^{-1/2}$ [53] in table-top setups in the standard two-beam configuration, where pump and probe beams propagate perpendicular to each other [1]. The orthogonal pump-probe configuration takes advantage of the dispersive resonance signal, displayed by the spin component perpendicular to the pumping axis, which is observed by optical rotation of the off-resonance probe beam using a balanced polarimeter (see Fig. 9). However, simpler and more practical geometries are realized with a single beam [78]. Single-beam zero-field magnetometers have been implemented in microfabricated cells in table-top setups [23], and fiber-coupled magnetometers as described below. Most single-beam SERF magnetometers are based on absorption measurements of the transmitted light, with dispersive resonances obtained by applying a modulating magnetic field orthogonal to the light

direction and using phase-sensitive detection of the transmitted light. However, if the pumping beam is off resonant and elliptically polarized, phase shift measurements can be implemented as well [94]. Typical modulation frequencies are on the order of 1 kHz, with corresponding modulation amplitudes of about 100 nT for ^{87}Rb atoms. To prevent cross-talk induced by the modulation field in array-based applications, optical modulation can be used instead [95].

4.3 Fiber-Coupled Magnetometers

Compact fiber-coupled magnetometers, where the light is coupled to the vapor cells through optical fibers, have been developed using microfabricated and glass-blown cells. One intent in this sensor design is to eliminate components that produce magnetic fields from the sensor package. A second intent is to enable the remote interrogation of the sensor heads. Figure 12 shows three fiber-coupled microfabricated magnetometer sensor packages recently developed at the National Institute of Standard and Technology (NIST) and two small fiber-coupled sensors developed at Sandia National Laboratories and QuSpin Inc.[1] The sensor in Fig. 12a used thin-film titanium resistive heaters on both windows of a (1.5 mm^3) ^{87}Rb vapor cell, suspended on a thin polyimide web that was attached to an outer silicon frame. A polarization-maintaining fiber delivered the pumping light to the package. The light beam was expanded, collimated, and circularly polarized, before reaching the vapor cell. The transmitted light was coupled into a multi-mode fiber and detected by a photodiode 5 m away from the sensor package. The sensor reached a sensitivity of 150 fT/Hz$^{1/2}$ in the SERF mode, limited by photon shot noise [6]. An improved version of this sensor, shown in Fig. 12b [74], implemented optical heating of the cell, which was suspended inside a vacuum package made from an anodically-bonded five-layer stack of silicon and glass wafers. A vacuum gap of 500 μm enabled a distance of 2.5 mm between the center of the ^{87}Rb vapor cell, with inner volume of 3 mm^3, and the outer surface of the sensor package. As in the previous design, pumping light at 795 nm was coupled into the cell from a polarization maintaining single-mode optical fiber. The light transmitted through the cell was focused and redirected by a dichroic mirror onto a silicon photodiode attached to the package. The current from the sensor photodiode was carried through a twisted pair of wires to a remotely-located transimpedance amplifier. The heat light was delivered to the sensor package with a multi-mode optical fiber. It was counter-propagating to the pump light on the sensor head and separated with a dichroic mirror. The sensor reached a sensitivity of 15 fT/Hz$^{1/2}$ in the SERF mode, while consuming 200 mW of heating optical power [74].

[1]Manufacturer is stated for technical clarity and does not imply endorsement by NIST. Products from other manufacturers may perform as well or better. Contribution of NIST an agency of the U. S. government; not subject to copyright.

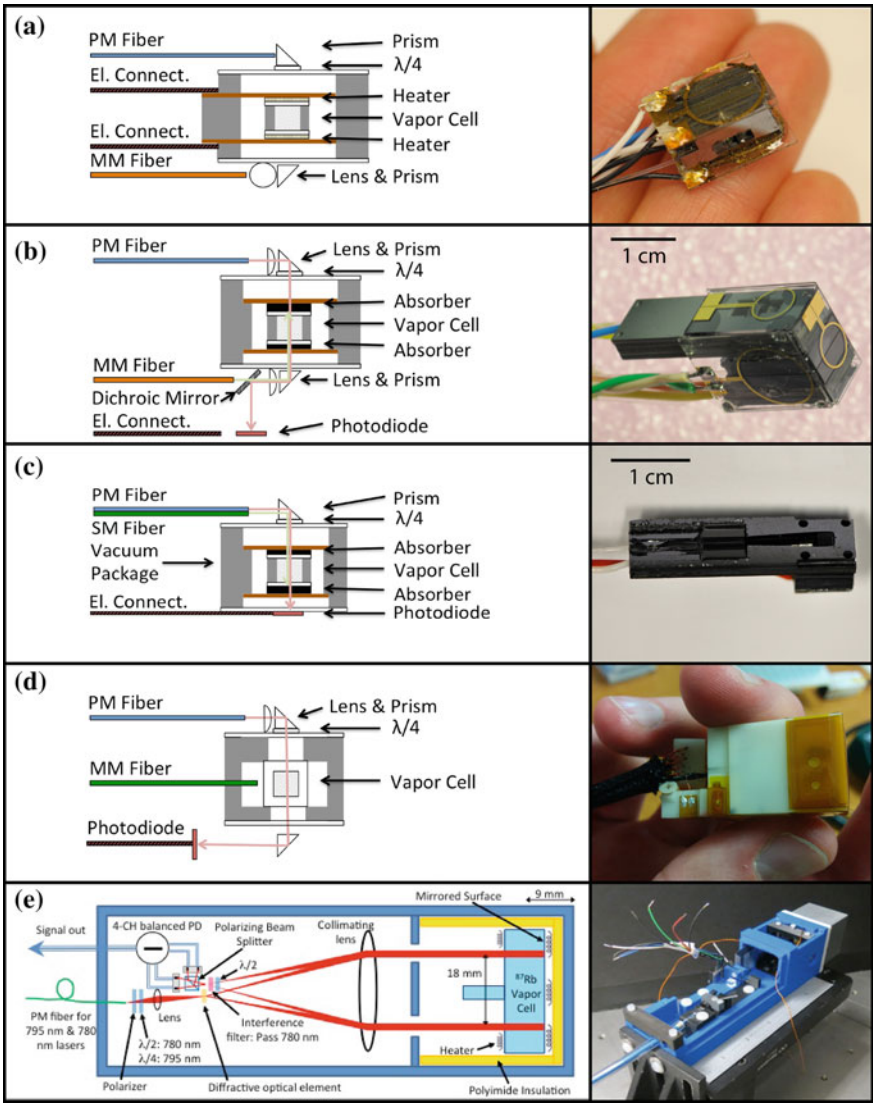

Fig. 12 Schematics and photographs of several small fiber-coupled OPMs. Fiber-coupled microfabricated magnetometer sensor packages recently developed at the National Institute of Standard and Technology **a**–**c** and two small fiber-coupled sensors developed at QuSpin Inc. **d** and Sandia National Laboratories **e**. *Source* **d** QuSpin Inc. (see footnote 1), https://www.quspin.com; with permission from QuSpin Inc. **e** Sandia National Laboratories, https://www.sandia.gov; with permission from Sandia National Laboratories)

The sensor package shown in Fig. 12c is a simplified version of the previous magnetometer but with similar performance and dimensions of $7.3 \times 8.5 \times 30$ mm^3. Contrary to the previous design, the pumping and heating light fibers

terminate in a single silicon V-groove ferrule. Both beams were not collimated and co-propagate through the sensor head. The heat light is mostly absorbed by filters on the cell windows, and its wavelength is outside the detection range of the photodiode.

The sensor shown in Fig. 12d is made by QuSpin Inc. (see footnote 1). It does not use microfabricated components, but could easily be fabricated with such. The setup is very similar to the one in Fig. 12c. The (3 mm^3) cell is heated through the absorption of light, and allows for a distance on 5 mm between the center of the cell and the outside of the housing, which has a volume of $19 \times 12 \times 60$ mm^3.

The sensor head in Fig. 12e is a compact version of a four-channel magnetometer, made by Sandia National Laboratories. While the sensor has a total dimension of $46 \times 46 \times 204$ mm^3, it uses a unique configuration of the physics package, amenable to microfabrication. The vapor cell has a thickness of 4 mm and a width of 25 mm to allow for four parallel laser beams of diameter 2.5 mm to pass through. The beam separation defines the gradiometer baseline of 18 mm. The light is reflected by a mirror behind the vapor cell, which allows for a distance of 9 mm between the center of the cell and the outside wall of the sensor [96]. This list is by no means exhaustive and many other small fiber-coupled sensor heads have been built with single-beam and more complicated multi-beam configurations.

5 Multichannel Systems

Currently, there is much interest in developing multichannel systems consisting of an array of OPMs. One goal of such systems is to perform non-invasive magnetic field mapping of the human body in an analogous way as instrumentation based on SQUID-magnetometers [20]. Several groups have made efforts to build large arrays of sensors and demonstrated their use for biomagnetics: Wyllie et al. [13] measured fetal magnetocardiograms (MCG) with four independent sensor heads, Bison et al. [8] did pioneering MCG measurements with a static array of 19 sensors. Xia et al. [14] presented the first magnetoencephalography (MEG) measurements with a large glass cell and a 16×16 channel CCD camera, which was refined later [97]. Johnson et al. [92] made MEG measurements with an eight-channel array.

The only microfabricated OPM array that has so far been demonstrated was a 32-channel imaging system by NIST with small sensor heads very similar to the one shown in Fig. 12c, fabricated by Draper Laboratories. The sensors are coupled to the control system through 5 m long optical fibers and can be placed in an arbitrary configuration. While several cells and vacuum packages were sealed in small parallel batches, the components were made on whole wafers. Charles Draper Laboratories also demonstrated an array of 100 thermally-suspended cells on a wafer (see Fig. 13).

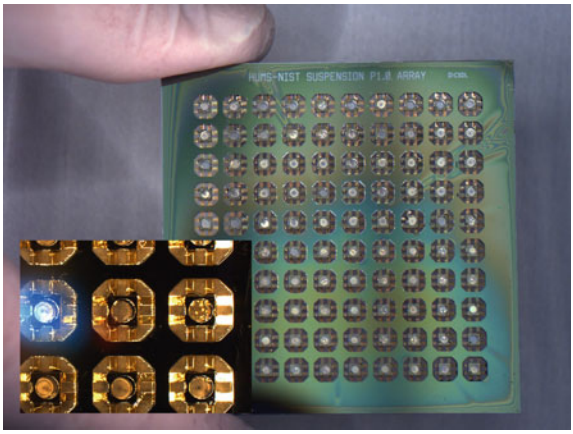

Fig. 13 Photographs on a 10×10 array of thermally suspended MEMS Cs cells. (*Source* Charles Stark Draper Laboratory Inc., http://www.draper.com; reproduced with permission from Draper Laboratory)

6 Non-alkali Based Magnetometers

Noble-gas magnetometers. Magnetometers using nuclear-spins of xenon gas have been implemented in sealed MEMS cells [98] and microfluidic platforms [99]. In these devices spin polarization of xenon atoms is achieved through spin-exchange collisions with optically-polarized alkali atoms [100]. Detection of the nuclear spin is then carried out with the co-located alkali atoms as in situ optical magnetometers to detect the xenon magnetization. With their long coherence times of up to 10 s in a 1 mm^3 MEMS cell [98], magnetometers based on nuclear spins are ideal for accurate magnetic field measurements. One application of such devices is in nuclear magnetic resonance gyroscopes, which detect rotation by measuring a corresponding shift in the Larmor frequency of nuclear spins in a bias magnetic field [82, 98, 101].

Metastable He-4 magnetometers. Because He-4 atoms have no nuclear spin, no hyperfine interaction is present. Therefore, magnetometers based on He-4 atoms are unaffected by the nonlinear Zeeman shifts. In He-4 magnetometers, a weak RF discharge excites a fraction of He-4 atoms from their ground (singlet) state $1\ ^1S_0$ into their metastable (triplet) state $2\ ^3S_1$, producing an ensemble of unpolarized atoms. Optical pumping with light from a diode laser, tuned to the D_0 (1083 nm) transition can be employed to polarize and detect the metastable atoms whose spin-precession about an external magnetic field can be driven either by RF or optical excitation. He-4 magnetometers have been used extensively in space missions due to their higher accuracy. Recently, a miniaturize He-4 magnetometer has been reported with measured sensitivities of 10 $pT/Hz^{1/2}$ in a frequency range from dc to 100 Hz [102]. In this He-4 magnetometer, pumping with linearly polarized light is employed to suppress heading errors caused by light shifts. To avoid dead zones, a miniature liquid-crystal polarization rotator, based on microfabrication techniques, is used to keep the linear polarization axis orthogonal to the ambient field. The reported sensitivity is one to two orders of magnitude worse than

larger-scale versions of this magnetometer design; however, its estimated spin-projection noise sensitivity is 10 $fT/Hz^{1/2}$. The current magnetometer is based on a glass vapor cell of 100 mm^3, and consumes about 100 mW to initiate the RF discharge; current work aims at its implementation and further miniaturization through microfabricated He-4 vapor cells [102]. A similar device has also been operated at zero field and simulated MCG signals have been detected [103].

7 Outlook

Microfabricated optically-pumped magnetometers are being developed for many applications, and validation experiments have been performed with several prototypes. For magnetic anomaly detection, small, low-power, low-cost magnetometers have been demanded. For geophysical surveying, unexploded ordinance detection, and space applications, scalar μOPMs with low heading errors and good long-term stability are being developed [67]. Zero-field μOPMs have shown promising results in the detection of microfluidic NMR at low magnetic fields [91] and for chemical analysis based on J-couplings of ethanol [104]. These high sensitivity magnetometers, combined with non-thermal spin-polarization methods allow the detection of NMR even in the absence of external magnetic fields. For this purpose, parahydrogen induced polarization was demonstrated in combination with detection by a μOPM [105] and, in a different experiment, a microfluidic xenon polarizer was demonstrated [99]. Finally, in the field of biomagnetics, the high sensitivity of zero-field μOPMs was found to be sufficient to measure MCG [5], fetal MCG [4], and MEG [6], as well as the field from magnetic micro- and nano-particles [5]. Research on better interrogation schemes along with better fabrication methods will open the way for many other applications of μOPMs in the future.

Acknowledgements R. Jiménez-Martínez acknowledges support from the ICFO-NEST Fellowship program.

References

1. J.C. Allred, R.N. Lyman, T.W. Kornack, M.V. Romalis, High-sensitivity atomic magnetometer unaffected by spin-exchange relaxation. Phys. Rev. Lett. **89**, 130801 (2002)
2. H.B. Dang, A.C. Maloof, M.V. Romalis, Ultrahigh sensitivity magnetic field and magnetization measurements with an atomic magnetometer. Appl. Phys. Lett. **97**, 151110 (2010)
3. I.K. Kominis, T.W. Kornack, J.C. Allred, M.V. Romalis, A subfemtotesla multichannel atomic magnetometer. Nature **422**, 596–599 (2003)
4. O. Alem, T.H. Sander, R. Mhaskar, J. LeBlanc, H. Eswaran, U. Steinhoff et al., Fetal magnetocardiography measurements with an array of microfabricated optically pumped magnetometers. Phys. Med. Biol. **60**, 4797 (2015)

5. S. Knappe, T.H. Sander, O. Kosch, F. Wiekhorst, J. Kitching, L. Trahms, Cross-validation of microfabricated atomic magnetometers with superconducting quantum interference devices for biomagnetic applications. Appl. Phys. Lett. **97**, 133703 (2010)
6. T.H. Sander, J. Preusser, R. Mhaskar, J. Kitching, L. Trahms, S. Knappe, Magnetoencephalography with a chip-scale atomic magnetometer. Biomed. Opt. Express **3**, 981–990 (2012)
7. J. Belfi, G. Bevilacqua, V. Biancalana, S. Cartaleva, Y. Dancheva, L. Moi, Cesium coherent population trapping magnetometer for cardiosignal detection in an unshielded environment. J. Opt. Soc. Am. B-Opt. Phys. **24**, 2357–2362 (2007)
8. G. Bison, N. Castagna, A. Hofer, P. Knowles, J.L. Schenker, M. Kasprzak et al., A room temperature 19-channel magnetic field mapping device for cardiac signals. Appl. Phys. Lett. **95**, 173701 (2009)
9. C. Johnson, P.D.D. Schwindt, M. Weisend, Magnetoencephalography with a two-color pump-probe, fiber-coupled atomic magnetometer. Appl. Phys. Lett. **97**, 243703 (2010)
10. M.N. Livanov, Recording of human magnetic fields. Dokl. Akad. Nauk SSSR **238**, 253–256 (1977)
11. V.K. Shah, R.T. Wakai, A compact, high performance atomic magnetometer for biomedical applications. Phys. Med. Biol. **58**, 8153 (2013)
12. S. Taue, Y. Sugihara, T. Kobayashi, S. Ichihara, K. Ishikawa, N. Mizutani, Development of a highly sensitive optically pumped atomic magnetometer for biomagnetic field measurements: a phantom study Magnetics. IEEE Trans. **46**, 3635–3638 (2010)
13. R. Wyllie, M. Kauer, R.T. Wakai, T.G. Walker, Optical magnetometer array for fetal magnetocardiography. Opt. Lett. **37**, 2247–2249 (2012)
14. H. Xia, A.B.-A. Baranga, D. Hoffman, M.V. Romalis, Magnetoencephalography with an atomic magnetometer, Appl. Phys. Lett. **89**, 211104–211103 (2006)
15. M. Díaz-Michelena, Small magnetic sensors for space applications. Sensors **9**, 2271–2288 (2009)
16. I. Mateos, B. Patton, E. Zhivun, D. Budker, D. Wurm, J. Ramos-Castro, Noise characterization of an atomic magnetometer at sub-millihertz frequencies. Sens. Actuators, A **224**, 147–155 (2015)
17. P.A. Bottomley, NMR imaging techniques and applications: a review. Rev. Sci. Instrum. **53**, 1319–1337 (1982)
18. P.C. Lauterbur, Image formation by induced local interactions: examples employing nuclear magnetic resonance. Nature **242**, 190–191 (1973)
19. D.C. Jiles, Review of magnetic methods for nondestructive evaluation. NDT International **21**, 311–319 (1988)
20. D. Cohen, Magnetoencephalography: detection of the brain's electrical activity with a superconducting magnetometer. Science **175**, 664–666 (1972)
21. S.R. Steinhubl, E.D. Muse, E.J. Topol, The emerging field of mobile health. Sci. Trans. Med. **7**, 283rv283 (2015)
22. W. Happer, Optical pumping. Rev. Mod. Phys. **44**, 169–249 (1972)
23. V. Shah, S. Knappe, P.D.D. Schwindt, J. Kitching, Subpicotesla atomic magnetometry with a microfabricated vapour cell. Nat. Photonics **1**, 649–652 (2007)
24. S.J. Smullin, I.M. Savukov, G. Vasilakis, R.K. Ghosh, M. Romalis, Low-noise high-density alkali-metal scalar magnetometer. Phys. Rev. A **80**, 033420 (2009)
25. I.M. Savukov, S.J. Seltzer, M.V. Romalis, K.L. Sauer, Tunable atomic magnetometer for detection of radio-frequency magnetic fields. Phys. Rev. Lett. **95**, 063004 (2005)
26. M.P. Ledbetter, I.M. Savukov, V.M. Acosta, D. Budker, M.V. Romalis, Spin-exchange-relaxation-free magnetometry with Cs vapor. Phys. Rev. A **77**, 033408 (2008)
27. D.A. Steck, Rubidium 87 D line data, revision 2.1.4 (2010)
28. V. Shah, G. Vasilakis, M.V. Romalis, High bandwidth atomic magnetometery with continuous quantum nondemolition measurements. Phys. Rev. Lett. **104**, 013601 (2010)

29. B. Patton, O.O. Versolato, D.C. Hovde, E. Corsini, J.M. Higbie, D. Budker, A remotely interrogated all-optical 87Rb magnetometer. Appl. Phys. Lett. **101**, 083502 (2012)
30. J. Belfi, G. Bevilacqua, V. Biancalana, Y. Dancheva, L. Moi, All optical sensor for automated magnetometry based on coherent population trapping. J. Opt. Soc. Am. B **24**, 1482–1489 (2007)
31. W.E. Bell, A.L. Bloom, Optically driven spin precession. Phys. Rev. Lett. **6**, 280 (1961)
32. V. Acosta, M.P. Ledbetter, S.M. Rochester, D. Budker, D.F.J. Kimball, D.C. Hovde et al., Nonlinear magneto-optical rotation with frequency-modulated light in the geophysical field range. Phys. Rev. A **73**, 053404 (2006)
33. G. Alzetta, A. Gozzini, L. Moi, G. Orriols, Experimental-method for observation of Rf transitions and laser beat resonances in oriented Na vapor. Nuovo Cimento Della Societa Italiana Di Fisica B-Gen. Phys. Relativ. Astron. Math. Phys. Methods **36**, 5–20 (1976)
34. C. Affolderbach, A. Nagel, S. Knappe, C. Jung, D. Wiedenmann, R. Wynands, Nonlinear spectroscopy with a vertical-cavity surface-emitting laser (VCSEL). Appl. Phys. B **70**, 407–413 (2000)
35. V. Gerginov, V. Shah, S. Knappe, L. Hollberg, J. Kitching, Atomic-based stabilization for laser-pumped atomic clocks. Opt. Lett. **31**, 1851–1853 (2006)
36. F. Gruet, F. Vecchio, C. Affolderbach, Y. Pétremand, N.F. de Rooij, T. Maeder et al., A miniature frequency-stabilized VCSEL system emitting at 795 nm based on LTCC modules. Opt. Lasers Eng. **51**, 1023–1027 (2013)
37. S. Knappe, H.G. Robinson, L. Hollberg, Microfabricated saturated absorption spectroscopy with alkali atoms. Opt. Express **15**, 6293–6299 (2007)
38. V. Venkatraman, H. Shea, F. Vecchio, T. Maeder, P. Ryser, in *LTCC Integrated Miniature Rb Discharge Lamp Module for Stable Optical Pumping in Miniature Atomic Clocks and Magnetometers*. 2012 IEEE 18th International Symposium for Design and Technology in Electronic Packaging (SIITME), pp. 111–114
39. V. Venkatraman, S. Kang, C. Affolderbach, H. Shea, G. Mileti, Optical pumping in a microfabricated Rb vapor cell using a microfabricated Rb discharge light source. Appl. Phys. Lett. **104**, 054104 (2014)
40. D.K. Serkland, K.M. Geib, G.M. Peake, R. Lutwak, A. Rashed, M. Varghese et al., in *VCSELs for Atomic Sensors*, eds. by K.D. Choquette, J.K. Guenter, Proceedings of SPIE 6484: Vertical-Cavity Surface-Emitting Lasers XI (2007)
41. S. Knappe, V. Velichansky, H.G. Robinson, J. Kitching, L. Hollberg, Compact atomic vapor cells fabricated by laser-induced heating of hollow-core glass fibers. Rev. Sci. Instrum. **74**, 3142–3145 (2003)
42. G. Wallis, D. Pomerantz, Field assisted glass-metal sealing. J. Appl. Phys. **40**, 3946–3949 (1969)
43. Y. Pétremand, C. Affolderbach, R. Straessle, M. Pellaton, D. Briand, G. Mileti et al., Microfabricated rubidium vapour cell with a thick glass core for small-scale atomic clock applications. J. Micromech. Microeng. **22**, 025013 (2012)
44. S. Knappe, V. Gerginov, P.D.D. Schwindt, V. Shah, H. Robinson, L. Hollberg et al., Atomic vapor cells for chip-scale atomic clocks with improved long-term frequency stability. Opt. Lett. **30**, 2351–2353 (2005)
45. L.-A. Liew, S. Knappe, J. Moreland, H.G. Robinson, L. Hollberg, J. Kitching, Microfabricated alkali atom vapor cells. Appl. Phys. Lett. **84**, 2694–2696 (2004)
46. F. Gong, Y.Y. Jau, K. Jensen, W. Happer, Electrolytic fabrication of atomic clock cells. Rev. Sci. Instrum. **77**, 076101 (2006)
47. L.-A. Liew, J. Moreland, V. Gerginov, Wafer-level filling of microfabricated atomic vapor cells based on thin-film deposition and photolysis of cesium azide. Appl. Phys. Lett. **90**, 114106 (2007)
48. S. Woetzel, V. Schultze, R. IJsselsteijn, T. Schulz, S. Anders, R. Stolz et al., Microfabricated atomic vapor cell arrays for magnetic field measurements, Rev. Sci. Instrum. **82**, 033111 (2001)

49. J. Haesler, L. Balet, J.A. Porchet, T. Overstolz, J. Pierer, R.J. James, et al., in *The Integrated Swiss Miniature Atomic Clock.* European Frequency and Time Forum & International Frequency Control Symposium (EFTF/IFC), 2013 Joint, pp. 579–581 (2013)
50. M. Hasegawa, R.K. Chutani, C. Gorecki, R. Boudot, P. Dziuban, V. Giordano et al., Microfabrication of cesium vapor cells with buffer gas for MEMS atomic clocks. Sens. Actuators, A **167**, 594–601 (2011)
51. L. Nieradko, C. Gorecki, A. Douahi, V. Giordano, J.C. Beugnot, J. Dziuban et al., New approach of fabrication and dispensing of micromachined cesium vapor cell. MOEMS **7**, 033013–033016 (2008)
52. S.-K. Lee, M.V. Romalis, Calculation of magnetic field noise from high-permeability magnetic shields and conducting objects with simple geometry. J. Appl. Phys. **103**, 084904 (2008)
53. W.C. Griffith, S. Knappe, J. Kitching, Atomic magnetometer with sub-5-femtotesla sensitivity using a microfabricated vapor cell. Opt. Express **18**, 27167–27172 (2010)
54. M.A. Perez, U. Nguyen, S. Knappe, E.A. Donley, J. Kitching, A.M. Shkel, Rubidium vapor cell with integrated Bragg reflectors for compact atomic MEMS. Sens. Actuators, A **154**, 295–303 (2009)
55. M.A. Perez, S. Knappe, J. Kitching, 45° silicon etching for chip scale atomic devices (unpublished)
56. E.J. Eklund, A.M. Shkel, S. Knappe, E.A. Donley, J. Kitching, Glass-blown spherical microcells for chip-scale atomic devices. Sens. Actuators, A **143**, 175–180 (2008)
57. D. Senkal, M.J. Ahamed, S. Askari, A.M. Shkel, MEMS micro-glassblowing paradigm for wafer-level fabrication of fused silica wineglass gyroscopes. Procedia Eng. **87**, 1489–1492 (2014)
58. N. Dural, M.V. Romalis, Gallium phosphide as a new material for anodically bonded atomic sensors. APL Mat. **2**, 086101 (2014)
59. S. Woetzel, E. Kessler, M. Diegel, V. Schultze, H.-G. Meyer, Low-temperature anodic bonding using thin films of lithium-niobate-phosphate glass. J. Micromech. Microeng. **24**, 095001 (2014)
60. R. Straessle, M. Pellaton, C. Affolderbach, Y. Petremand, D. Briand, G. Mileti et al., Low-temperature indium-bonded alkali vapor cell for chip-scale atomic clocks. J. Appl. Phys. **113**, 064501 (2013)
61. M.V. Balabas, T. Karaulanov, M.P. Ledbetter, D. Budker, Polarized alkali-metal vapor with minute-long transverse spin-relaxation time. Phys. Rev. Lett. **105**, 070801 (2010)
62. M.A. Bouchiat, J. Brossel, Relaxation of optically pumped Rb atoms on paraffin-coated walls. Phys. Rev. **147**, 41–54 (1966)
63. S.J. Seltzer, M.V. Romalis, High-temperature alkali vapor cells with antirelaxation surface coatings. J. Appl. Phys. **106**, 114905 (2009)
64. Y.W. Yi, H.G. Robinson, S. Knappe, J.E. Maclennan, C.D. Jones, C. Zhu et al., Method for characterizing self-assembled monolayers as antirelaxation wall coatings for alkali vapor cells. J. Appl. Phys. **104**, 023534 (2008)
65. R. Straessle, M. Pellaton, C. Affolderbach, Y. Pétremand, D. Briand, G. Mileti et al., Microfabricated alkali vapor cell with anti-relaxation wall coating. Appl. Phys. Lett. **105**, 043502 (2014)
66. G. Vasilakis, H. Shen, K. Jensen, M. Balabas, D. Salart, B. Chen et al., Generation of a squeezed state of an oscillator by stroboscopic back-action-evading measurement. Nat. Phys. **11**, 389–392 (2015)
67. H. Korth, K. Strohbehn, F. Tajeda, A. Andreou, S. McVeig, J. Kitching et al., Chip-scale absolute scalar magnetometer for space applications. Johns Hopkins APL Tech. Dig. **28**, 248–249 (2010)
68. R. Mhaskar, S. Knappe, J. Kitching, in *Low-Frequency Characterization of Mems-Based Portable Atomic Magnetometer*, Frequency Control Symposium (FCS), 2010 IEEE International, pp. 376–379

69. P.D.D. Schwindt, S. Knappe, V. Shah, L. Hollberg, J. Kitching, L.-A. Liew et al., Chip-scale atomic magnetometer. Appl. Phys. Lett. **85**, 6409–6411 (2004)
70. P.D.D. Schwindt, B. Lindseth, S. Knappe, V. Shah, J. Kitching, A chip-scale atomic magnetometer with improved sensitivity using the Mx technique. Appl. Phys. Lett. **90**, 081102 (2007)
71. R. Jiménez-Martínez, W.C. Griffith, S. Knappe, J. Kitching, M. Prouty, High-bandwidth optical magnetometer. J. Opt. Soc. Am. B **29**, 3398–3403 (2012)
72. J. Preusser, S. Knappe, V. Gerginov, J. Kitching, in *A Microfabricated Photonic Magnetometer*. 2009 European Conference on Lasers and Electro-Optics 2009 and the European Quantum Electronics Conference CLEO Europe—EQEC, pp. 1–1
73. M.J. Mescher, R. Lutwak, M. Varghese, in *An Ultra-Low-Power Physics Package for a Chip-Scale Atomic Clock*, The 13th International Conference on Solid-State Sensors, Actuators and Microsystems, 2005 Digest of Technical Papers TRANSDUCERS '05, Vol. 311, pp. 311–316 (2005)
74. R. Mhaskar, S. Knappe, J. Kitching, A low-power, high-sensitivity micromachined optical magnetometer. Appl. Phys. Lett. **101**, 241105 (2012)
75. M.A. Perez, S. Knappe, J. Kitching, in *MEMS Techniques for the Parallel Fabrication of Chip Scale Atomic Devices.* 2010 IEEE Sensors, pp. 2155–2158 (2010)
76. A. Bloom, Principles of operation of the rubidium vapor magnetometer. Appl. Opt. **1**, 61–68 (1962)
77. W.F. Stuart, M.J. Usher, S.H. Hall, Rubidium self-oscillating magnetometer for earth's field measurements. Nature **202**, 76 (1964)
78. J. Dupont-Roc, S. Haroche, C. Cohen-Tannoudji, Detection of very weak magnetic fields (10^{-9} gauss) by Rb zero-field level crossing resonances. Phys. Lett. A **28**, 628–639 (1969)
79. H.J. Lee, J.H. Shim, H.S. Moon, K. Kim, Flat-response spin-exchange relaxation free atomic magnetometer under negative feedback. Opt. Express **22**, 19887–19894 (2014)
80. S.J. Seltzer, M.V. Romalis, Unshielded three-axis vector operation of a spin-exchange-relaxation-free atomic magnetometer. Appl. Phys. Lett. **85**, 4804–4806 (2004)
81. R. Lutwak, P. Vlitas, M. Varghese, M. Mescher, D.K. Serkland, G.M. Peake, in *The MAC—A Miniature Atomic Clock.* Joint Meeting of the IEEE International Frequency Control Symposium and the Precise Time and Time Interval (PTTI) Systems and Applications Meeting, Vancouver, Canada, pp. 752–757 (2005)
82. M. Larsen, M. Bulatowicz, in *Nuclear Magnetic Resonance Gyroscope: For DARPA's Micro-technology for Positioning, Navigation and Timing Program*. 2012 IEEE International on Frequency Control Symposium (FCS), pp. 1–5 (2012)
83. J. Kitching, S. Knappe, P.D.D. Schwindt, V. Shah, L. Hollberg, L. Liew, J. Moreland, in *Power Dissipation in Vertically Integrated Chip-Scale Atomic Clocks.* Proceedings of the 2004 IEEE International Frequency Control Symposium, pp. 781–784 (2004)
84. B. Lindseth, P.D.D. Schwindt, J. Kitching, D. Fischer, V. Shusterman, *Non-Contact Measurement of Cardiac Electromagnetic Field in Mice Using a Microfabricated Atomic Magnetometer.* Proceedings of 2007 Conference on Computers in Cardiology (2007)
85. A. Pollinger, M. Ellmeier, W. Magnes, C. Hagen, W. Baumjohann, E. Leitgeb et al., in *Enable the Inherent Omni-Directionality of an Absolute Coupled Dark State Magnetometer for e.g. Scientific Space Applications*. 2012 IEEE International on Instrumentation and Measurement Technology Conference (I2MTC), pp. 33–36 (2012)
86. W. Magnes, R. Lammegger, A. Pollinger, M. Ellmeier, C. Hagen, I. Jernej et al., in *Space Qualification of a New Scalar Magnetometer*. Geophysical Research Abstracts. EGU 2013-9600-2011
87. Z.D. Grujić, A. Weis, Atomic magnetic resonance induced by amplitude-, frequency-, or polarization-modulated light. Phys. Rev. A **88**, 012508 (2013)
88. R. Jiménez-Martínez, W.C. Griffith, W. Ying-Ju, S. Knappe, J. Kitching, K. Smith et al., Sensitivity comparison of Mx and frequency-modulated bell-bloom Cs magnetometers in a microfabricated cell, instrumentation and measurement. IEEE Trans. **59**, 372–378 (2010)

89. V. Schultze, R. Ijsselsteijn, T. Scholtes, S. Woetzel, H.-G. Meyer, Characteristics and performance of an intensity-modulated optically pumped magnetometer in comparison to the classical Mx magnetometer. Opt. Express **20**, 14201–14212 (2012)
90. W. Happer, H. Tang, Spin-exchange shift and narrowing of magnetic resonance lines in optically pumped alkali vapors. Phys. Rev. Lett. **31**, 273 (1973)
91. M.P. Ledbetter, I.M. Savukov, D. Budker, V. Shah, S. Knappe, J. Kitching et al., Zero-field remote detection of NMR with a microfabricated atomic magnetometer. Proc. Nat. Acad. Sci. USA **105**, 2286–2290 (2008)
92. C.N. Johnson, P.D.D. Schwindt, M. Weisend, Multi-sensor magnetoencephalography with atomic magnetometers. Phys. Med. Biol. **58**, 6065–6077 (2013)
93. M.V. Romalis, H.B. Dang, Atomic magnetometers for materials characterization. Mater. Today **14**, 258–262 (2011)
94. V. Shah, M.V. Romalis, Spin-exchange relaxation-free magnetometry using elliptically polarized light. Phys. Rev. A **80**, 013416 (2009)
95. R. Jiménez-Martínez, S. Knappe, J. Kitching, An optically modulated zero-field atomic magnetometer with suppressed spin-exchange broadening. Rev. Sci. Instrum. **85**, 045124 (2014)
96. P.D.D. Schwindt, A. Colombo, T. Carter, Y.-Y Jau, C.W. Berry, J. McKay et al., in *Development of an Optically Pumped Atomic Magnetometer Array for Magnetoencephalography.* 2015 Joint Conference of the IEEE International Frequency Control Symposium & European Frequency and Time Forum, Denver (2015)
97. K. Kim, S. Begus, H. Xia, S.-K. Lee, V. Jazbinsek, Z. Trontelj et al., Multi-channel atomic magnetometer for magnetoencephalography: a configuration study. NeuroImage **89**, 143–151 (2014)
98. E.A. Donley, J.L. Long, T.C. Liebisch, E.R. Hodby, T.A. Fisher, J. Kitching, Nuclear quadrupole resonances in compact vapor cells: the crossover between the NMR and the nuclear quadrupole resonance interaction regimes. Phys. Rev. A **79**, 013420 (2009)
99. R. Jiménez-Martínez, D.J. Kennedy, M. Rosenbluh, E.A. Donley, S. Knappe, S.J. Seltzer et al., Optical hyperpolarization and NMR detection of 129Xe on a microfluidic chip. Nat Commun **5**, 3908 (2014)
100. T.G. Walker, W. Happer, Spin-exchange optical pumping of noble-gas nuclei. Rev. Mod. Phys. **69**, 629–642 (1997)
101. E.A. Donley, in *Nuclear Magnetic Resonance Gyroscopes.* 2010 IEEE Sensors, pp. 17–22 (2010)
102. J. Rutkowski, W. Fourcault, F. Bertrand, U. Rossini, S. Getin, O. Lartigue et al., in *Towards a Miniature Atomic Scalar Magnetometer Using Liquid Crystal Polarization Rotator.* The 17th International Conference on Solid-State Sensors, Actuators and Microsystems (TRANSDUCERS & EUROSENSORS XXVII), 2013 Transducers & Eurosensors XXVII. pp. 705–708 (2013)
103. M.-C. Corsi, E. Labyt, W. Fourcault, C. Gobbo, F. Bertrand, F. Alcouffe et al., Detecting Mcg Signals from a Phantom with a 4He Magnetometer (Biomag, Halifax, Canada, 2014)
104. M.P. Ledbetter, C.W. Crawford, A. Pines, D.E. Wemmer, S. Knappe, J. Kitching et al., Optical detection of NMR J-spectra at zero magnetic field. J. Magn. Reson. **199**, 25–29 (2009)
105. T. Theis, P. Ganssle, G. Kervern, S. Knappe, J. Kitching, M.P. Ledbetter et al., Parahydrogen-enhanced zero-field nuclear magnetic resonance. Nat. Phys. **7**, 571–575 (2011)
106. T. Scholtes, V. Schultze, R. Ijsselsteijn, S. Woetzel, H.G. Meyer, Light-narrowed optically pumped Mx magnetometer with a miniaturized Cs cell. Phys. Rev. A **84**, 043416 (2011)
107. H. Clevenson, M.E. Trusheim, C. Teale, T. Schroder, D. Braje, D. Englund, Broadband magnetometry and temperature sensing with a light-trapping diamond waveguide. Nat. Phys. **11**, 393–397 (2015)
108. D.D. Awschalom, J.R. Rozen, M.B. Ketchen, W.J. Gallagher, A.W. Kleinsasser, R.L. Sandstrom et al., Low-noise modular microsusceptometer using nearly quantum limited dc SQUIDs. Appl. Phys. Lett. **53**, 2108–2110 (1988)

109. D. Drung, S. Bechstein, K.-P. Franke, M. Scheiner, T. Schurig, Improved direct-coupled dc SQUID read-out electronics with automatic bias voltage tuning. IEEE Trans. Appl. Supercond. **11**, 880–883 (2001)
110. K. Fang, V.M. Acosta, C. Santori, Z. Huang, K.M. Itoh, H. Watanabe et al., High-sensitivity magnetometry based on quantum beats in diamond nitrogen-vacancy centers. Phys. Rev. Lett. **110**, 130802 (2013)
111. M.I. Faley, U. Poppe, R.E. Dunin-Borkowski, M. Schiek, F. Boers, H. Chocholacs et al., High-Tc DC SQUIDs for Magnetoencephalography. Appl. Supercond. IEEE Trans. **23**, 1600705 (2013)
112. J. Gallop, SQUIDs: some limits to measurement. Supercond. Sci. Technol. **16**, 1575 (2003)
113. M. Pannetier, C. Fermon, G. Le Goff, J. Simola, E. Kerr, Femtotesla magnetic field measurement with magnetoresistive sensors. Science **304**, 1648–1650 (2004)
114. S. Marauska, R. Jahns, C. Kirchhof, M. Claus, E. Quandt, R. Knöchel et al., Highly sensitive wafer-level packaged MEMS magnetic field sensor based on magnetoelectric composites. Sens. Actuators, A **189**, 321–327 (2013)
115. Y. Wang, J. Gao, M. Li, D. Hasanyan, Y. Shen, J. Li et al., Ultralow equivalent magnetic noise in a magnetoelectric Metglas/Mn-doped Pb(Mg1/3Nb2/3)O3-PbTiO3 heterostructure. Appl. Phys. Lett. **101**, 022903 (2012)
116. D. Robbes, Highly sensitive magnetometers—a review. Sens. Actuators, A **129**, 86–93 (2006)

Magnetometry with Nitrogen-Vacancy Centers in Diamond

Kasper Jensen, Pauli Kehayias and Dmitry Budker

Abstract This chapter covers magnetic sensing with nitrogen-vacancy (NV) defect centers in diamond. The NV center fundamentals are introduced and NV optically detected magnetic resonance techniques for dc and ac magnetic sensing are summarized. After reviewing some successful sensing applications, the advantages for using NV magnetometry, as well as some ongoing challenges, are enumerated.

1 Introduction

Magnetometers made with nitrogen-vacancy (NV) color centers in diamond are a recent addition to our collection of magnetometery tools. They are useful for magnetometry with high spatial resolution, are technically quite simple to use, work well in ambient conditions, and are a new system with many avenues for improvements and applications. These features have propelled much of the recent burst in NV magnetometer development in recent years, while ongoing work aims to extend the best achievable sensitivity and scope of their utility. This chapter provides an overview (including references to representative work) of NV basic

K. Jensen (✉)
Niels Bohr Institute, University of Copenhagen, Blegdamsvej 17,
2100 Copenhagen Ø, Denmark
e-mail: kjensen@nbi.dk

D. Budker
Department of Physics, University of California, Berkeley, CA 94720, USA
e-mail: dbudker@gmail.com

P. Kehayias
Harvard-Smithsonian Center for Astrophysics, Cambridge, MA 02138, USA
e-mail: pauli.kehayias@cfa.harvard.edu

D. Budker
Helmholtz-Institute Mainz, Johannes Gutenberg University, Mainz, Germany

A. Grosz et al. (eds.), *High Sensitivity Magnetometers*, Smart Sensors,
Measurement and Instrumentation 19, DOI 10.1007/978-3-319-34070-8_18

properties, magnetic sensing techniques, applications, and how NV centers fit into the broader scope of magnetometer technologies [1–4].

2 Physics of the NV Center

The NV center is a point defect in the diamond crystal lattice. It consists of a substitutional nitrogen atom and a neighboring vacancy, i.e. a missing carbon atom (Fig. 1). NV centers can have negative (NV^-), positive (NV^+), and neutral (NV^0) charge states, but NV^- is used for magnetometry and other applications. The NV^- center has six electrons. Five of the electrons are contributed from the dangling bonds of the three neighboring carbon atoms and the nitrogen atom. One extra electron is captured from an electron donor and gives rise to the negative charge state. The axis defined by the line connecting the nitrogen atom and the vacancy is called the NV axis. There are four possible ways that the nitrogen atom can be positioned with respect to the vacancy, leading to four possible NV alignments. The NV center has C_{3v} spatial point-group symmetry, i.e. its structure is symmetric with respect to rotations of 0, $2\pi/3$ and $4\pi/3$ around the NV axis and to reflections in the mirror planes defined by the NV axis and one of the three neighboring carbon atoms. We can construct the energy levels of NV^- using a linear combinations of atomic orbitals (LCAO) group-theoretical approach [5, 6]. Figure 2 shows an energy-level diagram for NV electronic spin-triplet states ($^3A_2$ and ^3E) and electronic spin-singlet states (^1E and $^1A_1$). The spin-triplet states each have three sublevels with magnetic quantum number $m = 0, \pm 1$ where the quantization axis is set by the NV axis.

The optical transition between $^3A_2$ and ^3E has a 637 nm wavelength (corresponding to red light) and the transition between ^1E and $^1A_1$ has a 1042 nm wavelength (corresponding to infrared light). Both transitions have phonon sidebands due to vibrations in the diamond lattice. These phonon sideband transitions broaden the NV absorption and fluorescence spectra by hundreds of nanometers.

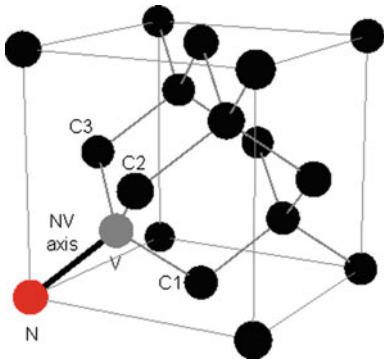

Fig. 1 Diamond crystal lattice with an NV center defect. The vacancy, nitrogen atom, and nearest-neighbor carbon atoms are labeled

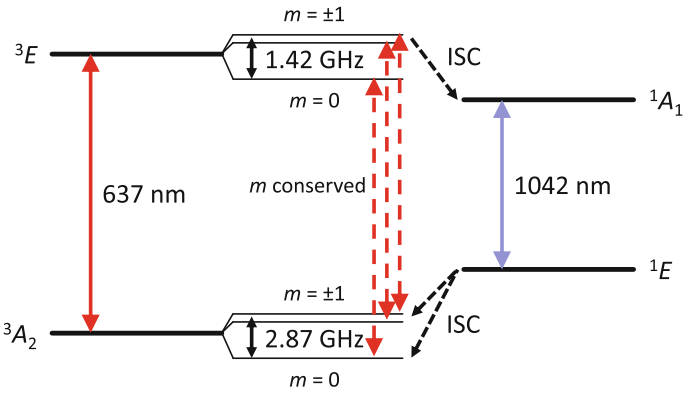

Fig. 2 NV electronic energy levels and optical transitions. The *m*-dependent intersystem crossing (ISC) from ^3E enables optical initialization and readout

The $^3A_2 \rightarrow {}^3E$ transition can be excited with light with wavelength from ~450 to 637 nm, and one typically uses a 532 nm diode-pumped solid state laser to drive this transition. The fluorescence from the $^3E \rightarrow {}^3A_2$ decay is in the 637 to ~800 nm wavelength range. The optical transitions are largely spin-conserving, but there is also an intersystem crossing (ISC) between the spin-singlet and spin-triplet states. There is non-radiative decay from ^3E to $^1A_1$, and the ISC rate is higher for the $m = \pm 1$ states than for the $m = 0$ state [7, 8]. There is also a non-radiative ISC from ^1E to $^3A_2$.

An important feature of the NV center is that it is possible to optically detect its spin state and optically pump it into the $m = 0$ sublevel. The mechanism for this is now described: assume the NV center is illuminated with resonant light that drives the $^3A_2 \rightarrow {}^3E$ transition. If the NV is initially in the $^3A_2, m = 0$ ground-state sublevel, it is excited to the $^3E, m = 0$ state as the optical transition is spin-conserving. The NV center decays back to the $^3A_2, m = 0$ sublevel, emitting fluorescence. This transition is cyclic and one detects a high fluorescence intensity when continuously illuminating the NV center. On the other hand, if the NV is initially in one of the $^3A_2$, $m = \pm 1$ ground-state sublevels, it is excited to the ^3E, $m = \pm 1$ states, which have a substantial probability to undergo ISC to the singlet states. From the $^1A_1$ state, the NV center first decays to the ^1E state, which has a 200 ns lifetime at room temperature [9]. Subsequently the NV center undergoes ISC to the $^3A_2$ state. Probabilistically, the NV center ends up in the $m = 0$ cycling transition after several excitation cycles, after which we say that the NV center has been optically pumped to the $m = 0$ state. When initially in one of the $^3A_2$, $m = \pm 1$ sublevels, an NV center emits less fluorescence from the $^3E \rightarrow {}^3A_2$ transition as it decays (largely nonradiatively) through the singlet states. By measuring fluorescence, one can read out the NV spin state from its fluorescence intensity.

The spin-triplet $^3A_2$ ground state is of particular importance. This state has a zero-field-splitting $D \approx 2.87$ GHz between the $m = 0$ and the $m = \pm 1$ sublevels

due to electron spin-spin interaction. Magnetic fields couple to the NV center through the Zeeman effect, which is described by the Hamiltonian $\mathcal{H}_B = \gamma \mathbf{B} \cdot \mathbf{S}$ (in units of hertz). Here, $\mathbf{S}$ is the dimensionless spin-projection operator for the NV electronic spin and $\gamma \approx 28.0$ GHz/T is the electron gyromagnetic ratio. If a magnetic field $\mathbf{B} = B_z \hat{\mathbf{z}}$ is aligned along the NV axis here chosen as the z direction, the energies of the m-sublevels are $E(m) = Dm^2 + \gamma B_z m$ (Fig. 3). Note that the energies of the $m = \pm 1$ sublevels depend linearly on the magnetic field. NV magnetometry is based on optical detection of this energy shift. The energies of the magnetic resonance transitions $m = 0 \leftrightarrow \pm 1$ are $\Delta E = D \pm \gamma B_z$, which are shown in Fig. 3 in frequency units as $f_\pm$. More generally, the vector magnetic field can be determined from these resonance frequencies.

The NV center has hyperfine structure due to the nuclear spin of the nitrogen atom. Nitrogen has two stable isotopes, ^{14}N (99.6 % natural abundance) with nuclear spin 1 and ^{15}N (0.4 % natural abundance) with nuclear spin 1/2. The nuclear spin state contributes additional terms to the Hamiltonian, written here in units of hertz as $\mathcal{H}_\mathcal{I} = PI_z^2 + \gamma_N \mathbf{B} \cdot \mathbf{I}$ and $\mathcal{H}_{\text{hf}} = A_\parallel S_z I_z + A_\perp (S_x I_x + S_y I_y)$, where $\mathbf{I}$ is the dimensionless spin-projection operator for the nuclear spin. When considering an ^{14}N nucleus, $P \approx -4.95$ MHz is the quadrupole splitting, $\gamma_N \approx 3.077$ MHz/T is the nuclear gyromagnetic ratio, and $A_\parallel \approx -2.16$ MHz and $A_\perp \approx -2.7$ MHz are the parallel and perpendicular hyperfine coupling parameters, respectively [10–12]. The nuclear Zeeman term $\gamma_N \mathbf{B} \cdot \mathbf{I}$ is usually small and can often be neglected. Due to the hyperfine coupling with the ^{14}N nuclear spin, each of the magnetic resonances f_+ and f_- will split into three transitions which conserve m_I. The hyperfine splittings can be observed in magnetic resonance spectra if the resonance linewidth is narrower than the splitting [13].

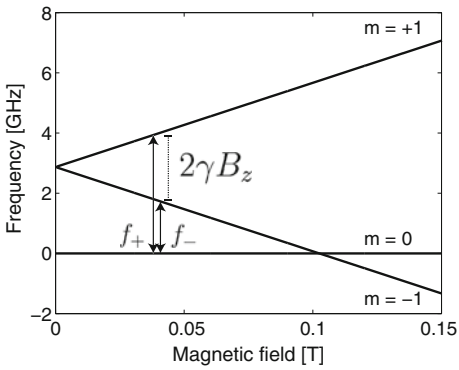

Fig. 3 Energy-level diagram for an NV center as a function of magnetic field when the magnetic field is aligned along the NV axis. The $m = 0 \leftrightarrow +1$ and $m = 0 \leftrightarrow -1$ transition frequencies are written as f_+ and f_-, respectively

3 Diamond Materials

Although natural diamonds can contain NV centers and other defects [14], one usually uses synthetic diamonds in order to have a better understanding of what the samples contain and to have a controlled and reproducible manufacturing method. There are several types of NV experiments that require different samples:

- NV ensemble experiments, where one interrogates many NV centers in a sample. The NV centers could be located in a thin sheet in the diamond or they could be distributed over a larger volume (throughout the entire diamond).
- Single-NV experiments, which use a diamond sample with few defects. One selects a particular NV with which to make measurements.
- NV nanodiamond experiments, which use nanodiamonds containing one or many NV centers. The nanodiamonds can be attached to atomic force microscopy (AFM) cantilevers, trapped in optical dipole traps, or functionalized and put into living cells [15–17].

There are several ways to manufacture diamond samples to suit these experimental requirements:

- High-pressure high-temperature (HPHT) growth, which is similar to natural diamond formation and is done in an anvil press at 5 GPa and 1700 K. After a solvent metal dissolves the carbon in a source graphite block, the carbon precipitates onto a seed crystal, which then grows. This growth technique yields samples with $\sim$100 ppm of nitrogen.
- Chemical vapor deposition (CVD), where diamond is grown layer-by-layer in a gaseous environment. CVD growth produces samples with fewer nitrogen impurities (roughly 1 ppb to 1 ppm).
- Explosives detonation, which produces nanodiamonds with high nitrogen and NV densities.

HPHT and CVD growth can yield a variety of diamond qualities, such as polycrystalline, monocrystalline, optical-grade (with minimal birefringence and absorption), and electronic-grade diamond (with minimal impurity concentration). With a given manufacturing technique, one has further control over how NV centers are formed:

- During HPHT and CVD growth, one can control the nitrogen concentration in the growth environment, though most embedded nitrogen atoms do not form NV centers. These samples can be used as-is (for instance, in a single-NV experiment), but they are often irradiated or implanted to improve the NV density.
- One can bombard diamond samples with electrons, protons, neutrons, N^+, N_2^+, C^+, or other particles to create vacancies and implant nitrogen. Varying the energy and species of the accelerated particles can create a uniform or near-surface defect layer. After creating vacancies, the NV density is not much

improved as the N and V locations are uncorrelated, but annealing the diamond samples after irradiation increases the NV yield. Annealing temperatures range from 700 to 1200 °C for several hours.

- The NV centers in an ensemble are usually randomly aligned, with 1/4 aligned along each crystallographic axis. However, CVD growth along certain crystallographic directions can create NV centers with preferential alignment, resulting in NV centers with primarily one or two alignments [18]. This is useful for NV ensemble magnetometry, where one might select NV centers with one alignment for sensing while the others contribute to background fluorescence.
- Delta doping is another technique for creating a nitrogen-doped layer during CVD growth. Nitrogen gas is introduced during slow CVD growth to embed a thin nitrogen layer in an otherwise pure diamond. Followed by irradiation and annealing, this can yield an NV layer (usually near the surface). To form the doped layer, ^{15}N is often added to the diamond growth environment to distinguish the near-surface NV centers from the deeper (^{14}N) NV centers. Delta doping ensures that CVD samples have few NV centers except near the surface, where they are most useful for sensing external fields. One can also use delta doping to create NV layers with known relative separations [19, 20].
- Bulk diamond samples can be turned into nanodiamonds by ball milling or chemical etching [21, 22].
- Diamond samples can be chemically etched to make diamond nanostructures, including optical waveguides, resonators, photonic crystals, or atomic force microscope (AFM) cantilevers [15, 23, 24].

4 Microscopy

One frequently optically probes NV centers with confocal microscopy setups, which are also used to characterize samples in biology and materials science. As shown in Fig. 4, a pump laser beam (often from a 532 nm solid-state laser) reflects off a dichroic mirror (which selectively reflects short optical wavelengths but transmits long wavelengths), is focused through a lens or microscope objective, and illuminates the diamond containing NV centers. The fluorescence from the NV centers is collected through the same lens, then passes through the dichroic mirror and onto a photodetector. A pinhole is used to filter out fluorescence from regions in the sample which are out of focus. NV confocal microscopy is used in several contexts:

- One can focus the pump laser beam onto the diamond and query a diffraction-limited volume of NV centers by measuring the collected fluorescence intensity with a single-pixel photodiode. One can sweep the interrogated volume by using scanning galvenometer mirrors or a piezo-driven objective or sample mount to obtain a wide-field image one pixel at a time [25].

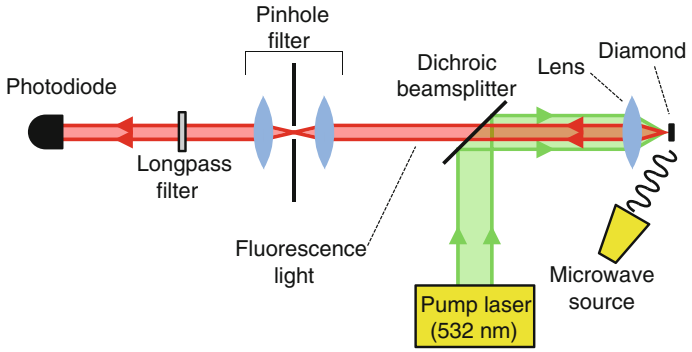

Fig. 4 A typical confocal microscopy setup for experiments with NV centers in diamond

- Another option for wide-field imaging is to instead illuminate a wide area on the diamond and image the fluorescence with a camera. This enables diffraction-limited spatial resolution (<1 μm) for imaging individual NV centers or mapping the magnetic field over a spatial region [26]. This can be extended using sub-diffraction-limited imaging to few-nm resolution [27].
- One can use diamonds and NV centers in scanning-probe microscopy (such as AFM) and use optical readout to query the NV centers. This yields few-nm spatial resolution [15, 28]. A microscope objective collects fluorescence light from a diamond AFM probe containing an NV center, and moving the probe interrogates different spatial regions without significantly affecting the light collection. A diamond nanopillar probe can also enhance the light collection by directing fluorescence light to the objective.

While magnetometers based on NV centers in diamond are currently less sensitive than other technologies such as SQUID magnetometers and vapor cell magnetometers, the high spatial resolution is their main advantage. Confocal microscopy is quite universal in experiments with NV centers, though work is ongoing to overcome its primary sensitivity limitation which is photon shot noise (see Eq. 2) due to poor fluorescence collection efficiency [29–31].

5 Light Detection and Collection

Photon shot noise of the detected NV fluorescence often limits the magnetic field sensitivity. It is therefore important to detect NV fluorescence efficiently; however, one is only able to collect a fraction of the light emitted. This problem is quite severe, as the NV centers are inside the diamond host material which has a high index of refraction ($n_d \approx 2.419$). The first issue is that only part of the light exiting the diamond is collected by the microscope objective (or lens) in a confocal microscope. The collection efficiency depends on the numerical aperture *NA* of the

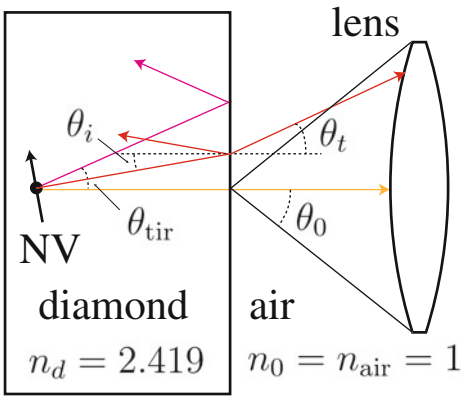

Fig. 5 NV fluorescence refraction and reflection at a diamond-air interface

objective, which is defined as $NA = n_0 \sin(\theta_0)$, where θ_0 is the maximum half-angle from which the objective can collect light and n_0 is the index of refraction outside the diamond (Fig. 5). For a given NA, light is collected within the angle $\theta_0 = \arcsin(NA/n_0)$. The numerical aperture typically ranges from 0.1 to 1 for air objectives and up to ~ 1.52 for oil-immersion objectives. The upper limit for NA is given by the index of refraction of either the air ($n_{\text{air}} \approx 1$) or the oil ($n_{\text{oil}} \approx 1.52$). There is also fluorescence refraction inside the diamond at the diamond interface. By Snell's law [$n_d \sin(\theta_i) = n_0 \sin(\theta_t)$], only light emitted within the angle $\theta_i^{\max} = \arcsin(NA/n_d)$ can exit the diamond and be collected by the objective. The maximum emission angles are $\theta_i^{\max} \approx 24^\circ$ and 39° for the best air ($NA = 1$) and oil-immersion objectives ($NA = 1.52$).

The second issue is that there are reflections of the emitted light from the diamond surface. As an example, for normal incidence the reflectance is $R = |(n_d - n_0)/(n_d + n_0)|^2$ using the Fresnel equations, which yields $R \approx 17\,\%$ at a diamond-air interface and $R \approx 5\,\%$ at a diamond-oil interface. As mentioned above, there is also total internal reflection at the diamond surface when $\theta_i \geq \theta_{\text{tir}} = \arcsin(n_0/n_d)$. The total collection efficiency of the light emitted from an NV center can be calculated taking the emission pattern of the NV center dipole into account (since the reflectance depends on the light polarization). The maximum collection efficiency is 4 or 10 % using either air (up to $NA = 1$) or oil-immersion objectives (up to $NA = 1.52$) [29].

There are several strategies for improving light collection efficiency. In Ref. [29] it was realized that when NV centers are excited from the top of a diamond plate, most of the fluorescent light undergoes multiple total internal reflections before it leaves the diamond plate at the sides perpendicular to the top. By placing photodiodes close to the four sides, a total of 47 % of the emitted fluorescence was collected. Other schemes use a solid-immersion lens (SIL), including lenses made from diamond [32, 33]. With this geometry, light emitted in the center of the SIL will not undergo refraction at the diamond-air interface as the light rays are perpendicular to the surface, improving the collection efficiency. Nanofabricated

diamond waveguides can also direct the emitted fluorescence out of the diamond, also improving the collection efficiency [23].

The fluorescence collection problem can be circumvented by instead detecting absorption of a probe laser beam. So far, schemes based on absorption of 637 nm red light and 1042 nm infrared (IR) light (see transitions in Fig. 2) have been demonstrated [34–37]. Red and infrared probe light can have spin-state-dependent absorption, a fact we can use to measure the $^3A_2$ magnetic resonance frequencies. When detecting the NV centers using infrared absorption one can in principle have an arbitrarily large photon flux without causing extra decoherence to the NV centers, thereby reducing the photon shot noise limitation to the magnetometer sensitivity (see Eq. 2). The amount of IR absorption depends on the $^1E \rightarrow {}^1A_1$sun cross-section, the NV density, and the thickness of the diamond. The first IR magnetometry experiment [35] was done at cryogenic temperatures ($T \approx 75$ K), where the absorption cross section is larger than at room temperature [38]. A later experiment employed an external optical cavity, enhancing the absorption by two orders of magnitude and enabling room-temperature operation of the magnetometer [37].

Another detection scheme is based on ionizing the NV^- to NV^0 conditionally on the NV^- $^3A_2$ sublevel, then reading out the charge state using a 594 nm probe laser [30]. Since NV^- fluoresces when illuminated with 594 nm light while NV^0 does not, this spin-to-charge-state readout scheme has high contrast with many readout photons. Yet another approach is to detect spin-state dependent photocurrent, making photon collection unnecessary [39]. Finally, cryogenic single-NV experiments can use a high-contrast optical readout technique that probes different $^3A_2 \rightarrow {}^3E$ transitions [31].

6 Optically Detected Magnetic Resonance

Many of the techniques for NV magnetometry require a bias magnetic field of a certain amplitude and direction. Such static magnetic fields can be measured with the following continuous wave (CW) optically detected magnetic resonance (ODMR) technique.

Consider the typical confocal microscopy setup shown in Fig. 4 where 532 nm green light continuously illuminates the diamond sample. For simplicity, assume that the sample contains a single NV center within the confocal volume. The NV center is optically pumped into the $m = 0$ sublevel by the green light, and a high level of fluorescence from the NV center is detected. Simultaneously, microwave (MW) radiation is applied to the NV center. The MW frequency is scanned within a certain range containing the magnetic resonances. When the MW frequency is on resonance with one of the $m = 0 \leftrightarrow \pm 1$ transitions, the fluorescence level decreases since the MW field spoils the NV optical pumping, transferring NV centers to the $m = \pm 1$ sublevels which fluoresce less brightly. The associated spectrum showing the fluorescence intensity as a function of MW frequency is called an ODMR

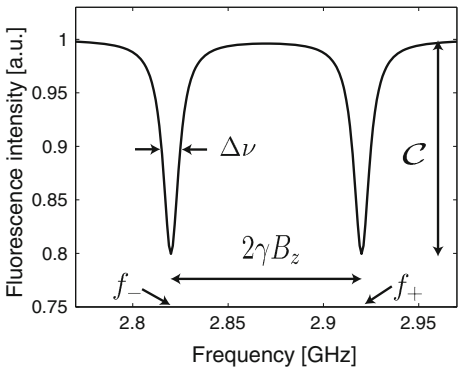

Fig. 6 Sketch of an optically-detected magnetic resonance spectrum for a single NV center. The magnetic field is assumed to be along the NV axis

spectrum and is sketched in Fig. 6. In this drawing, we assume that the magnetic field is pointing along the NV axis. The magnetic field amplitude can be determined from the resonance frequencies. The fractional difference in fluorescence intensity between MW on- and off-resonance is called the fluorescence contrast $\mathcal{C}$. For single NV centers, a $\mathcal{C} = 0.20$ contrast is typical. Another important parameter is the linewidth of the magnetic resonance $\Delta\nu$. The linewidth is related to the inhomogeneously-broadened transverse spin relaxation time $T_2^* = 1/(\pi\Delta\nu)$, which is ≈100 ns for NV centers in HPHT diamond material rich in nitrogen [13] and a few μs for NV centers in diamonds with low nitrogen concentration. In order to measure the transition frequencies and thereby the magnetic field accurately, it is advantageous to have a large contrast and a narrow linewidth.

If instead of a single NV center, one has an ensemble of NV centers in the confocal volume, there may be in total eight magnetic resonances due to the four possible alignments of the NV center. For certain directions of the magnetic field, some resonances are degenerate. Figure 7 shows an example ODMR spectrum with a bias magnetic field along an arbitrary direction. One option for NV magnetometry is to select one NV alignment by applying a bias field along the NV axis so that changes in the magnetic field projection along this axis affect the resonance frequencies approximately linearly. Another option is to use all four NV alignments; although the eight ODMR frequencies have more complicated dependence on **B**, this option yields vector information about the magnetic field.

7 DC Magnetometry

We will now discuss measurements of static or slowly-varying magnetic fields. To be more precise, with a dc magnetometer one can measure magnetic fields with frequency components from dc up to the bandwidth of the magnetometer (BW). The bandwidth can be measured by applying oscillating magnetic fields of increasing frequencies while recording the magnetometer response. The

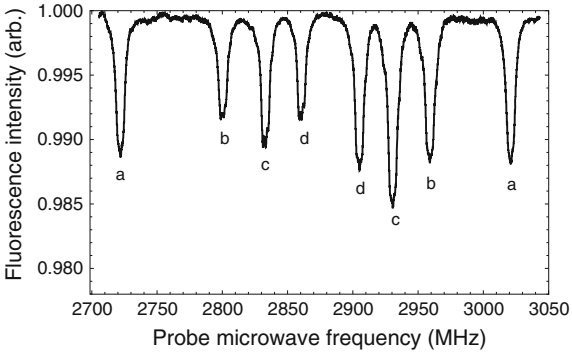

Fig. 7 An example ODMR plot with a magnetic field in an arbitrary direction. Each of the four NV alignments (labeled *a–d*) has a different magnetic field projection along its quantization axis, leading to eight ODMR peaks (two for each NV alignment). The ODMR frequencies are linear with **B** when aligned along the NV axis. Although the ODMR frequencies have more complicated dependence when **B** is along an arbitrary direction, we can extract the **B** vector information by using multiple NV alignments. The asymmetry between the two peaks arising from the same alignment is due to differences in the applied microwave power

magnetometer signal decreases with increasing frequency, and the bandwidth is defined as the frequency where the signal has decreased by a factor of two. The signal-to-noise ratio (SNR) typically decreases with increasing frequency since the signal decreases. However, if the noise also decreases, it is possible to measure magnetic fields with frequencies above the BW with good SNR.

One way to measure the magnetic field is with CW ODMR. In this case, the MW frequency is scanned across the magnetic resonance within a certain time τ_{scan}. One can obtain a value for the magnetic field during each such time interval, and the bandwidth of the magnetometer will then be $\text{BW} \sim 1/\tau_{\text{scan}}$. Many microwave generators can only scan the frequency slowly ($\tau_{\text{scan}} \geq 10$ ms) such that the bandwidth will be small ($\text{BW} \leq 100$ Hz). The slow scan also makes the measurement sensitive to low-frequency technical noise or drifts in the experimental apparatus. Examples of noise sources include moving magnetic objects (cars, trains, elevators, and so on), 50/60 Hz magnetic fields from the line voltage, laser power fluctuations, fluctuations in the MW power or frequency, light polarization noise, temperature drifts, and so on. In order to make a sensitive measurement of the magnetic field, one can instead utilize a modulation technique. One possibility is to apply an oscillating magnetic field using an external coil and use lock-in detection [35]. Alternatively, one can modulate the microwave frequency [34, 37]. Many microwave generators have build-in frequency modulation (FM), making FM an easy approach to implement.

Consider the case depicted in Fig. 8 where the microwave frequency is modulated with the frequency f_{mod} around a central value f_c. The maximum excursion from the center frequency is called the frequency deviation f_{dev}. The center frequency should be chosen to be close to one of the magnetic resonance frequencies,

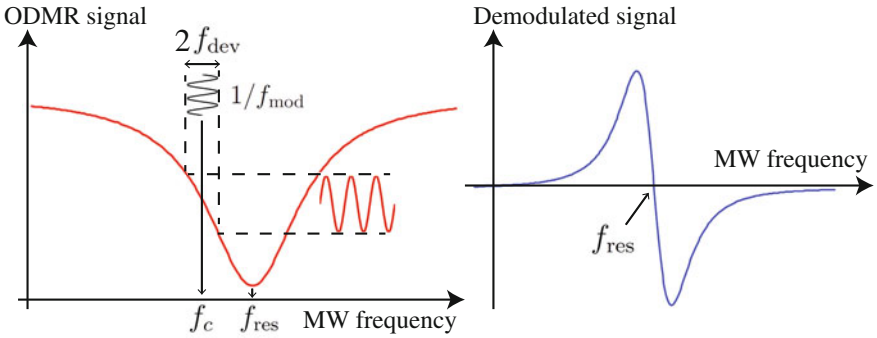

Fig. 8 *Left* Optically detected magnetic resonance signal. The MW frequency is modulated at the frequency f_{mod} around the central value f_c with a certain frequency deviation f_{dev}. *Right* The demodulated signal has a dispersive lineshape when sweeping the central frequency

here assumed to be the $m = 0 \rightarrow -1$ transition shown in Fig. 6. The detected fluorescence signal is then demodulated by a lock-in amplifier referenced to the modulation frequency. The demodulated signal S_{LI} has a dispersive lineshape with a zero crossing at $f_c = f_{res}$ and is linear $S_{LI} \approx \alpha(f_c - f_{res})$, where α is a proportionality constant, when $f_c - f_{res}$ is well within the linewidth of the magnetic resonance Δv. The demodulated signal can be used to measure slowly-varying magnetic fields $B(t) = B_0 + \Delta B(t)$, where B_0 is defined by the set value of the center frequency by the formula $f_c = D - \gamma B_0/(2\pi)$. The demodulated signal is linear in the magnetic field deviation $\Delta B(t) = -2\pi S_{LI}(t)/(\alpha\gamma)$ and therefore provides a good measure for $\Delta B(t)$. The magnetometer bandwidth depends on the optical pump power and the microwave power, and for high powers a bandwidth as large as a few MHz has been demonstrated [40]. The maximum achievable bandwidth will in the end be limited by the lifetime of the metastable singlet state (≈200 ns at room temperature).

Methods from atomic clock technology can be used to make a pulsed NV magnetometer for dc magnetic fields (Fig. 9), a complementary technique to the CW methods described above. One way to implement this is to initialize the NV centers to the $m = 0$ sublevel, switch off the pump laser, apply a frequency-dependent microwave π-pulse to interrogate the $m = 0 \rightarrow +1$ or $m = 0 \rightarrow -1$ resonance frequency, and read out the final-state fluorescence with a second laser pulse. Similar to CW magnetometry, the microwave π-pulse duration

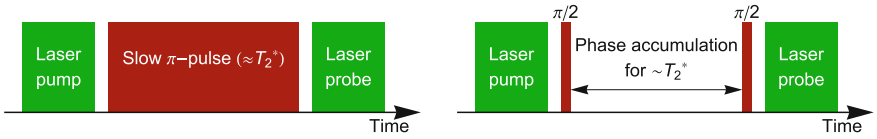

Fig. 9 Pulse sequences for ODMR experiments using a resonant π-pulse (*left*) or Ramsey spectroscopy (*right*)

τ_π and the inhomogeneously-broadened transverse spin relaxation time (T_2^*) contribute to the linewidth. A longer π-pulse has a narrower Fourier width, but excites fewer NV centers; choosing $\tau_\pi = T_2^*$ yields the best sensitivity [41]. Alternatively, one can measure the ODMR frequency with Ramsey interferometry, using two short $\pi/2$-pulses separated by an interaction time ($\approx T_2^*$) to accumulate magnetic-field-dependent phase, which one can read out to extract the magnetic field.

8 AC Magnetometry

An ac magnetometer is sensitive to synchronized magnetic fields or asynchronized magnetic noise within a narrow bandwidth around a specific frequency. This is in contrast to a dc magnetometer which is sensitive to frequency components from dc up to the bandwidth of the sensor. ac magnetometry with NV centers is inspired by nuclear magnetic resonance (NMR) techniques where pulse sequences (called dynamical decoupling, or DD) of microwave or radio-frequency radiation are used to remove magnetic inhomogeneity and extend coherence lifetime (one example is Hahn echo). Decoupling sequences can extend the T_2^* coherence time to a considerably longer T_2 coherence time (2 ms at room temperature and 0.6 s at 77 K), though this is easiest to achieve in ^{13}C-depleted diamond samples with few defects [42, 43]. Though designed to remove ac and dc inhomogeneity in NMR, DD pulse sequences are sensitive to ac magnetic fields (and can act as band-pass filters or lock-in detectors). Decoupling sequences can be used to sense coherent ac fields and incoherent ac fields (magnetic noise) at kHz-MHz frequencies.

Figure 10 illustrates how a DD sequence (Hahn echo in this case) is useful for ac magnetometry. After initializing the NV centers to an equal superposition of two Zeeman sublevels with the first $\pi/2$-pulse, the ac magnetic field (with frequency f_{AC} and period T_{AC}) with projection along the NV axis (B_{AC}) induces faster or slower Larmor precession, depending on its instantaneous sign. By choosing the pulse

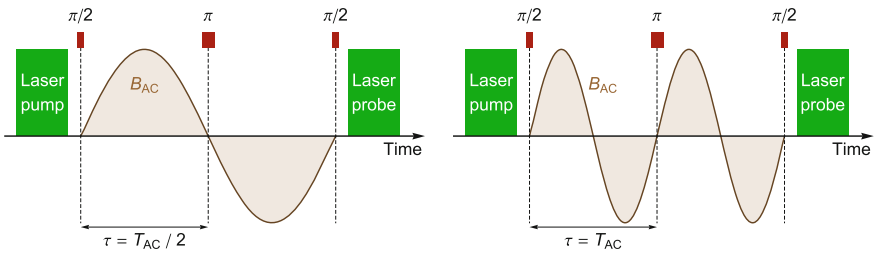

Fig. 10 *Left* The π-pulse allows us to keep the absolute value of the phase accumulation from B_{AC}. When sensing noise, this is how you get the most decoherence. *Right* Here, $\tau = T_{AC}$, and the phase accumulation cancels regardless of the relative phase and amplitude. This makes the NV centers immune to magnetic noise at f_{AC}, restoring coherence for this choice of τ (ESEEM)

spacing $\tau = T_{AC}/2$ and synchronizing the experiment and the ac magnetic field, one can maximize the phase accumulation the NV centers acquire from B_{AC}. Decoupling sequences also enable asynchronous ac magnetic noise detection. Choosing $\tau = T_{AC}/2$ also spoils the NV coherence if there is strong magnetic noise at f_{AC}, while choosing $\tau = T_{AC}$ makes the NV coherence immune to magnetic noise with frequency f_{AC}. This phenomenon is called electron spin echo envelope modulation (ESEEM) in electron paramagnetic resonance and is often used to sense and identify nearby magnetic nuclei [44]. Figure 11 shows some example measurements of ac magnetic noise detected with NV ensembles. The diamond samples contain a natural abundance of 1.1 % ^{13}C nuclear spins, which when located in a magnetic field will precess with the frequency of ≈ 10.705 MHz/T, leading to collapses and revivals in the NV coherence as the time τ is varied. The plot on the right includes data from an experiment with an externally-applied 707 kHz magnetic field from a function generator. The external field was not synchronized with the MW pulses and further spoiled the NV coherence for particular τ.

NV centers can also be used to sense incoherent nuclear and paramagnetic ac magnetic fields with other detection schemes. Correlation spectroscopy is a technique that extends DD sensing with some added benefits. It uses two DD sequences (separated by a time $\tilde{\tau}$) that each accumulate phase from an ac magnetic field [45]. This enables us to study the phase correlations in a nuclear spin bath with $\approx T_1^{-1}$ frequency resolution (instead of $\approx T_2^{-1}$ for DD). Another scheme is double electron-electron resonance (DEER), which can sense electronic spins using simultaneous NV and electronic π-pulses [28]. Similarly, one can detect NV decoherence when driving NV Rabi oscillations at a frequency that matches the desired ac frequency (a method called spin-locking) or driving both the NV centers and a target spin at the same Rabi frequency (called Hartmann-Hahn double resonance) [46, 47]. The resulting NV decoherence indicates the presence of an ac

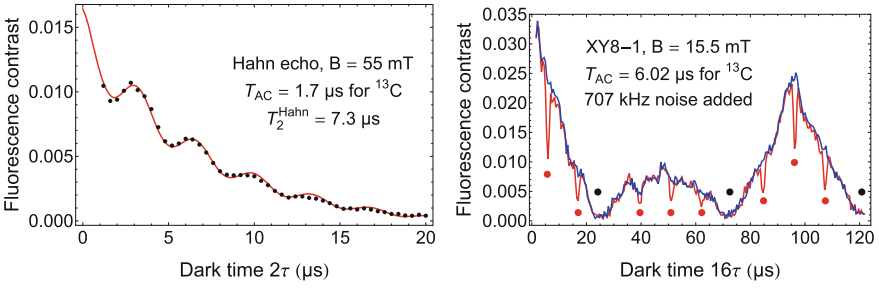

Fig. 11 *Left* Results of a Hahn echo experiment with an HPHT sample ($\sim$1 ppm NV^- concentration), showing the ESEEM coherence revivals caused by ^{13}C nuclei. *Right* Results of an XY8-1 experiment (another DD sequence with eight π-pulses) with a CVD sample ($\sim$10 ppb NV^- concentration). The *blue* data show how the NV coherence is most strongly spoiled by ^{13}C magnetic noise for dark times indicated by the *black circles*. The *red* data show the same experiment with an externally-applied (unsynchronized) 707 kHz magnetic field, which further spoils the coherence for dark times indicated by the *red circles*

magnetic field. One can also use NV T_1 measurements to detect paramagnetic spins or GHz-frequency magnetic white noise, as these sources spoil the NV T_1 lifetime [48–52].

9 Magnetic Field Sensitivity

The magnetic field sensitivity (in units of $\mathrm{T}/\sqrt{\mathrm{Hz}}$) describes the smallest change in magnetic field one can detect with a measurement bandwidth of 1 Hz. For a given measurement time τ_m, the measurement bandwidth is approximately $1/(2\tau_m)$; the exact numerical factor depends on the details of the measurement. For simplicity, we assume here that the magnetometer has a 100 % duty cycle and that the sensitivity equals $\delta B\sqrt{\tau_m}$, where δB is the uncertainty on the measured magnetic field. Notice that if the measurement is repeated N times in a duration $T = N\tau_m$, the uncertainty will decrease by a factor of $\sqrt{N}$ if the noise in the N measurements is uncorrelated. However, the sensitivity does not depend on the number of averages as the measurement time increases accordingly.

There are certain quantum limits to the sensitivity of an NV magnetometer. The most fundamental limit is due to the spin projection noise associated with the finite number of NV centers queried. The spin projection noise limited sensitivity is

$$\delta B_{\mathrm{PN}}\sqrt{\tau_m} \approx \frac{1}{\gamma\sqrt{N_{\mathrm{NV}}T_2}}, \tag{1}$$

where δB_{PN} is the magnetic field uncertainty due to the spin projection noise, γ is the electron gyromagnetic ratio, N_{NV} is the number of NV centers in the ensemble, and T_2 is the coherence time. The projection-noise limit can only be surpassed if one uses quantum entanglement of the sensing spins [53].

The photon shot noise of the light used to read out the NV spin state also limits the magnetic field sensitivity. This photon shot noise limited sensitivity is given by

$$\delta B_{\mathrm{SN}}\sqrt{\tau_m} \approx \frac{\Delta v}{\gamma\mathcal{C}\sqrt{\mathcal{R}}}, \tag{2}$$

where δB_{SN} is the magnetic field uncertainty due to the photon shot noise, $\mathcal{R}$ is the rate of detected photons, Δv is the FWHM of the magnetic resonance, and $\mathcal{C}$ is the contrast. The FWHM is related to the coherence time by the equation $T_2 = 1/(\pi\Delta v)$. The rate of detected photons can be calculated from the detected power $\mathcal{R} = P/(hc/\lambda)$, where P is the power, h is Planck's constant, c the speed of light, and λ is the wavelength of the detected light. Since the overall magnetometer signal S increases linearly with the rate of detected photons $S \propto \mathcal{R}$, and the uncertainty ΔS due to the photon shot noise increases only as the square-root $\Delta S \propto \sqrt{\mathcal{R}}$, the sensitivity improves as $\Delta S/S \propto \sqrt{\mathcal{R}}/\mathcal{R} = 1/\sqrt{\mathcal{R}}$.

The shot-noise-limited sensitivity and the projection-noise-limited sensitivity are in general different. However, under some conditions they can be of the same size. Consider an ensemble of NV centers continuously illuminated with pump light (as in a CW ODMR experiment). The excitation rate from the $^3A_2$ state to the ^3E state is denoted Γ_P. The rate of emitted fluorescence is approximately $N_{\mathrm{NV}}\Gamma_P$. The optimal excitation rate will be $\Gamma_P \approx 1/T_2$ as increasing the excitation rate beyond this will decrease the coherence time. Assuming that all the fluorescence is detected we find $\mathcal{R} \approx N_{\mathrm{NV}}/T_2$. Finally assuming 100 % contrast we calculate $\delta B_{\mathrm{SN}}\sqrt{\tau_m} \approx \delta B_{\mathrm{PN}}\sqrt{\tau_m}$. We note that in most realistic situations both the light detection efficiency and the contrast are much smaller than 100 %, such that the shot noise limited sensitivity is worse than the projection noise limited sensitivity.

The parameters used to calculate spin projection noise and photon shot noise vary drastically depending on the experiment and diamond sample. The coherence time is generally longer for ac magnetometers compared to dc magnetometers, as the T_2 time obtained using Hahn echo or dynamical decoupling techniques can be much longer than the T_2^* time relevant for dc magnetometers. The coherence times T_2^* and T_2 also depend strongly on the diamond material and the particular DD sequence used. The rate of detected photons depends on the number of NV centers in the probed volume, the input pump power, and the light detection efficiency, which is typically quite low (a few percent) for a confocal setup. The number of NV centers used depends on the size of the probed volume and on the NV density, which depends on the diamond material and on the irradiation dose and annealing procedure. Finally, the fluorescence contrast can be up to 20 % for a single NV center, while for ensembles of NV centers the contrast is typically much smaller due to background fluorescence.

There are several ways to assess magnetometer sensitivity experimentally. With a CW magnetometer, one can apply a constant field, measure this field continuously, and calculate the noise floor after taking the Fourier transform. With a pulsed magnetometer that reports discrete values, one can apply a constant field and calculate the standard deviation of the resulting magnetic field values (normalizing to 1 Hz bandwidth). A similar approach is to apply slightly different fields and determine how long it takes to distinguish them.

The highest sensitivities which have been demonstrated with an NV ensemble are 15 $\mathrm{pT}/\sqrt{\mathrm{Hz}}$ (dc sensing) and 1 $\mathrm{pT}/\sqrt{\mathrm{Hz}}$ (ac sensing) [54, 55]. The magnetometer sensitivity in Ref. [54] is nearly photon shot noise limited, though the spin projection noise is $\sim 10\ \mathrm{fT}/\sqrt{\mathrm{Hz}}$. There has been rapid progress in recent years on improving the magnetic field sensitivity of NV magnetometers, and with additional improvements sub-$\mathrm{pT}/\sqrt{\mathrm{Hz}}$ sensitivity will soon be achievable.

10 Applications

NV magnetometers are most appropriate for sensing applications requiring high spatial resolution, especially those where it is possible to put the NV centers close to the system being measured. As described above, NV centers can sense paramagnetic and nuclear spins a few nanometers away using T_1 and T_2 ac magnetometry schemes. NV T_1 relaxation is better suited for sensing GHz-frequency magnetic noise, which lends itself well to sensing paramagnetic spins and magnetic Johnson noise [48–52]. Since nuclei have 0.1–1 MHz Larmor precession at a few tens of millitesla, T_2 relaxation is useful for sensing magnetic nuclei (such as ^{1}H, ^{13}C, ^{19}F, ^{29}Si, and ^{31}P) [44, 56, 57, 58]. One eventual goal is to achieve single-molecule MRI, where an NV center can sense nearby magnetic nuclei and distinguish their positions, allowing us to reconstruct the structure of complex molecules such as proteins.

While many NV experiments seek new magnetic sensitivity limits or study a well-understood target system, the most exciting projects are those that use NV sensing in a new context. NV wide-field magnetic imaging examined 50 nm ferromagnetic grains in magnetotactic bacteria, 10–100 μm grains in meteorites, and immunomagnetically-labeled cancer cells [59–61]. Due to the high spatial resolution and non-toxicity of diamond, NV applications extend to neuroscience and biology. One experiment measured the magnetic field in a living cell to probe intracellular dynamics with nanodiamonds [17]. In neuroscience, NV magnetometers aim to sense the magnetic field from a firing neuron and study how neural networks form connections as they grow on a diamond [26, 54]. Soon NV magnetometry will enable NMR and MRI for molecules near the diamond surface. NV magnetometers have sensed the stray fields from magnetic domains in hard disk drives and show potential for characterizing read/write heads [15].

Finally, NV magnetometers are a promising tool for investigating magnetic phenomena in condensed-matter physics, such as the Meissner effect and magnetic flux vortices in superconductors [62]. NV AFM experiments have also examined domain walls and vortices in magnetic thin films [63, 64]. Another experiment used individual NV centers to study magnetic spin-wave excitations in a ferromagnetic microdisk [65]. NV magnetometers also show potential for investigating skyrmion, spin ice, and other exotic materials [3, 66]. Finally, NV decoherence measurements reveal information about the magnetic spin bath dynamics (for both nuclear and paramagnetic spins).

11 Advantages and Ongoing Challenges

As sensors, NV centers have unprecedented spatial resolution. The NV electronic wave function is constrained to a few atomic lattice sites ($\sim$0.5 nm) and the spatial resolution can be hundreds of nanometers when using diffraction-limited optics,

while optical superresolution techniques can do even better. An NV ensemble provides vector information about the magnetic field (instead of a projection). Furthermore, NV centers can work as simultaneous magnetic field, electric field, temperature, compression, and rotation sensors in the same device [67–72].

Another advantage is the technical simplicity of NV magnetometers. Often the pump laser is a common frequency-doubled 532 nm Nd:YAG laser, and high polarization and frequency stability are usually unnecessary (in contrast to other optical magnetometers). Furthermore, NV centers are easy to optically initialize and read out compared to other atomic physics systems. Other magnetic sensing technologies require specific environments (near-zero magnetic field, cryogenics, or ultra-high vacuum). Isolating the sensor in a cryogenic or vacuum environment separates it from the system being sensed, and with the additional distance comes reduced spatial resolution and reduced magnetic field from external sources. NV sensors are versatile and robust, allowing us to compensate for the lower magnetic field sensitivity by placing the NV centers a few nanometers away from the target, where the field is stronger. Most NV experiments are done in ambient conditions, though they also work at extreme pressures and temperatures [68, 73].

Many of these advantages come from the diamond material properties themselves. Diamond is chemically inert and biocompatible; living cells can rest on top of a diamond substrate and can uptake nanodiamonds without being poisoned. NV centers have long relaxation times at room temperature because of the strong carbon-carbon bonds in diamond, leading to a high Debye temperature ($\sim$2200 K [14]). With improvements in fabrication and implantation technology, one will be able to deterministically place NV centers in a diamond sample and fabricate diamond nanostructures (including diamond nanopillars) for increased light collection efficiency and for magnetometry with high spatial resolution.

Despite their advantages, NV centers have many technical challenges to overcome. Diamond has a high refractive index, so most of the fluorescence light emitted from an NV in a flat diamond is not collected in a confocal microscope. This means that despite the small spin-projection noise, NV experiments are instead limited by photon shot noise (or other noise sources), which is often many orders of magnitude larger. Inhomogeneous broadening is another problem; local magnetic fields and crystal strains broaden the ODMR resonances, reduce T_2^*, and diminish sensitivity. Using high-density samples with many NV centers may improve ensemble sensitivity, but this comes at the cost of more broadening from radiation damage, nitrogen defects, and crystal strain. Sample-dependent results also complicates development—diamond samples differ in crystal growth conditions, surface treatment, irradiation, NV depth, and impurity content. This makes some goals achievable only with certain samples, and one must study how to reproducibly produce desirable samples.

Compared to the atoms used in other optical magnetometers (Rb, Cs, He, and so on), which have well-understood basic properties (such as electronic configurations, transition frequencies, and electric dipole moments), NV centers are still not fully understood. The ${}^3A_2 \leftrightarrow {}^3E$ and ${}^1E \leftrightarrow {}^1A_1$ energies are known (Fig. 2), but the

relative triplet-singlet energies and their energies compared to the diamond valence and conduction bands are not known directly [74–76]. Similarly, the optical pumping mechanism, which all NV experiments take advantage of for initialization and readout, is not completely understood. Furthermore, although four of the six anticipated electronic states are experimentally confirmed, the remaining two have yet to be found.

NV magnetometers have some inconvenient limitations. Transverse crystal strain (which can be up to ~ 10 MHz) makes low-field magnetometry challenging. NV centers are also simultaneously a magnetometer and a thermometer, meaning uncompensated temperature drifts can be interpreted as changes in magnetic field. Querying both of the $m = 0 \leftrightarrow \pm 1$ transitions can mitigate this problem and cancel temperature drifts [77, 78]. Finally, although near-surface NV centers are best for sensing external magnetic fields, their properties (photostability and coherence time) deteriorate at shallower depths because of magnetic noise from unbonded electrons at the diamond surface [20].

12 Summary

It has only been a few years since NV-based sensors burst into the field of optical magnetometry, promising to revolutionize it with an unprecedented combination of high sensitivity and spatial resolution. While the technical challenges facing diamond sensors are substantial, the promise has already been fulfilled, largely through a plethora of novel applications that have become possible due to the unique properties of NV sensors. With the ongoing advances and ever-growing breadth of utility, we are sure this is only the beginning.

Acknowledgements We thank Victor Acosta, Yannick Dumeige, Demitry Farfurnik, Andrey Jarmola, and Nathan Leefer for insightful discussions and comments on the manuscript. Our research was supported in part by German-Israeli Project Cooperation (DIP) program, the NSF through grant No. ECCS-1202258, and the AFOSR/DARPA QuASAR program. K. J. acknowledges support from the Carlsberg Foundation.

References

1. R. Schirhagl, K. Chang, M. Loretz, C.L. Degen, Nitrogen-vacancy centers in diamond: nanoscale sensors for physics and biology. Annu. Rev. Phys. Chem. **65**(1), 83 (2014)
2. M.W. Doherty, N.B. Manson, P. Delaney, F. Jelezko, J. Wrachtrup, L.C.L. Hollenberg, The nitrogen-vacancy colour centre in diamond. Phys. Rep. **528**(1), 1 (2013)
3. L. Rondin, J.-P. Tetienne, T. Hingant, J.-F. Roch, P. Maletinsky, V. Jacques, Magnetometry with nitrogen-vacancy defects in diamond. Rep. Prog. Phys. **77**(5), 056503 (2014)
4. V.M. Acosta, D. Budker, P.R. Hemmer, J.R. Maze, R.L. Walsworth, Optical magnetometry with nitrogen-vacancy centers in diamond, in *Optical Magnetometry*, ed. by D. Budker, D.F. Jackson Kimball (Cambridge University Press, Cambridge, 2013), pp. 142–166

5. J.R. Maze, A. Gali, E. Togan, Y. Chu, A. Trifonov, E. Kaxiras, M.D. Lukin, Properties of nitrogen-vacancy centers in diamond: the group theoretic approach. New J. Phys. **13**(2), 025025 (2011)
6. M.W. Doherty, N.B. Manson, P. Delaney, L.C.L. Hollenberg, The negatively charged nitrogen-vacancy centre in diamond: the electronic solution. New J. Phys. **13**, 025019 (2011)
7. L. Robledo, H. Bernien, T. van der Sar, R. Hanson, Spin dynamics in the optical cycle of single nitrogen-vacancy centres in diamond. New J. Phys. **13**, 025013 (2011)
8. J.-P. Tetienne, L. Rondin, P. Spinicelli, M. Chipaux, T. Debuisschert, J.-F. Roch, V. Jacques, Magnetic-field-dependent photodynamics of single NV defects in diamond: an application to qualitative all-optical magnetic imaging. New J. Phys. **14**, 103033 (2012)
9. V.M. Acosta, A. Jarmola, E. Bauch, D. Budker, Optical properties of the nitrogen-vacancy singlet levels in diamond. Phys. Rev. B **82**, 201202 (2010)
10. S. Felton, A.M. Edmonds, M.E. Newton, P.M. Martineau, D. Fisher, D.J. Twitchen, J.M. Baker, Hyperfine interaction in the ground state of the negatively charged nitrogen vacancy center in diamond. Phys. Rev. B **79**, 075203 (2009)
11. B. Smeltzer, J. McIntyre, L. Childress, Robust control of individual nuclear spins in diamond. Phys. Rev. A **80**, 050302 (2009)
12. M. Steiner, P. Neumann, J. Beck, F. Jelezko, J. Wrachtrup, Universal enhancement of the optical readout fidelity of single electron spins at nitrogen-vacancy centers in diamond. Phys. Rev. B **81**, 035205 (2010)
13. V.M. Acosta, E. Bauch, M.P. Ledbetter, C. Santori, K.-M.C. Fu, P.E. Barclay, R.G. Beausoleil, H. Linget, J.F. Roch, F. Treussart, S. Chemerisov, W. Gawlik, D. Budker, Diamonds with a high density of nitrogen-vacancy centers for magnetometry applications. Phys. Rev. B **80**, 115202 (2009)
14. A.M. Zaitsev, *Optical Properties of Diamond: A Data Handbook* (Springer, New York, 2001)
15. P. Maletinsky, S. Hong, M.S. Grinolds, B. Hausmann, M.D. Lukin, R.L. Walsworth, M. Loncar, A. Yacoby, A robust scanning diamond sensor for nanoscale imaging with single nitrogen-vacancy centres. Nat. Nanotechnol. **7**, 320 (2012)
16. M. Geiselmann, M.L. Juan, J. Renger, J.M. Say, L.J. Brown, F.J.G. de Abajo, F. Koppens, R. Quidant, Three-dimensional optical manipulation of a single electron spin. Nat. Nanotechnol. **8**, 175 (2013)
17. L.P. McGuinness, Y. Yan, A. Stacey, D.A. Simpson, L.T. Hall, D. Maclaurin, S. Prawer, P. Mulvaney, J. Wrachtrup, F. Caruso, R.E. Scholten, L.C.L. Hollenberg, Quantum measurement and orientation tracking of fluorescent nanodiamonds inside living cells. Nat. Nanotechnol. **6**, 358 (2011)
18. M. Lesik, J.-P. Tetienne, A. Tallaire, J. Achard, V. Mille, A. Gicquel, J.-F. Roch, V. Jacques, Perfect preferential orientation of nitrogen-vacancy defects in a synthetic diamond sample. Appl. Phys. Lett. **104**(11), 113107 (2014)
19. K. Ohno, F.J. Heremans, L.C. Bassett, B.A. Myers, D.M. Toyli, A.C.B. Jayich, C. J. Palmstrom, D.D. Awschalom, Engineering shallow spins in diamond with nitrogen delta-doping. Appl. Phys. Lett. **101**(8), 082413 (2012)
20. B.A. Myers, A. Das, M.C. Dartiailh, K. Ohno, D.D. Awschalom, A.C. Bleszynski, Jayich. Probing Surface Noise with Depth-Calibrated Spins in Diamond. Phys. Rev. Lett. **113**, 027602 (2014)
21. L.-J. Su, C.-Y. Fang, Y.-T. Chang, K.-M. Chen, Y.-C. Yu, J.-H. Hsu, H.-C. Chang, Creation of high density ensembles of nitrogen-vacancy centers in nitrogen-rich type Ib nanodiamonds. Nanotechnology **24**(31), 315702 (2013)
22. P. Andrich, B.J. Aleman, J.C. Lee, K. Ohno, C.F. de las Casas, F.J. Heremans, E.L. Hu, D.D. Awschalom, Engineered micro- and nanoscale diamonds as mobile probes for high-resolution sensing in fluid. Nano Lett. **14**(9),4959 (2014)
23. B.J.M. Hausmann, T.M. Babinec, J.T. Choy, J.S. Hodges, S. Hong, I. Bulu, A. Yacoby, M.D. Lukin, M. Loncar, Single-color centers implanted in diamond nanostructures. New J. Phys. **13** (4), 045004 (2011)

24. M.J. Burek, Y. Chu, M.S. Z. Liddy, P. Patel, J. Rochman, S. Meesala, W. Hong, Q. Quan, M. D. Lukin, M. Loncar, High quality-factor optical nanocavities in bulk single-crystal diamond. Nat. Commun. **5** (2014)
25. J.R. Maze, P.L. Stanwix, J.S. Hodges, S. Hong, J.M. Taylor, P. Cappellaro, L. Jiang, M.V. Gurudev Dutt, E. Togan, A.S. Zibrov, A. Yacoby, R.L. Walsworth, M.D. Lukin, Nanoscale magnetic sensing with an individual electronic spin in diamond. Nature **455**, 644 (2008)
26. L.M. Pham, D. Le Sage, P.L. Stanwix, T.K. Yeung, D. Glenn, A. Trifonov, P. Cappellaro, P. R. Hemmer, M.D. Lukin, H. Park, A. Yacoby, R.L. Walsworth, Magnetic field imaging with nitrogen-vacancy ensembles. New J. Phys. **13**(4), 045021 (2011)
27. D. Wildanger, B.R. Patton, H. Schill, L. Marseglia, J.P. Hadden, S. Knauer, A. Schönle, J.G. Rarity, J.L. O'Brien, S.W. Hell, J.M. Smith, Solid immersion facilitates fluorescence microscopy with nanometer resolution and sub-angstrom emitter localization. Adv. Mater. **24** (44), OP309 (2012)
28. M.S. Grinolds, M. Warner, K. De Greve, Y. Dovzhenko, L. Thiel, R.L. Walsworth, S. Hong, P. Maletinsky, A. Yacoby, Subnanometre resolution in three-dimensional magnetic resonance imaging of individual dark spins. Nat. Nanotechnol. **9**, 279 (2014)
29. D. Le Sage, L.M. Pham, N. Bar-Gill, C. Belthangady, M.D. Lukin, A. Yacoby, R.L. Walsworth, Efficient photon detection from color centers in a diamond optical waveguide. Phys. Rev. B **85**, 121202 (2012)
30. B.J. Shields, Q.P. Unterreithmeier, N.P. de Leon, H. Park, M.D. Lukin, Efficient readout of a single spin state in diamond via spin-to-charge conversion. Phys. Rev. Lett. **114**, 136402 (2015)
31. L. Robledo, L. Childress, H. Bernien, B. Hensen, P.F.A. Alkemade, R. Hanson, High-fidelity projective read-out of a solid-state spin quantum register. Nature **477**, 574 (2011)
32. P. Siyushev, F. Kaiser, V. Jacques, I. Gerhardt, S. Bischof, H. Fedder, J. Dodson, M. Markham, D. Twitchen, F. Jelezko, J. Wrachtrup, Monolithic diamond optics for single photon detection. Appl. Phys. Lett. **97**, 241902 (2010)
33. J.P. Hadden, J.P. Harrison, A.C. Stanley-Clarke, L. Marseglia, Y.-L.D. Ho, B.R. Patton, J.L. O'Brien, J.G. Rarity, Strongly enhanced photon collection from diamond defect centers under microfabricated integrated solid immersion lenses. Appl. Phys. Lett. **97**, 241901 (2010)
34. V.M. Acosta, K. Jensen, C. Santori, D. Budker, R.G. Beausoleil, Electromagnetically induced transparency in a diamond spin ensemble enables all-optical electromagnetic field sensing. Phys. Rev. Lett. **110**, 213605 (2013)
35. V.M. Acosta, E. Bauch, A. Jarmola, L.J. Zipp, M.P. Ledbetter, D. Budker, Broadband magnetometry by infrared-absorption detection of nitrogen-vacancy ensembles in diamond. Appl. Phys. Lett. **97**, 174104 (2010)
36. Y. Dumeige, M. Chipaux, V. Jacques, F. Treussart, J.-F. Roch, T. Debuisschert, V. Acosta, A. Jarmola, K. Jensen, P. Kehayias, D. Budker, Magnetometry with nitrogen-vacancy ensembles in diamond based on infrared absorption in a doubly resonant optical cavity. Phys. Rev. B **87**, 155202 (2013)
37. K. Jensen, N. Leefer, A. Jarmola, Y. Dumeige, M. Acosta, V.P. Kehayias, B. Patton, D. Budker, Cavity-enhanced room-temperature magnetometry using absorption by nitrogen-vacancy centers in diamond. Phys. Rev. Lett. **112**, 160802 (2014)
38. P. Kehayias, M.W. Doherty, D. English, R. Fischer, A. Jarmola, K. Jensen, N. Leefer, P. Hemmer, N.B. Manson, D. Budker, Infrared absorption band and vibronic structure of the nitrogen-vacancy center in diamond. Phys. Rev. B **88**, 165202 (2013)
39. E. Bourgeois, A. Jarmola, P. Siyushev, M. Gulka, J. Hruby, F. Jelezko, D. Budker, M. Nesladek, Photoelectric detection of electron spin resonance of nitrogen-vacancy centres in diamond. Nat. Commun. **6**, 8577 (2015)
40. C.S. Shin, C.E. Avalos, M.C. Butler, D.R. Trease, S.J. Seltzer, J.P. Mustonen, D.J. Kennedy, V.M. Acosta, D. Budker, A. Pines, V.S. Bajaj, Room-temperature operation of a radiofrequency diamond magnetometer near the shot-noise limit. J. Appl. Phys. **112**(12), 124519 (2012)

41. A. Dréau, M. Lesik, L. Rondin, P. Spinicelli, O. Arcizet, J.-F. Roch, V. Jacques, Avoiding power broadening in optically detected magnetic resonance of single NV defects for enhanced dc magnetic field sensitivity. Phys. Rev. B **84**, 195204 (2011)
42. L.M. Pham, N. Bar-Gill, C. Belthangady, D. Le Sage, P. Cappellaro, M.D. Lukin, A. Yacoby, R.L. Walsworth, Enhanced solid-state multispin metrology using dynamical decoupling. Phys. Rev. B **86**, 045214 (2012)
43. N. Bar-Gill, L.M. Pham, A. Jarmola, D. Budker, R.L. Walsworth, Solid-state electronic spin coherence time approaching one second. Nat. Commun. **4**, 1743 (2012)
44. S.J. DeVience, L.M. Pham, I. Lovchinsky, A.O. Sushkov, N. Bar-Gill, C. Belthangady, F. Casola, M. Corbett, H. Zhang, M. Lukin, H. Park, A. Yacoby, R.L. Walsworth, Nanoscale NMR spectroscopy and imaging of multiple nuclear species. Nat. Nanotechnol. **10**, 129 (2015)
45. A. Laraoui, F. Dolde, C. Burk, F. Reinhard, J. Wrachtrup, C.A. Meriles, High-resolution correlation spectroscopy of ^{13}C spins near a nitrogen-vacancy centre in diamond. Nat. Commun. **4**, 1651 (2013)
46. C. Belthangady, N. Bar-Gill, L.M. Pham, K. Arai, D. Le Sage, P. Cappellaro, R.L. Walsworth, Dressed-state resonant coupling between bright and dark spins in diamond. Phys. Rev. Lett. **110**, 157601 (2013)
47. P. London, J. Scheuer, J.-M. Cai, I. Schwarz, A. Retzker, M.B. Plenio, M. Katagiri, T. Teraji, S. Koizumi, J. Isoya, R. Fischer, L.P. McGuinness, B. Naydenov, F. Jelezko, Detecting and polarizing nuclear spins with double resonance on a single electron spin. Phys. Rev. Lett. **111**, 067601 (2013)
48. A. Jarmola, V.M. Acosta, K. Jensen, S. Chemerisov, D. Budker, Temperature- and magnetic-field-dependent longitudinal spin relaxation in nitrogen-vacancy ensembles in diamond. Phys. Rev. Lett. **108**, 197601 (2012)
49. S. Steinert, F. Ziem, L.T. Hall, A. Zappe, M. Schweikert, N. Götz, A. Aird, G. Balasubramanian, L. Hollenberg, J. Wrachtrup, Magnetic spin imaging under ambient conditions with sub-cellular resolution. Nat. Commun. **4** (2013)
50. A.O. Sushkov, N. Chisholm, I. Lovchinsky, M. Kubo, P.K. Lo, S.D. Bennett, D. Hunger, A. Akimov, R.L. Walsworth, H. Park, M.D. Lukin, All-optical sensing of a single-molecule electron spin. Nano Lett. **14**(11), 6443 (2014)
51. S. Kolkowitz, A. Safira, A.A. High, R.C. Devlin, S. Choi, Q.P. Unterreithmeier, D. Patterson, A.S. Zibrov, V.E. Manucharyan, H. Park, M.D. Lukin, Probing Johnson noise and ballistic transport in normal metals with a single-spin qubit. Science **347**(6226), 1129 (2015)
52. L.T. Hall, P. Kehayias, D.A. Simpson, A. Jarmola, A. Stacey, D. Budker, L.C.L. Hollenberg, Detection of nanoscale electron spin resonance spectra demonstrated using nitrogen-vacancy centre probes in diamond. Nat. Commun. **7**, 10211 (2016)
53. W. Wasilewski, K. Jensen, H. Krauter, J.J. Renema, M.V. Balabas, E.S. Polzik, Quantum noise limited and entanglement-assisted magnetometry. Phys. Rev. Lett. **104**, 133601 (2010)
54. J.F. Barry, M.J. Turner, J.M. Schloss, D.R. Glenn, Y. Song, M.D. Lukin, H. Park, R.L. Walsworth, Optical magnetic detection of single-neuron action potentials using quantum defects in diamond. arXiv:1602.01056 (2016)
55. T. Wolf, P. Neumann, K. Nakamura, H. Sumiya, T. Ohshima, J. Isoya, J. Wrachtrup, Subpicotesla diamond magnetometry. Phys. Rev. X **5**, 041001 (2015)
56. H.J. Mamin, M. Kim, M.H. Sherwood, C.T. Rettner, K. Ohno, D.D. Awschalom, D. Rugar, Nanoscale nuclear magnetic resonance with a nitrogen-vacancy spin sensor. Science **339** (6119), 557 (2013)
57. T. Staudacher, F. Shi, S. Pezzagna, J. Meijer, J. Du, C.A. Meriles, F. Reinhard, J. Wrachtrup, nuclear magnetic resonance spectroscopy on a (5-Nanometer)^3 sample volume. Science **339** (6119), 561 (2013)
58. C. Müller, X. Kong, J.-M. Cai, K. Melentijević, A. Stacey, M. Markham, D. Twitchen, J. Isoya, S. Pezzagna, J. Meijer, J.F. Du, M.B. Plenio, B. Naydenov, L.P. McGuinness, F. Jelezko, Nuclear magnetic resonance spectroscopy with single spin sensitivity. Nat. Commun. **5**(4703) (2014)

59. D. Le Sage, K. Arai, D.R. Glenn, S.J. DeVience, L.M. Pham, L. Rahn-Lee, M.D. Lukin, A. Yacoby, A. Komeili, R.L. Walsworth, Optical magnetic imaging of living cells. Nature **496**, 486 (2013)
60. R.R. Fu, B.P. Weiss, E.A. Lima, R.J. Harrison, X.-N. Bai, S.J. Desch, D.S. Ebel, C. Suavet, H. Wang, D. Glenn, D. Le Sage, T. Kasama, R.L. Walsworth, A.T. Kuan, Solar nebula magnetic fields recorded in the Semarkona meteorite. Science **346**(6213), 1089 (2014)
61. D.R. Glenn, K. Lee, H. Park, R. Weissleder, A. Yacoby, M.D Lukin, H. Lee, R.L. Walsworth, C.B. Connolly, Single-cell magnetic imaging using a quantum diamond microscope. Nat. Methods (2015)
62. A. Waxman, Y. Schlussel, D. Groswasser, V.M. Acosta, L.-S. Bouchard, D. Budker, R. Folman, Diamond magnetometry of superconducting thin films. Phys. Rev. B **89**, 054509 (2014)
63. J.-P. Tetienne, T. Hingant, J.-V. Kim, L. Herrera Diez, J.-P. Adam, K. Garcia, J.-F. Roch, S. Rohart, A. Thiaville, D. Ravelosona, V. Jacques, Nanoscale imaging and control of domain-wall hopping with a nitrogen-vacancy center microscope. Science **344**(6190), 1366 (2014)
64. L. Rondin, J.-P. Tetienne, S. Rohart, A. Thiaville, T. Hingant, P. Spinicelli, J.-F. Roch, V. Jacques, Stray-field imaging of magnetic vortices with a single diamond spin. Nat. Commun. **4**, 2279 (2013)
65. T. van der Sar, F. Casola, R. Walsworth, A. Yacoby, Nanometre-scale probing of spin waves using single electron spins. Nat. Commun. **6**, 7886 (2015)
66. A. Dussaux, P. Schoenherr, K. Chang, N. Kanazawa, Y. Tokura, C.L. Degen, D. Meier, Observation of local magnetization dynamics in the helimagnet FeGe. arXiv:1503.06622 (2015)
67. F. Dolde, H. Fedder, M.W. Doherty, T. Nöbauer, F. Rempp, G. Balasubramanian, T. Wolf, F. Reinhard, L.C.L. Hollenberg, F. Jelezko, J. Wrachtrup, Electric-field sensing using single diamond spins. Nat. Phys. **7**, 459 (2011)
68. M.W. Doherty, V.V. Struzhkin, D.A. Simpson, L.P. McGuinness, Y. Meng, A. Stacey, T. J. Karle, R.J. Hemley, N.B. Manson, L.C.L. Hollenberg, S. Prawer, Electronic properties and metrology applications of the diamond NV center under pressure. Phys. Rev. Lett. **112**, 047601 (2014)
69. V.M. Acosta, E. Bauch, M.P. Ledbetter, A. Waxman, L.-S. Bouchard, D. Budker, Temperature dependence of the nitrogen-vacancy magnetic resonance in diamond. Phys. Rev. Lett. **104**, 070801 (2010)
70. D. Maclaurin, M.W. Doherty, L.C.L. Hollenberg, A.M. Martin, Measurable quantum geometric phase from a rotating single spin. Phys. Rev. Lett. **108**, 240403 (2012)
71. M.P. Ledbetter, K. Jensen, R. Fischer, A. Jarmola, D. Budker, Gyroscopes based on nitrogen-vacancy centers in diamond. Phys. Rev. A **86**, 052116 (2012)
72. A. Ajoy, P. Cappellaro, Stable three-axis nuclear-spin gyroscope in diamond. Phys. Rev. A **86**, 062104 (2012)
73. D.M. Toyli, C.F. de las Casas, D.J. Christle, V.V. Dobrovitski, D.D. Awschalom, Fluorescence thermometry enhanced by the quantum coherence of single spins in diamond. Proc. Natl. Acad. Sci. **110**(21), 8417 (2013)
74. N. Aslam, G. Waldherr, P. Neumann, F. Jelezko, J. Wrachtrup, Photo-induced ionization dynamics of the nitrogen vacancy defect in diamond investigated by single-shot charge state detection. New J. Phys. **15**(1), 013064 (2013)
75. D.M. Toyli, D.J. Christle, A. Alkauskas, B.B. Buckley, C.G. Van de Walle, D.D. Awschalom, Measurement and control of single nitrogen-vacancy center spins above 600 K. Phys. Rev. X **2**, 031001 (2012)
76. M.L. Goldman, M.W. Doherty, A. Sipahigil, N.Y. Yao, S.D. Bennett, N.B. Manson, A. Kubanek, M.D. Lukin, State-selective intersystem crossing in nitrogen-vacancy centers. Phys. Rev. B **91**, 165201 (2015)

77. K. Fang, V.M. Acosta, C. Santori, Z. Huang, K.M. Itoh, H. Watanabe, S. Shikata, R.G. Beausoleil, High-sensitivity magnetometry based on quantum beats in diamond nitrogen-vacancy centers. Phys. Rev. Lett. **110**, 130802 (2013)
78. H.J. Mamin, M.H. Sherwood, M. Kim, C.T. Rettner, K. Ohnoand, D.D. Awschalom, D. Rugar, Multipulse double-quantum magnetometry with near-surface nitrogen-vacancy centers. Phys. Rev. Lett. **113**, 030803 (2014)